



**Imaging of biogeochemical processes at the field scale –
advancing the application of geophysical electrical
methods for environmental investigations**

Habilitation Thesis

Submitted to the
Technische Universität Wien (TU-Wien)
Faculty of Mathematics and Geoinformation

by

Dr. Adrián Flores Orozco
Department of Geodesy and Geoinformation
Research Unit of Geophysics
Wiedner Hauptstraße 8, 1040 - Vienna

Vienna, October 2019

Abstract

Understanding subsurface biogeochemical processes, including their impact on the carbon budget, has become a key topic in environmental research, especially in frame of climate change. Hence, to-date environmental investigations demand time- and cost-efficient approaches to characterize in-situ subsurface biogeochemical processes both at a high resolution and on a large scale. Such efforts could help us to improve our understanding of a variety of processes ranging from carbon- and nutrient-cycling to the degradation of waste and other organic contaminants. Laboratory investigations have shown that geophysical electrical methods are sensitive to a variety of biogeochemical processes, in particular the spectral induced polarization (SIP) method. However, it is still open to debate whether observations made under the controlled conditions in the laboratory can be taken to the complex environments usually encountered in the field. One of the main challenges is the interpretation of the field SIP responses: while geophysical and geochemical laboratory data can help to understand the signatures for insolated process, the analyzed volumes are not representative for field-scale investigations. Moreover, laboratory data lacks the complexity inherent to real field data, which is commonly related to the superposition of different processes and lithological changes. Hence, the question remains whether the field application of the SIP imaging method is suited for the investigation of natural biogeochemical processes.

In this work, I will first address the basic principles of the SIP imaging method and then demonstrate that an adequate field-survey design together with a careful processing of the data permit to delineate biogeochemically active zones (i.e., hot-spots) on the floodplain scale in a non-invasive manner. To set these results in perspective, I will also present the comparison of imaging results collected under different geological settings. I will show the importance of taking into account the properties of the pore-scale for the correct interpretation of electrical

signatures at the field scale, permitting to understand results which to date were open to debate. Additionally, the ability to monitor changes in pore-space geometry and geochemical properties will be proven by the IP imaging results obtained before and during nanoparticles injections for the degradation of contaminants, which allowed to identify clogging of the pore-space, followed by fracking and the deviation in the trajectory of the injected particles off target. Overall, these results demonstrate that the IP imaging method can be used at the field scale as a diagnostic tool in biogeochemistry.

Contents

1. Introduction	1
1.1 General background	1
1.2 The Spectral Induced Polarization (SIP) imaging method	3
1.3 Motivation	7
1.4 Objectives	10
1.5 Hypothesis	11
1.6 Structure	12
2. Non-invasive delineation of biogeochemical active zones at the field scale: the untapped potential of the IP imaging method	19
2.1 Decay curve analysis for data error quantification in time-domain induced polarization imaging	21
2.2 Hierarchical Bayesian method for mapping biogeochemical hot spots using induced polarization imaging	33
3. Re-interpretation of electrical signatures in clay-rich soils and hydrocarbon contaminated sites: the contribution of surface conduction and microbial activity	53
3.1 Complex-conductivity imaging for the understanding of landslide architecture	55
3.2 Analysis of time-lapse data error in complex conductivity imaging to alleviate anthropogenic noise for site characterization	67
4. IP monitoring along nanoparticles injections: real-time evaluation of stimulated biogeochemical activity for the degradation of contaminants	81
4.1 Monitoring the injection of microscale zerovalent iron particles for groundwater remediation by means of complex electrical conductivity imaging	83
4.2 Complex-conductivity monitoring to delineate aquifer pore clogging during nanoparticles injection	91
5. Conclusions	107
References	112

6. Additional material	129
6.1 Investigations of cable effects in spectral induced polarization imaging using multicore and coaxial cables	131
6.2 Imaging biogeochemical active zones in landfills with induced polarization	169
6.3 An analytical membrane-polarization model to predict the complex conductivity signature of immiscible liquid hydrocarbon contaminants	201
6.4 Electrochemical polarization around metallic particles — Part 1: The role of diffuse-layer and volume-diffusion relaxation	217
6.5 Electrochemical polarization around metallic particles — Part 2: The role of diffuse surface charge	232
6.6 On the role of Stern- and Diffuse-layer polarization mechanisms in porous media	249
6.7 Curriculum Vitae	271

Imaging of biogeochemical processes at the field scale – advancing the application of geophysical electrical methods for environmental investigations

1. Introduction

1.1 General background

Microbial activity plays a critical role in a broad range of subsurface processes ranging from precipitation and dissolution of minerals (Achal et al., 2015), soil-root interactions (Bardgett et al., 1998; Vacheron et al., 2013), carbon and nutrient cycling (Heimann and Reichstein, 2008), to the decomposition of organic matter and waste (Barlaz et al., 1990), or the degradation of contaminants (Adams et al., 2015). In particular, due to the imminent threat of climate change, there is an urgent need for an improved understanding of mineral-organic matter-microorganism interactions towards a better quantification of subsurface carbon budgets as one of the key input parameters of climate models (e.g., Huang et al., 2005; Heimann and Reichstein, 2008). Taking into account the important role microbial activity plays in chemical reactions in geological media, the term biogeochemistry has been adopted since 1917. Biogeochemistry merges biology, geology and chemistry and aims at understanding the processes that transform organic and inorganic substances in soils, sediments and water (Madsen, 2011).

Biogeochemical investigations are to date based on laboratory analysis of soil, water and gas samples. Although ex-situ analysis provides direct measurement of the parameters of interest (e.g., chemical composition, soil textural properties), the resolution of the investigation depends on the number, location and volume of the samples. Due to the relatively high costs for sampling

and laboratory analysis, *ex-situ* investigations commonly rely on a limited number of scattered sampling points and thus, require the interpolation of discrete data points. However, due to the complexity of soil architecture and other field-scale heterogeneities, the interpolation of discrete direct data may not or only insufficiently reflect the actual geometry of, e.g., active zones in landfills. This lack of spatially continuous data might make the final interpretations weak or even misleading. Furthermore, the collection of samples is often time-consuming, posing serious limitations for the monitoring of fast biogeochemical processes (Flores Orozco et al., 2015). Furthermore, characterization of extensive areas based on direct methods may take from months to years (e.g., Cassini et al., 2014) and thus, may result in the comparison of data collected under different biogeochemical conditions.

In contrast to sampling-based site characterization, geophysical methods provide quasi-continuous information on subsurface properties in a non-invasive manner (e.g., Binley et al., 2015). Near-surface geophysical investigations are widely employed for the exploration of natural resources, including groundwater and ore deposits (e.g., Auken et al., 2006; Seigel et al 2007). Since the early 2000's, it has been noted that geophysical measurements may also be sensitive to microbial processes, giving birth to the emergent discipline of Biogeophysics (Atekwana and Slater, 2009). The earliest biogeophysical studies focused on laboratory measurements to investigate the sensitivity of the geophysical response to the accumulation of microbial cells and biofilms (e.g., Ntarlagiannis et al., 2005), the precipitation of iron-sulfides accompanying the stimulation of iron-reducing bacteria (e.g., Williams et al., 2005), or the transformation of hydrocarbon contaminants (e.g., Abdel Aal, 2004).

1.2 The Spectral Induced Polarization (SIP) imaging method

Among all geophysical techniques, those based on the measurement of electrical properties revealed the most promising results for the investigation of biogeochemical processes (Atekwana and Slater, 2009). In particular, the Induced Polarization (IP) method bears a great potential as it assesses the low-frequency electrical conductivity and capacitive properties of the subsurface (e.g., Waxman and Smits, 1968; Ward, 1990; Binley and Kemna, 2005). The SIP method is also referred to as the complex conductivity, complex resistivity or the electrical impedance spectrometry method. It is an electrical method based on 4-electrode arrays (consisting of metal bars inserted into the ground), where two electrodes are used to inject a current I into the subsurface (current-dipole) and two other electrodes measure the resulting electrical impedance Z (potential dipole). For imaging surveys, tens to hundreds of electrodes are deployed to investigate lateral and vertical variations along profiles (i.e., 2D sections) or over a certain area (3D volumes). Lateral changes can be detected by collecting 4-point measurements at different positions along the line (mapping), whereas information at different depths is gained by increasing the separation between current and potential dipoles (sounding). 2D imaging surveys combine a large number of mapping and sounding measurements. The near-surface resolution of the resulting images can be enhanced by using small electrode separations and dipole spacing, while the signal-to-noise ratio (S/N) and the depth of investigation are favored by a larger dipole length and separation between current and potential dipoles, respectively.

IP measurements can also be repeated at different frequencies of the injected alternating current to study the frequency dependence of the electrical properties of the subsurface. Measurements covering a broader range of frequencies are commonly referred to as spectral IP (SIP). In small laboratory setups with only a few 4-point measurements to be carried out, SIP data is typically collected between 1 mHz and 10 kHz. By contrast, for field measurements with a much larger

number of independent measurements, increasing the number of frequencies below 1 Hz would exponentially increase the acquisition time (e.g., Flores Orozco 2018a; 2018b). Thus, for practical reasons, SIP field data is commonly only collected between 0.06 and 100 Hz.

Besides the preparation of adequate measuring protocols, the IP imaging procedure requires the so-called “inversion” of the data. Such inversion permits to compute the distribution of physical properties (i.e., model parameters) in the subsurface that can explain the measurements (i.e., data parameters) collected at the surface. In case of IP measurements, the data parameters are the measured electrical impedances, while the model parameter are the electrical complex conductivity (σ^*) of the subsurface materials, or its inverse the complex resistivity (ρ^*). The use of complex-valued model parameters permits to represent both the electrical conductivity and capacitive properties of the subsurface. Accordingly, the real component (σ') represents an energy loss term (i.e., conductivity), and the imaginary component (σ'') the energy storage (i.e., polarization). Additionally, the complex conductivity can also be expressed in terms of its magnitude ($|\sigma|$) and phase (ϕ). In most subsurface investigations, the values of ϕ are sufficiently small (< 100 mrad), such that $\sigma' \approx |\sigma|$, which is typically referred to as the electrical conductivity (σ). Likewise, the phase of the complex conductivity can be approximated by the ratio of the imaginary to the real component ($\phi \approx \sigma'' / \sigma'$), which has been also suggested as a proxy for the subsurface electrical capacitive properties, or the IP effect.

After the collection and the inversion of the data, a third step comprises the interpretation of the computed electrical imaging results in terms of the targeted material properties and processes. For an adequate interpretation of the electrical signatures, it is important to understand the different electrochemical processes engaged in the conduction of electrical current in the subsurface.

Generally, the low-frequency σ^* of subsurface materials is controlled by three main mechanisms (e.g., Ward et al., 1988):

- (a) Matrix conduction through the solid phase, which is important only if a high metal content allows electronic conduction, which can be assumed to be negligible for most natural media;
- (b) ionic or electrolytic conduction (σ_{el}) through the fluid-filled pore space; and
- (c) surface conduction (σ_{surf}^*) through the electrical double layer (EDL), a charge-carrier rich and thus more conductive layer covering the fluid-grain interface.

In summary, the complex conductivity σ^* of geological media (free of metals) can be written as a superposition of the two main contributions:

$$\sigma^*(\omega) = \sigma_{el} + \sigma_{surf}^*(\omega), \quad (1)$$

where ω is the angular frequency. Due to different polarization processes that can take place within the EDL, the surface conduction σ_{surf}^* is a frequency-dependent quantity, while σ_{el} shows a negligible frequency dependence – at least in the low-frequency range (< 1 kHz), in which SIP measurements are typically conducted.

Rewriting σ_{el} using Archie's model (Archie, 1942) and σ_{surf}^* in terms of its real and imaginary components, the complex conductivity can also be expressed as (Lesmes and Frye, 2001):

$$\sigma^*(\omega) = [\Theta^m S^n \sigma_w + \sigma'_{surf}(\omega)] + i\sigma''_{surf}(\omega), \quad (2)$$

where Θ represents the porosity, S the saturation, m and n are empirical coefficients, and σ_w denotes the conductivity of the pore fluid.

To summarize, Figure 1.1 shows a schematic representation of the necessary steps for field-scale IP investigations.

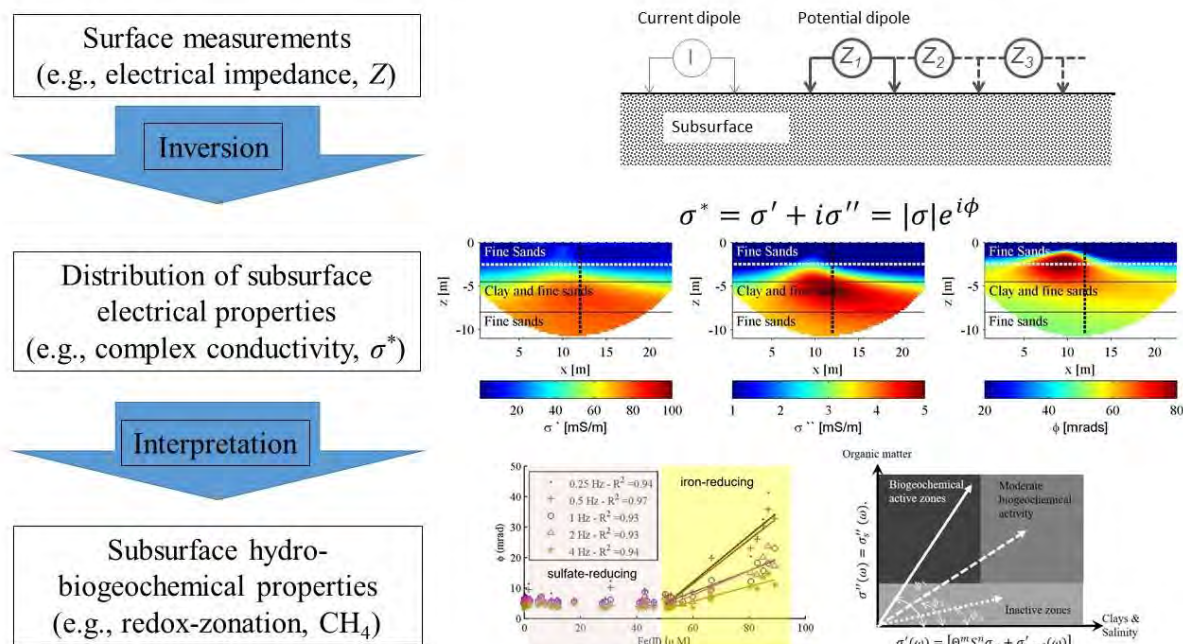


Figure 1.1: Schematic representation of the necessary steps in the application of the IP imaging method at the field scale: data collection, inversion and interpretation of subsurface electrical models. IP measurements are given in terms of the electrical impedances (Z), while the inversion solves for the distribution of the complex conductivity (σ^*) in the subsurface. In a third step, imaging results need to be interpreted to define geological units and, as investigated here, the delineation of biogeochemical processes

Built on the large evidence from laboratory studies, during the last years considerable efforts have been made to establish empirical relations to quantify the dependence of electrical properties on different biogeochemical parameters. In this context, the SIP response has been shown to correlate with the hydraulic conductivity (e.g., Binley et al., 2005; Revil et al., 2015a), induced redox reactions (Slater et al., 2007), the accumulation of microbial cells (Revil et al., 2012), changes in salinity and temperature (e.g., Weller et al., 2015; Hördt et al., 2017), or the concentration of hydrocarbon contaminants (e.g., Schmutz et al., 2010). However, most of these models are based on laboratory experiments using well defined materials and components, which largely simplifies the much more complex situation under real field conditions. To date, the knowledge of the dominating electrical responses or the interplay between different polarization processes at the field scale is limited. The few published field-scale investigations are often limited to measurements conducted along illustrative profiles under conditions where

a strong polarization response is expected. However, an extensive database covering a broad range of geological settings and, in particular, different biogeochemical conditions is still missing. Hence, the applicability of the IP method to characterize biogeochemical processes in natural media at the field scale is still open to debate.

1.3 Motivation

The potential of the SIP method to gain information on biogeochemical processes has opened new areas of research, which is reflected in an increasing number of publications in the field of biogeophysics within the last 10 years (see Figure 1.2). Although some studies may have been overlooked in the preparation of Figure 1.2, it is clear that during this time, the IP method and its application to biogeochemical problems has been gaining momentum. Recent IP research generally focusses on the improved estimation of hydrogeological or biogeochemical parameters. As most of the promising relationships between IP response and these parameters have only been measured in laboratory-scale column experiments, it remains open to debate if they are strong enough to be useful at the field scale.

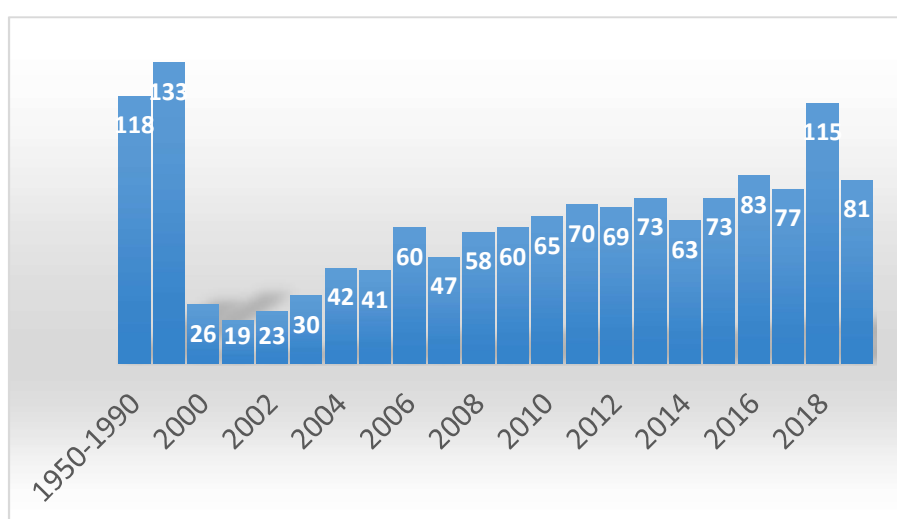


Figure 1.2: Number of published studies based on the IP method. The statistic is based on entries found in Google Scholar (last revised on September 24, 2019). This overview only includes contributions to peer-reviewed journals.

In order to underline the persisting demand for field-scale SIP research, it is worth having a look into the 60 contributions to the 5th international workshop on Induced Polarization (October 3-5, 2018, Rutgers University, US). Of all contributions, 50% corresponded to laboratory investigations, 30% were related to instrumental developments and inversion algorithms, and only 20% represented field experiments. As laid down in the proceedings of the round-table discussions of the workshop, two of the key questions regarding the SIP method are whether (1) the method is mature and ready to be applied on a large (industrial) scale; and whether (2) standardized guidelines for the acquisition and processing of SIP field data can be established, especially for new users or users beyond the geophysical community.

SIP data collected under field conditions is still scarce, with most of the measurements collected along short profiles (a few tens of meters) and on sites where high polarization signatures are expected in the subsurface (e.g., Hördt et al., 2007; Williams et al., 2009; Flores Orozco et al., 2011; Martin and Günther, 2013; Kemna et al., 2014; Maurya et al., 2018). Hence, building a comprehensive database of SIP field responses of different geological environments and biogeochemical settings remains one of the main tasks.

Primarily, variations in the electrical properties of the subsurface are related to lithological changes; however, an increase in the polarization response can also often be indicative of contaminants or bioremediation processes (e.g., Kemna et al., 2004; Williams et al., 2009). Natural biogeochemical processes in organic-rich subsurface materials may also accelerate weathering of the solid constituents resulting in changes in the pore-space geometry and the chemical composition of the pore water. In particular, chemical changes directly modify the properties of the electrical double layer formed at the grain-fluid interface where the polarization takes place and, thus, affect the SIP response. Hence, biogeochemically induced variations in the polarization response are not limited to anthropogenically disturbed media but do also take place in a variety of natural settings. In this regard, the application of the SIP

imaging method as a diagnostic tool in biogeochemistry on the catchment scale is a topic of research, which is relevant for a broad audience.

With respect to the applicability of the SIP method, the main question remains whether natural biogeochemical processes can produce a detectable response and if it can be discriminated from the variations related to the lithology. However, biogeochemical processes are as diverse as the geological media they take place in; thus, it is necessary to define clear research strategies. In the present work, a first step comprises the evaluation of the SIP imaging method for the delineation of microbiological hot-spots in different environments. Such microbiological hot spots are defined as relatively small volumes in the subsurface associated to disproportional rates of microbial activity (McClain et al., 2002; Vidon et al., 2010; Duncan et al., 2013). As their occurrence, distribution, and geometry is poorly known, such hot spots represent an important source of uncertainty for the understanding of soil-atmosphere interaction, for instance carbon and nutrient cycling. Here, the main challenge is that the delineation of such hot spots requires the investigation of extensive areas at a high spatial resolution. Together with the expected heterogeneity of geological settings and their different IP responses, this makes the geophysical search for microbiological hot spots a relevant topic to test innovative field procedures. If successful, SIP could then be used as an efficient tool for the investigation of extensive areas, and time and cost intensive detailed investigations by means of direct methods and laboratory experiments could be directed to a reduced number of spatially confined targets.

Among other reasons, the imbalance between laboratory and field studies as well as the lack of a comprehensive field data base, is the result of the technical and logistical challenges associated with the collection of reliable SIP data at the field scale. For instance, deep investigations of more than a few meters require the use of long cables connecting the instrument with the electrodes, which commonly results in the contamination of the data due to unwanted electromagnetic (EM) fields (e.g., Hallof, 1974; Pelton et al., 1978; Zimmermann et

al., 2008; 2019). The so-called EM coupling within the device, between cables or in conductive ground (e.g., due to a high clay content) can significantly affect the SIP readings, especially at high frequencies. Besides EM coupling, the conduction of SIP surveys in urban or industrial areas may also be challenging because of the contamination of the data due to anthropogenic sources of noise, such as buried infrastructure, power lines, among others (Caterina et al., 2007; Flores Orozco et al., 2019).

Moreover, SIP measurements require the collection of data at many different frequencies and, thus, larger acquisition times than, e.g., direct-current resistivity methods (e.g., Binley and Kemna, 2005; Flores Orozco et al., 2012a). Hence, SIP investigation at the field scale, and in particular for monitoring applications, also demand the development of efficient tools for the real-time evaluation of data quality and signal strength. Such analysis is critical to adjust the survey design, or to delineate areas of interest, for the collection of meaningful and interpretable data at a larger scale, or for the monitoring of fast biogeochemical processes.

1.4 Objectives

The overall goal of my research is to establish the SIP imaging method as a diagnostic tool for biogeochemistry. To achieve this overall goal, I define four specific objectives addressed within this work:

- 1) Develop a methodology for the collection and processing of SIP imaging data at the field scale that can readily be adopted by any practitioner. This is a crucial first step for the assessment of S/N and data uncertainty, considering the numerous sources of measurement errors in SIP surveys at the field scale.
- 2) Investigate the applicability of the SIP imaging method to map biogeochemical hot-spots in situ. The main interest here is to validate whether the SIP method is able to

detect lithological units and at the same time provide information on biogeochemical zonation and processes in natural media.

- 3) Investigate variations in the SIP response associated to changes in biogeochemical activity associated to solid waste and hydrocarbon-contaminant plumes. Besides the release of pollutants, landfills and hydrocarbons represents important subsurface sources of carbon and, thus, potential biogeochemical hot spots.
- 4) Investigate the applicability of the SIP imaging method as a tool for the monitoring of nanoparticles injections, e.g., for the remediation of groundwater contaminants. Due to the high reactivity of nanoparticles, they are used to accelerate biogeochemical degradation of contaminants. The monitoring experiments presented here provided a unique opportunity to investigate the temporal resolution of the SIP imaging method.

The four objectives of this work are closely related to each other, with some overlapping aspects. Such continuity is needed to present the different results in perspective, taking the reader from clean to contaminated sites, from lithological to biogeochemical investigations, and from static responses to the monitoring of fast processes.

1.5 Hypothesis

To achieve the objectives described above, investigations were conducted based on the following hypothesis:

- 1) Spatial consistency of the imaging data sets can be used for an automatized analysis of the field data. Based on such an approach, outliers can be detected and removed and data uncertainty can be quantified efficiently in order to allow for a real-time data analysis during field surveys.

- 2) Microbiological hot spots are related to the stimulation of different bacteria, for instance, iron reducers, which ultimately result in the precipitation of iron sulfides (e.g., pyrite). Considering the usually high polarization response of iron-minerals, these represent a suitable target for SIP measurements.
- 3) Natural degradation of waste and hydrocarbon contaminants results in the stimulation of microbial activity; thus, spatial variations in the SIP response can be used to discriminate between biogeochemically inactive and active zones (i.e., hot spots).
- 4) Temporal variations in SIP images can be used to assess the reactivity of nanoparticles in the subsurface and monitor the stimulation of biogeochemical processes towards the fast degradation of hydrocarbon-contaminated zones.

Although not specifically addressed here, these hypothesis could also be extended to other research questions in environmental investigations, for instance the quantification of ice and water content in permafrost environments, or the understanding of surface-groundwater interactions for investigations in the fields of hydrology or limnology.

1.6 Structure

This habilitation thesis is organized into six main chapters, in which the objectives and hypothesis described above are addressed. The structure also aims at taking the reader step-by-step following the workflow for a successful SIP imaging survey in the context of Biogeophysics: from the design and conduction of the field survey, and the processing of the data to the interpretation of the electrical imaging results in terms of geological units and biogeochemical processes. Such workflow is illustrated in Figure 1.3

The structure of the thesis can be summarized as:

1. Introduction: motivation, objectives and hypothesis
2. Non-invasive delineation of biogeochemical active zones at the field scale: the untapped potential of the IP imaging method
3. Re-interpretation of electrical signatures in clay-rich soils and hydrocarbon-contaminated sites: the contribution of surface conduction and microbial activity
4. IP monitoring along nanoparticles injections: real-time evaluation of stimulated biogeochemical activity for the degradation of contaminants
5. Conclusions
6. Additional material

Following this introductory chapter, chapter 2 addresses the non-invasive delineation of biogeochemical active zones at the field scale. It is built on two studies: one on a new methodology for the fully-automatized processing of IP imaging data sets (Flores Orozco et al., 2018a), and the second on the application of this methodology for the delineation of microbiological hot spots at the floodplain scale (Wainwright, Flores Orozco, et al., 2016). As discussed in Flores Orozco et al. (2018a), the proposed algorithm for the processing of IP data permits the identification of outliers based on the analysis of the spatial consistency of the readings of an imaging dataset. Deviations from a theoretical model can be used for the quantification of the data uncertainty. Flores Orozco et al. (2018a) also includes the first study case using the IP imaging method at the floodplain scale, where 22 profiles were collected in selected areas across a 45-ha site for the identification of biogeochemical hotspots. Following the same approach, the study by Wainwright and Flores Orozco et al (2016) presents the successful identification of biogeochemical hot spots at the Rifle site (~10 ha), where IP anomalies with high polarization magnitudes were used to define drilling targets for the subsequent recovery of sediments. Analysis of the recovered materials revealed high concentrations of organic matter and the accumulation of biominerals, i.e., iron sulfides. To the

best of my knowledge, these two studies are the first ground-based IP imaging surveys at the large scale evidencing the applicability of the method to delineate microbiological active zones. Chapter 3 discusses the contribution of surface conduction and microbial activity and uses the corresponding results for a reinterpretation of the electrical signatures of clay-rich soils and hydrocarbon-contaminated sites measured at La Valette (France) and Trecate (Italy), respectively. The La Valette site corresponds to a clay-rich landslide, where low to negligible rates of biogeochemical activity is expected, while at the Trecate site bioattenuation of a persistent contaminant plume of crude oil was studied, which resulted from the blowout of an oil exploration well. The purpose of this chapter is twofold. On the one hand, it can be understood as a follow-up of the interpretations provided in Chapter 2 towards the biogeochemical interpretation of SIP imaging results in other study areas. On the other hand, this chapter also addresses two intriguing electrical responses: the high electrical conductivity of (i) unsaturated clay-rich sediments and (ii) hydrocarbon-impacted sediments. Based on a discussion of the different conduction mechanisms, Chapter 3 demonstrates that the contribution of surface conduction (σ'_s) dominates over electrolytic conduction (σ_{el}) in clay-rich soils; thus resulting in higher conductivity values than those in coarser sediments (see Flores Orozco et al., 2018b). In the case of the hydrocarbon-impacted soils, the stimulation of microbial activity and the release of carbonic acids, carbon dioxide (CO_2), and methane (CH_4) as metabolic products result in the increase of salinity in pore-water (i.e., the fluid conductivity σ_w), which explains the high conductivity observed at the Trecate site (Flores Orozco et al., 2019a). The studies presented in Chapter 3 represent the first field applications of the SIP imaging method for landslide characterization (Flores Orozco et al., 2018b) and the first one-year IP monitoring of processes in a hydrocarbon-contaminant plume (Flores Orozco et al., 2019a).

Chapter 4 investigates the ability of the IP imaging method to monitor fast biogeochemical processes accompanying the injection of nanoparticles for the degradation of hydrocarbon contaminants in the subsurface. IP imaging is initially used to characterize the geometry of the contaminant plume and possible hydraulic barriers associated to clay-rich zones. Measurements are then repeated during the nanoparticles injections. The analysis of the temporal changes in the resulting time-laps complex-conductivity data are used to track the path of the injected particles and evaluate the delivery to the target and the degradation of the contaminants. Chapter 4 also comprises two studies corresponding to different types of particles and contaminants: (i) the injection of zero-valent iron (ZVI) particles for the degradation of trichloroethene (TCE), and (ii) the injection of nano-goethite particles (NGP) for the remediation of toluene. Baseline imaging results (i.e., those based on the data collected prior to the injection) permit to extend the observations made in Chapter 3 to other hydrocarbon contaminants. They furthermore demonstrate that the obtained IP images are not only sensitive to the geometry of the contaminant plume, but also to the polarity of the oil (Flores Orozco et al., 2015; 2019a; 2019b), which is consistent with corresponding laboratory observations. The monitoring results demonstrate the high spatio-temporal resolution of the IP imaging method and its capability to detect deviations in the trajectory of the injected particles (Flores Orozco et al., 2015) resulting from clogging of the pore space due to particle aggregation at the injection point (Flores Orozco et al., 2019b). Based on the results of two different field-scale particle injection experiments, Chapter 4 gives evidence of the capability of the IP method to monitor unintended fracking due to the subsurface amendment of nano-particle suspensions (Flores Orozco et al., 2015; 2019b). Moreover, variations in the complex conductivity can be used to assess biogeochemical transformations of the particle surface. The studies presented in Chapter 4 are the first field-scale IP applications to achieve a real-time monitoring of nanoparticles injections (Flores Orozco et al., 2015) and the first to assess pore clogging during subsurface amendment (Flores Orozco et al., 2019b).

Chapter 5 presents the conclusions. In the additional material provided in Chapter 6, two further studies are included, which are currently still undergoing peer-review process but also form part of the research effort presented here. In Flores Orozco and Gallistl (under revision in Geophysics), we provide a detailed analysis of the distortions in SIP imaging data collected with multicore cables from three different manufacturers. Such multicore cables are standard in the collection of geophysical resistivity and IP surveys. However, our results demonstrate that IP data collected with multicore cables, even at frequencies as low as 1 Hz, can be severely affected by EM coupling resulting in more than 40% of inconsistent readings. In this study, the use of coaxial cables is shown to be a suitable alternative that significantly improves the quality of the SIP readings (here less than 5% inconsistent readings at 1 Hz). Moreover, the readings collected with a single coaxial cable demonstrate an improved data quality compared to those collected with two (unshielded) separate cables for current and potential dipoles, a standard technique to minimize EM coupling. Hence, the cable setup proposed by Flores-Orozco and Gallistl (submitted to Geophysics) simplifies field procedures, as required for extensive investigations, and improves the quality, resolution and depth of investigation of SIP imaging surveys.

In the study by Flores Orozco et al. (submitted to Journal of Waste management), IP imaging is used on a landfill, where municipal solid waste (MSW) and construction and demolition waste (CDW) were disposed. The investigation aims at identifying microbiologically active zones associated to the generation of landfill gas (e.g., CO₂ and CH₄). This study reveals that conductivity images (magnitude) are mainly controlled by the landfill leachate, hindering a univocal delineation of the landfill geometry and assessment of the waste composition. However, IP images (ϕ) reveal sufficiently strong contrasts between the surrounding geological material and the waste volume, permitting to correctly delineate the geometry of the landfill. Moreover, the polarization effect reveals a clear positive correlation with the total organic

content (TOC) measured in leachate samples, a proxy of microbial activity. Hence, the study of Flores Orozco et al. (submitted to *J. of Waste Management*) proves the applicability of the IP imaging method to discriminate between waste composition and to delineate biogeochemical inactive and active zones (e.g., hot spots) in landfills.

The interpretation of the imaging results is the inherent step following the development of robust field procedures and efficient processing techniques. To achieve this, I co-supervised a PhD thesis aiming at the development of a numerical framework to predict the frequency-dependence of the IP response for different geometries at the pore scale (Bücker, 2018). Such work permitted us to investigate the theoretical response associated to different processes such as the variations in textural parameters (e.g., clay content), water content, and volumetric content of non-aqueous phase liquids (NAPL), among other properties. These manuscripts are also presented in Chapter 6 as they are critical for supporting the interpretation of SIP imaging results presented in the main part of this habilitation thesis.

Chapter 2, 3 and 4 are based on six manuscripts published in the highest ranked peer reviewed Journals in Geophysics. From these manuscripts, I am the leading author in five, while in one of these I am the second author. Additionally, in Chapter 6, I am including two studies undergoing revisions where I am the leading author, and four studies where I am co-supervisor of the leading author. The use of published manuscripts for this work aims at reaching a broad international community.

2. Non-invasive delineation of biogeochemical active zones at the field scale: the untapped potential of the IP imaging method

2.1 Decay curve analysis for data error quantification in time-domain induced polarization imaging

2.2 Hierarchical Bayesian method for mapping biogeochemical hot spots using induced polarization imaging

Decay curve analysis for data error quantification in time-domain induced polarization imaging

Adrian Flores Orozco¹, Jakob Gallistl¹, Matthias Buecker², and Kenneth H. Williams³

ABSTRACT

In recent years, the time-domain induced polarization (TDIP) imaging technique has emerged as a suitable method for the characterization and the monitoring of hydrogeologic and biogeochemical processes. However, one of the major challenges refers to the resolution of the electrical images. Hence, various studies have stressed the importance of data processing, error characterization, and the deployment of adequate inversion schemes. A widely accepted method to assess data error in electrical imaging relies on the analysis of the discrepancy between normal and reciprocal measurements. Nevertheless, the collection of reciprocals doubles the acquisition time and is only viable for a limited subset of commonly used electrode configurations (e.g., dipole-dipole [DD]). To overcome these limitations, we have developed a new methodology to quantify the

data error in TDIP imaging, which is entirely based on the analysis of the recorded IP decay curve and does not require recollection of data (e.g., reciprocals). The first two steps of the methodology assess the general characteristics of the decay curves and the spatial consistency of the measurements for the detection and removal of outliers. In the third and fourth steps, we quantify the deviation of the measured decay curves from a smooth model for the estimation of random error of the total chargeability and transfer resistance measurement. The error models and imaging results obtained from this methodology — in the following referred to as “decay curve analysis” — are compared with those obtained following a conventional normal-reciprocal analysis revealing consistent results. We determine the applicability of our methodology with real field data collected at the floodplain scale (approximately 12 ha) using multiple gradient and DD configurations.

INTRODUCTION

Initially developed for the prospection of metallic ores, the induced polarization (IP) method has emerged in recent years as a suitable technique for environmental and hydrogeologic studies. As an extension of the standard DC-resistivity method, IP measurements provide information about the electrical conductivity (i.e., energy loss) and capacitive (i.e., energy storage) properties of the subsurface permitting an improved lithologic characterization (Kemna et al., 2012; Weller et al., 2013). Particularly at the field scale, time-domain IP (TDIP) measurements have become popular within the past few years due to the robustness and accuracy of modern commercial measuring devices. An increasing number of studies report meaningful TDIP imaging results for a wide range

of applications, such as the characterization of contaminated sites (Flores Orozco et al., 2012a; Gazoty et al., 2012), the assessment of seasonal changes in permafrost (Doetsch et al., 2015a), the evaluation of processes associated with CO₂ injections to shallow aquifers (Dafflon et al., 2012; Doetsch et al., 2015b), and the monitoring of zero-valent iron nanoparticles injections (Flores Orozco et al., 2015). Furthermore, a recent study has described the prospection of microbial “hot spots” at the floodplain scale using TDIP imaging (Wainwright et al., 2015), demonstrating the applicability of the TDIP method for exploration at large scale (the floodplain covered approximately 12 ha). If based only on the analysis of soil and groundwater samples, floodplain-scale site characterization suffers from the limitations imposed by the characteristics of the sampling

Manuscript received by the Editor 30 December 2016; revised manuscript received 25 September 2017; published online 10 January 2018.

¹TU-Wien, Geophysics Research Group, Department of Geodesy and Geoinformation, Vienna, Austria. E-mail: flores@tuwien.ac.at; adrian.flores-orozco@geo.tuwien.ac.at; jakob.gallistl@geo.tuwien.ac.at.

²TU-Wien, Geophysics Research Group, Department of Geodesy and Geoinformation, Vienna, Austria and University of Bonn, Department of Geophysics, Steinmann Institute, Bonn, Germany. E-mail: buecker@geo.uni-bonn.de.

³Lawrence Berkeley National Laboratory, Earth Sciences Division, Berkeley, California, USA. E-mail: khwilliams@lbl.gov.

© 2018 Society of Exploration Geophysicists. All rights reserved.

and often lacks the spatial resolution needed to identify small heterogeneities such as microbial hot spots. The ability of the TDIP imaging method to gain quasi-continuous information about textural and geochemical properties of soil materials makes it an attractive technique for hydrogeologic investigations (Binley et al., 2016); in addition, the characteristic polarization response associated to biomass (e.g., microbial cells) and related metabolic products has been exploited for innovative applications in the emerging field of biogeophysics (Atekwana and Slater, 2009; Kemna et al., 2012). However, as pointed out by Wainwright et al. (2015), the modest polarization response of soil materials with low (to negligible) metallic content places high demands on the resolution of the IP imaging results.

An adequate characterization of the data error is critical to enhance the resolution of electrical images, considering that an underestimation of data error is typically associated to the creation of artifacts in the images, whereas data error overestimation generally leads to the loss of resolution (LaBrecque et al., 1996). Data errors can be systematic or random; the main source for systematic errors in electrical imaging measurements is due to poor contact between the electrodes and the ground, resulting in low current injections and noisy voltage readings. In addition, TDIP measurements are subject to other sources of systematic error due to (1) electromagnetic capacitive and inductive coupling, which affects potential readings collected in the early times (e.g., Dahlin and Leroux, 2012), and (2) distortions in potential measurements performed by electrodes placed within the current pathway or previously used for current injection, due to a (remnant) polarization of the electrode itself (e.g., Dahlin et al., 2002). Measurements affected by systematic error need to be removed as outliers before the inversion. To this end, a recent study proposed the analysis of TDIP data collected at high sampling rates (3.75 kHz) to reduce the effect due to the drift and polarization of the electrodes, spikes in the voltage readings, or harmonic noise due to AC power supplies (Olsson et al., 2016). Remaining uncertainties in the data can be considered random error, related to variations in magnitude and pathways of the injected current, electronic noise of the measuring instrument, etc., and they can generally be roughly described by the mean and standard deviation (e.g., Binley et al., 1995; LaBrecque et al., 1996; Slater et al., 2000). It has been widely documented that inversion algorithms minimizing an objective function subject to fitting the data to a predefined error level (given by the estimates of random error) might provide results less affected by artifacts than those computed by strictly minimizing the data misfit (e.g., Binley et al., 1995; LaBrecque et al., 1996; Kemna, 2000). Field studies have confirmed the advantages of accurately incorporating information about the data error for the inversion of TDIP imaging data sets (e.g., Slater and Binley, 2006; Kemna et al., 2012; Flores Orozco et al., 2015; Binley et al., 2016). Flores Orozco et al. (2012b) recently adopted a power-law model to characterize the data error in IP measurements (i.e., phase or chargeability) as a function of the associated transfer resistance, yielding imaging results with an improved resolution over those computed using previous assumptions of a constant error.

Therefore, during the processing of the data, quantitative information on the characteristics of data error is required to (1) assess the reliability of the data, (2) identify and remove outliers associated with systematic errors, and (3) adjust error models describing the characteristics of inherent random errors to be incorporated within

the inversion. Besides error quantification for data inversion, the characterization of large areas by means of IP imaging demands an onsite assessment of data quality to (1) eventually indicate the need to increase the signal-to-noise ratio (S/N), e.g., by modifying the measuring protocol and (2) determine areas of interest for the collection of denser data sets (e.g., higher resolution). To date, a widely used method to evaluate IP data quality is based on the analysis of the misfit between normal and reciprocal measurements, in which reciprocal measurements refer to the recollection of the data with interchanged current and potential electrodes (e.g., Slater et al., 2000; Slater and Binley, 2006; Flores Orozco et al., 2011, 2012a, 2012b). Nevertheless, the necessity to reduce the acquisition time for large-scale surveys compromises the collection of reciprocals. Furthermore, measuring configurations characterized by high S/N, such as the multiple-gradient (MG) array (Dahlin and Zhou, 2006), are not suited for the collection of reciprocals with multi-channel instruments without severely increasing the acquisition time. Accordingly, IP surveys at the large scale urge for the development of new techniques to quickly and reliably quantify data error without the need of reciprocal readings.

Here, we propose a new methodology for the processing of TDIP measurements based on the analysis of the voltage decay curve. Our decay curve analysis (DCA) permits us to identify and remove outliers prior to the inversion, and it is also suited to quantify data error in TDIP imaging measurements. To evaluate the accuracy of our approach, we compare its outcome with the one obtained from the widely used normal-reciprocal analysis (NRA). We further demonstrate the robustness and efficiency of the proposed DCA by applying it to an extensive TDIP data set collected at the floodplain scale (approximately 12 ha) for the characterization of a near-surface aquifer and the identification of possible naturally reduced zones (NRZ) associated to microbial hot spots in the aquifer sediments. In the following section, we will briefly describe the characteristics of the site and the field measurements, as well as the algorithm used for the inversion of the TDIP data; this is followed by the step-by-step description of our DCA. Then, we present the electrical imaging results as obtained by means of the DCA and the comparison with those obtained by the standard NRA, followed by the discussion and conclusions.

MATERIALS AND METHODS

Site description and TDIP survey

TDIP measurements were collected on the Shiprock site (New Mexico, USA) on the grounds of a former uranium-processing facility. The site has been remediated, but measurable concentrations of uranium are still present in groundwater samples. The affected floodplain of the San Juan River has a total extension of approximately 45 ha, and its stratigraphy consists of three main units: an impermeable clay-rich layer extending from the surface to approximately 2 m depth, followed by a sandy-gravel aquifer (approximately 3 m thickness) that rests on top of a shale unit of low hydraulic permeability known as the Mancos Shale formation. The groundwater level was located at a depth of approximately 3 m during the field survey. A previous study on a similar site (Wainwright et al., 2015) revealed that fluvially deposited organic material within aquifer sediments may result in the development of microbial hotspots, consequently leading to the natural immobilization of uranium and the accumulation of reduced end products, such

as biominerals (e.g., iron monosulfides, FeS) and pore fluids (e.g., methane and carbon dioxide). To map possible hot spots at the Shiprock site, a total of 22 TDIP profiles were collected (Figure 1). Six roll-along profiles (up to 350 m) were laid out to characterize large-scale changes in the electrical properties across the active margin of the floodplain (approximately 12 ha), with 16 shorter profiles included to improve the resolution of particular areas of interest. Separation between electrodes was 2 m for all profiles for an intended depth of investigation of 7 m, which fairly covers the aquifer and the contact to the Mancos Shale. Measurements were collected using the Syscal Pro Switch 72 equipment (from IRIS Instruments) with a square-wave current injection, 50% duty cycle, and a pulse length of 2 s. The voltage decay was measured along 20 windows using an arithmetic distribution of the IP windows, i.e., having the same duration of 80 ms and starting after an initial delay of 240 ms after current shutoff. Such settings were chosen as a trade-off between acquisition time (favored by a short pulse length) and the response due to slow polarization processes (favored by long pulse lengths), a fair sampling of the decay curve (for early and late times), and an ample delay to minimize the electromagnetic coupling in the data. Furthermore, data collected with the same settings yielded good results for the delineation of microbial hot spots at a site with similar characteristics (Wainwright et al., 2015). Measurements were collected using two configurations: (1) dipole-dipole (DD) skip 0 (i.e., a length of 2 m for the current and potential dipoles) and (2) MG configurations (after Dahlin and Zhou, 2006) with 10 potential dipoles (skip 0, skip 1, and skip 2) nested within the current dipole. DD measurements were collected as normal-reciprocal pairs. All data sets were inverted with CRTomo, a smoothness-constraint algorithm (by Kemna, 2000) that permits the inversion of the data to a confidence level determined by an error model. The algorithm calculates the complex resistivity distribution on a 2D grid of lumped finite element cells from a given data set of transfer impedances, in terms of magnitude and phase, at a given frequency (for further details, we refer to Kemna, 2000). Modeling errors in CRTomo have been estimated at less than 2% (Weigand et al., 2017). To compute the phase shift of the electrical impedance, apparent total chargeability values were linearly converted to frequency-domain phase values (at the fundamental frequency of 0.125 Hz) assuming a constant-phase response (van Voorhis et al., 1973), based on the approach proposed by Kemna et al. (1999). This approach demonstrated quantitatively consistent results obtained from time- and frequency-domain data sets (Flores Orozco et al., 2012a).

Data processing

Figure 2 illustrates typical manifestations of errors observed in TDIP data sets: Measurements collected with a small separation between current and potential electrodes (high S/N) are typically related to smoothly decaying curves (Figure 2a), whereas increasing the separation between the potential and current electrodes (Figure 2b and 2c) is associated with more erratic curves due to a decrease in the S/N. Although shape and magnitude of most decay curves are similar, some measurements clearly deviate from the general “decay” pattern, with voltage increasing after current shutoff (e.g., Figure 2d). These outliers are commonly a result of capacitive coupling (Dahlin and Loke, 2015) and need to be deleted before the inversion of the data.

The effects of systematic and random error on TDIP decay curves have been recognized earlier and previous studies proposed to manually remove measurements associated with an erratic behavior of the decay curves (Gazoty et al., 2013; Doetsch et al., 2015a; 2015b). However, an approach that relies on the manual identification of outliers is not suited for the processing of extensive data sets, which calls for automatable filtering schemes. Gazoty et al. (2013) and Olsson et al. (2015) suggest statistical analysis of repeated measurements (i.e., stacking) to remove outliers and the quantification of data error. Yet repeatability is not well-suited to reduce the acquisition time and does not offer any advantage in comparison with NRA (LaBrecque et al., 1996). Moreover, the existing approaches do not offer the possibility to quantify the random error on the TDIP measurements. This is particularly important for the inversion of measurements collected with large dipole separations, which typically suffer from a low S/N and cannot just be removed as outliers, considering that the information from these measurements is critical to improve the quantitative interpretation of electrical images at depth. Instead of eliminating curves with an erratic behavior, we propose to perform an adequate quantification of the error in the measured decay curves (i.e., deviating from a smooth decay curve) and incorporate such information into the inversion as part of the error model. Furthermore, systematic errors in the data may lead to measurements related to a smooth decay curve but associated to total chargeability values without spatial correlation within the data set, i.e., values inconsistent with measurements collected with neighbor electrodes. Such measurements also need to be removed before the inversion. Thus, analysis of TDIP data sets requires the assessment of the quality of the decay curve (for the quantification

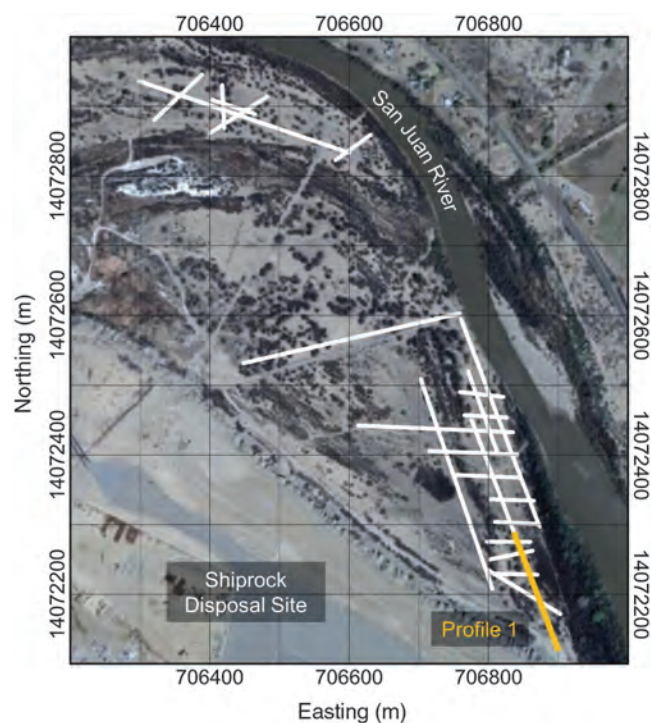


Figure 1. Layout of the geophysical survey at the Shiprock study area. The white lines indicate TDIP profiles, the yellow line highlights the first section (64 electrodes) of profile 1 used as an exemplary data set for the application of the DCA method. Satellite image modified from Google Earth.

of random error) and the spatial correlation of the measurements within the TDIP imaging data set (for the identification of systematic errors).

In the following section, we describe a novel four-step methodology that provides an improved and automatable outlier removal as well as an adequate quantification of data error for the transfer resistance and the total chargeability measurement.

By transfer resistance, we mean the ratio of the measured primary voltage to the injected current ($R = U/I$) and by apparent total chargeability the normalized sum of N individual chargeabilities m_i times the respective durations Δt_i of N IP windows (Binley and Kemna, 2005):

$$M = \frac{\sum_{i=1}^N (m_i \cdot \Delta t_i)}{\sum_{i=1}^N \Delta t_i}. \quad (1)$$

Note that much of the erratic variation of the decay curves observed in Figure 2 is averaged out by the calculation of the total chargeability M as the temporal average of the voltage decay (equation 1). The main idea of our methodology is to reconstruct the standard deviation of this average by comparing the measured decay curve with a representative smooth decay. This estimated standard deviation of the apparent chargeability can then be used to adjust the error model required for the inversion.

DECAY CURVE ANALYSIS

Power-law fit and first filter

The first step consists of fitting an approximate power-law model to each of the measured decay curves, for each profile:

$$m_f(t) = \alpha t^{-\beta} + \varepsilon. \quad (2)$$

Here, m_f represents the fitted apparent chargeability (in mV/V), t represents the time (in ms) after current shutoff, and α and β are the fitting parameters. We also include a constant term ε to account for deviations from a pure power law. Power-law models are well-suited to describe most TDIP responses and can be considered the time domain equivalent of the frequency-domain constant-phase model (van Voorhis et al., 1973). As can be observed in Figure 2, the power-law model yields a fair and robust fit of most decays in the sample data set. To assess the goodness of each fit, we calculate the root-mean-square deviation (rmsd) between the measured and fitted curves as

$$\text{rmsd} = \sqrt{\frac{1}{N} \sum_{i=1}^N (m_f(t_i) - m_{m,i})^2}, \quad (3)$$

where N is the number of IP windows of the curve and $m_{m,i}$ are the apparent chargeabilities at times t_i .

Considering that physically meaningful measured decay curves should be positive and decrease with time, we remove all measurements associated with nondecaying curves ($\beta < 0$ and $\alpha < 0$, or $\beta > 0$ and $\alpha > 0$). The incorporation of the so-called negative IP effect (e.g., Dahlin and Loke, 2015) into the analysis will be

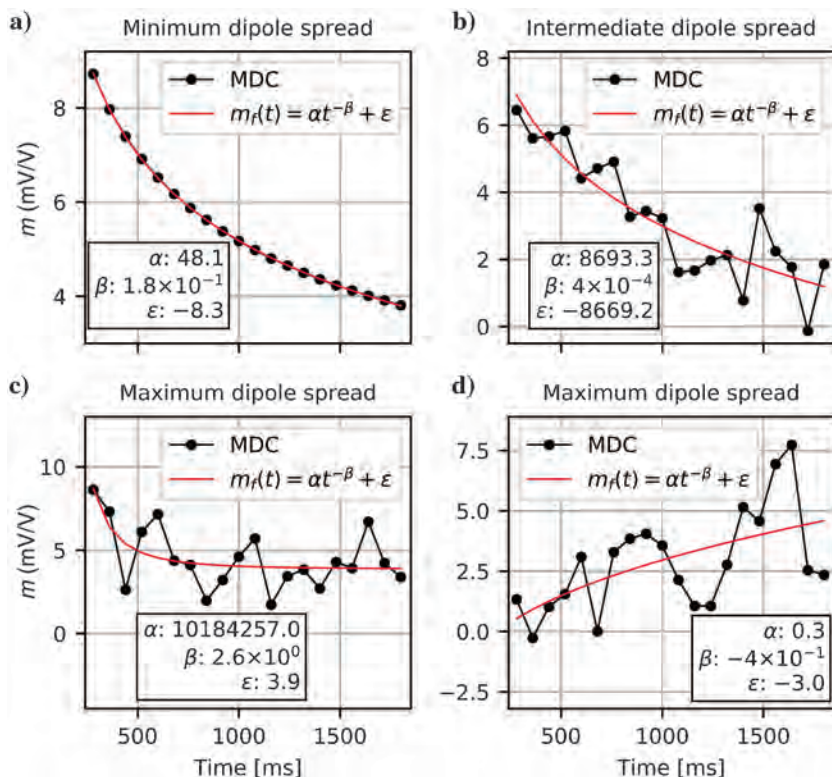


Figure 2. Plots of the measured decay curves with DD configurations (black symbols) for (a) small, (b) medium and (c and d) maximum separation between current and potential dipoles (i.e., representing different S/Ns). The negative power law model (after equation 2) fitted to each curve is indicated with the red line.

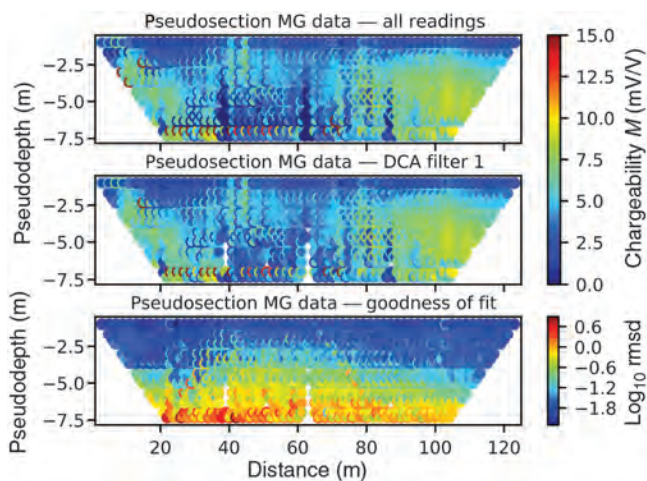


Figure 3. Pseudosections of the total chargeability measurements collected along the first section (64 electrodes) of profile 1, with MG configurations for the unfiltered data set (first plot) and following the removal of IP measurements associated to nondecaying curves (second plot) as well as the associated goodness of fit values as defined in equation 3 (third plot). Superimposed pixels in the pseudosections are related to measurements associated to the same position in the representation, but not necessarily in the subsurface.

discussed further below. Figure 3 shows the pseudosection of the MG apparent chargeability raw data collected along the first section (64 electrodes) of profile 1 before (top row) and after (second row) the removal of nondecaying curves. Measurements associated with erratic curves, i.e., with large RSMD, were not removed in this step because they are mainly related to larger separation between electrodes and, thus, to deeper information, as can be observed in Figure 3 (bottom row). As we mentioned before, one premise of our analysis is to preserve as many deep measurements as possible.

Construction of a reference curve and second filter

To this point, each decay curve has been fitted independently, which can still result in a high spatial variability of the apparent total chargeability readings, as observed in Figure 3. In particular, the first filter does not remove those readings characterized by anomalously high total chargeability values associated with a (smoothly) decaying curve. However, due to the nature of the imaging measurements, we expect apparent total chargeability values to vary in a relatively gradual manner across the pseudosection. Measurements lacking spatial correlation with neighbor readings clearly indicate systematic errors and need to be removed before the inversion as outliers.

Thus, in the second step of the DCA, we perform an analysis of the spatial consistency of the recorded decay curves. To this end, we first construct a reference decay curve taking into account all quadrupole measurements associated with the same injection dipole. Outliers are then identified as those measured decay curves related to a magnitude that largely varies from the magnitude of the reference curve. To minimize the effect of random noise in this step, we work with the fitted power-law model instead of the measured decay curve. The reference curve is computed as the median value of the apparent chargeability of each IP window of the M fitted curves for measurements collected within the same current injection. For the i th IP window, the apparent chargeability ($m_{r,i}$) of the reference curve is written as

$$m_{r,i} = \text{median}(m_{f,1}(t_i), m_{f,2}(t_i), \dots, m_{f,M}(t_i)). \quad (4)$$

The use of the fitted power law instead of the actual readings aims at reducing the influence of noisy curves, leading to a smooth reference curve. To avoid a distortion of the reference curve due to the effect of nondecaying curves, only measurements remaining after the first filtering step are taken into account. Figure 4 illustrates the shape and position of the reference curves for MG measurements considering three different lengths in the potential dipoles (skip 0, skip 1, and skip 2) and the corresponding spread of the current dipole.

Once the reference curve is defined for each subset, it is shifted along the vertical axis minimizing the rmsd between the reference curve and the fitted curve. Outliers are then defined as those readings that require a large vertical shift within the entire data set. To define numeric and, thus, automatable criteria for the filtering, we (1) quantify the “upshift” (k_u) or “downshift” (k_d) necessary for the reference curves to fit the corresponding measurements and (2) com-

pute the standard deviation of the shift values (k_u and k_d) within the data set (i.e., for all current injections). Outliers are then defined as those measurements associated with a shift value (k_u, k_d) larger than three times the standard deviation for the entire data set. In Figure 5, we present the pseudosection for DD and MG measurements after removal of outliers based on the filtering with the reference curve. Plots in Figure 5 demonstrate that for the measurements discussed here, both configurations have a consistent performance and are related to consistent values in the measured total chargeability, permitting to validate the results from the DCA in MG configurations with those obtained by means of the NRA with DD arrays.

Standard deviation estimate and bin analysis

In the third step, we compute the DCA misfit $\Delta m_{\text{DCA},i}$ between the measured decay curve and the power-law model fitted in step one for all measurements after applying filters one and two. For the i th IP window, the DCA misfit is defined as

$$\Delta m_{\text{DCA},i} = m_f(t_i) - m_{m,i}. \quad (5)$$

This allows us to quantify the temporal instability (i.e., erratic behavior) of the measured signal and estimate the standard deviation of the chargeability measurement.

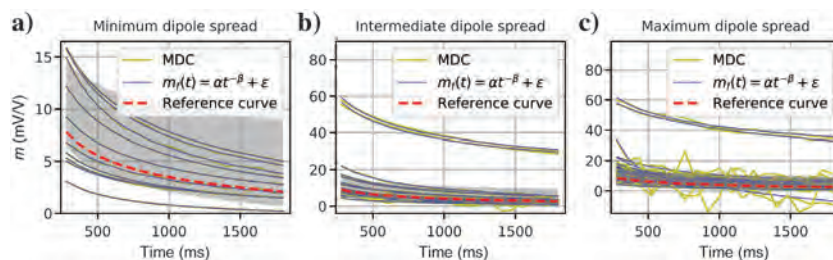


Figure 4. Plots of the measured decay curves MDC, fitted decay curves, and the reference curve after first filter (removal of nondecaying curves) of MG measurements for (a) small, (b) medium, and (c) maximum lengths in the current dipole.

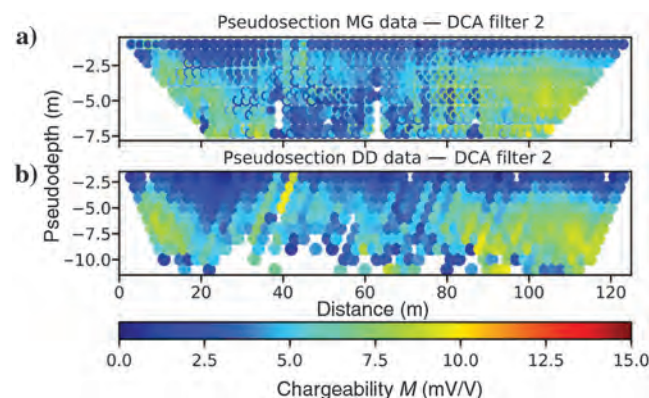


Figure 5. Pseudosections for data sets collected with MG and DD configurations after removal of nondecaying curves (filter 1) and spatially inconsistent measurements following the comparison with the reference curve (filter 2) from the DCA.

We propose to use the misfit $\Delta m_{DCA,i}$ between the fitted and measured decay curves in a similar way as other authors used the misfit between normal and reciprocal readings to describe the random

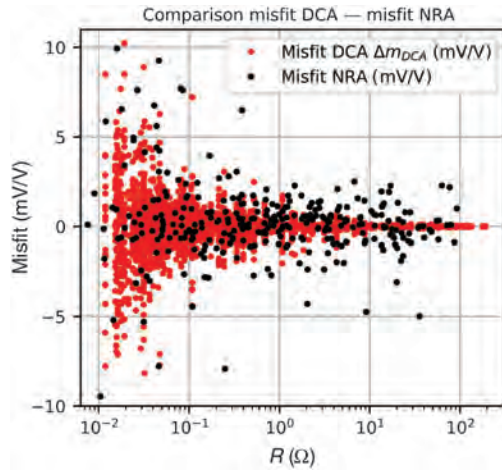


Figure 6. Chargeability error estimates based on DCA and NRA misfits plotted as a function of the transfer resistances

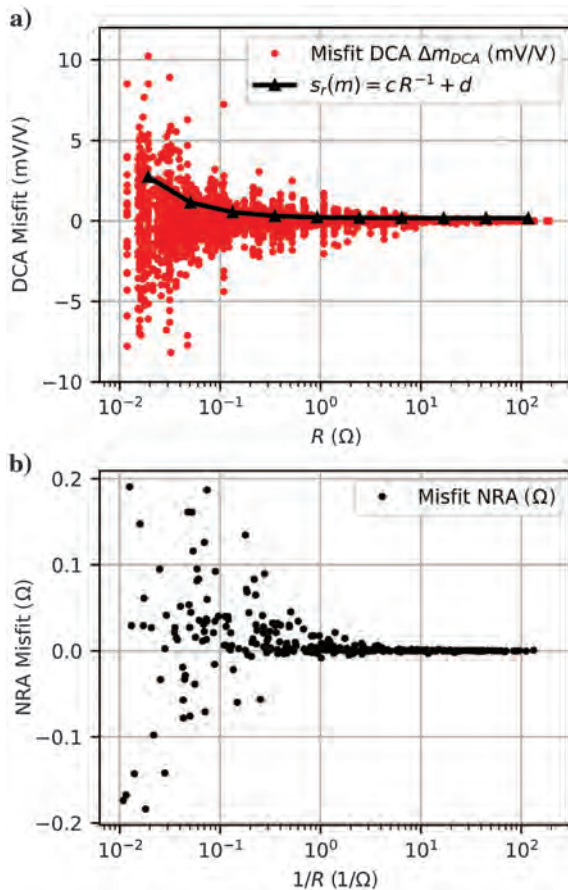


Figure 7. Distribution of (a) the DCA chargeability misfit and (b) the NRA transfer resistance misfit as a function of the transfer resistances. The black solid line shows the rational model adjusted to the binned DCA chargeability, which is then used to describe the error of the transfer resistance measurements.

error of the total chargeability readings of a data set (Slater and Binley, 2006; Flores Orozco et al., 2012b). To quantitatively evaluate this approach, Figure 6 shows the DCA and NRA misfits of the same DD data set, both in function of the respective transfer resistances $R = U/I$. The general dependence of the misfit on the transfer resistance is consistent for the DCA and NRA; namely, a decrease in the misfit is associated with an increase in the value of the associated transfer resistance. The data error for chargeability measurements ($s_p(m)$) can be modeled using a power law as proposed by Flores Orozco et al. (2012b) for phase measurements:

$$s_p(m) = aR^b, \quad (6)$$

with $b < 0$, as noted in Flores Orozco et al. (2012b), to account for the decrease in the chargeability data error for increasing the associated transfer resistances. Note that instead of adjusting the error-model parameters a and b to the actual misfit $\Delta m_{DCA,i}$, we follow the methodology described in Flores Orozco et al. (2012b), based on a partitioning of the data into several bins with respect to the transfer resistance (here 10 bins), in which the error model (equation 6) is fitted to the standard deviation computed for each bin. Such procedure honors the assumption that random error can be described by its standard deviation. An alternative approach is to define a constant error model based on the standard deviation of the misfits of the entire data set, as proposed by Slater and Binley (2006), which would assume $b = 0$ in equation 6. However, such approach ignores the dependence of the IP data error on the signal strength, as discussed in Flores Orozco et al. (2012a, 2012b) and recently in Binley et al. (2016).

Error model for the resistance measurement

To obtain an estimate for the error of the transfer resistance measurement, we propose to fit a rational function to the standard deviation of the same binned misfits of the apparent total chargeability values used before, based on the following model:

$$s_r(m) = \frac{c}{R} + d, \quad (7)$$

where the coefficients c and d are the fitting parameters and $s_r(m)$ refers to the error model of the chargeability as a function of the resistance. This is an empirical approach that honors the assumption that the resistance misfit increases with increasing transfer resistances (e.g., LaBrecque et al., 1996; Slater et al., 2000) and that the random error causing the erratic behavior observed in the measured decay curves affects the transfer resistances readings in a similar way. Thus, we use the DCA misfit as a proxy to quantify the resistance error as well. Figure 7a shows that this rational model also adjusts the variation of the $\Delta m_{DCA,i}$ misfits. For comparison, Figure 7b also shows that the normal-reciprocal misfit in resistance measurements follows the same pattern, when plotted as a function of the inverse of the associated transfer resistance. Significant deviations from the power-law error model (equation 6) only appear at large transfer resistances. Now, we insert the same fitting parameters into the linear model:

$$s(R) = c + dR, \quad (8)$$

where $s(R)$ is the error model for resistance measurements, widely used (La Brecque et al., 1996; Slater et al., 2000) to describe the error of the transfer resistance measurement. Such a model implies that error parameters for low resistances are defined by the absolute error (c in equation 8 for $R < 1 \Omega$), whereas the error is a percentage of the measured resistance for larger values (d in equation 8 for $R > 1 \Omega$).

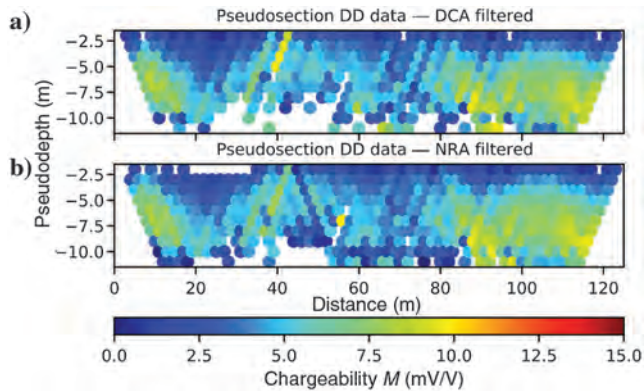


Figure 8. Pseudosections for DD data collected along the first section (64 electrodes) of profile 1 after the removal of outliers as defined by (a) the proposed DCA and (b) the widely used NRA.

Following this strategy, error parameters for apparent total chargeability and transfer resistance were defined for each TDIP profile separately, to account for variations of measurement quality across the floodplain.

RESULTS

To investigate the suitability of our methodology to identify measurements affected by systematic errors, we compare in Figure 8 the DD total chargeability pseudosection for profile 1 after the removal of outliers following steps 1 and 2 from our DCA approach and following the NRA. For the latter, outliers were defined as measurements with a normal-reciprocal misfit larger than two times the standard deviation of all NRA misfits of the data set (see Flores Orozco et al., 2012a). Plots in Figure 8 reveal that the DCA and NRA identify similar outliers for an exemplary DD data set. We present in Table 1 a summary of the total measurements for each profile for the configurations DD and MG, as well as the percentage of the readings removed as outliers following the NRA as well as steps 1 and 2 of the proposed DCA. Table 1 demonstrates that both approaches have a similar performance regarding the number of measurements identified and removed as outliers. As mentioned in the “Introduction” section, the NRA is not suited to be applied to MG data; thus, for such measurements, we only compare the data removed (from the total) after each step of the DCA. Figure 8 reveals

Table 1. Summary of the total of measurements collected along each of the 22 Profiles for the DD and MG configurations, as well as the total of measurements accepted after NRA (only for DD configurations), and after each filter from the DCA approach (nondecaying curves, and after comparison with the reference curve).

Line	Electrodes	Total DD	Outliers NRA (%)	Outliers DCA Filter 1 (%)	Outliers DCA Filter 2 (%)	Total MG	Outliers DCA Filter 1 (%)	Outliers DCA Filter 2 (%)
1	176	2260	18.8	16.8	22.2	8960	12.3	26.9
2	160	1695	26.3	22.0	25.8	5279	13.7	21.2
3	192	2085	33.0	36.6	47.5	5904	16.9	25.8
4	160	1695	56.6	48.3	62.5	5280	38.4	57.8
5	32	245	39.6	39.2	47.8	624	23.2	30.3
6	112	1129	51.7	34.9	48.4	1760	25.4	48.1
7	160	1695	11.3	17.9	20.6	5280	2.3	5.9
8	64	565	4.6	9.2	11.3	1760	1.1	2.6
9	48	405	4.2	6.2	8.6	1121	1.6	4.2
10	32	245	8.2	1.6	3.3	624	4.8	10.1
11	32	245	5.3	6.5	9.0	624	2.9	10.9
12	32	245	6.1	8.2	16.3	624	2.4	5.1
13	32	245	19.2	24.1	26.5	624	9.0	12.5
14	64	565	10.3	17.7	21.1	1760	4.7	10.0
15	32	245	6.5	2.4	4.5	624	2.7	5.9
16	32	245	6.9	2.9	5.3	624	6.4	11.7
17	32	245	1.6	1.2	3.3	624	3.0	7.1
18	64	565	4.4	2.3	4.4	1760	3.9	23.1
19	48	405	24.0	19.3	22.2	1120	10.0	36.3
20	32	245	21.2	22.4	25.3	624	6.7	25.3
21	32	245	55.5	52.7	54.3	624	27.4	32.5
22	48	405	13.3	23.7	27.3	1120	5.3	13.0

that the DCA filter removes fewer measurements associated with relatively high total chargeability values and/or small separations between electrodes. This illustrates the main difference between the two approaches. While the DCA only evaluates the similarity of all measured decay curves of a subset, the NRA is sensible to variations in the offset of the decay curves, the magnitude of which is higher at small dipole spacing.

Regarding the quantification of random error for the transfer resistances and total chargeability measurements, in Figure 9, we present the comparison of the adjusted models following steps 3 and 4 of the proposed DCA and the NRA. Figure 9 reveals the possibility to solve for consistent error parameters. Histograms of the transfer resistances and phase-shift values, presented in Figure 9, reveal variations in the data sets due to the different filters applied

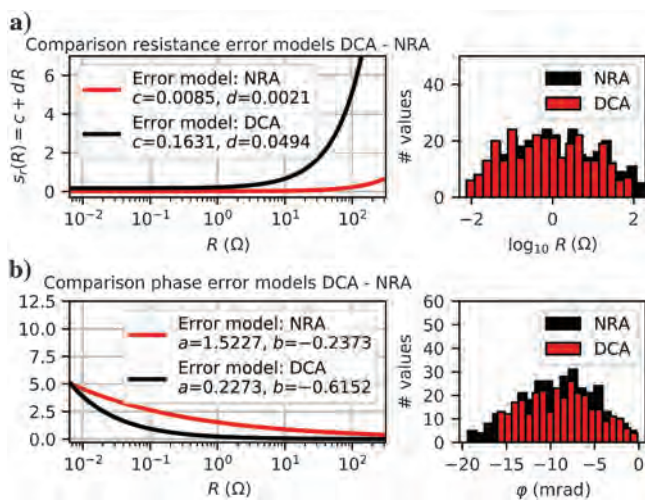


Figure 9. Comparison of error models (left column) and histograms of filtered raw data (right column) following the proposed DCA and the widely used NRA. Error models and histograms are presented for (a) transfer resistance and (b) the apparent phase shift data.

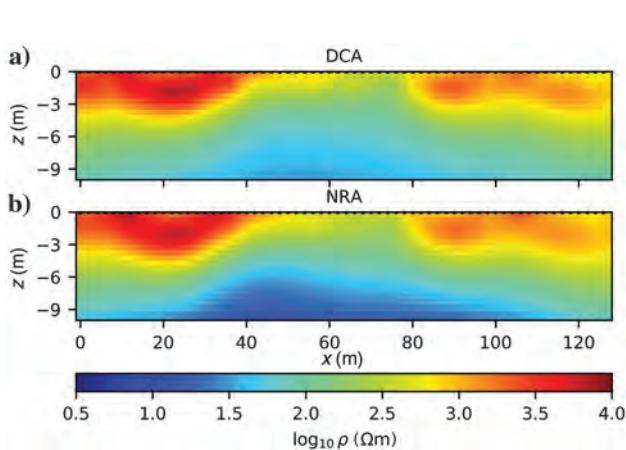


Figure 10. Resistivity imaging results for data processed after (a) the proposed DCA and (b) widely used NRA. Images obtained from the inversion of mixed DD and MG configurations collected along the first segment (64 electrodes) of profile 1.

in the DCA and NRA; such variations explain the slight differences in the error models obtained by the two techniques. The higher S/N in resistance measurements during the collection of normal and reciprocals lead to the estimation of lower error parameters for the inversion of the resistivity than those computed by the DCA, which is based on voltage readings after switching the current off. Nevertheless, plots of the inverted magnitude of the complex resistivity (hereafter resistivity, ρ) reveal consistent results following both approaches, as presented in Figure 10, clearly demonstrating the applicability of the DCA technique for the quantification of resistance data error in TDIP imaging.

Plots in Figure 10 present the electrical resistivity images obtained from the inversion of measurements collected along the first segment of profile 1 (64 electrodes) after data processing and error quantification using NRA and the DCA. Inversion results following the two different approaches yield practically the same resistivity images characterized by three units: Close to the ground surface (>3 mbgs), high resistivity values ($>1000 \Omega\text{m}$) are associated to the unsaturated materials mainly composed of gravels and sands, a few centimeters below the clay top soil. The modest resistivity values ($100 - 400 \Omega\text{m}$) are associated to the confined aquifer in fluvial sediments (e.g., dominating sands) and extend between 3 and 9 m depth; at the bottom, the low electrical resistivity values are related to the Mancos Shale formation. Variations in the actual depth of the aquifer are also reported from drillings on the floodplain (further information about the Shiprock site is available at U.S. Department of Energy, 2017).

Figure 11 presents a comparison of the imaging results, as obtained for the DCA and the NRA, for the polarization effect expressed in terms of the phase shift of the complex electrical resistivity (hereafter phase, ϕ). Both phase images presented in Figure 11 consistently resolve the main geologic units; the low phase values correspond to the unsaturated clay-rich top layer and the low permeable Mancos Shale at the bottom, whereas the intermediate to high phase values are associated with the sandy-gravel aquifer material. The imaging results presented in Figure 11 clearly show that the DCA analysis permits the inversion of quantitatively similar results to those obtained by the NRA. Analysis of all 22 profiles

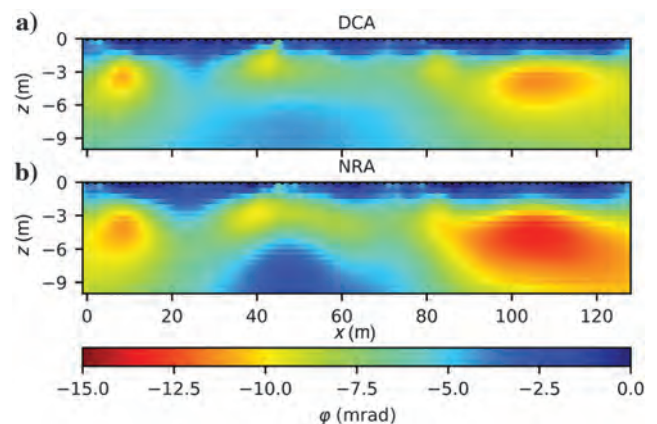


Figure 11. IP imaging results in terms of the phase of the complex electrical resistivity for data processed after (a) the proposed DCA and (b) widely used NRA. Images obtained from the inversion of mixed DD and MG configurations collected along the first segment (64 electrodes) of profile 1.

measured at the Shiprock site revealed consistent imaging results. However, a more detailed discussion of the electrical images is beyond the scope of this methodological study.

DISCUSSION

An important and novel step in our DCA is the identification of outliers based on the analysis of the spatial correlation within the data set avoiding the arbitrary definition of threshold values and permitting an automatable processing of large TDIP imaging data without supervision. To achieve this, we define a reference curve and shift it along the y -axis, and statistical analysis of this shifting is then used to define a confidence interval, with outliers defined as those measurements not encompassed within the limits of the confidence interval. An initial approach was to define a single reference curve and use it to evaluate the spatial consistency of the entire data set, as illustrated in Figure 12a. However, such an approach results in a poor identification of outliers, as the definition of the interval of confidence renders too broad due to the presence of measurements with a poor S/N and large distortions in the decay curve, as observed in Figure 12. To overcome this, we opted for a partitioning of the imaging data set in smaller subsets and define the reference curve and confidence interval for each of those subsets separately. Here, it is important to warrant a sufficient number of subsets to avoid the definition of too broad filters similar to the case of a single reference curve, as well as a sufficient number of measured decay curves in each subset to avoid the definition of narrow confidence intervals and the removal of acceptable measurements. Furthermore, considering that the DCA approach penalizes the magnitude of the total chargeability, it is necessary to have some dynamic in the measured values contained in each subset (i.e., variations in the measured decay curves) so that the adjustments of the reference take place over a broad range and minimize the risk of removing a large number of acceptable measurements as outliers.

Grouping the measurements based on the current injection provides a good trade-off regarding the number and size of the subsets. Furthermore, such approach takes into account that imaging data sets are collected with tens of electrodes with variable contact resistances, resulting in changes of the injected current along the imaging plane (as illustrated in Figure 12b), which also impose changes in the S/N of the recorded voltages. Thus, our approach compares measurements collected due to the same imposed electrical field and a relative volume of influence; thus, outliers can be defined as those readings revealing an abrupt change in the measured decay curve, based on the comparison with the reference model. Moreover, analysis of measurements based only on those collected for a given current injection permits to perform the DCA during data collection, in case that real-time information is required, for instance, in monitoring applications.

A second approach considers the definition of subsets associated to the depth in the pseudosection, which aims at the comparison of readings collected with the same separation between electrodes, another factor controlling the S/N. To illustrate this, Figure 12 presents the measured curves for shallow (Figure 12c), intermediate (Figure 12d), and deeper (Figure 12e) positions in the pseudosection, as well as the corresponding reference curve and computed interval of confidence. Such plots reveal that the shallow measurements (Figure 12c) contain a larger number of measurements than those related to deeper positions (Figure 12d); yet, it permits the comparison of curves with a roughly similar quality in the decay curves,

which is a significant advantage of such an approach. Furthermore, such approach can be used in imaging data sets collected with single-channel instruments or Wenner configurations, in which every potential measurement is made with a different current dipole. Although not presented here, we observed similar results regarding the number of measurements removed as outliers, and the distribution of data misfit and error parameters as the last two steps of the DCA are independent on the definition of subsets for the analysis of the reference curve. However, grouping the data set based on the depth level of the pseudosection needs to be performed carefully, as these subsets may contain decay curves associated to different S/N related to variations in the injected current (Figure 12b) and also due to lateral changes in the electrical properties of the subsurface (see Figures 5 and 8).

Analysis of the 22 TDIP profiles reveals that the rule described above applies to most of the cases; however, the filter might need to be adjusted for noisy or very consistent (clean) data sets. In the former case, the computed reference curve is obtained by averaging poorly comparable curves, leading to a nonrepresentative reference curve and only a poor filtering, whereas for the clean data sets, we do need to adjust the filter to avoid the filtering of valid measurements. In Table 2, we present a first approach to permit an automatable identification of the “noisy” and “clean” data sets, as well as a rule to define the maximum up- and down-shifts k_u and k_d and to adjust the maximum deviations accepted.

The case of noisy data sets poses further challenges considering that the computed k_u and k_d values could vary over a broad range resulting in an insufficient detection of outliers during the second filtering step. To overcome this possible problem, we propose a further filtering step based on the analysis of the histogram of the measured total chargeabilities of the entire data set. Such analysis considers that, for an adequate number of bins, the measured total chargeability without spatial correlation should appear as isolated

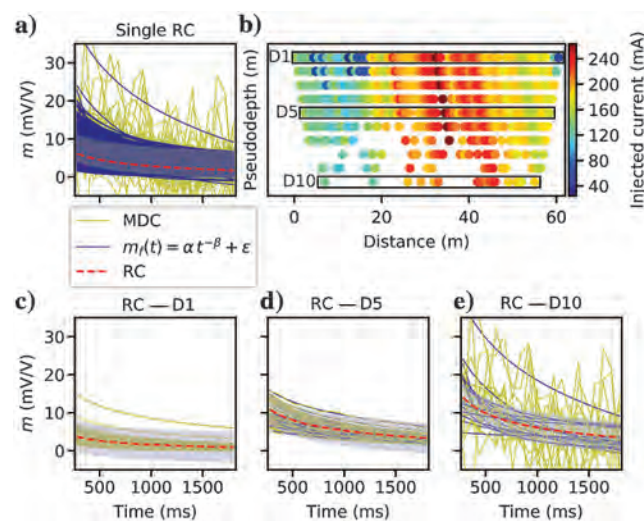


Figure 12. Presentation of the intervals of confidence after shifting of the reference curve based on two approaches: (1) grouping all measurements in a single set (a) and (2) subsets defined by the measurements collected at the same level of the pseudosection (c-e). The pseudosection (b) presents the injected current associated to each quadrupole measurement and highlights the three depth levels displayed in the bottom row.

clusters separated from the main distribution of valid measurements. Hence, the occurrence of empty bins can be used to identify spatial inconsistencies and to define the maximum and minimum values for total chargeability readings. Measurements outside the range defined in this manner can then be removed as outliers. The efficiency of such an approach depends largely on the number of bins selected for the analysis. Based on the normal-reference rule provided by [Sturges \(1926\)](#) and modified by [Larson \(1975\)](#), we define the number of bins (nb) as

$$\text{nb} = 1 + 4.5 \log_{10} n, \quad (9)$$

where n refers to the total number of measurements remaining in the data set after the second filter of the DCA. Although not discussed here, such histogram analysis could also be performed for the NRA or as a preliminary filter to remove readings associated to electrodes with high contact resistance or related to low current injections.

Our DCA is based on fitting the measured decays by means of a simple power-law model, which represents the voltage decay after switching the current injection off. As mentioned above, power-law models can be considered the time-domain equivalent of the frequency-domain constant phase model ([van Voorhis et al., 1973](#)). Further tests also included the fitting of the measured decay curve with a Cole-Cole model (CCM) which is the dispersion model commonly used to describe the frequency dependence of the IP response ([Pelton et al., 1978](#)) and lately has also been used to model the decay curve in TDIP measurements (e.g., [Fiandaca et al., 2012](#)). Although the implementation of the CCM into our analysis also reveals consistency in the computed total chargeability values and the definition of outliers, the goodness of fit and the retrieved Cole-Cole parameters strongly depend on the initial values defined for the fitting — in particular for noisy data. The processing of imaging data sets requires the fitting of hundreds to thousands of measurements; thus, a robust model with a small number of parameters is better suited. Furthermore, it has been demonstrated that not all IP signatures can be described by a CCM (e.g., [Nordsiek and Weller 2008](#); [Flores Orozco et al., 2012b, 2013](#)). Hence, we consider that fitting of the power-law model presented in equation 2 for the detection of outliers and quantification of data error is more than sufficient, and its advantages considering robustness and the weak dependency on the initial values outweigh by far the possible lack of a theoretical justification.

It is also worth highlighting that the use of the power-law model is strictly limited to the estimation of the error parameters and has no further implication on the inversion itself. Actually, as mentioned above, the conversion of the TDIP chargeability to frequency-domain phases assumes a constant-phase model (e.g., [van Voorhis et al., 1973](#); [Kemna et al., 1999](#)), which is also not a Cole-Cole type response. Furthermore, the inversion of the data is performed on the computed total chargeability; i.e., only the magnitude of the polarization is taken into account and no information about the shape of the measured decay curve. However, recent inversion schemes are based on the modeling of the full waveform of the received voltage (e.g., [Fiandaca et al., 2012a, 2012b](#)), in which the shape of the decay plays an important role. Moreover, the DCA approach can be used only for the removal of outliers (steps 1 and 2), and inversion can be performed using robust schemes ([Morelli and LaBrecque, 1996](#); [Kemna, 2000](#)), which do not require information on the data error.

A particular case to take into account is the occurrence of negative chargeability related to high polarization effects in areas of negative sensitivity, as presented in detail in the study by [Dahlin and Loke \(2015\)](#). These authors observe that for certain electrode configurations and under certain subsurface conditions, voltage readings after current switch off can be negative and increase with time (voltage values tending to zero). Yet it is important to differentiate actual negative IP effects from the occurrence of systematic error resulting in nondecaying curves (see [Figure 2d](#)) related to capacitive and inductive coupling, as also discussed by [Dahlin and Loke \(2015\)](#). Furthermore, keeping measurements related to negative decaying curves should be considered only if the inversion algorithm can model such negative IP effects.

Recent investigations have also demonstrated the possibility to significantly reduce acquisition times, for instance, by deploying 100% duty cycles ([Olson et al., 2015](#)) and modeling the entire waveform. Yet we note here that such measurements might also be affected by capacitive and inductive coupling, and the distortions in the signatures due to random error. Therefore, the analysis that we present can be applied to full waveform data as a first filtering of the data (i.e., to identify and remove outliers). In this regard, further investigations could focus on the incorporation of the full waveform analysis (i.e., penalize not only the magnitude but also the shape of the decay curve), as well as the incorporation of the error parameters obtained from our DCA into the inversion of the frequency dependence of TDIP using the formulation of the waveform, as well as into the analysis of monitoring data sets.

Table 2. Adjustments to the second filter in the DCA for noisy and clean data sets. Automatable rules are provided to differentiate between cases and the corresponding threshold to identify outliers based on the shift values (k_u and k_d) computed after the comparison with the reference curve.

Case	Definition	k_u	k_d
General	—	>3 times standard deviation	>3 times standard deviation
Noisy data set	Three times standard deviation of k_u computed for the entire data set > 2 times median of total chargeability measurements of data set	>1.5 times standard deviation	> single standard deviation
Clean data set	Three times standard deviation of k_u computed for the entire data set < median of total chargeability measurements of data set	>4 times standard deviation	>4 times standard deviation

CONCLUSION

We have presented a new methodology for the processing of TDIP imaging data sets entirely based on the analysis of the IP decay curve. Analysis of the data was performed on TDIP measurements using DD and MG configurations performed in an extensive area (approximately 12 ha) in a near-surface investigation (depth of investigation limited to 7 m). Our results demonstrate that our approach reliably identifies outliers and provides an adequate quantification of the data error. Our methodology is able to quantify magnitude and distribution of the data error in a very consistent manner comparable with the widely used NRA. In contrast to the latter, the new method does not require the collection of reciprocal readings, which reduces the acquisition time by 50% and makes field surveys much more efficient. Furthermore, based on our method, a quantitative data error description is also possible for data collected with configurations other than DD, e.g., pole-dipole or MG. Inverted chargeability images obtained from DCA-processed data also reveal consistency with those obtained using NRA.

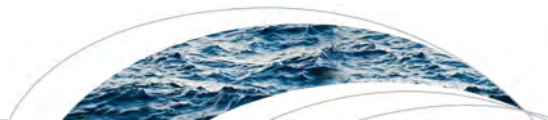
ACKNOWLEDGMENTS

This material is partially based upon work supported through the Lawrence Berkeley National Laboratory's Watershed Function Scientific Focus Area. The U.S. Department of Energy (DOE), Office of Science, and Office of Biological and Environmental Research (BER) funded the work under contract DE-AC02-05CH11231 (Lawrence Berkeley National Laboratory; operated by the University of California). The research supported by the SLAC Science Focus Area (SFA) program is also supported by DOE-BER under SLAC FWP 10094 and by the POTHAL project funded by the Austrian Federal Ministry of Education in frame of the Raw-Materials initiative. We thank L. Slater and two anonymous reviewers for their constructive comments that helped to improve the manuscript.

REFERENCES

- Atekwana, E. A., and L. D. Slater, 2009, Biogeophysics: A new frontier in Earth science research: *Reviews of Geophysics*, **47**, RG4004, doi: [10.1029/2009RG000285](https://doi.org/10.1029/2009RG000285).
- Binley, A., J. Keery, L. Slater, W. Barrash, and M. Cardiff, 2016, The hydrogeologic information in cross-borehole complex conductivity data from an unconsolidated conglomeratic sedimentary aquifer: *Geophysics*, **81**, no. 6, E409–E421, doi: [10.1190/geo2015-0608.1](https://doi.org/10.1190/geo2015-0608.1).
- Binley, A., and A. Kemna, 2005, DC resistivity and induced polarization methods, in Y. Rubin and S. Hubbard, eds., *Hydrogeophysics*: Springer, 129–156.
- Binley, A., A. Ramirez, and W. Daily, 1995, Regularised image reconstruction of noisy electrical resistance tomography data: 4th Workshop of the European Concerted Action on Process Tomography, European Concerted Action on Process Tomography.
- Dafflon, B., Y. Wu, S. S. Hubbard, J. T. Birkholzer, T. M. Daley, J. D. Pugh, J. E. Peterson, and R. C. Trautz, 2012, Monitoring CO₂ intrusion and associated geochemical transformations in a shallow groundwater system using complex electrical methods: *Environmental Science and Technology*, **47**, 314–321, doi: [10.1021/es301260e](https://doi.org/10.1021/es301260e).
- Dahlin, T., and V. Leroux, 2012, Improvement in time-domain induced polarization data quality with multi-electrode systems by separating current and potential cables: *Near Surface Geophysics*, **10**, 545–565.
- Dahlin, T., V. Leroux, and J. Nissen, 2002, Measuring techniques in induced polarisation imaging: *Journal of Applied Geophysics*, **50**, 279–298, doi: [10.1016/S0926-9851\(02\)00148-9](https://doi.org/10.1016/S0926-9851(02)00148-9).
- Dahlin, T., and M. H. Loke, 2015, Negative apparent chargeability in time-domain induced polarisation data: *Journal of Applied Geophysics*, **123**, 322–332.
- Dahlin, T., and B. Zhou, 2006, Multiple-gradient array measurements for multichannel 2D resistivity imaging: *Near Surface Geophysics*, **4**, 113–123.
- Doetsch, J., G. Fiandaca, E. Auken, A. V. Christiansen, A. G. Cahill, and R. Jakobsen, 2015a, Field-scale time-domain spectral induced polarization monitoring of geochemical changes induced by injected CO₂ in a shallow aquifer: *Geophysics*, **80**, no. 2, WA113–WA126, doi: [10.1190/geo2014-0315.1](https://doi.org/10.1190/geo2014-0315.1).
- Doetsch, J., T. Ingeman-Nielsen, A. V. Christiansen, G. Fiandaca, E. Auken, and B. Elberling, 2015b, Direct current (DC) resistivity and induced polarization (IP) monitoring of active layer dynamics at high temporal resolution: *Cold Regions Science and Technology*, **119**, 16–28, doi: [10.1016/j.coldregions.2015.07.002](https://doi.org/10.1016/j.coldregions.2015.07.002).
- Fiandaca, G., E. Auken, A. V. Christiansen, and A. Gazoty, 2012a, Time-domain-induced polarization: Full-decay forward modeling and 1D laterally constrained inversion of Cole-Cole parameters: *Geophysics*, **77**, no. 3, E213–E225, doi: [10.1190/geo2011-0217.1](https://doi.org/10.1190/geo2011-0217.1).
- Fiandaca, G., J. Ramm, A. Binley, A. Gazoty, A. V. Christiansen, and E. Auken, 2012b, Resolving spectral information from time domain induced polarization data through 2-D inversion: *Geophysical Journal International*, **192**, 631–646, doi: [10.1093/gji/ggs060](https://doi.org/10.1093/gji/ggs060).
- Flores Orozco, A., A. Kemna, C. Oberdörster, L. Zschornack, C. Leven, P. Dietrich, and H. Weiss, 2012a, Delineation of subsurface hydrocarbon contamination at a former hydrogenation plant using spectral induced polarization imaging: *Journal of Contaminated Hydrology*, **136–137**, 131–144, doi: [10.1016/j.jconhyd.2012.06.001](https://doi.org/10.1016/j.jconhyd.2012.06.001).
- Flores Orozco, A., A. Kemna, and E. Zimmermann, 2012b, Data error quantification in spectral induced polarization imaging: *Geophysics*, **77**, no. 3, E227–E237, doi: [10.1190/geo2010-0194.1](https://doi.org/10.1190/geo2010-0194.1).
- Flores Orozco, A., M. Velimirovic, T. Tosco, A. Kemna, H. Sapon, N. Klaas, R. Sethi, and B. Leen, 2015, Monitoring the injection of microscale zero-valent iron particles for groundwater remediation by means of complex electrical conductivity imaging: *Environmental Science and Technology*, **49**, 5593–5600, doi: [10.1021/acs.est.5b00208](https://doi.org/10.1021/acs.est.5b00208).
- Flores Orozco, A., K. H. Williams, and A. Kemna, 2013, Time-lapse spectral induced polarization imaging of stimulated uranium bioremediation: *Near Surface Geophysics*, **11**, 531–544.
- Flores Orozco, A., K. H. Williams, P. E. Long, S. S. Hubbard, and A. Kemna, 2011, Using complex resistivity imaging to infer biogeochemical processes associated with bioremediation of an uranium-contaminated aquifer: *Journal of Geophysical Research: Biogeosciences*, **116**, 2156–2206, doi: [10.1029/2010JG001591](https://doi.org/10.1029/2010JG001591).
- Gazoty, A., G. Fiandaca, J. Pedersen, E. Auken, A. V. Christiansen, and J. K. Pedersen, 2012, Application of time domain induced polarization to the mapping of lithotypes in a landfill site: *Hydrology and Earth System Sciences*, **16**, 1793–1804, doi: [10.5194/hess-16-1793-2012](https://doi.org/10.5194/hess-16-1793-2012).
- Gazoty, A., G. Fiandaca, J. Pedersen, E. Auken, and A. V. Christiansen, 2013, Data repeatability and acquisition techniques for time-domain spectral induced polarization: *Near Surface Geophysics*, **11**, 391–406, doi: [10.3997/1873-0604.2013013](https://doi.org/10.3997/1873-0604.2013013).
- Kemna, A., 2000, Tomographic inversion of complex resistivity: Theory and application: *Der Andere Verlag*.
- Kemna, A., A. Binley, G. Cassiani, E. Niederleithinger, A. Revil, L. Slater, K. H. Williams, A. Flores Orozco, F.-H. Haegel, A. Hördt, S. Kruschwitz, V. Leroux, K. Titov, and E. Zimmermann, 2012, An overview of the spectral induced polarization method for near-surface applications: *Near Surface Geophysics*, **10**, 453–468.
- Kemna, A., E. Råkers, and L. Dresen, 1999, Field applications of complex resistivity tomography: 69th Annual International Meeting, SEG, Expanded Abstracts, 331–334.
- LaBrecque, D. J., M. Miletto, W. Daily, A. Ramirez, and E. Owen, 1996, The effects of noise on Occam's inversion of resistivity tomography data: *Geophysics*, **61**, 538–548, doi: [10.1190/1.1443980](https://doi.org/10.1190/1.1443980).
- Larson, H. J., 1975, *Statistics: An introduction*: Wiley, 15.
- Morelli, G., and D. J. LaBrecque, 1996, Robust scheme for ERT inverse modelling: *Symposium on the Application of Geophysics to Engineering and Environmental Problems*: SEG, 629–638.
- Nordsiek, S., and A. Weller, 2008, A new approach to fitting induced-polarization spectra: *Geophysics*, **73**, no. 6, F235–F245, doi: [10.1190/1.2987412](https://doi.org/10.1190/1.2987412).
- Olsson, P. I., T. Dahlin, G. Fiandaca, and E. Auken, 2015, Measuring time-domain spectral induced polarization in the on-time: decreasing acquisition time and increasing signal-to-noise ratio: *Journal of Applied Geophysics*, **123**, 316–321, doi: [10.1016/j.jappgeo.2015.08.009](https://doi.org/10.1016/j.jappgeo.2015.08.009).
- Olsson, P. I., G. Fiandaca, J. J. Larsen, T. Dahlin, and E. Auken, 2016, Doubling the spectrum of time-domain induced polarization by harmonic de-noising, drift correction, spike removal, tapered gating and data uncertainty estimation: *Geophysical Journal International*, **207**, 774–784, doi: [10.1093/gji/ggw260](https://doi.org/10.1093/gji/ggw260).
- Pelton, W. H., S. H. Ward, P. G. Hallof, W. R. Sill, and P. H. Nelson, 1978, Mineral discrimination and removal of inductive coupling with multifrequency IP: *Geophysics*, **43**, 588–609, doi: [10.1190/1.1440839](https://doi.org/10.1190/1.1440839).
- Slater, L., and A. Binley, 2006, Synthetic and field-based electrical imaging of zerovalent iron barrier: Implications for monitoring long-term barrier performance: *Geophysics*, **71**, no. 5, B129–B137, doi: [10.1190/1.2235931](https://doi.org/10.1190/1.2235931).

- Slater, L., A. Binley, W. Daily, and R. Johnson, 2000, Cross-hole electrical imaging of a controlled saline tracer injection: *Journal of Applied Geophysics*, **44**, 85–102, doi: [10.1016/S0926-9851\(00\)00002-1](https://doi.org/10.1016/S0926-9851(00)00002-1).
- Sturgers, H. A., 1926, The choice of a class interval: *Journal of the American Statistical Association*, **21**, 65–66, doi: [10.1080/01621459.1926.10502161](https://doi.org/10.1080/01621459.1926.10502161).
- U.S. Department of Energy (DOE) Office of Legacy Management Data Disclaimer, 2017, <http://www.gems.lm.doe.gov/#site=SHP>, accessed December 2017.
- Van Voorhis, G. D., P. H. Nelson, and T. L. Drake, 1973, Complex resistivity spectra of porphyry copper mineralization: *Geophysics*, **38**, 49–60, doi: [10.1190/1.1440333](https://doi.org/10.1190/1.1440333).
- Wainwright, H. M., A. Flores Orozco, M. Bucker, B. Dafflon, J. Chen, S. S. Hubbard, and K. H. Williams, 2015, Hierarchical Bayesian method for mapping biogeochemical hot spots using induced polarization imaging: *Water Resources Research*, **52**, 533–551, doi: [10.1002/2015WR017763](https://doi.org/10.1002/2015WR017763).
- Weigand, M., A. Flores Orozco, and A. Kemna, 2017, Reconstruction quality of SIP parameters in multi-frequency complex resistivity imaging: *Near Surface Geophysics*, **15**, 187–199.
- Weller, A., L. Slater, and S. Nordsiek, 2013, On the relationship between induced polarization and surface conductivity: Implications for petrophysical interpretation of electrical measurements: *Geophysics*, **78**, no. 5, D315–D325, doi: [10.1190/geo2013-0076.1](https://doi.org/10.1190/geo2013-0076.1).



Water Resources Research

RESEARCH ARTICLE

10.1002/2015WR017763

Key Points:

- Naturally reduced zones (NRZs) are considered to be biogeochemical hot spots under floodplains
- We developed a noninvasive probabilistic mapping method of NRZs using induced polarization imaging
- This method provides a minimally invasive means to parameterize a floodplain biogeochemical model

Correspondence to:

H. M. Wainwright,
hmwainwright@lbl.gov

Citation:

Wainwright, H. M., A. Flores Orozco, M. Bückler, B. Dafflon, J. Chen, S. S. Hubbard, and K. H. Williams (2016), Hierarchical Bayesian method for mapping biogeochemical hot spots using induced polarization imaging, *Water Resour. Res.*, 52, 533–551, doi:10.1002/2015WR017763.

Received 1 JUL 2015

Accepted 27 DEC 2015

Accepted article online 30 DEC 2015

Published online 29 JAN 2016

Hierarchical Bayesian method for mapping biogeochemical hot spots using induced polarization imaging

Haruko M. Wainwright¹, Adrian Flores Orozco², Matthias Bückler^{2,3}, Baptiste Dafflon¹, Jinsong Chen¹, Susan S. Hubbard¹, and Kenneth H. Williams¹

¹Earth Sciences Division, Lawrence Berkeley National Laboratory, Berkeley, California, USA, ²Department of Geodesy and Geoinformation, Vienna University of Technology, Vienna, Austria, ³Steinmann Institute, Department of Geophysics, University of Bonn, Bonn, Germany

Abstract In floodplain environments, a naturally reduced zone (NRZ) is considered to be a common biogeochemical hot spot, having distinct microbial and geochemical characteristics. Although important for understanding their role in mediating floodplain biogeochemical processes, mapping the subsurface distribution of NRZs over the dimensions of a floodplain is challenging, as conventional wellbore data are typically spatially limited and the distribution of NRZs is heterogeneous. In this study, we present an innovative methodology for the probabilistic mapping of NRZs within a three-dimensional (3-D) subsurface domain using induced polarization imaging, which is a noninvasive geophysical technique. Measurements consist of surface geophysical surveys and drilling-recovered sediments at the U.S. Department of Energy field site near Rifle, CO (USA). Inversion of surface time domain-induced polarization (TDIP) data yielded 3-D images of the complex electrical resistivity, in terms of magnitude and phase, which are associated with mineral precipitation and other lithological properties. By extracting the TDIP data values collocated with wellbore lithological logs, we found that the NRZs have a different distribution of resistivity and polarization from the other aquifer sediments. To estimate the spatial distribution of NRZs, we developed a Bayesian hierarchical model to integrate the geophysical and wellbore data. In addition, the resistivity images were used to estimate hydrostratigraphic interfaces under the floodplain. Validation results showed that the integration of electrical imaging and wellbore data using a Bayesian hierarchical model was capable of mapping spatially heterogeneous interfaces and NRZ distributions thereby providing a minimally invasive means to parameterize a hydrobiogeochemical model of the floodplain.

1. Introduction

Terrestrial biogeochemical processes represent a significant uncertainty in our understanding of carbon and nutrient cycling [e.g., *Heimann and Reichstein*, 2009]. Recent studies have described how small zones in an environment can display enhanced biogeochemical reaction rates and/or fluxes relative to surrounding regions. Compared to contributions from neighboring regions, these biogeochemical hot spots can have a disproportionately large impact on larger-scale biogeochemical cycling [*McClain et al.*, 2002; *Vidon et al.*, 2010]. *Duncan et al.* [2013], for example, estimated that riparian-zone hollows (lower topographic regions) accounted for more than 99% of total denitrification in a catchment (37 ha), even though the hollows represent only 0.5%–1.0% of the total catchment area. Several other papers have described hot spots associated with regions where groundwater flow upwells or meets organic-rich sediments [*Hedin et al.*, 1998; *Hill et al.*, 2000]. Other hot spots include wetlands [*Johnston et al.*, 2001], hyporheic zones [*Triska et al.*, 1984; *Holmes et al.*, 1996], and vernal pools [*Capps et al.*, 2014].

Identifying and mapping hot spots in sufficient resolution, yet over spatial scales needed to inform modeling, is challenging [*Vidon et al.*, 2010]. *Duncan et al.* [2013] used a topographic wetness index (based on a digital elevation map from airborne LiDAR) to estimate the distribution of hot spots of intense denitrification (i.e., riparian-zone hollows). However, *Anderson et al.* [2015] estimated—using the same index—that drier upland soils would contribute to a larger portion of whole-catchment denitrification. Such discrepancy could be attributed to the fact that the subsurface terms (soil thickness and hydraulic conductivity) are often ignored or approximated in the topographic wetness index. Although the topography and other surface indicators (e.g., slope) are often strongly correlated with subsurface biological processes, other factors

(e.g., geology, soil type) may also play a critical role in subsurface biogeochemistry. However, direct measurements of subsurface properties have been mostly limited to drilling wells and sampling cores, which are often invasive and sparse, failing to identify the exact extent of the hot spots or associated controls.

Recently, *Campbell et al.* [2012] and *Qafoku et al.* [2014] reported the presence of naturally reduced zones (NRZs) within aquifer sediments at a former uranium mill-processing site near Rifle, Colorado (USA). This site is located on a floodplain adjacent to the Colorado River. The two studies found that NRZ sediments had elevated concentrations of uranium, organic matter, and geochemically reduced mineral phases, such as metal sulfides, and were often associated with predominantly fine-grained sediment textures. The historical monitoring of pore water chemistry also showed that the elevated concentrations were fairly persistent over time [*Zachara et al.*, 2013]. The conceptual model of NRZ formation is that roots, twigs, and other plant materials accumulated during the river depositional process, became buried, and formed the reduced sediments. In addition to these two studies, *Mouser et al.* [2014] found unique microbial characteristics within the NRZs, such as the abundance of iron-reducing Geobacteraceae communities. Recent modeling studies suggested that NRZs have a significant impact on subsurface carbon flux to the atmosphere as well as to the river [*Arora et al.*, 2015a, 2015b]. NRZs can therefore be considered the biogeochemical “hot spots” of the Rifle floodplain, having distinct microbial, mineralogical, and geochemical properties.

Floodplain-based NRZs could potentially play an important role in global carbon cycling. Although the floodplains cover a small portion of the Earth’s surface, overbank sedimentation at river floodplains is considered to be a significant terrestrial sink of carbon [*Walling et al.*, 2006; *Battin et al.*, 2009; *Aufdenkampe et al.*, 2011]. Floodplains also constantly exchange water, sediment, and geochemical constituents with rivers [*Neff and Asner*, 2001; *Grimm et al.*, 2003; *Gomez et al.*, 2012]. Subsurface carbon respiration and surface water-groundwater exchanges within floodplains contribute significantly to dissolved organic carbon concentrations and CO₂ outgassing in streams and rivers [*Schindler and Krabbenhoft*, 1998; *Cole et al.*, 2007; *Battin et al.*, 2008; *Melack*, 2011]. To develop a model describing the coupled hydrologic and biogeochemical behavior of floodplains, we must include the presence and distribution of such hot spots within the subsurface. Unfortunately, conventional borehole data (e.g., sediment properties, solid and aqueous phase geochemistry, microbial community composition) are often spatiotemporally sparse and thus insufficient for resolving subsurface heterogeneity within floodplain deposits [e.g., *Scheibe and Freyberg*, 1995; *Kowalsky et al.*, 2011; *Yabusaki et al.*, 2011].

Various geophysical methods have been developed in the past several decades to characterize heterogeneous subsurface environments in a noninvasive manner [e.g., *Rubin and Hubbard*, 2005; *Vereecken et al.*, 2006; *Hubbard and Linde*, 2011; *Binley et al.*, 2015]. Surface electrical methods—based on injecting an electrical current through one pair of electrodes on the ground surface and measuring the electrical potential between a second pair of electrodes—are amongst the most commonly used near-surface geophysical techniques. The geometrical distribution of electrical resistivity from such measurements has been used to delineate geological units, water saturation, and lithological properties [e.g., *Bowling et al.*, 2005; *Binley and Kemna*, 2005; *Doetsch et al.*, 2012; *Kennedy et al.*, 2013]. Particularly, electrical resistivity tomography (ERT) employs tens of electrodes along the profile and measures the electrical potential between them. Tomographic data are then converted to depth-discrete electrical resistivity values along the profile using suitable inversion schemes [e.g., *Binley and Kemna*, 2005]. Electrical resistivity (the inverse of electrical conductivity) is a bulk property of subsurface material associated with its tendency to resist electrical current flow, and has long been known to be correlated with water saturation, pore water chemistry and lithological properties [e.g., *Archie*, 1942].

Recently, the induced polarization (IP) imaging technique—also referred to as complex conductivity or complex resistivity imaging—has been increasingly used to provide additional information on subsurface conditions. Induced polarization phenomena are of electrochemical origin, depending mainly on the presence of metallic minerals and the pore structure. In the presence of metallic minerals, the change in the electrical conduction mechanisms from electrolytic (in the groundwater) to electronic (in the metallic minerals) results in strong polarization effects [e.g., *Pelton et al.*, 1978]. Previous studies have reported a linear correlation between the size of metallic minerals and the IP effect [*Wong*, 1979]. In case of porous media without metallic minerals, the polarization effect is primarily controlled by the total mineral-fluid surface area within the sample, which can be estimated from the total mineral surface area per unit pore volume [e.g., *Weller and Slater*, 2015]. As grain size and surface are inversely related, other workers have found a near-inverse

linear relation between the IP effect and effective grain [e.g., *Titov et al.*, 2004] and pore size [e.g., *Binley et al.*, 2005].

The IP method was initially used in the prospecting for metallic and certain sulfide ores [e.g., *Pelton et al.*, 1978] based upon strong polarization enhanced in the presence of metallic and semiconductive minerals [Wong, 1979]. More recently, polarization mechanisms occurring in geological materials without metallic admixtures, such as membrane polarization [e.g., *Marshall and Madden*, 1959; *Bücker and Hördt*, 2013] or the polarization of the Stern layer [e.g., *Revil and Florsch*, 2010], have been found to be sensitive to different hydrogeological (texture, grain/pore size, saturation, etc.) and geochemical (e.g., salinity, pH) parameters. Particularly, the membrane polarization model has been proposed for rocks with a dispersed clay fraction [e.g., *Marshall and Madden*, 1959], based on the theory that clay minerals coating the quartz grains or located in pore-throats produce local concentration gradients under applied external voltage [Titov et al., 2002; Scott and Barker, 2003]. In addition, the IP measurements have recently been used to detect and map subsurface (bio)geochemical properties associated with microbe-induced mineral precipitation [e.g., *Ntarlagiannis et al.*, 2005; *Williams et al.*, 2009; *Flores Orozco et al.*, 2011; *Chen et al.*, 2013; *Abdel Aal et al.*, 2014].

Ground-based tomographic IP measurements are typically acquired using a similar electrode configuration as ERT. In addition to the resistivity measurements, the time decay of the electric potential is measured after the current injection is stopped. Recently, multielectrode IP surveys (commonly referred to as tomographic surveys), in combination with appropriate inversion techniques, have enabled the high spatial resolution imaging of the complex electrical resistivity in the subsurface [Binley and Kemna, 2005].

Previous studies at the Rifle site reported the application of the IP method for monitoring subsurface microbial processes stimulated through organic carbon addition [Williams et al., 2009]. These field studies revealed that the IP method is suitable for detecting an increase in the polarization effect accompanying the precipitation of iron sulfides (e.g., FeS) and changes in the chemical composition of groundwater, particularly the concentration of electroactive ions, such as Fe (II) [Flores Orozco et al., 2011; Chen et al., 2013]. A recent study demonstrated that the polarization response in geochemically reduced, biostimulated sediments remained much higher than for background aquifer materials (i.e., those unimpacted by carbon addition) at the Rifle site over the broad frequency bandwidth (0.06–120 Hz) used for the IP measurements [Flores Orozco et al., 2013]. Given the natural enrichment in conductive and semiconductive metal sulfides in NRZ sediments relative to non-NRZ sediments [Campbell et al., 2012; Qafoku et al., 2014], surface IP methods are well suited for the noninvasive delineation of NRZs within aquifer sediments.

As with other geophysical methods, interpretation of IP imaging results in terms of biogeochemical properties is hindered by uncertainties and often site-specific relationships between the electrical parameters (in this case, the magnitude and phase shift of the complex electrical resistivity) and mineralogical-geochemical properties. Other mechanisms exist that can engender a measurable polarization response in the subsurface, which also complicates interpretation of IP data. In particular, the mixture of materials with different textural properties (e.g., grain size) is related to an increase in the polarization effect due to membrane polarization mechanisms [e.g., *Revil and Florsch*, 2010; *Bücker and Hördt*, 2013]. Hence, IP measurements collected over the full extent of a floodplain might be sensitive to subsurface properties not solely limited to the presence of reduced sediments within NRZ's, but also due to lithological boundaries and corresponding changes in mineralogical and textural properties [e.g., *Börner et al.*, 1996; *Slater et al.*, 2014].

Bayesian methods offer an approach to integrate geophysical data sets and point measurements, including their uncertainty, in a consistent manner [e.g., *Hubbard et al.*, 2001; *Chen et al.*, 2004, 2006; *Sassen et al.*, 2012; *Wainwright et al.*, 2014]. In particular, reactive facies or zonation approaches have recently been developed within the Bayesian framework to identify regions that have unique distribution of physical and geochemical properties using geophysical data [Chen et al., 2006; Sassen et al., 2012; Wainwright et al., 2014]. Instead of estimating hydrological or biogeochemical properties directly, the zonation approaches aim to delineate zones and their associated property distributions. These methods take advantage of the often-coupled nature of physical, microbiological, and geochemical properties of subsurface materials and the sensitivity of geophysical responses to at least one of the properties to identify and characterize reactive facies or zones.

In this study, we extend the zonation concept to estimate the distribution of NRZs in a three-dimensional (3-D) domain over the Rifle floodplain using surface time domain-induced polarization (TDIP) measurements.

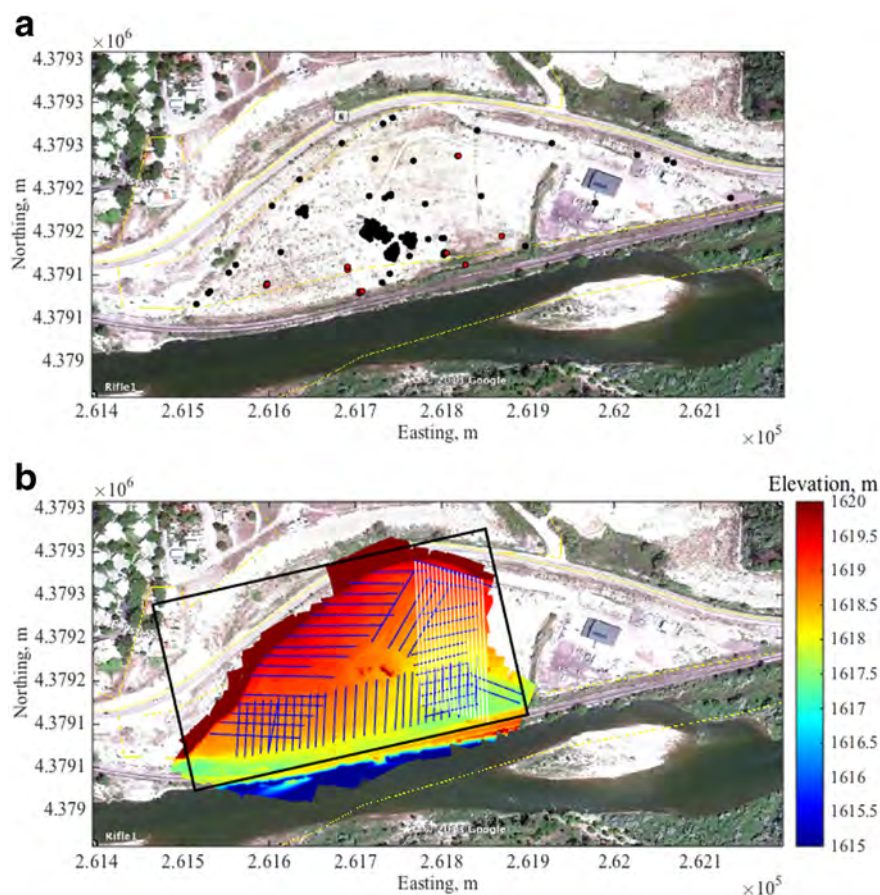


Figure 1. (a) Rifle floodplain with well locations, and (b) digital elevation model (in meter) with ERT lines (white region) and TDIP lines (blue lines). In Figure 1a, the black circles are the well locations constructed prior to 2013, and the red circles represent the wells that were drilled in 2014. The site picture is obtained from Google Earth. The Colorado River bounds the south of the site. In Figure 1b, the black rectangle represents the domain used for the estimation and reactive transport modeling.

The distribution of the complex electrical resistivity properties of the subsurface was obtained after the inversion of the TDIP data. We developed a Bayesian approach to integrate wellbore lithological data and IP inversion results, and estimated the distribution of NRZs in a probabilistic manner. In order to develop a high-resolution 3-D representation of the subsurface, we used a digital elevation model (DEM) inferred from an aerial landscape imaging survey and structure-from-motion techniques. We estimated hydrostratigraphic interfaces using electrical resistivity images from both the IP data sets and electrical resistivity tomography (ERT) data available at the site. Such hydrostratigraphic interfaces are important for hydrological and geochemical modeling at this site, as they control vertical infiltration and lateral groundwater flow. To the authors' knowledge, this is the first study to apply the IP method for delineating such biogeochemical hot spots in a probabilistic manner and to establish a methodology for integrating multiple spatially extensive above ground and below ground data sets capable of informing biogeochemical models at the floodplain scale.

2. Site Information and Data

2.1. Site Description

The Rifle site (Figure 1) is located on a floodplain adjacent to the Colorado River in northwestern Colorado [e.g., Williams *et al.*, 2009]. The site was formerly used as a vanadium and uranium ore processing facility, which caused soil and groundwater contamination by uranium and other heavy metals. The site is currently a part of the U.S. Department of Energy's (DOE) Uranium Mill Tailings Remedial Action program, which includes long-term monitoring activities following excavation and removal of mill tailings and tailings-contaminated surface materials. The Rifle site currently serves as a community field laboratory for research in

biogeochemical characterization, bioremediation, subsurface microbial characterization, and nutrient cycling [e.g., Williams *et al.*, 2011; Yabusaki *et al.*, 2011; Castelle *et al.*, 2013; Wrighton *et al.*, 2014].

The site hydrostratigraphy consists of three principal units, referred to hereafter from surface to base of the aquifer as: the fill layer, the Rifle Formation, and the Wasatch Formation. The fill layer—comprised of silt-rich loess deposits derived from a quarry abutting the site to the northeast—was artificially constructed to cover the ground surface postreclamation and also to reduce the amount of infiltration reaching the groundwater. The fill thickness is $\sim 1\text{--}3$ m over the area, although it is thicker in areas where a greater depth of contaminated soil was excavated due to higher contamination levels. A shallow unconfined aquifer, the Rifle Formation, is comprised of alluvium deposited by the Colorado River that includes unconsolidated clays, silts, sands, gravels, and cobbles (DOE, 1999). Primarily composed of weathered clayey siltstone, the low-permeability Wasatch Formation underlies the Rifle Formation at depths of 5–8 m below ground surface and serves as a local aquitard to the saturated alluvium at the site. Additionally, the Wasatch Formation includes discontinuous sandstone lenses, a small fraction of which contain visible pyrite grains, with such materials observed both within drilling-recovered materials and in outcrops adjoining the site.

2.2. Core Data and Lithological Logs

This site has 171 wells with well-documented lithological logs constructed over more than 20 years (in Figure 1a, the black circles are the well locations constructed prior to 2013). Sixteen new wells were added in 2014 for additional geochemical characterization (red circles in Figure 1a). Through extensive geochemical and microbiological analysis of Rifle core data, several studies [Campbell *et al.*, 2012; Qafoku *et al.*, 2014; Janot *et al.*, 2015] identified and characterized two NRZ localities at the site (spatially separated by ~ 65 m). To identify NRZ locations along each well, we relied on the lithological log constructed for each of those wells. These log reports have a standard format and include the description of core texture, color (using Munsell soil color chart), and other features. They also provide the interface depths of the fill, Rifle Formation, and Wasatch Formation. Those reports are archived, quality controlled, and made publically available by DOE at URL <http://gems.lm.doe.gov/#site=RFO>. By comparing the well log reports and the sample locations in Campbell *et al.* [2012] and Qafoku *et al.* [2014], we found that the sediment description of “dark color” or “reduced” provided an excellent match to the NRZ locations.

2.3. Surface Elevation Data

A high-resolution surface elevation map was provided by a kite-based aerial system, which lifts a consumer-grade digital camera (Sony Nex-5R) about 40 m above the ground surface [Smith *et al.*, 2009]. The reconstruction procedure was performed using a commercial computer vision software package (PhotoScan from Agisoft LLC). The reconstruction involved automatic image feature detection/matching, structure-from-motion and multiview-stereo techniques for 3-D point-cloud generation, and georeferenced mosaic reconstruction. High-accuracy georeferencing was enabled by using a network of ground control points surveyed with a high-precision centimeter-grade RTK DGPS system.

A digital terrain model was inferred from the digital surface model by using a moving average filter to remove sharp positive variations, which is adequate for this site because of the sparse and low vegetation and the relatively smooth changes in terrain elevation. The comparison to the ground surface elevation at wells surveyed with high-precision GPS showed excellent agreement. The digital elevation model was used to convert the depth information of the ERT and IP data to the elevation after the inversion. Since elevation variability is low along each line (< 1.5 m), no formal treatment of elevation effects on data inversion was undertaken.

2.4. Geophysical Data Acquisition and Inversion

The ERT data set was acquired on the eastern side of the site along 17 parallel profiles (white lines in Figure 1b), each one being 166.5 m long and 5 m distant from the adjacent profile. Resistance measurements were collected using the MPT-DAS-1 system with 112 stainless steel electrodes having an electrode separation of 1.5 m and using a dipole-dipole configuration involving dipole lengths ranging from 1.5 to 18 m with the distance between the closest injection and potential electrodes equal to or smaller than 3 times the dipole length. The survey configuration was chosen to obtain a high signal-to-noise ratio and to image both near-surface features and the deeper Rifle-Wasatch interface. Ten percent of measurements were collected in a normal and reciprocal mode to evaluate data quality.

The IP data set was collected using a time domain-induced polarization (TDIP) method along 65 profiles of various lengths over the floodplain (Figure 1b). In the TDIP method, the transient decay of voltage is measured after current shut-off, typically in the form of an integral of decay curves over a predefined time-window (so-called integral chargeability). TDIP measurements at the site were collected using the Syscal Iris Pro Switch equipment with a square-wave current injection, 50% duty cycle, and a pulse length of 2 s. The integral chargeability measurements were carried out using 20 windows during voltage decay between 240 and 1840 ms after current shut-off. Tomographic measurements were collected by deploying stainless steel electrodes with an electrode separation of 1.8 m and using a dipole-dipole “skip-2” and “skip-3” measuring protocol (i.e., for a dipoles length of 5.4 and 7.2 m, respectively). The sequence of dipole-dipole measurements was carefully arranged to (1) minimize unwanted electromagnetic coupling effects in the data, avoiding potential measurements with electrodes located inside the current dipole (as suggested in *Pelton et al.* [1978] and *Flores Orozco et al.* [2013]), (2) prevent voltage measurements using electrodes, which might be polarized due to previous current injection [*LaBrecque and Daily*, 2008; *Williams et al.*, 2009], and (3) increase the signal-to-noise ratio for an intended exploration depth of 8 m, i.e., the bottom of the aquifer [e.g., *Williams et al.*, 2011]. All measurements were collected as normal and reciprocal pairs for estimation of the data error. The IP measurements were collected with symmetric arrays (i.e., the measuring equipment placed at the center of the electrode array) with a maximum of 36 electrodes, considering that longer profiles revealed a significant increase in the normal-reciprocal misfit for the measurements of the decay curve, probably due to greater impact of electromagnetic coupling on the data.

Both the ERT and TDIP data sets were inverted in a two-dimensional domain along each transect using CRTomo, which is a smoothness-constraint inversion code based on a finite element algorithm [*Kemna*, 2000]. The resistivity and phase shift values at each pixel were then assigned at the corresponding point within the 3-D floodplain domain (the black rectangle Figure 1b) and used in the 3-D estimation. The TDIP inversion results provided the distribution of the complex resistivity, expressed in terms of its magnitude and phase-shift, while the inversion of ERT data was solved for the magnitude of resistivity. For the inversion of the ERT measurements, data have been cleaned from a very limited number of outliers. In the reciprocal-versus-normal measurements, the measurements with the highest misfit were related to lowest measured voltage. The analysis of the normal-reciprocal misfit was used to estimate the relative error. We removed the measurement with smallest voltage difference (<2 mV), representing about 2% variations in the data. For the inversion of TDIP measurements, chargeability values were linearly converted to frequency domain phase values (at the fundamental frequency of 0.125 Hz), by assuming a constant-phase response [*Kemna et al.*, 1997]. This approach has been demonstrated to provide consistent results in previous studies [*Slater and Binley*, 2006; *Mwakanyamale et al.*, 2012; *Flores Orozco et al.*, 2012a, 2012b]. *Flores Orozco et al.* [2012a] also showed that the two existing approaches—frequency domain measurements and converted time domain data sets—did not create a significant difference in the correlation (below 5%) between hydrocarbon concentrations and the magnitude and phase shift of the complex electrical resistivity.

The estimation of the data errors was performed on the analysis of the misfit between normal and reciprocal measurements, following the methodology developed by *Flores Orozco et al.* [2012b]. Prior to the inversion, we removed outliers in the data, which were defined as those measurements associated with large discrepancies between normal and reciprocal phase readings (i.e., the normal-reciprocal misfit of each configuration exceeding 2 times the normal-reciprocal standard deviation of the entire data set). After the inversion, we removed the low-sensitivity area from the 2-D image of the phase shift and resistivity. We used a threshold value in the cumulated sensitivity, which is a measure of how much the entire data set changes due to a changing model value in each cell [*Kemna*, 2000] and has been previously used to assess the variable image resolution [*Kemna*, 2000; *Nguyen et al.*, 2009]. As discussed in the study of *Flores Orozco et al.* [2013], the uncertainty in IP imaging results increases with decreasing the cumulated sensitivity.

3. Exploratory Data Analysis of Inverted Geophysical Images

Resistivity images obtained from the inversion of both ERT and TDIP data sets were used to map the depths of the fill-Rifle and Rifle-Wasatch interfaces, since both the fill layer and Wasatch Formation have lower resistivity (owing to higher clay and/or silt contents) than the Rifle Formation. While the dense ERT measurements were located only in the western part of the floodplain, the TDIP measurements covered most of the

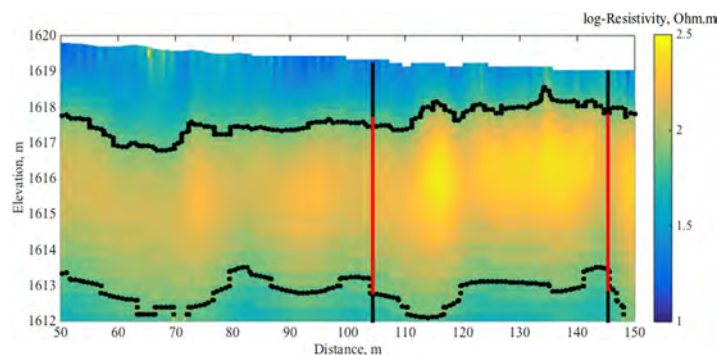


Figure 2. Two-dimensional Resistivity image from the surface ERT (one of 17 lines). The threshold resistivity value (70.0 Ohm m) is marked by the black curves, representing the two interfaces (Fill-Rifle and Rifle-Wasatch). The vertical black lines are the collocated well locations. The red portion represents the Rifle Formation, so that the black-red boundary represents the interface.

based on the threshold resistivity values and the ones from the wellbore lithology data in one of the ERT images.

Figures 3a and 3b show the significant correlations between the ERT-derived depths and borehole-derived depths for the fill-Rifle and Rifle-Wasatch interfaces. The correlation coefficients were 0.75 (p -value: 5.3×10^{-2}) for the Rifle-Wasatch interface and 0.85 (p -value: 5.2×10^{-5}) for the fill-Rifle interface, respectively. Since there is a shift (or bias) from the one-to-one line, we performed a linear regression, and used the linearly fitted line for estimating the interface depths. The standard deviation of the linear-fitting residuals was 0.48 m for the Rifle-Wasatch and 0.25 m for the fill-Rifle, respectively. We consider that the scatters resulted from the variability in the lithology and texture of each geologic layer over the floodplain. Similarly, Figure 3c shows a correlation between the TDIP-derived depths and wellbore-derived depths for the fill-Rifle interface (correlation coefficient: 0.83, and p -value: 6.4×10^{-6}). The standard deviation of the linear-fitting residuals was 0.24 m. Although the TDIP has a much larger coverage over the floodplain, we did not use the TDIP data for estimating the Rifle-Wasatch interface, since the TDIP data were focused on the shallower depths within the Rifle Formation, and had limited sensitivity to the Wasatch Formation.

Previous monitoring studies at the Rifle Site demonstrated an increase in the IP phase shift accompanying the precipitation of metallic minerals (e.g., FeS) resulting from stimulated microbial activity [Williams *et al.*, 2009; Flores Orozco *et al.*, 2011; Flores Orozco *et al.*, 2013]. These studies were, however, based on monitoring data sets collected over the same profile, i.e., with no changes in lithology. A diversity of polarization-generating mechanisms can underlie an anomalous IP response, with variations in sediment texture,

floodplain. We delineated the interfaces by setting the threshold resistivity values and correlated them to the depths reported for collocated wells. We determined the threshold values to maximize the correlations between the borehole-determined interface and the geophysically determined one. For ERT, the threshold value was 70.0 Ohm m for both the Wasatch and fill interfaces. For TDIP, 66.1 Ohm m was used for the fill interface. Figure 2 shows the correspondence between the interfaces

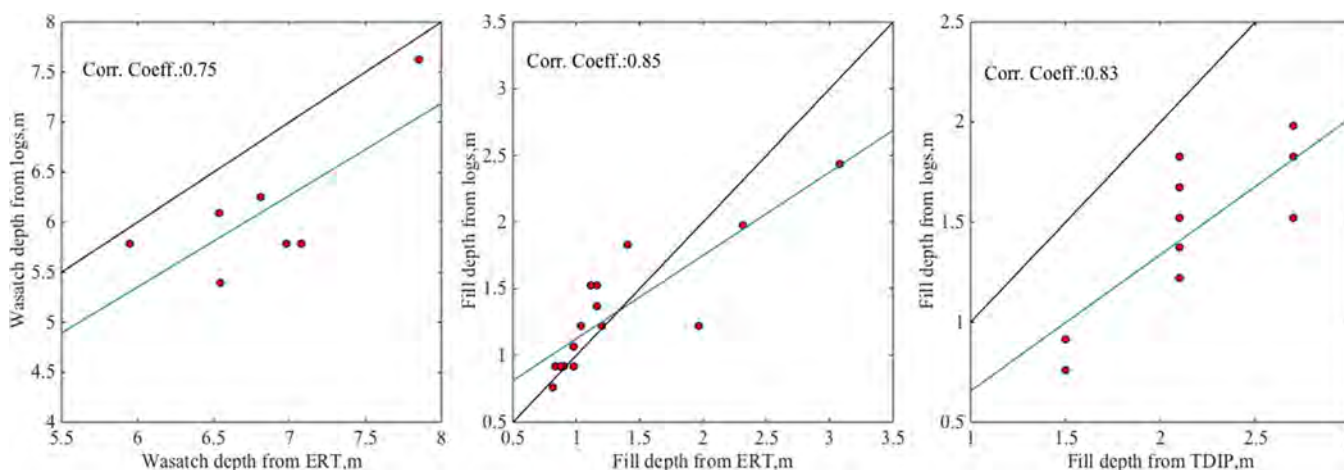


Figure 3. Correlations between (a) ERT-derived and well-derived Wasatch depths, (b) ERT-derived and well-derived Fill depths, and (c) IP-derived and well-derived Fill depths. In Figures 3a–3c, the red dots are data values, the black lines are the one-to-one lines, and the blue lines are the regression-based best fit lines. The correlation coefficient (Corr. Coeff.) is included in each plot.

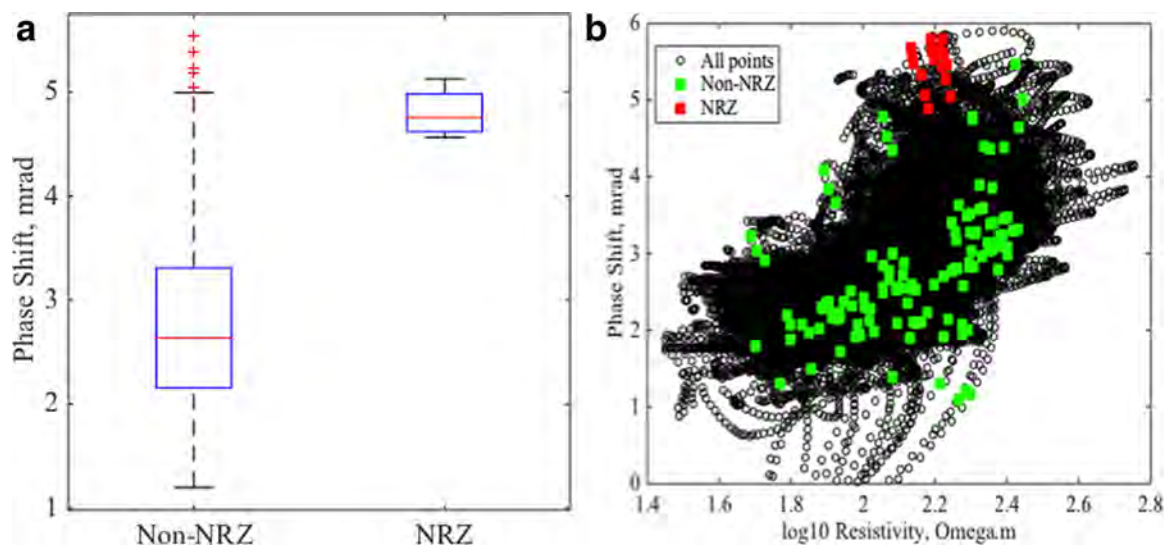


Figure 4. (a) Boxplot to show the phase shift distributions in Non-NRZs and NRZs, and (b) cross-correlation plot for resistivity and phase shift within the Rifle Formation. In Figure 4a, the central red line is the median, the edges of the box are the 25th and 75th percentiles, and the whiskers extend to the 99th percentiles. The red crosses are outliers plotted individually. In Figure 4b, geophysical NRZ and non-NRZ values at wellbore locations are plotted in red and green circles, respectively.

mineralogy, and fluid composition all contributing the polarization/resistivity signature of subsurface materials. Since the current study deals with the change in the electrical responses at a much larger scale (200×500 m) than previous studies at the site (30 m), we need to consider the variation in the lithology and other properties of the aquifer.

By comparing the TDIP images and collocated lithological data, we found that NRZs tend to have a higher phase shift, although there are some exceptions (Figure 4a). Plotting the phase shift along with the resistivity at each pixel in Figure 4b shows that the resistivity and phase shift are correlated to each other (the correlation coefficient is 0.72). It is consistent with several studies, in which the higher phase shift is associated with the higher resistivity [Slater *et al.*, 2005]. Based on the lithological logs, we identified two clusters in the resistivity-phase shift domain: one for NRZ (the red dots in Figure 4b) and the other for non-NRZ (the green dots in Figure 4b). The distribution of non-NRZ is much broader, possibly because the spatial extent of non-NRZ is much larger, and hence non-NRZs have a larger variability in the resistivity and phase shift associated with lithological properties. Taking into account these two clusters, we used both resistivity and phase shift data simultaneously to identify the NRZ locations and defined the NRZ response in the resistivity-phase shift space as bivariate distributions.

In addition, we observed that a small subset of the TDIP profiles revealed the highest phase-shift values within the Wasatch rather than the Rifle Formation. For example, the inversion results at two lines (in Figure 5) show that a clear IP anomaly associated with an NRZ (confirmed by the collocated wells; Figure 5a) and one line associated with high polarization effects in the Wasatch Formation (Figure 5b). These deeper anomalies were inferred to result from pyrite-bearing sandstone lenses reported in lithological data from collocated drilling locations. Plots in Figure 5 reveal that if the increased phase-shift is associated with an NRZ, the highest phase shift is located in the aquifer materials (Figure 5a). The high polarization due to metallic minerals in the Wasatch (but not NRZ) leads to the creation of artifacts with high phase shift values in the aquifer zone (Figure 5b). Their unintentionally shallow depth in the imaging results is thought to be an artifact resulting from the smoothness constraint used in the inversion.

To remove such artifacts, we considered polarizable anomalies as NRZs only when the highest phase-shift value was located within the Rifle Formation. Although different approaches have been suggested to solve for sharp contrasts in the inversion and improve the resolution of the electrical images [e.g., Blaschek *et al.*, 2008; Caterina *et al.*, 2014], such strategies require sufficient information about the geometry and characteristics of the interfaces to avoid the creation of further artifacts. Considering that it is not possible to know a priori the existence and geometry of NRZ locations, we believe that the smoothness inversion is an adequate approach to validate the application of the IP imaging method to characterize NRZs.

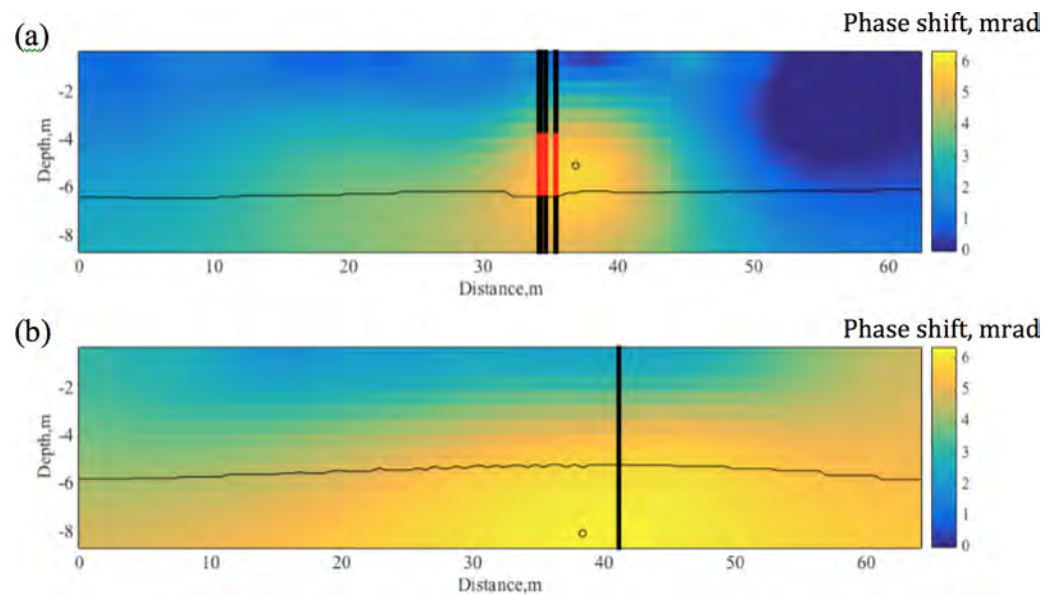


Figure 5. Two-dimensional cross section of the inverted phase shift (mrad) from the TDIP data at (a) the line that had a confirmed NRZ within the Rifle Formation, and at (b) the line that had a confirmed pyrite lens in the Wasatch Formation. The small circle in each figure is the highest phase shift in the domain, and the thin black line is the estimated Rifle-Wasatch interface. The thick black vertical lines indicate collocated well locations. The red lines in Figure 5a are the confirmed NRZs.

4. Statistical Method

Bayesian hierarchical models have been used in the past to integrate multitype and multiscale data sets in a consistent manner, as well as to integrate complex processes [e.g., *Wikle et al., 2001; Wainwright et al., 2014; Hermans et al., 2015*]. The goal of this estimation is to determine the posterior distribution of heterogeneous properties (or property fields) conditioned on all the given data sets and data model parameters α , $p(\text{field}|\text{data}, \alpha)$. In a Bayesian hierarchical model, the posterior distribution can be divided into three statistical submodels represented by conditional distributions: (1) a data model, $p(\text{data}|\text{field}, \alpha)$, which represents the data as a function of the property field and parameters α ; (2) a process model, $p(\text{field}|\beta)$, which describes the property field as function of process model parameters β ; and (3) a prior model, $p(\alpha, \beta)$, which defines the prior information of parameters [*Wikle et al., 2001*]. In the geological environment, one of commonly used process models is often a geostatistical model, which describes a subsurface heterogeneous field as a function of spatial dependence parameters. The hierarchical approach breaks down a complex posterior distribution into a series of simple models, and hence enables us to capture complex relationships easily.

4.1. Interface Estimation

We define each interface as a two-dimensional (2-D) field (e.g., a surface in the 3-D domain). We denote the interface at i th pixel by d_i , where $i = 1, \dots, n$. The goal is to estimate the posterior distribution $p(\{d_i\}|\mathbf{z}_{\text{ERT}}, \mathbf{z}_{\text{IP}}, \mathbf{z}_{\text{L}})$ of the interface field $\{d_i\}$ (i.e., the interface at all the pixels), conditioned on the ERT data (resistivity) \mathbf{z}_{ERT} , the IP data \mathbf{z}_{IP} , and well log data \mathbf{z}_{L} . By applying the Bayes' rule under the assumption that \mathbf{z}_{ERT} , \mathbf{z}_{IP} , and \mathbf{z}_{L} are conditionally independent given the interface locations $\{d_i\}$, we can write the posterior distribution of the interface field as $p(\{d_i\}|\mathbf{z}_{\text{ERT}}, \mathbf{z}_{\text{IP}}, \mathbf{z}_{\text{L}}) \propto p(\mathbf{z}_{\text{ERT}}|\{d_i\}) p(\mathbf{z}_{\text{IP}}|\{d_i\}) p(\{d_i\}|\mathbf{z}_{\text{L}})$, where C_{ERT} and C_{IP} are indices of pixels that are collocated either with ERT or IP data, respectively.

The first two conditional distributions $p(\mathbf{z}_{\text{ERT}}|\{d_i\})$ and $p(\mathbf{z}_{\text{IP}}|\{d_i\})$ represent the data model, specifically the dependence of the interface depth on data value at each pixel. At the geophysical data locations ($i \in C_{\text{ERT}}$ and $i \in C_{\text{IP}}$), we assume that the data values can be described by $z_{\text{ERT},i} = a_1 d_i + a_2 + \varepsilon_{\text{ERT}}$ and $z_{\text{IP},i} = b_1 d_i + b_2 + \varepsilon_{\text{IP}}$, where ε_{ERT} and ε_{IP} are the error terms associated with the uncertainty and/or variability of the correlations between the interface depths and ERT/IP imaging results (Figures 3a–3c), and a_l and b_l ($l = 1, 2$) are the linear-fitting terms to fix the bias from the one-to-one line in Figures 3a–3c. We also assume that ε_{ERT} and ε_{IP} follow the independent normal distribution with zero-mean and the variance σ_{ERT} and σ_{IP} , determined from the correlation plots (Figures 3a–3c).

Furthermore, we assume that $\{d_i\}$ is a multivariate Gaussian random field described by geostatistical parameters, we can derive an analytical form of this posterior distribution as a multivariate normal distribution with mean $Q^{-1}\mathbf{g}$ and variance Q^{-1} , where $Q = \Sigma_c^{-1} + A_{\text{ERT}}^T D_{\text{ERT}}^{-1} A_{\text{ERT}} + A_{\text{IP}}^T D_{\text{IP}}^{-1} A_{\text{IP}}$ and $\mathbf{g} = \Sigma_c^{-1} \boldsymbol{\mu}_c + A_{\text{ERT}}^T D_{\text{ERT}}^{-1} \mathbf{z}_{\text{ERT}} + A_{\text{IP}}^T D_{\text{IP}}^{-1} \mathbf{z}_{\text{IP}}$ (Appendix A). In Q and \mathbf{g} , $\boldsymbol{\mu}_c$ and Σ_c are the conditional mean and covariance given the point (i.e., well) data and geostatistical parameters. D_{ERT} and D_{IP} are the data covariance matrices; each of the diagonal components is σ_{ERT} and σ_{IP} . A_{ERT} and A_{IP} are m_{ERT} -by- n and m_{IP} -by- n sparse matrices, where $A_{\text{ERT},ji} = 1$ if i th pixel has j th data point; otherwise $A_{\text{ERT},ji}$ is 0. m_{ERT} and m_{IP} are the number of data points of ERT and IP, respectively.

4.2. Natural Reduced Zone Estimation

To map the NRZ locations, we define a indicator random field $\{f_i\}$ in the 3-D domain ($i = 1, \dots, n_{3D}$) such that

$$f_i = \begin{cases} 1, & \text{if } i\text{th pixel is in NRZs} \\ 0, & \text{otherwise} \end{cases} \quad (1)$$

We consider the resistivity and phase shift as the data vectors for resistivity (\mathbf{r}) and phase shift (ϕ). Each data point has the data values r_i and ϕ_i at a subset of pixels collocated with the IP data locations ($i \in C_{\text{IP},3D}$). We also define the depth-discrete well log data vector $\mathbf{z}_{W,3D}$, each element of which is either 0 or 1, since they are the direct measurements of indicators.

As a data model, we follow previous studies that defined geophysical data values having distinct distributions, depending on the indicator type [Chen *et al.*, 2004, 2006; Wainwright *et al.*, 2014]. We assume that the resistivity and phase shift in i th pixel (r_i and ϕ_i) follow distinct bivariate distributions, depending on whether i th pixel is in a NRZ ($f_i = 1$) or not ($f_i = 0$). Instead of univariate distributions used in previous studies [Chen *et al.*, 2006; Wainwright *et al.*, 2014], we assume that the bivariate distributions can represent the correlation coefficients found in the data sets (Figure 4b). We have two sets of distributions:

$$\begin{aligned} p(r_i, \phi_i | f_i = 0, \Phi_0) &= \text{BiN}(\boldsymbol{\mu}_0, \Phi_0) \\ p(r_i, \phi_i | f_i = 1, \Phi_1) &= \text{BiN}(\boldsymbol{\mu}_1, \Phi_1) \end{aligned} \quad (2)$$

where BiN represents the bivariate normal distribution with the mean vector $\boldsymbol{\mu}_l$ and the two-by-two covariance matrix Φ_l ($l = 0, 1$). The mean vector $\boldsymbol{\mu}_1$, for example, includes the mean resistivity and mean phase shift at the NRZ locations ($f_i = 1$). The covariance matrix is a function of the resistivity variance, phase shift variance, and their correlation coefficient (shown in Figure 4b). We assume that the covariance is uncertain and needs to be estimated, since the variances tend to be underestimated from a limited number of samples. We estimate the covariance matrices Φ_0 and Φ_1 together in the estimation. The data parameter matrix is defined as $\boldsymbol{\alpha} = \{\Phi_0, \Phi_1\}$.

The goal is to estimate the joint posterior distribution of the indicator field $\{f_i\}$ conditioned on the IP data (\mathbf{r} and ϕ) and well log data ($\mathbf{z}_{W,3D}$), which is the marginal distribution of $p(\{f_i\}, \boldsymbol{\alpha} | \mathbf{r}, \phi, \mathbf{z}_{W,3D})$. By assuming resistivity and phase pairs are independent given indicator variable, $\{f_i\}$, and using the Bayes rule, we can write this posterior distribution as:

$$\begin{aligned} p(\{f_i\}, \boldsymbol{\alpha} | \mathbf{r}, \phi, \mathbf{z}_{W,3D}) &\propto p(\mathbf{r}, \phi | \{f_i, i \in C_{\text{IP},3D}\}, \boldsymbol{\alpha}) p(\{f_i\} | \mathbf{z}_{W,3D}) p(\boldsymbol{\alpha}), \\ &= \prod_{i \in C_{\text{IP},3D}} p(r_i, \phi_i | f_i, \boldsymbol{\alpha}) p(\{f_i\} | \mathbf{z}_{W,3D}) p(\boldsymbol{\alpha}), \\ &= \prod_{i \in C_{\text{IP},3D}, f_i=0} p(r_i, \phi_i | f_i = 0, \Phi_0) \prod_{i \in C_{\text{IP},3D}, f_i=1} p(r_i, \phi_i | f_i = 1, \Phi_1) \\ &= p(\{f_i\} | \mathbf{z}_{W,3D}) p(\boldsymbol{\alpha}). \end{aligned} \quad (3)$$

The first conditional distribution $p(\mathbf{r}, \phi | \{f_i | i \in C_{\text{IP},3D}\}, \boldsymbol{\alpha})$ is a data model that defines the distribution of the data values given the occurrence of an NRZ or not, which is defined in equation (2). The latter conditional distribution $p(\{f_i\} | \mathbf{z}_{W,3D})$ represents the indicator field given the depth-discrete well log data as conditional points. The prior distribution must be defined for the covariances as $p(\boldsymbol{\alpha})$.

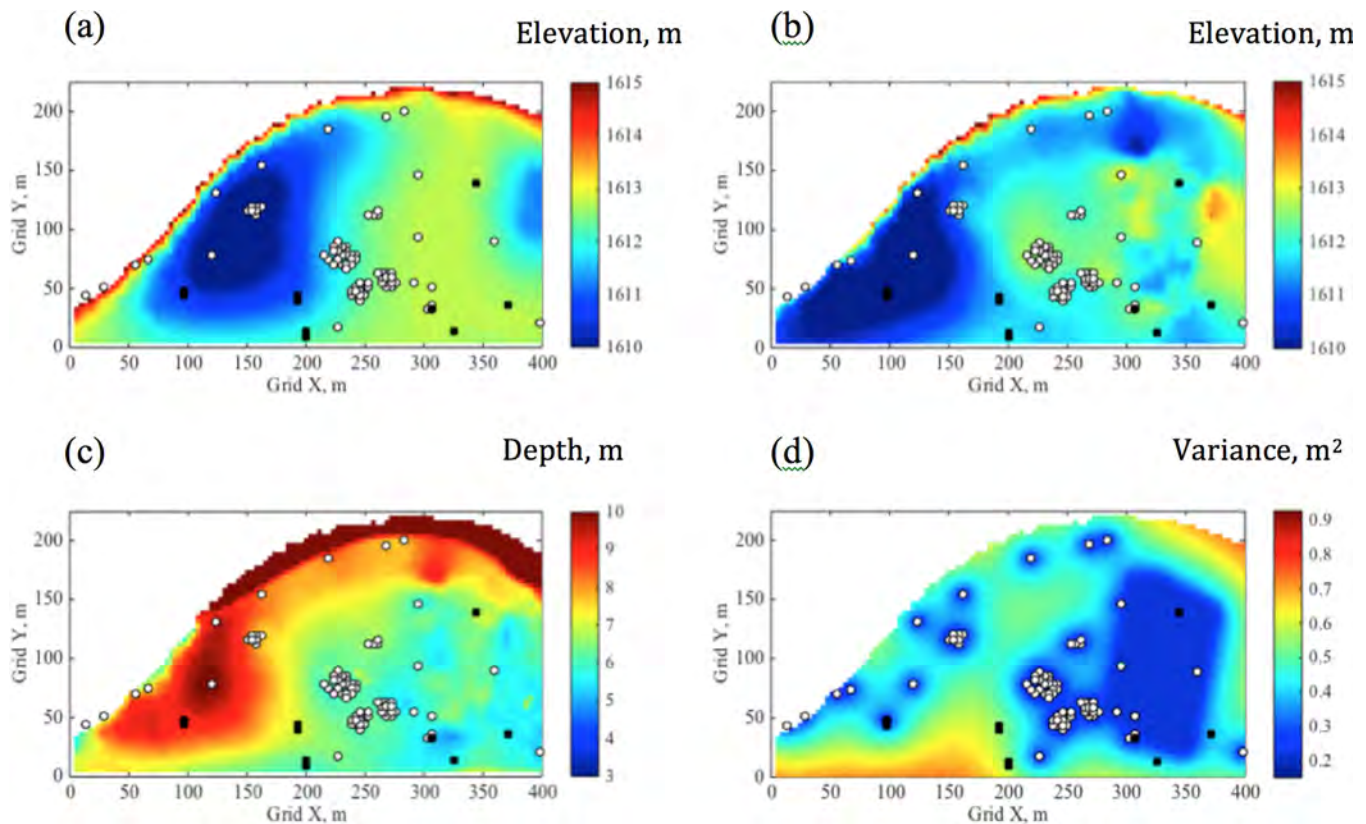


Figure 6. Rifle-Wasatch interface estimation results: (a) the previously estimated elevation in meters, (b) the mean estimate of the elevation in meters, (c) the depth in meters, and (d) the estimation variance in squared meters. The white circles are the well locations used for the estimation, and the black circles are the well locations used for validation.

To define $p(\{f_i\}|\mathbf{z}_{W,3D})$, we follow the approach developed by *Chen et al.* [2006]. Here $\{f_i\}$ is an indicator field such that the facies at each element f_i has a Bernoulli distribution given by:

$$p(f_i=1|\mathbf{z}_{W,3D}, \{f_{i,k \neq i}\}) = \text{Bernoulli}(p_i^*), \quad (4)$$

where p_i^* can be determined by simple indicator kriging:

$$p_i^* = \mu + \sum_{k \neq i} c_k (f_k - \mu), \quad (5)$$

where μ is the overall mean. Note that p_i is truncated within $[0, 1]$. The kriging coefficients c_k 's are a function of the correlation length and sill, derived from the exponential variogram model, and the distance between Pixel k and Pixel i . In this study, we assume that they are fixed and determined by the variogram analysis.

We use MCMC methods to sample from the joint posterior distribution $p(\{f_i\}|\mathbf{r}, \phi, \mathbf{z}_{W,3D})$, which is the marginal distribution of $p(\{f_i\}, \alpha|\mathbf{r}, \phi, \mathbf{z}_{W,3D})$. The MCMC sampling requires formulation of the probability distribution of each parameter c conditioned on the other parameters and all data sets. We sample the indicator at each pixel f_i .

$$p(f_i|\mathbf{r}, \phi, \mathbf{z}_{W,3D}, \{f_{k,k \neq i}\}, \alpha) \propto p(r_i, \phi_i|f_i, \alpha) p(f_i|\mathbf{z}_{W,3D}, \{f_{k,k \neq i}\}). \quad (6)$$

With a mathematical manipulation similar to that used in *Chen et al.* [2006], we can arrive at an analytical form of the distribution. The indicator f_i follows a Bernoulli distribution with the probability:

$$p(f_i=1|r_i, \phi_i, \{f_{k,k \neq i}\}, \alpha, \mathbf{z}_{W,3D}) = \frac{p_1 p_i^*}{p_1 p_i^* + p_0 (1 - p_i^*)}. \quad (7)$$

where $p_0 = p(r_i, \phi_i|f_i=0, \Phi_0)$ and $p_1 = p(r_i, \phi_i|f_i=1, \Phi_1)$, both of which are defined in equation (2) and represent likelihood information from the IP data.

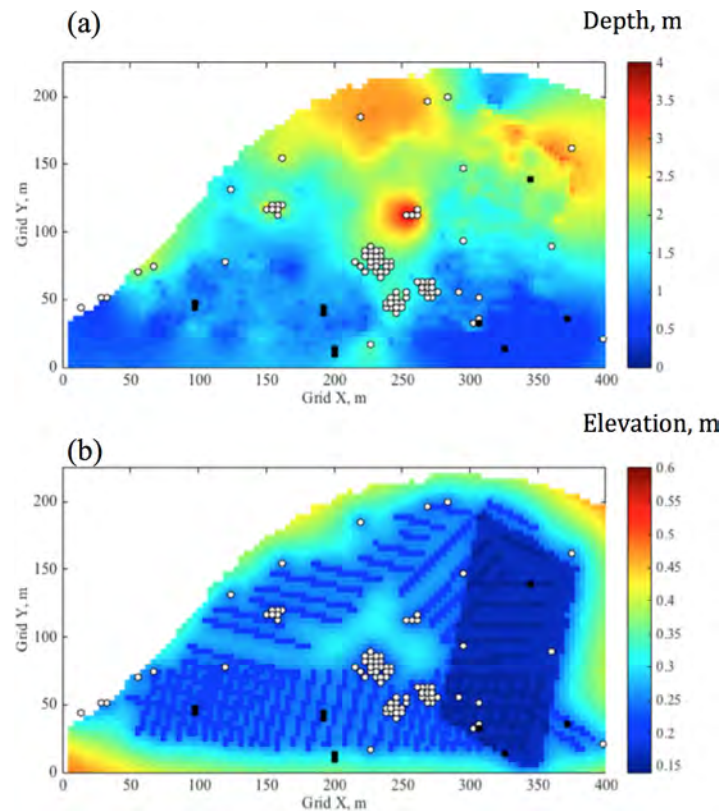


Figure 7. Fill-Rifle Interface estimation results: (a) the mean estimate of the depth in meters and (b) the variance in squared meters. The white circles are the well locations used for the estimation, and the black circles are the well locations used for validation.

To sample the covariance matrices in α (Φ_0 and Φ_1), we follow a similar approach to the univariate case developed by *Chen et al.* [2006]. While *Chen et al.* [2006] used the inverse gamma distribution as a conjugate prior, we use the Wishart distribution, which is multidimensional generalization of the inverse gamma distribution [Murphy, 2007]. We assume that the prior distribution for each of the covariance matrices (Φ_0 and Φ_1) is an inverse Wishart distribution with the degree of freedom m_0 and m_1 , and the inverse-scale matrices Ψ_0 and Ψ_1 , respectively. We determined these parameters from the collocated data sets shown in Figure 4b [Chen et al., 2006]. Since the inverse Wishart distribution is a conjugate prior for the covariance of a multivariate normal distribution, the posterior of Φ_0 and Φ_1 are defined by the inverse Wishart distribution (IW):

$$p(\Phi_l|\bullet) \sim IW(m_l + n_l, X^T X), \quad (8)$$

where $X = \{r - E[r], \phi - E[\phi]\}$ ($E[\cdot]$ is the mean), n_l is the number of IP data locations where $f_l = l$ ($l = 0$ or 1). In the MCMC sequence, we sample each pixel of $\{f_l\}$ and α sequentially. Since their conditional distributions are

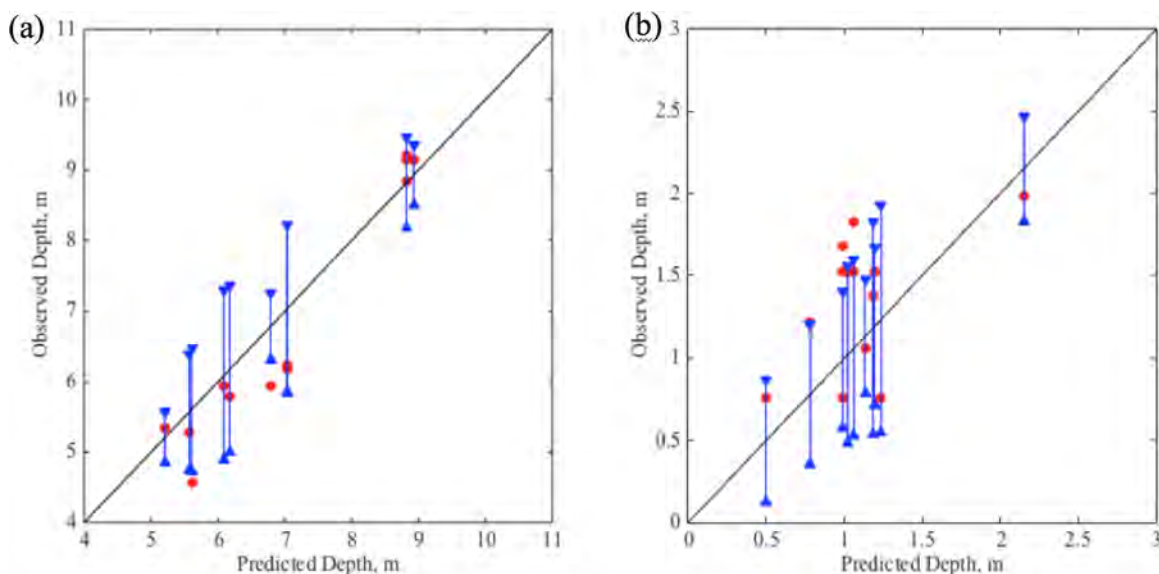


Figure 8. Estimated mean and confidence interval compared with the interpretations from the well data not used in the estimation; (a) the Rifle-Wasatch interface depth and (b) Rifle-Fill interface depth. The red dots represent the interfaces at wells, the blue lines are the confidence intervals based on the standard deviation (STD) multiplied by two, and the black lines are the one-to-one line.

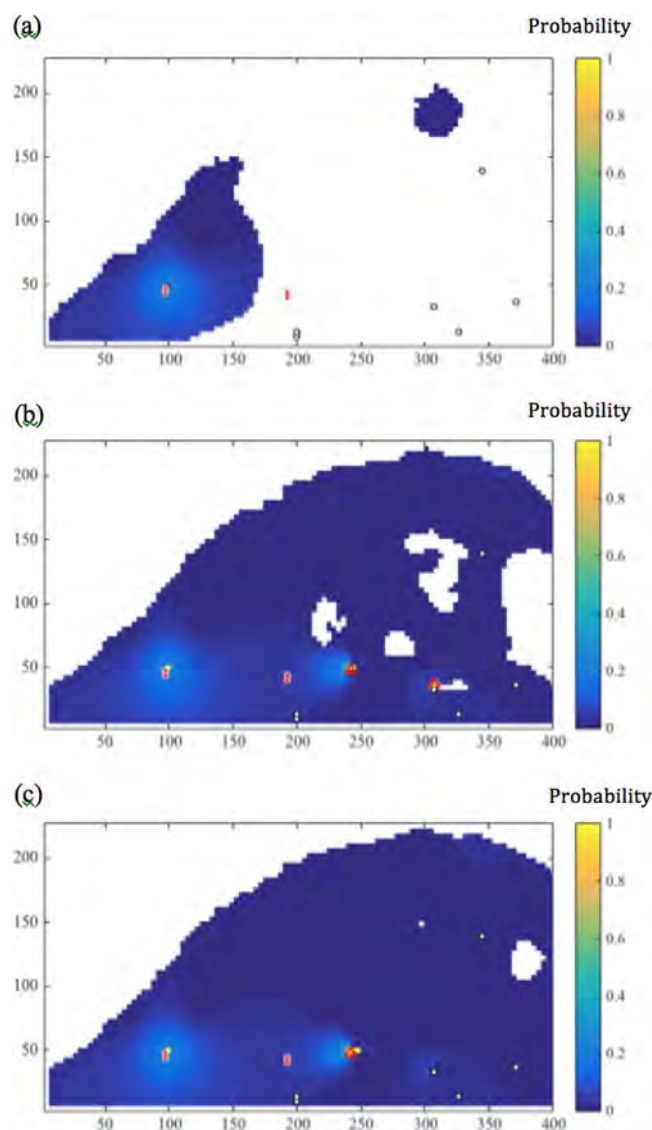


Figure 9. Probability field of NRZs based on well data only; 2-D horizontal slices at elevations (a) 1611.6 m, (b) 1613.2 m, and (c) 1613.8 m. The red filled circles are the wells that were confirmed to have NRZs, and the white circles are the wells that were confirmed not to have NRZs. These are validation wells, not included in the estimation. The red triangles were the NRZ sample locations in *Campbell et al.* [2012] and *Qafoku et al.* [2014]. The white region is either outside of the domain or outside of the Rifle Formation.

in addition, ERT identified the connectivity (or channel) between the depressions in the Rifle-Wasatch interface along the northern part of this floodplain ($x = 250\text{--}350$ m and $y = 150\text{--}200$ m). We interpret this channel to represent a former paleochannel of the Colorado River and a potential local control on groundwater flow direction in this area. The Wasatch Formation depth (Figure 6c) is highly variable (4–10 m) over the floodplain. The variance in Figure 6d represents the uncertainty associated with this mean estimate. This variance is smaller around the wells and ERT locations, since the estimate is better constrained by the data sets in their vicinity.

Figure 7 shows the mean estimate and variance of the Rifle-fill interface depth. In Figure 7a, we find that the fill layer is thicker in the northern portion of the floodplain, where soil contamination extended over a greater vertical profile. The southern portion near the river has a thinner layer reflecting the minimal need for excavation and removal of surficial soils in this area. In Figure 7b, the estimation variance is smaller near the ERT and IP data locations, meaning that there is lower uncertainty in the estimate for this region. Owing to its lower permeability, the fill layer is known to control infiltration into groundwater as well as evapotranspiration near the

known analytical distributions, we use Gibbs sampling, which is quite efficient compared to the other MCMC sampling methods.

5. Estimation Results and Discussions

5.1. Interface Estimation

We estimated the interfaces at each grid in the domain as needed for input into a biogeochemical model over the floodplain. The grid size is 3.8 m by 3.8 m, and the domain size is 400 m by 229 m. For the Rifle-Wasatch interface, there is a previously estimated interface elevation available, which is based on well data, outcrop, and geological observations. We estimated the difference from these previous estimates, by honoring the outcrop and geological observations, as well as wellbore and geophysical data. For the estimation, we only computed the mean and variance fields on the interfaces, rather than random fields, since most reactive transport models require fixed interfaces. However, it is possible to sample the random fields of the interfaces for stochastic simulations to include the uncertainty in interface estimates.

Figure 6 shows the Rifle-Wasatch interface elevation, including the previously estimated elevation (Figure 6a), mean estimation of the elevation (Figure 6b), and the mean estimation of depths and variance (Figure 6c). Compared to the previous estimation (Figure 6a), the new estimation (Figure 6b) captures more detailed heterogeneity around the ERT locations, even between wells. In addition,

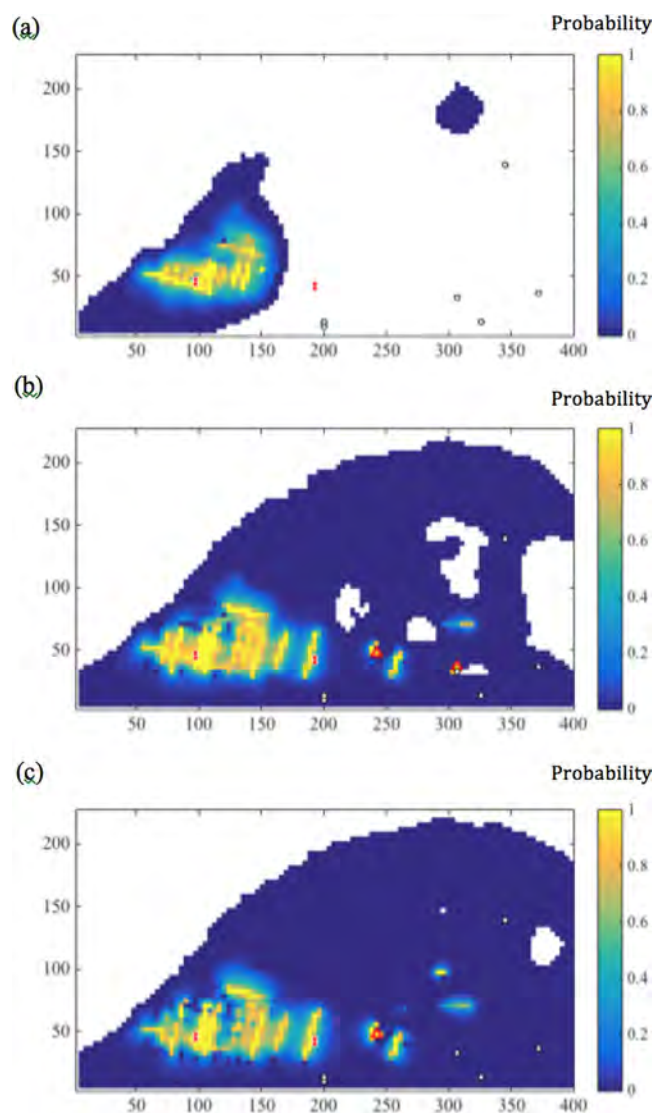


Figure 10. Posterior probability field of NRZs based on wells and TDIP data; 2-D horizontal slices at elevations (a) 1611.6 m, (b) 1613.2 m, and (c) 1613.8 m. The red filled circles are the wells that were confirmed to have NRZs (based on well-bore lithology), and the white circles are the wells that were confirmed not to have NRZs. These are validation wells, not included in the estimation. The red triangles were the NRZ sample locations in *Campbell et al.* [2012] and *Qafoku et al.* [2014]. The white region is either outside of the domain or outside of the Rifle Formation.

the cells within the Rifle Formation were considered, based on the interfaces estimated in Figures 6 and 7. Geostatistical parameters (i.e., mean, variance, and correlation length) were determined based on the lithological logs. We used the MCMC approach to generate 20,000 samples of the NRZ indicator field, the convergence of which was confirmed by the Geweke's convergence diagnostic [Geweke, 1992]. Wells installed prior to 2013 were used as conditioning data in the estimation, with 16 new wells installed in 2014 used as validation data to evaluate the performance of the estimation.

We compared two cases in the results: (1) well data only (Figure 9) and (2) well and TDIP data (Figure 10). In Figure 9, we see that the well-only case does not capture any of the major NRZs due to the lack of data. Capturing the full NRZ extent would require installation of innumerable wells at a cost that is prohibitive or logistically impossible. In Figure 10, including TDIP data allows us to capture the extent of NRZs, particularly in the western portion of the floodplain near the river ($x = 50\text{--}200$ m and $y = 30\text{--}100$ m). The additional high-probability regions appeared in Figure 10 (compared to Figure 9) is attributed to the TDIP data set. The results indicate that

surface. Since there is no record of the fill-layer thickness postreclamation, this newly derived, site-wide thickness estimate will be important for hydrobiogeochemical modeling at the site.

To validate the estimation results, Figure 8 shows a comparison of the estimated interface mean value and confidence interval, with the colocated (well-determined) interfaces not used in the estimation procedure. Among the 187 wells, 16 new wells (installed in 2014) were selected as validation wells (not used for estimation). We did not use this subset of wells for our estimation in order to simulate the situation that researchers would encounter when they plan well locations based on geophysical images and estimation results. The Wasatch depths (Figure 8a) are closely estimated at most of the locations (i.e., the confidence intervals capture the true depths), although the confidence intervals are larger for the wells that are away from the existing wells or ERT locations. Figure 8b shows that the true fill depth at the validation points is close to the mean estimates and mostly within the confidence intervals. Confidence intervals are wider for the validation wells far away from the conditioning wells or geophysical data. The comparison of the two figures suggests that the resistivity method is useful—indeed necessary—to estimate the spatially heterogeneous interfaces successfully.

5.2. NRZ Estimation Results

The presence or absence of NRZs was estimated within a 3-D hydrobiogeochemical modeling domain being developed in parallel to this study. Only

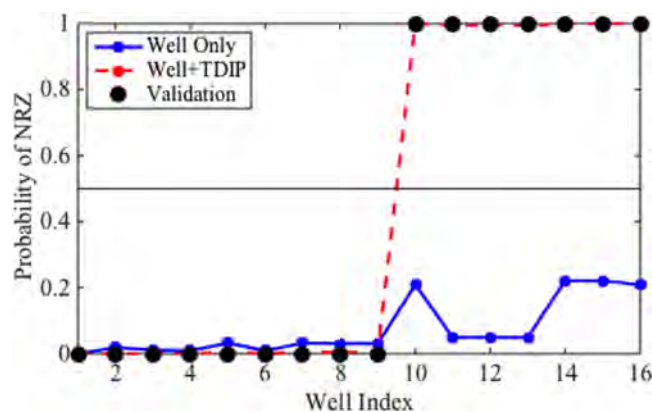


Figure 11. Probability of finding NRZs at each validation well. The lines are the probability computed based on well data only (blue) and bivariate data (phase shift and resistivity; red). The black dots represent the observations not used in the estimation; the value is 1 if the well is located within a NRZ, and 0 otherwise.

or close to zero at the observed non-NRZ locations. The well-only case does not capture any of the NRZ locations, since the probability is zero at those locations. These findings support the claim that it is impossible to characterize the full spatial extent of NRZs with well data only and that IP measurements greatly improve the mapping of NRZs.

Figure 12 shows the 3-D distribution of the high-probability region of NRZs (with threshold of 0.5) along with the two estimated interfaces. Both the interfaces and NRZ locations can be directly implemented in hydrobiogeochemical simulations serving to parameterize the modeling domain with regions inferred to have an outsized influence on reactions of interest (e.g., hot spot locations). In Figures 10 and 12, we find that the NRZs are generally parallel to and located 20–50 m from the active margin of the Colorado River (N.B. Closer access to the active river margin itself is impeded due to the presence of a railway corridor). Previous studies [Campbell *et al.*, 2012; Qafoku *et al.*, 2014; Janot *et al.*, 2015] found close association between NRZs and fine and/or organic-rich sediments. In fact, fine-grained and organic-rich sediments are often found near the river, based on the lithological descriptions. Based on this study, we may assume that those identified NRZ locations are the regions where fine-grained sediments were deposited.

6. Conclusion

In this study, we developed a methodology to integrate geophysical and wellbore data for mapping naturally reduced zones (NRZs) in a minimally invasive manner and to help biogeochemical model parameteriza-

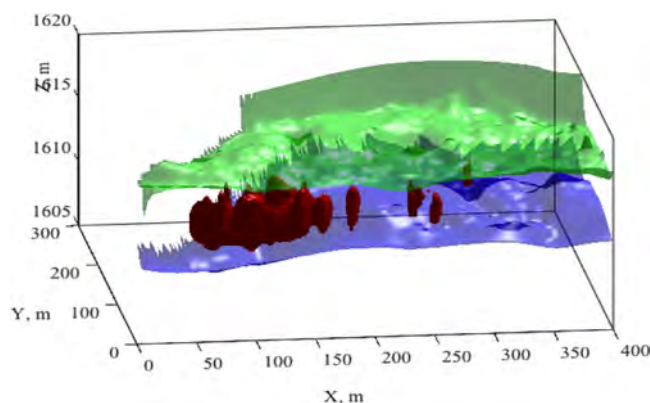


Figure 12. A three-dimensional modeling domain with the Rifle-Fill interface (green), Wasatch-Rifle interface (blue), and the high-probability region of naturally reduced zones (NRZs; red). To create the volume of the high-probability region, we used the threshold probability of 0.5.

NRZs are generally located in proximity to the active river margin and in portions of the aquifer where the depth to the Wasatch Formation is deeper (Figure 6).

To evaluate the performance of our estimation, we compared the predicted NRZ probabilities and observed NRZ indicators at the validation well locations. In Figure 11, the probability of finding an NRZ at each well is shown and compared with the indicator representing whether an NRZ was found at the well. The figure shows that when we used both wellbore and TDIP data, the probability is one or close to one at all the observed NRZ locations and zero

at the observed non-NRZ locations. Our study builds upon previous studies at the site that identified NRZs using detailed geochemical and microbial characterization [Campbell *et al.*, 2012; Qafoku *et al.*, 2014], as well as studies that used IP techniques to detect changes in subsurface redox conditions [Williams *et al.*, 2009; Flores Orozco *et al.*, 2011, 2013; Chen *et al.*, 2013]. Our approach took advantage of the data-defined correlations among collocated geochemical samples, lithological log data, and geophysical data. A Bayesian hierarchical method enabled us to integrate these data for

estimating the hydrostratigraphic interfaces, as well as the probability of NRZ presence or absence over the dimensions of the floodplain. This is the first study to demonstrate the ability of TDIP imaging surveys for characterizing hot spots that have unique distributions of subsurface lithological and biogeochemical properties.

Many recent studies use Bayesian or stochastic joint inversion approaches to estimate hydrological parameters or geological units directly from geophysical data sets by including geophysical forward models in the estimation framework [e.g., *Chen et al.*, 2004; *Chen and Hoversten*, 2012; *Dafflon and Barrash*, 2012; *Wainwright et al.*, 2014; *Hermans et al.*, 2015]. Such approaches, however, are computationally intensive and difficult to deploy in a 3-D setting over a large spatial domain. The two-step approach presented here—geophysical inversion first and then estimation along with other data sets—is flexible and computationally frugal enough to integrate multiple types of data sets together in a 3-D domain over a floodplain. Statistical analyses at collocated wells enabled us to identify correlations between inverted data and borehole data. This study also showed that it is important to evaluate various polarization-generating mechanisms for an improved interpretation of IP images particularly where the unambiguous delineation of NRZs is concerned.

As with the previous studies [*Sassen et al.*, 2012; *Wainwright et al.*, 2014], this study showed that the zonation approach is very powerful in transferring the information and parameters from grain-scale laboratory measurements to the field scale. Detailed biogeochemical characterization is often prohibitively expensive and time consuming, such that it is generally impossible to obtain sufficient data to fully constrain many natural environments owing to their large size and inherent heterogeneity. By exploiting spatially extensive geophysical data sets and correlations among various data sets, we can capture the subsurface heterogeneity required for parameterizing hydrobiogeochemical models.

The approach developed in this study can be transferable to other floodplains or other near-surface terrestrial environments, advancing the characterization of biogeochemical hot spots in a minimally invasive manner and distributing critical biogeochemical properties across scales. Future development should include the use of geophysical monitoring to use a temporal signature for estimating dynamic properties associated with NRZs and non-NRZs (such as changes in pore water chemistry) and also for further refining the estimation of hydraulic and geochemical properties (e.g., permeability, porosity, and texture). Another important refinement will be to couple geophysical methods and remote sensing techniques. While the denitrification hot spots by *Duncan et al.* [2013] have been mapped in 2-D as an “area” over the catchment, geophysical methods could provide more refined estimates of their depth distribution, and hence could provide the 3-D volume of biogeochemical hot spots. Although the IP measurements presented here are labor intensive and are unlikely to be taken to the catchment scale, correlating the subsurface signatures (from geophysical data) and surface structures (from remote sensing data) could help upscaling the subsurface properties to a much larger scale [e.g., *Wainwright et al.*, 2015]. Probabilistic mapping—such as the one presented here—will be essential for such a large-scale characterization due to increased uncertainty and disparity of scales among data sets.

Appendix A: Analytical Form of $p(\{d_i\}|\mathbf{z}_{\text{ERT}}, \mathbf{z}_{\text{IP}}, \mathbf{z}_{\text{L}})$

To estimate the posterior distribution of the interface $\{d_i\}$, we derive the analytical form of $p(\{d_i\}|\mathbf{z}_{\text{ERT}}, \mathbf{z}_{\text{IP}}, \mathbf{z}_{\text{L}})$ defined in section 2.1. Following the data model definition, we write the ERT and IP data vector by

$$\begin{aligned}\mathbf{z}_{\text{ERT}} &\sim \text{MVN}(\mathbf{A}_{\text{ERT}}\{d_i\}, \mathbf{D}_{\text{ERT}}), \\ \mathbf{z}_{\text{IP}} &\sim \text{MVN}(\mathbf{A}_{\text{IP}}\{d_i\}, \mathbf{D}_{\text{IP}}),\end{aligned}\tag{A1}$$

where MVN represents the multivariate normal distribution, and \mathbf{D}_{ERT} and \mathbf{D}_{IP} are the data error matrices, only having the diagonal components of σ_{ERT} and σ_{IP} , respectively. \mathbf{A}_{ERT} and \mathbf{A}_{IP} are sparse matrices to connect the interface depth value at each pixel and the data point such that

$$A_{\text{ERT},ji} = \begin{cases} 1 & \text{if } i\text{th pixel is } j\text{th ERT data point} \\ 0 & \text{otherwise.} \end{cases}$$

and

$$A_{IP,ji} = \begin{cases} 1 & \text{if } i\text{th pixel is } j\text{th IP data point} \\ 0 & \text{otherwise} \end{cases} \quad (A2)$$

We can write the posterior distribution of the interface as:

$$\begin{aligned} p(\{d_i\} | \mathbf{z}_{ERT}, \mathbf{z}_{IP}, \mathbf{z}_L) &\propto p(\mathbf{z}_{ERT} | \{d_i\}) p(\mathbf{z}_{IP} | \{d_i\}) p(\{d_i\} | \mathbf{z}_L), \\ &\propto \exp \left[-\frac{1}{2} (\mathbf{z}_{ERT} - A_{ERT} \{d_i\})^T D_{ERT}^{-1} (\mathbf{z}_{ERT} - A_{ERT} \{d_i\}) \right] \\ &\exp \left[-\frac{1}{2} (\mathbf{z}_{IP} - A_{IP} \{d_i\})^T D_{IP}^{-1} (\mathbf{z}_{IP} - A_{IP} \{d_i\}) \right] \exp \left[-\frac{1}{2} (\{d_i\} - \boldsymbol{\mu}_c)^T \boldsymbol{\Sigma}_c^{-1} (\{d_i\} - \boldsymbol{\mu}_c) \right]. \end{aligned} \quad (A3)$$

Since both ERT and IP data are linear functions of interface depths according to equations (A1) and (A2), the resultant posterior distribution has a multivariate Gaussian distribution, which is given below:

$$p(\{d_i\} | \mathbf{z}_{ERT}, \mathbf{z}_{IP}, \mathbf{z}_L) \propto \exp \left[-\frac{1}{2} (\{d_i\} - Q^{-1} \mathbf{g})^T Q (\{d_i\} - Q^{-1} \mathbf{g}) \right]. \quad (A4)$$

where

$$\begin{aligned} Q &= \boldsymbol{\Sigma}_c^{-1} + A_{ERT}^T D_{ERT}^{-1} A_{ERT} + A_{IP}^T D_{IP}^{-1} A_{IP}, \\ \mathbf{g} &= \boldsymbol{\Sigma}_c^{-1} \boldsymbol{\mu}_c + A_{ERT} D_{ERT}^{-1} \mathbf{z}_{ERT} + A_{IP} D_{IP}^{-1} \mathbf{z}_{IP}, \end{aligned} \quad (A5)$$

$\{d_i\}$ is the multivariate normal distribution with the mean $Q^{-1} \mathbf{g}$ and covariance Q^{-1} .

Acknowledgment

This material is partially based upon work supported through the Lawrence Berkeley National Laboratory's Sustainable Systems Scientific Focus Area (SFA). The U.S. Department of Energy (DOE), Office of Science, and Office of Biological and Environmental Research funded the work under contract DE-AC02-05CH11231 (Lawrence Berkeley National Laboratory; operated by the University of California). We would like to thank Joel Rowland at Los Alamos National Laboratory for providing advice that helped to strengthen the conceptual model of floodplain-related hot spots. Data sets are available upon request by contacting the corresponding author (Haruko M. Wainwright, hmwainwright@lbl.gov).

References

- Abdel Aal, G. Z., E. A. Atekwana, and A. Revil (2014), Geophysical signatures of disseminated iron minerals: A proxy for understanding subsurface biophysicochemical processes, *J. Geophys. Res. Biogeosci.*, *119*, 1831–1849, doi:10.1002/2014JG002659.
- Anderson, T., P. Groffman, and M. Walter (2015), Using a soil topographic index to distribute denitrification fluxes across a northeastern headwater catchment, *J. Hydrol.*, *522*, 123–134, doi:10.1016/j.jhydrol.2014.12.043.
- Archie, G. (1942), The electrical resistivity log as an aid in determining some reservoir characteristics, *Trans. AIME*, *146*, 54–62.
- Arora, B., et al. (2015a), Influence of hydrological, biogeochemical and temperature transients on subsurface carbon fluxes in a flood plain Environment, *Biogeochemistry*, doi:10.1007/s10533-016-0186-8, in press.
- Arora, B., D. Dwivedi, N. F. Spycher, and C. I. Steefel (2015b), Modeling processes affecting carbon dynamics at a biogeochemical hotspot in a floodplain aquifer, in *Proceedings of the TOUGH Symposium 2015*, pp. 456–463, Lawrence Berkeley National Laboratory, Berkeley, Calif.
- Aufdenkampe, A. K., E. Mayorga, P. A. Raymond, J. M. Melack, S. C. Doney, S. R. Alin, and K. Yoo (2011), Riverine coupling of biogeochemical cycles between land, oceans, and atmosphere, *Frontiers Ecol. Environ.*, *9*(1), 53–60.
- Battin, T. J., L. A. Kaplan, S. Findlay, C. S. Hopkinson, E. Marti, A. I. Packman, J. D. Newbold, and F. Sabate (2008), Biophysical controls on organic carbon fluxes in fluvial networks, *Nat. Geosci.*, *1*(2), 95–100, doi:10.1038/ngeo101.
- Battin, T. J., S. Luysaert, L. A. Kaplan, A. K. Aufdenkampe, A. Richter, and L. J. Tranvik (2009), The boundless carbon cycle, *Nat. Geosci.*, *2*(9), 598–600, doi:10.1038/ngeo618.
- Binley, A., and A. Kemna (2005), DC resistivity and induced polarization methods, in *Hydrogeophysics*, edited by Y. Rubin and S. Hubbard, pp. 129–156, Springer, Dordrecht, Netherlands, doi:10.1007/1-4020-3102-5_5.
- Binley, A., L. D. Slater, M. Fukes, and G. Cassiani (2005), Relationship between spectral induced polarization and hydraulic properties of saturated and unsaturated sandstone, *Water Resour. Res.*, *41*, W12417, doi:10.1029/2005WR004202.
- Binley, A., S. S. Hubbard, J. A. Huisman, A. Revil, D. A. Robinson, K. Singha, and L. D. Slater (2015), The emergence of hydrogeophysics for improved understanding of subsurface processes over multiple scales, *Water Resour. Res.*, *51*, 3837–3866, doi:10.1002/2015WR017016.
- Blaschek, R., A. Hördt, and A. Kemna (2008), A new sensitivity-controlled focusing regularization scheme for the inversion of induced polarization data based on the minimum gradient support, *Geophysics*, *73*, F45–F54.
- Börner, F. D., J. R. Schopper, and A. Weller (1996), Evaluation of transport and storage properties in the soil and groundwater zone from induced polarization measurements, *Geophys. Prospect.*, *44*, 583–601, doi:10.1111/j.1365-2478.1996.tb00167.x.
- Bowling, J. C., A. B. Rodriguez, D. L. Harry, and C. Zheng (2005), Delineating alluvial aquifer heterogeneity using resistivity and GPR data, *Ground Water*, *43*(6), 890–903.
- Bücker, M., and A. Hördt (2013), Analytical modelling of membrane polarization with explicit parametrization of pore radii and the electrical double layer, *Geophys. J. Int.*, *194*(2), 804–813.
- Campbell, K. M., et al. (2012), Characterizing the extent and role of natural subsurface bioreduction in a uranium-contaminated aquifer, *Appl. Geochem.*, *27*, 1499–1511.
- Capps, K., R. Rancatti, N. Tomczyk, T. Parr, A. Calhoun, and M. Hunter (2014), Biogeochemical hotspots in forested landscapes: The role of vernal pools in denitrification and organic matter processing, *Ecosystems*, *17*(8), 1455–1468, doi:10.1007/s10021-014-9807-z.
- Castelle, C. J., L. A. Hug, K. C. Wrighton, B. C. Thomas, K. H. Williams, D. Wu, S. G. Tringe, S. W. Singer, J. A. Eisen, and J. F. Banfield (2013), Extraordinary phylogenetic diversity and metabolic versatility in aquifer sediment, *Nat. Commun.*, *4*, 2120.
- Caterina, D., T. Hermans, and F. Nguyen (2014), Case studies of incorporation of prior information in electrical resistivity tomography: Comparison of different approaches, *Near Surf. Geophys.*, *12*(4), 451–465.
- Chen, J., and M. Hoversten (2012), Joint inversion of marine seismic AVA and CSEM data using statistical rock-physics models and Markov random fields, *Geophysics*, *77*, R65–R80, doi:10.1190/GEO2011-0219.1.

- Chen, J., S. Hubbard, Y. Rubin, C. Murray, E. Roden and E. Majer (2004), Geochemical characterization using geophysical data and Markov chain Monte Carlo methods: A case study at the South Oyster Bacterial Transport Site in Virginia, *Water Resour. Res.*, *40*, W12412, doi:10.1029/2003WR002883.
- Chen, J., S. S. Hubbard, J. E. Peterson, K. Williams, M. Fioren, P. Jardine, and D. Watson (2006), Development of a joint hydrogeophysical inversion approach and application to a contaminated fractured aquifer, *Water Resour. Res.*, *42*, W06425, doi:10.1029/2005WR004694.
- Chen, J., S. S. Hubbard, and K. H. Williams (2013), Data-driven approach to identify field-scale biogeochemical transitions using geochemical and geophysical data and hidden Markov models: Development and application at a uranium-contaminated aquifer, *Water Resour. Res.*, *49*, 6412–6424, doi:10.1002/wrcr.20524.
- Cole, J., et al. (2007), Plumbing the global carbon cycle: Integrating inland waters into the terrestrial carbon budget, *Ecosystems*, *10*, 172–185.
- Dafflon, B., and W. Barrash (2012), Three-dimensional stochastic estimation of porosity distribution: Benefits of using ground-penetrating radar velocity tomograms in simulated-annealing-based or Bayesian sequential simulation approaches, *Water Resour. Res.*, *48*, W05553, doi:10.1029/2011WR010916.
- Doetsch, J., N. Linde, M. Pessognelli, A. G. Green, and T. Günther (2012), Constraining 3-D electrical resistance tomography with GPR reflection data for improved aquifer characterization, *J. Appl. Geophys.*, *78*, 68–76.
- Duncan, J., P. Groffman, and L. Band (2013), Towards closing the watershed nitrogen budget: Spatial and temporal scaling of denitrification, *J. Geophys. Res. Biogeosci.*, *118*, 1105–1119, doi:10.1002/jgrg.20090.
- Flores Orozco, A., K. H. Williams, P. E. Long, S. S. Hubbard and A. Kemna (2011), Using complex resistivity imaging to infer biogeochemical processes associated with bioremediation of a uranium-contaminated aquifer, *J. Geophys. Res.*, *116*, G03001, doi:10.1029/2010JG001591.
- Flores Orozco A., A. Kemna, C. Oberdörster, L. Zschornack, C. Leven, P. Dietrich, and H. Weiss (2012a), Delineation of subsurface hydrocarbon contamination at a former hydrogenation plant using spectral induced polarization imaging, *J. Contam. Hydrol.*, *136–137*, 131–144.
- Flores Orozco, A., A. Kemna, and E. Zimmermann (2012b), Data error quantification in spectral induced polarization imaging, *Geophysics*, *77*(3), E227–E237.
- Flores Orozco, A., K. H. Williams, and A. Kemna (2013), Time-lapse spectral induced polarization imaging of stimulated uranium bioremediation, *Near Surf. Geophys.*, *11*(1988), 531–544, doi:10.3997/1873-0604.2013020.
- Geweke, J. (1992), Evaluating the accuracy of sampling-based approaches to calculating posterior moments, in *Bayesian Statistics*, vol.4, edited by J. M. Bernardo et al., pp. 169–193, Clarendon, Oxford, N. Y.
- Grimm, N. B., et al. (2003), Merging aquatic and terrestrial perspectives of nutrient biogeochemistry, *Oecologia*, *137*, 485–501.
- Gomez, J. D., J. L. Wilson, and M. B. Cardenas (2012), Residence time distributions in sinuosity-driven hyporheic zones and their biogeochemical effects, *Water Resour. Res.*, *48*, W09533, doi:10.1029/2012WR012180.
- Hedin, L. O., J. C. Fischer, N. E. Ostrom, B. P. Kennedy, M. G. Brown, and P. G. Robertson (1998), Thermodynamic constraints on nitrogen transformations and other biogeochemical processes at soil-stream interfaces, *Ecology*, *79*(2), 684–703, doi:10.1890/0012-9658(1998)079.
- Heimann, M., and M. Reichstein (2009), Terrestrial ecosystem carbon dynamics and climate feedbacks, *Nature*, *451*, 289–292.
- Hermans, T., F. Nguyen, and J. Caers (2015), Uncertainty in training image-based inversion of hydraulic head data constrained to ERT data: Workflow and case study, *Water Resour. Res.*, *51*, 5332–5352, doi:10.1002/2014WR016460.
- Hill, A. R., K. J. Devito, S. Campagnolo, and K. Sanmugas (2000), Subsurface denitrification in a forest riparian zone: Interactions between hydrology and supplies of nitrate and organic carbon, *Biogeochemistry*, *51*(2), 193–223.
- Holmes, R. M., J. B. Jones Jr., S. G. Fisher, and N. B. Grimm (1996), Denitrification in a nitrogen-limited stream ecosystem, *Biogeochemistry*, *33*(2), 125–146.
- Hubbard, S. S., and N. Linde (2011), Hydrogeophysics, in *Treatise on Water Science*, vol. 2, edited by P. Wilderer, Academic, Oxford, U. K.
- Hubbard, S. S., J. Chen, J. E. Peterson, E. Majer, K. W. Williams, D. Swift, B. Mailloux, and Y. Rubin (2001), Hydrogeological characterization of the D.O.E. bacterial transport site in Oyster Virginia using geophysical data, *Water Resour. Res.*, *37*(10), 2431–2456.
- Janot, N., et al. (2015), Physico-chemical heterogeneity of organic-rich sediments in the Rifle aquifer, CO: Impact on uranium biogeochemistry, *Environ. Sci. Technol.*, *50*(1), 46–53, doi:10.1021/acs.est.5b03208.
- Johnston, C. A., S. D. Bridgman, and J. P. Schubauer-Berigan (2001), Nutrient dynamics in relation to geomorphology of riverine wetlands, *Soil Sci. Soc. Am. J.*, *65*(2), 557–577.
- Kemna, A. (2000), Tomographic inversion of complex resistivity: Theory and application, PhD thesis, Ruhr Univ., Bochum, Germany.
- Kemna, A., E. Räkens, and A. Binley (1997), Application of complex resistivity tomography to field data from a Kerosene-contaminated site, in *Proceedings of 3rd Meeting of Environmental and Engineering Geophysics Society*, *Environ. Eng. Geophys. Soc.*, pp. 151–154, Denver, Colo.
- Kennedy, D. O., C. Leven, and O. A. Cirpka (2013), Delineating subsurface heterogeneity at a loop of River Steinlach using geophysical and hydrogeological methods, *Environ. Earth Sci.*, *69*(2), 335–348.
- Kowalsky, M. B., E. Gasperikova, S. Finsterle, D. Watson, G. Baker, and S. S. Hubbard (2011), Coupled modeling of hydrogeochemical and electrical resistivity data for exploring the impact of recharge on subsurface contamination, *Water Resour. Res.*, *47*, W02509, doi:10.1029/2009WR008947.
- LaBrecque, D., and W. Daily (2008), Assessment of measurement errors for galvanic-resistivity electrodes of different composition, *Geophysics*, *73*(2), F55–F64.
- Marshall, D. J., and T. R. Madden (1959), Induced polarization, a study of its causes, *Geophysics*, *24*(4), 790–816.
- McClain, M., et al. (2002), Biogeochemical hot spots and hot moments at the interface of terrestrial and aquatic ecosystems, *Ecosystems*, *6*, 301–312, doi:10.1007/s10021-003-0161-9.
- Melack, J. (2011), Biogeochemistry: Riverine carbon dioxide release, *Nat. Geosci.*, *4*, 821–822.
- Mouser, P. J., et al. (2014), Influence of carbon and microbial community priming on the attenuation of uranium in a contaminated floodplain aquifer, *Ground Water*, *53*, 600–613, doi:10.1111/gwat.12238.
- Murphy, K. P. (2007), Conjugate Bayesian analysis of the Gaussian distribution, technical report. [Available at <http://www.devel.cs.ucb.cam.ac.uk/Papers/bayesGauss.pdf>.]
- Mwakanyamale, K., L. Slater, A. Binley, and D. Ntarlagiannis (2012), Lithologic imaging using induced polarization: Lessons learned from the Hanford 300 area, *Geophysics*, *77*, 397–409.
- Neff, J. C., and G. P. Asner (2001), Dissolved organic carbon in terrestrial ecosystems: Synthesis and a model, *Ecosystems*, *4*, 29–48.
- Nguyen, F., et al. (2009), Characterization of seawater intrusion using 2D electrical imaging, *Near Surface Geophysics*, *7*, 377–390.
- Ntarlagiannis, D., K. H. Williams, L. D. Slater, and S. S. Hubbard (2005), Low frequency electrical response to microbial induced sulfide precipitation, *J. Geophys. Res.*, *110*, G02009, doi:10.1029/2005JG000024.

- Pelton, W. H., S. H. Ward, P. G. Hallof, W. R. Sill, and P. H. Nelson (1978), Mineral discrimination and removal of inductive coupling with multifrequency IP, *Geophysics*, *43*(3), 588–609.
- Qafoku, N. P., et al. (2014), Geochemical and mineralogical investigation of uranium in multi-element contaminated, organic-rich subsurface sediment, *Appl. Geochem.*, *42*, 77–85, doi:10.1016/j.apgeochem.2013.12.001.
- Revil, A., and N. Florsch (2010), Determination of permeability from spectral induced polarization in granular media, *Geophys. J. Int.*, *181*, 1480–1498.
- Rubin, Y., and S. S. Hubbard (Eds.) (2005), *Hydrogeophysics*, vol. 50, Springer, Berlin.
- Sassen, D. S., S. S. Hubbard, S. A. Bea, J. Chen, N. Spycher, and M. E. Denham (2012), Reactive facies: An approach for parameterizing field-scale reactive transport models using geophysical methods, *Water Resour. Res.*, *48*, W10526, doi:10.1029/2011WR011047.
- Scheibe, T. D., and D. L. Freyberg (1995), Use of sedimentological information for geometric simulation of natural porous media structure, *Water Resour. Res.*, *31*(12), 3259–3270, doi:10.1029/95WR02570.
- Schindler, J. E., and D. P. Krabbenhoft (1998), The hyporheic zone as a source of dissolved organic carbon and carbon gases to a temperate forested stream, *Biogeochemistry*, *43*(2), 157–174.
- Scott, J. B. T., and R. D. Barker (2003), Determining pore-throat size in Permian-Triassic sandstones from low-frequency electrical spectroscopy, *Geophys. Res. Lett.*, *30*(9), 1450, doi:10.1029/2003GL016951.
- Slater, D. L., D. Choi, and Y. Wu (2005), Electrical properties of iron-sand columns: Implications for induced polarization investigation and performance monitoring of iron wall barriers, *Geophysics*, *70*(4), G87–G94.
- Slater, L., and A. Binley (2006), Synthetic and field-based electrical imaging of zerovalent iron barrier: Implications for monitoring long-term barrier performance, *Geophysics*, *71*, 129–137.
- Slater, L., W. Barrash, J. Montrey, and A. Binley (2014), Electrical-hydraulic relationships observed for unconsolidated sediments in the presence of a cobble framework, *Water Resour. Res.*, *50*, 5721–5742, doi:10.1002/2013WR014631.
- Smith, M. J., J. Chandler, and J. Rose (2009), High spatial resolution data acquisition for the geosciences: Kite aerial photography, *Earth Surf. Processes Landforms*, *34*(1), 155–161.
- Vereecken, H., A. Binley, G. Cassiani, A. Revil, and K. Titov (2006), *Applied Hydrogeophysics*, Springer, N. Y.
- Titov, K., V. Komarov, V. Tarasov, and A. Levitski (2002), Theoretical and experimental study of time-domain-induced polarization in water saturated sands, *J. Appl. Geophys.*, *50*(4), 417–433.
- Titov, K., A. Kemna, A. Tarasov, and H. Vereecken (2004), Induced polarization of unsaturated sands determined through time domain measurements, *Vadose Zone J.*, *3*, 1160–1168.
- Triska, F. J., J. R. Sedell, K. Cromack Jr., S. V. Gregory, and F. M. McCorison (1984), Nitrogen budget for a small coniferous forest stream, *Ecol. Monogr.*, *54*(1), 119–140.
- Vidon, P., C. Allan, D. Burns, T. P. Duval, N. Gurwick, S. Inamdar, R. Lowrance, J. Okay, D. Scott, and S. Sebestyen (2010), Hot spots and hot moments in riparian zones: Potential for improved water quality management, *J. Am. Water Resour. Assoc.*, *46*, 278–298, doi:10.1111/j.1752-1688.2010.00420.x.
- Wainwright, H. M., J. Chen, D. S. Sassen, and S. S. Hubbard (2014), Bayesian hierarchical approach and geophysical data sets for estimation of reactive facies over plume scales, *Water Resour. Res.*, *50*, 4564–4584, doi:10.1002/2013WR013842.
- Wainwright, H. M., B. Dafflon, L. J. Smith, M. S. Hahn, J. B. Curtis, Y. Wu, C. Ulrich, J. E. Peterson, M. S. Torn, and S. S. Hubbard (2015), Identifying multiscale zonation and assessing the relative importance of polygon geomorphology on carbon fluxes in an Arctic tundra ecosystem, *J. Geophys. Res. Biogeosci.*, *120*, 788–808, doi:10.1002/2014JG002799.
- Walling, D., D. Fang, A. P. Nicholas, R. J. Sweet, J. S. Rowan, R. W. Duck, and A. Werritty (2006), River flood plains as carbon sinks, in *Sediment Dynamics and the Hydromorphology of Fluvial Systems*, pp. 460–470, IAHS Publication, Oxfordshire OX10 8BB, U. K.
- Weller, A., and D. L. Slater (2015), Induced polarization dependence on pore space geometry: Empirical observations and mechanistic predictions, *J. Appl. Geophys.*, *123*, 310–315, doi:10.1016/j.jappgeo.2015.09.002.
- Wikle, C. K., R. F. Milliff, D. Nychka, and L. M. Berliner (2001), Spatiotemporal hierarchical Bayesian modeling: Tropical ocean surface winds, *J. Am. Stat. Assoc.*, *96*(454), 382–397.
- Williams K.H., A. Kemna, M.J. Wilkins, J. Druhan, E. Arntzen, A. L. N'Guessan, P. E. Long, S. S. Hubbard and J. F. Banfield (2009), Geophysical monitoring of coupled microbial and geochemical processes during stimulated subsurface bioremediation, *Environ. Sci. Technol.*, *43*, 6717–6723.
- Williams, K. H., et al. (2011), Acetate availability and its influence on sustainable bioremediation of uranium-contaminated groundwater, *Geomicrobiol. J.*, *28*(5–6), 519–539, doi:10.1080/01490451.2010.520074.
- Wong, J. (1979), An electrochemical model of the induced polarization phenomenon in disseminated sulfide ores, *Geophysics*, *44*(7), 1245–1265.
- Wrighton, K. C., et al. (2014), Metabolic interdependencies between phylogenetically novel fermenters and respiratory organisms in an unconfined aquifer, *ISME J.*, *8*(7), 1452–1463.
- Yabusaki, S. B., Y. Fang, K. H. Williams, C. J. Murray, A. L. Ward, R. Dayvault, S. R. Waichler, D. R. Newcomer, F. A. Spane, and P. E. Long (2011), Variably saturated flow and multicomponent biogeochemical reactive transport modeling of a uranium bioremediation field experiment, *J. Contam. Hydrol.*, *126*(3–4), 271–290, doi:10.1016/j.jconhyd.2011.09.002.
- Zachara, J. M., et al. (2013), Persistence of uranium groundwater plumes: Contrasting mechanisms at two DOE sites in the groundwater–river interaction zone, *J. Contam. Hydrol.*, *147*, 45–72.

3. Re-interpretation of electrical signatures in clay-rich soils and hydrocarbon contaminated sites: the contribution of surface conduction and microbial activity

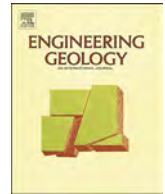
3.1 Complex-conductivity imaging for the understanding of landslide architecture

3.2 Analysis of time-lapse data error in complex conductivity imaging to alleviate anthropogenic noise for site characterization



Contents lists available at ScienceDirect

Engineering Geology

journal homepage: www.elsevier.com/locate/enggeo

Complex-conductivity imaging for the understanding of landslide architecture

Adrián Flores Orozco^{a,*}, Matthias Bucker^a, Matthias Steiner^{a,b}, Jean-Philippe Malet^c

^a Geophysics Research Division, Department of Geodesy and Geoinformation, TU-Wien, Vienna, Austria

^b Institute of Applied Geology, University of Natural Resources and Life Sciences, Vienna, Austria

^c Institut de Physique du Globe de Strasbourg, CNRS UM7516, University of Strasbourg/EOST, Strasbourg, France

ABSTRACT

Geophysical methods are widely used for landslide investigation to delineate depth and geometry of the sliding plane. In particular, electrical resistivity tomography (ERT) is often used because both porosity and water saturation control the electrical resistivity of the subsurface materials and are critical for slope stability. Moreover, ERT can be employed to monitor changes in pore-fluid pressure which is an important factor triggering landslides. However, the interpretation of ERT results in clay-rich landslides can be challenging considering that high electrical conductivity values may not only be related to an increase in saturation but also to the surface conduction mechanism, which becomes dominant in the presence of clays. Recently, environmental investigations have demonstrated an improved subsurface characterization through induced polarization (IP) imaging, an extension of the ERT method, which permits to gain information about electrical conductive and capacitive (i.e., polarization effect) properties of the subsurface. As the polarization effect is mainly controlled by surface charge, which is large in clays, IP images are expected to improve the lithological interpretation and overcome the limitations of the ERT method. Additionally, measurements collected over a broad frequency bandwidth, the so-called spectral IP (SIP), have been successfully used in laboratory experiments to quantify textural and hydrogeological parameters. However, the application of SIP field measurements for the delineation of hydrogeological structures in landslides has not been addressed to date. To fill this gap, in this study we present SIP imaging results for data collected at the La Valette landslide (South East French Alps), where an existing geotechnical model of the landslide is available for evaluation. Moreover, our study provides a detailed revision on the collection and processing of SIP datasets, as well as a description of the diverse sources of error in IP surveys, to stress the importance of data-error quantification for a quantitative application of the SIP method. Our results demonstrate that adequate data processing allows obtaining consistent results at different frequencies and independently of the measuring protocol. Furthermore, the frequency dependence of the complex conductivity obtained in the field-scale SIP survey is consistent with earlier laboratory experiments. In conclusion, our study shows the potential of the SIP method to improve our understanding of subsurface properties, and an improved delineation of the contact between the mobilized material and the bedrock as well as variations in the clay content within the landslide and the bedrock.

1. Introduction

Landslides pose a high geological hazard on human settlements, infrastructure, and agricultural areas. One of the most important processes triggering landslides refers to the increase in pore-fluid pressure, for instances following intense rainfall events (Samyn et al., 2012; Brückl et al., 2013). Hence, a characterization of the internal structure and geometry of landslides with high spatial resolution is critical to identify preferential groundwater flow paths as well as clay-rich areas, where water could accumulate. Such information is critical in the management and control of landslides, taking into account that climate change models predict an increase of rainfall during the winter and rainy seasons in humid regions, such as Europe (Maraun et al., 2010), and a possible increase of landsliding rates (Malet et al., 2007).

Subsurface landslide characterization is commonly performed through geological and geotechnical methods, which require drilling or

trenching. Although such techniques provide direct information about deformation, lithology, water content, and geotechnical properties, their spatial resolution is often limited to the immediate vicinity of the sampling point. Furthermore, direct investigations commonly require interpolation of the data, which may lead to inaccuracies or a bias in the interpretation of the resulting investigations. Due to the increase in costs and time required for a repeated sampling and analysis, direct methods may also not be suited for monitoring purposes. The application of geophysical methods can help to overcome some of these limitations, as they permit to gain quasi-continuous spatial and temporal information about subsurface materials without disturbing the study area.

In the case of landslide investigations, seismic refraction and reflection (SRR) techniques have been used for decades to characterize the landslide internal structure, in particular the geometry of the sliding planes (e.g., Gance et al., 2012; Brückl et al., 2013). Geophysical

* Corresponding author.

E-mail address: flores@tuwien.ac.at (A. Flores Orozco).

<https://doi.org/10.1016/j.enggeo.2018.07.009>

Received 22 December 2017; Received in revised form 6 June 2018; Accepted 8 July 2018

Available online 10 July 2018

0013-7952/ © 2018 Published by Elsevier B.V.

electrical methods, such as electrical resistivity tomography (ERT), have also been applied to delineate the geometry of the sliding plane and assess lithological changes (Friedel et al., 2006; Supper et al., 2014), to estimate landslide hydrological properties (Travelletti et al., 2012; Gance et al., 2016) or to complement seismic surveys (Hibert et al., 2012; Travelletti et al., 2009). Making use of the dependency of the electrical conductivity on the water content, ERT applications have also been used to monitor water content and pore-fluid pressure, which allowed forecasting local failures leading to landslides or debris flow (Friedel et al., 2006; Travelletti et al., 2012; Supper et al., 2014). However, the interpretation of ERT results in terms of water content may be challenging. High electrical conductivity (σ) values are not always related to an increase in water saturation, through electrolytic conduction (Archie, 1942), but can also be due to a high contribution of surface conduction. Particularly in clay-rich materials, surface conduction along the microscopic solid-liquid interfaces, which are covered by an electrical double layer (EDL), might be dominant and mask the saturation dependence of the electrical conductivity (Waxman and Smits, 1968; Revil and Glover, 1998; Slater, 2006). The reader is referred to Ward (1988) for a detailed revision.

Recent hydro-geophysical investigations (Kemna et al., 2012; Binley et al., 2015; Flores Orozco et al., 2015) have demonstrated an improved understanding of lithological structures by means of the Induced Polarization (IP) imaging method, an extension of the ERT, which provides information about the conductive and capacitive (i.e., polarization) properties of the subsurface. Because the polarization effect is mainly controlled by surface charges in the EDL, IP images can help discriminating between saturated sediments and clay-rich materials and, thus, improve the estimation of hydrogeological parameters (Slater and Lesmes, 2002; Slater, 2006). From laboratory studies and theoretical modeling, it is also evident that the frequency dependence of the IP effect, which can be assessed by spectral IP (SIP) measurements, is strongly correlated with the geometrical properties of the pore space (Binley et al., 2005; Bucker and Hördt, 2013). Consequently, SIP imaging has the potential to contribute to the quantification of textural and hydrogeological parameters (Revil and Florsch, 2010) and, thus, improve the geophysical characterization of units with different hydrogeological properties in landslides.

Despite this expected potential, to date only rare studies have addressed the application of IP methods for landslide characterization (Marescot et al., 2008; Sastry and Mondal, 2012). In addition, these studies did not discuss the frequency dependence of the polarization effect nor the number of systematic error affecting IP measurements, which can be neglected in ERT surveys. Hence, in this work, we investigate the possible contributions of single-frequency IP and SIP imaging methods to the non-invasive geophysical investigation of landslides. We present imaging results for data collected at the La Valette landslide located in the French Alps, where numerous studies have been conducted and detailed information on the subsurface conditions of the landslide is available.

In order to set the basis for future IP and SIP surveys on landslides, we test different parameters for data collection, especially the electrode configuration, and discuss the particular sources of systematic errors in SIP measurements. With the same objective, we provide sufficient details on the data processing and the quantification of data error.

2. Material and methods

2.1. The time- and frequency-domain IP methods

The IP method is based on four-electrode measurements, where two electrodes are used to inject a current (I) into the ground and the two other electrodes measure the resulting voltages (V). IP measurements can be performed in either time domain (TDIP) or frequency domain (FDIP). TDIP data are commonly expressed in terms of the measured resistance (R), which is the voltage-to-current ratio (V/I), and the

integral chargeability, which measures the magnitude of the secondary voltage observed after switching the current off. The measured resistance R largely depends on the geometric arrangement of the four-electrode measurement (i.e. the distances between the four electrodes). Knowing the geometric arrangement, each measured R can be converted to the so-called apparent resistivity (ρ_{app}), which is the electrical resistivity of an equivalent homogeneous half space.

In FDIP, current injections are performed with alternating current, and the measurements are usually given in terms of the measured resistance (R) and an apparent phase shift (ϕ_{app}) between current and voltage. FDIP measurements repeated at different frequencies of the injected current (typically < 1 kHz) are commonly referred to as spectral induced polarization (SIP) and provide information about the frequency dependence of the electrical properties.

Inversion results of FDIP and SIP data are commonly given in terms of the complex conductivity (σ^*). Detailed reviews of IP methods can be found in Sumner (1976), Ward (1988), and Kemna et al. (2012), amongst others.

2.2. The complex conductivity (σ^*)

The electrical properties of the subsurface materials in the low-frequency range (below ~ 100 kHz) can be represented by the complex conductivity, CC (σ^*), or its inverse, the complex resistivity (ρ^*). The CC consists of a real (σ') and an imaginary (σ'') component, which represent the conductive (loss) and capacitive (storage) electrical properties of subsurface materials, respectively. Alternatively, the σ^* can be expressed in terms of its magnitude ($|\sigma|$) and phase (ϕ):

$$1/\rho^* = \sigma^* = \sigma' + i\sigma'' = |\sigma| e^{i\phi} \quad (1)$$

where $i = \sqrt{-1}$. In most practical applications, measured phase shifts are sufficiently small (< 100 mrad) to assume that $\sigma' \approx |\sigma|$ and to approximate the phase ϕ with the ratio between real and imaginary component, i.e. $\phi \approx \sigma''/\sigma'$.

The low-frequency CC of subsurface materials is controlled by three main mechanisms (Ward, 1988): (a) matrix conduction through the solid phase, which is important only if a high metal content allows electronic conduction; (b) ionic or electrolytic conduction through the fluid-filled pore space; and (c) surface conduction through the EDL covering the fluid-grain interface.

Due to its high surface area and cation exchange capacity, clay minerals are related to a high contribution of surface conduction, which usually dominates the electric response of clay-rich materials (Waxman and Smits, 1968; Slater and Lesmes, 2002; Revil and Glover, 1998). Hence, the interpretation of electrical images of clay-rich landslides needs to take into account the contribution of surface conductivity, as the electrical response is not only controlled by the conduction through the pore water. Moreover, typical materials involved in landslide processes do not contain significant concentrations of metallic minerals, such that the contribution of matrix conduction may be neglected. Thus, the measured CC can be understood in terms of two mechanisms: electrolytic (σ_{el}) and surface conduction (σ_{surf}). Taking into account the frequency dependence of the surface conduction, the CC can be written as:

$$\sigma^*(\omega) = \sigma_{el} + \sigma_{surf}^*(\omega) \quad (2)$$

where ω is the angular frequency. As noted in Eq. (2), in the low-frequency range, in which the SIP measurements are conducted, σ_{el} shows a negligible frequency dependence, which is not the case of σ_{surf}^* . Rewriting σ_{el} using Archie's model (Archie, 1942) and σ_{surf}^* in terms of its real and imaginary components, the CC can be expressed as (Lesmes and Frye, 2001):

$$\sigma^*(\omega) = [\Theta^m S^n \sigma_w + \sigma'_{surf}(\omega)] + i\sigma''_{surf}(\omega) \quad (3)$$

where Θ represents the porosity, S the saturation, m and n are empirical

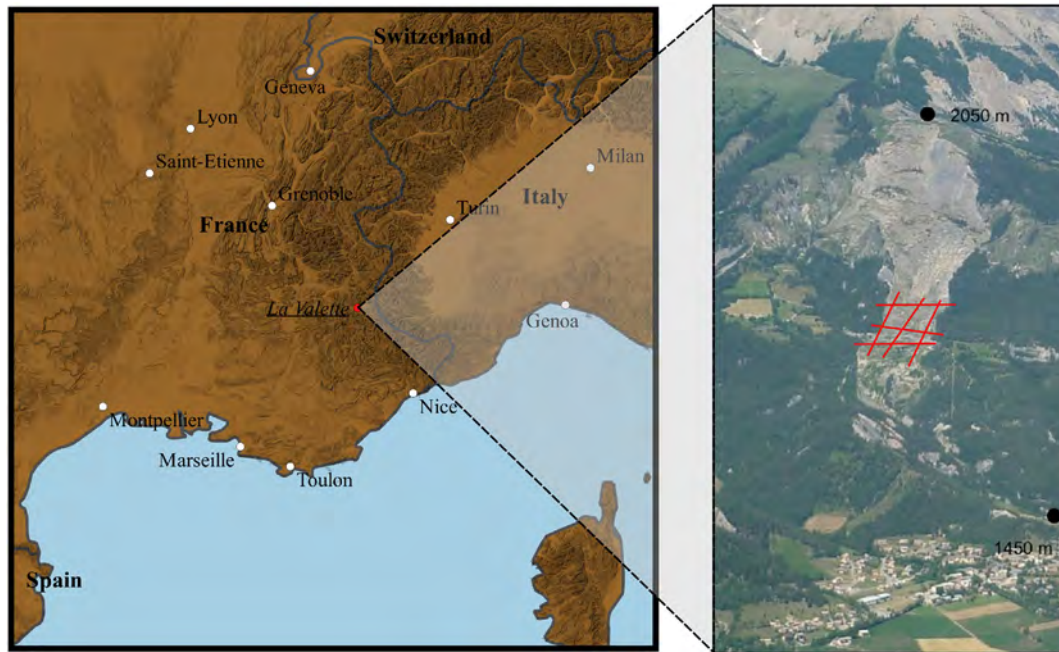


Fig. 1. The La Valette landslide, with its location depicted by the red marker (left) and a picture of the landslide (right) indicating the height (above sea level) of its highest and lowest topographic features. (For interpretation of the references to colour in this figure legend, the reader is referred to the web version of this article.)

coefficients, and σ_w the conductivity of the pore fluid. Eq. (3) shows that the conductivity magnitude $|\sigma|$, as for instance obtained from ERT, is affected by all three components; whereas the imaginary conductivity σ'' assessed by IP measurements only depends on the imaginary part of the surface conductivity. This explains the huge potential of the IP method for an improved lithological characterization of clay-rich landslides.

2.3. The La Valette landslide (South East French Alps)

The La Valette landslide is located in the South East French Alps (Fig. 1), where the presence of a thrust fault separating highly susceptible clay-shale sediments (Jurassic black marls) at the bottom and sandstone and limestone competent rocks at the top is responsible for many landslides in the region (Samyn et al., 2012; Travelletti et al., 2013). The landslide has been triggered in March 1982 at the contact between these two main geological units. The deformation is attributed to the steep slopes and the increase in pore-fluid pressure resulting from the different hydraulic conductivities of the two geological units (Samyn et al., 2012).

The landslide has been subject to numerous investigations using a variety of direct and indirect methods, such as remote sensing (terrestrial and airborne LiDAR), geotechnical analysis of samples recovered from boreholes, and geodetic measurements (e.g., extensometers, inclinometers, GPS), for the spatio-temporal assessment of surface deformation (Raucoules et al., 2013; Malet et al., 2013; Travelletti et al., 2013). Moreover, the internal structure of the La Valette landslide has been characterized through a series of ERT and seismic surveys (Travelletti et al., 2009; Samyn et al., 2012; Hibert et al., 2012). Low electrical resistivity (ρ) values and P-wave seismic velocities (v_p) were generally found to be associated with both the sliding mass consisting of mobilized flysch sediments and the underlying black marls. The lowest values ($\rho < 50 \Omega\text{m}$ and $v_p < 1200 \text{ m}\cdot\text{s}^{-1}$) were observed in the flysch unit, which extends to a maximum depth of 30 m (see Fig. 2), whereas only slightly higher values (ρ between 60 and 150 Ωm and $v_p > 2000 \text{ m}\cdot\text{s}^{-1}$) are representative of the underlying black marls (Travelletti et al., 2009, 2013; Samyn et al., 2012; Hibert et al., 2012). Furthermore, the combination of direct and geophysical methods

permitted to reconstruct the depth and geometry of the bedrock (Samyn et al., 2012) as presented in Fig. 2.

Nevertheless, the relatively weak electrical contrast between the clay-rich sediments of the sliding mass and the stable black marls limits the applicability of ERT results for an improved hydrogeological understanding, i.e. the delineation of clay-rich zones or preferential groundwater flow paths. Moreover, the subsurface high electrical conductivity is controlled by high clay contents in both the flysch and the black marl units (Ghorbani et al., 2009), which limits the potential of ERT for the monitoring of water saturation (Gance et al., 2016).

2.4. IP measuring protocols and inversion algorithms

SIP measurements were conducted in the central part of the landslide, in the vicinity of the existing borehole B3, where lithological information is available (see Fig. 2) for the validation of the imaging results. SIP data were collected along three long profiles (96 electrodes each) oriented parallel to the flanks (along the main direction of the landslide), and three shorter profiles (64 electrodes each) perpendicular to them, as depicted in Fig. 2. The separation between electrodes in all profiles was 5 m to warrant a depth of investigation of at least 50 m. The measuring device was always placed at the center of the profile (i.e., between electrodes 48 and 49 or 32 and 33, respectively) to reduce the maximum cable length.

SIP data were acquired using an eight-channel impedance tomographer DAS-1 (Multi-Phase Technologies) at 12 frequencies: 0.5, 1, 1.5, 2.5, 5, 7.5, 12, 25, 37.5, 75, 112, and 225 Hz. We tested multiple-gradient (MG) and dipole-dipole (DD) protocols to evaluate their performances in terms of acquisition time, spatial resolution, depth of investigation, and Signal-to-Noise ratio (S/N). These two configurations were selected as they permit the collection of multi-channel sequences (i.e., multiple voltage readings for a given current injection), which is not the case with often-used Wenner or Schlumberger configurations. Furthermore, DD protocols help avoiding potential readings with electrodes previously used for current injection. This is an important consideration because the persistent polarization of electrodes, which have been used for current injections, can result in systematic errors in subsequent voltage readings.

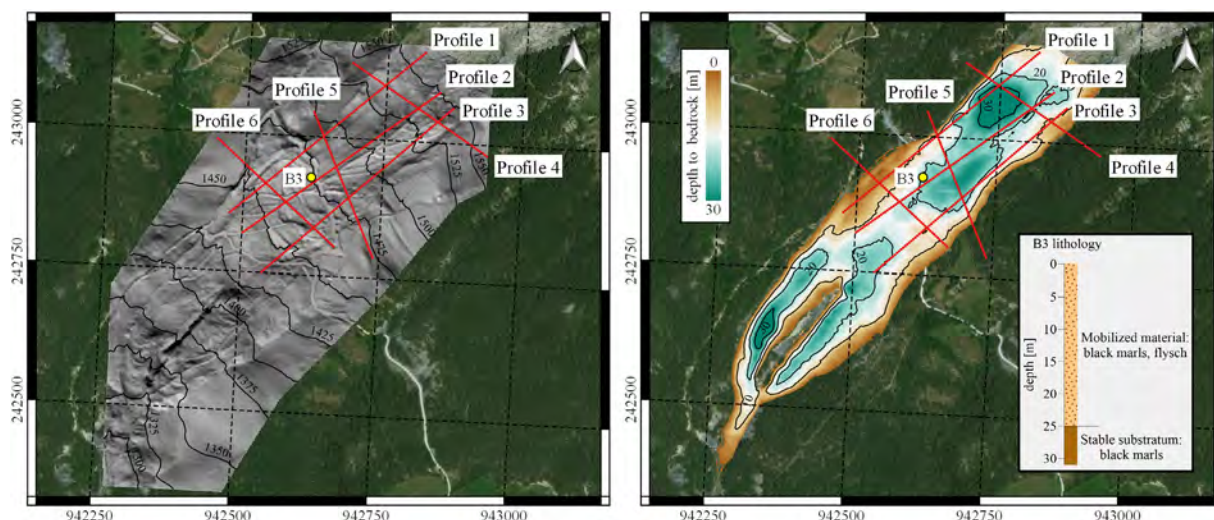


Fig. 2. Location of the SIP profiles at the La Valette landslide (red lines). Left: Terrain relief from an airborne LIDAR-derived digital surface model represented by a hillshade map and elevation contour lines (black lines). The position of the borehole B3 is indicated by the solid circle. Right: Depth to the contact between flysch and black marls (modified from Samyn et al., 2012), with the lithological column of borehole B3 indicated in the inset.

DD data were collected using a constant dipole length, which we define by the number of electrodes “skipped” within a current/potential dipole. For instance, a DD skip-0 denotes measurements with adjacent electrodes. In this study, DD protocols consider measurements to a maximum separation possible between current and potential dipoles. MG protocols were constructed after Dahlin and Zhou (2006), with eight potential dipoles arranged within the current dipole, the length of which increases with the length of the nested potential dipoles (here, skip-0, skip-1, skip-2, and skip-3).

In total, four different measuring protocols were tested: MG, DD skip-0 (DD0), DD skip-3 (DD3) and a combination of skip0 to skip5 (DDmix). Several studies have addressed the comparison of different configurations for the collection of ERT data, while for IP surveys this topic has only been discussed in rare studies (Dahlin and Zhou, 2006). Moreover, previous studies have not addressed the evaluation of the different sources of random and systematic error affecting SIP data. Therefore, our tests consider configurations related to high signal strength (favored by large dipole lengths, such as MG, DD3) and configurations with high spatial resolution (favored by smaller dipole lengths, e.g., DD0).

Inversion algorithms solve for the distribution of electrical properties in the subsurface that explain the measured data. In this study, all datasets were inverted with CRTomo, a smoothness-constraint algorithm by Kemna (2000), which permits the inversion of the data to the confidence level determined by an error model. From a given data set in terms of transfer resistances (R) and apparent phase shifts (ϕ_{app}), the algorithm solves for the distribution of complex resistivity on a 2D grid of lumped finite-element cells. Inversions with CRTomo were performed independently for each frequency. For further details on the inversion procedure, the readers are referred to Kemna (2000).

3. Results and discussion

3.1. Pre-processing of IP datasets

In order to assess the effect on the S/N of the four different measurement configurations, i.e. DD0, DD3, DDmix, and MG, the histograms in Fig. 3 illustrate the distribution of apparent resistivity (ρ_{app}), measured resistance (R), and apparent phase shift (ϕ_{app}) data collected at 1 Hz along Profile 4. In the distributions of ρ_{app} , no significant dependence on the measurement configuration can be observed. This behavior meets the expectations, because for all four configurations, the

values of ρ_{app} represent the mean resistivities of comparable volumes of the subsurface, and geometric parameters, such as dipole lengths and the separation between current and potential dipoles, only have a second-order effect. Furthermore, the S/N of the measurement of R (from which ρ_{app} is computed) is high, which prevents the distributions from “smearing out” at the lower and upper limits. The latter effect, however, can be observed in the distribution of ϕ_{app} in the third line of Fig. 3. Especially the DD configurations reveal a large amount of anomalously high and low ϕ_{app} values, which clearly indicates a lower S/N than the one of the MG configuration.

The dependence of the signal strength itself on the measurement configuration can be seen from the distributions of R illustrated in the second line of Fig. 3. The histograms of R reveal variations over three to four orders of magnitude depending on the selected configuration. Moreover, the range of recorded R for the different configurations also changes significantly, with the broadest range related to DD configurations (between 10^{-4} and 1Ω), evidencing the large dynamic range of recorded voltages (remember that $R \propto V$). Consistently, Fig. 3 exhibits larger variability in ϕ_{app} values for DD measurements, whereas values populate a smaller range for MG measurements.

Although, some authors have proposed to directly analyze voltage readings to assess signal strength, we use the transfer resistances R , which are also sensitive to variations in the injected current I . Besides the measured voltage, I is an important parameter controlling the S/N, which can vary considerably throughout an imaging dataset (e.g., Flores Orozco et al., 2018) depending e.g. on the galvanic contact between electrodes and the ground.

As FDIP measurements are expected to record the response of a chargeable subsurface, the measured resistivity phase shifts should be negative or zero ($\phi_{app} \leq 0$). Thus, positive ϕ_{app} values indicate the presence of random and systematic error in the data. In Fig. 3, particularly DD measurements seem to be affected, whereas the higher S/N reduces the effect of noise on the ϕ_{app} values in MG readings.

However, it is not always indicated to remove all positive ϕ_{app} values: The so-called “negative IP effect” (resulting in positive ϕ_{app} values) has been observed in layered media, where the deepest layer is more conductive than the layer immediately above and the shallowest layer is polarizable (Sumner, 1976). Moreover, negative IP effects have also been reported recently for TDIP (Dahlin and Loke, 2015) under certain geometrical conditions. Although it might be justifiable in some cases, the negative IP effect needs to be treated with caution, as it is the result of systematic errors in most other cases (Flores Orozco et al., 2018). The

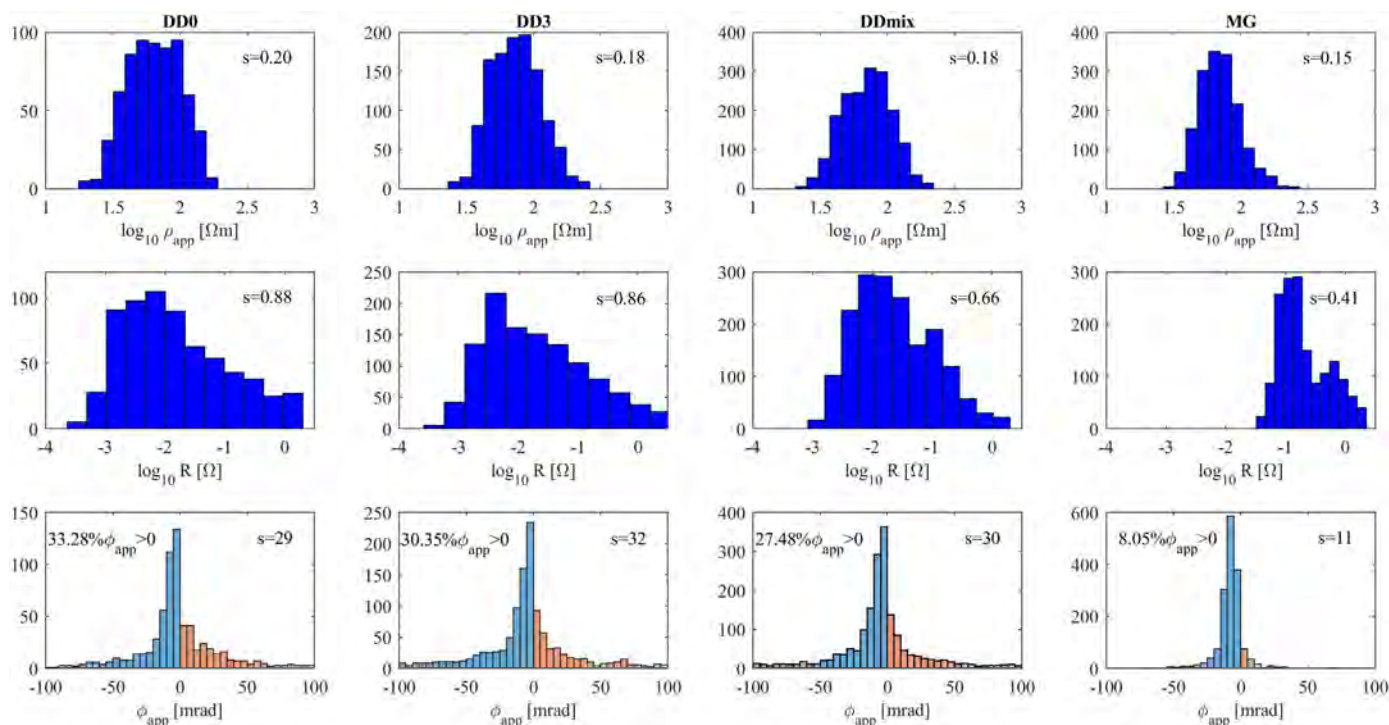


Fig. 3. Histograms of the apparent resistivity ρ_{app} (first line), measured resistance R (second line), and apparent phase shift ϕ_{app} (third line) at 1 Hz along Profile 4 at the La Valette landslide using four different measuring protocols (DD0, DD3, DDmix, and MG). To better assess the variability in the measured values, plots also present the standard deviation (s) computed for each dataset.

latter might be caused by electromagnetic coupling effects, cross talking between wires, poor S/N, or anthropogenic noise (e.g., buried metallic structures) (Dahlin and Leroux, 2012; Flores Orozco et al., 2011, 2012a, 2013; Schmutz et al., 2014; Dahlin and Loke, 2015).

To define the actual range of valid ϕ_{app} readings for the subsequent inversion, it is important to identify outliers in the data. The analysis of the normal and reciprocal misfit (NRM) is a common practice for the characterization of data error in electrical imaging, where reciprocal refer to the re-collection of the normal quadrupole after interchanging the current and potential dipoles. As noted in earlier studies (Labrecque et al., 1996; Slater et al., 2000), the NRM has an important advantage over other methods (e.g., stacking), as it is based on the comparison of two independent measurements and not the repetition of the same reading including the same systematic error. Hence, measurements related to large NRM may indicate those affected by systematic errors, in particular related to poor galvanic contact or problems with the cables (Labrecque et al., 1996). Fig. 4 shows the comparison between normal and reciprocal readings for DD0 measurements along Profile 4. Such plots reveal practically a perfect agreement in transfer resistance for normal (R_n) and reciprocal (R_r) readings. The good agreement of the measurements suggests a negligible level of systematic errors and a minimal distortion due to random errors even for readings with large separations between current and potential dipoles (typically associated with low R values). The apparent robustness of the R measurements also explains the consistency in the ρ_{app} values for measurements with different configurations observed in Fig. 3. Despite of this, Fig. 4 shows large NRM for ϕ_{app} clearly indicating distortions due to systematic and random error.

The NRM of measured resistance (ΔR) and apparent phase shift ($\Delta\phi_{app}$) are analyzed to identify measurements associated with systematic errors or largely dominated by random errors, which need to be removed as outliers prior to the inversion. Here, outliers are defined as those readings related to a NRM exceeding (i) 25% of the value of the corresponding normal or reciprocal; and (ii) two times the standard deviation computed for the entire NRM dataset (~ 2 m Ω for ΔR and ~ 5

mrad for $\Delta\phi_{app}$). Before the analysis of NRM, first outliers were defined as those potential readings collected with current injections below 0.001 A, and negative apparent resistivity values, as those readings are clearly related to poor contact between the electrodes and the ground. As observed in the comparison between ϕ_n and ϕ_r (Fig. 4d), following the removal of outliers after the analysis of NRM, it is possible to define maximum and minimum threshold values (here, between ~ 20 and 0 mrad), which can then be used for the identification of outliers in MG measuring schemes lacking reciprocal readings. Pseudo-sections for the data collected along Profile 4 after removal of outliers based on the aforementioned approach are presented in Fig. 5. It is notable that most of the outliers are mainly associated to deep levels with a low S/N.

After the removal of outliers, the remaining measurements are assumed to be affected only by random errors, the magnitude of which can be incorporated into the inversion, by means of error models as proposed by Labrecque et al. (1996), and Slater et al. (2000). These studies recognized a linear increase of the data error of the measured resistance (ΔR) with R (Figure 4c), whereas a negative power-law model (Figure 4f) has recently been adopted to describe $\Delta\phi_{app}$ as a function of R (Flores Orozco et al., 2012a;). As we can see from Fig. 4, these error models also describe the data uncertainty for the measurements collected at La Valette landslide. Hence, error parameters were computed using the bin analysis described in Flores Orozco et al. (2012a).

The advantage of deploying error models, instead of individual errors, is that the same error parameters can be used for the inversion of datasets lacking reciprocal readings, such as MG configurations (e.g., Flores Orozco et al., 2018). Inversions were conducted independently for each dataset collected with different electrode configurations, using the error models defined as $\Delta R = 0.001\Omega + 1.3R$, and $\Delta\phi = 1.19$ mrad $(R/\Omega)^{-0.23}$. The resulting imaging results are presented in Fig. 6, in terms of the real (σ') and imaginary (σ'') components of the complex conductivity. Blanked regions in the electrical images are related to low cumulative sensitivity values (< -3 in the logarithmic normalized value), a parameter that can be used as a proxy for the depth of

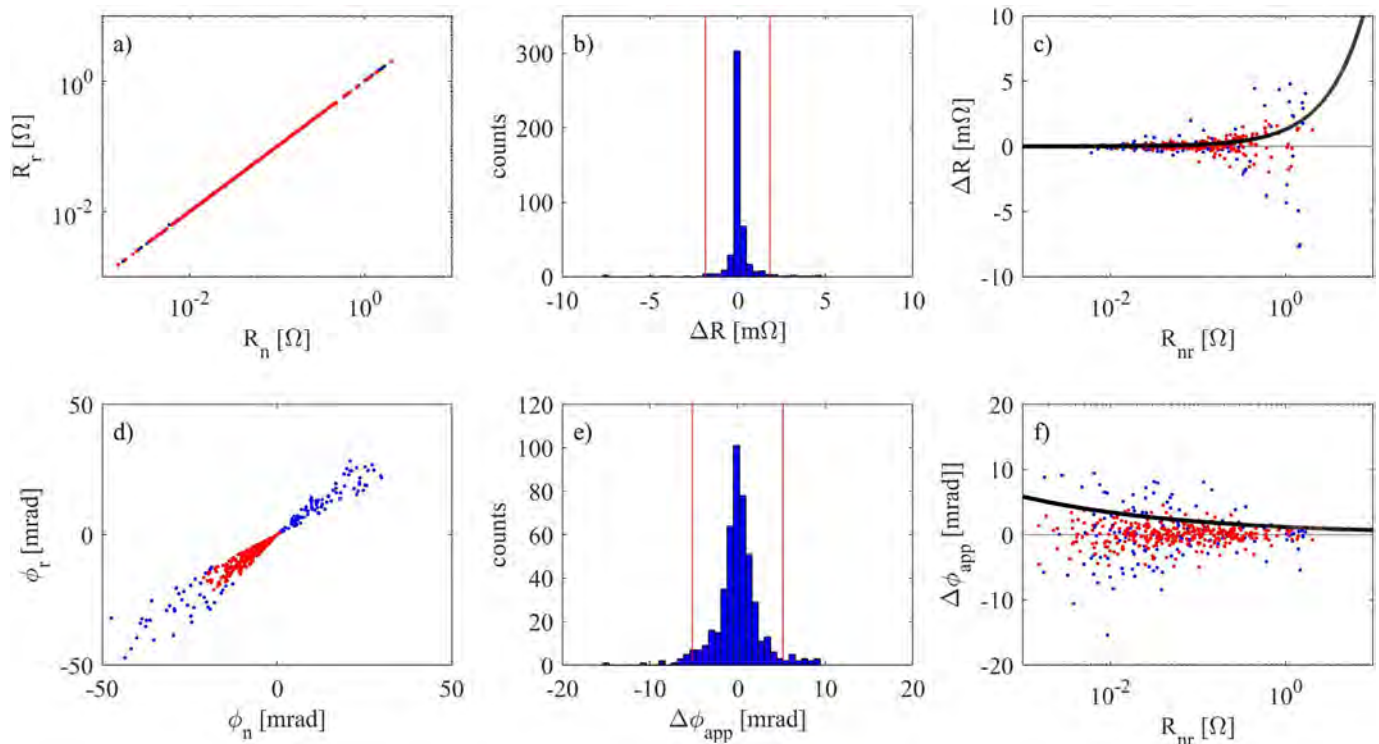


Fig. 4. (a) Comparison between normal and reciprocal readings for transfer resistances R and (d) the apparent phase shifts ϕ_{app} . (b) Histograms of the data error for resistance (ΔR) and (e) apparent phase shift ($\Delta\phi_{app}$) measurements reveal a normal distribution. The values of two standard deviations, which we used as limiting values for the identification of outliers, are indicated by red lines. The dependencies of ΔR (c) and $\Delta\phi_{app}$ (f) on the signal strength R are consistent with previous observations, permitting to define error models (solid black lines). The plots show all readings (blue symbols) and those accepted after removal of outliers (red symbols). (For interpretation of the references to colour in this figure legend, the reader is referred to the web version of this article.)

investigation of IP inversion results (see Weigand et al., 2017, for further details).

3.2. SIP imaging results

Fig. 6 shows SIP imaging results obtained for data collected with DDmix configurations at 0.5, 2.5 and 15 Hz along profiles parallel to the main landslide direction (Profiles 1, 2, and 3). The σ' model is only visualized for the lowest frequency of 0.5 Hz, as the results revealed no changes for data collected at higher frequencies. In general, all sections

reveal high electrical conductivities in all subsurface materials, with σ' varying over a narrow range (between 10 and 30 mS/m). These results are consistent with previous investigations at the La Valette landslide (Travelletti et al., 2009; Hibert et al., 2012) and the nearby Super-Sauze landslide (Schmutz et al., 2000) developed in the same lithology. At the same time, the σ'' images, i.e. the polarization effect, reveal a much larger variability with σ'' values ranging between 1 and 800 $\mu\text{S}\cdot\text{m}^{-1}$.

In the case of the real component of the electrical conductivity (σ'), high values correspond to the landslide body, i.e., the mix of weathered blocks of black marls and flysch, indicated by the dashed line in Fig. 6;

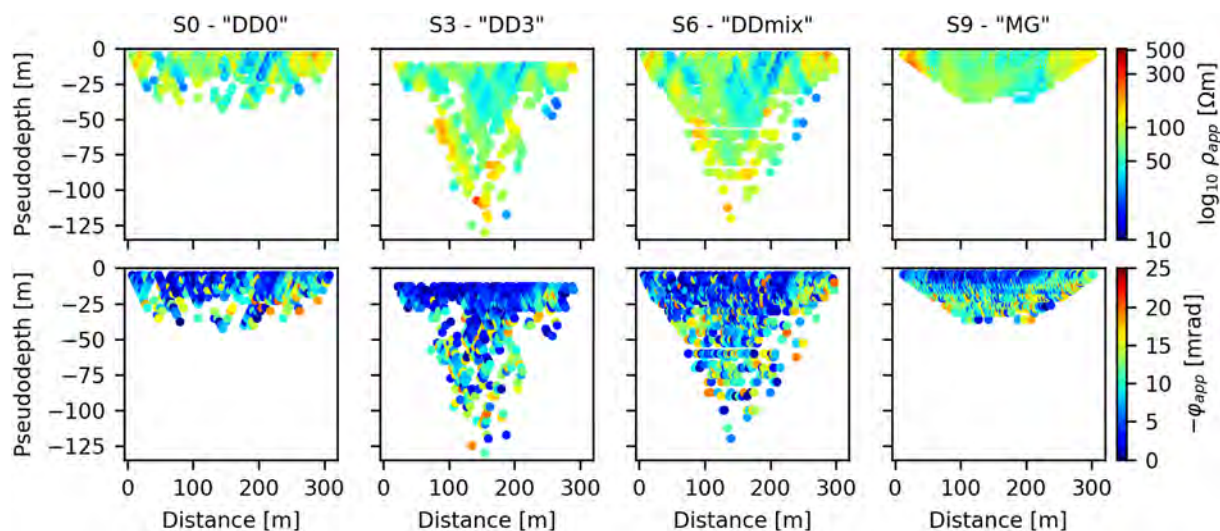


Fig. 5. Raw data measurements presented in pseudo-sections in terms of the apparent resistivity (ρ_{app} - top row) and apparent phase shift (ϕ_{app} - bottom row) for data collected along Profile 4 using DD0, DD3, DDmix, and MG protocols.

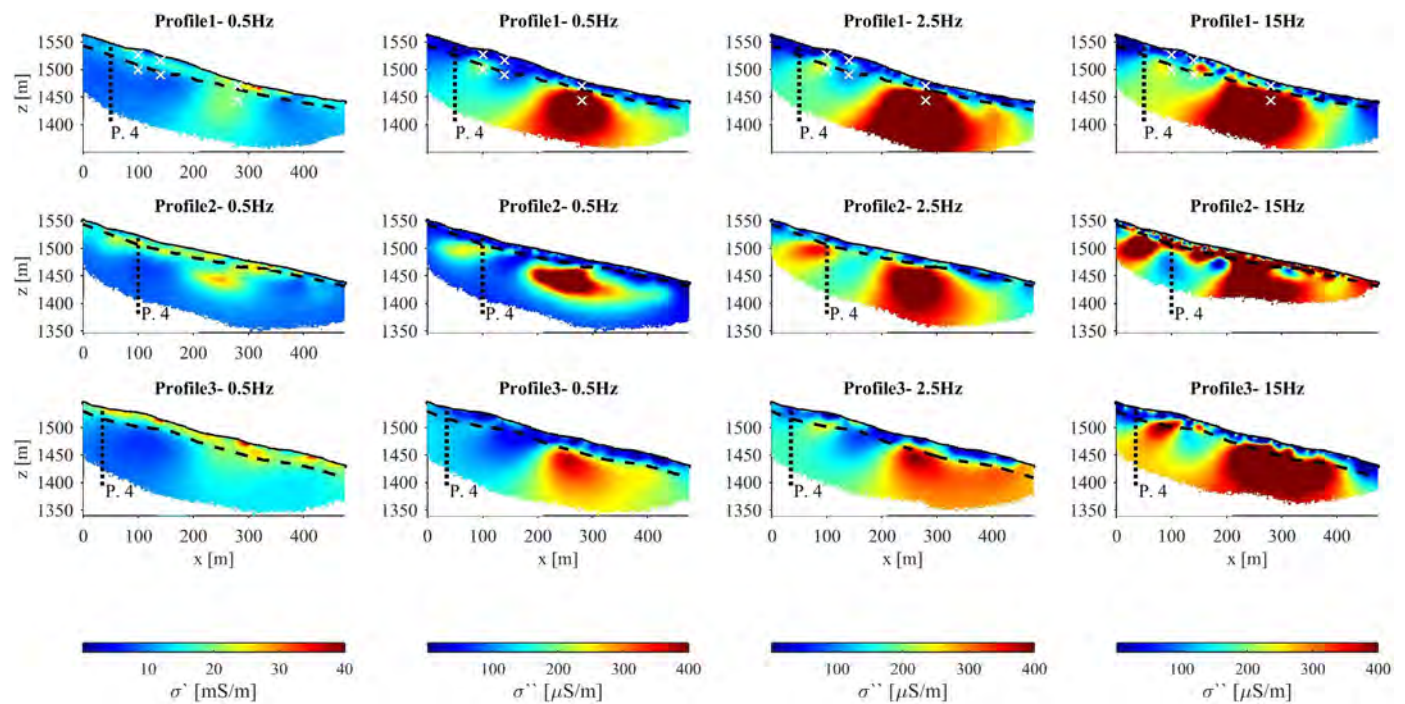


Fig. 6. SIP imaging results obtained from DDmix data collected along Profile 1, 2 and 3 expressed in terms of the real (first column - for data collected at 0.5 Hz) and imaginary components (columns 2 to 4 for data collected at 0.5, 2.5, and 15 Hz) of the CC. Dashed lines parallel to the surface indicate the position of the sliding plane as obtained from wellbore and seismic data (Samyn et al., 2012). The position of the intersection with the perpendicular Profile 4 is indicated by the dashed vertical line. The position of the pixel values extracted for the discussion of the spectral response is indicated by the white symbols (x) along Profile 1.

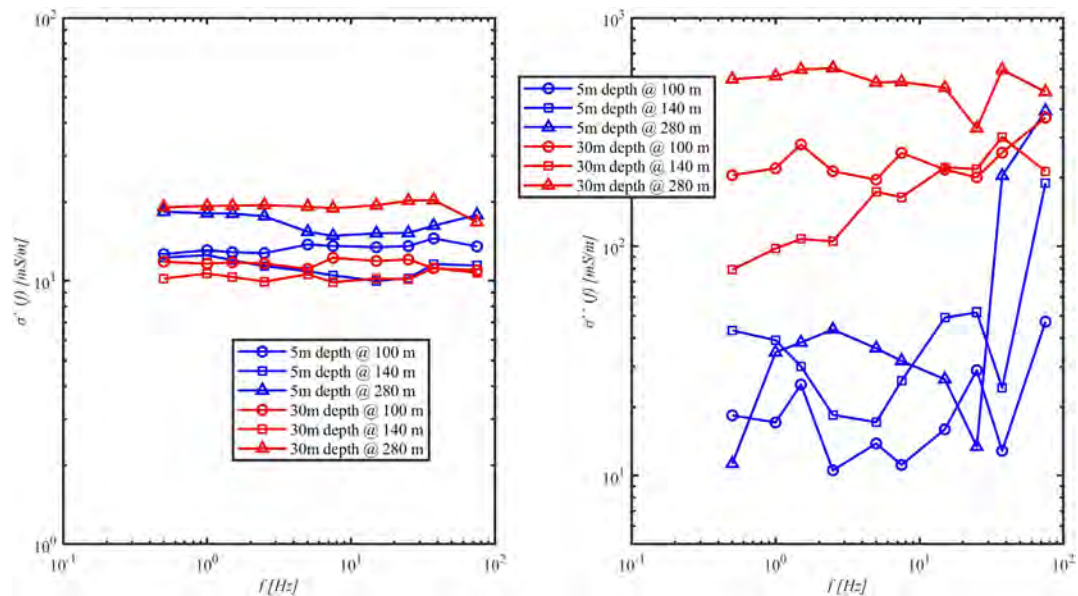


Fig. 7. SIP response for selected pixels retrieved from imaging results obtained for data collected along Profile 1 using the DDmix configuration. The data plotted represent the median of model parameters within a pixel of 4 m radius centered at 100 m (circles), 140 m (squares) and 270 m (triangles), and at depths of 5 m (in blue) and 30 m (in red) associated to the sliding mix of weathered black marls and flysch unit and the underlying black-marl bedrock, respectively. (For interpretation of the references to colour in this figure legend, the reader is referred to the web version of this article.)

lower values ($\sigma' < 10 \text{ mS m}^{-1}$) are generally observed within the underlying stable unit, corresponding to the black marls. However, locally, high conductivities also appear well below this lithological contact between the loose materials and the black-marl bedrock (particularly between 200 and 300 m along Profiles 1 and 2) reducing the usefulness of the real component of the CC for the delineation of this geometrical boundary. Similar ambiguities, which make the determination of the landslide body from ERT profiles alone difficult, have been

reported before (Travelletti et al., 2009, 2012, 2013; Gance et al., 2016).

As the visualization of the imaginary component of the electrical conductivity (σ'') in Fig. 6 illustrates, this additional property can largely reduce the ambiguity of electrical imaging. Here, the landslide body stands out clearly by a weak polarization response ($\sigma'' < 100 \mu\text{S m}^{-1}$), whereas the underlying black marls are generally more polarizable. Particularly, the conductive anomalies below the sliding

plane (dashed lines), which make the σ' (or equally ERT) images inconclusive, are associated with the highest polarization responses (σ'' up to $800 \mu\text{S}\cdot\text{m}^{-1}$) and help to distinguish the conductive landslide body from conductive anomalies within the bedrock unit.

While the amplitude of the polarization effect (σ'') turns out to be particularly helpful to reduce the uncertainty of electrical imaging on the La Valette landslide and aid the delineation of the landslide body, the large variability of σ'' values below the sliding plane raise new questions regarding the electrical response of the underlying unit. Based on information available near the SIP lines (lithological description in sediments recovered at B3), we must assume that the black marls underlie the entire landslide body at an average depth of ~ 25 m (Travelletti et al., 2009; Samyn et al., 2012). Consequently, we do not expect any lithological changes in the bedrock along the SIP Profiles 1 to 3. Thus, the observed lateral changes in σ'' must be attributed to local variations in the composition, fracturing, and/or weathering of the black marls.

In the absence of sufficiently dense borehole data, a more detailed analysis of the frequency dependence of the CC can further aid the interpretation of the electrical imaging results. Fig. 7 shows the spectral variation (i.e., frequency dependence) of σ' and σ'' at three different positions along Profile 1 and two different depths: (i) the flysch unit at 5 m depth and (ii) the black marls at 30 m depth. The σ' spectra in the left panel reconfirm the aforementioned observation that the real part of the conductivity is not indicative for the two principal lithological units, as the conductivity of the black marl unit varies over a wide range. In addition, they reveal practically no frequency dependence for σ' . Meanwhile, the polarization effect, presented in terms of σ'' , reveals different magnitudes and spectral behaviors for the two units. The mix of weathered blocks of black marls and flysch materials exhibit low and practically constant σ'' values at frequencies below 30 Hz, whereas within the more polarizable black-marl unit, the σ'' values are approximately one order of magnitude higher and small peaks can be observed around 1.5–2.5 Hz (at 100 m and 280 m) and at 5–15 Hz (100 m and 140 m). In particular the spectra for pixel values recovered at 140 m (along profile direction) in the black marls reveal a linear increase in σ'' with increasing the frequency, consistent to the observations from Ghorbani et al. (2009), for measurements in the laboratory in black marls samples recovered in the Super-Sauze landslide, which is located in the same lithology as the La Valette landslide.

Imaging results presented in Figure 6 and 7 show the potential of the SIP method for the investigation of landslide architecture. However, the SIP measurements are related to lower S/N than ERT, as well as additional sources of systematic errors. Hence, an adequate processing of SIP data is critical for the inversion of quantitative meaningful electrical models. Hence, in Fig. 8, we present a workflow illustrating

the iterative steps for an adequate processing of single-frequency and spectral IP datasets: (1) identification of clear outliers; (2) normal-reciprocal analysis; (3) detailed identification of outliers; (4) quantification of data error; (5) inversion of the dataset; (6) verification of the imaging results through complementary information; and (7) interpretation of subsurface electrical properties.

3.3. Electrical properties of geological units

The amplitude and frequency dependence of both components of the CC (σ' and σ'') in pixels retrieved from the black-marl bedrock are in good agreement with existing laboratory SIP measurements on clay-rock samples. In our field measurements, σ' roughly varies between 10 and 20 mS/m in the intact black marls and exhibits a constant value at the different frequencies here investigated (< 100 Hz). In their analysis of seven clay-rock samples from three different formations, including black marls, Ghorbani et al. (2009) found a slightly larger variability in the σ' values (~ 5 to $80 \text{ mS}\cdot\text{m}^{-1}$) but the same negligible frequency dependence. As written in Eq. (2), the surface conduction contributes to both the real and imaginary components of the CC. Hence, the comparably high electrical conductivities are largely due to the contribution of surface conduction (σ_{surf} in Eq. (3)) associated to clay minerals. Accordingly, in the study by Ghorbani et al. (2009) the σ' values roughly correlate with the clay content of the investigated samples. For the present data set, this implies that observed changes in σ' below the sliding plane (for instance in spectra presented in Fig. 7) are indicative of variations in the clay fraction in the stratified black marls.

The mobilized flysch of the landslide body tends to be associated with slightly higher electrical conductivity (σ') values. Also in this clay-rich unit, surface conduction is expected to contribute a significant part to the overall conduction. Thus, besides a higher contribution of electrolytic conduction through the porous sediments (compared to the tight black marls), the higher σ' values might be due to a higher clay content of the loose material.

Furthermore, the imaginary part of the conductivity σ'' inferred from our SIP field measurements are in good agreement with the laboratory studies by Ghorbani et al. (2009). While our field measurements resulted in σ'' values between 80 and $600 \mu\text{S}\cdot\text{m}^{-1}$ in the black marls, the laboratory study reports values between 1 and $600 \mu\text{S}/\text{m}$ over a comparable frequency range. The frequency dependencies of field and laboratory data also show a similar behavior. Both the near-linear increase (on a log-log scale) of σ'' observed in the less polarizable zone at 140 m (see Fig. 7) as well as the near-constant behavior with slight peaks observed in the more polarizable zones around 100 m and 280 m can also be found in the laboratory data set. In both data sets, σ'' peaks tend to be associated with higher polarization magnitudes.

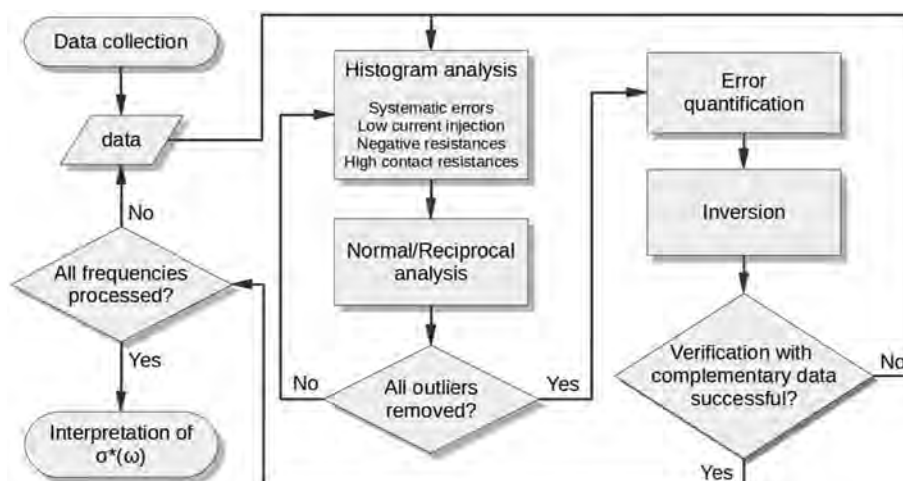


Fig. 8. Workflow chart presenting the iterative processes for the processing of IP and SIP datasets.

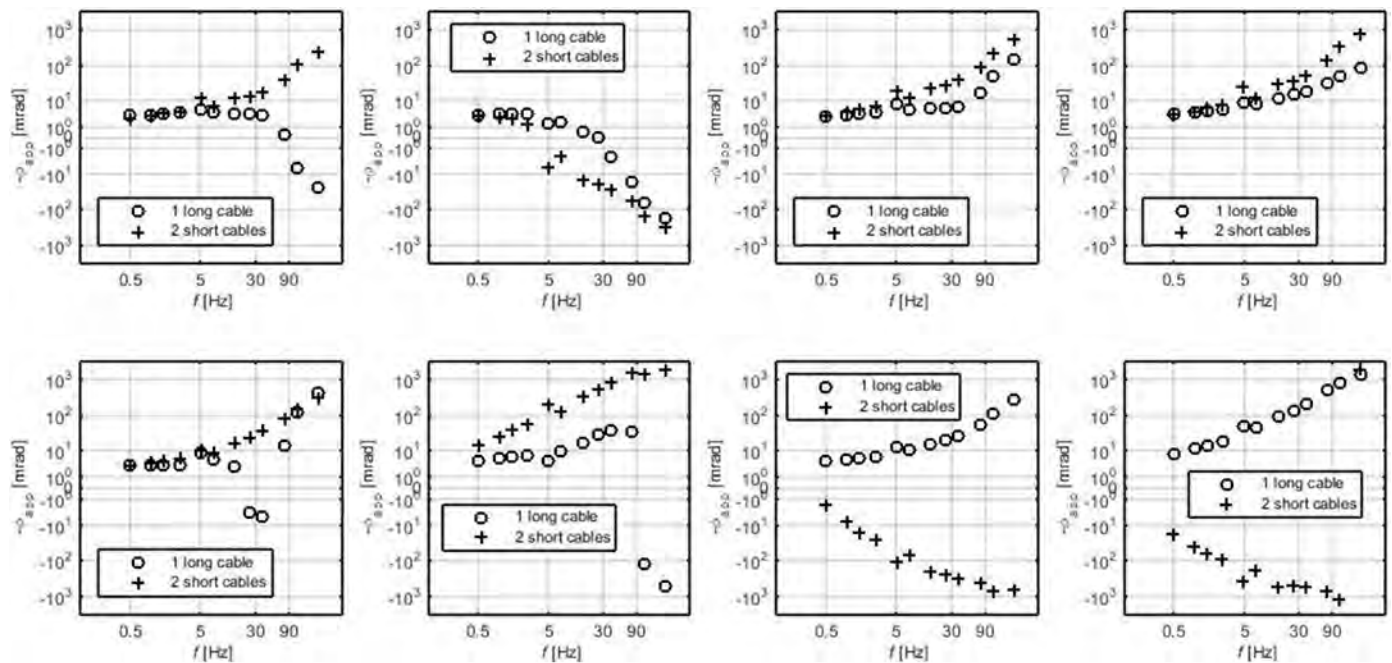


Fig. 9. Representative apparent phase-shift (ϕ_{app}) spectra collected with current and potential dipoles in the same cable bundle (open circles) and using separate cable bundles for current and potential electrodes (crosses). For the measurements in the same cables, current injections were performed between electrodes 1 and 2 and the potential readings were collected by adjacent electrode pairs between electrodes 3 to 11, representing the longest separations from the measuring device. Whereas measurements with separate cables used current injections between electrodes 31 and 32 and potential readings performed with electrodes between 33 and 41 using adjacent electrode pairs, which represent the shorter cable lengths to the measuring device. Measurements refer to the eight potential differences collected with adjacent electrodes (DD0 protocol) for a given current injection.

Changes in the shape of the σ'' spectra are, consistently to Ghorbani et al. (2009), based on variations in the clay content and the chemical composition of the clay minerals.

The spectral position of the polarization (σ'') maximum is generally attributed to a characteristic grain size (e.g., Revil and Florsch, 2010) or a characteristic pore size (e.g., Binley et al., 2005). The low-frequency (i.e. 1.5–2.5 Hz) polarization maximum observed in the black marls points to a slow polarization processes dominated by large grains (or pores). As Ghorbani et al. (2009) argue, relatively large non-clayey (i.e. quartz and calcite) grains surrounded by much smaller clay minerals are the most probable reason for the slow polarization process.

The lack of a clear polarization maximum and the smaller polarization magnitude in the mix of weathered black marls and flysch unit indicates a homogeneous distribution of large non-clay grains, with the increase in σ'' at high frequencies (> 10 Hz) likely indicating a fast polarization resulting from disperse (i.e. not attached to the larger grains) fine grains in flysch materials. Moreover, plots in Fig. 7 reveal an erratic behavior at higher frequencies (> 30 Hz) in the black marls and a steep increase of σ'' in the flysch sediments. This high-frequency response in SIP measurements is generally related to the occurrence of electromagnetic coupling in the data.

3.4. Electromagnetic coupling in SIP imaging data

The critical frequency (f_c) refers to the frequency at which the polarization response has a maximum (i.e., peak), and, as mentioned before, is attributed to a length scale (grain or pore size), which is also controlling groundwater flow (Binley et al., 2005; Slater, 2006). Hence, petrophysical relationships linking hydrogeological and electrical parameters are based on the relaxation time (Revil and Florsch, 2010), which is inversely proportional to f_c . However, SIP field measurements performed at relatively high frequencies (> 25 Hz) are often affected by distortions due to electromagnetic (EM) coupling, impeding a quantitative determination of relaxation times at high frequencies.

In SIP data, EM coupling is known to be an important source of

systematic error, in particular at high frequencies. However, some studies have shown that even at relatively low frequencies (around 4 Hz), EM distortions can affect ϕ_{app} readings (Flores Orozco et al., 2011). EM coupling may occur due to (i) inductive effects taking place in conductive subsurface materials due to current flowing during current injections (Schmutz et al., 2014); (ii) mutual impedances between the wires connecting the potential and the current dipoles (Zimmermann et al., 2008, and references therein); and (iii) capacitive effects due to parasitic EM fields resulting from differences in the contact impedances between the electrodes and the subsurface or between the conductive shield of the cable and the surface (Zhao et al., 2013).

EM (inductive) coupling is proportional to the conductivity of the ground, the frequency and the squared cable length connecting the electrodes (Halloy, 1974). Consequently, it can be expected to affect high-frequency IP measurements (> 1 Hz), in particular in clay-rich materials related to high σ' , as observed at the La Valette landslide. Over the last decades, several studies have proposed to use numerical modeling of the high-frequency EM response of homogeneous and layered conductive media to remove the effect of EM coupling from different dipole configurations (Halloy, 1974; Routh and Oldenburg, 2001). However, rough topographies, such as the one of the La Valette landslide, significantly influence the geometry of the cables and put a limit to such EM decoupling approaches. Moreover, such corrections do not address capacitive coupling.

A different approach fits a Cole-Cole relaxation model to the high-frequency response and subtracts this response from the measured values (Pelton et al., 1978). Kemna (2000) demonstrated the applicability of such approach in tomographic applications and extended the method to account for positive and negative EM effects, which reflect dominating inductive or capacitive coupling. Meanwhile, other authors have investigated field methodologies to avoid, or minimize, EM coupling, such as the deployment of separate cables for current injections and potential measurements (Dahlin et al., 2002; Dahlin and Leroux, 2012).

To assess EM coupling in our SIP measurements and illustrate some practical limitations of the aforementioned decoupling approaches, Fig. 9 shows representative DD0 apparent phase spectra for eight potential dipoles. SIP measurements were collected using two different setups: (a) current injection between electrodes 1 and 2 and potential readings between adjacent electrode pairs between electrodes 3 to 10, to illustrate the effect of EM coupling due to one long multi-core cable (160 m length); and (b) current injection between electrodes 31 and 32 and potential readings between adjacent electrode pairs between electrodes 33 to 41 using two short (10 m) and separate cables, one for current injection and the other for potential dipoles. Although the geometries of the measurements vary significantly, all apparent phase spectra in Fig. 9 reveal similar trends at high frequencies: a linear increase (or decrease) of ϕ_{app} with frequency, which sets on at about 25 Hz and is clearly indicative of EM coupling.

The spectra in Fig. 9 demonstrate that even separating current from potential cables does not yield a significant improvement of high-frequency measurements. Most likely, either capacitive coupling or induction in the conductive subsurface dominates over cable effects. Furthermore, EM coupling may result in sign reversals, which can be attributed to dominating inductive (commonly negative ϕ_{app} values) or capacitive (commonly positive ϕ_{app} values) effects. Although not discussed here, the recollection of measurements after splitting dipoles for current injection and potential readings in separate cables (Dahlin and Leroux, 2012) may help to distinguish which IP readings are still within the range of negligible EM coupling.

Application of the decoupling method proposed by Pelton et al. (1978) resulted in corrected ϕ_{app} values below 1 mrad (data not shown). This clearly indicated that the readings were dominated by EM coupling and no information about the subsurface polarization response could be recovered from high-frequency (above 25 Hz) readings.

The deployment of instruments using fiber optic instead of ERT multicore cables has also been proposed to improve the collection of IP data at high frequencies (Schmutz et al., 2014). However, previous studies deploying such instruments also revealed EM coupling in the data starting at ~ 30 Hz (Flores Orozco et al., 2012b). Alternatively, the use of coaxial cables demonstrated the possibility to collect SIP data without apparent EM coupling over the frequency range between 0.06 and 100 Hz (Flores Orozco et al., 2013), maybe offering a possibility for further research in the investigation of clay-rich landslides.

The collection of data with potential electrodes placed within the current dipole (MG, Wenner or Schlumberger arrays) is also related to strong EM coupling in SIP datasets (Flores Orozco et al., 2013). Furthermore, such configurations bear the risk of contamination of the apparent phase readings due to polarization of the electrodes placed within the current pathways. Hence, DD configurations are commonly recommended for the collection of both single frequency IP and SIP measurements.

3.5. IP imaging results for different electrode configurations

To evaluate possible effects of the electrode configuration on the SIP imaging results, Fig. 10 shows CC images obtained from data at 1 Hz collected along Profile 4 using different electrode configurations, DD0, DD3, DDmix, and MG. All datasets were pre-processed following the procedure presented in the section Pre-processing of IP data sets described above.

In general, the images of the real component of CC (σ' , first column in Fig. 10) show consistent results for measurements collected with different measuring protocols. Yet, it is noticeable that the DD0 protocol has the lowest depth of investigation (≤ 50 m, as indicated by the blanked-out areas), whereas DD3, DDmix and MG configurations yield similar depths of investigation of about 70 m and deeper. The low depth of investigation of the DD0 configuration is expected and can be explained by the reduced maximum separation between current and potential dipoles. Nevertheless, all configurations are sensitive down to

depths well below the sliding plane located between 5 and 30 m below ground surface (see dashed line in Fig. 10). Regarding the main units resolved in the σ' images presented in Fig. 10, results are consistent with those along Profile 2 (see Fig. 6), where the flysch unit stands out with high electrical conductivity values and the stable black marls exhibit slightly lower σ' .

Images of the polarization effect (σ'' , second column in Fig. 10) also show structures, which are consistent with those observed along Profile 2 (see Fig. 6). Maximum σ'' values along Profile 4 do not exceed $\sim 200 \mu\text{S}/\text{m}$, which are in agreement with maximum σ'' values in the upper part of Profile 2, where the two profiles intersect. Again, the flysch unit above the sliding plane is found to have a low polarization response ($\sigma'' < 100 \mu\text{S}\cdot\text{m}^{-1}$), whereas higher polarization responses ($\sigma'' \sim 200 \mu\text{S}\cdot\text{m}^{-1}$) can be found right below the contact between the mix of weathered black marls and flysch unit and the intact black-marl bedrock.

Regarding the spatial resolution of the different σ'' anomalies, Fig. 10 reveals differences between the four measurement configurations. Sharp contacts of the polarizable anomalies, especially those located between ~ 100 and ~ 200 m, indicate a higher spatial resolution of the three DD configurations as compared to the MG configuration. Furthermore, the four different measurement configurations resolve different polarizable anomalies. The DD0 results reveal polarizable anomalies only in the vicinity of the sliding plane; whereas DD3, DDmix and MG configurations resolve deeper anomalies, which are located below the sliding plane and extend beyond the limits of the sliding mass deep into the black marls forming the left and right flank (anomaly between ~ 200 and ~ 300 m). These deep anomalies are most pronounced in the images obtained from the MG data, which might be related to the high S/N of this configuration (c.f., Fig. 3). Performing the inversion with error parameters determined from the normal-reciprocal misfit of the DD configurations (associated to lower S/N) may over-estimate data error in MG measurements, which are associated to much larger transfer resistance values than those in DD measurements as observed in Fig. 3; thus resulting in a slight over-fitting in MG images, leading to the creation of the high polarizable anomaly values observed in Fig. 10.

Conclusively, the DDmix measuring protocol presents a good trade-off between spatial resolution and S/N. Furthermore, as mentioned before, DD measuring protocols can be designed to avoid the collection of voltage readings with electrodes previously used for current injection. An adequate processing of the raw data (see section Pre-processing of IP data sets) permits the computation of consistent imaging results independently of the selected measuring protocol. Furthermore, nested potential dipoles within the current dipole may enhance electromagnetic coupling in the data.

4. Conclusions

We present the application of single-frequency IP and SIP imaging results for the understanding of hydrogeological units at the La Valette landslide. We demonstrate that a careful processing of the IP data regarding (1) the detection and removal of outliers and (2) the quantification of random error permits to solve for consistent imaging results obtained along different profiles, and independently of the deployed electrode configuration. We also demonstrate the distortion in the SIP measurements due to EM coupling, a topic rarely addressed in field IP application but that may largely affect the interpretation of the electrical images. Our data reveal EM coupling even at the low frequencies, starting at ~ 25 Hz, even for data collected using separate cables for current injections and potential measurements.

Our results demonstrate the possibility to improve the interpretation of electrical conductivity images in clay-rich landslides by adding the information gained by means of the images of the polarization effect. Results presented here revealed two main units: a conductive and low polarizable unit corresponding to the sliding mix of black marls and

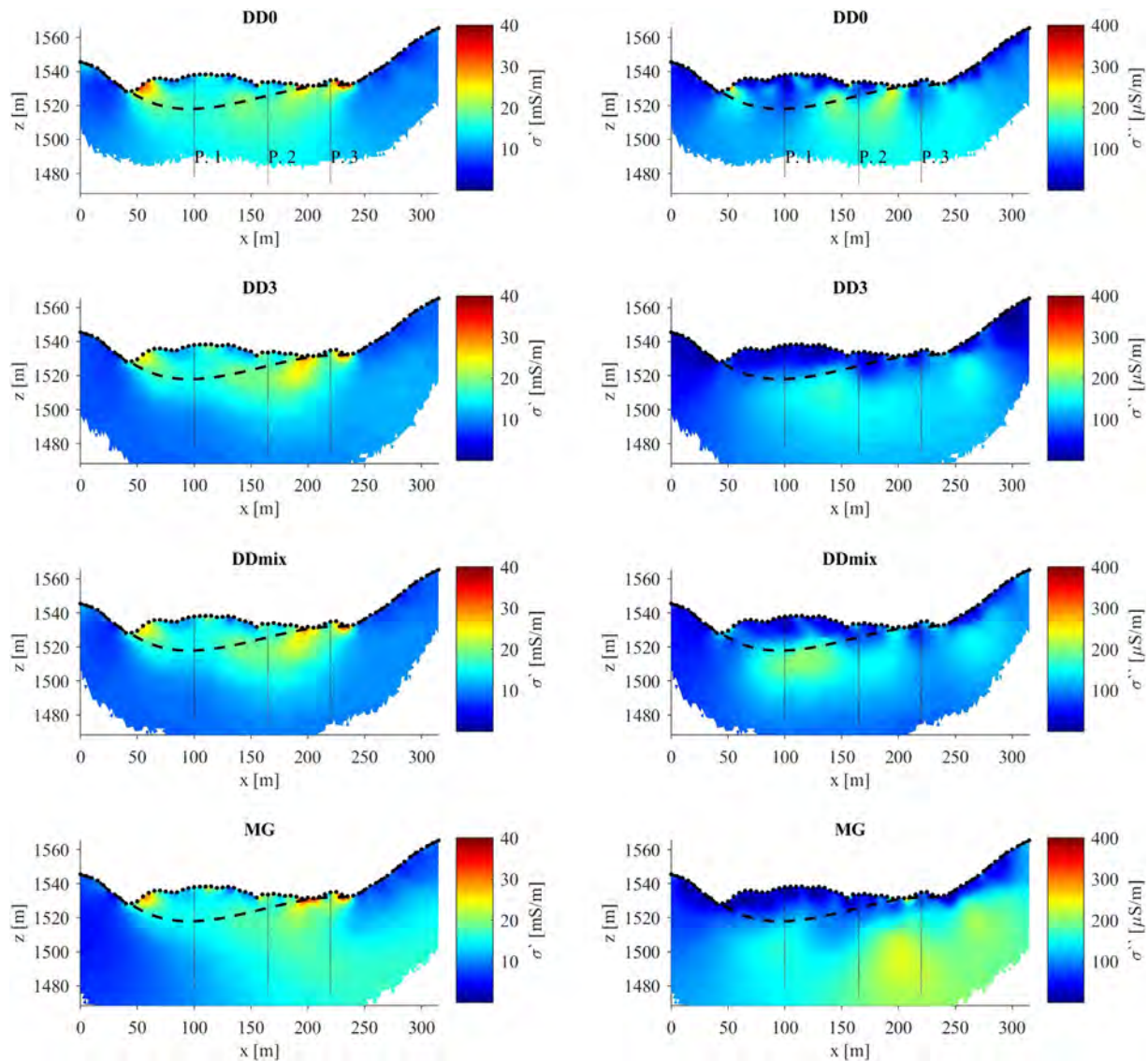


Fig. 10. CC imaging results for data collected along Profile 4 using different electrode configurations, expressed in terms of the real (left row) and imaginary (right row) component of the CC. Dashed horizontal lines indicate the position of the sliding plane as obtained from wellbore and seismic data (Samyn et al., 2012). Vertical lines indicate the intersections with Profiles 1, 2, and 3 (from left to right).

flysch materials on top of slightly less conductive black-marl bedrock, which is correlated to an enhanced polarization response. Imaging results of the polarization effect help to better delineate the contact between the two units, as well as lateral variations in the black marls, which may be indicative of variable hydraulic properties. The contact between materials with different hydraulic properties is commonly associated to zones vulnerable to landslides due to the undesired increase in pore-fluid pressure following rainfall events. Hence, the lateral changes observed in the black marls through the SIP images are likely indicative of changes in the clay fractions and the corresponding variations in hydraulic conductivity. It is also worth noting here that seismic surveys would also fail to identify the anomaly revealed in the SIP images, considering that the mechanical properties of flysch and alluvial sediments are similar. Furthermore, the interpretation of solely resistivity properties gained by means of ERT is limited, as observed in σ' plots in Fig. 6.

Our results suggest that SIP imaging is a suitable method to improve the understanding of landslides, in particular, to improve the interpretation of electrical conductive materials such as clay-rich geological media. Nevertheless, further investigations at La Valette landslide are required to fully validate the interpretation of the SIP imaging results

presented here. We believe that SIP imaging results could be used to help designing the collection of soil and water sampling campaigns to fully understand the electrical, hydraulic and geotechnical properties of the subsurface.

Acknowledgments

The preparation of this material is supported through the Austrian Science Fund (FWF) – Agence Nationale de la Recherche (ANR) research project FWF-I-2619-N29 and ANR-15-CE04-0009-01 HYDROSLIDE: *Hydro-geophysical observations for an advanced understanding of clayey landslides*. We also want to thank Veronika Rieckh, Martine Trautmann, Kusnahadi Susanto, Eric Stell, and Colas Bohy for their help during the fieldwork. We also want to thank the Editor, the Guest Editor Michel Jaboyedoff and three anonymous reviewers for their comments and suggestions that significantly improved the quality of this manuscript.

References

Archie, G.E., 1942. The electrical resistivity log as an aid in determining some reservoir

- characteristics. *Trans. AIME* 146 (1), 54–62.
- Binley, A., Slater, L.D., Fukes, M., Cassiani, G., 2005. Relationship between spectral induced polarization and hydraulic properties of saturated and unsaturated sandstone. *Water Resour. Res.* 41, W12417.
- Binley, A., Hubbard, S.S., Huisman, J.A., Revil, A., Robinson, D.A., Singha, K., Slater, L.D., 2015. The emergence of hydrogeophysics for improved understanding of subsurface processes over multiple scales. *Water Resour. Res.* 51 (6), 3837–3866.
- Brückl, E., Brunner, F.K., Lang, E., Mertl, S., Müller, M., Stary, U., 2013. The Gradenbach observatory—monitoring deep-seated gravitational slope deformation by geodetic, hydrological, and seismological methods. *Landslides* 10, 815–829.
- Bücker, M., Hördt, A., 2013. Long and short narrow pore models for membrane polarization. *Geophysics* 78 (6), E299–E314.
- Dahlin, T., Leroux, V., 2012. Improvement in time-domain induced polarization data quality with multi-electrode systems by separating current and potential cables: near surface. *Geophysics* 10 (6), 545–565.
- Dahlin, T., Loke, M.H., 2015. Negative apparent chargeability in time-domain induced polarisation data. *J. Appl. Geophys.* 123, 322–332.
- Dahlin, T., Zhou, B., 2006. Multiple-gradient array measurements for multichannel 2D resistivity imaging: near surface. *Geophysics* 4 (2), 113–123.
- Dahlin, T., Leroux, V., Nissen, J., 2002. Measuring techniques in induced polarisation imaging. *J. Appl. Geophys.* 50 (3), 279–298.
- Flores Orozco, A., Williams, K.H., Long, P.E., Hubbard, S.S., Kemna, A., 2011. Using complex resistivity imaging to infer biogeochemical processes associated with bioremediation of an uranium-contaminated aquifer. *J. Geophys. Res.* 116 (G3), 2156–2206 Biogeosciences.
- Flores Orozco, A., Kemna, A., Zimmermann, E., 2012a. Data error quantification in spectral induced polarization imaging. *Geophysics* 77 (3), E227–E237.
- Flores Orozco, A., Kemna, A., Oberdörster, C., Zschornack, L., Leven, C., Dietrich, P., Weiss, H., 2012b. Delineation of subsurface hydrocarbon contamination at a former hydrogenation plant using spectral induced polarization imaging. *Journal of Contaminated Hydrology* 136–137, 131–144.
- Flores Orozco, A., Williams, K.H., Kemna, A., 2013. Time-lapse spectral induced polarization imaging of stimulated uranium bioremediation: near surface. *Geophysics* 11 (5), 531–544.
- Flores Orozco, A., Velimirovic, M., Tosco, T., Kemna, A., Sapion, H., Klaas, N., Sethi, R., Leen, B., 2015. Monitoring the injection of microscale zero-valent iron particles for groundwater remediation by means of complex electrical conductivity imaging. *Environ. Sci. Technol.* 49 (9), 5593–5600.
- Flores Orozco, A., Gallistl, J., Bücker, M., Williams, K., 2018. Decay-curve analysis for data error quantification in time-domain induced polarization imaging. *Geophysics* 83 (2), E75–E86.
- Friedel, S., Thielen, A., Springman, S.M., 2006. Investigation of a slope endangered by rainfall-induced landslides using 3D resistivity tomography and geotechnical testing. *J. Appl. Geophys.* 60 (2006), 100–114.
- Gance, J., Grandjean, G., Samyn, K., Malet, J.-P., 2012. Quasi-Newton inversion of seismic first arrivals using source finite bandwidth assumption: application to subsurface characterization of landslides. *J. Appl. Geophys.* 87, 94–106.
- Gance, J., Malet, J.-P., Supper, R., Sailhac, P., Ottowitz, D., Jochum, B., 2016. Permanent electrical resistivity measurements for monitoring water circulation in clayey landslides. *J. Appl. Geophys.* 126, 98–115.
- Ghorbani, A., Cosenza, P., Revil, A., Zamora, M., Schmutz, M., Florsch, N., Jougnot, D., 2009. Non-invasive monitoring of water content and textural changes in clay-rocks using spectral induced polarization: a laboratory investigation. *Appl. Clay Sci.* 43 (3), 493–502.
- Hallof, P.G., 1974. The IP phase measurement and inductive coupling. *Geophysics* 39 (5), 650–665.
- Hibert, C., Grandjean, G., Bitri, A., Travelletti, J., Malet, J.-P., 2012. Characterizing landslides through geophysical data fusion: example of the La Valette landslide (France). *Eng. Geol.* 128, 23–29.
- Kemna, A., 2000. *Tomographic Inversion of Complex Resistivity: Theory and Application*. Der Andere Verlag, Osnabrück.
- Kemna, A., Binley, A., Cassiani, G., Niederleithinger, E., Revil, A., Slater, L., Williams, K.H., Flores Orozco, A., Haegel, F.H., Hördt, A., Kruschwitz, S., Leroux, V., Titov, K., Zimmermann, E., 2012. An overview of the spectral induced polarization method for near-surface applications: near surface. *Geophysics* 10 (6), 453–468.
- Labrecque, D.J., Miletto, M., Daily, W., Ramirez, A., Owen, E., 1996. The effects of noise on Occam's inversion of resistivity tomography data. *Geophysics* 61, 538–548.
- Lesmes, D.P., Frye, K.M., 2001. Influence of pore fluid chemistry on the complex conductivity and induced polarization responses of Berea sandstone. *J. Geophys. Res.* Solid Earth 106 (B3), 4079–4090.
- Malet, J.-P., Durand, Y., Remaitre, A., Maquaire, O., Etchevers, P., Guyomarch, G., Dégué, M., van Beek, L.P.H., 2007. Assessing the influence of climate change on the activity of landslides in the Ubaye Valley. In: McInnes, R., Jakeways, J., Fairbank, H., Mathie, E. (Eds.), *Proceedings International Conference on Landslides and Climate Change – Challenges and Solutions*. Taylor & Francis, London, pp. 195–205.
- Malet, J.-P., Ulrich, P., Déprez, A., Masson, F., Lissak, C., Maquaire, O., 2013. Continuous Monitoring and Near-Real Time Processing of GPS Observations for Landslide Analysis: A Methodological Framework. In: Margottini, C., Canuti, P., Sassa, K. (Eds.), *Landslide Science and Practice*. Springer, Berlin, Heidelberg.
- Maraun, D., Wetterhall, F., Ireson, A.M., Chandler, R.E., Kendon, E.J., Widmann, M., Brienen, S., Rust, H.W., Sauter, T., Themeßl, M., Venema, V.K.C., Chun, K.P., Goodes, C.M., Jones, R.G., Onof, C., Vrac, M., Thiele-Eich, I., 2010. Precipitation downscaling under climate change: Recent developments to bridge the gap between dynamical models and the end user. *Rev. Geophys.* 48 (3), RG3003.
- Marescot, L., Monnet, R., Chapellier, D., 2008. Resistivity and induced polarization surveys for slope instability studies in the Swiss Alps. *Eng. Geol.* 98 (1), 18–28.
- Pelton, W.H., Ward, S.H., Hallof, P.G., Sill, W.R., Nelson, P.H., 1978. Mineral discrimination and removal of inductive coupling with multifrequency IP. *Geophysics* 43 (3), 588–609.
- Raucoules, D., Michele, M., Malet, J.P., Ulrich, P., 2013. Time-variable 3D ground displacements from High-Resolution Synthetic Aperture Radar (SAR). Application to La Valette landslide (South French Alps). *Remote Sens. Environ.* 139, 198–204.
- Revil, A., Florsch, N., 2010. Determination of permeability from spectral induced polarization in granular media. *Geophys. J. Int.* 181 (3), 1480–1498.
- Revil, A., Glover, P.W.J., 1998. Nature of surface electrical conductivity in natural sands, sandstones, and clays. *Geophys. Res. Lett.* 25 (5), 691–694.
- Routh, P.S., Oldenburg, D.W., 2001. Electromagnetic coupling in frequency-domain induced polarization data: a method for removal. *Geophys. J. Int.* 145, 59–76.
- Samyn, K., Travelletti, J., Bitri, A., Grandjean, G., Malet, J.-P., 2012. Characterization of a landslide geometry using 3D seismic refraction traveltimes tomography: the La Valette landslide case history. *J. Appl. Geophys.* 86, 120–132.
- Sastry, R.G., Mondal, S.K., 2012. Geophysical characterization of the Salna Sinking Zone, Garhwal Himalaya, India. *Surv. Geophys.* 1–31.
- Schmutz, M., Albouy, Y., Guérin, R., Maquaire, O., Vassal, J., Schott, J.J., Desclôitres, M., 2000. Joint electrical and time domain electromagnetism (TDEM) data inversion applied to the Super Sauee earthflow (France). *Surv. Geophys.* 21 (4), 371–390.
- Schmutz, M., Ghorbani, A., Vaudelet, P., Blondel, A., 2014. Cable arrangement to reduce electromagnetic coupling effects in spectral-induced polarization studies. *Geophysics* 79 (2), A1–A5.
- Slater, L., 2006. Near surface electrical characterization of hydraulic conductivity: from petrophysical properties to aquifer geometries – a review. In: 18th IAGA WG 1.2 Workshop on Electromagnetic Induction in the Earth. El Vendrell, Spain (September 17–23, 2006).
- Slater, L., Lesmes, D., 2002. IP interpretation in environmental investigations. *Geophysics* 67 (1), 77–88.
- Slater, L., Binley, A., Daily, W., Johnson, R., 2000. Cross-hole electrical imaging of a controlled saline tracer injection. *J. Appl. Geophys.* 44, 85–102.
- Sumner, J.S., 1976. *Principles of Induced Polarization for Geophysical Exploration*. Elsevier, Amsterdam.
- Supper, R., Ottowitz, D., Jochum, B., Roemer, A., Pfeiler, S., Kauer, S., Keuschnig, M., Ita, A., 2014. Geoelectrical monitoring of frozen ground and permafrost in alpine areas: field studies and considerations towards an improved measuring technology: near surface. *Geophysics* 12 (1), 93–115.
- Travelletti, J., Malet, J.-P., Hibert, C., Grandjean, G., 2009. Integration of geomorphological, geophysical and geotechnical data to define the 3D morpho-structure of the La Valette mudslide (Ubaye Valley, French Alps). In: Malet, J.P., Remaitre, A., Boogard, T. (Eds.), *Proceedings of the International Conference on Landslide Processes: From Geomorphologic Mapping to Dynamic Modelling*, Strasbourg, CERG Editions, pp. 203–208.
- Travelletti, J., Sailhac, P., Malet, J.-P., Grandjean, G., Ponton, J., 2012. Hydrological response of weathered clay-shale slopes: water infiltration monitoring with time-lapse electrical resistivity tomography. *Hydrol. Process.* 26 (14), 2106–2119.
- Travelletti, J., Malet, J.-P., Samyn, K., Grandjean, G., Jaboyedoff, M., 2013. Control of landslide retrogression by discontinuities: evidence by the integration of airborne- and ground-based geophysical information. *Landslides* 10 (1), 37–54.
- Ward, S.H., 1988. The Resistivity and Induced Polarization Methods: In *Symposium on the Application of Geophysics to Engineering and Environmental Problems 1988*. Society of Exploration Geophysicists, pp. 109–250.
- Waxman, M.H., Smits, L.J.M., 1968. Electrical conductivities in oil-bearing shaly sands. *Soc. Pet. Eng. J.* 8 (02), 107–122.
- Weigand, M., Flores Orozco, A., Kemna, A., 2017. Reconstruction quality of SIP parameters in multi-frequency complex resistivity imaging: near surface. *Geophysics* 15 (2), 187–199.
- Zhao, Y., Zimmermann, E., Huisman, J.A., Treichel, A., Wolters, B., van Waasen, S., Kemna, A., 2013. Broadband EIT borehole measurements with high phase accuracy using numerical corrections of electromagnetic coupling effects. *Meas. Sci. Technol.* 24 (8), 085005.
- Zimmermann, E., Kemna, A., Berwix, J., Glaas, W., Münch, H.M., Huisman, J.A., 2008. A high-accuracy impedance spectrometer for measuring sediments with low polarizability. *Meas. Sci. Technol.* 19 (10), 105603.

Case History

Analysis of time-lapse data error in complex conductivity imaging to alleviate anthropogenic noise for site characterization

Adrian Flores Orozco¹, Andreas Kemna², Andrew Binley³, and Giorgio Cassiani⁴

ABSTRACT

Previous studies have demonstrated the potential benefits of the complex conductivity (CC) imaging over electrical resistivity tomography for an improved delineation of hydrocarbon-impacted sites and accompanying biogeochemical processes. However, time-lapse CC field applications are still rare, in particular for measurements performed near anthropogenic structures such as buried pipes or tanks, which are typically present at contaminated sites. To fill this gap, we have developed CC imaging (CCI) results for monitoring data collected in Trecate (northwest Italy), a site impacted by a crude oil spill. Initial imaging results reveal only a poor correlation with seasonal variations of the groundwater table at the site (approximately 6 m). However, it is not clear to which extent such results are affected by anthropogenic structures present at the site. To address this, we performed a detailed analysis of the

misfit between direct and reciprocal time-lapse differences. Based on this analysis, we were able to discriminate spatial and temporal sources of systematic errors, with the latter commonly affecting measurements collected near anthropogenic structures. Following our approach, CC images reveal that temporal changes in the electrical properties correlate well with seasonal fluctuations in the groundwater level for areas free of contaminants, whereas contaminated areas exhibit a constant response over time characterized by a relatively high electrical conductivity and a negligible polarization effect. In accordance with a recent mechanistic model, such a response can be explained by the presence of immiscible fluids (oil and air) forming a continuous film through the micro and macropores, hindering the development of ion-selective membranes and membrane polarization. Our results demonstrate the applicability of CCI for an improved characterization of hydrocarbon-contaminated areas, even in areas affected by cultural noise.

INTRODUCTION

Management of hydrocarbon-impacted sites, in particular the design of adequate remediation strategies, encourages the development of new methodologies for the spatial characterization of contaminant plumes and associated biogeochemical processes (e.g., Schädler et al., 2012). Ideally, the characterization techniques should help to define the geometry of the hydrogeologic units and the extent of the contaminant plumes with enhanced resolution,

as well as assess possible biogeochemical transformations of contaminants. To date, site characterization relies mainly on laboratory analysis of gas, soil, and groundwater samples. Although *ex-situ* analysis provides the direct measurement of the parameters of interest (e.g., chemical concentrations), investigations using direct methods are strongly limited by the sampling procedure (i.e., location and volume), thus, reducing the resolution of the investigation — given the spatial and temporal variability of the observed phenomena (e.g., Atekwana and Atekwana, 2010). In most cases,

Manuscript received by the Editor 15 November 2017; revised manuscript received 27 September 2018; published ahead of production 13 December 2018; published online 05 March 2019.

¹TU-Wien, Department of Geodesy and Geoinformation, Geophysics Research Division, Vienna, Austria. E-mail: flores@tuwien.ac.at (corresponding author).

²University of Bonn, Steinmann Institute, Department of Geophysics, Bonn, Germany. E-mail: kemna@geo.uni-bonn.de.

³Lancaster University, Lancaster Environment Centre, Lancaster, UK. E-mail: a.binley@lancaster.ac.uk.

⁴University of Padova, Department of Geosciences, Padova, Italy. E-mail: giorgio.cassiani@unipd.it.

© 2019 Society of Exploration Geophysicists. All rights reserved.

ex-situ investigations rely on the interpretation of too few and largely spaced sampling points requiring the interpolation of the data, which may then not reflect the actual geometry of, e.g., the contaminant plumes, making the relevant interpretations weak and potentially misleading. Furthermore, the collection of samples and laboratory analyses are time-consuming, causing the site characterization to last several months (or even years), potentially resulting in the comparison of data collected under different hydro-geochemical conditions.

Several studies have investigated the applicability of geophysical methods for site characterization taking into account the possibility to gain quasicontinuous spatiotemporal information about the subsurface properties. In particular, given the significant contrasts in the electrical properties between hydrocarbon contaminants (typically associated with low electrical conductivity) and groundwater (low to intermediate electrical conductivity), several studies have suggested the application of electrical resistivity tomography (ERT) (e.g., Sauck, 2000; Chambers et al., 2005; Heenan et al., 2014; Naudet et al., 2014). Nevertheless, over the past two decades, extensive laboratory and field studies have demonstrated that the electrical response of mature hydrocarbon plumes might reveal high electrical conductivity values following biotic and abiotic transformations of the contaminants (for details, we refer to the revision from Atekwana and Atekwana, 2010). Hydrocarbons can act as an energy source promoting microbial growth and the release of metabolic products, such as carbonic acids. Hence, the anomalous high electrical conductivity values observed in mature hydrocarbon plumes have mainly been attributed to an increase in the ionic concentration, and, thus, the fluid electrical conductivity σ_w accompanying the accumulation of carbonic acids (e.g., Cassidy et al., 2001; Werkema et al., 2003; Atekwana et al., 2004). Moreover, carbonic acids may contribute to the weathering of grain surfaces and enhancement of secondary porosity, further increasing the σ' observed in ERT surveys (e.g., Abdel Aal et al., 2006; Atekwana and Atekwana, 2010).

In addition to this, field investigations have also demonstrated the applicability of the complex electrical conductivity (CC), an extension of the ERT method, for improved site characterization (e.g., Kemna et al., 2004; Schmutz et al., 2010; Revil et al., 2011; Deceuster and Kaufmann, 2012; Johansson et al., 2015), and the characterization of the source zone and plume of contaminants (e.g., Flores Orozco et al., 2012a). The CC imaging (CCI) results are expressed in terms of its real σ' and imaginary σ'' components, which refers to the electrical conductivity and capacitive properties of the subsurface, respectively (e.g., Marshall and Madden, 1959; Slater and Lesmes, 2002; Kemna et al., 2012). For geologic media free of metallic minerals, the conductivity is mainly controlled by the saturation σ_w , the connectivity of the pore space (e.g., Archie, 1942), and by surface-conduction processes taking place at the grain-water interface (e.g., Slater and Lesmes, 2002; Slater et al., 2007; Kemna et al., 2012). The imaginary component σ'' is only caused by the polarization of charges in the electrical double layer (EDL) built at the interface between grain and pore water (e.g., Marshall and Madden, 1959; Kemna et al., 2012).

Initial studies (e.g., Olhoeft, 1985; Vanhala, 1997; Kemna et al., 2004) revealed a significant increase in the polarization effect with increasing concentrations of aromatic hydrocarbons (e.g., toluene, kerosene). These are “nonpolar” compounds, which are unable to interact with water molecules, due to their lack of ionic or polar groups. Hence, in the subsurface, they form immiscible droplets

caged within the water filling pores, without direct contact with the grain surface, and thus, are referred to as nonwetting oil. Accordingly, Schmutz et al. (2010) propose a modification of the model describing the polarization of the EDL, formed at the grain-fluid interface, to include the effect of the nonwetting hydrocarbons. Such a model predicts an increase in the polarization response with increasing the volumetric content of nonwetting hydrocarbons.

Contrary to previous studies, Ustra et al. (2012) report a negligible polarization response in laboratory measurement with sand-clay mixtures for different toluene concentrations. At the field scale, Flores Orozco et al. (2012a) observed an initial increase in the polarization response with increasing the concentrations of benzene and toluene, consistent with the response observed in the laboratory by Schmutz et al. (2010). However, the polarization response fades for contaminant concentrations above the saturation concentration (i.e., the occurrence of hydrocarbons as the free-phase), in agreement with the response observed by Ustra et al. (2012). Johansson et al. (2015) also observed similar results in field measurements in a site impacted by perchloroethylene, an “oil-wetting” hydrocarbon. Moreover, Cassiani et al. (2009) observe an inconclusive response for laboratory measurements performed in sand samples mixed with different concentrations of crude oil.

An extension to previous experiments, Revil et al. (2011) reported the decrease in the polarization response with increasing the volumetric content of polar compounds, or oil-wetting hydrocarbons, i.e., the scenario when the oil is in direct contact with the grain surface. However, such observations does not explain the observed increase in the polarization response at low hydrocarbon concentrations observed in field studies (e.g., Flores Orozco et al., 2015). An increase in the polarization response for aged hydrocarbon plumes, in laboratory studies, has been related to the accumulation of negatively charged microbial cells (e.g., Abdel Aal et al., 2006; Atekwana and Slater, 2009; Revil et al., 2012). However, biostimulation experiments at the field scale reported negligible changes in the polarization effects following biofilm formation, but a much larger response due to the precipitation of minerals accompanying microbial activity (e.g., Flores Orozco et al., 2011, 2013). Therefore, recently it has been suggested that the increase in the polarization effect observed in aged hydrocarbon contaminant plumes might be related to the precipitation of metallic minerals accompanying microbial activity (Mewafy et al., 2013; Abdel Aal et al., 2014). Moreover, changes in the chemical composition of groundwater, as well as the accumulation of metabolic by-products (e.g., organic acids), can also modify the surface properties in the hydrocarbons (e.g., Cassidy et al., 2001), for instance, promote the changes from nonwetting oil to oil-wetting, thus resulting in modifications of the geophysical response.

The noteworthy differences observed in laboratory and field investigations clearly demonstrate the necessity for further investigations to better evaluate the applicability of the CCI method and improve the interpretation of the imaging results. Monitoring studies at the field scale are necessary to understand the dynamics in the geophysical response, considering the impossibility to reproduce in the laboratory the variety of processes taking place (simultaneously) in hydrocarbon-impacted sites. Moreover, existing field studies have been conducted in areas without anthropogenic structures. However, hydrocarbon contaminants are typically located at (often derelict) industrial areas and they are commonly associated with their proximity to anthropogenic structures, such as power lines,

or buried pipes and tanks. The electrical response of such anthropogenic structures may mask the one of the subsurface, thus hindering an adequate interpretation of the CCI results and its application for site characterization. Therefore, field investigations need to address the capabilities of the CCI method to discriminate between signatures due to anthropogenic structures, lithology, and contaminants, as required for an improved site characterization.

In this study, we present the results of one-year CC monitoring measurements collected at a site impacted by a crude oil spill. Petroleum crude oil is a light nonaqueous phase liquid (LNAPL) mainly composed of nonpolar compounds; thus, it is expected to result in an increase in the polarization response with increasing the concentration (at least at early stages), after the model by [Schmutz et al. \(2010\)](#). Strong variations in the depth to the groundwater table at the site permitted the investigation of changes in the electrical response due to the vertical transport of the contaminant and biogeochemical processes. Extensive geochemical data have been collected since the time of an oil spill accident in 1994. Such data are necessary to constrain the interpretation of CCI results. At the site, relatively few anthropogenic structures are present; yet, their response can distort or mask the electrical signatures associated with the lithology and contaminant. Considering that such distortions might also control temporal fluctuations in the measured data, anthropogenic structures can then be defined as sources of temporal error. To better investigate this, we performed a detailed analysis of the time-lapse data-error, aiming at the identification and removal of spatial and temporal outliers (i.e., systematic errors) and the quantification of uncertainties in CC monitoring measurements. The analysis of the data presented here aims at evaluating the possibility of minimizing the distortion due to cultural noise in CC monitoring images in areas impacted by high hydrocarbon concentrations, a step forward for soil contamination assessment and site characterization.

MATERIAL AND METHODS

Study area

The study area is located close to Trecate (Novara, Italy), where a blowout from a deep oil well in February 1994 resulted in the spill of approximately 15,000 m³ of crude oil ([Cassiani et al., 2014](#)). The subsequent site remediation has been reported, for example, in the study of [Brandt et al. \(2002\)](#). The area is mainly agricultural with a prevalence of man-made rice paddies, partly converted to other crops, such as soy and maize. The main zone of hydrocarbon contamination covers approximately 96 ha, affecting the soil, vadose zone, and groundwater. The saturated and unsaturated zones have been monitored for natural attenuation and evolution of contamination conditions since the time of the accident. Measurable levels of hydrocarbon contamination have been observed in soil samples collected at different depths between 2 and 10 m below ground surface (bgs) between 1995 and 2007. Figure 1 shows the

total petroleum hydrocarbon (TPH) volumetric content in the soil as reported from chemical analysis of samples collected at more than 115 points, distributed at depths of 2, 6, and 10 m bgs and sampled using direct-push techniques. The groundwater samples collected in the contaminated area show a brown oil phase emulsion in the aqueous phase, and high dissolved hydrocarbon concentrations limited essentially to the same area of elevated contamination in the soil at 10 m in depth, shown in Figure 1. Further spread of the contaminant plume in groundwater downstream (approximately southeast) of the site is strongly limited by strong biodegradation of the hydrocarbons, as shown, e.g., by the study of [Burberry et al. \(2004\)](#). The contamination in the soil is likely to have been controlled over the years by the strong seasonal water table oscillations between 6 and 12 m bgs, which produces a clear smear zone, also spreading the contaminant laterally at greater depths (see Figure 1).

Geologically, the site is characterized by a thick sequence of poorly sorted silty sands and gravels in extensive lenses, typical of braided river sediments ([Cassiani et al., 2004](#)). Braided rivers are related to high energy but are also typical of environments that dramatically decrease the channel depth and velocity, and, thus could lead to the intercalation of fine sediments, such as clay ([Williams and Rust, 1969](#)). Such intercalations lead to the formation of paleochannels at the site, which can be found now filled by fine

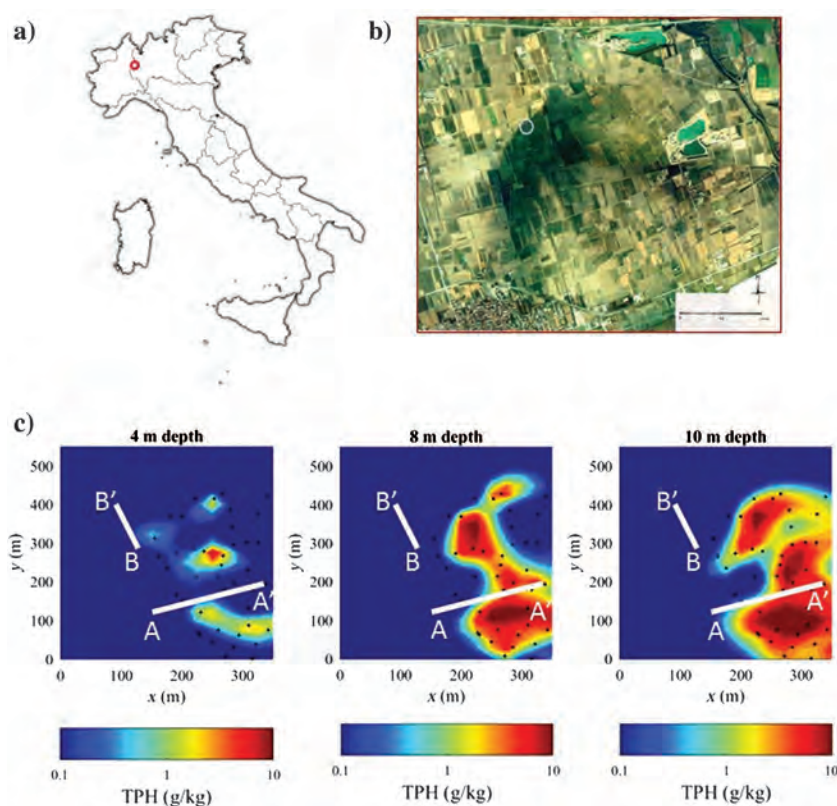


Figure 1. (a) The location of the study area, (b) satellite image revealing the extension of the contaminant plume at the surface following the crude oil well blowout in 1994, and (c) contaminant distribution in the subsurface at different depths as obtained from the chemical analysis of soil samples (black dots). The contaminant concentrations are expressed in terms of the TPH per unit soil mass. CC monitoring data sets were collected in lines A-A' (west-east) and B-B' (south-north) indicated by the solid white lines. Note that line B-B' lies in the uncontaminated area; thus, it can be considered as a "blank" line, whereas line A-A' crosses a heavily contaminated zone.

sediments (clay and silt), as discussed by Cassiani et al. (2004). Additionally, an artificial layer of clayey-silty material, approximately 1–2 m thick, placed as a liner for rice paddies about a century ago, overlies most of the site (Cassiani et al., 2014). The seasonal fluctuation in the water table is primarily a result of recharge from regional irrigation and flooding of the rice paddies. During the experiments presented here, the depth to the water table was observed at its maximum by the end of February (10.5 m bgs) and at its minimum at the end of September (5 m bgs). Further details on the site can be found in the study by Cassiani et al. (2014).

Complex conductivity monitoring measurements

The CC method — also known as the induced polarization (IP) method — is based on measurements using a four-electrode array, where two electrodes are used to inject electric current and the other two are used to measure the resulting electrical voltages. In the present study, measurements were collected in the time domain with a Syscal Pro (IRIS Instruments, France) using a square wave with a 50% duty cycle and a pulse length of 2 s. Integral chargeability readings were performed between 240 and 1840 ms after shutting current injection off using a linear distribution of 20 windows. Measurements were conducted using stainless steel electrodes with a separation of 2.5 m and a dipole-dipole “skip-3” configuration for a dipole length of 10 m (i.e., the dipole length defined by the number of skipped electrodes along the electrode array) to reach an estimated depth of investigation of approximately 12 m.

Monitoring measurements were collected along the two lines shown in Figure 1: (1) Line A-A', using a total of 81 electrodes in a roll-along scheme (an extension of 33 electrodes) for a total length of 200 m, with a rough west–east orientation, the latter designed to cover areas from negligible to high contaminant concentrations; and (2) line B-B', a control line deploying a total of 48 electrodes for a length of 117.5 m, approximately oriented south–north and located in the uncontaminated area of the site (Figure 1). Measurements were collected every two months, starting in May 2009 and with the last data set collected in February 2010. All data sets were collected as direct-reciprocal pairs for data error (ϵ) analysis, with reciprocal readings referred to the recollection of the data after interchanging current and potential dipoles. Error analysis of independent data sets (i.e., collected at each time) was performed following the methodology described by Flores Orozco et al. (2012b). Additionally, we present here a methodology aiming at characterizing the data error in time-lapse differences.

Inversion of the data was performed using CRTomo, a smoothness-constrained inversion algorithm by Kemna (2000). The code solves for the distribution of the complex electrical resistivity ρ^* , the inverse of the CC ($\sigma^* = 1/\rho^*$) from a tomographic electrical impedance data sets Z^* . Hence, integral chargeability measurements were linearly converted to electrical impedance phase-shift values using the approach of Kemna et al. (1997) assuming a constant phase response (at the fundamental frequency of 0.125 Hz). The assumption of a constant-phase response is valid considering the relatively narrow frequency-range for the measurements of the integral chargeability, equivalent to approximately 0.5–4 Hz. To account for the known geologic layering at the site (Cassiani et al., 2004, 2014), all inversions presented here were performed using a preferential horizontal smoothing with a ratio of 40:1 of the horizontal versus the vertical smoothing parameters (for details in the implementation, see, e.g., Kemna et al., 2002).

To avoid the interpretation of model parameters with a poor sensitivity, we blanked in the imaging results those pixels associated with cumulated sensitivity values two orders of magnitude smaller than the highest cumulated sensitivity (i.e., the sum of absolute, data-error weighted, sensitivities of all considered measurements; see, e.g., Kemna et al., 2002; Weigand et al., 2017).

Complementary geophysical data

To assess lateral variations of the electrical properties at the site, mapping measurements were conducted with low-induction-number electromagnetic (EMI) methods using a CMD-4 (GF Instruments, Czech Republic), which has an effective depth of investigation of 6 m.

To support the interpretation of the CCI results, ground-penetrating radar (GPR) data sets were collected along the same CC monitoring profiles using a PulseEKKO Pro system (Sensors & Software, Canada) with 100 MHz antennas. The GPR surface profiles presented here were based on a common-offset acquisition. Borehole GPR data, also using 100 MHz antennas, were collected with two schemes: (1) a multiple offset gather with 0.5 m vertical spacing between antenna stations and (2) a zero-offset profile (ZOP) with 0.25 m spacing between antenna stations. The complete description of the GPR processing and results is presented in the study of Cassiani et al. (2014).

To better differentiate in this study between the different geophysical data and modeled quantities, CCI results are presented in terms of its real σ' and imaginary σ'' components, whereas the measurements are represented by the apparent resistivity ρ_a and phase-shift φ_a . The EMI mapping data are presented in terms of the measured apparent conductivity σ_a because we are only interested in the lateral changes.

RESULTS AND DISCUSSIONS

Baseline characterization

Figure 2 presents the imaging results in terms of the electrical conductivity (expressed in terms of the real component of the CC, σ') and polarization (expressed in terms of the imaginary component of the CC, σ''), as solved for baseline measurements collected in May 2009, related to a groundwater level located at 6 m bgs. The electrical images for the control line (B-B') exhibit the lowest values in the electrical conductivity (σ' : approximately 1 mS/m), and a modest polarization effect (σ'' : approximately 10–20 μ S/m). A similar response is also observed in the first 60 m along the A-A' profile, which corresponds to the clean area. Variations in the CC at depth in line B-B' appear to be controlled by lithologic changes, for instance, the areas associated with the lowest polarization effect (σ'' : approximately 20 μ S/m) and conductivity values (σ' : < 1 mS/m) reveal poor agreement with the location of the groundwater level, yet they are consistent with intercalations of unsaturated silty sands and saturated gravels (e.g., between 5 and 10 m in depth). To aid in the interpretation of the electrical signatures, we present in Figure 2 the lithologic description from a core recovered during the drilling of a well in the vicinity of line B-B' (borehole BB reported in Cassiani et al., 2004). Moreover, CC images for line B-B' illustrate lateral variations in the thickness of the geologic units, associated with the existence of paleochannels at the site typical of braided river environments. Lateral variations in

Data error in time-lapse CCI

the electrical properties resolved for profile B-B' are consistent with previous observations at the site (Cassiani et al., 2004).

Electrical values associated with the contaminated area of profile A-A' (between 60 and 200 m along the profile direction) reveal different anomalies in σ' and σ'' . The most prominent structures are marked in Figure 2 and can be summarized as (1) two shallow anomalies characterized by modest conductive and high polarization values, located approximately 60 and 100 m along the profile direction; (2) an anomaly between 1 and 5 m depth and between approximately 60 and 100 m along the profile direction revealing the lowest conductivity values and lateral changes from high to low polarization values; and (3) a shallow anomaly in the unsaturated zone exhibiting the highest σ' and σ'' values between 120 and 180 m along the profile direction. The last anomaly also reveals a vertical transition to a deeper structure characterized by low polarization effect ($\sigma'' < 5 \mu\text{S/m}$) in the saturated zone.

To help with the interpretation of the anomalies observed in the CC images, we present in Figure 3 the map of the apparent electrical conductivity σ_a as obtained from the EMI measurements, as well as the common-offset GPR

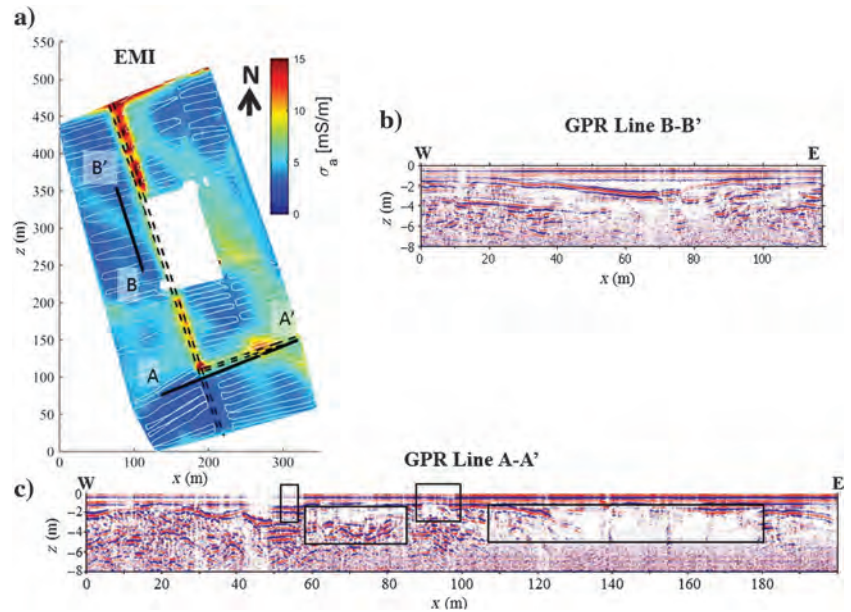


Figure 3. Complementary geophysical data sets: (a) Interpolated map of the apparent electrical conductivity σ_a measured with EMI at a nominal depth of investigation of 6 m with the position of the EMI readings indicated by the white dots, the location of the profile A-A' and B-B' by the solid black lines, and unpaved roads by the dashed lines; common offset GPR profile along line (b) B-B' and (c) A-A'. The anomalies depicted by the solid lines in the GPR profile for line A-A' indicates the position of the anomalies observed in the CCI results.

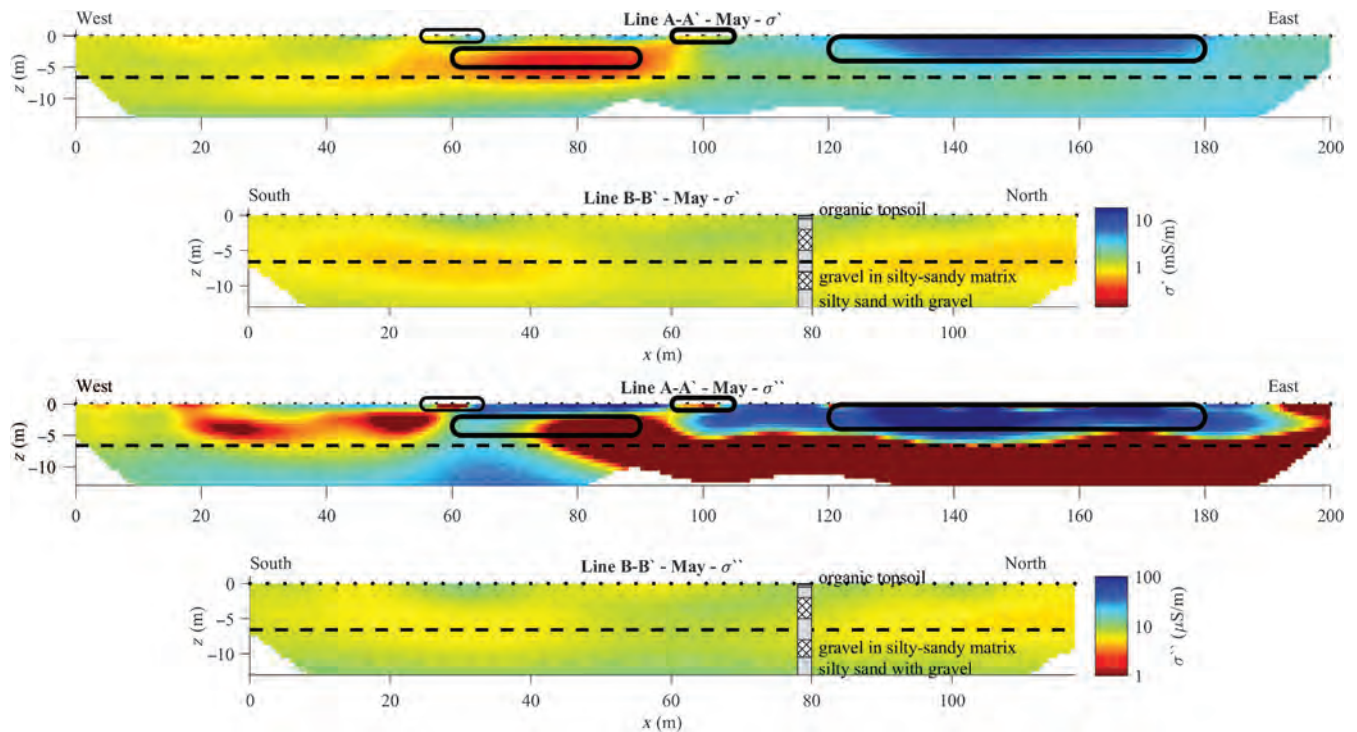


Figure 2. The CCI results for baseline measurements (May 2009) collected along lines A-A' and B-B', expressed in terms of the real σ' and imaginary σ'' components of the CC. The water table at the time of acquisition is shown by the dashed black line, and the position of the electrodes is marked with the solid dots at the surface. Anomalies marked by the solid lines along profile A-A' refer to possible anthropogenic structures, whereas available lithologic information from previous drillings is imposed at the corresponding position in profile B-B'.

profiles for measurements along lines A-A' and B-B'. The position of the CC anomalies is also marked in the radargram presented in Figure 3. The apparent conductivity σ_a map presented in Figure 3a clearly reveals high σ_a anomalies in the vicinity of profile A-A'. In particular, the elongated feature roughly oriented north–south between 150 and 300 m in the x -direction of the EMI map. Such an anomaly is coincident with the position of an unpaved road. Due to the compacted materials at the surface, such roads are expected to result in low electrical conductivity values. The high σ_a anomaly observed in Figure 3a might indicate the location of at least one buried pipe. The unpaved road crosses line A-A' at approximately 60 m, where the GPR image (Figure 3c) reveals shallow reflections, as expected for measurements near metallic structures, confirming the position of a possible pipe. Moreover, similar reflections are observed in the near surface at approximately 95 m, pointing out the presence of a second anthropogenic structure. This is the location of the shallow anomaly (a) observed in the CC images (see Figure 2), characterized by modest σ' , and high σ'' values. City documents indicate the location of a cast iron water pipe. Yet, no information is available about its exact size, nor about the possible coating, which is a common method used to prevent oxidation.

In addition to the interpreted pipe, the CC images reveal an anomaly characterized by a high polarization response between 60 and 80 m (along line A-A') also consistent with reflection hyperbolas observed in the GPR profile (between approximately 2 and 5 m bgs), as well as with high σ_a values in EMI measurements. Although such an anomaly may be interpreted as possible further anthropogenic structures, the deep extension of the anomaly might also be indicative of a lithologic contact. At present, no information is available to aid in the interpretation.

Furthermore, the lack of reflections in the radargram of line A-A', between 120 and 180 m, spatially corresponds to the high σ_a , σ' , and σ'' values in the EMI and CC images and thus can be explained by the attenuation of EMI waves in conductive media (von Hippel, 1954). Such an observation suggests the presence of a clay-rich layer that is likely to be the filling of a paleochannel of a braided river. Traces of these channels can be also seen in Figure 3a as relatively more conductive features elongated roughly in the north-northwest–south-southeast direction, with the bottom of one such channel clearly visible in the GPR line along B-B' (for a more detailed discussion, see Cassiani et al., 2004). Alternatively, this anomaly may be interpreted as the result of an increase in fluid conductivity accompanying the accumulation of carbonic acids accompanying the well-documented degradation of hydrocarbons at the site (e.g., Burberry et al., 2004). Accordingly, the increase in σ'' could be explained by the expected increase in the polarization response with increasing contaminant concentration predicted by the model from Schmutz et al. (2010).

In contrast to line A-A', the control line B-B' does not reveal indications of possible anthropogenic structures and exhibits only vertical interfaces between 4 and 8 m bgs reflecting the sand and gravel intercalations, which are consistent in both GPR and CC images, as well as with the lateral variations observed in the EMI between low and moderate σ_a values.

Cultural noise in CC monitoring results

An initial analysis of the inversion results, based on the independent analysis of monitoring data sets collected along line A-A' revealed inconclusive spatial and temporal patterns, hindering their

interpretation (Appendix A). Whereas the σ' monitoring images show relatively minimal variations for data collected at different periods, the polarization images show significant temporal variations, especially in the uncontaminated area. This region shows, in general, high σ'' values in the saturated zone, with vertical variations along the monitoring period well-correlated with changes in the groundwater table. Although promising, imaging results in the uncontaminated area resolved for November do not reflect the shallow position of the groundwater. Moreover, in the contaminated area of profile A-A' (between 60 and 200 m), the response is practically constant along the entire monitoring experiments. The apparent lack of variations in the electrical monitoring images for the contaminated areas may be indicative of (1) a constant response over time due to the contaminant plume, (2) electrical signatures being controlled by static (i.e., time-invariable) subsurface properties such as the lithology, or (3) the presence of anthropogenic structures (such as the water pipe) masking the electrical response of subsurface materials and contaminants.

Accounting for the time-lapse differences between the monitoring and the baseline images should permit to mute the effect due to lithology and anthropogenic structures, assuming that those do not change over the monitoring time (e.g., Kemna et al., 2002). A further alternative may be given by the direct inversion of the time-lapse differences, or the inversion of the data using temporal regularization (e.g., Lesparre et al., 2017). However, the presence of systematic errors in the data, as well as cultural noise, might mislead the application of such approaches. Hence, the quantification of random errors is critical for an adequate performance of time-lapse differences and time-regularization inversion schemes (Lesparre et al., 2017). In the case of the Trecate monitoring data sets, anthropogenic structures such as the unpaved road and the water pipe represent important sources of error. Moreover, monitoring measurements can also be affected by further sources of systematic errors related to the comparison of data collected with varying contact resistance of the electrodes, which can arise due to variations in temperature, surface moisture, or the presence of snow and ice in the surface during the winter measurements.

To overcome these deficiencies and improve the resolution of the electrical images, it is critical to (1) identify and remove outliers (i.e., systematic errors) and (2) quantify random error in the measurements, which can be taken into account within the inversion (e.g., Kemna, 2000; Flores Orozco et al., 2012b; Binley et al., 2016). In particular, for this study, we consider outliers to be not only related to spatially inconsistent in the independent measurements, but also, and most importantly, to data errors in the time-lapse differences for the CC measurements collected over the monitoring period, which hereafter are referred to as temporal outliers. Such temporal outliers are related to misplaced electrodes, variations in surface properties, and the contact resistance as well as to possible changes in the signatures of anthropogenic structures.

Raw-data analysis and identification of spatial and temporal outliers

Analysis of each independent data set (i.e., tomographic data collected at each time during the monitoring period) shows a good reciprocity for measurements along profile A-A', as presented in Figure 4 in terms of the apparent resistivity ρ_a and the apparent phase-shift ϕ_a . The plots in Figure 4 show the highest ($|\phi_a| > 20$ mrad) values between electrodes 32 and 48, which

include variations from large negative to large positive values. The collection of anomalous positive phase-shift values in electrical impedance measurements is associated with the so-called negative IP effect (for further details, see Sumner, 1976, pp. 195–196) and is not strictly erroneous measurements. Such negative IP effects (Sumner, 1976) can be observed in two main situations: (1) adjacent to a conductor (i.e., metal) close to the electrodes, where an electrical field is enhanced within the conductor with a reversed direction to the injected current; thus, resulting in a change in the sign for measurements collected with dipoles located on different sides of the conductor and (2) layered media in which the lowest unit is more conductive than the layer immediately above and the material closest to the electrodes is polarizable.

It is also possible to observe in Figure 4 that the negative IP effects reveal good consistency between direct and reciprocal readings, supporting the argument that the negative IP effects are not erroneous measurements. In this regard, a recent study by Dahlin and Loke (2015) investigates the inversion of negative chargeability in time-domain IP, further demonstrating that those are not necessarily erroneous measurements. Hence, the negative IP effect observed in Figure 4 might be controlled by two different, and likely concurrent, conditions: (1) the water pipe located near the surface, close to electrode 40 (approximately 100 m along the profile direction) and (2) the contact between subsurface materials characterized by contrasting electrical properties at the other two anomalies (i.e., between 60 and 90 m, as well as between 120 and 180 m along the profile direction).

Additional to the detection of negative IP polarization effects, Figure 4 shows that phase-shift measurements away of the anthropogenic structures (measurements with electrodes 1–30 and electrodes 45–80) are related to lower polarization effects ($-\phi_a < 10$ mrad), with the lowest values associated with those measurements within the contaminated area ($-\phi_a < 5$ mrad). Additionally, measurements associated with larger separations between current and potential dipoles (more than 25 electrodes) reveal spatially incoherent patterns, as expected due to a decrease in the signal-to-noise ratio (S/N) for “deeper” measurements. These erratic measurements are due to

random error and low S/N leading to large discrepancies between direct and reciprocal measurements; the corresponding data points need to be removed before the inversion.

As observed in the plots presented in Figure 4, the ϕ_a values recorded close to the anthropogenic structures (the unpaved road and the water pipe) dominate over the weaker response associated to subsurface materials. Visual comparison of the plots in Figure 4 also reveals that the ϕ_a values for measurements collected between electrodes 32 and 48 vary dramatically at different times. These temporal variations in the data collected between electrodes 32 and 48 can only be explained by (1) changes in the contact resistance of the electrodes placed on the paved road and associated changes in the signal strength and (2) changes in the moisture at the contact between the soil and the water pipe due to seasonal fluctuations in the groundwater level.

The high ϕ_a values of measurements over anthropogenic structures (between electrodes 32 and 48) are not increasing the misfits between direct and reciprocal readings because those are not outliers in the independent data sets. Thus, the data error ϵ estimated for independent data sets cannot be used to quantify temporal distortions in the data due to cultural noise. Other methods proposed for the identification of outliers, and quantification of data quality, such as stacking (i.e., repeatability), or the analysis of the voltage-decay curve for time-domain IP readings (e.g., Gazoty et al., 2013; Flores Orozco et al., 2018), will also face the same problem, considering that the measurements over anthropogenic structures are spatially well-resolved and associated to a high S/N.

Hence, as a second step, we investigated the reciprocity of time-lapse differences to identify possible systematic errors affecting temporal variations in the measurements. Here, we refer to the difference between the measurements collected at time j ($j > 0$) and baseline measurements ($j = 0$, corresponding to data collected in May) for apparent resistivity $\Delta\rho_a$ and phase shift $\Delta\phi_a$ as

$$\Delta\rho_a = \log \rho_{aj} - \log \rho_{a0}, \quad (1)$$

$$\Delta\phi_a = \phi_{aj} - \phi_{a0}. \quad (2)$$

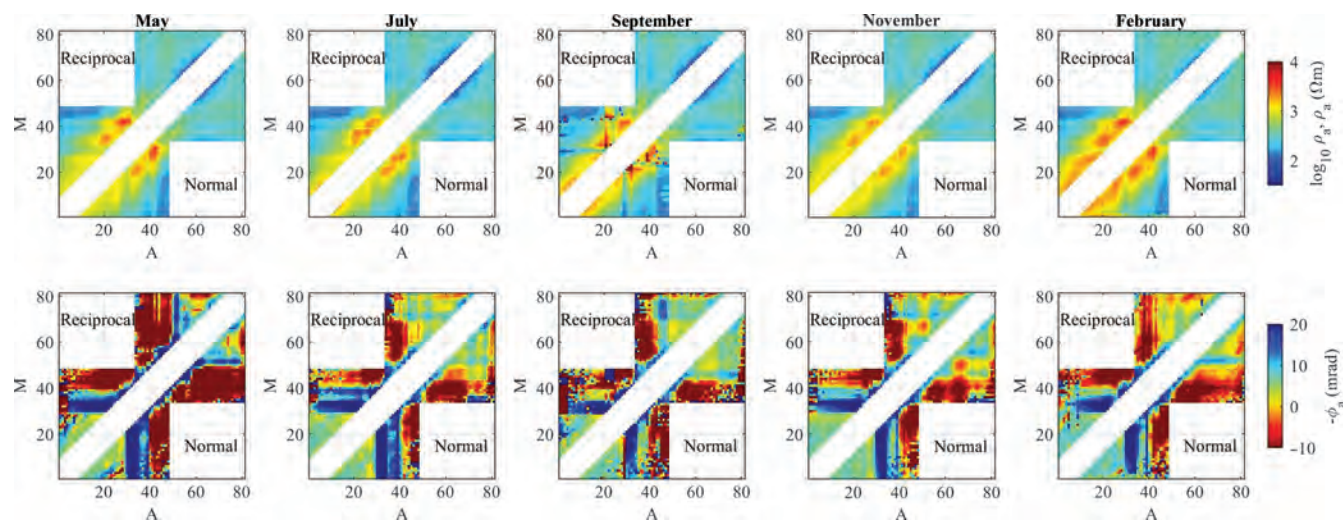


Figure 4. Plots of the raw data expressed in terms of the apparent resistivity, ρ_a (top) and impedance phase-shift ϕ_a (bottom) for each quadrupole along line A-A'. Each measurement is represented as a pixel value with the x- and y-coordinates given by the electrode number of the positive current (A) and potential (M) electrode.

We quantify the data error, at the time-lapse j , as the misfit between direct and reciprocal values of the computed time-lapse differences, which can be written for the apparent resistivity $\epsilon(\Delta\rho_a)$ as

$$\epsilon(\Delta\rho_{aj}) = \Delta\rho_{aj,D} - \Delta\rho_{aj,R}, \quad (3)$$

where $\Delta\rho_{aj,D}$ and $\Delta\rho_{aj,R}$ refer to the time-lapse difference in direct and reciprocal readings, respectively. In analogous way, the data error for time-lapse differences in phase-shift readings can be written as

$$\epsilon(\Delta\phi_{aj}) = \Delta\phi_{aj,D} - \Delta\phi_{aj,R}. \quad (4)$$

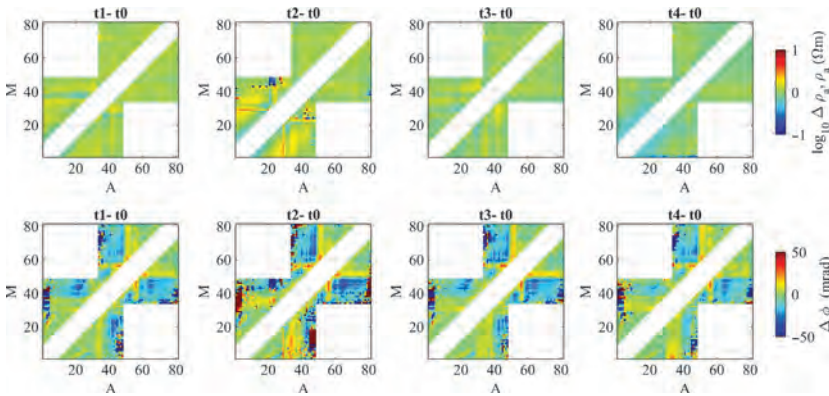


Figure 5. Plots of the time-lapse difference between baseline ($j = 0$) and time lapse ($j = 1, 2, 3, 4$) expressed in terms of the apparent resistivity, $\Delta\rho_a$ (top) and impedance phase shift $\Delta\phi_a$ (bottom) measurements in line A-A'. Each measurement is represented as a pixel value with the x - and y -coordinates given by the electrode number of the positive current (A) and potential (M) electrode.

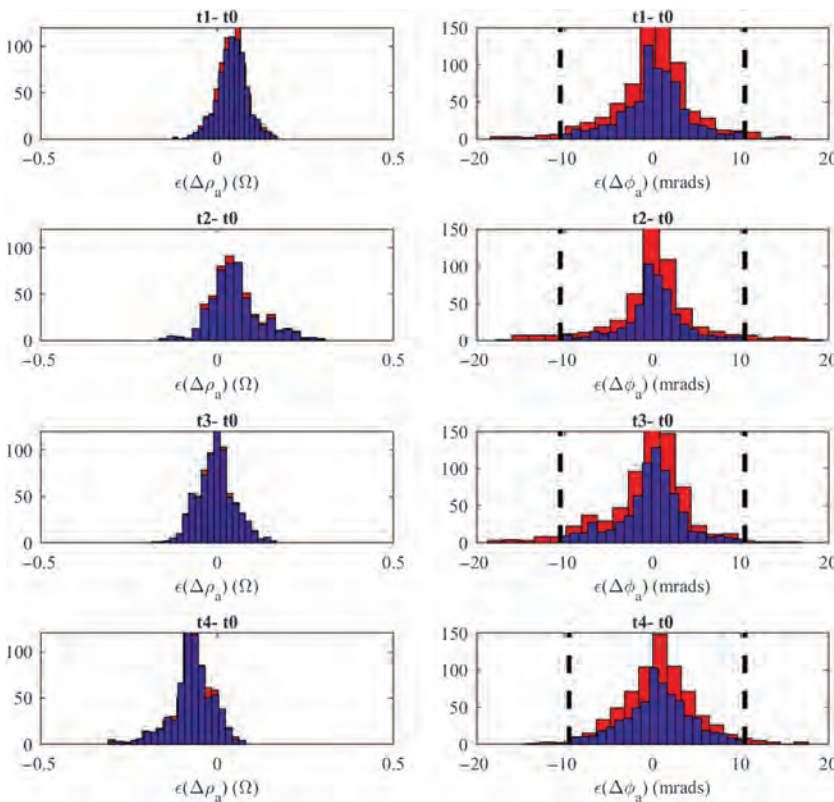


Figure 6. Plots of the data error for time-lapse differences as computed for the measured transfer resistance ($\epsilon(\Delta R)$, left) and phase-shift ($\epsilon(\Delta\phi_a)$, right). Histograms in red represent the complete time-lapse difference data set, and the imposed histogram in blue represents the resulting values after filtering the temporal outliers. The dashed lines indicate the maximum data error accepted for each time-lapse based after the analysis of misfit between direct-reciprocal time-lapse differences.

Figure 5 shows the computed time-lapse differences for data collected along line A-A'. The plots in Figure 5 reveal consistent values for the direct and reciprocal differences with the larger uncertainties observed for $\Delta\phi_a$, in measurements between electrodes 32 and 55, in the vicinity of the unpaved road, water pipe, and possible lithologic contacts. In particular, Figure 5 shows a poor reciprocity in time-lapse differences computed for readings between electrodes 50 and 55, which correspond to those electrodes installed directly on the unpaved road. Thus, such measurements could be removed before the inversion as temporal outliers.

To summarize, the outliers were identified (and removed) based on the analysis of direct-reciprocal misfit in two steps: (1) for independent data sets and (2) after the computation of the time-lapse differences ($\Delta\rho_{aj}$ and $\Delta\phi_{aj}$). In both cases, measurements were removed when the direct-reciprocal misfit exceeded the value of the corresponding average value between readings (i.e., $[\phi_{a,N} - \phi_{a,N}] > \frac{1}{2}[\phi_{a,N} + \phi_{a,R}]$). This filter assumes that measurements affected only by random error should provide a consistent value for direct and reciprocal readings for independent and time-lapse differences. From the initial 608 measurements, only 233 measuring points were used for the inversion of each independent data set, with the rest of the readings being deleted as outliers. Figures 4 and 5 demonstrate the validity of such an assumption. Histograms of the data error (i.e., $\epsilon(\Delta\rho_{aj})$ and $\epsilon(\Delta\phi_{aj})$) presented in Figure 6 demonstrate a normal distribution, as expected for random (time-lapse) data error. In addition to this, such plots reveal a few measurements related to larger $\epsilon(\Delta\phi_{aj})$ as isolated clusters separated from the main distribution of valid measurements. Hence, the occurrence of gaps in the histograms can be used to identify maximum and minimum threshold values for $\Delta\phi_{aj}$ (the dashed lines in Figure 6).

Monitoring results after removal of spatiotemporal outliers

Here, we discuss monitoring imaging results obtained from the inversion of independent data sets after the removal of temporal outliers based on the analysis of the direct-reciprocal misfit for independent measurements and time-lapse differences as described above. Furthermore, before the inversion, we removed those quadrupoles not present in all five monitoring data sets to ensure we are comparing imaging results with similar resolution

(i.e., based on the same number and distribution of quadrupoles). Accordingly, for the quantification of the data error, we performed a bin analysis as described in Flores Orozco et al. (2012b) based on the joined direct-reciprocal time-lapse misfits from all five data sets.

Hence, the error parameters were the same for the inversion of the entire monitoring data sets, following the recommendation by Lesparre et al. (2017). The underlying assumption is that by using the same error parameters, we fit all measurements to the same error level for a fair comparison of the inversion results. Such approach seems to be adequate considering that all our measurements revealed a consistent distribution of the data error (Figure 5) and of the measured ϕ_a and ρ_a values (Figures 4 and 6).

The inversion results computed for the monitoring data sets collected in line A-A' after the removal of temporal outliers following the methodology described above are presented in Figure 7. The electrical images reveal clear changes in the electrical properties for the contaminated and the clean sediments in line A-A', but most importantly, they do not reflect spatial variations between 60 and 120 m, where the anthropogenic structures (the unpaved road and the water pipe) are located. Yet, the removal of measurements close to these structures leads to a decrease of sensitivity in the computed images, as observed in the blanked pixels between 60 and 120 m. The first 60 m of profile A-A' reveal a shallow anomaly characterized by low conductivity values ($\sigma' < 1$ mS/m), the depth of which changes over time in agreement with fluctuations in the depth of the groundwater level. The high σ'

values (approximately 5 mS/m) observed in the uncontaminated area of line A-A' clearly delineate the saturated zone because they are consistently found below the groundwater table. As expected, a similar pattern is observed in the polarization (imaginary conductivity σ'') images, with low σ'' values associated with the unsaturated materials and higher values with the areas below the groundwater level. The low polarization values in the unsaturated zone show less spatial consistency, likely related to variations in the content of clay, which is polarizable even at low saturations (e.g., Titov et al., 2004). The higher σ'' values observed between May and September in the uncontaminated area at larger depths (approximately 12 m bgs) are likely to reflect the vertical contact between sand and gravel (Cassiani et al., 2004, 2014). Such contact is not visible in data sets collected for deeper positions of the groundwater table (November, February), which is explained by a decrease in the depth of investigation due to the long pathways of current injections through the unsaturated zone (Flores Orozco et al., 2013).

Regarding the contaminated area in profile A-A', here only minimal changes are observed for measurements collected at different periods. The shallow conductive unit (down to 4 m bgs) is related to the paleochannel discussed above. The interpreted high clay content in that area explains the high CC values (σ' and σ''). The response of such a layer is constant over time, thus it is not affected by the analysis of time-lapse reciprocity. Below this unit only low values for the polarization effect ($\sigma'' \ll 1$ μ S/m) are observed in all monitoring images for line A-A', corresponding with the area where

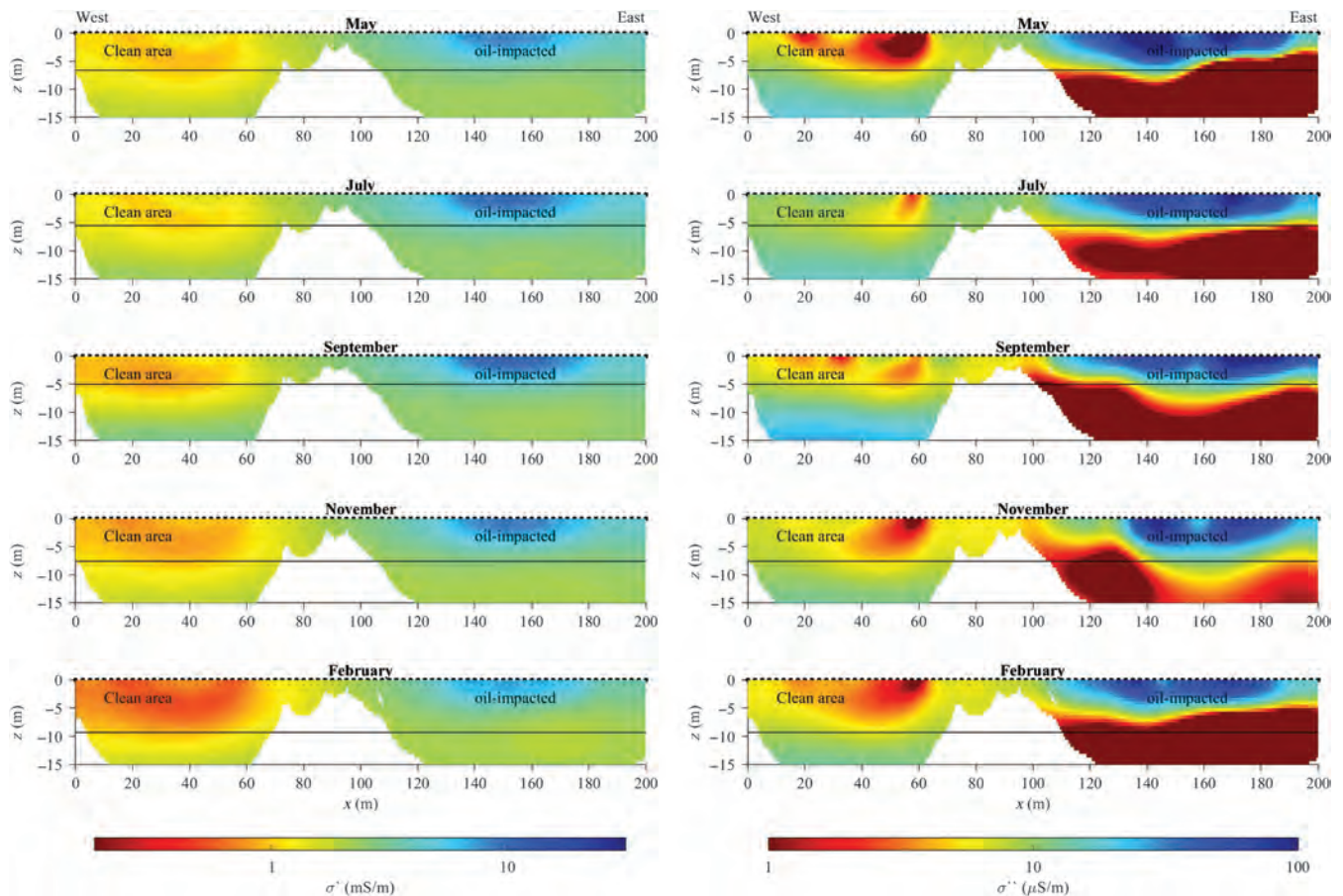


Figure 7. Monitoring imaging results after the removal of spatiotemporal outliers for data collected in line A-A' in terms of the real (left) and imaginary (right) component of the CC. The water table at each time is indicated by the solid line.

higher concentrations of hydrocarbon have been reported (and confirmed by the detailed data shown, e.g., in Cassiani et al., 2014). The geometry of the low polarization unit shows no correlation with fluctuations in the water table.

The negligible polarization effect associated with high hydrocarbon concentrations observed in Figure 7 is consistent with observations reported in the previous laboratory (Ustra et al., 2012; Personna et al., 2013) and field studies (Flores Orozco et al., 2012a; Johansson et al., 2015). However, the model proposed by Schmutz et al. (2010) does not explain the observed decrease in the polarization response, even if crude oil is mainly composed of nonpolar compounds. In this regard, some authors have argued that carbonic acids and other metabolic products might change the surface properties of hydrocarbons, promoting oil-wetting conditions (Cassidy et al., 2001; Zhao and Ioannidis, 2007). Hence, the negligible polarization response is consistent with the predicted response by the model of Revil et al. (2011).

A recent mechanistic model describing the membrane polarization for immiscible fluids trapped within the pore-space predicts a decrease in the polarization response for high concentrations of nonwetting hydrocarbons (Bücker et al., 2017). Based on the formulation of the membrane polarization, this model demonstrates that σ'' values are only dependent on the variations in the pore-space geometry imposed by the hydrocarbon droplets. Hence, the negligible polarization response observed in the contaminated area can be explained by the presence of immobile oil trapped within the micropores forming a continuous oil film with the mobile fraction occupying the macropores. As demonstrated by Bücker et al. (2017), such a continuous film hinders the formation of ion-selective membrane required for the

development of membrane polarization, and it could result in the negligible σ'' response observed in profile A-A' for the periods with a shallow water table. Accordingly, the polarization effect is still negligible for measurements between November and May, for deeper positions of the groundwater table because the oil trapped within the micropores forms a continuous film with air, another electrical insulator. Such an explanation is supported by the high TPH concentrations reported at the position of profile A-A' (Figure 1). The hindered polarization response over the entire depth, and not only on top of the saturated zone, as expected for a LNAPL such as oil, could be explained by the seasonal fluctuations in the water table depth, which transported the hydrocarbons into deeper sediments as observed in the TPH concentrations presented in Figure 1. Monitoring images in Figure 7 suggest that the sediments are not washed off following the recovery of the groundwater, which is also consistent with the persistence of the contaminant concentrations observed at the site (Cassiani et al., 2014). To support our interpretation, we present in Figure 8 the electrical properties (in terms of the σ' and σ'' values) as extracted from the electrical images from A-A' for pixel values located in the clean (30–40 m along the profile direction) and contaminated (160–170 m along the profile direction) regions at different periods, as well as the water content profile as obtained from GPR ZOP measurements performed between two boreholes located in the contaminated region practically along line A-A' (close to 150 m along profile direction) (Cassiani et al., 2014). ZOP measurements were performed at different periods associated with different depths of the groundwater level. The results indicate only relatively small changes in the water content, in agreement with the interpretation of the CC monitoring results. This is in contrast with the large moisture-content variations observed by the ZOP data at another pair of boreholes in the uncontaminated zone close to the control line B-B' (Cassiani et al., 2014). Figure 8 also reveals vertical changes between 4 and 12 m depths in the ZOP data, consistent with the limits of the clay-rich layer (4 m bgs) and with the depth interface (12 m bgs) observed in the σ'' images.

The hydrocarbons act as electrical insulators; thus, the relatively high σ' observed in the contaminated sediments of profile A-A' confirms the changes in the electrical properties in mature hydrocarbon plumes due to microbial activity, e.g., the release of carbonic acids (Sauck, 2000; Werkema et al., 2003; Atekwana and Atekwana, 2010; Caterina et al., 2017). Microbial activity has been reported at the site (Burbery et al., 2004), and high concentrations of total organic carbon observed at the site (Cassiani et al., 2014) support the interpretation of the high σ' values in hydrocarbon-impacted sediments. Recent laboratory studies report an increase in the polarization effect due to the accumulation of metallic minerals accompanying the stimulation of microbial activity in soil samples obtained from hydrocarbon-contaminated sites (e.g., Mewafy et al., 2013; Atekwana and Abdel Aal, 2015). However, our results do not reveal any increase in the σ'' ; neither has the formation of iron sulfides been reported at the site.

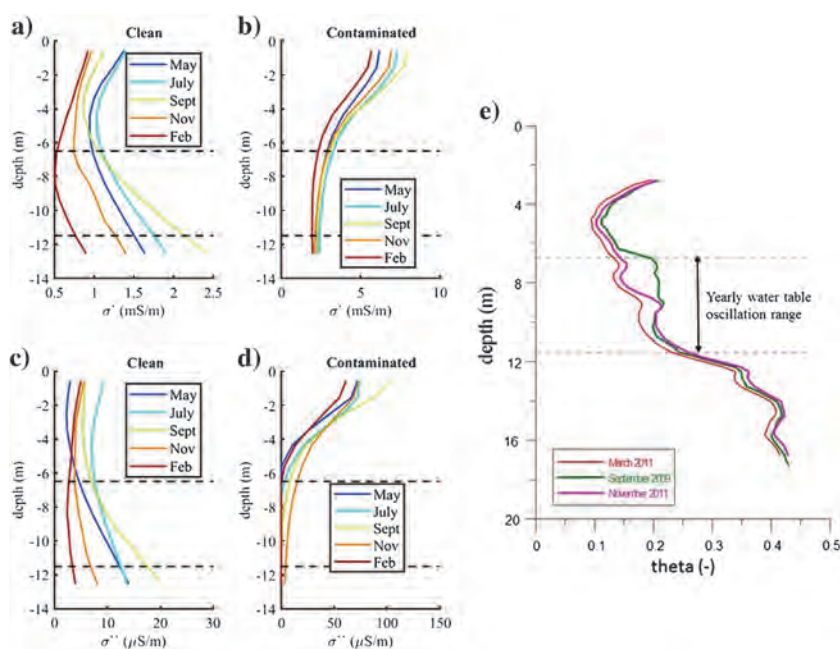


Figure 8. Temporal variations in electrical properties expressed in terms of the (a, b) real and (c, d) imaginary components of the CC for pixel values extracted from the electrical images computed for line A-A' in (a, c) clean (between 30 and 40 m along the profile direction) and (b, d) contaminated (between 160 and 170 m along the profile direction) regions. The dashed lines represent the yearly water table variations during the collection of the data (2009–2010). For comparison, (e) shows the estimated soil moisture content derived from crosshole GPR ZOP for data collected at different time instants in the heavily contaminated zone, after Cassiani et al. (2014).

CONCLUSION

We have presented a detailed analysis of the data error in time-lapse differences of apparent resistivity $\varepsilon(\Delta\rho_a)$ and phase-shift $\varepsilon(\Delta\phi_a)$ for monitoring CCI data sets. The data error was computed by means of the widely accepted analysis of direct and reciprocal misfit, taking it one step further to investigate the reciprocity for time-lapse differences. The CC data sets were collected in the vicinity of different anthropogenic structures, such as a water pipe, unpaved roads, and in prevalence of negative IP effects. Analysis of the independent data sets reveals that such measurements are associated with a high S/N, which also show a high correlation between direct and reciprocal measurements (variations <10% of the mean value), demonstrating that readings exhibiting a negative IP effect are not necessarily erratic measurements.

CCI results obtained after the removal of outliers in time-lapse differences revealed significant differences between the electrical signatures from clean subsurface materials and those impacted by the oil spill. For an uncontaminated region, CC images exhibited changes in agreement with seasonal variations in the position of the groundwater level; whereas contaminated sediments exhibited a constant response over the entire monitoring period associated with a negligible polarization effect and relatively high electrical conductivities. The increase in the electrical conductivity in contaminated sediments is explained by degradation processes of the contaminant plume, such as the release of carbonic acids accompanying microbial activity in mature hydrocarbon plumes. The reduction of the polarization response can be explained by the presence of hydrocarbon droplets trapped within the macro and micropores, which results in the formation of a water film surrounding grain minerals

with a constant thickness, hindering the development of ion-selective membranes and the membrane polarization.

The CCI results are consistent with independent results obtained with other geophysical methods, namely, GPR and low-induction-number EMI methods. The electrical images computed after the removal of the temporal outliers reveal no anomalies associated with anthropogenic structures validating the suitability of the proposed approach.

ACKNOWLEDGMENTS

This research was made possible by funding from the EU FP7 collaborative project ModelPROBE "Model Driven Soil Probing, Site Assessment and Evaluation." The authors thank K. Haaken, C. Oberdörster, R. Deiana, J. Boaga, M. Rossi, and A. Godio for their help in the collection of geophysical data. We appreciate L. Slater, D. Ntargiannis, and M. Weigand for the observations and comments that permitted us to improve significantly the quality of the manuscript.

DATA AND MATERIALS AVAILABILITY

Data associated with this research are available and can be obtained by contacting the corresponding author.

APPENDIX A

COMPLEX CONDUCTIVITY MONITORING PRIOR THE REMOVAL OF TEMPORAL OUTLIERS

In Figure A-1, we present the CC imaging results obtained for monitoring data collected along profile A-A' before the temporal

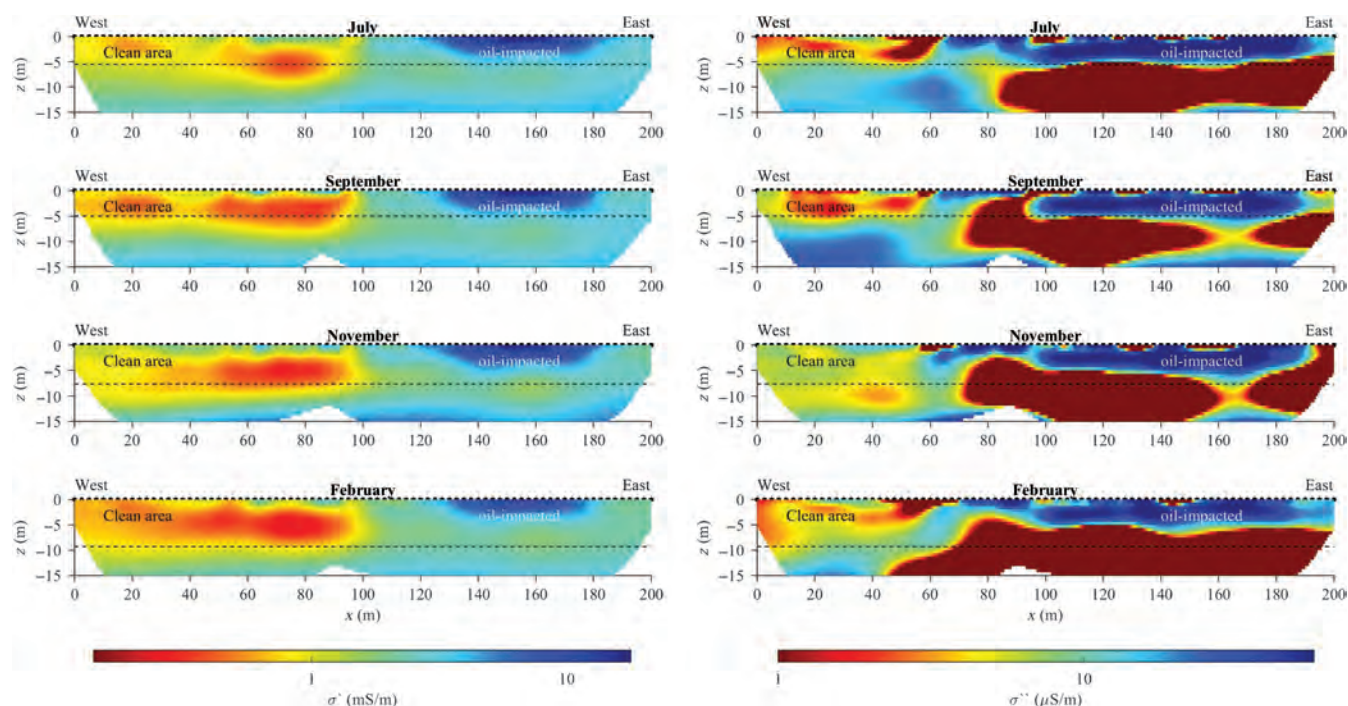


Figure A-1. The CCI results obtained for monitoring data collected at the Trecate site. Each data set was processed independently following the analysis of the misfit between direct and reciprocal readings described in Flores Orozco et al. (2012a). Accordingly, outliers and error parameters were defined independently for each data set. Imaging results are presented in terms of the real and imaginary component of the CC. The dashed line represents the position of the groundwater level at each monitoring period. The position of the electrodes is indicated at the surface by the black points.

analysis of reciprocity in time-lapse differences and the removal of temporal outliers. Images presented in Figure A-1 show a poor consistency with temporal variations of the groundwater level, for both contaminated and uncontaminated areas. Plots in Figure A-1 clearly reveal the limitations of reciprocal analysis in monitoring data sets, in particular for measurements collected in areas affected by cultural noise.

REFERENCES

- Abdel Aal, G. Z., E. A. Atekwana, and A. Revil, 2014, Geophysical signatures of disseminated iron minerals: A proxy for understanding subsurface biophysicochemical processes: *Journal of Geophysical Research: Biogeosciences*, **119**, 1831–1849.
- Abdel Aal, G. Z., L. D. Slater, and E. A. Atekwana, 2006, Induced-polarization measurements on unconsolidated sediments from a site of active hydrocarbon biodegradation: *Geophysics*, **71**, no. 2, H13–H24, doi: [10.1190/1.2187760](https://doi.org/10.1190/1.2187760).
- Archie, G. E., 1942, The electrical resistivity log as an aid in determining some reservoir characterization: *Transactions of the American Institute of Mining, Metallurgical, and Petroleum Engineers*, **146**, 54–62.
- Atekwana, E. A., and G. Z. Abdel Aal, 2015, Iron biomineralization controls on geophysical signatures of hydrocarbon contaminated sediments: *Journal of Earth Science*, **26**, 835–843, doi: [10.1007/s12583-015-0611-2](https://doi.org/10.1007/s12583-015-0611-2).
- Atekwana, E. A., and E. A. Atekwana, 2010, Geophysical signatures of microbial activity at hydrocarbon contaminated sites: A review: *Survey of Geophysics*, **31**, 247–283, doi: [10.1007/s10712-009-9089-8](https://doi.org/10.1007/s10712-009-9089-8).
- Atekwana, E. A., E. A. Atekwana, D. D. Werkema, P. J. Allen, L. A. Smart, J. W. Duris, D. P. Cassidy, W. A. Sauck, and S. Rossbach, 2004, Evidence for microbial enhanced electrical conductivity in hydrocarbon-contaminated sediments: *Geophysical Research Letters*, **31**, L23501.
- Atekwana, E. A., and L. D. Slater, 2009, Biogeophysics: A new frontier in earth science research: *Reviews of Geophysics*, **47**, RG4004, doi: [10.1029/2009RG000285](https://doi.org/10.1029/2009RG000285).
- Binley, A., J. Keery, L. Slater, W. Barrash, and M. Cardiff, 2016, The hydrogeologic information in cross-borehole complex conductivity data from an unconsolidated conglomeratic sedimentary aquifer: *Geophysics*, **81**, no. 6, E409–E421, doi: [10.1190/geo2015-0608.1](https://doi.org/10.1190/geo2015-0608.1).
- Brandt, C. A., J. M. Becker, and A. Porta, 2002, Distribution of polycyclic aromatic hydrocarbons in soils and terrestrial biota after a spill of crude oil in Trecate, Italy: *Environmental Toxicology Chemistry*, **21**, 1638–1643, doi: [10.1002/etc.v21.8](https://doi.org/10.1002/etc.v21.8).
- Bücker, M., A. Flores Orozco, A. Hördt, and A. Kemna, 2017, An analytical membrane-polarization model to predict the complex conductivity signature of immiscible liquid hydrocarbon contaminants: *Near Surface Geophysics*, **15**, 547–562.
- Burbery, L., G. Cassiani, G. Andreotti, T. Ricchiuto, and K. T. Semple, 2004, Well test and stable isotope analysis for the determination of sulphate-reducing activity in a fast aquifer contaminated by hydrocarbons: *Environmental Pollution*, **129**, 321–330, doi: [10.1016/j.envpol.2003.10.017](https://doi.org/10.1016/j.envpol.2003.10.017).
- Cassiani, G., A. Binley, A. Kemna, M. Wehrer, A. Flores Orozco, R. Deiana, J. Boaga, M. Rossi, P. Dietrich, U. Werban, L. Zschornack, A. Godio, A. JafarGandomi, and G. P. Deidda, 2014, Non-invasive characterization of the Trecate (Italy) crude-oil contaminated site: Links between contamination and geophysical signals: *Environmental Science and Pollution Research*, Special Issue on New approaches for low-invasive contaminated site characterization, monitoring and modeling, **21**, 8914–8931, doi: [10.1007/s11356-014-2494-7](https://doi.org/10.1007/s11356-014-2494-7).
- Cassiani, G., A. Kemna, A. Villa, and E. Zimmermann, 2009, Spectral induced polarization for the characterization of free-phase hydrocarbon contamination of sediments with low clay content: *Near Surface Geophysics*, **7**, 547–562.
- Cassiani, G., C. Strobbia, and L. Gallotti, 2004, Vertical radar profiles for the characterization of deep vadose zones: *Vadose Zone Journal*, **3**, 1093–1115, doi: [10.2136/vzj2004.1093](https://doi.org/10.2136/vzj2004.1093).
- Cassidy, D. P., D. D. Werkema, Jr., W. Sauck, E. Atekwana, S. Rossbach, and J. Duris, 2001, The effects of LNAPL biodegradation products on electrical conductivity measurements: *Journal of Environmental and Engineering Geophysics*, **6**, 47–52, doi: [10.4133/JEEG6.1.47](https://doi.org/10.4133/JEEG6.1.47).
- Caterina, D., A. Flores Orozco, and F. Nguyen, 2017, Long-term ERT monitoring of biogeochemical changes of an aged hydrocarbon contamination: *Journal of Contaminant Hydrology*, **201**, 19–29, doi: [10.1016/j.jconhyd.2017.04.003](https://doi.org/10.1016/j.jconhyd.2017.04.003).
- Chambers, J. E., P. I. Meldrum, R. D. Ogilvy, and P. B. Wilkinson, 2005, Characterization of a NAPL-contaminated former quarry site using electrical impedance tomography: *Near Surface Geophysics*, **3**, 79–90, doi: [10.3997/1873-0604.2005003](https://doi.org/10.3997/1873-0604.2005003).
- Dahlin, T., and M. H. Loke, 2015, Negative apparent chargeability in time-domain induced polarization data: *Journal of Applied Geophysics*, **123**, 322–332, doi: [10.1016/j.jappgeo.2015.08.012](https://doi.org/10.1016/j.jappgeo.2015.08.012).
- Deceuster, J., and O. Kaufmann, 2012, Improving the delineation of hydrocarbon impacted soils and water through induced polarization (IP) tomographies: A field study at an industrial waste land: *Journal of Contaminant Hydrology*, **136**, 25–42, doi: [10.1016/j.jconhyd.2012.05.003](https://doi.org/10.1016/j.jconhyd.2012.05.003).
- Flores Orozco, A., J. Gallistl, M. Bücker, and K. H. Williams, 2018, Decay curve analysis for data error quantification in time-domain induced polarization imaging: *Geophysics*, **83**, no. 2, E75–E86, doi: [10.1190/geo2016-0714.1](https://doi.org/10.1190/geo2016-0714.1).
- Flores Orozco, A., A. Kemna, C. Oberdörster, L. Zschornack, C. Leven, P. Dietrich, and H. Weiss, 2012a, Delineation of subsurface hydrocarbon contamination at a former hydrogenation plant using spectral induced polarization imaging: *Journal of Contaminant Hydrology*, **136–137**, 131–144, doi: [10.1016/j.jconhyd.2012.06.001](https://doi.org/10.1016/j.jconhyd.2012.06.001).
- Flores Orozco, A., A. Kemna, and E. Zimmermann, 2012b, Data error quantification in spectral induced polarization imaging: *Geophysics*, **77**, no. 3, E227–E237, doi: [10.1190/geo2010-0194.1](https://doi.org/10.1190/geo2010-0194.1).
- Flores Orozco, A., M. Velimirovic, T. Tosco, A. Kemna, H. Sapion, N. Klaas, R. Sethi, and B. Leen, 2015, Monitoring the injection of microscale zero-valent iron particles for groundwater remediation by means of complex electrical conductivity imaging: *Environmental Science and Technology*, **49**, 5593–5600, doi: [10.1021/acs.est.5b00208](https://doi.org/10.1021/acs.est.5b00208).
- Flores Orozco, A., H. K. Williams, and A. Kemna, 2013, Time-lapse spectral induced polarization imaging of stimulated uranium bioremediation: *Near Surface Geophysics*, **11**, 531–544, doi: [10.3997/1873-0604.2013020](https://doi.org/10.3997/1873-0604.2013020).
- Flores Orozco, A., H. K. Williams, P. E. Long, S. S. Hubbard, and A. Kemna, 2011, Using complex resistivity imaging to infer biogeochemical processes associated with bioremediation of an uranium-contaminated aquifer: *Journal of Geophysical Research*, **116**, G03001, doi: [10.1029/2010JG001591](https://doi.org/10.1029/2010JG001591).
- Gazoty, A., G. Fiandaca, J. Pedersen, E. Auken, and A. V. Christiansen, 2013, Data repeatability and acquisition techniques for time-domain spectral induced polarization: *Near Surface Geophysics*, **11**, 391–406.
- Heenan, J., L. D. Slater, D. Ntarlagiannis, E. A. Atekwana, B. Z. Fathepure, S. Dalvi, C. Ross, D. D. Werkema, and E. A. Atekwana, 2014, Electrical resistivity imaging for long-term autonomous monitoring of hydrocarbon degradation: Lessons from the deepwater Horizon oil spill: *Geophysics*, **80**, no. 1, B1–B11, doi: [10.1190/geo2013-0468.1](https://doi.org/10.1190/geo2013-0468.1).
- Johansson, S., G. Fiandaca, and T. Dahlin, 2015, Influence of non-aqueous phase liquid configuration on induced polarization parameters: Conceptual models applied to a time-domain field case study: *Journal of Applied Geophysics*, **123**, 295–309, doi: [10.1016/j.jappgeo.2015.08.010](https://doi.org/10.1016/j.jappgeo.2015.08.010).
- Kemna, A., 2000, Tomographic inversion of complex resistivity: Theory and application: Ph.D. thesis, Ruhr-University of Bochum.
- Kemna, A., A. Binley, G. Cassiani, E. Niederleithinger, A. Revil, L. Slater, K. H. Williams, A. Flores Orozco, F. H. Haegel, A. Hördt, S. Kruschwitz, V. Leroux, K. Titov, and E. Zimmermann, 2012, An overview of the spectral induced polarization method for near-surface applications: *Near Surface Geophysics*, **10**, 453–468.
- Kemna, A., A. Binley, and L. Slater, 2004, Crosshole IP imaging for engineering and environmental applications: *Geophysics*, **69**, 97–107, doi: [10.1190/1.1649379](https://doi.org/10.1190/1.1649379).
- Kemna, A., E. Räkera, and A. Binley, 1997, Application of complex resistivity tomography to field data from a Kerosene-contaminated site: *Proceedings of the 3rd Meeting Environmental and Engineering Geophysics*, European Section, 151–154.
- Kemna, A., J. Vanderborght, B. Kulesa, and H. Vereecken, 2002, Imaging and characterization of subsurface solute transport using electrical resistivity tomography (ERT) and equivalent transport models: *Journal of Hydrology*, **267**, 125–146, doi: [10.1016/S0022-1694\(02\)00145-2](https://doi.org/10.1016/S0022-1694(02)00145-2).
- Lesparre, N., F. Nguyen, A. Kemna, T. Robert, T. Hermans, M. Daoudi, and A. Flores Orozco, 2017, A new approach for time-lapse data weighting in electrical resistivity tomography: *Geophysics*, **82**, no. 6, E325–E333, doi: [10.1190/geo2017-0024.1](https://doi.org/10.1190/geo2017-0024.1).
- Marshall, D., and T. Madden, 1959, Induced polarization, a study of its causes: *Geophysics*, **24**, 790–816, doi: [10.1190/1.1438659](https://doi.org/10.1190/1.1438659).
- Mewafy, F. M., D. D. Werkema, E. A. Atekwana, L. D. Slater, G. Z. Abdel Aal, A. Revil, and D. Ntarlagiannis, 2013, Evidence that bio-metallic mineral precipitation enhances the complex conductivity response at a hydrocarbon contaminated site: *Journal of Applied Geophysics*, **98**, 113–123, doi: [10.1016/j.jappgeo.2013.08.011](https://doi.org/10.1016/j.jappgeo.2013.08.011).
- Naudet, V., J. C. Gourry, F. Girard, F. Mathieu, and A. Saada, 2014, 3D electrical resistivity tomography to locate DNAPL contamination around a housing estate: *Near Surface Geophysics*, **12**, 351–360, doi: [10.3997/1873-0604.2012059](https://doi.org/10.3997/1873-0604.2012059).
- Olhoeft, G. R., 1985, Low-frequency electrical-properties: *Geophysics*, **50**, 2492–2503, doi: [10.1190/1.1441880](https://doi.org/10.1190/1.1441880).

- Personna, Y. R., L. Slater, D. Ntarlagiannis, D. Werkema, and Z. Szabo, 2013, Complex resistivity signatures of ethanol biodegradation in porous media: *Journal of Contaminant Hydrology*, **153**, 37–50, doi: [10.1016/j.jconhyd.2013.07.005](https://doi.org/10.1016/j.jconhyd.2013.07.005).
- Revil, A., E. Atekwana, C. Zhang, A. Jardani, and S. Smith, 2012, A new model for the spectral induced polarization signature of bacterial growth in porous media: *Water Resources Research*, **48**, W09545.
- Revil, A., M. Schmutz, and M. L. Batzle, 2011, Influence of oil wettability upon spectral induced polarization of oil-bearing sands: *Geophysics*, **76**, no. 5, A31–A36, doi: [10.1190/geo2011-0006.1](https://doi.org/10.1190/geo2011-0006.1).
- Sauck, W. A., 2000, A model for the resistivity structure of LNAPL plumes and their environs in sandy sediments: *Journal of Applied Geophysics*, **44**, 151–165, doi: [10.1016/S0926-9851\(99\)00021-X](https://doi.org/10.1016/S0926-9851(99)00021-X).
- Schädler, S., M. Morio, S. Bartke, and M. Finkel, 2012, Integrated planning and spatial evaluation of megasite remediation and reuse options: *Journal of Contaminant Hydrology*, **127**, 88–100, doi: [10.1016/j.jconhyd.2011.03.003](https://doi.org/10.1016/j.jconhyd.2011.03.003).
- Schmutz, M., A. Revil, P. Vaudelet, M. Batzle, P. F. Vĩñao, and D. D. Werkema, 2010, Influence of oil saturation upon spectral induced polarization of oil-bearing sands: *Geophysical Journal International*, **183**, 211–224, doi: [10.1111/j.1365-246X.2010.04751.x](https://doi.org/10.1111/j.1365-246X.2010.04751.x).
- Slater, L., and D. Lesmes, 2002, Electrical-hydraulic relationships observed for unconsolidated sediments: *Water Resources Research*, **38**, 31–31-13, doi: [10.1029/2001WR001075](https://doi.org/10.1029/2001WR001075).
- Slater, L., D. Ntarlagiannis, Y. R. Personna, and S. Hubbard, 2007, Pore-scale spectral induced polarization (SIP) signatures associated with FeS biomineral transformations: *Geophysical Research Letters*, **34**, L21404, doi: [10.1029/2007GL031840](https://doi.org/10.1029/2007GL031840).
- Sumner, J. S., 1976, *Principles of induced polarization for geophysical exploration*: Elsevier Science Publishing Co.
- Titov, K., A. Kemna, A. Tarasov, and H. Vereecken, 2004, Induced polarization of unsaturated sands determined through time domain measurements: *Vadose Zone Journal*, **3**, 1160–1168, doi: [10.2136/vzj2004.1160](https://doi.org/10.2136/vzj2004.1160).
- Ustra, A., L. Slater, D. Ntarlagiannis, and V. Elis, 2012, Spectral induced polarization (SIP) signatures of clayey soils containing toluene: *Near Surface Geophysics*, **10**, 503–515, doi: [10.3997/1873-0604.2012015](https://doi.org/10.3997/1873-0604.2012015).
- Vanhala, H., 1997, Mapping oil-contaminated sand and till with the spectral induced polarization (SIP) method: *Geophysical Prospecting*, **45**, 303–326, doi: [10.1046/j.1365-2478.1997.00338.x](https://doi.org/10.1046/j.1365-2478.1997.00338.x).
- Von Hippel, A. R., 1954, *Dielectric and waves*: John Wiley and Sons.
- Weigand, M., A. Flores Orozco, and A. Kemna, 2017, Reconstruction quality of SIP parameters in multi-frequency complex resistivity imaging: *Near Surface Geophysics*, **15**, 187–199.
- Werkema, D. D., E. A. Atekwana, A. L. Endres, W. A. Sauck, and D. P. Cassidy, 2003, Investigating the geoelectrical response of hydrocarbon contamination undergoing biodegradation: *Geophysical Research Letters*, **30**, 49, doi: [10.1029/2003GL017346](https://doi.org/10.1029/2003GL017346).
- Williams, P. F., and B. R. Rust, 1969, The sedimentology of a braided river: *Journal of Sedimentary Research*, **39**, 1641–1643, doi: [10.1306/74D71EE2-2B21-11D7-8648000102C1865D](https://doi.org/10.1306/74D71EE2-2B21-11D7-8648000102C1865D).
- Zhao, W., and M. A. Ioannidis, 2007, Effect of NAPL film stability on the dissolution of residual wetting NAPL in porous media: A pore-scale modeling study: *Advances in Water Resources*, **30**, 171–181, doi: [10.1016/j.advwatres.2005.03.025](https://doi.org/10.1016/j.advwatres.2005.03.025).

4. IP monitoring along nanoparticles injections: real-time evaluation of stimulated biogeochemical activity for the degradation of contaminants

4.1 Monitoring the injection of microscale zerovalent iron particles for groundwater remediation by means of complex electrical conductivity imaging

4.2 Complex-conductivity monitoring to delineate aquifer pore clogging during nanoparticles injection

Monitoring the Injection of Microscale Zerovalent Iron Particles for Groundwater Remediation by Means of Complex Electrical Conductivity Imaging

Adrián Flores Orozco,^{*,†} Milica Velimirovic,^{‡,§} Tiziana Tosco,[⊥] Andreas Kemna,[¶] Hans Sapon,^{||} Norbert Klaas,[#] Rajandrea Sethi,[⊥] and Leen Bastiaens[‡]

[†]Geophysics Research Group, Vienna University of Technology, Gusshausstraße 27-29, E120-3, 1040 Vienna, Austria

[‡]Flemish Institute for Technological Research (VITO), Boeretang 200, 2400 Mol, Belgium

[§]Department of Environmental Geosciences, University of Vienna, Althanstrasse 14, 1090 Vienna, Austria

[⊥]DIATI-Dipartimento di Ingegneria del Territorio, dell'Ambiente e delle Infrastrutture, Politecnico di Torino, Corso Duca degli Abruzzi 24, 10129 Torino, Italy

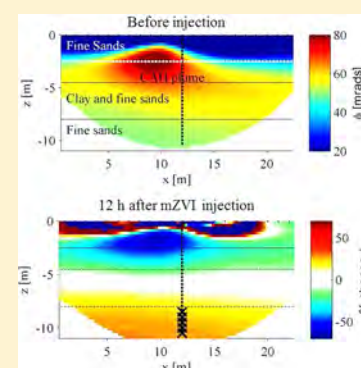
[¶]Department of Geophysics, Steinmann Institute, University of Bonn, Meckenheimer Allee 176, 53115 Bonn, Germany

^{||}SAPION, Oude Bevelsesteenweg 51, 2560 Nijlen, Belgium

[#]VEGAS, University of Stuttgart, Pfaffenwaldring 61, 70569 Stuttgart, Germany

S Supporting Information

ABSTRACT: The injection of microscale zerovalent iron (mZVI) particles for groundwater remediation has received much interest in recent years. However, to date, monitoring of mZVI particle injection is based on chemical analysis of groundwater and soil samples and thus might be limited in its spatiotemporal resolution. To overcome this deficiency, in this study, we investigate the application of complex electrical conductivity imaging, a geophysical method, to monitor the high-pressure injection of mZVI in a field-scale application. The resulting electrical images revealed an increase in the induced electrical polarization ($\sim 20\%$), upon delivery of ZVI into the targeted area, due to the accumulation of metallic surfaces at which the polarization takes place. Furthermore, larger changes ($>50\%$) occurred in shallow sediments, a few meters away from the injection, suggesting the migration of particles through preferential flowpaths. Correlation of the electrical response and geochemical data, in particular the analysis of recovered cores from drilling after the injection, confirmed the migration of particles (and stabilizing solution) to shallow areas through fractures formed during the injection. Hence, our results demonstrate the suitability of the complex conductivity imaging method to monitor the transport of mZVI during subsurface amendment in quasi real-time.



■ INTRODUCTION

Recent research addresses the injection of reactive nano- and microscale particles into the subsurface for the stimulated in situ degradation of pollutants present in aquifers.¹ Particles may be injected directly into the targeted contaminated zone, or close to the source of contamination for deep plumes, not only decreasing the remediation time, but also permitting the remediation of areas not accessible with other techniques such as underneath buildings, deep contaminant plumes, or areas characterized by low hydraulic conductivity.^{2–4} Furthermore, in situ site remediation is significantly faster compared to other conventional approaches.⁵ In particular, microscale zerovalent iron (mZVI) particles have received much attention for field applications due to their lower costs and extended longevity in comparison with nanosized ZVI (nZVI) particles.^{6,7} Although promising, the main difficulty of this remediation technique is related to the successful delivery of the ZVI into the subsurface. Injected ZVI particles are prone to rapid aggregation due to

strong non-DLVO (Derjaguin–Landau–Verwey–Overbeek) magnetic attraction forces (particularly nZVI),^{8,9} sedimentation (particularly for mZVI),^{10,11} and oxidation;¹² these can also cause a loss in reactivity and decreased mobility, thus limiting the efficacy of the remediation.^{4,5} To overcome this deficiency, different studies have explored the coating of ZVI particles with different surface modifiers.^{1,13} An alternative approach consists in the dispersion of mZVI particles in viscous non-Newtonian fluids^{11,14} to increase stability. Laboratory studies have demonstrated that solutions of biopolymers (e.g., guar gum) are effective in this sense, reducing sedimentation and aggregation.^{3,11,14} Recent experiments at the field scale have demonstrated the enhanced stability of guar gum (GG) coated

Received: January 14, 2015

Revised: April 9, 2015

Accepted: April 17, 2015

Published: April 17, 2015

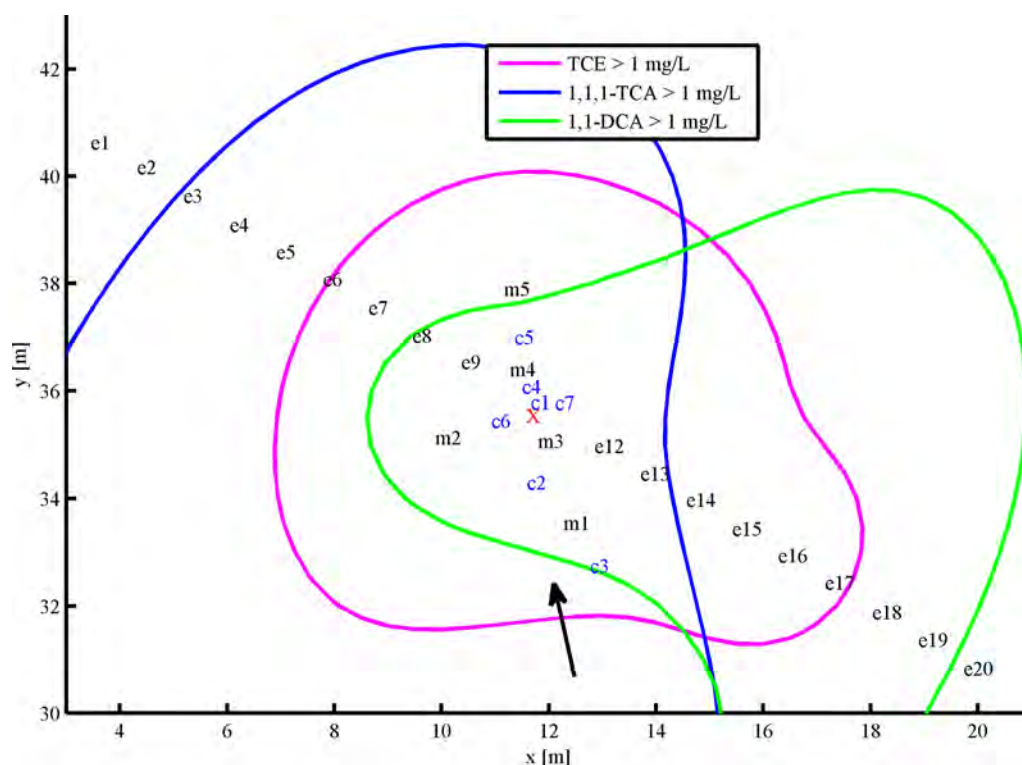


Figure 1. Schematic representation of the experimental setup, with the position of the mZVI-injection point indicated by the red cross. The extension of the contaminant plumes for concentrations above 1 mg/L are indicated by the contour lines. The arrow indicates the groundwater flow direction. The positions of the electrodes (e1, e2, etc.), the multilevel samplers (MLS) (m1–m5), and the core samplers (CS) (c1–c7) are indicated by the respective initial letters.

mZVI particles (hereafter GG-mZVI), with particles migrating over several meters from the injection point.³

To date, the monitoring of ZVI particle injection is performed through geochemical analysis of soil and water samples.^{3,5} Although geochemical analyses provide direct and precise measurements of the properties of interest, they are strongly limited by the characteristics of the samples (e.g., location of the boreholes, sampling volumes and rates) and thus the spatial resolution of the monitoring results. Moreover, sample collection and chemical analyses are time-consuming and not suitable for real-time monitoring of field activities like reagent delivery. Furthermore, one of the main advantages of the remediation through ZVI amendment is its applicability in aquifers characterized by low hydraulic conductivity. Here, the injection is performed at high pressure to create preferential flow paths (fractures).^{3,15} Particle injection via fracturing is also required in aquifers characterized by sediments with pore size comparable to particle size.¹⁶ In this case, the geochemical monitoring may be limited by the distribution of sampling wells, as well as by the geometry and location of the fractures controlling the flow, relevant to water sampling. Therefore, the application of mZVI for subsurface remediation urges the development of a monitoring technique, able to track the migration path of the particles, to delineate the extension and distribution of the iron slurry as well as to characterize processes accompanying particle injection, such as aggregation, oxidation, and clogging.⁵ Geophysical methods seem to be a suitable alternative to conventional approaches, as they permit to obtain continuous information on the subsurface properties based on noninvasive measurements performed on the surface or in existing boreholes.¹⁷ Although geophysical methods may provide information with enhanced spatiotemporal resolution,

geochemical data (from water and soil analyses) are still required to calibrate models linking the geophysical properties with parameters of interest (e.g., ZVI volumetric-content, contaminant concentrations).

Given the strong induced electrical polarization response observed in the presence of electronic conductors (e.g., metallic minerals), the complex electrical conductivity method, or simply complex conductivity (CC), has been established as a standard tool for the exploration of metallic ores.¹⁸ Taking this into account, CC images resulting from tomographic surveys have been utilized to evaluate changes in the reactivity of ZVI permeable reactive barriers¹⁹ (PRB) and to assess changes in pore-space geometry due to the accumulation of metallic minerals following biostimulation.^{20,21} Furthermore, because of the sensitivity of the CC to geochemical processes taking place at the mineral grain–water interface, CC imaging has been successfully applied at the field scale to delineate changes in the dominating redox-status of sediments in the course of bioremediation^{21,22} and to discriminate between the source zone and the plume for hydrocarbon contaminants.²³

A study by Joyce et al.²⁴ investigated the CC response in laboratory experiment of different metallic nanoparticles in a sand matrix. Their study reported an increase in the polarization effect for silver (Ag) and ZVI particles with increasing particle concentration, whereas a negligible polarization response was observed for metallic oxides. However, their study was performed on bare nanoscale particles without any coating or solution to increase the stability of the particles. To our knowledge, to date, there is no study investigating the applicability of the CC imaging method to monitor the injection of stabilized mZVI at the field scale. In particular, experiments at the field scale are required to investigate the

signal strength and the electrical response for measurements performed during the injection of stabilized mZVI.

The present study reports the application of the CC imaging method to characterize the delivery of GG-stabilized mZVI (GG-mZVI) during a field-scale injection by hydraulic fracturing. Our objective is to evaluate the application of CC monitoring images to delineate the migration pathway of the injected mZVI. Particles injection was conducted in the framework of the EU FP7-AQUAREHAB project along with geochemical monitoring, which was recently reported in detail.³ We hypothesize that the comparison of the electrical images obtained at different steps during and after the injection of GG-mZVI provides information on the migration pathway followed by the particles associated with an increase in the polarization response due to the accumulation of metallic surfaces, for example, ZVI. Because of the lack of a generally accepted petrophysical model linking geochemical parameters (e.g., contaminant concentration) and the electrical response, this study is not designed to explore the long-term effect in the contaminant plume. Instead, we focus on the imaging results obtained during the delivery of GG-mZVI and 12 h after the injection was concluded.

MATERIALS AND METHODS

Study Area. The site is located in an industry area in Belgium where the production of solvent-based painting and coating led to a severe contamination of the aquifer, mainly by chlorinated aliphatic hydrocarbons (CAHs), in particular trichloroethene (TCE) and 1,1,1-trichloroethane (1,1,1-TCA). Initial hydrogeological characterization of the site revealed three main units: a shallow sandy unit (0–4.5 m depth), followed by a clayey-sandy aquitard (4.5–8 m depth), and a deeper aquifer consisting of fine sands (8–20 m depth). According to an analysis of the aquifer sediments recovered during the installation of monitoring wells, individual grains of glauconite are present in materials below 5 m depth. Groundwater was located at 2.5 m below ground surface (bgs) with a flow direction toward south–southwest and an estimated flow velocity of ~ 10 m/year. Pumping and slug tests performed at the site³ estimated an average hydraulic conductivity of 8.2×10^{-5} m/s for the aquifer (depth >8 m bgs) and 2.4×10^{-6} m/s for the clayey-sandy aquitard. Analysis of recovered sediments from the deep aquifer reported a grain size distribution of $d_{10} = 52 \mu\text{m}$ and $d_{90} = 374 \mu\text{m}$, and an effective porosity of 18%. A complete description of the chemical composition of groundwater is presented in the Supporting Information.

Geochemical analysis of water samples collected previously at the site reported that the 1,1,1-TCA plume reaches a depth of 13.5 m bgs, while the TCE plume reaches 15.5 m bgs. The distribution of the TCE, 1,1,1-TCA, and 1,1-dichloroethane (1,1-DCA) plumes for concentrations above 1 mg/L are presented in Figure 1, as obtained from the interpolation of existing data. Further details of the site can be found in a previous study.³

GG-mZVI Injection. Subsurface amendment in this study targeted the materials underlying the known source zone (Figure 1). A total volume of 1.5 m^3 GG-mZVI was injected into the subsurface, consisting of 70 g/L mZVI and 7 g/L GG (HV7000, Rantec). Injections were performed at high pressure from bottom to top at 10.5, 10.0, 9.5, 9.0, and 8.5 m bgs, with an average of ~ 21 kg injected mZVI at each depth. Each injection lasted approximately 15 min, with 15 min periods

between successive injections to move the pump to the next injection depth. The employed reactive mZVI particles are reported to have a particle size distribution of $d_{10} = 24 \mu\text{m}$, $d_{50} = 56 \mu\text{m}$, $d_{90} = 69 \mu\text{m}$, and specific surface areas according to Burnauer–Emmett–Teller (BET) of $57 \text{ m}^2/\text{kg}$. Enzymes (LEB-H, Rantec) were added to the pump tank at the end of each injection period to induce fast degradation of the GG for the recovery of mZVI reactivity.^{3,7,25}

Laboratory Tests. Relevant properties of the GG-mZVI slurry were measured in the laboratory on slurry similar to that injected in the field and were prepared using tap water. Electrical conductivity of GG solution with and without mZVI particles, prior and after enzyme addition, was measured using a multiparameter probe. Zeta-potential of mZVI particles dispersed in GG prior and after enzyme addition was measured using an acoustic spectrometer (DT. 1200, Dispersion Technology Inc.).

Geochemical Monitoring. Groundwater samples before and after GG-mZVI injection were collected at depths of 4.5, 8.0, 8.5, 9.0, 9.5, 10.0, and 10.5 m bgs by means of multilevel samplers (MLS) located at the positions shown in Figure 1. To better assess the distribution of the injected mZVI, a total of seven core samples (CS) were collected after stopping the mZVI amendment, located at the positions shown in Figure 1. ZVI-concentrations in the recovered core-samples were quantified through hydrogen measurements after acid digestion of subsamples.⁵

Complex Conductivity Imaging. The CC method, also known as induced polarization (IP) method, is based on four-electrode impedance measurements, where two electrodes are used to inject electric current, and the other two to measure the resulting voltage. In the present study, measurements were collected in the time-domain, where the injected current signal is a square wave with on and off times. Here, CC measurements are given by the ratio of the recorded voltage to the injected current amplitude (resistance), and the measurement of the voltage decay, once the current is switched off (chargeability). Inversion of tomographic data sets collected with tens of electrodes provides the distribution of the CC (σ^*) in the subsurface.¹⁷ The resulting images can be expressed in terms of the real (σ') and imaginary (σ'') components of the CC or, alternatively, by its magnitude ($|\sigma|$) and phase (ϕ). The CC can also be described in terms of its inverse, the complex resistivity, ρ^* ($\rho^* = 1/\sigma^*$).

The real component (σ'), or magnitude ($|\sigma|$), of the CC is mainly controlled by the electrical conductivity of the fluid (σ_f), porosity, and the connectivity of the pore space,²⁶ and to a lesser extent by surface conductivity (σ_s) in the presence of metallic minerals (i.e., particles). The imaginary component of the CC (σ'') is solely related to surface conductivity (i.e., interface polarization effects), which arises due to electrochemical processes taking place at the interface between mineral grains and pore fluid.

Strong polarization effects are related to the presence of metallic minerals (or particles) in contact with an electrolyte. Here, the application of an external electrical field induces oxidation–reduction reactions at the metal–electrolyte interface, which involve charge transfer mechanisms from ionic to electronic: in the forward half reaction, a metal ion in solution accepts an electron from the metal and is reduced to the atomic state, while at another location of the metal, the reverse process takes place.¹⁸ Laboratory measurements²⁴ have revealed a measurable induced polarization response for ZVI nanoparticles

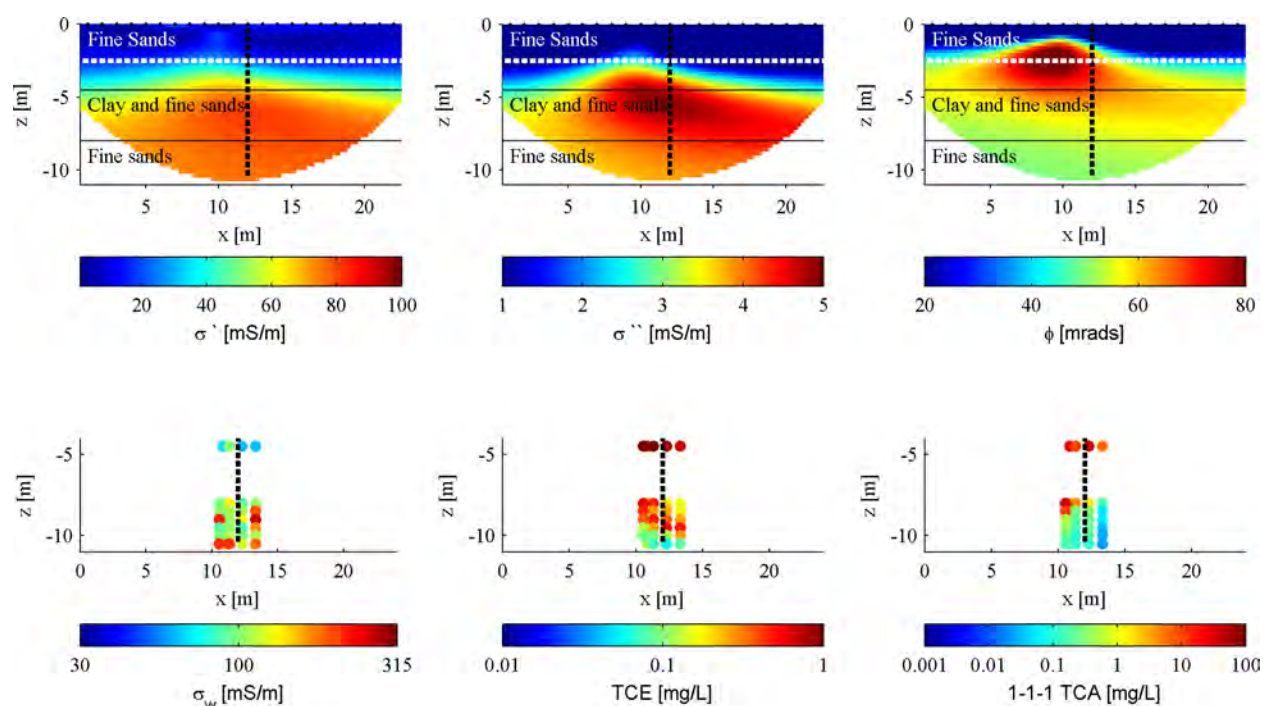


Figure 2. Electrical imaging results for data collected before the injection of GG-mZVI (top) as well as fluid conductivity (σ_f), TCE, and 1,1,1-TCA concentrations measured in MLS (bottom). The vertical black dashed line indicates the position of the injection well. In the electrical images, the electrodes at the surface are indicated with the black points, while the white dashed line indicates the groundwater level and the black solid lines the lithological contacts.

in a sand matrix with increasing phase values (ϕ) for increasing particle concentrations. However, we note here that in the study of Joyce et al.,²⁴ the nanoparticles were mixed to the sand during the preparation, that is, they did neither consider the injection of particles nor the effect of the stabilizing solution.

In the present study, tomographic CC surveys were conducted with a Syscal Pro (Iris Instruments) using 24 stainless steel electrodes with a separation of 1 m along a surface profile (see Figure 1). Data were collected using a dipole–dipole configuration, which combines “skip-3”, “skip-4”, and “skip-5” measurements with dipole lengths of 4, 5, and 6 m, respectively (i.e., dipole length defined by the number of skipped electrodes along the electrode array). The selection of the measurement configurations plays a key role regarding the resolution and depth of investigation of the imaging results. Usually the aim is to find the best compromise between signal-to-noise ratio (favored by large dipole lengths), image resolution (favored by small dipole lengths), and depth of investigation (favored by larger separation between the current and potential dipoles). Hence, the use of a reduced number of measurements will not only reduce the time required for data collection, but also the resolution of the resulting images. Further details on the characteristics of different measurement configurations can be found in other studies.^{17,21,27,28}

The measurement protocol was carefully designed to minimize electromagnetic coupling, avoid voltage measurements using electrodes previously used for current injection,²¹ and increase the signal-to-noise ratio for deep measurements. For the particular purpose of this study, it was important to collect an entire data set in less than 15 min, which was the time required, after each injection, to relocate the injection pump to the next depth. The intended exploration depth was 11 m, considering the maximal depth of the particle injection of 10.5 m. Initial and final measurements were collected as normal

and reciprocal pairs for quantification of the data error, where a reciprocal reading consists in the repetition of the measurements after interchanging current and potential dipoles. Monitoring measurements collected during particle injection were performed only as normal readings to reduce acquisition time. A square-wave current (50% duty cycle) was injected with a pulse length of 2 s. Integral chargeability measurements were obtained through 20 voltage readings recorded between 240 and 1840 ms after current shut-off. We note here that it was impossible to increase the length of the profile to avoid the vicinity of walls and other sources of anthropogenic noise. Shorter separation of electrodes would have increased the resolution in shallow areas but undesirably increased the acquisition time. For the purpose of this study, we opted for a single 2D profile given the significantly increased acquisition time associated with 3D surveys.

The electrical images were computed with CRTomo, a smoothness-constraint inversion algorithm by Kemna.²⁷ To enhance the quality of the inverted images, data-error parameters were defined in the inversion as stopping criterion. Data error was quantified based on the analysis of normal-reciprocal discrepancies, as described in a previous study.²⁸ For the inversion of time-domain measurements, chargeability values were linearly converted to frequency-domain phase values (at the fundamental frequency of 0.125 Hz), which assumes a constant-phase response.²⁷ This approach has been demonstrated to provide accurate results in previous studies.²³ Although not discussed here, we also tested inversions with other regularization schemes.²⁹ However, these results revealed no improvement over the images computed with the standard smoothness-constraint regularization and adequate data-error quantification, as presented here.

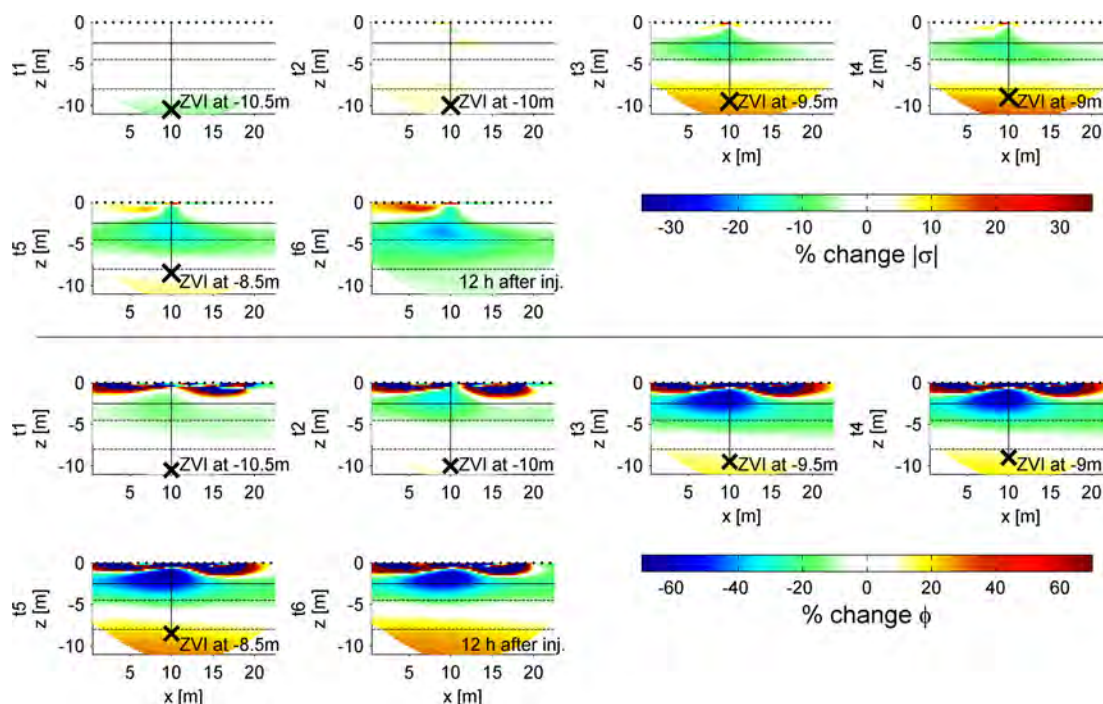


Figure 3. Relative change between the baseline (t_0) images and those obtained for data collected during (t_1 – t_5) and after (t_6) the GG-mZVI injection. The vertical line and black crosses indicate the respective positions of the injection point; black dots represent the electrodes placed at the surface; the solid horizontal line indicates the position of groundwater level; and the dashed horizontal lines indicate the upper and lower limit of the aquitard (clayey sandy materials).

RESULTS AND DISCUSSION

CC Imaging for CAH Plume Characterization: In Situ CAHs Targeting. Figure 2 shows the CC imaging results and geochemical parameters (i.e., σ_f , TCE, and 1,1,1-TCA concentrations) for the data collected 1 day before the GG-mZVI injection in MLS. The CC is presented in terms of real (σ') and imaginary (σ'') components as well as phase (ϕ). To guide the interpretation of the electrical images, we marked the interfaces between the lithological units.

The electrical images in Figure 2 reveal four main units in agreement with the lithology: low electrical conductivity values at the top, characteristic of unsaturated sands, followed by a unit revealing a slight increase in σ' and σ'' , corresponding to saturated sands. The highest σ' and σ'' values are observed for clayey materials in the aquitard (between 5 and 8 m bgs), and slightly lower values are associated with the deeper sandy aquifer. Furthermore, Figure 2 reveals two local anomalies in the polarization images: a shallow anomaly (between ~ 5 and 10 m along profile direction) characterized by high ϕ values, and a deeper anomaly (between ~ 10 and 20 m along profile direction) characterized by high σ'' values.

The position of the high-polarization anomalies corresponds to the region at which the highest CAHs concentrations (e.g., TCE and 1,1,1-TCA) were reported in MLS samples (Figure 2, bottom). From MLS data, the highest concentration of CAHs was measured at 4.5 m bgs (>15 mg CAHs/L), it slightly decreases for measurements at 8 m bgs (3–14 mg CAHs/L), and it further decreases for measurements at 10.5 m bgs (0.1–4 mg CAHs/L). Hence, it seems that the anomalies observed in the polarization images (ϕ and σ'') are correlated with the occurrence of high concentrations of CAHs. In detail, for the unsaturated zone, the high CAHs concentrations and the low water saturation correspond to an increase of the polarization

effect and a decrease of the electrical conductivity, respectively, resulting in the high ϕ values observed in Figure 2. Likewise, the occurrence of high CAHs concentrations should also explain the high polarization (σ'') values observed between ~ 4 and 8 m bgs in the image of the imaginary component. The increase in both the real and imaginary components in the clayey sand materials (>5 m bgs) leads to the observed decrease in the ϕ values in the aquitard materials, masking the response due to the high CAHs concentrations observed in the σ'' images. A recent study reported an increase in the electrical conductivity for increasing TCE concentrations in laboratory measurements.³⁰ However, our data reveal no correlation between σ' and TCE concentration or between σ_f and TCE. Nevertheless, the anomalies observed in the polarization images (σ'' and ϕ) reveal correspondence with high CAHs concentrations. A previous study at the field scale also revealed a correlation between the increase in the polarization response and increasing concentrations of dissolved hydrocarbons.^{23,31} Hence, images presented in Figure 2 suggest that the geometry of the anomaly characterized by high ϕ and σ'' values is mostly controlled by the occurrence of high CAHs concentrations and not by the lithology. However, the lack of high-resolution geochemical data in the area of the aquitard (5–8 m bgs) and for areas away from the injection point impedes the confirmation of this hypothesis.

Our results show the potential of CC imaging to delimit the subsurface distribution of CAH compounds in areas where the collection of groundwater samples is not feasible. Although the objective of this study is not the delineation of the contaminant plume, a good characterization is critical for the design of the particle injection, such as defining the location for injection and sampling wells.

The uncertainty in our measurements was estimated by means of statistical analysis of the misfit between normal-

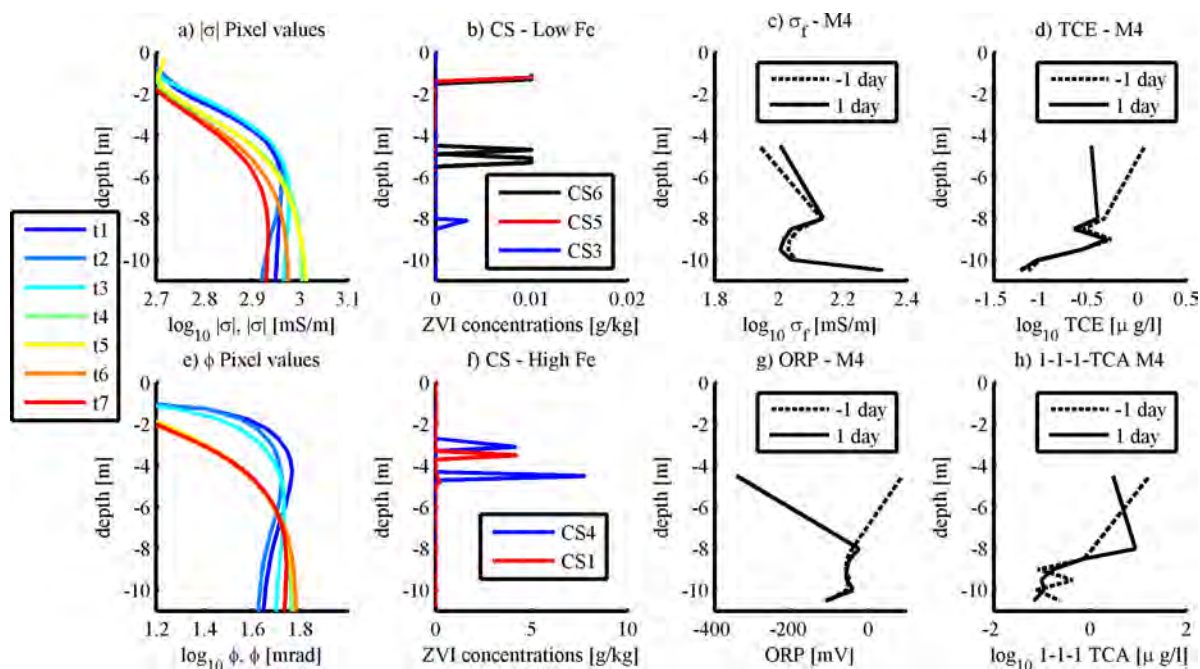


Figure 4. Comparison of geophysical and geochemical parameters. Temporal variations of conductivity (a) and polarization (e) at each depth can be compared with Fe-concentrations measured in the core samples, CS (b,f), as well as with fluid conductivity (c), oxidation–reduction potential (g), as well as TCE (d) and 1,1,1-TCA (h) concentrations.

reciprocal readings, as described in previous studies.²⁸ To assess the uncertainty in the inverted images, procedures were followed as those described in the study of Flores Orozco et al.²¹ On the basis of such analysis, we blanked and neglected in the interpretation the areas associated with a high uncertainty (>10%) in the inverted image, as shown in the bottom left and right regions of the electrical images in Figure 2. A similar analysis was performed for all the imaging results presented here.

CC Monitoring for Delineation of GG-mZVI Transport and Delivery. The imaging results for the data collected during GG-mZVI injection are presented in Figure 3 in terms of the percentage change between the data collected after each injection (including 12 h after stopping the last injection) and the baseline images (Figure 2). These monitoring images show three main aspects: (1) although a constant increase in the ϕ values is observed in the targeted area (between 8 and 10.5 m bgs), as expected due to the delivery of mZVI particles, the changes are modest (25%), even for data collected 12 h after the last injection; (2) only a minimal increase (<10%) is observed in the electrical conductivity for aquifer sediments during the injections, which is likely related to an increase in the surface conduction due to the delivered metallic particles. However, the conductivity images ($|\sigma|$) reveal modest changes (~10%) immediately after the last injection and 12 h later, probably due to geochemical changes at the particle surfaces hindering electronic conduction; (3) an unexpected decrease is observed between 2 and 5 m bgs for both the conductivity and polarization properties, in particular a modest decrease in the conductivity (~10%) and a more pronounced one in the polarization (~50%) for data collected during GG-mZVI injection and 12 h after the last injection. The images in Figure 3 reveal that the fractures generated during the high-pressure injection were acting as preferential flow paths and allowed the GG-mZVI to migrate to shallow areas, which are mostly associated with higher porosity and lower pressure. This

hypothesis is coherent with pressure logs shown by Velimirovic et al.,³ which revealed an initial peak due to opening of fractures, followed by two abrupt decreases corresponding to fracture propagation and to reaching of high permeable and lower pressure (shallow) layer.

Large ϕ variations observed in Figure 3 in the first 1 m bgs are probably artifacts resulting from computing relative changes to the values close to zero observed in the baseline image (cf. Figure 2) and will not be further discussed.

Figure 4 presents pixel values extracted from the CC images at the location of the injection, as well as relevant geochemical parameters, to evaluate their correlation. The $|\sigma|$ and ϕ curves (first column in Figure 4) represent the median of pixel values extracted from the CC images at each depth in a radius of 2 m around the injection point. These curves highlight the larger changes observed in shallow areas (between 2 and 4 m bgs) in comparison with the modest variations in the aquifer sediments (between 8 and 10 m bgs). Figure 4 also presents the iron (Fe) concentrations measured in the CS collected after the injection (second column). From the six cores recovered, only CS3 revealed measurable Fe concentrations in the targeted area (~3 mg/kg). Nonetheless, measurements in CS4 and CS1 reported high Fe concentrations (>3 g/kg) between 2 and 5 m bgs, with measurements CS5 and CS6 also revealing measurable Fe concentrations in that region. Furthermore, geochemical data revealed no changes for water samples collected in the aquifer, as previously reported.³ Changes in the geochemical parameters were observed only in water samples collected at 4.5 m depth from MLS4 (Figure 4c,d,g,h).

The σ_f measured by means of MLS revealed minimal changes in samples collected before and after the injection. To confirm this observation, we realized measurements in the laboratory using tap water, which demonstrated a consistent pattern with our field data: the electrical conductivity for tap water (~54.34 mS/m) revealed only a minimal increase after the mixture with GG solutions (to ~54.54 mS/m), and only a slight increase in

the electrical conductivity (values of ~ 56.7 mS/m) for samples containing GG and mZVI, in mixtures with similar ratios as those injected in the field experiment. Thus, σ_f seems to be unsuitable to monitor the injection of GG-mZVI. In addition to this, we concluded that changes observed in the CC are not related to variations in the σ_f of the electrolyte. Nevertheless, similar to variations observed in the monitoring CC images, TCE and 1,1,1-TCA concentrations revealed modest changes for samples collected within the aquifer (below 8 m depth), whereas they decreased significantly at one location (MLS4) at 4.5 m depth. Furthermore, as demonstrated in previous studies,³² variations in the oxidation–reduction potential (ORP) can be used to infer the accumulation of ZVI. In this regard, our independent measurements also agree with the results observed in CC images, considering that measurements performed at the MLS4 at 4.5 m depth revealed a decrease in the ORP values, as presented in Figure 4.

Both geochemical and geophysical data give evidence that the GG-mZVI was not effectively delivered into the deeper aquifer (8.5–10.5 m bgs) but mostly migrated into the sandy materials on the top of the aquitard. As a result, the CC images would be expected to exhibit an increase of the conduction and polarization response in the shallow zone due to the accumulation of metallic particles, as observed in the aquifer. The slight decrease ($\sim 10\%$) in the conductivity (σ' or $|\sigma|$) observed for shallow sediments, as well as for deeper locations, can be explained by a reduction of the porosity due to the viscous GG clogging the pore space. The reduction in the polarization effect (ϕ) is a consequence of the GG adsorbed onto the surface of the mZVI forming the so-called “brush-layer”^{33,34} hindering electronic conduction and electrode polarization processes. Once the external electrical field is applied (i.e., current injection), the migration of ions is only taking place through the electrolyte and the brush-layer (ionic conduction), with none to minimal interactions between the ions and the metallic surface of the mZVI, that is, no charge transfer at the electrolyte–metallic interface.

Previous studies have demonstrated a significant decrease in the zeta-potential of bare ZVI nanoparticles after they are coated by the GG brush layer.^{33,34} In addition to this, we performed measurements in the laboratory on GG-mZVI samples with similar concentrations as those used in the field injection. These laboratory measurements revealed, as expected, low zeta-potential values (0.37 ± 0.07 mV), which further decreased (to -0.4 ± 0.04 mV) after the addition of LEB-H enzymes, as those used in the field injection. Thus, the covering of the metallic surface due to the brush-layer, impeding the charge transfer mechanisms at the particles surface, explains the strong decrease observed in the polarization images (ϕ).

Samples retrieved for CS3 represent larger distances to the injection point, which suggests the development of preferential flow paths not only toward the shallow sandy materials. However, the monitoring by means of MLS was not able to track geochemical changes in that area. Nevertheless, a noticeable increase in the polarization response is observed for the aquifer materials. This response suggests the delivery of mZVI, dispersed in lower GG concentrations, as reported by Velimirovic et al.³

OUTLOOK

CC monitoring measurements during a field GG-mZVI injection experiment provided not only information about the

contaminant distribution, but also valuable information to identify the migration pathway of the injected GG-mZVI. The relatively short acquisition time permitted to obtain monitoring data with enhanced temporal resolution, that is, after each injection (every ~ 15 min), while it still covered an extended area of investigation in comparison with conventional geochemical monitoring by means of soil and water samples. Hence, CC imaging is a suitable method for the monitoring of GG-mZVI injection at the field scale. Nevertheless, geochemical data are required to fully understand the electrical signatures.

We decided to focus our investigation on the injection-period time frame, as it is critical for the effective remediation of contaminants. In this regard, CC imaging might also be used to guide the collection of soil and water samples, following the injection, to improve the characterization of transport and fate of injected GG-mZVI.

Although not addressed here, further studies should consider the performance of 3D surveys to address the spatial variability of the CC response due to ZVI injections. The deployment of electrodes placed in boreholes might also be considered to increase the vertical resolution of the resulting electrical images, or to reach deeper areas of interest, not accessible by means of surface measurements. Future studies may also consider investigating the geophysical response due to the electrical double layer surrounding the GG-mZVI particles.^{35,36} Furthermore, CC monitoring measurements may also be performed to assess long-term changes of the geochemical properties resulting from the ZVI-driven degradation of the contaminants.

ASSOCIATED CONTENT

Supporting Information

Complete description on the chemical composition of groundwater reported at the site 1 day before the injection of mZVI. The Supporting Information is available free of charge on the ACS Publications website at DOI: 10.1021/acs.est.5b00208.

AUTHOR INFORMATION

Corresponding Author

*E-mail: adrian.flores-orozco@geo.tuwien.ac.at.

Notes

The authors declare no competing financial interest.

ACKNOWLEDGMENTS

Part of this research was conducted in the framework of the European Union Project No. SQUAREHAB (FP7—Grant Agreement No. 226565). We thank Matthias Bucker for the helpful observations on an earlier version of this manuscript.

REFERENCES

- (1) Johnson, R. L.; Nurmi, J. T.; O'Brien Johnson, G. S.; Fan, D.; O'Brien Johnson, R. L.; Shi, Z.; Salter-Blanc, A. J.; Tratnyek, P. G.; Lowry, G. V. Field-scale transport and transformation of carboxymethylcellulose-stabilized nano zero-valent iron. *Environ. Sci. Technol.* **2013**, *47* (3), 1573–1580.
- (2) Elliott, D. W.; Zhang, X. W. Field assessment of nanoscale bimetallic particles for groundwater treatment. *Environ. Sci. Technol.* **2001**, *35*, 4922–4926.
- (3) Velimirovic, M.; Tosco, T.; Uytteboeck, M.; Luna, M.; Gastone, F.; De Boer, C.; Klaas, N.; Spaion, H.; Eisenmann, H.; Lasson, P. O.; Braun, J.; Sethi, R.; Bastiaens, L. Field assessment of guar gum

stabilized microscale zerovalent iron particles for in situ remediation of 1,1,1-trichloroethane. *J. Contam. Hydrol.* **2014**, *164*, 88–99.

(4) Tosco, T.; Petrangeli Papini, M.; Cruz Viggi, C.; Sethi, R. Nanoscale iron particles for groundwater remediation: A review. *J. Cleaner Prod.* **2014**, *77*, 10–21.

(5) Grieger, K. D.; Fjordboge, A.; Hartmann, N. B.; Eriksson, E.; Bjerg, P. L.; Baun, A. Environmental benefits and risks of zero-valent iron nanoparticles (nZVI) for in situ remediation: Risk mitigation or trade-off? *J. Contam. Hydrol.* **2010**, *118*, 165–183.

(6) Tosco, T.; Sethi, R. Transport of non-Newtonian suspension of highly concentrated micro- and nanoscale iron particles in porous media: A modeling approach. *Environ. Sci. Technol.* **2010**, *44* (23), 9062–9068.

(7) Velimirovic, M.; Larsson, P. O.; Simons, Q.; Bastiaens, L. Reactivity screening of microscale zerovalent iron and iron sulfides towards different CAHs under standardized experimental conditions. *J. Hazard. Mater.* **2013**, *252–253*, 204–212.

(8) Phenrat, T.; Saleh, N.; Sirk, K.; Tilton, R. D.; Lowry, G. V. Aggregation and sedimentation of aqueous nanoscale zerovalent iron dispersions. *Environ. Sci. Technol.* **2007**, *41*, 284–290.

(9) Phenrat, T.; Kim, H. J.; Fagerlund, F.; Illangasekare, T.; Tilton, R. D.; Lowry, G. V. Particle size distribution, concentration, and magnetic attraction affect transport of polymer-modified Fe0 nanoparticles in sand columns. *Environ. Sci. Technol.* **2009**, *43* (13), 5079–5085.

(10) Dalla Vecchia, E.; Luna, M.; Sethi, R. Transport in porous media of highly concentrated iron micro- and nanoparticles in the presence of xanthan gum. *Environ. Sci. Technol.* **2009**, *43* (23), 8942–8947.

(11) Gastone, F.; Tosco, T.; Sethi, R. Green stabilization of microscale iron particles using guar gum: Bulk rheology, sedimentation rate, and enzymatic degradation. *J. Colloid Interface Sci.* **2014**, *421*, 33–43.

(12) Velimirovic, M.; Carniato, L.; Simons, Q.; Schoups, G.; Seuntjens, P.; Bastiaens, L. Corrosion rate estimations of microscale zerovalent iron particles via direct hydrogen production measurements. *J. Hazard. Mater.* **2014**, *270*, 18–26.

(13) Saleh, N.; Sirk, K.; Liu, Y.; Phenrat, T.; Dufour, B.; Matyjaszewski, K.; Tilton, R. D.; Lowry, G. V. Surface modifications enhance nanoiron transport and NAPL targeting in saturated porous media. *Environ. Eng. Sci.* **2007**, *24*, 45–57.

(14) Tosco, T.; Gastone, F.; Sethi, R. Guar gum solutions for improved delivery of iron particles in porous media (Part 2): Iron transport tests and modeling in radial geometry. *J. Contam. Hydrol.* **2014**, *166* (0), 34–51.

(15) Phenrat, T.; Cihan, A.; Kim, H. J.; Mital, M.; Illangasekare, T.; Lowry, G. V. Transport and deposition of polymer-modified Fe0 nanoparticles in 2D heterogeneous porous media: Effects of particle concentration, Fe0 content, and coatings. *Environ. Sci. Technol.* **2010**, *44* (23), 9086–9093.

(16) Raychoudhury, T.; Tufenkj, N.; Ghoshal, S. Aggregation and deposition kinetics of carboxymethyl cellulose-modified zero-valent iron nanoparticles in porous media. *Water Res.* **2012**, *46* (6), 1735–1744.

(17) Kemna, A.; Binley, A.; Cassiani, G.; Niederleithinger, E.; Revil, A.; Slater, L.; Williams, H. K.; Flores Orozco, A.; Haegel, F.-H.; Hördt, A.; Kruschwitz, S.; Leroux, V.; Titov, K.; Zimmermann, E. An overview of the spectral induced polarization method for near-surface applications. *Near Surf. Geophys.* **2013**, *10* (6), 453–468.

(18) Wong, J. An electrochemical model of the induced polarization phenomenon in disseminated sulfide ores. *Geophysics* **1979**, *44* (7), 1245–1265.

(19) Slater, L.; Binley, A. Synthetic and field-based electrical imaging of a zerovalent iron barrier: Implications for monitoring long-term barrier performance. *Geophysics* **2006**, *71*, B129–B137.

(20) Williams, K. H.; Ntarlagiannis, D.; Slater, L. D.; Dohnalkova, A.; Hubbard, S. S.; Banfield, J. F. Geophysical imaging of stimulated microbial biomineralization. *Environ. Sci. Technol.* **2005**, *39*, 7592–7600.

(21) Flores Orozco, A.; Williams, H. K.; Kemna, A. Time-lapse spectral induced polarization imaging of stimulated uranium

bioremediation. *Near Surf. Geophys.* **2013**, *11*, 531–544 DOI: 10.3997/1873-0604.2013020.

(22) Flores Orozco, A.; Williams, K. H.; Long, P. E.; Hubbard, S. S.; Kemna, A. Using complex resistivity imaging to infer biogeochemical processes associated with bioremediation of a uranium-contaminated aquifer. *J. Geophys. Res.* **2011**, *116*, G03001.

(23) Flores Orozco, A.; Kemna, A.; Oberdörster, C.; Zschornack, L.; Leven, C.; Dietrich, P.; Weiss, H. Delineation of subsurface hydrocarbon contamination at a former hydrogenation plant using spectral induced polarization imaging. *J. Contam. Hydrol.* **2012**, *136–137*, 131–144.

(24) Joyce, R. A.; Glaser Li, D. R.; Werkema, D. D., Jr; Atekwana, E. A. Spectral induced polarization response to nanoparticles in a saturated sand matrix. *J. Appl. Geophys.* **2012**, *77*, 63–71.

(25) Velimirovic, M.; Chen, H.; Simons, Q.; Bastiaens, L. Reactivity recovery of guar gum coupled mZVI by means of enzymatic breakdown and rinsing. *J. Contam. Hydrol.* **2012**, *142–143*, 1–10.

(26) Archie, G. E. The electrical resistivity log as an aid in determining some reservoir characteristics. *Trans. Am. Inst. Min., Metall., Pet. Eng., Soc. Min. Eng. AIME* **1942**, *146*, 54–62.

(27) Kemna, A. *Tomographic Inversion of Complex Resistivity—Theory and Application*, Ph.D. Thesis, Ruhr University of Bochum, Bochum, Germany, 2000.

(28) Flores Orozco, A.; Kemna, A.; Zimmermann, E. Data error quantification in spectral induced polarization imaging. *Geophysics* **2012**, *77* (3), E227–E237.

(29) Blaschek, R.; Hördt, A.; Kemna, A. A new sensitivity-controlled focusing regularization scheme for the inversion of induced polarization data based on the minimum gradient support. *Geophysics* **2012**, *73*, F45–F54.

(30) Hort, R. D.; Revil, A.; Munakata-Marr, J. Analysis of sources of bulk conductivity change in saturated silica sand after unbuffered TCE oxidation by permanganate. *J. Contam. Hydrol.* **2012**, *165*, 11–23.

(31) Kemna, A.; Binley, A.; Slater, L. Crosshole IP imaging for engineering and environmental applications. *Geophysics* **2004**, *69*, 97–107.

(32) Shi, Z.; Nurmi, J. T.; Tratnyek, G. P. Effects of nano zero-valent iron on oxidation–reduction potential. *Environ. Sci. Technol.* **2011**, *45* (4), 1586–1592.

(33) Tiraferri, A.; Chen, K. L.; Sethi, R.; Elimelech, M. Reduced aggregation and sedimentation of zero-valent iron nanoparticles in the presence of guar gum. *J. Colloid Interface Sci.* **2008**, *324* (1), 71–79.

(34) Tiraferri, A.; Sethi, R. Enhanced transport of zerovalent iron nanoparticles in saturated porous media by guar gum. *J. Nanopart. Res.* **2009**, *11* (3), 635–645.

(35) Louie, S. M.; Phenrat, T.; Small, M. J.; Tilton, R. D.; Lowry, G. V. Parameter identifiability in application of soft Particle Electrokinetic Theory to determine polymer and polyelectrolyte coating thicknesses on colloids. *Langmuir* **2012**, *28* (28), 10334–10347.

(36) Phenrat, T.; Saleh, N.; Sirk, K.; Kim, H. J.; Tilton, R. D.; Lowry, G. V. Stabilization of aqueous nanoscale zerovalent iron dispersions by anionic polyelectrolytes: Adsorbed anionic polyelectrolyte layer properties and their effect on aggregation and sedimentation. *J. Nanopart. Res.* **2008**, *10*, 795–814.

Complex-conductivity monitoring to delineate aquifer pore clogging during nanoparticles injection

Flores Orozco Adrián,¹ Vesna Micić,² Matthias Bucker,³ Jakob Gallistl,¹ Thilo Hofmann² and Frederic Nguyen⁴

¹Geophysics Research Division, Department of Geodesy and Geoinformation, TU-Wien, Austria. E-mail: flores@tuwien.ac.at

²Environmental Geosciences, Centre for Microbiology and Environmental Systems Science, University of Vienna, Austria

³Institute of Geophysics and Extraterrestrial Physics, TU Braunschweig, Germany

⁴Urban and Environmental Engineering, University of Liege, Belgium

Accepted 2019 May 31. Received 2019 May 5; in original form 2019 January 15

SUMMARY

Laboratory and field studies have demonstrated the applicability of nanoparticles (NP) for accelerated contaminant degradation. Beside other limitations (e.g. costs, delivery, longevity, non-target specific reactions), concerns of regulators arose regarding toxicity of injected NP and particles delivered off-target (i.e. renegade particles). Renegade particles also significantly reduce the efficiency of the remediation. The delivery of particles off-target is caused, mainly, by unintended fracking, where the fractures act then as preferential flow paths changing the trajectory of the particles. Hence, the real-time monitoring of particle injection is of major importance to verify correct particle delivery and thus help to optimize the remediation strategy. However, to date NP monitoring techniques rely on the analysis of soil and water samples, which cannot provide information about clogging or the formation of fractures away of the sampling points. To overcome these limitations, in this study we investigate the applicability of complex-conductivity imaging (CCI), a geophysical electrical method, to characterize possible pore clogging and fracking during NP injections. We hypothesize that both processes are related to different electrical footprints, considering the loss of porosity during clogging and the accumulation of NP in areas away of the target after fracking. Here, we present CCI results for data collected before and during the injection of Nano-Goethite particles (NGP) applied to enhance biodegradation of a BTEX (benzene, toluene, ethylbenzene and xylene) contaminant plume. Imaging results for background data revealed consistency with the known lithology, while overall high electrical conductivity values and a negligible induced-polarization magnitude correspond with the expected response of a mature hydrocarbon plume. Monitoring images revealed a general increase (~15 per cent) in the electrical conductivity due to the injected NGP suspension in agreement with geochemical data. Furthermore, abrupt changes in this trend, shortly before daylighting events, show the sensitivity of the method to pore clogging. Such interpretation is in line with the larger variations in CCI resolved in the unsaturated zone, clearly indicating the accumulation of renegade NGP close to the surface due to fracking. Our results demonstrate the applicability of the CCI method for the assessment of pore clogging accompanying particles injection.

Key words: Hydrogeophysics; Electrical resistivity tomography (ERT); Permeability and porosity; High-pressure behaviour.

1 INTRODUCTION

An extensive number of laboratory studies have demonstrated that nanoparticles (NP) could speed up the degradation of groundwater contaminants, taking into account their large specific surface area and high surface reactivity (for a review see Grieger *et al.*

2010; Trujillo-Reyes *et al.* 2014; Adeleye *et al.* 2016 and references therein). Moreover, NP injection offers a promising cost-effective approach for the *in-situ* remediation of contaminated areas inaccessible for other techniques such as deep contaminant plumes, areas beneath infrastructure, as well as for multisource contaminated areas in low hydraulic permeable media (e.g. Karn *et al.* 2009; Tosco

et al. 2014 and references therein). Given their relatively low costs, zero-valent iron (ZVI) and iron-oxide NP have become popular due to their ability to promote the degradation of a variety of pollutants (e.g. Grieger *et al.* 2010; Tosco *et al.* 2014; Velimirovic *et al.* 2014; Chen *et al.* 2015; Schmid *et al.* 2015; Bhattacharjee & Ghoshal 2018). Iron-oxide particles are of special interest due to their non-toxicity, adsorption capacity and ability to stimulate bioremediation (Hua *et al.* 2012; Xu *et al.* 2012; Braunschweig *et al.* 2013; Lei *et al.* 2018). Especially, goethite (α -FeOOH) has demonstrated a high sorption capacity for metal cations (e.g. Hua *et al.* 2012), as well as the potential to enhance contaminant degradation by iron-reducing bacteria (Bosch *et al.* 2010). Specifically, ferric iron can act as an electron acceptor for microbial respiration (Fe³⁺-reduction coupled with the oxidation of contaminants) and can overcome limitations in electron-acceptor availability.

Results observed in laboratory have encouraged field-scale NP injections, with pilot and full-scale experiments reported to date in 92 sites worldwide (e.g. Mueller *et al.* 2012; Patil *et al.* 2016; Bardos *et al.* 2018 and including interactive map). Yet, there are still concerns regarding the effective delivery to the targeted areas and potential toxicity of the particles (e.g. Grieger *et al.* 2010; Bianco *et al.* 2017). Subsurface heterogeneities play an important role in the actual trajectory of the injected particles, for instance unintended injections into preferential flow paths might lead to particles traveling off target. Nathanail *et al.* (2016) adopted the term 'renegade particles' to describe those NP that deviate from the intended trajectory, either not reaching the targeted pollutant or passing through it. A particular case refers to the so-called daylighting, the incident in which renegade particles emerge to the surface along preferential flow paths, for instance through fractures developed by non-intended fracking. Fracking results from pressure building up during the NP injections due to continuous injections performed at high pressure (Hosseini & Tosco 2015; Luna *et al.* 2015), as well as from clogging of the pore space following aggregation and sedimentation of the injected particles (e.g. Tosco & Sethi 2010) enhanced by slow injections (e.g. Luna *et al.* 2015).

Hence, the real-time assessment of pore clogging during NP injection offers the opportunity to relocate the injection and may be the best approach to minimize unintended fracking and, thus, improve the efficiency of NP delivery into the target zone. However, to-date, the monitoring of NP injections still relies on direct methods based on the analysis of soil and groundwater samples (Tosco *et al.* 2014). Although such methods provide information about chemical parameters of interest, they are not suited for real-time monitoring and cannot identify pore clogging.

Geophysical methods can provide essential information about subsurface properties in quasi real-time and with high spatial resolution, offering a unique possibility to identify pore clogging during NP injections. In particular, the complex-conductivity imaging (CCI) method appears to be a suitable technique, considering that laboratory investigations have demonstrated the ability of the method to gain information about pore-space properties (e.g. grain size, pore length) controlling water flow (e.g. Slater 2007; Revil & Florsch 2010; Kemna *et al.* 2012; Okay *et al.* 2013; Binley *et al.* 2016; Gallistl *et al.* 2018; Mainault *et al.* 2018). Based on the electrical properties of contaminants, the CCI has also shown to be a well-suited method for characterization of contaminated sites (e.g. Deceuster & Kaufman 2012; Flores Orozco *et al.* 2012a; Johansson *et al.* 2015; Deng *et al.* 2018; Ntarlagiannis *et al.* 2018). Moreover, it has been observed that microbial activity also modifies the CCI response, either by the electrical properties of the microbial cells

themselves (e.g. Revil *et al.* 2012) or by induced chemical transformations (e.g. Atekwana and Slater 2009; Abdel Aal *et al.* 2014 and references therein). Built on such observations, the method has also been applied at the field-scale for the monitoring of bio-geochemical processes accompanying a variety of remediation techniques (e.g. Slater & Binley 2006; Williams *et al.* 2009; Flores Orozco *et al.* 2011; Chen *et al.* 2012; Saneiyani *et al.* 2019).

Regarding NP investigations, column studies have demonstrated variations in the electrical response due to different nanoparticles (e.g. Joyce *et al.* 2012; Abdel Aal *et al.* 2017; Mellage *et al.* 2018). However, only the study of Flores Orozco *et al.* (2015) has reported the application of the CCI method at the field scale. The authors revealed changes in the electrical images associated with accumulation of bare and coated microscale ZVI particles.

In this study, we extend previous investigations to evaluate the capabilities of the CCI method to monitor the fate and transport of a suspension of nano-goethite particles (NGP) injected in a BTEX-contaminated site. CCI measurements were conducted at the field scale with high temporal resolution aiming at identifying potential pore clogging due to particle sedimentation. The possible pore clogging indicated by the electrical images is supported by extensive geochemical data. Information on pore clogging and the reduction of hydraulic conductivity is critical towards the development of strategies for the effective delivery of NP and the improved remediation of contaminant plumes. To our best knowledge, this is the first field-scale study presenting the CCI monitoring results along nanoparticles injections.

2 MATERIAL AND METHODS

2.1 Pilot site: Spolchemie II in the Czech Republic

Our study presents imaging results for data collected during the injection of NGP at the Spolchemie II site within the scope of the NanoRem project. The Spolchemie II site is located in an industrial area near Ústí nad Labem (Czech Republic) characterized by an unconfined aquifer underlain by a clay layer of low hydraulic permeability at a depth of ~ 10 m; while an anthropogenic layer (with a thickness of ~ 1 m) covers the surface. The aquifer, located below this anthropogenic layer, is composed of quaternary sediments, mainly sand and gravel, with a hydraulic conductivity of $\sim 5.9 \times 10^{-5} \text{ m s}^{-1}$, and the main groundwater flow goes in south-eastern direction (NanoRem Bulletin 8). The groundwater table was found at 5 m below ground level (bgl) during our experiments.

The production of synthetic resin as well as the storage of various raw materials at the site has led to extensive groundwater contamination by BTEX compounds, with toluene representing the main contaminant, followed by xylene and ethylbenzene, and a negligible amount of benzene. The experimental area for the NP injection covers an area of approximately $10 \times 10 \text{ m}^2$, where seven existing wells permit the collection of groundwater samples for geochemical analysis (Fig. 1). At the time of our experiments, BTEX concentration at the water table exceeded 50 mg l^{-1} (as presented in Fig. 1), with lower concentrations for samples collected at larger depths, as expected considering that BTEX compounds are light non-aqueous phase liquids (LNAPL).

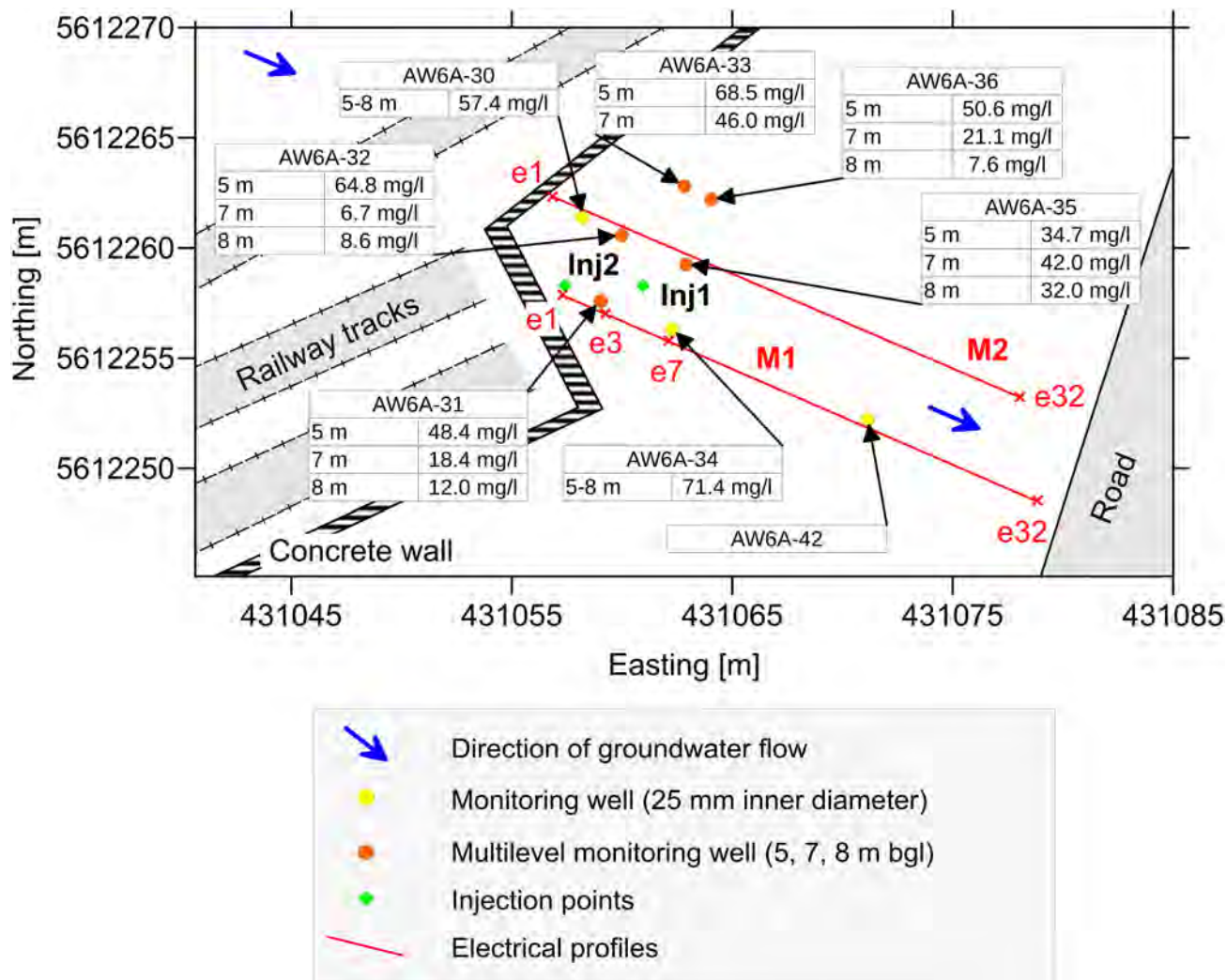


Figure 1. Schematic plan view of the Spolchemie II, CZ site, indicating the position of the monitoring wells and the injection points, BTEX concentrations (in mg l^{-1}) in the monitoring wells, as well as the layout of the electrical profiles M1 and M2 (red lines). The shaded areas indicate the position of infrastructure such as buildings, roads, etc.

2.2 Nano-Goethite particles, particle injections and geochemical monitoring

NGP coated with humic acids to reduce particle aggregation and enhance their mobility (Tirafferri *et al.* 2017), were provided in a stock suspension by the University of Duisburg-Essen and are described elsewhere (Meckenstock & Bosch 2014). The injection suspension was prepared on site by diluting the stock suspension with the filtrated water from the nearby Elbe River and adding a potassium-bromide (KBr) tracer and stored in two tanks.

The injection suspension was intended to contain a particle concentration of 5 g l^{-1} , aiming at delivering a total of 300 kg of NGP. Injections were planned between 5 and 8 m bgl (from top to bottom) in half-metre intervals at low pressure (between 1 and 12 bars) using a direct-push probe. Although injections were planned at five locations, in this study we are only presenting results observed for injections performed at two locations (Inj1 and Inj2 as depicted in Fig. 1) while groundwater sampling was possible. Clogging of the observations wells (as described in the following sections) hindered sampling required for geochemical analysis and therefore will not be presented here.

Prior to the NP injection, geochemical measurements were performed in all observation wells using the membrane-interface well logging probe (MIP) Ecoprobe-5 (from RS Dynamics). The Ecoprobe-5 is equipped with a photo-ionization detector (PID) and an InfraRed (IR) sensor permitting the *in-situ* screening for total petroleum hydrocarbons (TPH) and volatile organic compounds (VOC). For the monitoring of geochemical parameters upon the NGP injections, seven observation wells were available. Five of those were equipped with micro pumps at 5, 7 and 8 m bgl (multi-level monitoring wells). Two additional observation wells, screened between 4 m and 8 m bgl, were situated up- and down-gradient from the injection points aiming at the detection of renegade NP. Along the NGP injection, *in-situ* groundwater parameters, such as temperature, electrical conductivity (i.e. fluid conductivity, σ_f), pH and redox potential, were determined with calibrated probes. It was not possible to employ an on-site turbidity probe, as the diameter of the turbidity probe exceeded that of the groundwater monitoring well. Therefore, turbidity was determined in non-filtered groundwater samples upon return to the laboratory using a turbidimeter 2100 N IS (Hach Lange, Germany) calibrated with formazine standards. Total iron (Fe_{tot}) content in groundwater samples, determined by

ICP-OES Optima 5300DV (PerkinElmer, USA) after acid digestion (with 30 per cent HCl and 5 M HNO₃), was used as a proxy of NGP concentration.

2.3 Indirect monitoring method: complex-conductivity imaging

Complex-conductivity measurements, also referred to as induced polarization (IP), are based on four-electrode arrays and can be performed in the time- or frequency-domain (Ward 1990). When performed in the frequency-domain (as in this study), two electrodes are used to inject a sinusoidal current to the ground, and the second pair of electrodes is used to record the associated phase-shifted voltage. The deployment of tens of electrodes, for the collection of hundreds of measurements, permits to solve for spatially quasi-continuous models (i.e. images) of the subsurface complex conductivity (Binley & Kemna 2005; Kemna *et al.* 2012). The real (σ') and imaginary (σ'') components of the complex conductivity (σ^*) represent the low-frequency (<1 kHz) electrical conductivity (i.e. energy loss) and capacitive (i.e. energy storage) properties of the subsurface, which can also be expressed in terms of magnitude ($|\sigma|$) and phase (ϕ):

$$\frac{1}{\rho^*} = \sigma^* = \sigma' + i \sigma'' = |\sigma| e^{i\phi}, \quad (1)$$

where $i = \sqrt{-1}$ represents the imaginary unit. In most subsurface investigations, the values of ϕ are sufficiently small (<100 mrad), such that $\sigma' \approx |\sigma|$, which is typically referred to as the electrical conductivity (σ) or its inverse the electrical resistivity ($\rho = 1/\sigma$). Equally, for sufficiently small values, the phase of the complex conductivity can be approximated by the ratio of the imaginary to the real component ($\phi \approx \frac{\sigma''}{\sigma'}$), which has been also suggested as a valid proxy to quantify the IP effect.

In most subsurface materials, electrical conduction is carried by the electrolyte (i.e. ionic conduction) and through the electrical double layer (EDL) covering the pore surface (e.g. Waxman and Smits 1968; Leroy *et al.* 2008, and references therein). Ionic conduction is controlled by porosity, saturation and fluid conductivity (σ_f) (e.g. Slater 2007 and references therein); surface conduction along the EDL mainly depends on surface charge and surface area (Schwarz 1962; Schurr 1964; Leroy *et al.* 2008). For clay and other materials characterized by high surface charge and surface area, surface conduction is the dominating conduction mechanism under most conditions (i.e. for low and intermediate ionic strengths of the pore water) and commonly related to high σ values (e.g. Marshall & Madden 1959; Revil & Florsch 2010).

The IP effect in such (metal-free) media results from the migration and accumulation of charge carriers within the different parts of the EDL and has been described by means of two principle mechanisms (e.g. Kemna *et al.* 2012 and references therein): (i) the polarization of the Stern layer (e.g. Leroy *et al.* 2008; Revil & Florsch 2010; Revil *et al.* 2017) or the diffuse layer (e.g. Fixman 1980; Shilov *et al.* 2001) around isolated mineral grains; and (ii) the polarization of overlapping diffuse layers in pore throats better known as membrane polarization (Marshall & Madden 1959; Ward 1990; Bückler & Hördt 2013; Hördt *et al.* 2017). If highly conductive inclusions are present as a discontinuous phase (e.g. metallic nanoparticles or disseminated minerals), the conductor-electrolyte interfaces polarize giving rise to a strong polarization response. This so-called electrode polarization has been described for perfectly conducting inclusions, such as metallic conductors

(e.g. Wong 1979; Bückler *et al.* 2018) and more recently for semi-conducting inclusions, such as most natural metal ores (e.g. Revil *et al.* 2015; Misra *et al.* 2016).

2.4 Complex-conductivity imaging monitoring set-up

CCI monitoring data sets were collected in the frequency domain (at 1 Hz) using the eight-channel DAS-1 (from Multi-Phase technologies) along two profiles (M1 and M2, as depicted in Fig. 1). Each profile comprised 32 electrodes with a separation of 0.75 m between electrodes, aiming at a depth of investigation of 8 m. The presence of concrete walls and roads impeded to extend the length of the profiles for a larger investigation depth. A multiple-gradient configuration (Dahlin & Zhou 2006) was used for both profiles with eight potential dipoles (with lengths of $a = 0.75, 1.5, 2.25$ and 3 m) nested within the current dipole yielding 380 quadrupoles per profile. We opted for this electrode configuration considering that it provides measurements with a larger signal-to-noise ratio (S/N) than other configurations (Dahlin & Zhou 2006; Flores Orozco *et al.* 2018a). Moreover, initial measurements proved sensitive within the required depth of investigation (between 5 and 8 m bgs) and showed negligible distortions due to anthropogenic noise. Monitoring data sets were collected independently along each transect, i.e., no 3-D acquisition schemes to reduce the acquisition time. We aimed at collecting an entire data set in less than 7 min to enhance the temporal resolution of the CCI monitoring. The only gaps in the CCI monitoring corresponds to the overnight break, where the instrument needed to be retrieved from the field.

For the inversion of the observed CCI data, we used CRTomo, a finite-element smoothness-constraint algorithm (by Kemna 2000), which solves for the subsurface distribution of σ^* . This algorithm was selected, as it permits to fit the data within the inversion to a confidence interval, which is defined by an error model (e.g. Kemna 2000; Flores Orozco *et al.* 2012b). Such approach minimizes the risk of overfitting the data during the inversion and the associated creation of artefacts (e.g. Kemna 2000; Slater & Binley 2006; Flores Orozco *et al.* 2012b; Lesparre *et al.* 2017). Blanked areas in the imaging results correspond to regions associated with cumulated sensitivity values two orders of magnitude smaller than the highest cumulated sensitivity (i.e. the sum of absolute, data-error weighted, sensitivities of all considered measurements; see e.g. Weigand *et al.* 2017).

The error model aims at describing the magnitude of random error present in the data; yet it cannot be used to describe a systematic error. Hence, as a first step in the data processing, we removed physically implausible measurements, namely those associated with a negative current amplitude, geometrical factor or apparent resistivity. Then we performed a histogram analysis as proposed by Flores Orozco *et al.* (2018b) to assess the spatial consistency within the data set. Such approach suggests that the occurrence of empty bins in the histogram can be used to define maximum and minimum threshold values in the measured resistances and apparent phase-shift. Yet, no measurement was removed after those analyses demonstrating the good quality of the data. To better illustrate this, we present in the complementary material exemplary pseudo-sections for data collected at different time-lapses.

The analysis of normal and reciprocal readings has been widely accepted for the quantification of random error (e.g. Slater *et al.* 2000; Flores Orozco *et al.* 2012b). However, the fast process under investigation in this study and the collection of gradient configurations limited the possibility to collect reciprocal readings. Hence,

error parameters were estimated based on the analysis of the data quality computed by the instrument (standard deviation from three repetitions) and for the linear error model (e.g. Slater *et al.* 2000)

$$\varepsilon(R) = a + bR, \quad (2)$$

where, a and b refer to an absolute ($a = 1 \text{ m}\Omega$ in our study) and relative ($b = 5$ per cent in our study) error parameters (Slater *et al.* 2000). In case of phase measurements, we used a constant error equal to 1 mrad (e.g. Slater & Binley 2006). All inversion results presented here converged to a root-mean-square (RMS) equal to 1, where the RMS refers to the error-weighted misfit between the data and the modelled forward response (for a comprehensive description of the inverse modelling, we refer to Kemna 2000). CCI monitoring data sets were processed and independently.

3 RESULTS AND DISCUSSIONS

3.1 Background electrical imaging results delineate lithology and contamination levels

Background measurements were collected approximately 24 hr before the first NGP injection. Fig. 2 presents imaging results for background data expressed in terms of the electrical conductivity ($|\sigma|$) and the IP effect (ϕ) along M1, where lithological information is available (core drilling of the observation well AW6-42). Imaging results for background data collected along M2 are consistent to those presented in Fig. 2 (data not shown). The top panel of Fig. 2 shows that spatial variations in the electrical conductivity ($|\sigma|$) are in agreement with lithological changes. The lowest $|\sigma|$ values ($<50 \text{ mS m}^{-1}$) correspond with unsaturated loess and sandy gravels, with a slight increase in $|\sigma|$ associated to the occurrence of finer grains (sandy gravel) at depths between 4 and 5.5 m bgl in the unsaturated zone. The highest $|\sigma|$ values ($>80 \text{ mS m}^{-1}$) below 5.5 m bgl correspond with the saturated sandy clay. The ϕ image presented in the bottom panel of Fig. 2 shows no clear correlation with the lithological units. While the lower part of the image ($<2\text{--}4$ m bgl) is dominated by low values (<5 mrad), the shallow part of the image reveals locally high IP responses, yet these anomalies are most likely due to anthropogenic structures (e.g. pipes, backfill material).

The presence of two shallow cast-iron pipes (located at a depth between 1 and 2 m) is reported at the site, approximately at 7 and 15 m (along direction of profile M1). The pipes have a diameter of 12 cm (smaller than a fifth of the electrode separation), and are coated and wrapped with rubberized products to prevent contact with soil and groundwater and hinder corrosion. Such coating explains the lack of an IP response, as expected due to electrode polarization typical of blank metallic structures. Nonetheless, small phase anomalies ($\phi \sim 3$ mrad) can be distinguished in the shallow areas (between the surface and 2 m depth), which may be related to the heterogeneities in the anthropogenic (gravel) layer around the pipes and likely also distort the magnitude image in the shallow areas (1–2 m depth). Hence, monitoring imaging results presented in this study are only related to model parameters below 2 m depth, at which the distortion caused by the anthropogenic structures might be negligible (e.g. Flores Orozco *et al.* 2012a; Flores Orozco *et al.* 2019).

BTEX compounds are non-polar and, thus, tend to form droplets caged between the water molecules; these are also referred to as non-wetting hydrocarbons considering that they are not in direct contact with the grain surfaces (e.g. Schmutz *et al.* 2010). Early

laboratory investigations on non-wetting hydrocarbons reported an increase in the IP effect for increasing hydrocarbon concentration (e.g. Olhoeft 1985). Based on laboratory observations, an empirical model was proposed by Schmutz *et al.* (2010), which predicts a monotonous increase in the polarization response with increasing saturation of non-polar hydrocarbons (e.g. toluene). Such model is based on the polarization of the Stern layer and incorporates variations of the polarization response due to the presence of an electrically insulating and non-polarizable contaminant. A recent study demonstrated its applicability for laboratory measurements conducted on clayey soils (Deng *et al.* 2018).

At the same time, recent studies have revealed the opposite response, that is, a decrease of the polarization response with increasing saturation of hydrocarbon contaminants, at frequencies below 100 Hz (e.g. Schwartz *et al.* 2012; Ustra *et al.* 2012; Shefer *et al.* 2013). This behaviour may be explained by an increase of the wettability of the non-polar hydrocarbons, as proposed by Revil *et al.* (2011). These authors suggest that absorption of polar compounds to the grain surface will result in an increase of the bulk conductivity and a decrease of the polarization response. Microbial activity is also known to increase the wettability of hydrocarbons, due to the release of metabolic products that change the electrical properties of the hydrocarbons (e.g. Cassidy *et al.* 2001).

Investigations at the field scale (Flores Orozco *et al.* 2012a) have permitted to differentiate two behaviours: (i) a linear increase of the IP response ϕ for BTEX concentrations below the saturation concentration of the hydrocarbon; and (ii) a negligible IP response ($\phi < 5$ mrad) for hydrocarbon concentrations above the saturation concentration—at which the contaminant is present in free-phase. The change in the IP response around the saturation concentration has also been studied by Bucker *et al.* (2017) based on an analytical membrane-polarization model. These authors argue that low BTEX concentrations are related to the presence of small isolated hydrocarbon droplets within the large macro pores and a large membrane-polarization effect (i.e. an increase in ϕ) is caused by the small ion-selective pore throats, which are essentially contaminant free, if the hydrocarbon is non-wetting. However, if hydrocarbon concentration increases, the contaminant phase becomes continuous and fills both macro pores and pore throats, hindering the formation of ion-selective throats and, thus, reducing the IP effect (Bucker *et al.* 2017). Based on this model, the negligible IP response observed in Fig. 2 seems to be a consequence of toluene concentrations, which in fact exceed saturation concentration at the study site (saturation concentration of toluene is around 520 mg l^{-1}).

3.2 Mature hydrocarbon plumes show an increased electrical conductivity

Chemical transformations of hydrocarbon contaminant plumes may change the electrical footprint sensed in the subsurface, as observed in laboratory investigations (e.g. Heenan *et al.* 2014; Ntarlagianis *et al.* 2018 and references therein). Besides this, hydrocarbon plumes represent a source of organic carbon, which may stimulate microbial activity (Huling *et al.* 2002). Microbial activity enhances the transformation of contaminants (e.g. Schirmer *et al.* 2006), as well as the release of metabolic products, such as carbonic acids, commonly resulting in an increase of fluid conductivity and, thus, of the bulk electrical conductivity $|\sigma|$ (e.g. Atekwana & Atekwana 2010; Cassiani *et al.* 2014; Heenan *et al.* 2014; Caterina *et al.* 2017 and references therein). Moreover, carbonic acids have also been related to grain weathering and the development

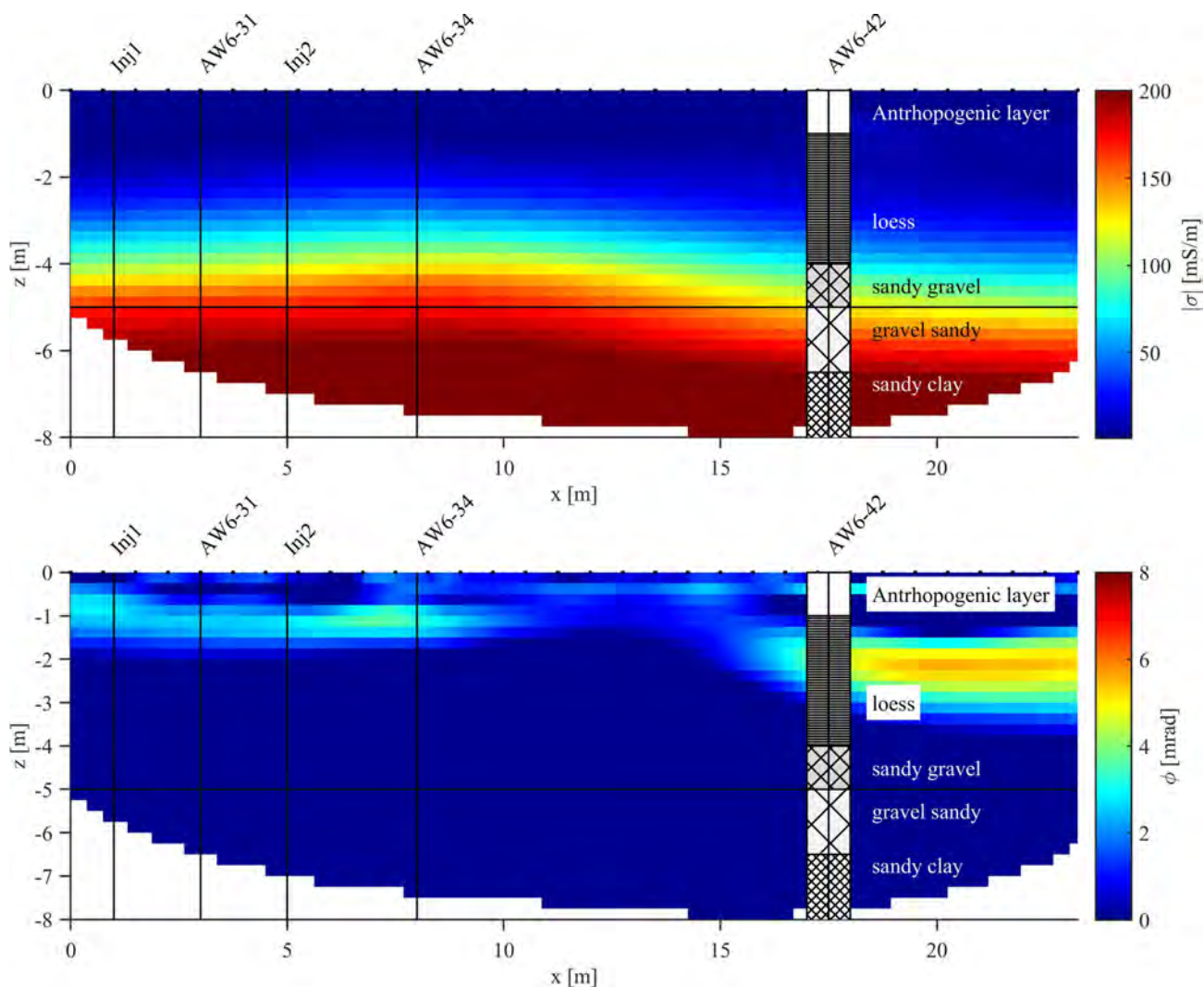


Figure 2. Electrical imaging results for data collected one day prior to the NGP injection expressed in terms of the magnitude ($|\sigma|$) and phase (ϕ) of the complex electrical conductivity. The positions of the monitoring wells (AW6-31, AW6-34 and AW6-42) and the injection points are indicated (solid vertical lines), as well as the depth to the groundwater table during the experiments (solid horizontal line). The overimposed lithological log of well AW6-42 aids the interpretation of the electrical units.

of secondary porosity and biofilms, further increasing the electrical conductivity of mature hydrocarbon plumes (Abdel Aal *et al.* 2004; 2006). Hence, chemical transformations related to a mature contaminant plume explain the high $|\sigma|$ values observed in Fig. 2, which might seem to be in contradiction to the low conductivity of fresh hydrocarbon spills (Cassiani *et al.* 2009). Furthermore, an increase in σ_f also has an effect on the IP response, as it reduces the contribution of the EDL to the overall conduction and, thus, further decreases the ϕ due to membrane polarization (Hördt *et al.* 2016).

TPH and VOC well-logs revealed high values around the water table (~ 5 m bgl), which was in agreement with the analysis of groundwater samples (Fig. 1) and the highest $|\sigma|$ values observed in Fig. 2. Moreover, MIP measurements of methane (CH_4) and carbon dioxide (CO_2) also revealed high concentrations in both the vadose and the saturated zone (Fig. 3), likely due to the stimulated microbial activity at the site, supporting the interpretation of the electrical images presented above.

3.3 Daylighting and other problems observed during the injection of the nano-goethite particles

NGP injection began at well Inj1 using the suspension from the first storage container, which at the site revealed a larger than intended particle concentration (ca. 20 g l^{-1} measured in the storage tank). The particle injection at the first, second and third injection depth (5, 5.5 and 6 m bgl in Inj1) were performed at a low pressure (5–6 bar, for a duration of ~ 75 min at each depth) aiming at preventing fracturing. Nevertheless, even if the injections were performed at low pressures, during the third injection (at 6 m bgl) in Inj1, solution escaped to the surface (daylighting) through wells AW6-30, AW6-31 and AW6-32 (a picture from the field conditions during daylighting is presented in Fig. 4). Furthermore, daylighting was also occurring at observation well AW6-30, which is located up-gradient from Inj1, clearly indicating the transport of particles away from the target areas and opposed to the main direction of groundwater flow, sustaining the interpretation of ongoing pore clogging close to the injection point.

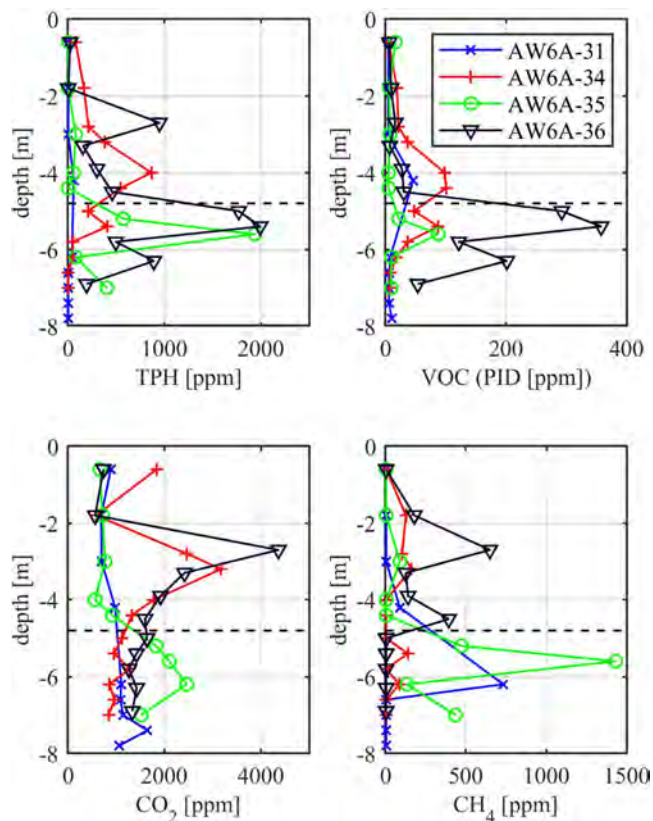


Figure 3. Geochemical data in selected monitoring wells measured *in situ* prior to the injection of the NGP. TPH: total petroleum hydrocarbons, VOC: volatile organic compounds. Data provided by AQUATEST a.s. (CZ).

NGP injections became less regular after the first daylighting; namely, injection in Inj1 at 6 m depth was suspended after a few minutes due to solution flowing to the surface. Injections at the next depth (6.5 m) were performed at higher pressure (>10 bar) to force the delivery of NGP in the subsurface, but after a few minutes, suspension was again flowing to the surface hindering further injection at that depth. At this point, the solution flowing out near the observations wells AW6-30, 31 and 32 was visibly containing iron (see picture in Fig. 4). To allow the delivery of the slurry, injections at 7 and 7.5 m depth were performed at even higher pressure (>12 bar), reducing the injection time to ~40 min for each step.

Injections at the second injection point (Inj2) started ~50 min after the last amendment in Inj1, at depths of 5, 5.5 and 6 m (at 12 bar and a delivery time of ~40 min). Yet, suspension flowing to the surface still occurred in several observation wells during the injection periods. Furthermore, geochemical sampling was hindered due to clogging of the tubing in observation wells affected by daylighting.

After an overnight break, which impeded the collection of CCI and geochemical data, NGP injections were restarted using suspension from the second container (initial particle concentration of ca. 10 g l^{-1}). During the second day, NGP injections were performed at 6.5, 7 and 7.5 m in Inj2 (also at 12 bar). Yet, daylighting was observed also for these injections and geochemical sampling was compromised again. Hence, in the following sections, we do not consider further injections points and only present results for data collected during the delivery of the NGP suspension from the first container in Inj1 (all injection depths) and Inj2 (only down to 6.5 m bgl).

3.4 Electrical monitoring images evidence fracking following particles injection

CCI measurements were collected every 7 min along the monitoring transect (i.e. profiles M1 and M2), with a long break overnight due to safety regulations within the facilities. CCI monitoring data sets were processed and inverted independently before the calculation of percentage changes between the baseline and the monitoring imaging results, as presented in Fig. 4.

As discussed above, anthropogenic structures close to the surface resulted in the creation of artefacts in the electrical images within the first 1 m depth. Under similar conditions, earlier studies have demonstrated the capability of the CCI method to characterize subsurface processes accurately at depths below the anthropogenic structures (e.g. Flores Orozco *et al.* 2012a, 2015; Caterina *et al.* 2017; Lesparre *et al.* 2017). Accordingly, here, we present only the temporal changes below the cover layer (between 1 and 8 m bgl), which reveal consistent results during the entire experiment, as observed in exemplary images presented in Fig. 4. Monitoring data sets in profile M2 were mainly collected along the injection of the solution of the second NGP storage tank and, as mentioned above, are not further discussed.

The imaging results in Fig. 4 show a modest increase (~10 per cent) in $|\sigma|$ in the saturated zone after concluding the first NGP injection (at 5 m depth). Images for data collected at later times (and injections) reveal a further increase in $|\sigma|$, with the last images, showing an increase of up to ~20 per cent in the electrical conductivity of the saturated zone, when compared to the baseline image. These recorded changes in the electrical conductivity correspond to subsurface amendment of NGP suspension, characterized by a fluid conductivity (σ_f) ~27 per cent higher than the groundwater (Table 1).

The increase in $|\sigma|$ (between 10 and 20 per cent over baseline measurements) in Fig. 4 close to the injection wells is clearly related to the addition of the NGP suspension. Nevertheless, changes in the electrical properties are not only confined to the depth of the NGP injection (between 5 and 8 m bgl), but are also observed in the unsaturated zone, in particular, between 2 and 4 m bgl. A straightforward explanation for such variations is that fractures developed during the NGP delivery extended from the injection point to the unsaturated zone, which led to the accumulation of the injected solution containing free humic acids, and likely NGP, close to the surface. The accumulation of particles away from its initial target has been previously reported for field-scale particles injection (e.g. Flores Orozco *et al.* 2015; Luna *et al.* 2015).

The impossibility to collect water samples in the unsaturated zone hinders the quantitative interpretation of the CCI anomalies. Nevertheless, our interpretation of the shallow electrically conductive anomaly is supported by the occurrence of daylighting in monitoring wells AW6-31 and AW6-32 during the third injection step (at 6 m bgl). Following this argumentation, the shallow conductive anomaly observed in Fig. 4 (after a few minutes after starting the very first injection) indicates that the fracking started much earlier than the daylighting (~160 min after starting the first injection), likely already during the first injection in Inj1 (at 5 m bgl). The position of the main conductive anomaly observed in the CCI monitoring results in Fig. 4 corresponds with loess material, which offers a perfect environment for the capture of renegade NGP due to its high porosity.

The monitoring results for images of the IP effect are not presented, as the monitoring images revealed negligible ϕ values along the entire experiments, similar to those resolved for the background

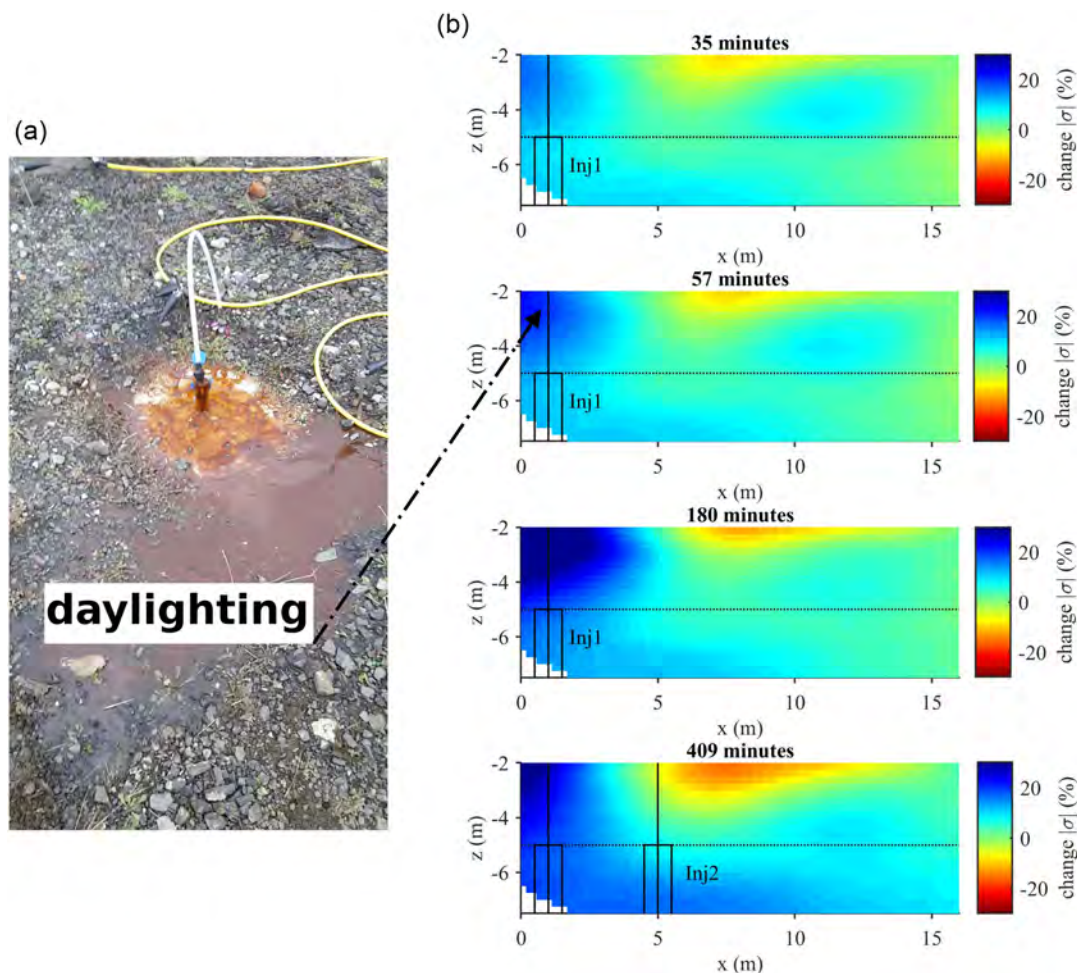


Figure 4. CCI monitoring results: (a) Daylighting observed in the vicinity of observation wells AW6-31 and AW6-32 after starting NGP delivery at 6.5 and 7 mg/l in Inj1. (b) CCI time-lapse imaging results for profile M1 in terms of the percentage change in $|\sigma|$ at different steps of the monitoring period. In Fig. 4(b), the dashed line indicates the depth to groundwater during the experiments, whereas the solid vertical lines show the position of the injection wells, with the rectangles indicating the injection areas.

Table 1. Fluid conductivity (σ_f) of NGP stock and injection suspension as well as the reference value of the groundwater and the Elbe River water. n.a.: not available.

Sample	Br ⁻ concentration	σ_f ($\mu\text{S cm}^{-1}$)	pH
NGP stock suspension	Stock suspension + ca. 1 g L ⁻¹ Br ⁻	4640	n.a.
NGP injection suspension (particle concentration ca. 20 g l ⁻¹)	Sample 1 + ca. 50 mg L ⁻¹ Br ⁻	1621	7.6
	Elbe River water	504	7.53
	On-site groundwater (containing BTEX)	1279	6.78

data (e.g. Fig. 2). The lack of an IP response following the injection can be explained by an increase in the fluid conductivity due to the injection of NGP suspension, characterized by a higher fluid conductivity than the one of the groundwater at the site (Table 1). A previous study in the laboratory revealed an initial increase in the polarization response with increasing fluid conductivity associated with sorption of ions into the Stern layer (Revil & Skold 2011). These authors also report a decrease in the polarization response at high salinity values for some samples, which they suggests may be due to membrane polarization. Based on the analysis of different samples, Weller *et al.* (2015) propose that the decrease in ion

mobility at high salinity values causes the decrease in the IP response. Based on the modelling of membrane polarization, Hördt *et al.* (2016), argue that a decrease in the zeta-potential needs also to be taken into account to explain the decrease in the IP response at high salinity values.

To better investigate the spatiotemporal changes in the electrical signature and their correlation with subsurface processes along the entire monitoring period, we present in Fig. 5 the values of representative geochemical parameters measured in water samples collected in different observation wells (AW6- 30, 31, 32, 34), as well as pixel values retrieved from the electrical images. Such pixel

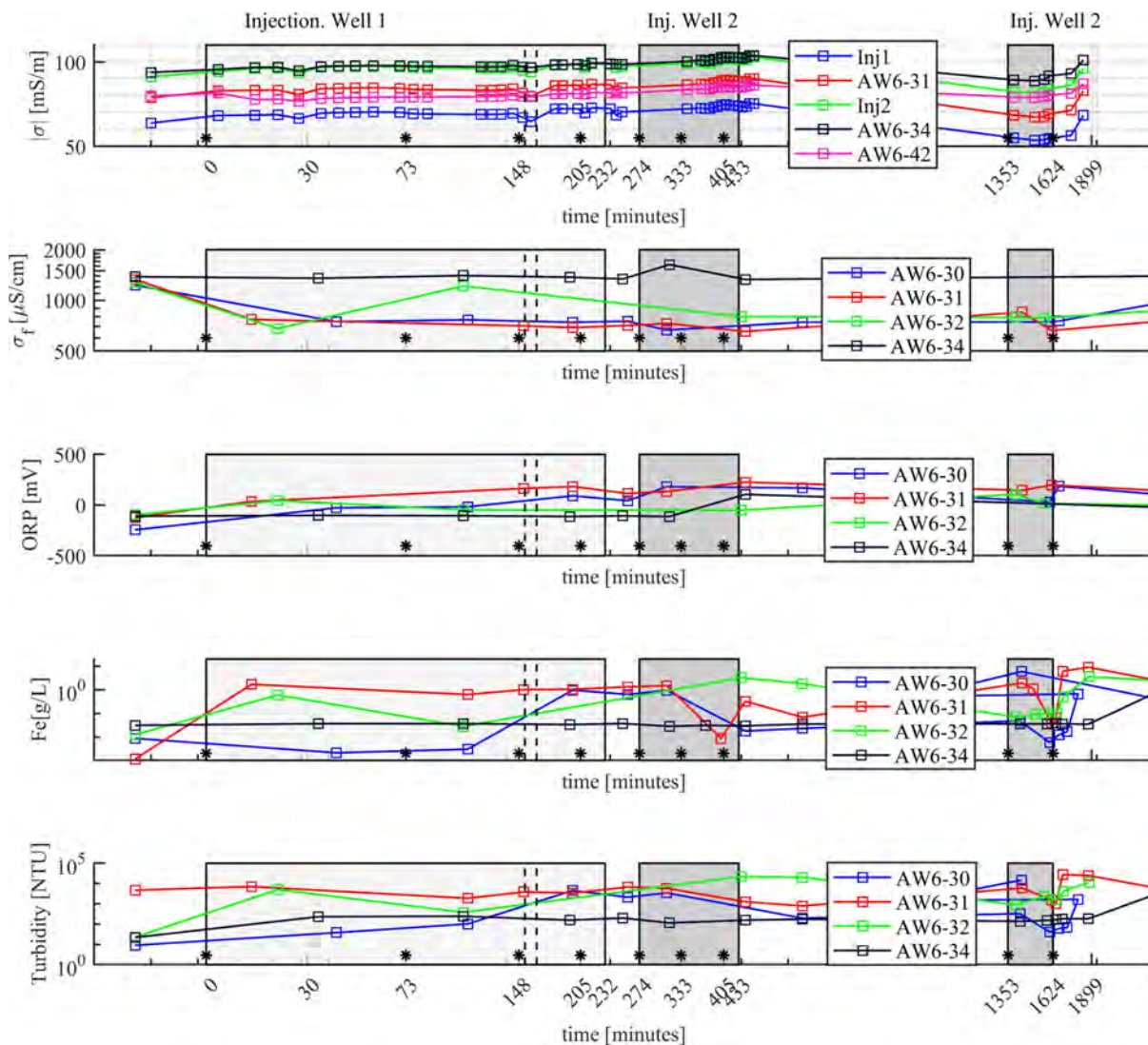


Figure 5. Geophysical and geochemical results for the monitoring period of the NGP injection. The electrical conductivity ($|\sigma|$) represents pixel values extracted from the electrical images between 5 and 7 m depth at the position of the injection points (Inj1 and Inj2) and observation wells (5a) along with the fluid electrical conductivity (5b), oxidation–reduction potential (5c), total iron content (5e) and turbidity (5e) measured in water samples. The grey-shaded zones represent the injection periods at each injection well. The vertical dashed line indicates the time of the first two daylighting events reported. The symbols (*) represent the beginning of injections at depths of 5, 5.5, 6 and 7.5 m at Inj1, as well as at depths of 5, 5.5 and 6 m depth at Inj2.

values represent the median $|\sigma|$ values between 5 and 8 m depth at the position of the observation wells and the first injection point (Inj1). The injection periods at Inj1 and Inj2 are indicated by the grey shaded areas. The blank area in Fig. 5 (between ~500 min and 24 hr) is due to overnight breaks, during which it was not possible to collect geophysical or geochemical data.

Fig. 5 reveals a slight increase in $|\sigma|$ during the injection period for most of the retrieved pixels, with the exception of observation well AW6-42. After finishing the injection in Inj1, Fig. 5 reveals a drop in the $|\sigma|$ values, which bounce back once the injection starts in Inj2. However, a more significant decrease in $|\sigma|$ is observed during the overnight break, which evidences a change from 75 mS m^{-1} to 55 mS m^{-1} for pixels extracted at the position of Inj1. Similar variations in $|\sigma|$ are also observed for the rest of the extracted pixels, with the exception of observation well AW6-42. This well is located 15 m down gradient from the injection point, where only a slight change in $|\sigma|$ is observed, suggesting that only minimal amounts of NGP suspension were transported to such distance during the first

injection day. In agreement with those observations, NGP injections at the second point (Inj2) are also related to a slight increase in $|\sigma|$.

Opposite to the trend observed in $|\sigma|$ values, *in-situ* measurements of σ_f revealed a significant decrease (~45 per cent) directly after starting the injection for water samples collected in observation wells close to the injection point (AW6-31 and 32). Such observation is not easy to explain, considering that the fluid conductivity of the injected NGP suspension is higher than the one of the groundwater (Table 1). Instead, we hypothesize that the mixing of shallow and deeper groundwater due to the NGP injection concurrent with the pumping in the observation wells causes the observed decrease in σ_f . This hypothesis is consistent with the lack of changes in observation wells located down gradient (e.g. AW6-42) the injection points.

Due to the high reactivity of the particles, Oxidation-Reduction Potential (ORP) measurements can be used as a proxy to monitor particle delivery (see Shi *et al.* 2011 and references therein). Consistently, during our experiments subsurface enrichment with NGP

can be evidenced by the continuous increase in ORP values in observation wells AW6-30 and AW6-31 along the entire monitoring period (Fig. 5c). Yet, such trend is followed by a decrease to pre-injection values after ~30 min, which is the time at which fracking can be inferred from the CCI results. Hence, ORP variations are also consistent to the interpretation of the electrical images.

Distinctive to such trend, ORP measurements reported 15 m down gradient from the injection point (AW6-42) reveal negligible changes over the first 450 min of the NGP amendment. Nevertheless, samples collected after concluding injections at 5.5 m depth at Inj2 show an increase in the ORP values, suggesting that some NGP suspension might have been transported 15 m after 8 hr. Such observation is also consistent with the slight increase in $|\sigma|$ resolved through the electrical monitoring. However, the negligible changes in Fe_{tot} indicate that no NGP were transported to such distances and the observed changes may be related only to the accumulation of the stabilizing solution of humic acids.

Measurements of the Fe_{tot} (Fig. 5d) can be used in the interpretation of CCI results and to evaluate the delivery of NGP. As expected, following the first injection, iron concentration increases in the observation wells near the injection (AW6-31 and AW6-32). Accordingly, Fe_{tot} also increases in the observation well located up gradient the injection point (AW6-30) after the reported daylighting (~160 min after starting the first injection). However, the Fe_{tot} concentration in AW6-30 dropped significantly before finishing the first injection period. Such observation in well AW6-30 is consistent with the turbidity measurements (another proxy to assess the presence of NP in water samples, see Shi *et al.* 2015), which also reveal an increase concurrent with the reported daylighting (Fig. 5e). However, turbidity bouncing back to initial values after starting the second NGP amendment (in Inj2) can be related to problems with the sampling or deviations in the particles due to fractures created during the first injection (e.g. daylighting). Additionally, turbidity measurements reveal an initial increase in AW6-30 and AW6-32 after starting the injections; yet, this is followed by fluctuations poorly correlated with the NGP injections. Furthermore, turbidity values show negligible changes in samples collected in observation wells AW6-31 (directly next to the injection well) and AW6-34 (15 m downgradient), suggesting that particles were mainly delivered to fractures connecting the injection point to the surface. Both, temperature and pH revealed only negligible changes along the monitoring period, with values around a mean value of 13 °C and a quasi-neutral pH of 7.2 (data not shown).

3.5 The lack of sensitivity of induced polarization images following the injection of nano-goethite particles

As an induced-polarization method, CCI is known to be highly sensitive to metallic particles in the subsurface (e.g. Pelton *et al.* 1978; Ward 1990). The large polarization magnitude of the underlying electrode-polarization process is mainly caused by the high electrical conductivity of the particles compared to the one of the surrounding electrolyte solution (e.g. Wong 1979). Although it is an iron-bearing mineral, goethite is a semiconductor and its relatively large band gap (2.1 eV) results in a very low electrical conductivity (approx. $10\text{--}3 \mu\text{S cm}^{-1}$) at room temperature (Cornell & Schwertmann 2003). Thus, the polarization response of goethite cannot be attributed to electrode polarization. More likely, it is caused by the polarization of the electrical double layer covering the charged surface of non-conducting particles as discussed by Abdel Aal *et al.* (2014). A non-zero charge at the surface of goethite particles is

well documented (e.g. Cornell & Schwertmann 2003; and references therein), such that it is straightforward to assume the action of a Stern-layer (e.g. Leroy *et al.* 2008) or diffuse-layer (e.g. Fixman 1980; Shilov *et al.* 2001) polarization process around the goethite particles. Laboratory IP measurements on goethite indicate a low (Huisman *et al.* 2014) or negligible low-frequency polarization (Olhoeft 1982; Abdel Aal *et al.* 2014) of goethite surfaces compared to those on conductive minerals (e.g. pyrite, magnetite, graphite). Thus, the absence of a characteristic CC signature of the NGP at frequencies around 1 Hz in our experiments is in perfect agreement with both theoretical considerations and earlier experimental findings.

A possible technical means to increase the phase response of the particles or particle aggregates would be to use (much) higher frequencies: Laboratory measurements with goethite nanoparticles conducted by Huisman *et al.* (2014) found a measureable increase of the imaginary part of the conductivity around 1 kHz and for comparable particle concentrations. However, in field applications, inductive and capacitive coupling effects generally mask the IP response and render the interpretation of high-frequency CCI data challenging (e.g. Pelton *et al.* 1978; Flores Orozco *et al.* 2013, 2018a and references therein). In particular, inductive coupling effects arise due to the conduction of current along the cables connecting the measuring instrument and the electrodes, which are proportional to the bulk conductivity of the subsurface, the acquisition frequency and the square of the cable length (Hollof *et al.* 1974). Hence, collection of high-frequency IP data in areas characterized by high electrical conductivity (e.g. mature hydrocarbon plumes) or by the injection of NP dispersions with high fluid conductivity may be challenging due to contamination of the IP data by inductive coupling. Clearly, the problem will increase with increasing the depth of investigation, which requires the collection of data with longer cables. A recommendation for future campaigns would be to find a trade-off between signal strength and adverse high-frequency effects in order to maximize the information on NPG in the phase response. Accordingly, the development of dispersion solutions characterized by low fluid conductivity could also be beneficial to improve the sensitivity of the CCI method for the characterization of nanoparticles injections. The collection of IP data over a long time-span might also be important for further studies to assess long-term variations in the signatures associated with the agglomeration of the particles, which may result in larger particle sizes and measurable IP signatures at the low frequencies. Moreover, further changes in the IP signatures might also be related to chemical transformations of the contaminant (e.g. Revil *et al.* 2011) or the accumulation of iron-minerals (Flores Orozco *et al.* 2011, 2013; Abdel Aal *et al.* 2014) due to the expected stimulation of microbial activity (e.g. Braunschweig *et al.* 2013).

3.6 The potential of geophysical monitoring to reveal pore-space clogging and to guide geochemical sampling

To facilitate the quantitative interpretation of changes in the electrical conductivity along the monitoring period, we present in Fig. 6 the response of the same extracted pixels presented in Fig. 5, but plotted as the change in the $|\sigma|$ from baseline.

Fig. 6 clearly reveals a significant decrease in the bulk electrical conductivity concurrent with the daylighting reported in wells AW6-31 and 32 (indicated by the dashed lines). A straightforward explanation of such sudden drop can be given by the pore-space clogging due to the accumulation and sedimentation

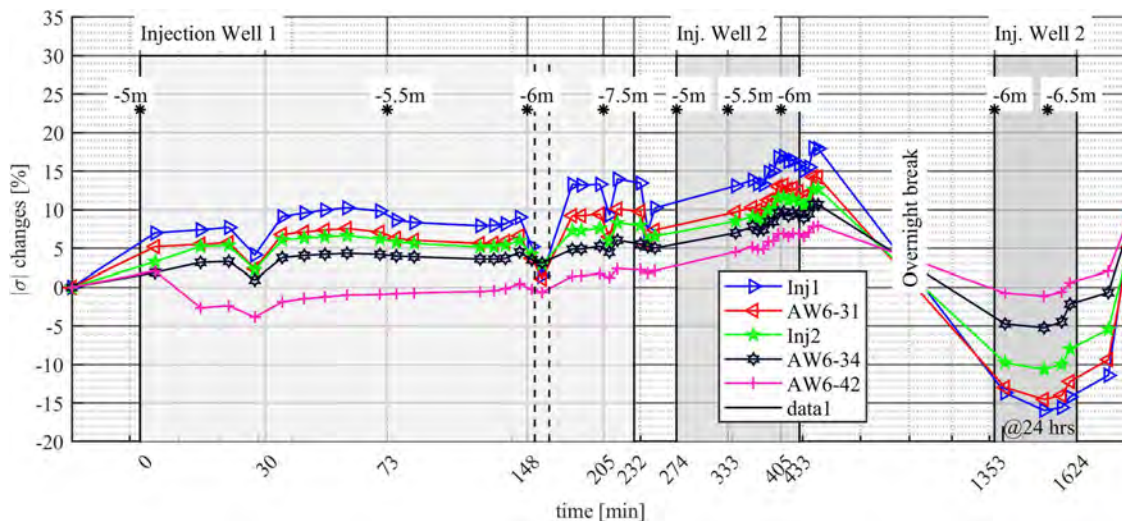


Figure 6. Percentage changes in the electrical conductivity ($|\sigma|$) for the inversion results between the baseline and monitoring measurements. Electrical parameters represent the median for pixel values extracted from the electrical images between 5.5 and 7 m depth at the position of the injection and observation wells. The vertical dashed line represents the time at which the first daylighting was observed in well AW6-30. The grey polygons represent the delivery periods in Inj1 and Inj2.

of NGP near the injection point. The interaction between NP and the corresponding agglomeration and loss of mobility over time have been largely documented, including coated iron oxides (e.g. Vecchia *et al.* 2009; Tiraferri *et al.* 2017); furthermore, as discussed by Luna *et al.* (2015), long injections commonly result in the sedimentation of the particles. Hence, a two-step process can explain the $|\sigma|$ patterns observed in Fig. 6: (1) first a decrease in porosity (and $|\sigma|$) due to the clogging of the pore space; followed by (2) an increase in the porosity (and $|\sigma|$) due to fracturing and the filling of the associated fractures with NGP solution and groundwater.

To better illustrate this, we can look in detail at the changes in $|\sigma|$ accompanying the first injection (i.e. at Inj1 and 5 m depth). Here, the NGP delivery was performed at low pressure (5–6 bar) and over a long injection time (>60 min), which are conditions promoting particle sedimentation (e.g. Luna *et al.* 2015). Accordingly, the observed decrease in $|\sigma|$ values (at ~ 28 min), is most likely an indication of pore clogging. Hence, the further delivery of NGP suspension resulted in an increase in pore-pressure and the development of fracturing, which can be evidenced in the geophysical imaging by the rapid increase in $|\sigma|$, for instance at ~ 35 min. Hence, the slight decrease in the electrical conductivity observed during the injections at 5.5 m depth can be related to clogging of both the pores and the previously created fractures. Consequently, further injections at 6 m depth, and related plugging of the pore space, resulted in the strong decrease in $|\sigma|$ observed at ~ 160 min, which also led to the further development of the fractures and the daylighting events.

While geochemical analysis cannot help to validate the interpretation of the electrical images, the presence of iron in the solution flowing to the surface, clearly indicates that the injected solution was delivered through fractures to observations wells and the surface. Moreover, the increase in the $|\sigma|$ values in the unsaturated zone close to the injections wells observed in Fig. 4 also supports our interpretation. Here, such anomalies suggest that NGP and/or the dispersion solution found preferential flow paths leading to their accumulation in the unsaturated loss materials.

Following the overnight break, CCI results reveal a significant decrease in $|\sigma|$, even below baseline values. In particular, pixel values close to Inj1 (e.g. AW6-31) show a decrease of 16 per cent in comparison to baseline values and about 26 per cent when compared to the measurement before the overnight break. A first explanation for this conductivity drop can be the degradation of the humic acids coating the NGP particles, and, thus, pore clogging due to particle aggregation. Yet, no hydro-geochemical data are available to sustain this possible interpretation. Nonetheless, our results suggest that CCI may be a suitable method to evaluate changes in porosity following the subsurface enrichment with NP, either associated to fracturing developed during the injection or pore clogging after finishing the delivery of the slurry.

While geochemical data are available only in ca. 12 samples for each observation well, CCI data sets were collected every 7 min allowing tracking the fate of NP in 54 time steps. In addition to that, not all observation wells were sampled along the 12 geochemical time lapses, for instance, observations wells up and down gradient (AW6-30 and -34, respectively) were sampled only 30 min after starting the injection, and then only every 60 min. Moreover, clogging in the tubing of the monitoring wells affected by the daylighting (AW6-32) impeded the collection of water samples, further limiting the resolution of the geochemical monitoring. CCI may overcome some of these limitations in monitoring applications, especially regarding the spatial and temporal resolution.

Although our results show that CCI is a promising method for the monitoring of NP injections, geochemical monitoring is still critical to permit an adequate interpretation of the electrical signatures. We suggest that following experiments consider adjusting the geochemical sampling in order to take into account the geophysical response. Hence, a coupled geochemical–geophysical monitoring could improve the quantitative interpretation of CCI images and permit to improve the efficiency of the remediation method by providing real-time information.

Further information is needed to evaluate the uncertainty in geochemical data. The geochemical variations observed in well AW6-34 illustrate the problem: geochemical monitoring revealed no changes in σ_f , Fe_{tot} and turbidity, suggesting that NGP were not

transported 15 m down gradient the injection points. However, ORP measurements revealed an increase in AW6-34 after starting the first injection (~480 min), which are also consistent with a slight increase in $|\sigma|$ in that area after concluding the NGP amendment at 6 m depth in Inj2 (~453 min after starting the first injection as presented in Fig. 6). We explain our observations as the effect of the injected solution consisting only of humic acids (causing the increase in $|\sigma|$ and ORP), but negligible NGP concentrations. On the one hand, the lack of changes in the σ_f seems to challenge such interpretation. On the other hand, well AW6-34 is fully screened between 6 and 8 m depth, which might induce the mixing of groundwater from different depths and distances during the sampling. Hence, the discrepancy observed between $|\sigma|$ and σ_f might be related to mixed water samples, which may also bias other geochemical parameters such as Fe_{tot} .

4 CONCLUSIONS

We presented the first field-scale application of the CCI method to monitor subsurface processes accompanying the injection of nanoparticles, in particular NGP. Our imaging results permitted to identify clogging of the pore space, that is, a decrease of hydraulic conductivity at the injection point. The continuous injection resulted in the unintended development of preferential flow paths and the delivery of NGP in areas away of the target, leading to an overall decrease in the efficiency of the remediation technique.

Spatial variations in the electrical conductivity $|\sigma|$ for baseline images revealed a good correlation with the lithological units. The IP effect, a measure of the capacitive properties, revealed only a weak response, which can be explained by the occurrence of the contaminant in free-phase (displacing groundwater) and the high fluid conductivity of groundwater; the latter possibly being a result of the release of carbonic acids as metabolic products of hydrocarbon-degrading organisms, a well-documented process in mature plumes.

CCI monitoring results revealed four consecutive steps in the electrical signatures governed by the delivery and transport of NGP suspension, namely: (i) an increase in the electrical conductivity ($|\sigma|$) associated to the subsurface enrichment of the NGP solution, characterized by a fluid conductivity 26 per cent higher than that of groundwater; (ii) a sudden drop in $|\sigma|$, likely associated to pore clogging and permeability loss; which is followed by (iii) an increase in $|\sigma|$, accompanying daylighting events, likely indicating the occurrence of fracturing and the development of secondary porosity and (iv) an important decrease of ~14 per cent below baseline values in $|\sigma|$ during the overnight brake, which can be explained by clogging due to changes in the surface properties of injected NGP. Our study demonstrates that geophysical monitoring data—if incorporated into the design of NP injections—offers unique possibilities to improve the efficiency of groundwater remediation measures. On the one hand, CCI results for background data demonstrate that pre-injection information could be used in the design of the injection strategy (e.g. to avoid injection to low hydraulic conductive areas). On the other hand, monitoring results can be used to gain information in quasi real-time to assess clogging of the pore space; thus, permitting re-locating the NP injection and a more effective delivery of particles. Although CCI monitoring provides information with enhanced spatial and temporal resolution, the complete advantages of the method cannot be fully exploited without additional geochemical information for the quantitative interpretation of the results. Hence, we suggest that the geochemical sampling should be performed taking into account real-time CCI results.

ACKNOWLEDGEMENTS

This material is partially based upon work supported by the Austrian Federal Ministry of Education, Science and Research (BMBWF) through the POTHAL project (Development of geophysical exploration methods for the characterization of mine-tailings towards exploitation). The NanoRem project has received funding from the European Union's Seventh Framework Programme for research, technological development and demonstration under grant agreement no 309517. The authors would like to thank AQUATEST a.s., CZ, for providing the information about the investigated site, as well as the geochemical data prior to the NGP injection. The authors like to thank Doris Schmid for fieldwork and analysis of geochemical data.

REFERENCES

- Abdel Aal, G., Atekwana, E.A. & Werkema, D.D., Jr, 2017. Complex conductivity response to silver nanoparticles in partially saturated sand columns, *J. appl. Geophys.*, **137**, 73–81.
- Abdel Aal, G.Z., Atekwana, E.A. & Revil, A., 2014. Geophysical signatures of disseminated iron minerals: a proxy for understanding subsurface biogeochemical processes, *J. geophys. Res.*, **119**(9), 1831–1849.
- Abdel Aal, G.Z., Atekwana, E.A., Slater, L.D. & Atekwana, E.A., 2004. Effects of microbial processes on electrolytic and interfacial electrical properties of unconsolidated sediments, *Geophys. Res. Lett.*, **31**(12).
- Abdel Aal, G.Z., Slater, L.D. & Atekwana, E.A., 2006. Induced-polarization measurements on unconsolidated sediments from a site of active hydrocarbon biodegradation: Geophysics, **71**(2), H13–H24.
- Adeleye, A.S., Conway, J.R., Garner, K., Huang, Y., Su, Y. & Keller, A.A., 2016. Engineered nanomaterials for water treatment and remediation: costs, benefits, and applicability, *Chem. Eng. J.*, **286**, 640–662.
- Atekwana, E.A. & Atekwana, E.A., 2010. Geophysical signatures of microbial activity at hydrocarbon contaminated sites: a review, *Surv. Geophys.*, **31**, 247–283.
- Bardos, P., Merly, C., Kvapil, P. & Koschitzky, H.P., 2018. Status of nanoremediation and its potential for future deployment: risk-benefit and benchmarking appraisals, *Remediation J.*, **28**(3), 43–56.
- Bhattacharjee, S. & Ghoshal, S., 2018. Optimal design of sulfidated nanoscale zerovalent iron for enhanced trichloroethene degradation, *Environ. Sci. Technol.*, **52**(19), 11 078–11 086.
- Bianco, C., Higuaita, J.E.P., Tosco, T., Tiraferri, A. & Sethi, R., 2017. Controlled deposition of particles in porous media for effective aquifer nanoremediation, *Sci. Rep.*, **7**(1), 12992.
- Binley, A., Keery, J., Slater, L., Barrash, W. & Cardiff, M., 2016. The hydrogeologic information in cross-borehole complex conductivity data from an unconsolidated conglomeratic sedimentary aquifer: Cross-borehole complex conductivity, *Geophysics*, **81**(6), E409–E421.
- Binley, A. & Kemna, A., 2005. DC resistivity and induced polarization methods, in *Hydrogeophysics*, pp. 129–156, eds Rubin, Y. & Hubbard, S.S., Springer, Dordrecht.
- Bosch, J., Heister, K., Hofmann, T. & Meckenstock, R.U., 2010. Nanosized iron oxide colloids strongly enhance microbial iron reduction, *Appl. Environ. Microbiol.*, **76**(1), 184–189.
- Braunschweig, J., Bosch, J. & Meckenstock, R.U., 2013. Iron oxide nanoparticles in geomicrobiology: from biogeochemistry to bioremediation, *New Biotechnol.*, **30**(6), 793–802.
- Bücker, M., Flores Orozco, A., Hördt, A. & Kemna, A., 2017. An analytical membrane-polarization model to predict the complex conductivity signature of immiscible liquid hydrocarbon contaminants, *Near Surf. Geophys.*, **15**(6), 547–562.
- Bücker, M., Flores Orozco, A. & Kemna, A., 2018. Electro-chemical polarization around metallic particles—Part 1: the role of diffuse-layer and volume-diffusion relaxation, *Geophysics*, **83**(4), 1–53.
- Bücker, M. & Hördt, A., 2013. Long and short narrow pore models for membrane polarization, *Geophysics*, **78**(6), E299–E314.

- Cassiani, G., Kemna, A., Villa, A. & Zimmermann, E., 2009. Spectral induced polarization for the characterization of free-phase hydrocarbon contamination of sediments with low clay content, *Near Surf. Geophys.*, **7**, 547–562.
- Cassiani, G. et al., 2014. Non-invasive characterization of the Trecate (Italy) crude-oil contaminated site: links between contamination and geophysical signals: Environmental Science and Pollution Research, Special Issue on “New approaches for low-invasive contaminated site characterization, monitoring and modelling”, *Environ. Sci. Pollut. Res.*, **21**, 8914–8931.
- Cassidy, D.P., Werkema Jr, D.D., Sauck, W., Atekwana, E., Rossbach, S. & Duris, J., 2001. The effects of LNAPL biodegradation products on electrical conductivity measurements, *Journal of Environmental and Engineering Geophysics*, **6**(1), 47–52.
- Caterina, D., Flores Orozco, A. & Nguyen, F., 2017. Long-term ERT monitoring of biogeochemical changes of an aged hydrocarbon contamination, *J. Contam. Hydrol.*, **201**, 19–29.
- Chen, C.F., Binh, N.T., Chen, C.W. & Dong, C.D., 2015. Removal of polycyclic aromatic hydrocarbons from sediments using sodium persulfate activated by temperature and nanoscale zero-valent iron, *J. Air Waste Manage. Assoc.*, **65**(4), 375–383.
- Chen, J., Hubbard, S.S., Williams, K.H., Flores Orozco, A. & Kemna, A., 2012. Estimating the spatiotemporal distribution of geochemical parameters associated with biostimulation using spectral induced polarization data and hierarchical Bayesian models, *Water Resour. Res.*, **48**(5), doi:10.1029/2011WR010992.
- Cornell, R.M. & Schwertmann, U., 2003. *The Iron Oxides: Structure, Properties, Reactions, Occurrences and Uses*, John Wiley & Sons, Hoboken, NJ.
- Dahlin, T. & Zhou, B., 2006. Multiple-gradient array measurements for multichannel 2D resistivity imaging: near surface geophysics, **4**(2), 113–123.
- Deceuster, J. & Kaufmann, O., 2012. Improving the delineation of hydrocarbon impacted soils and water through induced polarization (IP) tomographies: a field study at an industrial waste land, *J. Contam. Hydrol.*, **136**, 25–42.
- Deng, Y., Shi, X., Revil, A., Wu, J. & Ghorbani, A., 2018. Complex conductivity of oil-contaminated clayey soils, *J. Hydrol.*, **561**, 930–942.
- Estella, A., Atekwana & Lee, D. Slater, 2009. Biogeophysics: A new frontier in Earth science research, *Reviews of Geophysics*, **47**(4), 30.
- Fixman, M., 1980. Charged macromolecules in external fields. I. The sphere, *J. Chem. Phys.*, **72**(9), 5177–5186.
- Flores Orozco, A., Bückner, M., Steiner, M. & Malet, J.P., 2018a. Complex-conductivity imaging for the understanding of landslide architecture, *Eng. Geol.*, **243**, 241–252.
- Flores Orozco, A., Gallistl, J., Bückner, M. & Williams, K.H., 2018b. Decay curve analysis for data error quantification in time-domain induced polarization imaging, *Geophysics*, **83**(2), E75–E86.
- Flores Orozco, A., Kemna, A., Binley, A. & Cassiani, G., 2019. Analysis of time-lapse data error in complex conductivity imaging to alleviate anthropogenic noise for site characterization, *Geophysics*, **84**(2), B181–B193.
- Flores Orozco, A., Kemna, A., Oberdörster, C., Zschornack, L., Leven, C., Dietrich, P. & Weiss, H., 2012a. Delineation of subsurface hydrocarbon contamination at a former hydrogenation plant using spectral induced polarization imaging, *J. Contam. Hydrol.*, **136**, 131–144.
- Flores Orozco, A., Kemna, A. & Zimmermann, E., 2012b. Data error quantification in spectral induced polarization imaging, *Geophysics*, **77**(3), E227–E237.
- Flores Orozco, A., Velimirovic, M., Tosco, T., Kemna, A., Sapion, H., Klaas, N., Sethi, R. & Bastiaens, L., 2015. Monitoring the injection of microscale zerovalent iron particles for groundwater remediation by means of complex electrical conductivity imaging, *Environ. Sci. Technol.*, **49**(9), 5593–5600.
- Flores Orozco, A., Williams, K.H. & Kemna, A., 2013. Time-lapse spectral induced polarization imaging of stimulated uranium bioremediation, *Near Surf. Geophys.*, **11**(5), 531–544.
- Flores Orozco, A., Williams, K.H., Long, P.E., Hubbard, S.S. & Kemna, A., 2011. Using complex resistivity imaging to infer biogeochemical processes associated with bioremediation of a uranium-contaminated aquifer, *J. geophys. Res.*, **116**, G03001, doi:10.1029/2010JG001591.
- Gallistl, J., Weigand, M., Stumvoll, M., Ottowitz, D., Glade, T. & Flores Orozco, A., 2018. Delineation of subsurface variability in clay-rich landslides through spectral induced polarization imaging and electromagnetic methods, *Eng. Geol.*, **245**, 292–308.
- Grieger, K.D., Fjordbøge, A., Hartmann, N.B., Eriksson, E., Bjerg, P.L. & Baun, A., 2010. Environmental benefits and risks of zero-valent iron nanoparticles (nZVI) for in situ remediation: risk mitigation or trade-off? *J. Contam. Hydrol.*, **118**(3–4), 165–183.
- Hallof, P.G., 1974. The IP phase measurement and inductive coupling, *Geophysics*, **39**(5), 650–665.
- Heenan, J. et al., 2014. Electrical resistivity imaging for long-term autonomous monitoring of hydrocarbon degradation: Lessons from the Deepwater Horizon oil spill, *Geophysics*, **80**(1), B1–B11.
- Hosseini, S.M. & Tosco, T., 2015. Integrating NZVI and carbon substrates in a non-pumping reactive wells array for the remediation of a nitrate contaminated aquifer, *J. Contam. Hydrol.*, **179**, 182–195.
- Hua, M., Zhang, S., Pan, B., Zhang, W., Lv, L. & Zhang, Q., 2012. Heavy metal removal from water/wastewater by nanosized metal oxides: a review, *J. Hazard. Mater.*, **211**, 317–331.
- Huisman, J.A., Moradi, S., Zimmermann, E., Bosch, J. & Vereecken, H., 2014. Spectral induced polarization of goethite nanoparticles, i AGU Fall Meeting Abstracts 2014, San-Francisco.
- Huling, S.G., Pivetz, B. & Stransky, R., 2002. Terminal electron acceptor mass balance: light nonaqueous phase liquids and natural attenuation, *J. Environ. Eng.*, **128**, 246–252.
- Hördt, A., Bairlein, K., Bielefeld, A., Bückner, M., Kuhn, E., Nordsiek, S. & Stebner, H., 2016. The dependence of induced polarization on fluid salinity and pH, studied with an extended model of membrane polarization, *J. appl. Geophys.*, **135**, 408–417.
- Hördt, A., Bairlein, K., Bückner, M. & Stebner, H., 2017. Geometrical constraints for membrane polarization, *Near Surf. Geophys.*, **15**(6), 579–592.
- Johansson, S., Fiandaca, G. & Dahlin, T., 2015. Influence of non-aqueous phase liquid configuration on induced polarization parameters: Conceptual models applied to a time-domain field case study, *J. appl. Geophys.*, **123**, 295–309.
- Joyce, R.A., Glaser, D.R., II, Werkema, D.D., Jr & Atekwana, E.A., 2012. Spectral induced polarization response to nanoparticles in a saturated sand matrix, *J. appl. Geophys.*, **77**, 63–71.
- Karn, B., Kuiken, T. & Otto, M., 2009. Nanotechnology and in situ remediation: a review of the benefits and potential risks, *Environ. Health Perspect.*, **117**(12), 1813, doi:10.1289/ehp.0900793.
- Kemna, A., 2000. *Tomographic Inversion of Complex Resistivity: Theory and Application*, Der Andere Verlag, Osnabrück.
- Kemna, A. et al., 2012. An overview of the spectral induced polarization method for near-surface applications, *Near Surf. Geophys.*, **10**(6), 453–468.
- Lei, C., Sun, Y., Tsang, D.C. & Lin, D., 2018. Environmental transformations and ecological effects of iron-based nanoparticles, *Environ. Pollut.*, **232**, 10–30.
- Leroy, P., Revil, A., Kemna, A., Cosenza, P. & Ghorbani, A., 2008. Complex conductivity of water-saturated packs of glass beads, *Journal of Colloid and Interface Science*, **321**(1), 103–117.
- Lesparre, N., Nguyen, F., Kemna, A., Robert, T., Hermans, T., Daoudi, M. & Flores Orozco, A., 2017. A new approach for time-lapse data weighting in ERT, *Geophysics*, **82**(6), 325–E333.
- Luna, M. et al., 2015. Pressure-controlled injection of guar gum stabilized microscale zerovalent iron for groundwater remediation, *J. Contam. Hydrol.*, **181**, 46–58.
- Maineult, A., Jougnot, D. & Revil, A., 2018. Variations of petrophysical properties and spectral induced polarization in response to drainage and imbibition: a study on a correlated random tube network, *Geophys. J. Int.*, **212**(2), 1398–1411.
- Marshall, D.J. & Madden, T.R., 1959. Induced polarization, a study of its causes, *Geophysics*, **24**(4), 790–816.

- Meckenstock, R.U. & Bosch, J., 2014. Method for the degradation of pollutants in water and/or soil, United States patent.
- Mellage, A., Holmes, A.B., Linley, S., Vallée, L., Rezanezhad, F., Thomson, N., Gu, F.X. & Van Cappellen, P., 2018. Sensing coated iron-oxide nanoparticles with spectral induced polarization (SIP): experiments in natural sand packed flow-through columns, *Environ. Sci. Technol.*, **52**, 14 256–14 265.
- Misra, S., Torres-Verdín, C., Revil, A., Rasmus, J. & Homan, D., 2016. Interfacial polarization of disseminated conductive minerals in absence of redox-active species. Part 1: mechanistic model and validation, *Geophysics*, **81**(2), E139–E157.
- Mueller, N.C., Braun, J., Bruns, J., Cerník, M., Rissing, P., Rickerby, D. & Nowack, B., 2012. Application of nanoscale zero valent iron (NZVI) for groundwater remediation in Europe, *Environ. Sci. Pollut. Res.*, **19**(2), 550–558.
- NanoRem Bulletin 8- NanoRem Pilot Site – Spolchemie II, Czech Republic: Remediation of BTEX Compounds Using Nano-Goethite. Available at: www.nanorem.eu, Access 12 June 2019.
- Nathanail, C.P., Gillett, A., McCaffrey, C., Nathanail, J. & Ogden, R., 2016. A preliminary risk assessment protocol for renegade nanoparticles deployed during nanoremediation, *Remediation J.*, **26**(3), 95–108.
- Ntarlagiannis, D., Ustra, A., Kessouri, P. & Flores Orozco, A., 2018. The untapped potential of the induced polarization method: characterization and monitoring of hydrocarbon contamination in soils, *FastTIMES*, **23**(4), 64–75.
- Okay, G., Cosenza, P., Ghorbani, A., Camerlynck, C., Cabrera, J., Florsch, N. & Revil, A., 2013. Characterization of macroscopic heterogeneities in clay-rocks using induced polarization: Field tests at the experimental underground research laboratory of Tournemire (Aveyron, France), *Geophys. Prospect.*, **61**, 134–152.
- Olhoeft, G.R., 1982. Warburg impedances at single water-mineral interfaces, in *SEG Technical Program Expanded Abstracts 1982*, pp. 516–518, Society of Exploration Geophysicists, Tulsa, OK.
- Olhoeft, G.R., 1985. Low-frequency electrical-properties, *Geophysics*, **50**, 2492–2503.
- Patil, S.S., Shedbalkar, U.U., Truskewycz, A., Chopade, B.A. & Ball, A.S., 2016. Nanoparticles for environmental clean-up: a review of potential risks and emerging solutions, *Environ. Technol. Innov.*, **5**, 10–21.
- Pelton, W.H., Ward, S.H., Hallof, P.G., Sill, W.R. & Nelson, P.H., 1978. Mineral discrimination and removal of inductive coupling with multifrequency IP, *Geophysics*, **43**, 588–609.
- Revil, A., Abdel Aal, G.Z., Atekwana, A., Mao, D. & Florsch, N., 2015. Induced polarization response of porous media with metallic particles — Part 2. Comparison with a broad database of experimental data, *Geophysics*, **80**(5), D539–D552.
- Revil, A., Atekwana, E., Zhang, C., Jardani, A. & Smith, S., 2012. A new model for the spectral induced polarization signature of bacterial growth in porous media, *Water Resour. Res.*, **48**, W09545, doi:10.1029/2012WR011965.
- Revil, A. & Florsch, N., 2010. Determination of permeability from spectral induced polarization data in granular media, *Geophys. J. Int.*, **181**, 1480–1498.
- Revil, A., Schmutz, M. & Batzle, M.L., 2011. Influence of oil wettability upon spectral induced polarization of oil-bearing sands, *Geophysics*, **76**(5), A31–A36.
- Revil, A. & Skold, M., 2011. Salinity dependence of spectral induced polarization in sands and sandstones, *Geophys. J. Int.*, **187**(2), 813–824.
- Revil, A. *et al.*, 2017. Complex conductivity of soils, *Water Resour. Res.*, **53**(8), 7121–7147.
- Saneiyani, S., Ntarlagiannis, D., Ohan, J., Lee, J., Colwell, F. & Burns, S., 2019. Induced polarization as a monitoring tool for in-situ microbial induced carbonate precipitation (MICP) processes, *Ecol. Eng.*, **127**, 36–47.
- Schirmer, M. *et al.*, 2006. Natural attenuation research at the contaminated megasite Zeitz, *J. Hydrol.*, **328**, 393–407.
- Schmid, D., Micic, V., Laumann, S. & Hofmann, T., 2015. Measuring the reactivity of commercially available zero-valent iron nanoparticles used for environmental remediation with iopromide, *J. Contam. Hydrol.*, **181**, 36–45.
- Schmutz, M., Revil, A., Vaudelet, P., Batzle, M., Femenía Viñao, P. & Werkema, D., 2010. Influence of oil saturation upon spectral induced polarization of oil bearing sands, *Geophys. J. Int.*, **183**, 211–224.
- Schurr, J.M., 1964. On the theory of the dielectric dispersion of spherical colloidal particles in electrolyte solution1, *The Journal of Physical Chemistry*, **68**(9), 2407–2413.
- Schwartz, N., Huisman, J.A. & Furman, A., 2012. The effect of NAPL on the electrical properties of unsaturated porous media, *Geophys. J. Int.*, **188**(3), 1007–1011.
- Schwarz, G., 1962. A theory of the low-frequency dielectric dispersion of colloidal particles in electrolyte solution1, 2, *J. Phys. Chem.*, **66**(12), 2636–2642.
- Shefer, I., Schwartz, N. & Furman, A., 2013. The effect of free-phase NAPL on the spectral induced polarization signature of variably saturated soil, *Water Resour. Res.*, **49**(10), 6229–6237.
- Shilov, V.N., Delgado, A.V., Gonzalez-Caballero, F. & Grosse, C., 2001. Thin double layer theory of the wide-frequency range dielectric dispersion of suspensions of non-conducting spherical particles including surface conductivity of the stagnant layer, *Colloids Surf. A*, **192**(1–3), 253–265.
- Shi, Z., Fan, D., Johnson, R.L., Tratnyek, P.G., Nurmi, J.T., Wu, Y. & Williams, K.H., 2015. Methods for characterizing the fate and effects of nano zerovalent iron during groundwater remediation, *J. Contam. Hydrol.*, **181**, 17–35.
- Shi, Z., Nurmi, J.T. & Tratnyek, P.G., 2011. Effects of nano zero-valent iron on oxidation–reduction potential, *Environ. Sci. Technol.*, **45**(4), 1586–1592.
- Slater, L., 2007. Near surface electrical characterization of hydraulic conductivity: From petrophysical properties to aquifer geometries—A review, *Surv. Geophys.*, **28**(2–3), 169–197.
- Slater, L. & Binley, A., 2006. Synthetic and field-based electrical imaging of a zerovalent iron barrier: Implications for monitoring long-term barrier performance, *Geophysics*, **71**(5), B129–B137.
- Slater, L., Binley, A.M., Daily, W. & Johnson, R., 2000. Cross-hole electrical imaging of a controlled saline tracer injection, *J. appl. Geophys.*, **44**(2–3), 85–102.
- Tiraferrri, A., Hernandez, L.A.S., Bianco, C., Tosco, T. & Sethi, R., 2017. Colloidal behavior of goethite nanoparticles modified with humic acid and implications for aquifer reclamation, *J. Nanopart. Res.*, **19**(3), 107, doi:10.1007/s11051-017-3814-x.
- Tosco, T., Papini, M.P., Viggì, C.C. & Sethi, R., 2014. Nanoscale zerovalent iron particles for groundwater remediation: a review, *J. Cleaner Prod.*, **77**, 10–21.
- Tosco, T. & Sethi, R., 2010. Transport of non-Newtonian suspensions of highly concentrated micro-and nanoscale iron particles in porous media: a modeling approach, *Environ. Sci. Technol.*, **44**(23), 9062–9068.
- Trujillo-Reyes, J., Peralta-Videa, J.R. & Gardea-Torresdey, J.L., 2014. Supported and unsupported nanomaterials for water and soil remediation: are they a useful solution for worldwide pollution? *J. Hazard. Mater.*, **280**, 487–503.
- Ustra, A., Slater, L., Ntarlagiannis, D. & Elis, V., 2012. Spectral induced polarization (SIP) signatures of clayey soils containing toluene, *Near Surf. Geophys.*, **10**(6), 503–515.
- Vecchia, E.D., Luna, M. & Sethi, R., 2009. Transport in porous media of highly concentrated iron micro-and nanoparticles in the presence of xanthan gum, *Environ. Sci. Technol.*, **43**(23), 8942–8947.
- Velimirovic, M. *et al.*, 2014. Field assessment of guar gum stabilized microscale zerovalent iron particles for in-situ remediation of 1, 1, 1-trichloroethane, *J. Contam. Hydrol.*, **164**, 88–99.
- Ward, S.H., 1990. Resistivity and induced polarization methods, *Geotech. Environ. Geophys.*, **1**, 147–189.
- Waxman, M.H. & Smits, L.J.M., 1968. Electrical conductivities in oil-bearing shaly sands, *Society of Petroleum Engineers Journal*, **8**(2), 107–122.
- Weigand, M., Flores Orozco, A. & Kemna, A., 2017. Reconstruction quality of SIP parameters in multi-frequency complex resistivity imaging, *Near Surface Geophysics*, **15**(2), pp. 187–199.

- Weller, A., Zhang, Z. & Slater, L., 2015. High-salinity polarization of sandstones, *Geophysics*, **80**(3), D309–D318.
- Williams, K.H. *et al.*, 2009. Geophysical monitoring of coupled microbial and geochemical processes during stimulated subsurface bioremediation, *Environ. Sci. Technol.*, **43**, 6717–6723.
- Wong, J., 1979. An electrochemical model of the induced-polarization phenomenon in disseminated sulfide ores, *Geophysics*, **44**, 1245–1265.
- Xu, P. *et al.*, 2012. Use of iron oxide nanomaterials in wastewater treatment: a review, *Sci. Total Environ.*, **424**, 1–10.

5 SUPPORTING INFORMATION

Supplementary data are available at [GJI](#) online.

Appendix A.docx

Please note: Oxford University Press is not responsible for the content or functionality of any supporting materials supplied by the authors. Any queries (other than missing material) should be directed to the corresponding author for the paper.

5. Conclusions

This work has proven the possibility to delineate in-situ and non-invasively biogeochemical active zones in natural geological media and contaminated sites by means of the Spectral Induced Polarization (SIP) imaging method. This work has focused on the evaluation of field signatures, with a particular interest on the investigation of extensive areas towards establishing the method as a standard technique for environmental studies as well as for applications beyond the academia. To achieve such purpose, this work conducted SIP investigations in different geological environments, ranging from clay-rich landslides, alluvial sediments, to landfills and hydrocarbon impacted-soils in industrial areas.

As stressed within the studies presented here, an adequate quantification of data-uncertainty and the inversion of the data to its respective error level permit to solve for imaging results with enhanced resolution and to minimize the risk of creating artifacts due to over-fitting within the inversion (e.g., Flores Orozco et al., 2018a; 2019a). Therefore, this work proposes two methodologies for the processing of SIP imaging datasets: (a) quasi real-time analysis of data uncertainty based on the spatial consistency of the readings within the imaging dataset for static measurements (the decay-curve analysis proposed in Flores Orozco et al. 2018a); and (b) the analysis of reciprocity in time-lapse differences for error-quantification in monitoring measurements (Flores Orozco et al., 2019a). Following these methodologies it was possible to solve for images of the complex conductivity revealing structures consistent with the expected lithological units, as well as the identification of structures in the subsurface not resolved through borehole data. In particular, imaging results permitted the identification of paleo-channels at the Trecate, Rifle and Shiprock Rifle sites (Flores Orozco et al., 2019a; 2018a; Wainwright and Flores Orozco et al., 2016), and to improve the geometrical delineation of the sliding plane at La Valette landslide (Flores Orozco et al., 2018b).

In case of IP investigations at the flood-plain scale presented in Chapter 2, IP measurements permitted to delineate anomalies correlated with the presence of naturally reduced minerals in biogeochemical hot-spots. In such hot-spots, organic-rich subsurface sediments stimulate the enzymatic reduction of ferric minerals by iron-reducing bacteria, resulting in the accumulation of aqueous iron (FeII), which in presence of aqueous sulfide results in the precipitation of iron sulfides (FeS). Iron sulfides are related to a measurable increase in the polarization response (e.g., Flores Orozco et al., 2018a; Wanwright and Flores Orozco et al., 2016), which is stressed in the images of the phase (ϕ). The interpretation of ϕ anomalies as biogeochemical hot-spots was validated through extensive borehole data available at the Rifle site, which confirmed the presence of reduced sediments (i.e., iron sulfides).

Taking into account that different soil parameters such as saturation, porosity, pH, salinity, and temperature affect both the conductivity (σ') and the capacitive (σ'') electrical properties, imaging results of the ϕ permits a better visualization of the polarizable anomalies, considering that it represents the ratio of the polarization-to-conductivity (i.e., $\phi \approx \sigma'' / \sigma'$), as mentioned in Chapter 1. Hence, ϕ offers the best parameter to identify areas where polarization dominates over conductivity, for instance resulting from the accumulation of iron sulfides in biogeochemical hot-spots (Flores Orozco et al., 2018a; Wainwright and Flores Orozco et al., 2016). The superior ability of the ϕ over σ'' images to highlight dominating polarizable anomalies for the discrimination of biogeochemical active zones was also proven in measurements conducted in municipal solid waste landfills presented in Chapter 6.2 (Flores Orozco et al., submitted to Journal of Waste Management).

For an adequate interpretation of the IP imaging results, it is critical to properly understand the interplay between the different subsurface conduction mechanisms, as discussed in Chapter 3, high σ' and a σ'' values can be observed for measurements conducted at completely different geological conditions, such as clay-rich landslides and hydrocarbon-impacted sites, even if both

conditions should favor the polarization response due to the high surface charge of clay (in the former one), or the biogeochemical degradation of contaminants (for the latter one). Such intriguing responses highlight the interplay between electrolytic (σ_w) and surface conduction (σ_s^*), as well as the contribution of the latter to both conduction (σ_s') and polarization (σ_s''). In case of clay-rich materials, such as for measurements at La Valette landslide, σ_s' plays a dominating role, resulting in highly conductive anomalies, even if the sediments are poorly saturated (Flores Orozco et al., 2018b). However, the contribution of σ_s' is commonly ignored in landslide investigations, with changes in the electrical conductivity commonly explained only due to variations in saturation. Electrical imaging of mature hydrocarbon-contaminated sites represent the opposite case, where the electrolytic conduction (σ_w) dominates over σ_s' and σ_s'' . Here, the activity of hydrocarbon-degrading bacteria is stimulated resulting in the release of metabolic products such as carbonic acids, increasing the salinity in pore-water and the fluid conductivity. By increasing the electrical conductivity of pore water, electrolytic conduction (σ_w) dominates over surface conduction and contributes to the reduction in polarization response (i.e., σ''), as observed in Flores Orozco et al. (2015; 2019a; 2019b).

Moreover, field investigations presented here reveal variations in the polarization response associated to the characteristics of the oil, in agreement with laboratory investigations. In case of the measurements conducted at the Trecate and Spolchemie II sites, where non-polar compounds are present, we observed a decrease in the polarization response with increasing the hydrocarbon concentration, which is explained by the formation of a continuous water film surrounding mineral grains once that the hydrocarbon fills both the micro- and macro-pores (Flores Orozco et al., 2019a; 2019b). Whereas in case of polar compounds (e.g., TCE), for instance for measurements at the Aarschot site (Flores Orozco et al., 2015), the high polarization response is explained by modifications of the electrical double layer (EDL) due to the adsorption of the hydrocarbon into the grain surface. This interpretation is validated by the

extension of the analytical model for membrane polarization mechanism that predicts the IP response for both polar or non-polar hydrocarbons presented in Chapter 6.3 (Bücker and Flores Orozco et al., 2017).

Chapter 4 presented the first real-time monitoring of nano- and micro-sized particles at the field-scale in an imaging framework. Here IP imaging was performed to monitor fast processes accompanying the injection of particles along two different experiments conducted at full field-scale: (a) injection of micro-scale guar-guar coated zero-valent iron (GG-mZVI) for the remediation of TCE; and (b) the injection of Nano-Goethite Particles (NGP) for the remediation of toluene. While zero-valent iron is an electric semi-conductor, commonly related to high polarization response, goethite is an iron oxide, commonly related to low electrical conductive values and negligible polarization. For both experiments, the variations in the electrical images for data collected before, during and after subsurface amendment permitted to obtain monitoring data with enhanced higher temporal resolution than conventional geochemical monitoring, and yet covering an extended area of investigation. In particular, IP monitoring permitted to identify deviations in the trajectory of the injected particles away from the target area due to fracking. Here, the accumulation of particles at the injection point resulted in clogging of the pore-space (Flores Orozco et al., 2019b), followed by fracking and the transport of the particles back to the surface through the developed fractures (Flores Orozco et al., 2015; 2019b). Analysis of shallow samples and daylighting observed during the injection confirmed the interpretation of the IP images.

Furthermore, for the injection of GG-mZVI particles presented in Chapter 4, IP monitoring results revealed two different electrical responses, permitting to demonstrate the ability of the method to distinguish between coated and bare particles, as illustrated in Figure 5.1. In the former case, the coating adsorbed to the particle surface hinders electrode polarization; thus the observed decrease in σ'' and ϕ following the injection is related to contribution to the σ'_s from

the injected particles, which also explains the results observed in case of NGP injections. Once the coating is degraded, bare particles results in an increase in the polarization response (observed in both σ'' and ϕ) due to electrode polarization mechanisms, as illustrated in Figure 5.1. To validate the interpretation of the polarization effect observed along the monitoring of particles injections, Chapter 6.4, and 6.5 present the full analytical solution for the electrode polarization mechanism for both uncharged and charged particles. Whereas Chapter 6.6 discusses the polarization of the Stern- and Diffuse-layer in porous media, which validates the interpretation of the non-metallic particles (i.e., NGP).

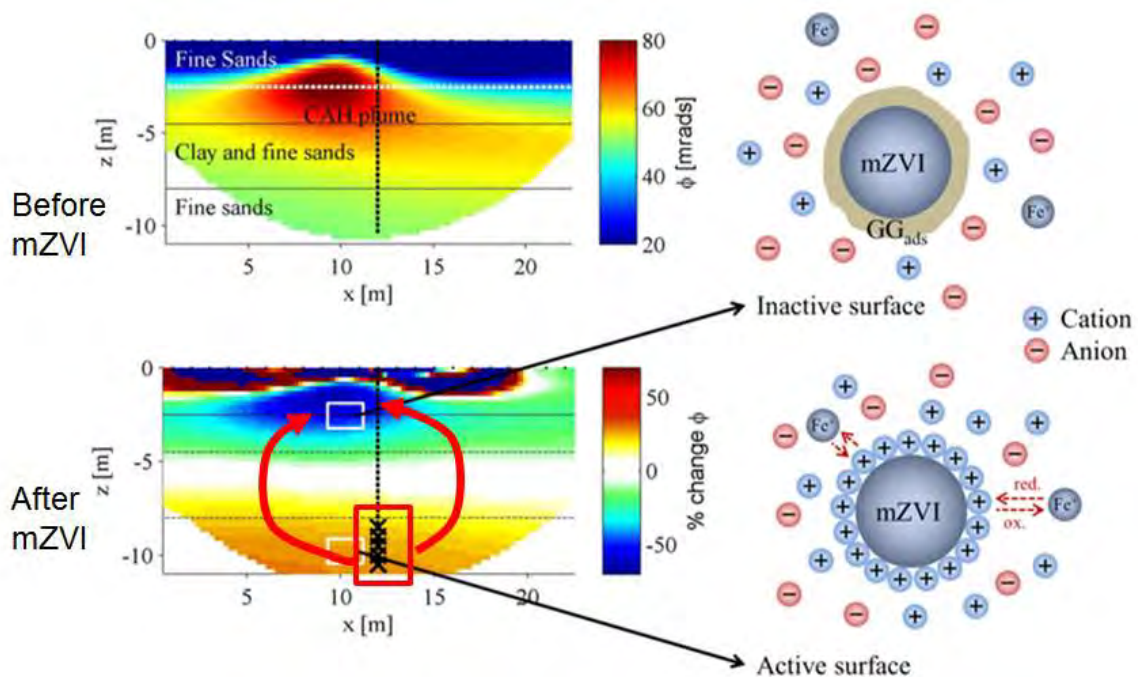


Figure 5.1: IP response before (top left) and after (bottom left) the injection of guar-gum coated micro zero-valent iron (GG-mZVI) particles for the remediation of a (CAH) contaminant plume. Spatial variations in the IP response are related to the accumulation of: bare particles at the injection points (between 8 and 10 m depth - indicated by “x” symbols), and coated GG-mZVI off-target in the unsaturated zone, delivered through fractures during the injection (indicated by the red arrows). The position of the electrodes and the injection well are indicated by the black dots and the vertical dashed line, respectively, whereas the dashed horizontal lines represent lithological contacts (black) and the groundwater table (white). Figure modified from Flores Orozco et al. (2015)

References

- Abdel Aal, G. Z., Atekwana, E. A., and Revil, R., 2014, Geophysical signatures of disseminated iron minerals: A proxy for understanding subsurface biophysicochemical processes. *Journal of Geophysical Research. Biogeosciences*, 119, 1831-1849.
- Abdel Aal, G. Z., Atekwana, E.A., Slater, L.D. and Atekwana, E.A., 2004, Effects of microbial processes on electrolytic and interfacial electrical properties of unconsolidated sediments. *Geophysical Research Letters*, 31(12).
- Abdel Aal, G., Atekwana, E. A., Werkema Jr, D. D., 2017, Complex conductivity response to silver nanoparticles in partially saturated sand columns. *J. of Applied Geophysics*, 137, 73-81.
- Abdel Aal, G. Z., Slater, L.D., and Atekwana, E.A., 2006, Induced-polarization measurements on unconsolidated sediments from a site of active hydrocarbon biodegradation. *Geophysics*, 71(2), H13-H24.
- Achal, V., Mukherjee, A., Kumari, D. and Zhang, Q., 2015, Biomineralization for sustainable construction—A review of processes and applications. *Earth-science reviews*, 148, 1-17.
- Adams, G.O., Fufeyin, P.T., Okoro, S.E. and Ehinomen, I., 2015, Bioremediation, biostimulation and bioaugmentation: a review. *International Journal of Environmental Bioremediation & Biodegradation*, 3(1), 28-39.
- Adeleye, A.S., Conway, J.R., Garner, K., Huang, Y., Su, Y., Keller, A.A., 2016, Engineered nanomaterials for water treatment and remediation: Costs, benefits, and applicability. *Chemical Engineering Journal*, 286, 640-662.
- Anderson, T., Groffman, P., and Walter, M., 2015, Using a soil topographic index to distribute denitrification fluxes across a northeastern headwater catchment, *J. Hydrol.*, 522, 123–134
- Archie, G. E., 1942, The electrical resistivity log as an aid in determining some reservoir characteristics. *Transactions of the AIME*, 146(1), 54-62.
- Arora, B., Dwivedi, D., Spycher, N. F., and Steefel, C. I., 2015b, Modeling processes affecting carbon dynamics at a biogeochemical hotspot in a floodplain aquifer, in *Proceedings of the TOUGH Symposium 2015*, pp. 456–463, Lawrence Berkeley National Laboratory, Berkeley, Calif.
- Arora, B., Spycher, N.F., Steefel, C.I., Molins, S., Bill, M., Conrad, M.E., Dong, W., Faybishenko, B., Tokunaga, T.K., Wan, J. and Williams, K.H., 2016, Influence of hydrological, biogeochemical and temperature transients on subsurface carbon fluxes in a flood plain environment. *Biogeochemistry*, 127(2-3), 367-396.
- Atekwana, E. A., and Abdel Aal, G.Z., 2015, Iron biomineralization controls on geophysical signatures of hydrocarbon contaminated sediments. *Journal of Earth Science*, 26, 835-843.
- Atekwana, E. A., and Atekwana, E. A., 2010, Geophysical signatures of microbial activity at hydrocarbon contaminated sites: a review: *Survey Geophysics*, 31, 247–283.
- Atekwana, E.A., Atekwana, E.A., Werkema, E. A., Allen, P. J., Smart, L. A., Duris, J.W., Cassidy, D.P., Sauck, W.A., and Rossbach, S., 2004, Evidence for microbial enhanced electrical conductivity in hydrocarbon-contaminated sediments. *Geophysical Research Letters*, 31, L23501.

- Atekwana E.A., and Slater, L. D., 2009, Biogeophysics: A new frontier in Earth science research. *Reviews of Geophysics* 47, RG4004.
- Atkins, P., and De Paula, J., 2010, *Elements of physical chemistry*: Oxford University Press.
- Aufdenkampe, A. K., Mayorga, E., Raymond, P. A., Melack, J. M., Doney, S. C., Alin, S. R., and Yoo, K., 2011, Riverine coupling of biogeochemical cycles between land, oceans, and atmosphere. *Frontiers Ecol. Environ.*, 9(1), 53–60.
- Auken, E., Pellerin, L., Christensen, N.B. and Sørensen, K., 2006, A survey of current trends in near-surface electrical and electromagnetic methods. *Geophysics*, 71(5), G249-G260
- Bardgett, R.D., Wardle, D.A. and Yeates, G.W., 1998, Linking above-ground and below-ground interactions: how plant responses to foliar herbivory influence soil organisms. *Soil Biology and Biochemistry*, 30(14), 1867-1878.
- Bardos, P., Merly, C., Kvapil, P. and Koschitzky, H.P., 2018, Status of nanoremediation and its potential for future deployment: Risk-benefit and benchmarking appraisals. *Remediation Journal*, 28(3), 43-56.
- Barlaz, M.A., Ham, R.K., and Schaefer, D.M., 1990, Methane production from municipal refuse: A review of enhancement techniques and microbial dynamics. *Critical Reviews in Environmental Control*, 19(6), 557-584.
- Battin, T. J., Kaplan, L. A., Findlay, S., Hopkinson, C. S., Marti, E., Packman, A. I., Newbold, J. D., and Sabate F., 2008, Biophysical controls on organic carbon fluxes in fluvial networks, *Nat. Geosci.*, 1(2), 95–100
- Battin, T. J., Luysaert, S., Kaplan, L. A., Aufdenkampe, A. K., Richter, A., and Tranvik, L. J., 2009, The boundless carbon cycle, *Nat. Geosci.*, 2(9), 598–600
- Bhattacharjee, S., and Ghoshal, S., 2018, Optimal Design of Sulfidated Nanoscale Zerovalent Iron for Enhanced Trichloroethene Degradation. *Environmental science and technology*, 52(19), 11078-11086.
- Beaver, C. L., Williams, A. E., Atekwana, A. E., Mewafy, F. M., Abdel Aal, G. Z., Slater, L. D., and Rossbach, S., 2016, Microbial communities associated with zones of elevated magnetic susceptibility in hydrocarbon-contaminated sediments. *Geomicrobiology Journal*, 33, 441-452.
- Bianco, C., Higueta, J.E.P., Tosco, T., Tiraferri, A. Sethi, R., 2017, Controlled deposition of particles in porous media for effective aquifer nanoremediation. *Scientific reports*, 7(1), 12992.
- Binley A., Keery, J., Slater, L., Barrash, W., and Cardiff, M., 2016, The hydrogeologic information in cross-borehole complex conductivity data from an unconsolidated conglomeratic sedimentary aquifer: *Geophysics*, 81(6), E409-E421
- Binley, A., and Kemna, A., 2005, *DC resistivity and induced polarization methods: Hydrogeophysics*. Springer Netherlands. 129-156.
- Binley, A., Slater, L. D., Fukes, M., and Cassiani, G., 2005, Relationship between spectral induced polarization and hydraulic properties of saturated and unsaturated sandstone. *Water Resources Research* 41, W12417
- Binley, A., Hubbard, S. S., Huisman, J. A., Revil, A., Robinson, D. A., Singha, K., and Slater, L. D., 2015, The emergence of hydrogeophysics for improved understanding of subsurface processes over multiple scales. *Water Resources Research*, 51(6), 3837-3866.

- Binley, A., Ramirez, A., and Daily, W., 1995, Regularised image reconstruction of noisy electrical resistance tomography data: 4th Workshop of the European Concerted Action on Process Tomography, Eur. Concerted Action on Process Tomography, Bergen.
- Blaschek, R., Hördt, A., and Kemna, A. A new sensitivity-controlled focusing regularization scheme for the inversion of induced polarization data based on the minimum gradient support. *Geophysics* 2012, 73, F45-F54.
- Bosch, J., Heister, K., Hofmann, T., Meckenstock, R.U., 2010. Nanosized iron oxide colloids strongly enhance microbial iron reduction. *Applied and environmental microbiology*, 76(1), 184-189
- Bowling, J. C., Rodriguez, A. B., Harry, D. L., and Zheng, C., 2005, Delineating alluvial aquifer heterogeneity using resistivity and GPR data. *Ground Water*, 43(6), 890–903.
- Brandt, C.A., Becker, J.M., and Porta, A., 2002, Distribution of polycyclic aromatic hydrocarbons in soils and terrestrial biota after a spill of crude oil in Trecate, Italy. *Environmental Toxicology Chemistry*, 21, 1638–1643.
- Braunschweig, J., Bosch, J., and Meckenstock, R.U., 2013, Iron oxide nanoparticles in geomicrobiology: from biogeochemistry to bioremediation. *New biotechnology*, 30(6), 793-802.
- Burbery L., Cassiani, G. Andreotti, G., Ricchiuto, T., and Semple, K. T., 2004, Well test and stable isotope analysis for the determination of sulphate-reducing activity in a fast aquifer contaminated by hydrocarbons. *Environmental Pollution*, 129, 321-330.
- Börner, F. D., Schopper, J. R., and Weller, A., 1996, Evaluation of transport and storage properties in the soil and groundwater zone from induced polarization measurements. *Geophys. Prospect.*, 44, 583–601
- Bücker, M., Flores Orozco, A. Hördt, A., and Kemna, A., 2017, An analytical membrane-polarization model to predict the complex conductivity signature of immiscible liquid hydrocarbon contaminants. *Near Surface Geophysics*, 15, 547-562.
- Bücker, M., Flores Orozco, A. Kemna, A., 2018, Electro-chemical polarization around metallic particles—Part 1: The role of diffuse-layer and volume-diffusion relaxation. *Geophysics*, 83(4), 1-53.
- Bücker, M., and Hördt, A., 2013a, Analytical modelling of membrane polarization with explicit parametrization of pore radii and the electrical double layer. *Geophys. J. Int.*, 194(2), 804–813.
- Bücker, M. and Hördt, A., 2013b, Long and short narrow pore models for membrane polarization. *Geophysics*, 78(6), E299-E314
- Brückl, E., Brunner, F.K., Lang, E., Mertl, S., Müller, M. and Stary, U., 2013, The Gradenbach Observatory—monitoring deep-seated gravitational slope deformation by geodetic, hydrological, and seismological methods. *Landslides*, 10, 815–829.
- Campbell, K. M., et al., 2012, Characterizing the extent and role of natural subsurface bioreduction in a uranium-contaminated aquifer. *Appl. Geochem.*, 27, 1499–1511.
- Capps, K., Rancatti, R., Tomczyk, N., Parr, T., Calhoun, A., and Hunter, M., 2014, Biogeochemical hotspots in forested landscapes: The role of vernal pools in denitrification and organic matter processing. *Ecosystems*, 17(8), 1455–1468

Castelle, C. J., Hug, L. A., Wrighton, K. C., Thomas, B. C., Williams, K. H., Wu, D., Tringe, S. G., Singer, S. W., Eisen, J. A., and Banfield, J. F., 2013, Extraordinary phylogenetic diversity and metabolic versatility in aquifer sediment. *Nat. Commun.*, 4, 2120.

Carmichael, R.S. (Ed.), 1989. *Practical handbook of physical properties of rocks and minerals*. Band III, CRC Press, Boca Raton.

Cassiani, G., Binley, A., Kemna, A., Wehrer, M., Orozco, A.F., Deiana, R., Boaga, J., Rossi, M., Dietrich, P., Werban, U. and Zschornack, L., 2014, Noninvasive characterization of the Trecate (Italy) crude-oil contaminated site: links between contamination and geophysical signals. *Environmental Science and Pollution Research*, 21(15), 8914-8931.

Cassiani, G., Kemna, A., Villa, A. and Zimmermann, E., 2009, Spectral induced polarization for the characterization of free-phase hydrocarbon contamination of sediments with low clay content. *Near Surface Geophysics* 7, 547-562.

Cassiani G., Strobbia, C., and Gallotti, L., 2004, Vertical radar profiles for the characterization of deep vadose zones, *Vadose Zone Journal*, 3, 1093-1115.

Cassidy, D. P., Werkema Jr, D. D., Sauck, W., Atekwana, E.A., Rossbach, S., and Duris, J., 2001, The effects of LNAPL biodegradation products on electrical conductivity measurements. *Journal of Environmental and Engineering Geophysics*, 6(1), 47-52.

Caterina, D., Flores Orozco, A., and Nguyen, F., 2017, Long-term ERT monitoring of biogeochemical changes of an aged hydrocarbon contamination. *Journal of Contaminant Hydrology*, 201, 19-29.

Caterina, D., Hermans, T., and Nguyen, F., 2014, Case studies of incorporation of prior information in electrical resistivity tomography: Comparison of different approaches. *Near Surf. Geophys.*, 12(4), 451–465.

Chambers, J. E., Meldrum, P.I., Ogilvy, R. D., and Wilkinson, P.B., 2005, Characterisation of a NAPL-contaminated former quarry site using electrical impedance tomography. *Near Surface Geophysics*, 3, 79-90.

Chen, C.F., Binh, N.T., Chen, C.W., Dong, C.D., 2015, Removal of polycyclic aromatic hydrocarbons from sediments using sodium persulfate activated by temperature and nanoscale zero-valent iron. *Journal of the Air and Waste Management Association*, 65(4), 375-383.

Chen, J., and Hoversten, M., 2012, Joint inversion of marine seismic AVA and CSEM data using statistical rock-physics models and Markov random fields. *Geophysics*, 77, R65–R80

Chen, J., Hubbard, S. S., Williams, K. H., Flores Orozco, A., and Kemna, A., 2012, Estimating the spatiotemporal distribution of geochemical parameters associated with biostimulation using spectral induced polarization data and hierarchical Bayesian models. *Water Resources Research*, 48(5).

Cornell, R.M. and Schwertmann, U., 2003. *The iron oxides: structure, properties, reactions, occurrences and uses*. John Wiley & Sons.

Dafflon, B., Wu, Y., Hubbard, S. S., Birkholzer, J. T., Daley, T. M., Pugh, J. D., Peterson, J. E. and Trautz, R. C., 2012, Monitoring CO₂ intrusion and associated geochemical transformations in a shallow groundwater system using complex electrical methods. *Environmental science and technology*, 47(1), 314-321.

Dahlin, T., and Leroux, V., 2012, Improvement in time-domain induced polarization data quality with multi-electrode systems by separating current and potential cables. *Near Surface Geophysics*, 10(6), 545-565.

Dahlin, T., Leroux, V., and Nissen, J., 2002, Measuring techniques in induced polarisation imaging. *Journal of Applied Geophysics* 50.3, 279-298.

Dahlin, T. and Loke, M. H., 2015. Negative apparent chargeability in time-domain induced polarisation data. *Journal of Applied Geophysics*, 123, 322-332.

Dahlin, T., and Zhou, B., 2006, Multiple-gradient array measurements for multichannel 2D resistivity imaging. *Near Surface Geophysics*, 4(2), 113-123.

Dalla Vecchia, E., Luna, M. and Sethi, R. Transport in Porous Media of Highly Concentrated Iron Micro- and Nanoparticles in the Presence of Xanthan Gum. *Environmental Science and Technology* 2009, 43(23), 8942-8947.

Deceuster, J. and Kaufmann, O., 2012, Improving the delineation of hydrocarbon impacted soils and water through induced polarization (IP) tomographies: A field study at an industrial waste land. *Journal of Contaminant Hydrology*, 136, 25-42.

Deng Y., Shi, X., Revil, A., Wu, J., and Ghorbani, A., 2018. Complex conductivity of oil-contaminated clayey soils. *Journal of Hydrology*, 561, 930–942

Doetsch, J., Fiandaca, G., Auken, E., Christiansen, A. V., Cahill, A. G., and Jakobsen, R., 2015a, Field-scale time-domain spectral induced polarization monitoring of geochemical changes induced by injected CO₂ in a shallow aquifer. *Geophysics*, 80(2), WA113-WA126.

Doetsch, J., Ingeman-Nielsen, T., Christiansen, A.V., Fiandaca, G., Auken, E., and Elberling, B., 2015b, Direct current (DC) resistivity and induced polarization (IP) monitoring of active layer dynamics at high temporal resolution. *Cold Regions Science and Technology*, 119, 16-28.

Duncan, J.M., Groffman, P.M. and Band, L.E., 2013, Towards closing the watershed nitrogen budget: Spatial and temporal scaling of denitrification. *Journal of Geophysical Research: Biogeosciences*, 118(3), 1105-1119.

Fetter, C. W. (2018). *Applied hydrogeology*. Waveland Press.

Elliott, D.W., and Zhang, X.W., 2001, Field Assessment of Nanoscale Bimetallic Particles for Groundwater Treatment. *Environmental Science and Technology* 35, 4922-4926.

Fiandaca, G., Auken, E., Christiansen, A.V., and Gazoty, A., 2012, Time-domain-induced polarization: Full-decay forward modeling and 1D laterally constrained inversion of Cole-Cole parameters. *Geophysics*, 77(3), E213-E225.

Fiandaca, G., Ramm, J., Binley, A., Gazoty, A., Christiansen, A.V. and Auken, E., 2012, Resolving spectral information from time domain induced polarization data through 2-D inversion. *Geophysical Journal International*, ggs060.

Fixman, M., 1980. Charged macromolecules in external fields. I. The sphere. *The Journal of Chemical Physics*, 72(9), 5177-5186.

Flores Orozco A., Bücker, M., Steiner, M. Malet, J.P., 2018, Complex-conductivity imaging for the understanding of landslide architecture. *Engineering geology*, 243, 241-252.

- Flores Orozco, A., Gallistl, J., Bucker, M., and Williams, K., 2018. Decay-curve analysis for data error quantification in time-domain induced polarization imaging. *Geophysics*, 83(2), E75-E86.
- Flores Orozco, A., Kemna, A., Oberdörster, C., Zschornack, L., Leven, C., Dietrich, P., Weiss, H., 2012a, Delineation of subsurface hydrocarbon contamination at a former hydrogenation plant using spectral induced polarization imaging. *Journal of Contaminated Hydrology*, 136-137, 131-144.
- Flores Orozco, A., Kemna, A., Zimmermann, E., 2012b, Data error quantification in spectral induced polarization imaging. *Geophysics*, 77(3), E227-E237.
- Flores Orozco, A., Velimirovic, V., Tosco, T., Kemna, A., Sapion, H., Klaas, N., Sethi, R., and Leen, B., 2015, Monitoring the injection of microscale zero-valent iron particles for groundwater remediation by means of complex electrical conductivity imaging. *Environmental Science and Technology*: 49 (9), 5593–5600.
- Flores Orozco, A., Williams, K. H., Long, P. E., Hubbard, S.S., and Kemna, A., 2011, Using complex resistivity imaging to infer biogeochemical processes associated with bioremediation of an uranium-contaminated aquifer. *Journal of Geophysical Research: Biogeosciences* 116(G3), 2156-2206.
- Flores Orozco, A., Williams, K., H., Kemna, A., 2013, Time-lapse spectral induced polarization imaging of stimulated uranium bioremediation. *Near Surface Geophysics*: 11(5), 531-544.
- Friedel S., Thielen A., and Springman, S.M., 2006, Investigation of a slope endangered by rainfall-induced landslides using 3D resistivity tomography and geotechnical testing. *Journal of Applied Geophysics.*, 60 (2006), 100-114
- Gallistl, J., Weigand, M., Stumvoll, M., Ottowitz, D., Glade, T. and Flores Orozco, A., 2018. Delineation of subsurface variability in clay-rich landslides through spectral induced polarization imaging and electromagnetic methods. *Engineering Geology*, 245, 292-308.
- Gance, J., Grandjean, G., Samyn, K., and Malet, J.-P., 2012, Quasi-Newton inversion of seismic first arrivals using source finite bandwidth assumption: application to subsurface characterization of landslides. *Journal of Applied Geophysics*, 87: 94-106.
- Gance, J., Malet, J.-P., Supper, R., Sailhac, P., Ottowitz, D., and Jochum, B., 2016, Permanent electrical resistivity measurements for monitoring water circulation in clayey landslides. *Journal of Applied Geophysics*, 126: 98-115.
- Gastone, F., Tosco, T., and Sethi, R. 2014, Green stabilization of microscale iron particles using guar gum: bulk rheology, sedimentation rate and enzymatic degradation. *Journal of Colloid and Interface Science* 2014, 421, 33-43.
- Gazoty, A., Fiandaca, G., Pedersen, J., Auken, E., Christiansen, A.V., and Pedersen, J.K., 2012, Application of time domain induced polarization to the mapping of lithotypes in a landfill site. *Hydrology and Earth System Sciences*, 16, 1793–1804.
- Gazoty, A., Fiandaca, G., Pedersen, J., Auken, E., and Christiansen, A.V., 2013, Data repeatability and acquisition techniques for time-domain spectral induced polarization. *Near Surface Geophysics*, 11(4), 391-406.
- Ghorbani, A., Cosenza, P., Revil, A., Zamora, M., Schmutz, M., Florsch, N., and Jougnot, D., 2009, Non-invasive monitoring of water content and textural changes in clay-rocks using spectral induced polarization: A laboratory investigation. *App. Clay Science*, 43(3), 493-502.

- Grieger, K. D., Fjordbøge, A., Hartmann, N. B., Eriksson, E., Bjerg, P. L., and Baun, A., 2010, Environmental benefits and risks of zero-valent iron nanoparticles (nZVI) for in situ remediation: risk mitigation or trade-off? *J. of Contaminant Hydrology*, 118(3-4), 165-183.
- Haldar, S. K., 2013, *Introduction to mineralogy and petrology*. Elsevier.
- Hallof, P. G., 1974, The IP phase measurement and inductive coupling. *Geophysics* 39(5), 650-665
- Hallaji, M., Seppänen, A., and Pour-Ghaz, M., 2015, Electrical resistance tomography to monitor unsaturated moisture flow in cementitious materials. *Cement and Concrete Research*, 69, 10-18.
- Heenan, J., Slater, L.D., Ntarlagiannis, D., Atekwana, E.A., Fathepure, B.Z., Dalvi, S., Ross, C., Werkema, D.D., and Atekwana, E.A., 2014, Electrical resistivity imaging for long-term autonomous monitoring of hydrocarbon degradation: Lessons from the Deepwater Horizon oil spill. *Geophysics*, 80(1), B1-B11.
- Hibert, C., Grandjean, G., Bitri, A., Travelletti, J., and Malet, J.-P., 2012, Characterizing landslides through geophysical data fusion: Example of the La Valette landslide (France). *Engineering Geology*, 128, 23-29.
- Hort, R. D. Revil, A., and Munakata-Marr, J., 2012, Analysis of sources of bulk conductivity change in saturated silica sand after unbuffered TCE oxidation by permanganate. *Journal of Contaminant Hydrology* 165, 11-23.
- Hosseini, S. M., and Tosco, T., 2015, Integrating NZVI and carbon substrates in a non-pumping reactive wells array for the remediation of a nitrate contaminated aquifer. *Journal of contaminant hydrology*, 179, 182-195.
- Hua, M., Zhang, S., Pan, B., Zhang, W., Lv, L., Zhang, Q., 2012, Heavy metal removal from water/wastewater by nanosized metal oxides: a review. *Journal of hazardous materials*, 211, 317-331.
- Huang, P.M., Wang, M.K. and Chiu, C.Y., 2005, Soil mineral–organic matter–microbe interactions: impacts on biogeochemical processes and biodiversity in soils. *Pedobiologia*, 49(6), 609-635.
- Huisman, J.A., Moradi, S., Zimmermann, E., Bosch, J. and Vereecken, H., 2014, Spectral induced polarization of goethite nanoparticles. In *AGU Fall Meeting Abstracts 2014*.
- Huling, S.G., Pivetz, B. and Stransky, R., 2002, Terminal electron acceptor mass balance: light nonaqueous phase liquids and natural attenuation. *J Environ Eng* 128, 246–252
- Hördt, A., Bairlein, K., Bielefeld, A., Bücken, M., Kuhn, E., Nordsiek, S. and Stebner, H., 2016, The dependence of induced polarization on fluid salinity and pH, studied with an extended model of membrane polarization. *Journal of Applied Geophysics* 135, 408-417.
- Hördt, A., Bairlein, K., Bücken, M., and Stebner, H., 2017, Geometrical constraints for membrane polarization. *Near Surface Geophysics* 15(6), 579-592.
- Hördt, A., Blaschek, R., Kemna, A., and Zisser, N., 2007, Hydraulic conductivity estimation from induced polarisation data at the field scale - the Krauthausen case history. *Journal of Applied Geophysics*, 62(1), 33-46.
- Johansson, S., Fiandaca, G., and Dahlin, T., 2015, Influence of non-aqueous phase liquid configuration on induced polarization parameters: Conceptual models applied to a time-domain field case study. *Journal of Applied Geophysics* 123, 295-309.

- Johnson, T. C., and D. Wellman, 2015, Accurate modelling and inversion of electrical resistivity data in the presence of metallic infrastructure with known location and dimension. *Geophysical Journal International* 202, 1096-1108.
- Johnson, R.L, Nurmi. J.T, O'Brien Johnson, G.S, Fan, D., O'Brien Johnson, R.L., Shi, Z., Salter-Blanc, A.J., Tratnyek, P.G., Lowry, G.V., 2013, Field-scale transport and transformation of carboxymethylcellulose-stabilized nano zero-valent iron. *Environmental Science and Technology* 47(3), 1573-1580.
- Joyce, R. A., Glaser II, D. R., Werkema Jr, D. D., Atekwana, E. A., 2012, Spectral induced polarization response to nanoparticles in a saturated sand matrix. *Journal of applied geophysics* 77, 63-71.
- Karn, B., Kuiken, T., Otto, M., 2009, Nanotechnology and in situ remediation: a review of the benefits and potential risks. *Environmental health perspectives*, 117(12), 1813.
- Karhunen, K., Seppänen, A., Lehtikoinen, A., Monteiro, P.J., and Kaipio, J.P., 2010, Electrical resistance tomography imaging of concrete. *Cement and Concrete Research* 40, 137-145.
- Kemna, A., 2000. *Tomographic Inversion of Complex Resistivity: Theory and Application*, Der Andere Verlag, Osnabrück.
- Kemna, A., Binley, A., Cassiani, G., Niederleithinger, E., Revil, A., Slater, L., Williams, K.H., Flores Orozco, A., Haegel, F.H., Hoerd, A. and Kruschwitz, S., 2012, An overview of the spectral induced polarization method for near-surface applications. *Near Surface Geophysics*, 10(6), 453-468.
- Kemna, A., Binley, A., and Slater, L., 2004, Crosshole IP imaging for engineering and environmental applications. *Geophysics* 69, 97-107.
- Kemna, A., Räckers, E., and Binley, A., 1997, Application of complex resistivity tomography to field data from a Kerosene-contaminated site. in *Proc. 3rd Mtg. Environmental and Engineering Geophysics. Environ. Eng. Geophys. Soc., Eur. Section* 151-154.
- Kemna, A., Vanderborght, J., Kulesa, B., and Vereecken, H., 2002, Imaging and characterisation of subsurface solute transport using electrical resistivity tomography (ERT) and equivalent transport models. *Journal of Hydrology* 267, 125-146.
- Larson, H.J, 1975, *Statistics: An Introduction*. New York: Wiley, pp 15.
- LaBrecque, D. J., Miletto, M., Daily, W., Ramirez, A., and Owen, E., 1996, The effects of noise on Occam's inversion of resistivity tomography data. *Geophysics* 61, 538-548.
- Lei, C., Sun, Y., Tsang, D.C., Lin, D., 2017, Environmental transformations and ecological effects of iron-based nanoparticles. *Environmental Pollution* 232, 10-30
- Lesmes, D.P. and Frye, K.M., 2001, Influence of pore fluid chemistry on the complex conductivity and induced polarization responses of Berea sandstone. *Journal of Geophysical Research - Solid Earth*, 106(B3), 4079-4090.
- Lesparre, N., Nguyen, F., Kemna, A., Robert, T., Hermans, T., Daoudi, M., and Flores Orozco, A., 2017, A new approach for time-lapse data weighting in ERT. *Geophysics* 82(6), 325-E333.
- Louie, S.M., Phenrat, T., Small, M.J., Tilton, R.D., Lowry, G.V., 2012, Parameter identifiability in application of soft Particle Electrokinetic Theory to determine polymer and polyelectrolyte coating thicknesses on colloids. *Langmuir* 28 (28), 10334–10347

- Luna, M., Gastone, F., Tosco, T., Sethi, R., Velimirovic, M., Gemoets, J., Muysshondt, R., Sapion, H., Klaas, N., Bastiaens, L., 2015, Pressure-controlled injection of guar gum stabilized microscale zerovalent iron for groundwater remediation. *Journal of contaminant hydrology* 181, 46-58.
- Maineult, A., Jougnot, D., and Revil, A., 2018, Variations of petrophysical properties and spectral induced polarization in response to drainage and imbibition: a study on a correlated random tube network, *Geophysical Journal International* 212(2), 1398-1411
- Maineult, A., Revil, A., Camerlynck, C., Florsch, N., and Titov, K., 2017, Upscaling of spectral induced polarization response using random tube networks. *Geophysical Journal International* 209(2), 948-960
- Malet J.-P., Ulrich P., Déprez A., Masson F., Lissak C., Maquaire O., 2013, Continuous Monitoring and Near-Real Time Processing of GPS Observations for Landslide Analysis: A Methodological Framework. In: Margottini C., Canuti P., Sassa K. (eds) *Landslide Science and Practice*. Springer, Berlin, Heidelberg
- Malet, J.-P., Durand, Y., Remaître, A., Maquaire, O., Etchevers, P., Guyomarch' G., Déqué, M., van Beek, L.P.H., 2007, Assessing the influence of climate change on the activity of landslides in the Ubaye Valley. In: McInnes, R, Jakeways, J., Fairbank, H. and Mathie E. (Eds): *Proceedings International Conference on Landslides and Climate Change – Challenges and Solutions*, Taylor & Francis, London, 195-205.
- Maraun, D., Wetterhall, F., Ireson, A. M., Chandler, R. E., Kendon, E. J., Widmann, M., Brienen, S., Rust, H.W., Sauter, T., Themeßl, M., Venema, V. K. C., Chun, K. P., Goodes, C. M., Jones, R. G., Onof, C., Vrac, M., and Thiele-Eich, I., 2010, Precipitation downscaling under climate change: Recent developments to bridge the gap between dynamical models and the end user. *Reviews of Geophysics* 48(3), RG3003
- Marescot, L., Monnet, R. and Chapellier, D., 2008, Resistivity and induced polarization surveys for slope instability studies in the Swiss Alps. *Engineering Geology* 98(1), 18-28.
- Marshall, D. and Madden, T., 1959, Induced polarization, a study of its causes: *Geophysics* 24, 790.
- Maurya, P.K., Fiandaca, G., Christiansen, A.V., and Auken, E., 2018, Field-scale comparison of frequency-and time-domain spectral induced polarization. *Geophysical Journal International*, 214(2), 1441-1466.
- McClain, M.E., Boyer, E.W., Dent, C.L., Gergel, S.E., Grimm, N.B., Groffman, P.M., Hart, S.C., Harvey, J.W., Johnston, C.A., Mayorga, E. and McDowell, W.H., 2003, Biogeochemical hot spots and hot moments at the interface of terrestrial and aquatic ecosystems. *Ecosystems*6(4), 301-312.
- Meckenstock, R. U. and Bosch, J., 2014, Method for the degradation of pollutants in water and/or soil. United States patent.
- Mellage, A., Holmes, A.B., Linley, S., Vallée, L., Rezanezhad, F., Thomson, N., Gu, F. and Van Cappellen, P., 2018, Sensing coated iron-oxide nanoparticles with spectral induced polarization (SIP): experiments in natural sand packed flow-through columns. *Environmental science & technology*, 52(24), 14256-14265.
- Mewafy, F. M., Werkema, D. D., Atekwana, E. A., Slater, L. D., Abdel Aal, G. Z., Revil, A., and Ntarlagiannis, D., 2013, Evidence that bio-metallic mineral precipitation enhances the complex conductivity response at a hydrocarbon contaminated site. *Journal of Applied Geophysics* 98, 113-123.

- Misra S., Torres-Verdín, C., Revil, A., Rasmus, J., and Homan, D., 2016, Interfacial polarization of disseminated conductive minerals in absence of redox-active species. Part 1: Mechanistic model and validation. *Geophysics* 81(2), E139-E157
- Morelli, G., and LaBrecque, D.J., 1996, Robust scheme for ERT inverse modelling: In Symposium on the Application of Geophysics to Engineering and Environmental Problems, Society of Exploration Geophysicists 629-638
- Mueller, N. C., Braun, J., Bruns, J., Cerník, M., Rissing, P., Rickerby, D., Nowack, B., 2012, Application of nanoscale zero valent iron (NZVI) for groundwater remediation in Europe. *Environmental Science and Pollution Research* 19(2), 550-558.
- NanoRem Bulletin 8 - NanoRem Pilot Site – Spolchemie II, Czech Republic: Remediation of BTEX Compounds Using Nano-Goethite
- Nathanail, C.P., Gillett, A., McCaffrey, C., Nathanail, J. and Ogden, R., 2016, A preliminary risk assessment protocol for renegade nanoparticles deployed during nanoremediation. *Remediation Journal*, 26(3), 95-108.
- Naudet, V., Gourry, J. C., Girard, F., Mathieu, F., and Saada, A., 2014, 3D electrical resistivity tomography to locate DNAPL contamination around a housing estate. *Near Surface Geophysics* 12, 351-360.
- Nordsiek, S., and Weller, A., 2008, A new approach to fitting induced-polarization spectra. *Geophysics* 73, F235-F245.
- Ntarlagiannis, D., Ustra, A., Kessouri, P., and Flores Orozco, A., 2018, The untapped potential of the induced polarization method: characterization and monitoring of hydrocarbon contamination in soils. *FastTIMES* 23(4), 64 - 75
- Ntarlagiannis, D., Yee, N., and Slater, L., 2005, On the low-frequency electrical polarization of bacterial cells in sands. *Geophysical Research Letters*, 32, L24402.
- Okay G., Cosenza, P., Ghorbani, A., Camerlynck, C., Cabrera, J., Florsch, N., and Revil, A., 2013, Characterization of macroscopic heterogeneities in clay-rocks using induced polarization: Field tests at the experimental underground research laboratory of Tournemire (Aveyron, France). *Geophysical Prospecting*, 61, 134-152
- Olhoeft, G.R., 1982, Warburg impedances at single water-mineral interfaces. In SEG Technical Program Expanded Abstracts 1982. Society of Exploration Geophysicists 516-518.
- Olhoeft, G.R., 1985, Low-Frequency Electrical-Properties. *Geophysics* 50, 2492-2503.
- Olsson, P.I., Fiandaca, G., Larsen, J. J., Dahlin, T., and Auken, E., 2016, Doubling the spectrum of time-domain induced polarization by harmonic de-noising, drift correction, spike removal, tapered gating and data uncertainty estimation. *Geophysical J. Int.* 207(2), 774-784.
- Olsson, P.I., Dahlin, T., Fiandaca, G., and Auken, E., 2015, Measuring time-domain spectral induced polarization in the on-time: decreasing acquisition time and increasing signal-to-noise ratio. *Journal of applied Geophysics* 123,316–321.
- Patil, S. S., Shedbalkar, U. U., Truskewycz, A., Chopade, B. A., and Ball, A. S., 2016, Nanoparticles for environmental clean-up: a review of potential risks and emerging solutions. *Environmental Technology and Innovations* 5, 10-21.

- Pelton, W.H., Ward, S. H., Hallof, P. G., Sill, W. R., and Nelson, P. H., 1978, Mineral discrimination and removal of inductive coupling with multifrequency IP. *Geophysics* 43, 588-609.
- Personna, Y. R., Slater, L., Ntarlagiannis, D., Werkema, D., and Szabo, Z., 2013, Complex resistivity signatures of ethanol biodegradation in porous media. *Journal of Contaminant Hydrology*, 153, 37-50.
- Phenrat, T., Cihan, A., Kim, H.J., Mital, M., Illangasekare, T., and Lowry, G. V., 2010, Transport and Deposition of Polymer-Modified Fe₀ Nanoparticles in 2-D Heterogeneous Porous Media: Effects of Particle Concentration, Fe₀ Content, and Coatings. *Environmental Science and Technology* 44 (23), 9086–9093.
- Phenrat, T., Kim, H.J., Fagerlund, F., Illangasekare, T., Tilton, R.D., and Lowry, G.V., 2009, Particle Size Distribution, Concentration, and Magnetic Attraction Affect Transport of Polymer- modified Fe₀ Nanoparticles in Sand Columns. *Environmental Science and Technology* 43 (13), 5079–5085.
- Phenrat, T., Saleh, N., Sirk, K., Tilton, R., D., and Lowry, G., V., 2007, Aggregation and sedimentation of aqueous nanoscale zerovalent iron dispersions. *Environmental Science and Technology* 41 284-290.
- Phenrat, T., Saleh, N., Sirk, K., Kim, H.J., Tilton, R., D., and Lowry, G., V., 2008, Stabilization of aqueous nanoscale zerovalent iron dispersions by anionic polyelectrolytes: adsorbed anionic polyelectrolyte layer properties and their effect on aggregation and sedimentation. *Journal of Nanoparticle Research* 10, 795-814.
- Polder, R. B., and Peelen, W. H. A., 2002, Characterisation of chloride transport and reinforcement corrosion in concrete under cycling wetting and drying by electrical resistivity. *Cement and Concrete Composites*, 24, 427 – 435.
- Raucoules, D., Michele, M., Malet, J. P., and Ulrich, P., 2013, Time-variable 3D ground displacements from High-Resolution Synthetic Aperture Radar (SAR). Application to La Valette landslide (South French Alps). *Remote Sensing of Environment*, 139, 198-204.
- Raychoudhury, T., Tufenkj, N., and Ghoshal, S., 2012, Aggregation and deposition kinetics of carboxymethyl cellulose-modified zero-valent iron nanoparticles in porous media. *Water Research* 46(6), 1735-1744.
- Revil A., Abdel Aal, G.Z., Atekwana, A., Mao, D., and N. Florsch, 2015, Induced polarization response of porous media with metallic particles — Part 2. Comparison with a broad database of experimental data, *Geophysics* 80(5), D539-D552
- Revil, A., E. Atekwana, C. Zhang, A. Jardani, and S. Smith, 2012, A new model for the spectral induced polarization signature of bacterial growth in porous media: *Water Resources Research* 48, W09545.
- Revil A., Coperey, A., Mao, D., Abdulsamad, F., Ghorbani, A., Rossi, M., and Gasquet, D., 2018, Induced polarization response of porous media with metallic particles – Part 8. Influence of temperature and salinity, *Geophysics* 83(6), 1-22
- Revil, A. and Florsch, N., 2010, Determination of permeability from spectral induced polarization in granular media: *Geophysical Journal International* 181(3), 1480-1498.
- Revil A., Florsch, N., and Mao, A., 2015, Induced polarization response of porous media with metallic particles — Part 1: A theory for disseminated semiconductors, *Geophysics* 80(5), D525–D538

- Revil, A., and Glover, P. W. J., 1998, Nature of surface electrical conductivity in natural sands, sandstones, and clays: *Geophysical Research Letters* 25(5), 691-694.
- Revil, A., M. Schmutz, M., and M. L. Batzle, 2011, Influence of oil wettability upon spectral induced polarization of oil-bearing sands: *Geophysics* 76(5), A31-A36.
- Revil, A. and Skold, M., 2011, Salinity dependence of spectral induced polarization in sands and sandstones. *Geophysical Journal International* 187(2), 813-824.
- Routh, P. S., and Oldenburg, D. W., 2001, Electromagnetic coupling in frequency-domain induced polarization data: A method for removal. *Geophysical J. Int.* 145, 59–76,
- Saleh, N., Sirk, K., Liu, Y., Phenrat, T., Dufour, B., Matyjaszewski, K., Tilton, R.D., Lowry, G.V., 2007, Surface modifications enhance nanoiron transport and NAPL targeting in saturated porous media. *Environmental Engineering Science* 24, 45-57.
- Saneiyan, S., Ntarlagiannis, D., Ohan, J., Lee, J., Colwell, F., and Burns, S., 2019, Induced polarization as a monitoring tool for in-situ microbial induced carbonate precipitation (MICP) processes. *Ecological Engineering* 127, 36-47.
- Samyn, K., Travelletti, J., Bitri, A., Grandjean, G., and Malet, J.-P., 2012, Characterization of a landslide geometry using 3D seismic refraction traveltime tomography: The La Valette landslide case history. *Journal of Applied Geophysics* 86, 120-132.
- Sastry, R.G. and Mondal, S.K., 2012, Geophysical Characterization of the Salna Sinking Zone, Garhwal Himalaya, India: *Surveys in Geophysics*, 1-31.
- Sauck, W.A., 2000, A model for the resistivity structure of LNAPL plumes and their environs in sandy sediments. *Journal of Applied Geophysics* 44, 151-165.
- Schmid, D., Micic, V., Laumann, S., Hofmann, T., 2015, Measuring the reactivity of commercially available zero-valent iron nanoparticles used for environmental remediation with iopromide. *Journal of contaminant hydrology* 181, 36-45.
- Seigel, H., Nabighian, M., Parasnis, D.S., and Vozoff, K., 2007, The early history of the induced polarization method. *The Leading Edge* 26(3), 312-321.
- Shi, Z., Fan, D., Johnson, R. L., Tratnyek, P. G., Nurmi, J. T., Wu, Y., and Williams, K. H., 2015, Methods for characterizing the fate and effects of nano zerovalent iron during groundwater remediation. *Journal of contaminant hydrology* 181, 17-35.
- Shi, Z., Nurmi, J. T., and Tratnyek, P. G., 2011, Effects of nano zero-valent iron on oxidation–reduction potential. *Environmental science and technology* 45(4), 1586-1592.
- Shilov, V. N., Delgado, A. V., Gonzalez-Caballero, F., and Grosse, C., 2001, Thin double layer theory of the wide-frequency range dielectric dispersion of suspensions of non-conducting spherical particles including surface conductivity of the stagnant layer. *Colloids and Surfaces A: Physicochemical and Engineering Aspects* 192(1-3), 253-265.
- Schirmer, M., Dahmke, A., Dietrich, P., Dietze, M., Gödeke, S., Richnow, H.H., Schirmer, K., Weiß, H., Teutsch, G., 2006, Natural attenuation research at the contaminated megasite Zeitz. *Journal of Hydrology* 328, 393–407

- Schmutz, M., Albouy, Y., Guérin, R., Maquaire, O., Vassal, J., Schott, J. J., and Descloîtres, M., 2000, Joint electrical and time domain electromagnetism (TDEM) data inversion applied to the Super Sauze earthflow (France). *Surveys in Geophysics*, 21(4), 371-390.
- Schmutz, M., Ghorbani, A., Vaudelet, P., and Blondel, A., 2014, Cable arrangement to reduce electromagnetic coupling effects in spectral-induced polarization studies. *Geophysics*, 79(2), A1-A5.
- Schmutz, M., Revil, A., Vaudelet, P., Batzle, M., Viñao, P. F., and Werkema, D. D., 2010, Influence of oil saturation upon spectral induced polarization of oil-bearing sands. *Geophysical Journal International* 183, 211-224
- Schwartz, N., Huisman, J. A., and Furman, A., 2012, The effect of NAPL on the electrical properties of unsaturated porous media. *Geophysical Journal Int.* 188(3), 1007-1011.
- Schwarz, G., 1962, A theory of the low-frequency dielectric dispersion of colloidal particles in electrolyte solution^{1, 2}. *The Journal of Physical Chemistry* 66(12), 2636-2642.
- Schädler, S., Morio, M., Bartke, S., and Finkel, M., 2012, Integrated planning and spatial evaluation of megasite remediation and reuse options. *J. of Cont. Hyd.* 127, 88-100.
- Shefer, I., Schwartz, N., and Furman, A., 2013, The effect of free-phase NAPL on the spectral induced polarization signature of variably saturated soil. *Water Resources Research*, 49(10), 6229-6237.
- Slater, L., 2006, Near surface electrical characterization of hydraulic conductivity: from petrophysical properties to aquifer geometries – a review: 18th IAGA WG 1.2 Workshop on Electromagnetic Induction in the Earth, El Vendrell, Spain, September 17-23, 2006
- Slater, L. and Binley, A., 2006, Synthetic and field-based electrical imaging of a zerovalent iron barrier: Implications for monitoring long-term barrier performance. *Geophysics* 71(5), B129-B137.
- Slater, L., Binley, A., Daily, W., and Johnson, R., 2000, Cross-hole electrical imaging of a controlled saline tracer injection. *Journal of Applied Geophysics* 44, 85–102.
- Slater L., and Lesmes, D., 2002a, IP interpretation in environmental investigations. *Geophysics* 67(1), 77-88
- Slater, L., and D. Lesmes, 2002b, Electrical-hydraulic relationships observed for unconsolidated sediments. *Water Resources Research*, 38, 31.
- Slater, L., D. Ntarlagiannis, Y. R. Personna, and S. Hubbard, 2007, Pore-scale spectral induced polarization signatures associated with FeS biomineral transformations. *Geophysical Research Letters* 34(21).
- Sturgers, H.A., 1926, The choice of a class interval: *Journal of the American Statistical Association* 21 (153), 65.
- Supper, R., Ottowitz, D., Jochum, B., Roemer, A., Pfeiler, S., Kauer, S., Keuschnig, M., and Ita, A., 2014, Geoelectrical monitoring of frozen ground and permafrost in alpine areas: field studies and considerations towards an improved measuring technology. *Near Surface Geophysics*, 12(1), 93-115.
- Sumner, J.S., 1976, *Principles of induced polarization for geophysical exploration*. Elsevier, Amsterdam.
- Tiraferrri, A., Chen, K. L., Sethi, R., and Elimelech, M., 2008, Reduced aggregation and sedimentation of zero-valent iron nanoparticles in the presence of guar gum. *Journal of Colloid and Interface Science* 324(1), 71-79.

- Tirafferri, A., Hernandez, L.A.S., Bianco, C., Tosco, T., and Sethi, R., 2017, Colloidal behavior of goethite nanoparticles modified with humic acid and implications for aquifer reclamation. *Journal of Nanoparticle Research* 19(3), 107.
- Tirafferri, A., and Sethi, R., 2009, Enhanced transport of zerovalent iron nanoparticles in saturated porous media by guar gum. *Journal of Nanoparticle Research* 11(3), 635-645.
- Titov, K., A. Kemna, A. Tarasov, and H. Vereecken, 2004, Induced polarization of unsaturated sands determined through time domain measurements. *Vadose Zone Journal* 3, 1160-1168.
- Tosco, T., Gastone, F., and Sethi, R., 2014, Guar gum solutions for improved delivery of iron particles in porous media (Part 2): Iron transport tests and modeling in radial geometry. *Journal of Contaminant Hydrology* 166(0), 34-51.
- Tosco, T., Papini, M.P., Viggi, C.C., and Sethi, R., 2014, Nanoscale zerovalent iron particles for groundwater remediation: a review. *Journal of Cleaner Production*, 77, 10-21.
- Tosco, T. and Sethi, R., 2010, Transport of non-Newtonian suspensions of highly concentrated micro- and nanoscale iron particles in porous media: a modeling approach. *Environmental science and technology* 44(23), 9062-9068.
- Travelletti J, Malet J.-P, Hibert, C., Grandjean, G., 2009, Integration of geomorphological, geophysical and geotechnical data to define the 3D morpho-structure of the La Valette mudslide (Ubaye Valley, French Alps). In: Malet J. P, Remaître A, Boogard T (eds) *Proceedings of the International Conference on Landslide Processes: from geomorphologic mapping to dynamic modelling*, Strasbourg, CERG Editions, 203-208
- Travelletti, J., Malet, J.-P., Samyn, K., Grandjean, G., and Jaboyedoff, M., 2013, Control of landslide retrogression by discontinuities: evidence by the integration of airborne- and ground-based geophysical information. *Landslides* 10(1), 37-54.
- Travelletti, J., Sailhac, P., Malet, J.-P., Grandjean, G., and Ponton, J., 2012, Hydrological response of weathered clay-shale slopes: water infiltration monitoring with time-lapse electrical resistivity tomography. *Hydrological processes* 26(14), 2106-2119.
- Trujillo-Reyes, J., Peralta-Videa, J.R., and Gardea-Torresdey, J.L., 2014, Supported and unsupported nanomaterials for water and soil remediation: are they a useful solution for worldwide pollution? *Journal of hazardous materials* 280, 487-503.
- Ustra, A., Slater, L., Ntarlagiannis, D., and Elis, V., 2012, Spectral induced polarization (SIP) signatures of clayey soils containing toluene. *Near Surface Geophysics* 10, 503-515.
- Vanhala, H., 1997, Mapping oil-contaminated sand and till with the spectral induced polarization (SIP) method. *Geophysical Prospecting* 45, 303-326.
- Vacheron, J., Desbrosses, G., Bouffaud, M.-L., Touraine, B., Moëgne-Loccoz, Y., Muller, D., Legendre, L., Wisniewski-Dyé, F., and Prigent-Combaret, C., 2013, Plant growth-promoting rhizobacteria and root system functioning. *Front. Plant Sci.* 4, 356.
- Van Voorhis, G.D., Nelson, P. H., and Drake, T. L., 1973, Complex resistivity spectra of porphyry copper mineralization. *Geophysics*, 38(1), 49-60.
- Vecchia, E.D., Luna, M. and Sethi, R., 2009, Transport in porous media of highly concentrated iron micro- and nanoparticles in the presence of xanthan gum. *Environmental Science and Technology* 43(23), 8942-8947.

- Velimirovic, M., Carniato, L., Simons, Q., Schoups, G., Seuntjens, P. and Bastiaens, L., 2014, Corrosion rate estimations of microscale zerovalent iron particles via direct hydrogen production measurements. *Journal of Hazardous Materials* 270: 18-26.
- Velimirovic, M., Chen, H., Simons, Q., and Bastiaens, L., 2012, Reactivity recovery of guar gum coupled mZVI by means of enzymatic breakdown and rinsing. *J. Contam. Hydrology* 142-143, 1-10.
- Velimirovic, M., Larsson, P.O., Simons, Q., and Bastiaens, L., 2013, Reactivity screening of microscale zerovalent irons and iron sulfides towards different CAHs under standardized experimental conditions, *J. Hazard. Materials* 252-253, 204-212.
- Velimirovic, M., Tosco, T., Uyttebroek, M., Luna, M., Gastone, F., De Boer, C., Klaas, N., Sapion, H., Eisenmann, H., Larsson, P.O. and Braun, J., 2014, Field assessment of guar gum stabilized microscale zerovalent iron particles for in-situ remediation of 1, 1, 1-trichloroethane. *Journal of contaminant hydrology* 164, 88-99.
- Vidon, P., Allan, C., Burns, D., Duval, T.P., Gurwick, N., Inamdar, S., Lowrance, R., Okay, J., Scott, D. and Sebestyen, S., 2010, Hot spots and hot moments in riparian zones: potential for improved water quality management 1. *JAWRA Journal of the American Water Resources Association*, 46(2), 278-298.
- Ward, S.H., 1988. The resistivity and induced polarization methods: In *Symposium on the Application of Geophysics to Engineering and Environmental Problems 1988*, 109-250: Society of Exploration Geophysicists
- Ward, S.H., 1990, Resistivity and induced polarization methods. *Geotechnical and environmental geophysics* 1,147-189.
- Waxman, M. H. and Smits, L.J.M., 1968, Electrical conductivities in oil-bearing shaly sands. *Society of Petroleum Engineers Journal*8(02), 107-122.
- Wainwright, H. M., Flores Orozco, A., Bücker, M., Dafflon, B., Chen, J., Hubbard, S.S., and Williams, K.H., 2015, Hierarchical Bayesian method for mapping biogeochemical hot spots using induced polarization imaging. *Water Resources Research* 52, 533-551.
- Weigand, M., Flores Orozco, A., and Kemna, A., 2017, Reconstruction quality of SIP parameters in multi-frequency complex resistivity imaging. *Near Surface Geophysics* 15(2), 187-199.
- Weller, A., Slater, L., and Nordsiek, S., 2013, On the relationship between induced polarization and surface conductivity: Implications for petrophysical interpretation of electrical measurements. *Geophysics* 78(5), D315 – D325.
- Weller, A., Zhang, Z. and Slater, L., 2015, High-salinity polarization of sandstones. *Geophysics* 80(3), D309-D318.
- Werkema, D.D., Atekwana, E. A., Endres, A. L., Sauck, W. A, and Cassidy, D. P., 2003, Investigating the geoelectrical response of hydrocarbon contamination undergoing biodegradation. *Geophysical Research Letters* 30, 49.
- Williams, K.H., Ntarlagiannis, D., Slater, L.D., Dohnalkova, A., Hubbard, S.S., and Banfield, J.F., 2005, Geophysical imaging of stimulated microbial biomineralization. *Environmental Science and Technology* 39, 7592-7600.
- Williams, K.H., Kemna, A., Wilkins, M. J., Druhan, J., Arntzen, E., N'Guessan, A. L., Long, P. E., Hubbard, S. S., and Banfield, J. F., 2009, Geophysical monitoring of coupled microbial and

geochemical processes during stimulated subsurface bioremediation. *Environmental Science and Technology* 43, 6717-6723.

Wong, J., 1979, An electrochemical model of the induced-polarization phenomenon in disseminated sulfide ores. *Geophysics* 44, 1245-1265.

Xu, P., Zeng, G.M., Huang, D.L., Feng, C.L., Hu, S., Zhao, M.H., Lai, C., Wei, Z., Huang, C., Xie, G.X., and Liu, Z.F., 2012, Use of iron oxide nanomaterials in wastewater treatment: a review. *Science of the Total Environment* 424, 1-10.

Zhao, W., and Ioannidis, W.A., 2007, Effect of NAPL film stability on the dissolution of residual wetting NAPL in porous media: A pore-scale modeling study. *Advances in water resources* 30(2), 171-181.

Zhao, Y., Zimmermann, E., Huisman, J. A., Treichel, A., Wolters, B., van Waasen, S., and Kemna, A., 2013, Broadband EIT borehole measurements with high phase accuracy using numerical corrections of electromagnetic coupling effects. *Measurement Science and Technology* 24(8), 085005.

Zimmermann, E., Kemna, A., Berwix, J., Glaas, W., Münch, H. M., and Huisman, J. A., 2008, A high-accuracy impedance spectrometer for measuring sediments with low polarizability. *Measurement Science and Technology* 19(10), 105603

6. Additional material

6.1 Investigation of cable effects in spectral induced polarization imaging using multicore and coaxial cables

6.2 Imaging biogeochemical active zones in landfills with induced polarization

6.3 An analytical membrane-polarization model to predict the complex conductivity signature of immiscible liquid hydrocarbon contaminants

6.4 Electrochemical polarization around metallic particles — Part 1: The role of diffuse-layer and volume-diffusion relaxation

6.5 Electrochemical polarization around metallic particles — Part 2: The role of diffuse surface charge

6.6 On the role of Stern- and Diffuse-layer polarization mechanisms in porous media

6.7 Curriculum Vitae

1 Investigation of cable effects in spectral induced polarization imaging using
2 multicore and coaxial cables

3

4

5 Adrian Flores Orozco¹, and Jakob Gallistl¹

6

7 Right Running Head: Cable effects in SIP imaging

8

9 1) TU-Wien, Department of Geodesy and Geoinformation, Geophysics Research Division,
10 Vienna, Austria. E-mail: flores@tuwien.ac.at, jakob.gallistl@geo.tuwien.ac.at

11

12

13 Manuscript submitted to Geophysics

14

15

16

17

18

19

20
21
22
23
24
25
26
27
28
29
30
31
32
33
34
35
36
37
38
39
40
41
42
43

ABSTRACT

The Spectral Induced Polarization (SIP) has proven itself as an optimal laboratory method to characterize hydrogeological and biogeochemical parameters in samples. However, over the last years there has been limited advances in field procedures to improve the collection of deeper, or extensive, SIP data sets. Field surveys are facilitated by the use of multicore cables; however, these enhance the induction of parasitic electromagnetic field, reducing the SIP data quality at high frequencies. To minimize cable effects, field procedures to date rely on the use of two different cables separating the current and potential dipoles. This may reduce the depth of investigation and increase the efforts at the field. To overcome these limitations, we investigate here the use of a single coaxial cable, as an alternative to improve data quality and simplify field procedures. We present a meticulous evaluation of SIP imaging data collected with the same measuring device using a coaxial cable and a combination of multicore cables of different length and manufacturers). Data sets collected with a single coaxial cable reveal a significantly lower amount of outliers removed and high consistency between the phase-lag readings, yielding smooth pseudosections, even for measurements collected with a coaxial cable five times longer than the length of the profile. Furthermore, the data collected with coaxial cables reveal an improved quality for deeper measurements (associated to lower signal-to-noise ratios) in comparison to data sets collected with separated cables. For the sake of completeness, we also present the comparison of data collected in time-domain (TDIP). Our results demonstrate that the use of coaxial cables might represent a first step in establishing the SIP imaging method as a standard technique in applications beyond research and academia.

INTRODUCTION

44

45 The Induced Polarization (IP) is an extension of the DC-resistivity method, which provides
46 information about the conductive and capacitive properties of the subsurface. The
47 measurements can be re-collected at different frequencies, in the so-called spectral IP (SIP), to
48 gain information about the frequency dependence of the electrical properties, commonly in
49 the frequency range between 0.06 and 1000 Hz (e.g., Kemna et al., 2012; Flores Orozco et al.,
50 2018a). Traditionally, spectral induced polarization (SIP) measurements are performed in the
51 frequency-domain (FD), with imaging measurements deploying tens to hundreds of electrodes
52 to perform thousands of readings based on 4-electrode arrays (for further details on the
53 method we recommend Binley and Kemna, 2005; Kemna et al., 2012; Flores Orozco et al.,
54 2018a). Taking into account the strong induced polarization effect (hereafter referred only to
55 as polarization) of metallic minerals under the appliance of an external electrical field, the SIP
56 is a method commonly used for the prospection of mineral ores, among other mining
57 applications (Pelton et al., 1978, Seigel et al., 2007). Moreover, developments in the
58 instrumentation (e.g., Zimmermann et al., 2008) have permitted to extend the application of
59 the SIP method to investigate processes and materials associated to weaker polarization
60 response for a variety of engineering, hydrogeological and environmental applications (we
61 refer to Kemna et al., 2012; Revil et al., 2012a; Binley et al., 2015; Flores Orozco et al.,
62 2018a). In particular, within the last two decades, extensive laboratory studies have
63 demonstrated a strong link between the SIP parameters and soil properties controlling water
64 flow permitting an improved quantification of hydraulic conductivity (e.g., Börner et al.,
65 1996; Revil and Florsch, 2010; Weller, 2013; Binley et al., 2016). Additionally, laboratory
66 experiments have demonstrated the sensitivity of the SIP measurements to parameters of
67 relevance accompanying different biological and geochemical processes in the emerging
68 discipline of Biogeophysics (Atekwana and Slater, 2009). Among these processes are the

69 stimulation of microbial activity (e.g., Ntarlagiannis et al., 2005; Williams et al., 2005; Slater
70 et al., 2007), the accumulation of biofilms (Abdel Aal et al., 2006; Revil et al., 2012), and
71 more recently, the geometry and growth of root systems (e.g., Corona-Lopez et al., 2019;
72 Weigand and Kemna, 2019). However, to date SIP field applications are still rare.

73 The necessity to recollect data at different frequencies leads to significantly longer acquisition
74 time for SIP imaging surveys than for standard electrical resistivity tomography (ERT),
75 especially for data collected at the low frequencies (< 1 Hz). Such long acquisition time may
76 hinder the collection of broadband SIP data in surveys performed under time constraints.
77 Hence, some studies have reported SIP data collected only at a single frequency - or a few
78 frequencies-, for instance for the monitoring of groundwater remediation by means of
79 nanoparticles injections (Flores Orozco et al., 2015; 2019a) or bioremediation techniques
80 (e.g., Williams et al., 2009; Flores Orozco et al., 2011). To date, broadband SIP imaging has
81 been reported for the estimation of hydraulic conductivity (Hördt et al., 2007), the monitoring
82 of microbial activity during the immobilization of radionuclides (Flores Orozco et al., 2013),
83 the delineation of hydrocarbon-impacted sites (Flores Orozco et al., 2012a), the investigation
84 of landslides (Gallistl et al., 2018; Flores Orozco et al., 2018a), and - in a smaller spatial scale
85 - to detect fungi infection in trees (Martin and Günther, 2013).

86 Besides long acquisition times, the main limitation of field SIP imaging is related to the
87 contamination of the data (especially at frequencies above 10 Hz) due to parasitic
88 electromagnetic (EM) fields. Commonly referred to as EM coupling, it represents a source of
89 error, which increases proportionally with the acquisition frequencies. Hence, SIP data
90 collected at high frequencies commonly show a systematic increase in the polarization
91 response as a consequence of coupling dominating over the response from subsurface
92 materials, as reported initially by Pelton et al. (1978). Some studies have already observed

93 EM coupling dominating the SIP response at frequencies around 5 Hz (e.g., Kemna et al.,
94 2000; Gasperikova and Morrison, 2001; Williams et al., 2009; Flores Orozco et al., 2011).

95 EM coupling is caused by either inductive or capacitive sources (e.g., Zimmermann et al.,
96 2008; 2019; Flores Orozco et al., 2018a). Capacitive coupling results from differences in the
97 contact impedances between the electrodes and the subsurface, or between the conductive
98 shield of the cable and the surface, resulting in leakage currents and capacitive (i.e., involving
99 displacement currents) cross talking between transmitter and receiver, for instance between
100 cables used for current injection and voltage measurements (e.g., Zimmermann et al., 2008;
101 2019; Zhao et al., 2013; 2015). Inductive coupling is related to temporal variations in the
102 current flow along the wires connecting the electrodes and the measuring device, which result
103 in the induction of parasitic EM fields in conductive materials (metallic wires in multicore
104 cables or conductive soils). The inductive coupling is known to be proportional to the
105 conductivity of the subsurface, the acquisition frequency and the square of the cable length
106 (Hallof, 1974; Pelton et al., 1978). Thus, inductive coupling represents an inherent problem to
107 modern SIP imaging applications, which require tens to hundreds of cable cores (i.e., one for
108 each electrode), with their length increasing for deeper investigations.

109 To facilitate data collection at the field scale, the use of multicore cables is a common
110 practice, as these are easier to handle than separated wires and are low maintenance,
111 permitting the collection of data in practically all terrains from landslides to frozen rocks (e.g.,
112 Doetsch et al., 2015; Gallistl et al., 2018). However, the isolation between the independent
113 wires does not provide enough separation between wires to avoid cross talking within the
114 multi-core cable, which in turn can result in poor data quality in measurements close to 1 Hz
115 (e.g., Gasperikova and Morrison, 2001). Some alternatives have been proposed, for instance,
116 to digitize the response directly at the electrode using so-called remote units (RUs)

117 minimizing cross talking between the transmitter and receiver, or between the cables (Radic,
118 2016). However, such instruments lack the robustness and flexibility of multicore cables,
119 complicating field procedures, or limiting the application of the method in rough terrains and
120 for the mapping of extensive areas. Deploying different cables for current injection and
121 potential readings, through separated cables (Dahlin et al., 2002), permits the use of multicore
122 cables and reduces the contamination of the data due to cross talking. However, without the
123 use of additional multiplexers, such practice reduces the total length of the profile by a half
124 and, thus, limits the depth of investigation. Moreover, the separation between the separated
125 cables needs to be large enough to hinder the cross talking (Telford, 1990). Alternatively, the
126 use of shielded cables has been suggested to minimize capacitive cross talking and inductive
127 coupling between wires (Telford et al., 1990; Flores Orozco et al., 2013); however, such
128 practice has not been widely implemented in field investigations. Recent investigations (e.g.,
129 Zhao et al., 2013; 2014; Huisman et al., 2016; Zimmermann et al., 2019) have proposed
130 different techniques to model the EM response and correct SIP data at high frequencies;
131 however, such methods require detailed knowledge on the geometry of the wires, which may
132 hinder its application for large scale surveys. Moreover, correction of the data does not
133 substitute adequate field procedures.

134 Although the quality of the SIP readings at a broad frequency range is critical to extend the
135 observations from the laboratory to the field scale, to date, rare studies have addressed in
136 detail the field procedures to enhance data quality in field SIP readings. In this regard, there is
137 a considerable gap between laboratory- and field-scale studies addressing methodologies for
138 the collection of SIP data with improved quality. In particular, the quality of the SIP readings
139 by deploying different cable set-ups has not been addressed since the early studies by Dahlin
140 et al., (2002). Hence, in this study we thoughtfully investigate the quality of SIP
141 measurements performed with shielded coaxial cables, and standard multicore cables. To

142 better investigate cable effects, in this study we present measurements collected with a variety
143 of multicore cables (covering different lengths and manufacturers) using both a single lay-out
144 and separated cables for current and potential dipoles. For completeness, we also investigate
145 possible cable effects by deploying coaxial, and different multicore cables (and set-ups), for
146 the collection of time-domain (TDIP) measurements. Such extensive analysis aims at
147 stressing the importance of using adequate cable set-ups for the collection of reliable SIP
148 imaging data sets at the field scale.

149

150

MATERIAL AND METHODS

151 We present data collected at the Hydrological Open Air Laboratory (HOAL) located in Lower
152 Austria (Austria). The HOAL site is a small catchment (66 ha) where different investigations
153 are being conducted to understand run-off generation (Blöschl et al., 2016). The SIP data sets
154 presented in this study were acquired in a forest-covered area characterized by heavy soils
155 (clay and silt content above 70%), within a selected area where previous measurements have
156 revealed a relatively high phase-lag measurements. Such polarization response is associated to
157 electrode polarization mechanisms (e.g., Bucker et al., 2018; 2019) associated to disseminated
158 iron sulfides accompanying naturally stimulated microbial activity, in so-called bio-
159 geochemical hot-spots, similar to the response reported in Wainwright et al. (2016). However,
160 the interpretation of the electrical response is beyond the scope of this study.

161 The clay-rich sediments from the HOAL are related to elevated values in the bulk electrical
162 conductivity ($\sigma > 50$ mS/m) due to high electrical surface conduction mechanisms in fine
163 grains (e.g., Leroy et al., 2008; Revil and Florsch, 2010). Hence, the study area offers an
164 excellent opportunity to investigate cable effects in IP associated to inductive coupling in

165 conductive soils, yet exhibiting relatively high signal-to-noise ratios in IP measurements due
166 to the presence of a highly polarizable target (i.e., disseminated iron sulfides).

167 Regarding the cables deployed in this study, we opted to compare three different multicore
168 cables purchased from three different companies: two of them from well-known
169 manufacturers of measuring devices and geophysical components, and the third one from a
170 company specialized in the construction of cables. The coaxial cable was constructed at the
171 TU-Wien and permits to connect the shields of all coaxial wires to the mass of the grounded
172 instrument. In our experiments, we refer to short and long cables, with the short cables
173 corresponding to a length of 31 m and a separation of 1 m between the take-outs, and the long
174 cables corresponding to a length of 155 m and a separation of 5 m; both short and long cables
175 have 32 take-outs and 2m lead to the device. The coaxial cable used in this study was built
176 with 32 independent wires with lengths between 5 and 155 m, yielding a total of 32 take-outs
177 with a separation of 5 m between them. The purpose of this study is to evaluate the quality in
178 the data for different cables and set-ups, but not to recommend a particular manufacturer;
179 thus, our results are anonymized and only referred to as multicore (MC) X, Y, Z. In the
180 following, we refer to the different multicore cables as MCX5, MCY5, MCZ5, and MCX1,
181 MCY1, with the name referring to the three different manufacturers and the separation
182 between take-outs. Table 1 presents a summary of the different cables deployed and the
183 corresponding names.

184 For the collection of IP readings we deployed a DAS-1 instrument (from Multi-Phase
185 Technologies), which permits to conduct both TDIP and FDIP measurements. In this regard,
186 we can investigate the influence of the cables on data quality for both measuring techniques,
187 but based on the same instrument (e.g., for consistent resolution and accuracy). Measurements
188 were collected with a dipole-dipole skip-0 configuration, where the skip refers to the number

189 of electrodes separating the pair of electrodes used for current injection, as well as for the
 190 voltage measurement (i.e., the dipole length). In case of our measurements with a skip-0,
 191 dipoles were formed between adjacent electrodes; with potential electrodes always located in
 192 front of the current dipole covering the entire length of the profile. Hence, our configuration
 193 covers a range between 1 and 29 levels, with these levels referring to the number of electrodes
 194 separating current and potential dipoles. Due to the decay in the electrical potential with the
 195 square of the distance, a decrease in signal strength is expected with increasing the separation
 196 between current and potential dipoles; hence, the configuration used here allows us to identify
 197 a decrease in data quality for different cables as well as for a varying range in the signal-to-
 198 noise ratio (S/N).

199

Cable	Manufacturer	Length	Take-out spacing	Take-outs
MCX5	X	157	5	32
MCY5	Y	157	5	32
MCZ5	Z	157	5	32
MCX1	X	33	1	32
MCZ1	Z	33	1	32
Coaxial	TU-Vienna	157	5	32

200 *Table 1: Summary of the different cables used in this study, as well as the notation used to*
 201 *differentiate them in the following sections.*

202

203 SIP measurements were collected along a profile with 32 stainless steel electrodes,
 204 considering separations of 1 and 5 m between electrodes, aiming at investigating the effect of
 205 the cable length in the quality of the data. The dipole-dipole sequence contains 435
 206 quadrupoles, as normal measurements, and exemplary collections were re-collected as
 207 reciprocal (i.e., after interchanging current and potential dipoles, e.g., Flores Orozco et al.,

208 2012b). Special care was taken in the construction of the measuring protocol to avoid
209 potential readings with electrodes previously used for current injection (e.g., Slater et al.,
210 2000; Flores Orozco et al., 2018a).

211

212

RESULTS AND DISCUSSIONS

213 **Frequency-domain (FD) measurements with different cable lengths and electrode** 214 **separation**

215 SIP measurements were collected along 12 frequencies in the range between 0.5 and 225 Hz.
216 Outliers were defined as those measurements associated with an electrical impedance phase-
217 lag (ϕ , hereafter referred only as phase-lag) below -100 mrad or above 20 mrad. The broad
218 range of accepted ϕ values was chosen taking into account an expected increase in the IP
219 response with increasing the frequency, associated to polarization of the media or to EM
220 coupling, as well as possible negative IP effects (e.g., Dahlin and Loke, 2015; Flores Orozco
221 et al., 2019b). Measurements were collected along two perpendicular profiles: (1) one profile
222 roughly oriented south-north, considering 5 m electrode separation, and (2) a shorter profile,
223 with an electrode separation of 1 m, roughly oriented east-west.

224 We use pseudosections to evaluate the data quality as they permit to easily assess the
225 distribution of the measurements and their spatial consistency. The expectation for “clean”
226 datasets is that the measurements should be distributed in a limited range of values, with
227 smooth variations along the pseudosection plane due to the (spatial) correlation between
228 adjacent measurements (e.g., Flores Orozco et al., 2018b). Accordingly, “noisy”
229 measurements are those where the pseudosection shows large variability between the values
230 in nearby measurements. The variability in our study is quantified by the standard deviation of
231 the phase measurements in the imaging data set. Hence, in each pseudosection, we present the

232 percentage of data remaining after removal of outliers and the standard deviation (s) of the
233 phase (ϕ) readings. We do not present plots of the apparent resistivity as all data collected
234 with different cables revealed similar pseudosections.

235

236 **FDIP data with 5m separation between electrodes: comparison between long multicore**
237 **and coaxial cables**

238 Figure 1 shows the pseudosections after removal of outliers for data collected with the long
239 cables and a 5 m separation between electrodes. Smooth pseudosections can be observed for
240 measurements collected at the lowest frequency (0.5 Hz) with all multicore cables, yet only
241 within the first 8 levels (pseudodepth up to 10 m) where most of the phase-lag readings are
242 found in the range of values between -20 and 0 milliradians (mrads). A similar distribution is
243 also observed for readings collected at 1 Hz, yet the multicore data sets reveal an increase in
244 the variability of the readings (s increasing from ~ 18 to ~ 22) and a larger number of noisy
245 measurements even within the first 8 levels. The lack of spatially consistent measurements for
246 data collected at high levels (i.e., pseudodepth > 5 m) with multicore cables can be argued to
247 be expected for quadrupoles associated with high geometrical factors and poor S/N. However,
248 measurements collected with the coaxial cables show clean (i.e., smooth) pseudosection
249 practically for the entire data set collected at 0.5 Hz. Moreover, still at 1 Hz, the
250 pseudosections reveal consistent readings with the coaxial cable for up to 18 levels (maximum
251 pseudodepth of ~ 20 m), which is twice as depth as with multicore readings.

252 The high number of measurements removed as outliers for data collected with multicore
253 cables (between 40 and 45%) at the low frequencies points to clear systematic errors related to
254 the cables, considering that at such low frequencies induction effects in the shallow soils
255 might be negligible. This is particularly evidenced by the high quality revealed by the data

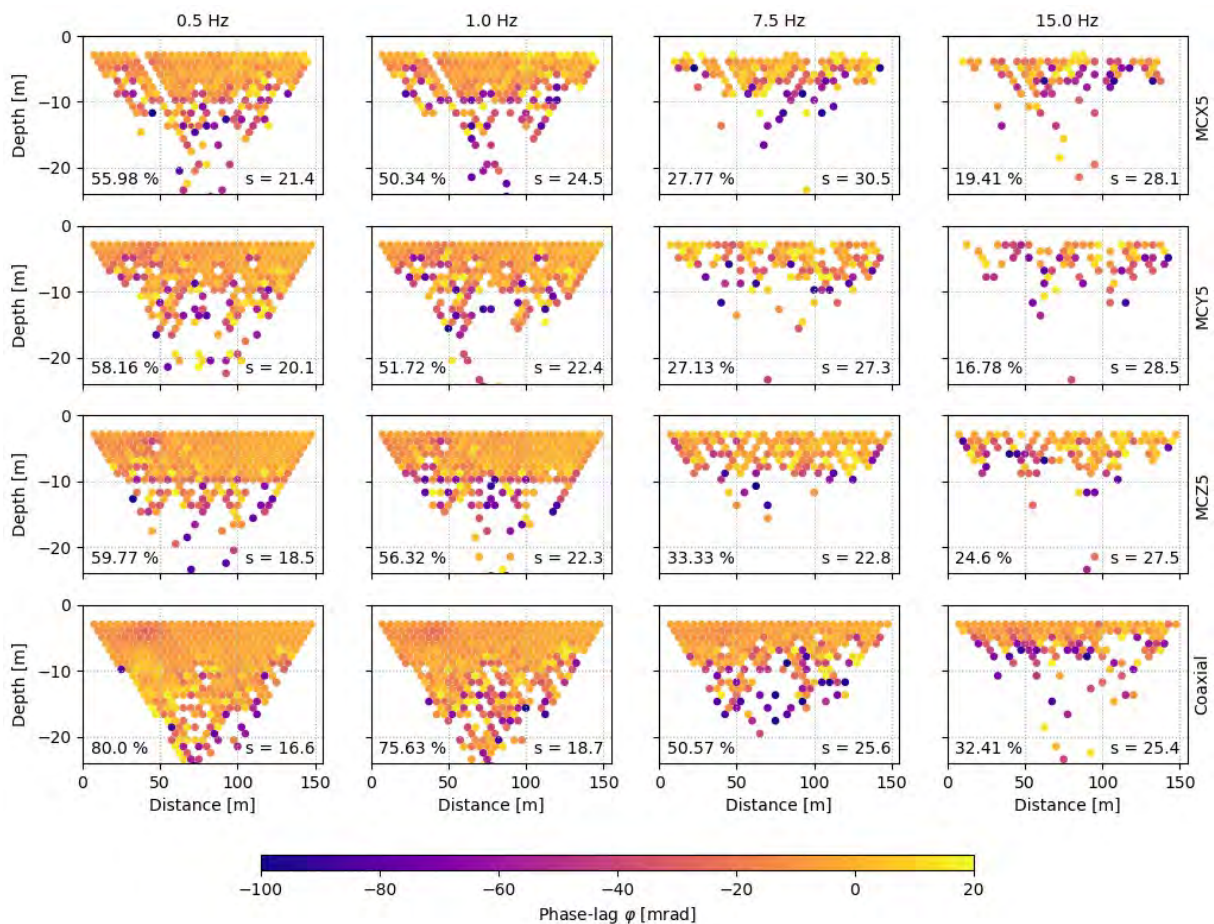
256 collected with coaxial cables, where less than 25 % of the readings are removed as outliers,
257 with consistent readings still visible for the larger separations between current and potential
258 dipoles.

259 At 7.5 Hz, the coaxial cables still permit to collect data characterized by clean pseudosections
260 for the first 8 levels (e.g., pseudodepth of 10 m), which are comparable only to the readings
261 collected with the MCZ5 cables. However, multicore cables still reveal a much larger number
262 of readings removed as outliers than the coaxial data sets. Pseudosections for MCX5 and
263 MCY5 reveal scattered data ($s > 27$) even if more than 70% of the readings have been filtered
264 as outliers, resulting in practically useless data sets.

265 For measurements collected at 15 Hz, the pseudosection for coaxial cables still shows a large
266 number of measurements with a high spatial consistency (i.e., smooth pseudosection) within
267 the first 8 levels (i.e., the first 10 m in the pseudodepth); whereas most of the deeper
268 measurements are removed as outliers. At 15 Hz, all multicore cables show a poor
269 performance, with more than 75 % of the readings removed as outliers, and the remaining
270 readings revealing a poor spatial consistency, with noisy pseudosections. The MCZ5 cables
271 are performing the best among the multicore, yet revealing much more scattered readings and
272 a higher number of removed outliers compared to the data set collected with the coaxial
273 cables.

274 Figure 1 shows that for an electrode separation of 5 m, the best SIP data set is the one
275 collected with the coaxial cables, followed by the MCZ5, and the MCX5. Whereas the MCY5
276 cables perform the worst, with most of the data severely affected by low S/N. Inductive
277 coupling is expected to affect the SIP readings at high frequencies (> 1 Hz) due to the
278 relatively long cable lengths and the high conductivity typically observed in heavy soils, such
279 as those in the HOAL site. Yet, it is expected that inductive coupling should be similar for

280 different multicore cables, as induction effects are only dependent on the conductivity of the
 281 soil and the cable length. However, Figure 1 evidences that the quality of the data collected at
 282 low frequencies (< 1 Hz), where EM coupling is commonly neglected, is also affected by the
 283 characteristics of the cable itself. At 0.5 Hz, only the coaxial cable provides a clean data set
 284 (for practically all levels), which clearly reveals the limitations of the field SIP data collected
 285 with standard multicore cables, in particular, the limited depth of investigation. Moreover,
 286 pseudosections presented in Figure 1 suggest that MCY5 cables might not be suited for
 287 collection of SIP data with 5 m separation between electrodes.



288

289 *Figure 1: Pseudosections for SIP data collected at the HOAL site using 32 electrodes*
 290 *deployed with a separation of 5 m. SIP measurements were conducted using long multicore*
 291 *(MCX5, MCY5 and MCZ5) and coaxial cables (a total length of 155 m). Labels inserted show*

292 *the percentage of remaining measurements after removal of outliers and the standard*
293 *deviation (s) in the phase readings.*

294

295 **FDIP data with 1 m separation between electrodes: comparison between long multicore**
296 **and coaxial cables**

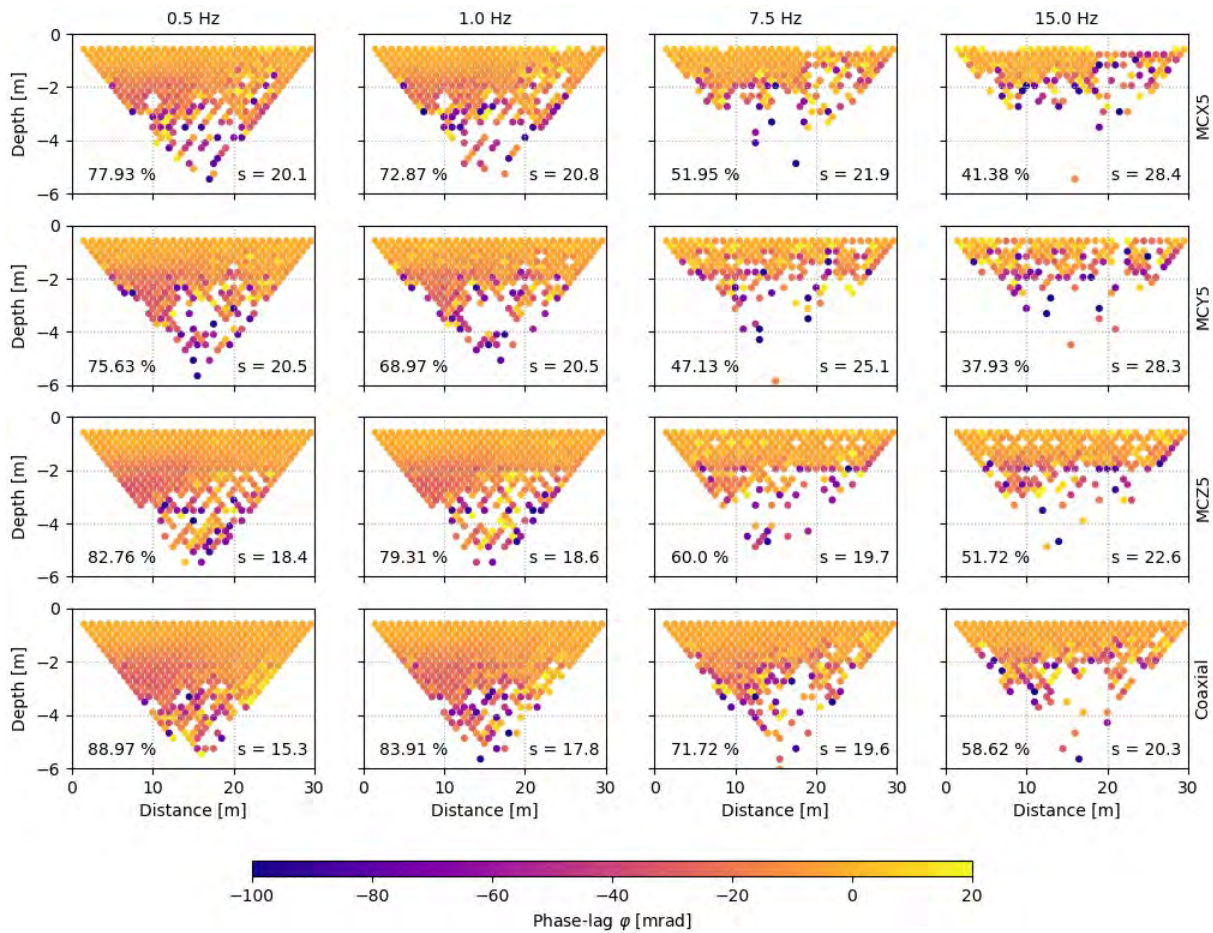
297 For long separation between electrodes (5 m) all multicore cables show a similar performance
298 with a significant increase in data quality evidenced for measurements collected with coaxial
299 cables, especially at higher frequencies (i.e., 15 Hz in Figure 1). In a second step, we
300 investigate the performance of the same long cables (115 m length, with 5 m spacing between
301 the take-outs), but for measurements collected with shorter electrode separation (1m for a
302 profile length of 31 m). A shorter separation between electrodes favors higher S/N, and may
303 help to reduce the contamination of the data due to EM coupling. At the field, the cables were
304 laid carefully to avoid the formation of loops within the 4 m of cable exceeding the separation
305 between electrodes to minimize the induction of electromagnetic fields in the near subsurface
306 or within the wires of the multicore cables.

307 As expected, the small separation between electrodes resulted in higher voltage readings,
308 ranging between 0.5 mV and 1 V (data not shown), which are two orders of magnitude higher
309 than those observed for measurements collected with 5 m separation between electrodes (data
310 not shown). Accordingly to the enhanced S/N, Figure 2 reveals only minimal readings
311 removed as outliers in the lower frequencies (0.5 and 1 Hz) for multicore measurements
312 (< 30 %), yet still coaxial cables perform the best (less than 15 % outliers removed).
313 Moreover, pseudosections for data collected at 7.5 Hz still reveal more than 50 % valid
314 readings for all but MCY5 cables deployed. Similar to the previous measurements, Figure 2
315 shows that the smoothest pseudosections are those related to measurements with the coaxial

316 cables. However, readings collected with the MCZ5 are also comparable (and to some extent
317 also MCX5), with relatively clean pseudosections up to 7.5 Hz within the first 8 to 12 levels
318 (pseudodepth < 3 m).

319 At 15 Hz, measurements collected with MCX5 and MCY5 are scattered over a larger range
320 and yielding noisy pseudosections, indicating poor quality in the phase readings. Whereas
321 MCZ5 and coaxial cables show clean pseudosections within the first 8 levels (pseudodepth
322 < 2 m) and relatively consistent distribution within the readings ($s \sim 21$). Clearly the long
323 cables cause a gain in the inductive coupling at 15 Hz (Hallof, 1974), even if the separation
324 between electrodes is small. Nonetheless, measurements collected with coaxial cables at
325 15 Hz still show a clean pseudosection with only a few outliers removed within the first 8
326 levels, suggesting that such effects might be minimal in this frequency range.

327 Pseudosections presented in Figure 2 evidence that the deployment of multicore cables longer
328 than the actual separation between electrodes, might significantly reduce the quality of SIP
329 readings, even at low frequencies, as observed for 0.5 Hz readings with MCX5 and MCY5.
330 This observation is consistent with the discussion above regarding the construction of the
331 multicore cables for SIP surveys. However, Figure 2 suggests that the deployment of coaxial
332 cables significantly improves data quality with reducing electrode separation, even if the
333 coaxial cable is much longer than the actual separation between electrodes.



334

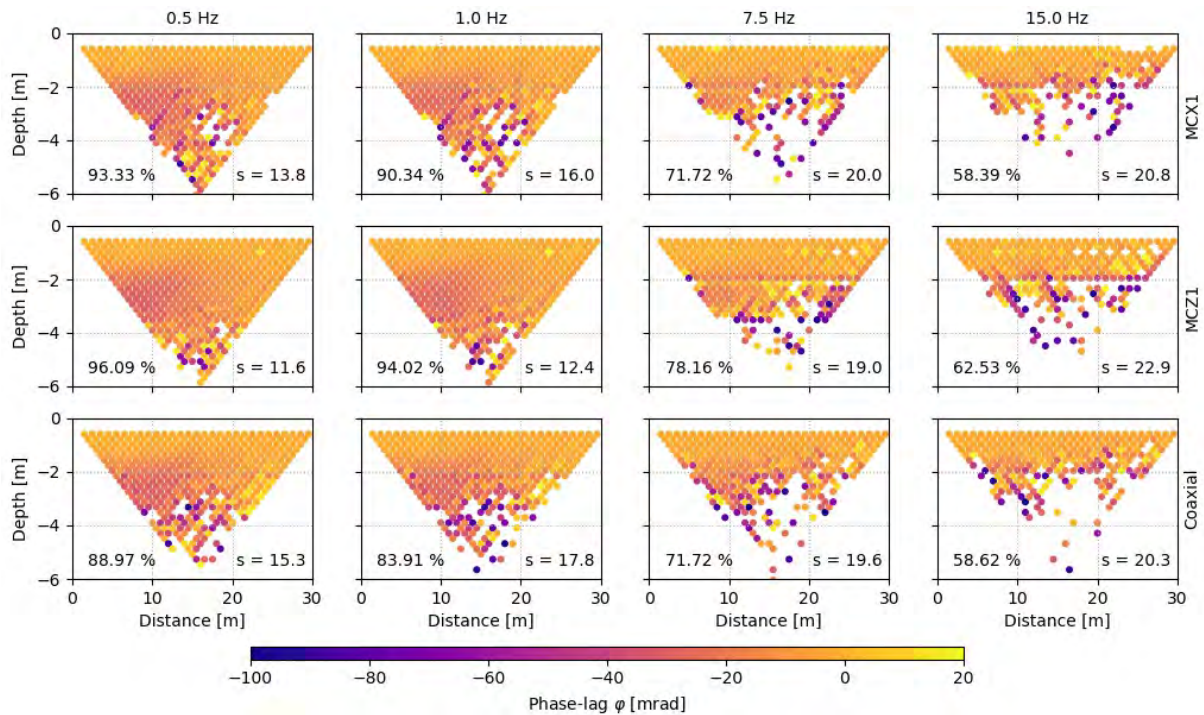
335 *Figure 2: Pseudosections for SIP data collected at the HOAL site using 32 electrodes*
 336 *deployed with a separation of 1 m. SIP readings were collected using long multicore (MCX5,*
 337 *MCY5 and MCZ5) and coaxial cables (a total length of 115 m each). Labels inserted show the*
 338 *percentage of remaining measurements after removal of outliers and the standard deviation*
 339 *(s) in the phase readings.*

340

341 **FDIP data with 1 m separation between electrodes: comparison between short multicore** 342 **cables and long coaxial cables**

343 Pseudosections presented in Figure 3 permit us to investigate the data quality in
 344 measurements collected with a short electrode separation and short multicore cables (1 m for
 345 a total profile length of 31 m), in comparison with the long coaxial cables (5 m spacing

346 between take-outs for a length of 115 m). Measurements with MCY1 were not conducted
 347 taking into account that those cables demonstrated the worst performances in previous tests.
 348 Figure 3 shows that data quality is significantly improved by reducing the length of the
 349 multicore cables to the exact size of the separation between electrodes.



350

351 *Figure 3: Pseudosections for SIP data collected at the HOAL site using 32 electrodes*
 352 *deployed with a separation of 1 m. SIP readings were collected using short multicore (MCX1*
 353 *and MCZ1 – a total length of 31m each) and long coaxial cables (a total length of 115 m).*
 354 *Labels inserted show the percentage of remaining measurements after removal of outliers and*
 355 *the standard deviation (s) in the phase readings.*

356 In general, all measurements presented in Figure 3 show smooth pseudosections for all cables
 357 in the low frequencies (0.5 and 1 Hz), with less than 10 % of measurements removed as
 358 outliers for multicore cables. Moreover, pseudosections reveal consistent phase readings also
 359 for 16 levels (pseudodepth < 5 m) for measurements collected at low frequencies; whereas
 360 only within the first 8-10 levels (for maximum pseudodepth of 2.5 m) at high frequencies (7.5

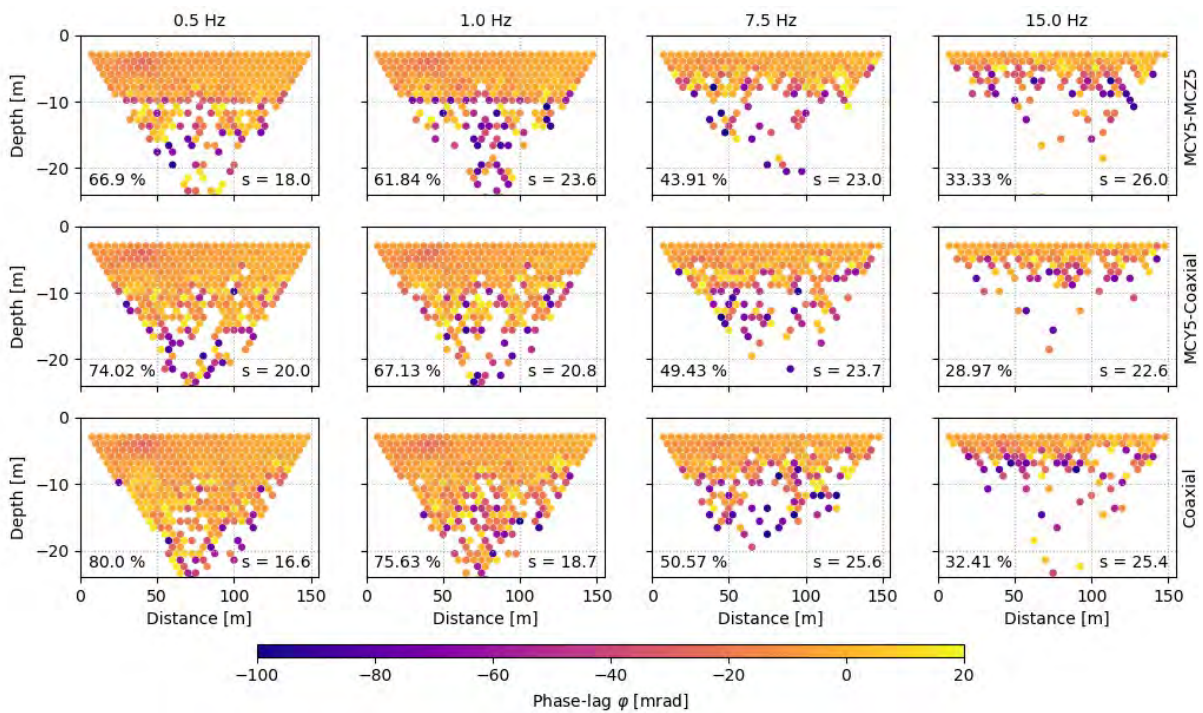
361 and 15 Hz). However, data quality decreases with increasing the acquisition frequency for
362 larger separations between current and potential dipoles (i.e., pseudodepth). Consistent to
363 previous observations, the MCZ cables perform still slightly better than the MCX cables.

364 Clearly, the short cables minimize EM coupling associated to both, inductive effects in the
365 subsurface and capacitive cross talking between the cables. Thus, field procedures deploying
366 the smallest-possible multicore cables are recommended to significantly improve the quality
367 of SIP data. Nonetheless, data collected with coaxial cables exhibit less dependence on the
368 actual length of the cable, with similar pseudosections obtained with long coaxial cables and 5
369 times smaller multicore cables, as revealed in Figure 3. In case of coaxial cables, the most
370 affected measurements are those with the larger separation between current and potential
371 dipoles (i.e., larger pseudodepth), associated to lower S/N and, as observed in Figure 3, more
372 susceptible to being dominated by parasitic EM fields.

373 **Comparison between single coaxial and separated cables**

374 Initially proposed by Dahlin et al. (2002), the use of separated cables for current and potential
375 dipoles is one of the most accepted methods to improve the data quality in SIP readings. Such
376 procedure limits the contamination of the data due to cross talking between the wires, if the
377 separation between both cables is large enough to overcome displacement currents. Such
378 cable layout permits to use any kind of multi-core cables for the collection of reliable of IP
379 data, and likely is independent on the actual length of the multicore cables, yet such issue has
380 not been explicitly addressed before. Alternatively, measurements presented so far
381 demonstrate that the deployment of coaxial cables enhances the quality of the IP data, as the
382 shield of the cables reduces inductive effects (in the ground and within the cable bundle) as
383 well as cross talking between the wires, at least up to 15 Hz.

384 To better evaluate both procedures, in Figure 4 we compare the pseudosections for data
 385 collected using a single coaxial cable, and a separated cable layout for a separation of 5 m in
 386 both electrode and take-outs. Moreover, we compare the readings for separated cables after (i)
 387 using two multicore cables (MCY5 and MCZ5) for current and potential readings, (ii) using
 388 the combination of coaxial and multicore cables (MCY5), and (iii) a single coaxial cable. We
 389 note here that we observed the same data quality using different combination of multicore
 390 cables. However, we present here pseudosections for data collected in combination with the
 391 MCY5 cable to demonstrate that a multicore performing bad as a single cable can be used to
 392 collect reliable data in lay-outs separating current and potential dipoles, especially when used
 393 in combination with a coaxial cable.



394

395 *Figure 4: Pseudosections for SIP data collected at the HOAL site using 32 electrodes with a*
 396 *separation of 5 m between them. SIP readings were collected using: (1) current injections and*
 397 *potential readings in a multicore cable (plots in the first row), followed by (2) current*
 398 *injections in the multicore cable and potential readings in the coaxial (plots in the second*

399 *row). For comparison, pseudosections are also presented for data collected with single*
400 *coaxial (third row). Labels inserted indicates the total of remaining measurements after*
401 *removal of outliers and the standard deviation (s) in the phase readings.*

402

403 Figure 4 shows practically the same pseudosections for data collected with a single coaxial
404 cable and separate cables, if the coaxial cable is used for the collection of data with separated
405 cables. In both cases, similar pseudosections are observed in all frequencies under
406 investigations. The use of separated cables clearly helps to improve the readings in
407 comparison with single multicore cables, with at least 10 % less measurements removed as
408 outliers in comparison to those presented above (see Figure 1). Especially the use of separated
409 cables helps to reduce the number of noisy measurements in high levels (between 10 and
410 20 m pseudodepth) for low frequency readings (0.5 and 1 Hz). However, in the same
411 frequency range, coaxial cables still perform better, with a lower amount of readings removed
412 as outliers, a higher spatial consistency between the measurements (i.e., smoother
413 pseudosections) and a much shorter variability ($s = 16$).

414 For measurements at higher frequencies, a single coaxial cable and the separated MCY5-
415 coaxial still show consistent pseudosections, with relatively good data quality (smooth
416 pseudosections) within the first 8 levels (i.e., pseudodepth no larger than 10 m). However,
417 Figure 4 also reveals that measurements with separated cables are significantly noisier if two
418 multicore cables are deployed (i.e., in comparison to multicore-coaxial lay-out or single
419 coaxial). The variations between the two data sets collected with separated cables are not easy
420 to explain, especially because both datasets revealed a similar distribution in the injected
421 current and voltage readings (data not shown). Hence, both measurements refer to similar
422 S/N. Likely, even if the current and potential dipoles are separated, the use of only multicore

423 cables still results in cross talking, leading to the decrease in data quality for IP readings,
424 which is already visible at 1 Hz.

425 Measurements presented in Figure 4 were collected as after interchanging current and
426 potential cables (i.e., a cable previously used for current dipoles is then used for potential
427 measurements), revealing the same pseudosection (data not shown), clearly indicating a
428 further advantage in protocols deploying separated cables, again with further improvements if
429 one is a coaxial cable. Still, the deployment of single coaxial cable provides the higher quality
430 for data collected with a long separation between electrodes, even over the data collected with
431 separated cables.

432 To address the use of separated short cables, in Figure 5 we present a similar comparison but
433 for a shorter separation (1 m) between electrodes and the take-outs of the MCX1 cables.
434 Similar to previous observations, the data quality improves with decreasing electrode
435 separation, corresponding to a higher S/N (voltage readings are consistently above 1 mV),
436 which likely dominates over parasitic EM fields (inductive and capacitive). Contrary to the
437 previous test, the pseudosections for data collected at 0.5 Hz clearly reveal an advantage of
438 using separated short multicore cables (MCX1-MCZ1), with a data sets revealing almost no
439 outliers (less than 2 % of the readings removed) and high spatial consistency between the
440 readings ($s \sim 10$). The data quality is only slightly reduced if the data is collected with
441 combination of a long multicore and coaxial cables, with 6 to 8 % of readings being removed
442 as outliers. The decrease in data quality is clearly related to the use of a much longer cable
443 than the actual separation between the electrodes. Accordingly, the data collected with
444 MCX1-MCZ1 shows the best quality as this corresponds to data collected with two short
445 cables and separated current and potential dipoles. Nonetheless, the data collected with a
446 single long coaxial cable is still comparable at 0.5 and 1 Hz.

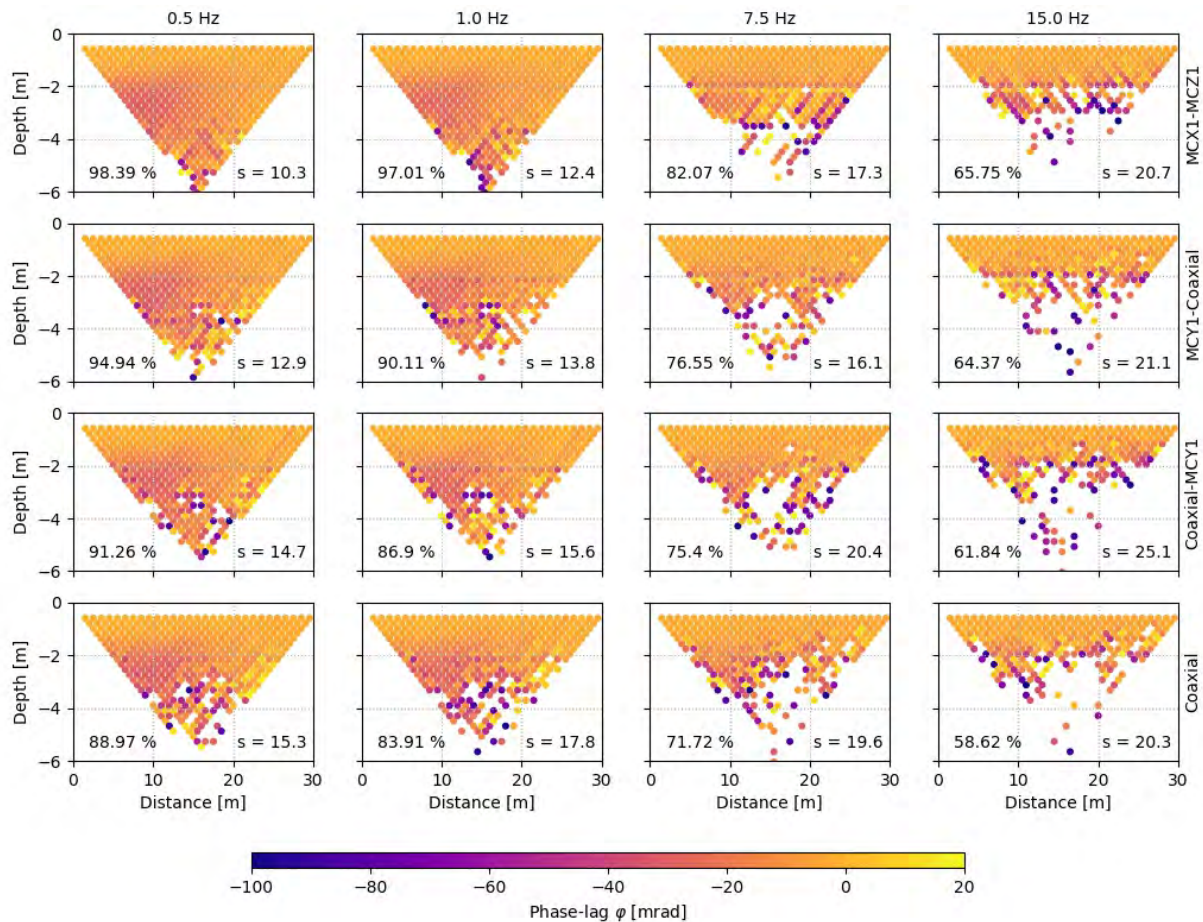
447 Readings with short separated cables reveal the best quality in IP measurements at 1 and
448 7.5 Hz, with smooth pseudosections and still a negligible amount of outliers removed. As
449 mentioned above, the data quality decreases at 7.5 Hz when the coaxial cable is used, which is
450 five times larger than the actual separation between electrodes. However, Figure 5 also shows
451 that data collected at 15 Hz are consistent for the different cables layouts, with all
452 pseudosections revealing about 40 % of the readings removed as outliers, and information
453 only within the first 8 levels. Moreover, Figure 5 reveals a slight increase in data quality for
454 current injections performed with the multicore and potential readings collected with the
455 coaxial cable. This may be a result of the extra isolation in the coaxial cables, which
456 minimizes cross talking in the voltage readings.

457 Our results have clearly demonstrated that the use of coaxial cables improved FDIP readings
458 in all frequencies under investigation; thus, measurements were not performed with short
459 electrode spacing and short coaxial cables, where even a higher data quality is expected.
460 However, we believe that the results here presented are relevant to establish low frequency
461 FDIP imaging as a robust method for field applications. In this regard, Figure 2 and Figure 4
462 show that, analogous to resistivity surveys, measurements conducted with single coaxial
463 cables can provide a clean data set. Moreover, it might not be necessary to construct different
464 cables for different electrode separations since, at least in the low frequencies (0.5 and 1 Hz),
465 IP readings show a good data quality even if the coaxial cable is much longer than the actual
466 separation between electrodes.

467 The use of separated short cables clearly helps to minimize cross talking, as visible in the
468 pseudosection for data collected at 0.5 Hz in Figure 5. However, the data is still comparable to
469 the one collected by a single long coaxial cable. Moreover, the collection of IP data with
470 separated cables might limit the depth of investigation without using extra multiplexers, or

471 require of much longer field procedures to reach the same depth of investigation as obtained
472 with a single coaxial cable. Moreover, data collected with separated multicore cables are only
473 improved if the cable has a similar separation between the take-outs as the electrode
474 separation. In case of data collected with separated long cables, the related pseudosections
475 show more noisy measurements than those for the single coaxial cable.

476 We also believe that the distortions observed for the measurements at high frequencies
477 collected with coaxial cables are related to the lack of a galvanic separation between the
478 transmitter and the receiver in the DAS-1. Hence, high frequency data might be subject to
479 capacitive coupling in the device and not to cables effects when coaxial cables are deployed.
480 Hence, SIP data could further be improved using coaxial cables and improved measuring
481 instruments. A previous study demonstrated the possibility to collect reliable SIP readings in
482 frequencies about 200 Hz using coaxial cables (Flores Orozco et al., 2013), based on data
483 collection with the Zonge GDP.



484

485 *Figure 5: Pseudosections for SIP data collected at the HOAL site using 32 electrodes with a*
 486 *separation of 1 m between them. SIP readings were collected using: (1) current injections*
 487 *potential readings in separated multicore cables, followed by (2) current injections in the*
 488 *multicore cable and potential readings in the coaxial, as well as (3) current injections in the*
 489 *coaxial and potential readings in the multicore cables. For comparison, pseudosections are*
 490 *also presented for data collected with a single coaxial cable. The label indicates the total of*
 491 *remaining measurements after removal of outliers and the standard deviation (s) in the phase*
 492 *readings.*

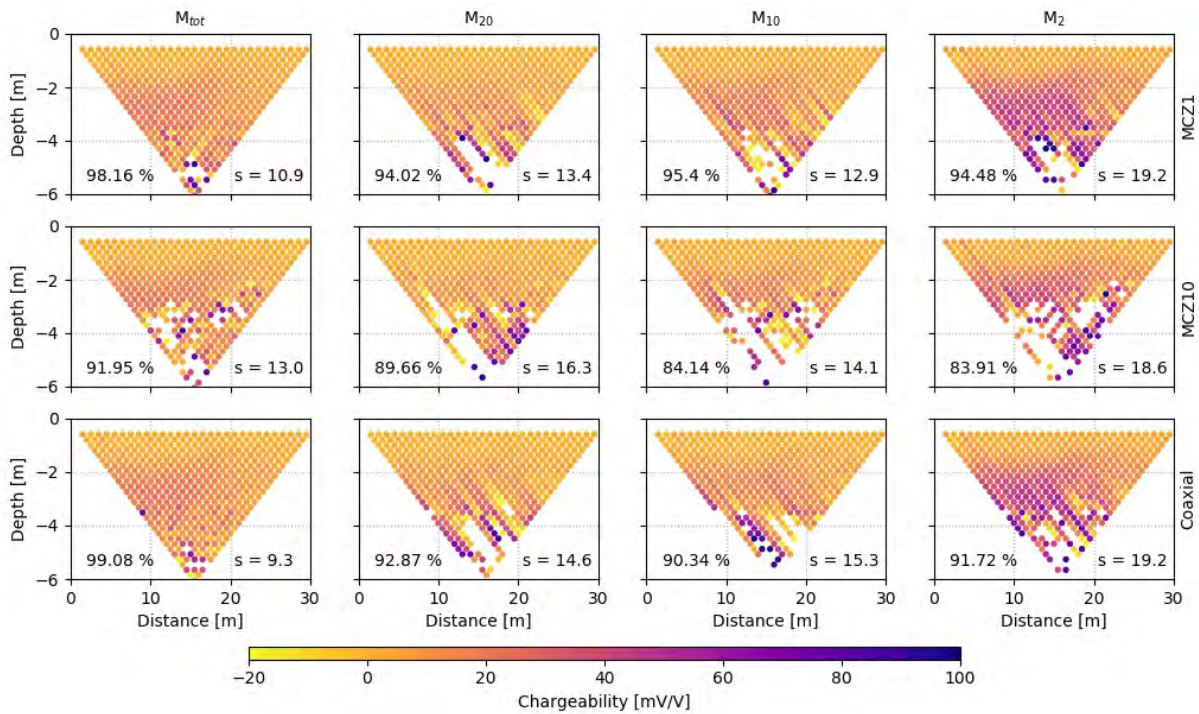
493 **Comparison of coaxial, multicore and separated cables for TD measurements**

494 Regarding EM coupling, TDIP measurements offer the advantage that potential readings are
 495 collected with a delay after the current injection is switched-off, which permits to minimize

496 the effect of electromagnetic effects in the data (Fiandaca, 2018). Hence, we investigate here
497 if the use of coaxial cables provide any advantage for TDIP measurements. TD measurements
498 were acquired for pulse lengths of 500 and 2000 milliseconds (ms), using a square wave, with
499 50 % duty cycle.

500 After current switch-off, the decay curve was sampled after an initial delay of 10 ms using 24
501 and 34 windows respectively for the 500 and 2000 ms pulse length. In the first case, all IP
502 windows have a constant width of 20 ms; whereas for 2000 ms pulse length, the decay curve
503 was sampled using a length of 20 ms for IP windows 1 to 10, a length of 40 ms for window 11
504 to 17 and a length of 80 ms for windows 18 to 34. Such sampling aims at increasing the S/N
505 for late measurements, where the lower voltages are expected.

506 For our analysis we present the pseudosections for chargeability measurements at three
507 different sampling windows (2, 20 and 29, for 2000 pulse length; whereas 2, 10 and 20 for
508 500 ms pulse length), analogous to the high, intermediate and low frequencies in FDIP. We
509 also present pseudosections for the integral chargeability (M_{tot}), which is a quantity commonly
510 used for the interpretation of TDIP surveys (more details can be found, for instance, in Binley
511 and Kemna, 2005). Similar to the FDIP data, the apparent resistivity pseudosections are
512 consistent for measurements with different cables and are not discussed here. We define and
513 remove outliers as those measurements for which the corresponding chargeability exceeds the
514 limits of -20 to 100 mV/V, with the broad range selected to permit the visualization of
515 possible negative chargeability values (e.g., Dahlin et al., 2015) or contamination in the data
516 due to EM coupling.



517

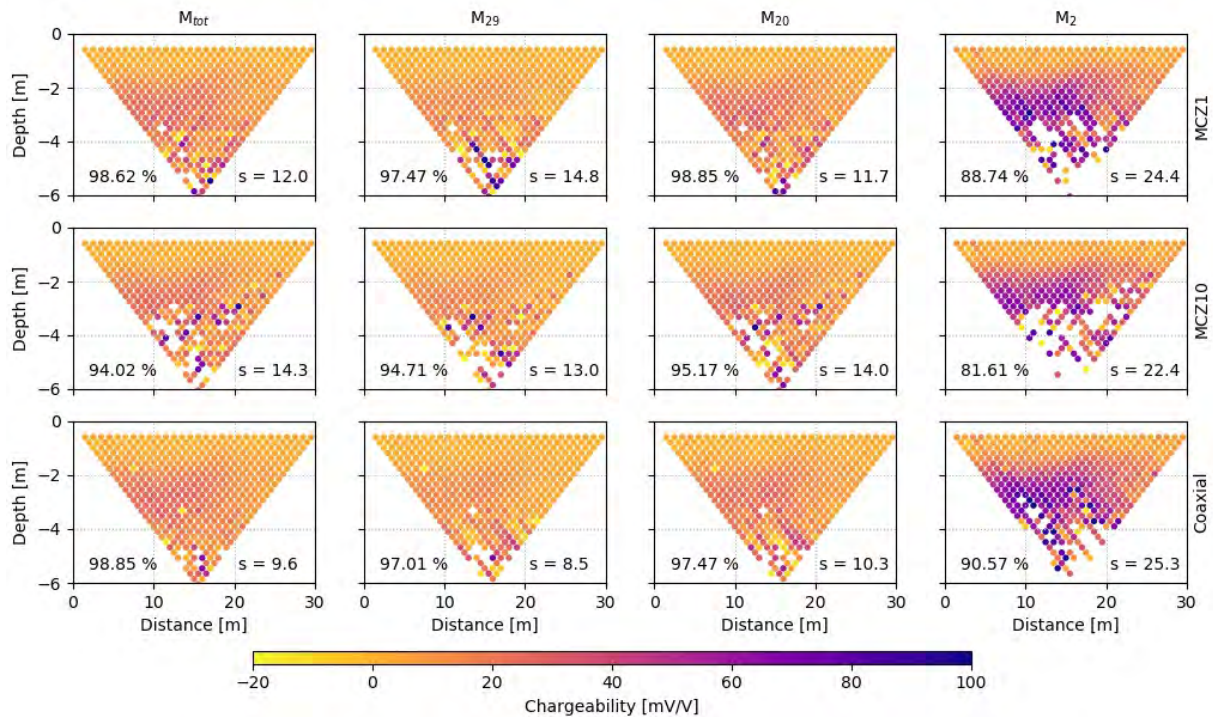
518 *Figure 6: Pseudosections for TDIP data collected (with a pulse length of 500 ms) at the*
 519 *HOAL site using 32 electrodes with a separation of 1 m between them and a multi-core cable*
 520 *with 1 m and 10 m separation between take-outs (MCZ1 and MCZ10 respectively), as well as*
 521 *the coaxial cable with 5 m separation between take-outs. The label indicates the total of*
 522 *remaining measurements after removal of outliers and the standard deviation (s) in the phase*
 523 *readings.*

524

525 Figure 6 shows in general clean pseudosections, at least to pseudodepth of 4 m (at least 14
 526 levels), and with less than 5 % of the data removed as outliers (for the M_{tot} plots), clearly
 527 evidencing the good quality in the TDIP readings. As expected, the noisier pseudosections are
 528 those related to measurements collected with the long MCZ10 cables (10 m separation
 529 between take-outs for a total cable length of 310 m), which reveals poor spatial consistency
 530 between the readings collected below 10 levels (i.e., 10 electrodes separating the current and
 531 potential electrodes). Such poor data quality might be related to possible inductive coupling

532 dominating over the low voltage measurements (i.e., lower S/N). The data quality improves
533 significantly for data collected with shorter multicore cables (from the same manufacturer), as
534 evidenced by pseudosections for MCZ1 data. These readings show smooth pseudosections,
535 with again some noisy measurements only for the deepest measurements (above 5 m
536 pseudodepth), TDIP measurements collected with the coaxial cable show the smoothest
537 pseudosections and the lowest amount of removed outliers ($< 1\%$ for the M_{tot}), clearly
538 demonstrating similar advantages for the collection of TDIP, as observed above for FDIP.

539 As expected, early IP windows (i.e., M_2 and M_{10}), reveal the largest number of filtered data
540 (15 % and 5 % for long and short multicore cables respectively, and 10 % for coaxial cables),
541 and noisy pseudosections for the readings with large levels (> 4 m pseudodepth). EM
542 coupling effects are expected in the early times (analogously to high frequencies in FDIP),
543 and clearly affect the quality of the measurements with weak S/N associated with large
544 separation between current and potential dipoles (i.e., large pseudodepth). Such contamination
545 of the data is only visible for the longest cables (MCZ10) in the integral chargeability plots,
546 but almost negligible for the coaxial cable (or the short multicore cable). Similar conclusions
547 can be drawn for TDIP data collected with 2000 ms pulse length, as presented in Figure 7.
548 However, in this case, the data collected with the long multicore cables (MCZ10) reveal a
549 larger distortion in the deep measurements, likely related to cross talking within the multicore.
550 Yet, the readings collected with the coaxial and MCZ1 cables reveal both high quality and
551 have distortions only in the early times readings (M_2)



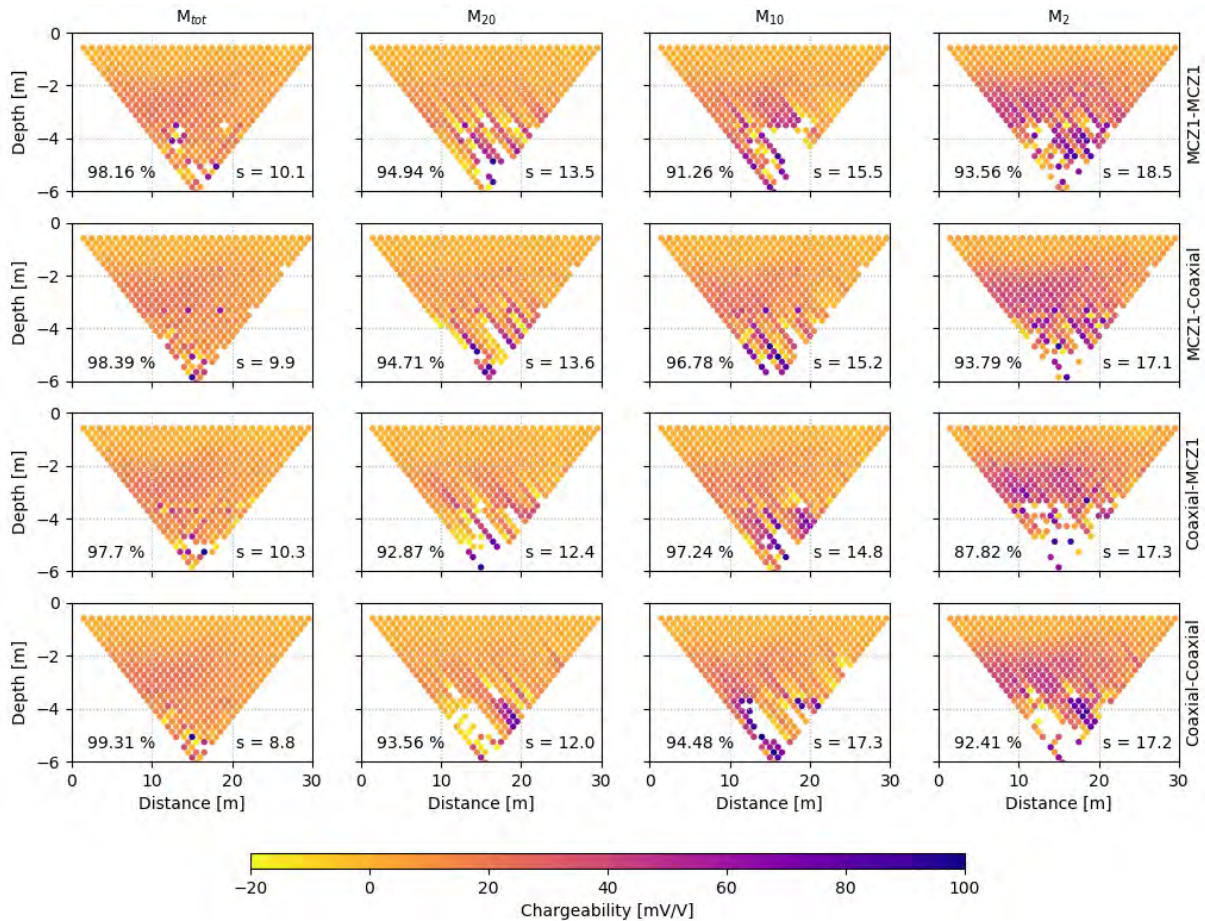
552

553 *Figure 7: Pseudosections for TDIP data collected (with a pulse length of 2000 ms) at the*
 554 *HOAL site using 32 electrodes with a separation of 1 m between them and multicore cables*
 555 *with 1 m and 10 m separation between take-outs (MCZ1 and MCZ10 respectively), as well as*
 556 *a coaxial cable with 5 m separation between take-outs. The label indicates the total of*
 557 *remaining measurements after removal of outliers and the standard deviation (s) in the phase*
 558 *readings.*

559

560 For completeness, we present in Figure 8 the pseudosections for TDIP data collected with
 561 separated cables and single coaxial cable, for the measurements conducted with a pulse length
 562 of 500 ms. As discussed above similar trends are observed for TDIP collected with 2000 ms;
 563 thus, such pseudosections are not presented. In Figure 8 we also present pseudosections for
 564 data collected with two separated coaxial cables (one for current and a second one for
 565 potential dipoles), to avoid redundancy with previous results. Pseudosections presented in
 566 Figure 8 show practically full pseudosections (less than 3 % of the data removed as outliers)

567 with high spatial consistency ($s < 10$) for integral chargeability values (M_{tot}). However, our
 568 data show larger discrepancies in early time readings for deep measurements (pseudodepth $>$
 569 4 m), which are related to large separations between current and potential dipoles, as
 570 mentioned above.



571

572 *Figure 8: Pseudosections for TDIP data collected (with a pulse length of 500 ms) at the*
 573 *HOAL site using 32 electrodes with a separation of 1 m between them and two cables to*
 574 *separate the current and potential dipole: a combination of short multicore cables (MCZ1-*
 575 *MCZ1), the combination of coaxial and multicore cable (MCZ1-coaxial and vice versa), and*
 576 *the combination of coaxial-coaxial cables (each one with a spacing of 5 m between take-outs).*
 577 *The label indicates the total of remaining measurements after removal of outliers and the*
 578 *standard deviation (s) in the phase readings.*

579 The distortion observed in early time TDIP measurements cannot be avoided even if two
580 coaxial cables are used to separate current and potential dipoles. It might be argued that such
581 distortion is only visible for the deep measurements, where the lowest S/N are expected.
582 Nonetheless, it might also highlight that coupling effects cannot be neglected in TDIP
583 measurements in early times. These cable effects might be even more important for the case
584 of voltage measurements at earlier times in case of full-wave form collections. Although not
585 investigated here, our results may be of special interest for TDIP measurements performed in
586 100 % duty cycle, i.e., for measurements of the charging curve during the current injection
587 (e.g., Olsson et al., 2015). Based on our study, the use of the coaxial cables might further
588 enhance the quality of the TDIP data, when the chargeability measurements are collected
589 during the current injection. As demonstrated before, the use of coaxial cables significantly
590 reduces cable effects in IP readings, permitting to collect data with better quality than
591 common procedures deploying separated cables (c.f., Figure 4 and Figure 5).

592 The use of multicore cables, either as a single or separated cable layout reveal a decrease in
593 the quality of the data for both FDIP and TDIP measurements. However, the distortion of the
594 TDIP data are much lower, taking into account that sampling of the decay-curve starts only
595 after the current injection is switch-off; thus, minimizing the influence of parasitic EM fields
596 only to early time readings. Different corrections methods taking into account the geometry of
597 the cables (e.g., Zhao et al., 2015) can still be performed to further improve the quality of the
598 phase measurements at higher frequencies, yet the application of such corrections is beyond
599 the scope of the present study. Likewise, the collection of IP data deploying other
600 configurations characterized by higher S/N, such as Wenner or Multiple-Gradient, are also not
601 addressed within this study as they do not provide new insights into the discussion. Our
602 results suggest that FDIP measurements should not be collected with a single multicore cable.

CONCLUSIONS

603
604 Our results show that SIP phase measurements collected with single multicore cables already
605 at low frequencies 0.5 Hz might be distorted by coupling effects taking place within the cable.
606 SIP data collected at low frequencies with long multicore cables (5 m separation between
607 take-outs) revealed moderately clean pseudosections only within the first 8 levels (i.e., a
608 maximum separation between current and potential dipoles of 8 electrodes); whereas shorter
609 multicore cables (1 m separation between take-outs) permitted to collect fairly clean
610 pseudosections up to ~12 levels. However, from the three multicore cables (MCX, MCY and
611 MCZ) tested here, only one of the short multicore cables (MCZ1) seems to provide clear
612 pseudosections at 7.5 and 15 Hz, yet only for shallow measurements (a maximum of 4 to 6
613 levels). Consistent to previous studies, multicore cables revealed an improved data quality in
614 comparison to single cables; however, the quality of the data is still dependent on the
615 construction and length of the multicore cables deployed, with cleaner pseudosections
616 observed only for those collected with short cables (1 m spacing in the take-outs).

617 In particular, our results demonstrate that the use of coaxial cables permit to collect SIP data
618 with high quality even if the cable is much longer than the actual separation between
619 electrodes. Hence, it might be sufficient to have a good set of coaxial cables to perform
620 surveys with different geometries, unlike having to deploy different multicore cables to adjust
621 for different electrode separations. Additionally, the use of coaxial cables permits to double
622 the depth of investigation in SIP surveys when compared to those performed with single or
623 separate layout of multicore cables.

624 Our results reveal that the use of coaxial cables permits to deploy the same field procedures
625 for the collection of SIP data as used for ERT surveys. Moreover, our results show that the
626 deployment of coaxial cables further increases the depth of investigations based on relative

627 simple field procedures, and thus, represent a first step to make the SIP imaging an attractive
628 method for applications beyond research and academia.

629

630

631

REFERENCES

632 Aal, G.Z.A., L.D. Slater, and E.A. Atekwana, 2006, Induced-polarization measurements on
633 unconsolidated sediments from a site of active hydrocarbon biodegradation: *Geophysics*,
634 **71**(2), H13-H24.

635 Atekwana, E. A., and L.D Slater, 2009, Biogeophysics: A new frontier in Earth science
636 research: *Reviews of Geophysics*, **47**(4).

637 Blöschl, G., A.P. Blaschke, M. Broer, C. Bucher, G. Carr, X. Chen, A. Eder, M. Exner-
638 Kittridge, A. Farnleitner, A. Flores-Orozco, and P. Haas, 2016, The Hydrological Open Air
639 laboratory (HOAL) in Petzenkirchen: a hypothesis-driven observatory: *Hydrology and Earth
640 System Sciences*, **20**(1), 227-255.

641 Binley, A., S.S. Hubbard, J.A. Huisman, A. Revil, D.D. Robinson, K. Singha, and L.D. Slater,
642 2015, The emergence of hydrogeophysics for improved understanding of subsurface
643 processes over multiple scales: *Water resources research*, **51**(6), 3837-3866.

644 Binley, A., J. Keery, L.D. Slater, W. Barrash, and M. Cardiff, 2016, The hydrogeologic
645 information in cross-borehole complex conductivity data from an unconsolidated
646 conglomeratic sedimentary aquifer: *Geophysics*, **81**(6), E409-E421.

647 Binley, A. and A. Kemna, 2005, DC resistivity and induced polarization methods. In
648 *Hydrogeophysics*. Springer, Dordrecht. 129-156.

- 649 Börner, F.D., J.R. Schopper, and A. Weller, 1996, Evaluation of transport and storage
650 properties in the soil and groundwater zone from induced polarization measurements.
651 Geophysical prospecting, **44**(4), 583-601.
- 652 Bücken, M., A. Flores Orozco, A., A. Kemna, 2018, Electrochemical polarization around
653 metallic particles—Part 1: The role of diffuse-layer and volume-diffusion relaxation:
654 Geophysics, **83**(4), E203-E217.
- 655 Bücken, M., S. Undorf, A. Flores Orozco, A. Kemna, 2019, Electrochemical polarization
656 around metallic particles—Part 2: The role of diffuse surface charge. Geophysics, **84**(2), E57-
657 E73.
- 658 Corona-Lopez, D. D.J., S. Sommer, S. A. Rolfe, F. Podd, and B. D. Grieve, 2019, Electrical
659 impedance tomography as a tool for phenotyping plant roots: Plant methods **15**(1), 15-49.
- 660 Dahlin, T., V. Leroux, and J. Nissen, 2002, Measuring techniques in induced polarisation
661 imaging: Journal of Applied Geophysics, **50**(3), 279-298.
- 662 Dahlin, T. and M. H. Loke, 2015, Negative apparent chargeability in time-domain induced
663 polarisation data: Journal of Applied Geophysics, 123, 322-332.
- 664 Doetsch, J., T. Ingeman-Nielsen, A.V. Christiansen, G. Fiandaca, E. Auken, and B. Elberling,
665 2015, Direct current (DC) resistivity and induced polarization (IP) monitoring of active layer
666 dynamics at high temporal resolution: Cold Regions Science and Technology, 119, 16-28.
- 667 Fiandaca, G., 2018, Induction-free acquisition range in spectral time-and frequency-domain
668 induced polarization at field scale: Geophysical Journal International.
- 669 Flores Orozco, A., M. Bücken, M. Steiner, and J.P. Malet, 2018a, Complex-conductivity
670 imaging for the understanding of landslide architecture: Engineering geology, 243, 241-252.

- 671 Flores Orozco, A., J. Gallistl, M. Bucker, and K.H. Williams, 2018b. Decay curve analysis for
672 data error quantification in time-domain induced polarization imaging: *Geophysics*, **83**(2),
673 pp.E75-E86.
- 674 Flores Orozco, A., A. Kemna, A. Binley, and G. Cassiani, 2019b, Analysis of time-lapse data
675 error in complex conductivity imaging to alleviate anthropogenic noise for site
676 characterization: *Geophysics*, **84**(2), B181-B193.
- 677 Flores Orozco, A., A. Kemna, C. Oberdörster, L. Zschornack, C. Leven, P. Dietrich, P. and
678 Weiss, H., 2012a, Delineation of subsurface hydrocarbon contamination at a former
679 hydrogenation plant using spectral induced polarization imaging. *Journal of Contaminant*
680 *Hydrology*, *136*, 131-144.
- 681 Flores Orozco, A., A. Kemna, and E. Zimmermann, 2012b, Data error quantification in
682 spectral induced polarization imaging. *Geophysics*, **77**(3), E227-E237.
- 683 Flores Orozco, A., V. Micić, M. Bucker, J. Gallistl, T. Hofmann, and F. Nguyen, 2019a,
684 Complex-conductivity monitoring to delineate aquifer pore clogging during nanoparticles
685 injection: *Geophysical Journal International*, *218*, 1838-1852
- 686 Flores Orozco, A., M. Velimirovic, T. Tosco, A. Kemna, H. Sapon, N. Klaas, R. Sethi, and
687 L. Bastiaens, 2015, Monitoring the injection of microscale zerovalent iron particles for
688 groundwater remediation by means of complex electrical conductivity imaging:
689 *Environmental science and technology*, **49**(9), 5593-5600.
- 690 Flores Orozco, A., K.H. Williams, P. Long, S.S. Hubbard, and A. Kemna, 2011, Using
691 complex resistivity imaging to infer biogeochemical processes associated with bioremediation
692 of an uranium-contaminated aquifer: *Journal of Geophysical Research: Biogeosciences*,
693 *116*(G3).

- 694 Flores Orozco, A., K.H Williams, and A. Kemna, 2013, Time-lapse spectral induced
695 polarization imaging of stimulated uranium bioremediation: *Near Surface Geophysics*, **11**(5),
696 531-544.
- 697 Gallistl, J., M. Weigand, M. Stumvoll, D. Ottowitz, T. Glade, and A. Flores Orozco, 2018,
698 Delineation of subsurface variability in clay-rich landslides through spectral induced
699 polarization imaging and electromagnetic methods: *Engineering geology*, **245**, 292-308.
- 700 Gasperikova, E., and H.F Morrison, 2001, Mapping of induced polarization using natural
701 fields: *Geophysics*, **66**, 137–147
- 702 Hallof, P. G., 1974, The IP phase measurement and inductive coupling: *Geophysics* **39**(5),
703 650-665
- 704 Huisman, J.A., E. Zimmermann, O. Esser, F.H. Haegel, A. Treichel, and H. Vereecken, 2016,
705 Evaluation of a novel correction procedure to remove electrode impedance effects from
706 broadband SIP measurements: *Journal of Applied Geophysics*, **135**, 466-473.
- 707 Kemna, A., A. Binley, A. Ramirez, and W. Daily, 2000, Complex resistivity tomography for
708 environmental applications: *Chemical Engineering Journal*, **77**, 11-18.
- 709 Kemna, A., A. Binley, C. Cassiani, E. Niederleithinger, A. Revil, L.D. Slater, W. Williams,
710 A. Flores Orozco, F.H. Haegel, A. Hoerdt, and S. Kruschwitz, 2012, An overview of the
711 spectral induced polarization method for near-surface applications: *Near Surface Geophysics*,
712 **10**(6), 453-468.
- 713 Martin, T. and T. Günther, 2013, Complex resistivity tomography (CRT) for fungus detection
714 on standing oak trees: *European journal of forest research*, **132**(5-6), 765-776.
- 715 Leroy, P. and A. Revil, 2009, A mechanistic model for the spectral induced polarization of
716 clay materials. *Journal of Geophysical Research: Solid Earth*, **114**(B10).

- 717 Ntarlagiannis, D., K.H. Williams, L.D. Slater, and S.S. Hubbard, 2005, Low-frequency
718 electrical response to microbial induced sulfide precipitation. *Journal of Geophysical*
719 *Research: Biogeosciences*, 110(G2).
- 720 Pelton, W. H., S.H. Ward, P.G. Hallof, W.R. Sill, and P.H. Nelson, 1978, Mineral
721 discrimination and removal of inductive coupling with multifrequency IP: *Geophysics*, 43(3),
722 588-609.
- 723 Radic, T., 2016, September. New Modular Multi-channel Field Equipment for SIP
724 Measurements up to 20 kHz. In *Near Surface Geoscience 2016-22nd European Meeting of*
725 *Environmental and Engineering Geophysics*.
- 726 Revil, A., E. Atekwana, C. Zhang, A. Jardani, and S. Smith, 2012b, A new model for the
727 spectral induced polarization signature of bacterial growth in porous media: *Water Resources*
728 *Research*, 48(9).
- 729 Revil, A. and N. Florsch, 2010, Determination of permeability from spectral induced
730 polarization in granular media. *Geophysical Journal International*, 181(3), 1480-1498.
- 731 Revil, A., M. Karaoulis, T. Johnson, and A. Kemna, 2012a, Some low-frequency electrical
732 methods for subsurface characterization and monitoring in hydrogeology. *Hydrogeology*
733 *Journal*, 20(4), 617-658.
- 734 Seigel, H., M. Nabighian, D.S. Parasnis, and K. Vozoff, 2007, The early history of the
735 induced polarization method: *The Leading Edge*, 26(3), 312-321.
- 736 Slater, L., A. Binley, W. Daily, and R. Johnson, 2000, Cross-hole electrical imaging of a
737 controlled saline tracer injection. *Journal of applied geophysics*, 44(2-3), 85-102.

- 738 Slater, L., D. Ntarlagiannis, Y.R. Personna, and S.S. Hubbard, 2007, Pore-scale spectral
739 induced polarization signatures associated with FeS biomineral transformations: Geophysical
740 Research Letters, 34(21).
- 741 Telford, W.M., L.P. Geldart, and R.E. Sheriff, 1990. Applied geophysics (Vol. 1). Cambridge
742 university press.
- 743 Wainwright, H.M., A. Flores Orozco, M. Bucker, B. Dafflon, J. Chen, S.S. Hubbard, and
744 K.H. Williams, 2016, Hierarchical Bayesian method for mapping biogeochemical hot spots
745 using induced polarization imaging. Water Resources Research, 52(1), 533-551.
- 746 Weigand, M. and A. Kemna, A., 2019, Imaging and functional characterization of crop root
747 systems using spectroscopic electrical impedance measurements: Plant and Soil, 435(1-2),
748 201-224.
- 749 Weller, A., L.D. Slater, and S. Nordsiek, 2013, On the relationship between induced
750 polarization and surface conductivity: Implications for petrophysical interpretation of
751 electrical measurements: Geophysics, 78(5), D315-D325.
- 752 Williams, K.H., A. Kemna, M.J. Wilkins, J. Druhan, E. Arntzen, A.L.N'Guessan, P.E. Long,
753 S.S. Hubbard, and J.F. Banfield, 2009, Geophysical monitoring of coupled microbial and
754 geochemical processes during stimulated subsurface bioremediation: Environmental Science
755 and Technology, 43(17), 6717-6723.
- 756 Slater, L. and A. Binley, 2006, Synthetic and field-based electrical imaging of a zerovalent
757 iron barrier: Implications for monitoring long-term barrier performance: Geophysics 71(5),
758 B129-B137.
- 759 Zhao, Y., E. Zimmermann, J.A. Huisman, A. Treichel, B. Wolters, S. van Waasen, and A.
760 Kemna, 2013, Broadband EIT borehole measurements with high phase accuracy using

761 numerical corrections of electromagnetic coupling effects: Measurement Science and
762 Technology, 24(8), 085005.

763 Zhao, Y., E. Zimmermann, J.A. Huisman, A. Treichel, B. Wolters, S. van Waasen, and A.
764 Kemna, 2014, Phase correction of electromagnetic coupling effects in cross-borehole EIT
765 measurements: Measurement science and technology, 26(1), 015801.

766 Zimmermann, E., J.A. Huisman, A. Mester, and S. van Waasen, 2019, Correction of phase
767 errors due to leakage currents in wideband EIT field measurements on soil and sediments:
768 Measurement science and technology, 30(8), 084002.

769 Zimmermann, E., A. Kemna, J. Berwix, W. Glaas, and H. Vereecken, 2008, EIT measurement
770 system with high phase accuracy for the imaging of spectral induced polarization properties of
771 soils and sediments: Measurement science and technology, 19(9), 094010.

772

773

774

775

1 Imaging biogeochemical active zones in landfills with induced polarization

2

3

4 A. Flores-Orozco¹, J. Gallistl¹, M. Steiner¹, C. Brandstätter², and J. Fellner²

5 ¹TU-Wien, Department of Geodesy und Geoinformation, Geophysics Research Unit

6 ²TU Wien, Institute for Water Quality and Resource Management

7

8 Manuscript submitted Waste Management Journal

9

10
11
12
13
14
15
16
17
18
19
20
21
22
23
24
25
26
27
28
29
30
31
32
33

Abstract

Here we investigate the applicability of the Induced Polarization (IP) imaging method to discriminate between biogeochemically active and inactive areas of a landfill. Elevated amount of degradable organic carbon in landfills results in the development of biogeochemical hot spots associated with high rates of microbial activity and the generation of landfill gas and leachate as metabolic products. The delineation of such hot pots is needed for the design of adequate stabilization systems and minimization of the environmental impact of landfills. Our results demonstrate that the electrical conductivity is mainly sensitive to the increase in the fluid conductivity associated to leachate production and migration. Whereas images of the polarization effect, expressed in terms of the phase of the complex conductivity (ϕ), revealed an improved contrasts to characterize variations in the architecture and activity of the landfill. Our results reveal that biogeochemically active zones (leachable TOC contents above 1500 mg/kg dry waste) are related to high polarization values ($\phi > 50$ mrad), whereas low leachable TOC contents (< 300 mg/kg dry waste) in the inactive areas are characterized by low polarization values ($10 > \phi > 25$). Additionally, landfill sections corresponding to construction and demolition waste (CDW), associated to negligible TOC content, exhibited the lowest polarization response ($\phi < 15$). We prove that IP imaging is a well-suited method for landfill investigations permitting an improved characterization of landfill geometry, variation in waste composition, and the delineation of biogeochemically active and inactive zones.

Keywords: municipal solid waste; geophysical imaging methods; electrical conductivity; induced polarization; landfills; microbiological active zones

34

1. Introduction

35 Within the last years, there has been a growing interest in the economical exploitation of
36 landfills, either for energy production or for the mining of raw materials. For landfill mining,
37 the characterization of the internal structure and waste composition is critical for an adequate
38 valorization of the landfill economic potential. Landfill investigations with high spatial
39 resolution are also critical for environmental protection, for instance to evaluate the potential
40 release of pollutants associated to landfill leachate production (Rinne et al., 2005; Fellner et
41 al., 2009), or the emission of landfill gas (Chiemchaisri et al., 2007; Laner et al., 2011,
42 Ritzkowski and Stegmann, 2013). In this regard, a high content of organic matter disposed in
43 municipal solid waste (MSW) landfills may enhance the development of biogeochemical hot-
44 spots associated with high rates of microbial activity, resulting in the production of landfill
45 gas and leachate as metabolic products. The accumulation of landfill gas accompanying
46 microbial activity in MSW landfills may result in spontaneous combustion and fires (Frid et
47 al., 2010). Furthermore, MSW landfills are responsible for ~ 5 % of the global greenhouse gas
48 emissions (Zhang et al., 2019), which may continue for decades after landfill closure
49 (Christensen and Kjeldsen, 1989; Huber-Humer et al., 2008; Laner et al., 2012; Brandstätter
50 et al., 2015). Therefore, understanding microbial activity in landfills is critical to reduce the
51 production of methane (CH₄) and carbon dioxide (CO₂) and minimize their environmental
52 impact.

53 The availability of MSW containing high amount of organic carbon stimulate the activity of
54 fermentative and acid-forming bacteria being able to degrade waste biomass into organic
55 acids, carbon dioxide (CO₂) and hydrogen, whereas CO₂ and carbonic acids stimulate the
56 activity of methanogenic bacteria, resulting in the emission of methane (CH₄) as a metabolic
57 product (Barlaz et al., 1990). Beside the content of organic matter, other factors such as the
58 moisture content or redox conditions prevailing in the landfill (presence or absence of

59 oxygen) strongly determine the metabolic products, in particular the generation of methane
60 (Gurijala and Suflita, 1993). Landfill aeration systems, based on air injections into the landfill,
61 switch degradation processes from anaerobic and aerobic, which increases the production of
62 CO₂ and H₂O, but at the same time hinders the generation of CH₄ (Ritzkowski et al., 2006).
63 Although water is produced during aerobic waste degradation, the water content of the
64 landfilled waste tends to decrease, as the temperature of waste increases and a significantly
65 higher volume of water saturated off gas is released in comparison to anaerobic degradation.
66 Accordingly, a detailed characterization of waste composition, landfill geometry and internal
67 structure is critical to evaluate the landfill potential for the generation of greenhouse gasses,
68 and the design of adequate stabilization systems.

69 To date, landfill characterization still relies on chemical analyses of soil, water and gas
70 samples. Although these provide direct concentration of chemical parameters and the waste
71 composition, the number and distribution of samples limit the resolution of the investigation.
72 While increasing the number of samples can improve the resolution of the investigations, high
73 number of samples and analyses, may render landfill investigations prohibitively expensive.
74 Thus, ex-situ studies commonly rely on data interpolation, which may bias the interpretation
75 of the results given the spatial (and temporal) variability and complexity of landfills.
76 Geophysical methods have proven to be well suited for landfill investigations with adequate
77 spatial and temporal resolution, as they provide quasi-continuous spatial and temporal
78 information about subsurface properties in a non-invasive manner (Konstantaki et al., 2013;
79 2016; Soupios and Ntarlagiannis, 2017; Nguyen et al., 2018 and references therein).

80 In particular, the electrical resistivity tomography (ERT) has become a widely-used method
81 for landfill investigations considering its sensitivity to variations in water content, salinity and
82 temperature, as demonstrated in the review by Nguyen et al (2018). Particularly, the decrease
83 in the electrical resistivity due to an increase in salinity and fluid conductivity permits the

84 application of ERT to delineate leachate production, migration and leakages (e.g., De Carlo et
85 al., 2013; Tsourlos et al., 2014). Additionally, temporal variations in the electrical resistivity
86 images have also been used for the characterization of water content changes within the
87 landfill (e.g., Dumont et al., 2018; Neyamadpour, 2019). Furthermore, the Induced
88 Polarization (IP) method has also proven to be a useful technique to improve the lithological
89 characterization of landfills (e.g., Dahlin et al., 2010; Gazoty et al., 2012). As an extension of
90 the ERT technique, the IP method gains information about the electrical conductivity and
91 capacitive properties of the subsurface, with the latter being related to the polarization of the
92 ions in the electrical double layer (EDL) formed at the fluid-grain interface during the
93 injection of an electric field.

94 The IP method was initially applied for the prospection of metallic ores due to the strong
95 polarization observed in electronic conductors and semi-conductors (Seigel et al., 2007).
96 However, recent laboratory investigations have demonstrated a high sensitivity of the method
97 to textural parameters of soil and rocks; thus, its applicability for the characterization of
98 subsurface hydraulic properties (e.g., Revil et al., 2015a; Binley et al., 2015; Osterman et al.,
99 2019). Additionally, laboratory experiments revealed that the high surface area of microbial
100 cells may also be subject of polarization allowing the IP method to delineate biofilm
101 formation (Ntarlagiannis et al., 2005; Revil et al., 2012), as well as microbiologically
102 mediated processes (Atekwana and Slater, 2009 and references therein). Field IP
103 measurements conducted during biostimulation of iron-reducing bacteria for the
104 immobilization of radionuclides have confirmed the ability of the method to characterize
105 changes in microbial activity (e.g., Williams et al., 2009), the accompanying variations in
106 redox-status (Flores Orozco et al., 2011) and the precipitation of biominerals (Flores Orozco
107 et al., 2013). Based on such findings, the method has been used recently to map (at the

108 floodplain scale) naturally reduced zones (i.e., biogeochemical hot-spots), characterized by
109 high IP response due to the presence of iron sulfides (Wainwright et al., 2016).

110 Built on results mentioned above, we propose here the IP as a method to differentiate between
111 biogeochemically active and inactive zones in MSW landfills. Considering that active zones
112 behave as biogeochemical hot-spots, we expect a moderate to high IP response and low
113 electrical resistivity values, associated to the precipitation of secondary minerals and the
114 accumulation of organic acids accompanying high rates of microbial activity. IP
115 measurements are performed in a MSW landfill being stabilized by means of in-situ aeration,
116 were biogeochemical active zones are then related to elevate production of CO₂. Additionally,
117 we investigate the ability of the IP method for an improved characterization of landfill
118 geometry and waste composition.

119 In the next section, we present the details of the IP method and a review of the current
120 conduction mechanisms required for an adequate interpretation of the imaging results. This is
121 followed by the description of the study area and the geophysical survey. In a third section,
122 we present the IP imaging results and discuss their interpretation, followed by our
123 conclusions. To the authors' knowledge, this is the first study to apply the IP method for
124 delineating biogeochemically active (i.e., hot-spots) and inactive zones in landfills.

125

126

2. Material and methods

127 2.1 The induced polarization (IP) method and the complex conductivity (σ^*)

128 The IP imaging method is an extension of the ERT, and is also based on current injection
129 through an electrode pair, while a second pair measures the resulting voltages. Measurements
130 can be performed either in time domain (TDIP) or in the frequency domain (FDIP) depending
131 on the characteristics of the measuring device, with TDIP typically working with direct

132 current (DC) and FDIP with alternating current (AC). In this study, we will focus on TDIP
 133 measurements, considering that these can be collected with the majority of commercially
 134 available ERT instruments. In TDIP, current injection is performed using a square-wave (i.e.,
 135 switching the current injection on – off – on – off), and the measurements are commonly
 136 expressed in terms of the measured resistance (R), corresponding to the voltage-to-current
 137 ratio (V/I) during the current injection (i.e., primary field), and the integral chargeability (M),
 138 which measures the voltage decay after current switch-off. This secondary field (i.e., the
 139 voltage decay) develops due to the polarization of the free charges in the electrical double
 140 layer at the grain-fluid interface (illustrated in Figure 1), which dissipates over time after
 141 switching the current off. Hence, the IP method provides information about the low frequency
 142 capacitive (i.e., energy storage) and conductivity (i.e., energy loss) electrical properties of the
 143 subsurface, while ERT only measures the conductivity.

144 Imaging applications deploy hundreds of electrodes to solve for 2D sections or 3D models of
 145 the subsurface electrical properties by means of data inversion. The inversion of the ERT data
 146 provides subsurface models in terms of the electrical resistivity (ρ), or its inverse the electrical
 147 conductivity ($\rho=1/\sigma$). The inversion of TDIP data can be expressed in terms of the complex
 148 resistivity (ρ^*), i.e., complex conductivity ($\rho^*=1/\sigma^*$), which permits to represent both the
 149 conductive and capacitive properties of the subsurface. The real component of the complex
 150 conductivity (σ') represents the energy loss, i.e., conduction; whereas the imaginary
 151 component (σ'') represents the energy storage, i.e., polarization. Alternatively, the σ^* can also
 152 be given in terms of its magnitude ($|\sigma|$) and phase (ϕ), such as:

$$153 \quad 1/\rho^* = \sigma^* = \sigma' + i\sigma'' = |\sigma|e^{i\phi}, \quad (1)$$

154 where $i = \sqrt{-1}$. In most practical applications, measured phase shifts are sufficiently small ($<$
 155 100 mrad) to assume that $\sigma' \approx |\sigma|$ and to approximate the phase ϕ with the ratio between
 156 real and imaginary component, i.e. $\phi \approx \sigma''/\sigma'$. A detailed review of the TDIP and FDIP

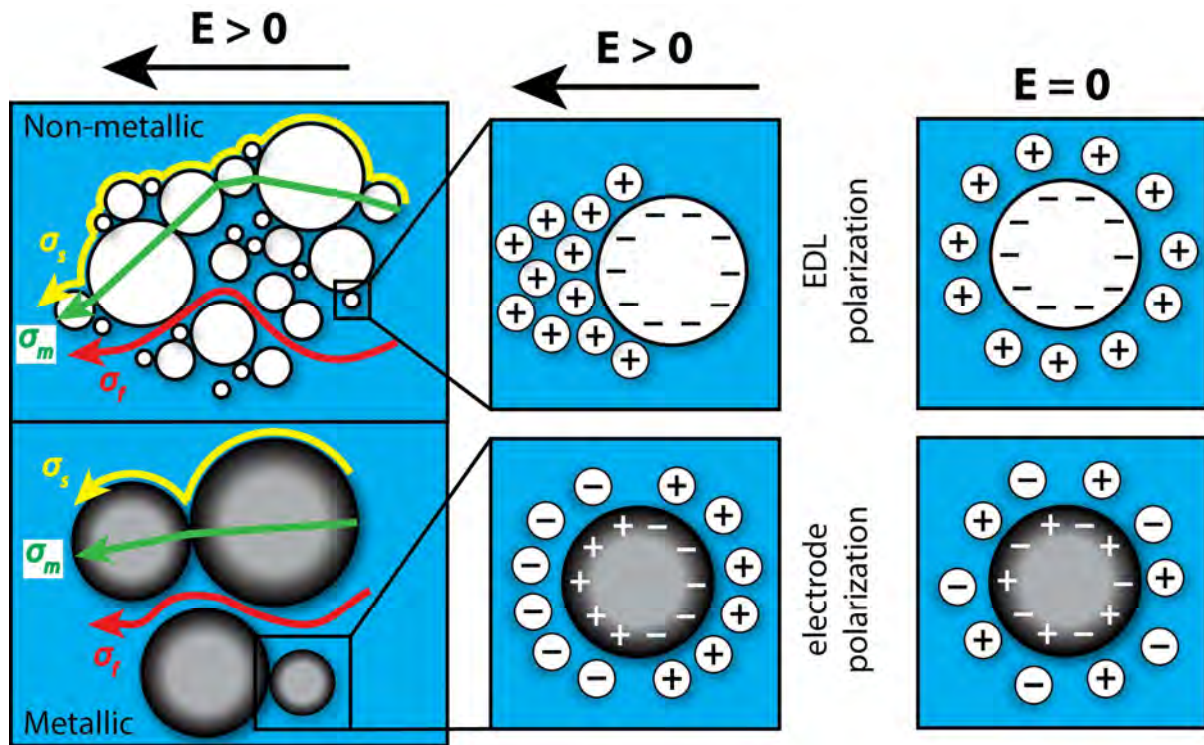
157 method can be found in Sumner (1976), Ward (1988), and Binley and Kemna (2005),
 158 amongst others.

159 **2.2 Conduction mechanisms in the subsurface, i.e., landfills – the importance of the** 160 **surface conduction to understand electrical signatures**

161 As illustrated in Figure 1, the complex conductivity in the subsurface, i.e., in landfills, is
 162 controlled by three mechanisms acting in parallel: matrix, ionic and surface conduction (e.g.,
 163 Waxman and Smits, 1968; Ward, 1988). The matrix conduction (σ_m) takes place along the solid
 164 phase (relevant only for metals and other materials permitting electronic conduction); ionic or
 165 electrolytic (σ_f) conduction through the fluid-filled pore space; and (σ_s) surface conduction
 166 along the electrical double layer (EDL) formed at the fluid-grain interface. While σ_m and σ_f
 167 contribute only to the ohmic conduction, the surface conduction is complex-valued contributing
 168 to both, conduction and polarization. Accordingly, the real component of the complex
 169 conductivity can be written as:

$$170 \quad \sigma' = \sigma_f + \sigma_m + \sigma'_s, (2)$$

171 The electrolytic conductivity (σ_f) is controlled primarily by the porosity and the interconnection
 172 between pores (i.e., tortuosity) as well as by the saturation and the conductivity of the pore
 173 water (σ_w) parameter of interest in landfill investigations. Commonly high electrical
 174 conductivity (σ') values in landfill investigations are associated to high volumes of
 175 (interconnected) metallic waste due to the contribution of matrix, i.e., electronic conduction
 176 (σ_m). However, a larger increase in the electrical conductivity (σ') is expected in fine-grained
 177 materials (e.g., silt, clay and organic matter), which are characterized by a high surface area and
 178 charge and, thus, contributing to surface conduction (e.g., Revil et al., 2017). Although
 179 commonly ignored, surface conduction can dominate over electrolytic conduction even for the
 180 case of clean sandstones i.e., clay-free (e.g., Revil et al., 2014).



181

182 Figure 1: Schematic representation of low frequency subsurface conduction mechanisms, i.e.,
 183 in landfills: matrix (σ_m), electrolytic (σ_f), and surface (σ_s) conduction. The subplots illustrate
 184 the distribution of charges in the electrical double layer (EDL) formed at the grain-fluid
 185 interface of non-metallic (top) and metallic (bottom) minerals before and during the injection
 186 of an electric current.

187 As illustrated in Figure 1, for any grain in contact with an electrolyte, the surface charge of the
 188 grains will attract counterions (ions from the opposite charge) from the electrolyte forming the
 189 EDL, which describes the inner and outer layers of the ions cloud formed in the electrolyte. The
 190 inner layer, or Stern layer, is formed by the ions adsorbed at the grain surface, whereas the outer
 191 layer, or diffuse layer, is populated by co-ions at some distance from the grain surface (e.g.,
 192 Schwarz, 1962; Leroy et al., 2008). The movement of the ions in the Stern layer is restricted to
 193 the grain surface, whereas in the diffuse layer it is unrestricted within the electrolyte. Hence,
 194 current injections enhance the migration of the ions in the diffuse layer and the polarization of
 195 the Stern layer, causing an excess of charge responsible for the surface conduction (σ_s). The

196 imaginary component of the complex conductivity is only related to the imaginary component
197 of the surface conduction, such as:

$$198 \quad \sigma'' = \sigma_s'', (3)$$

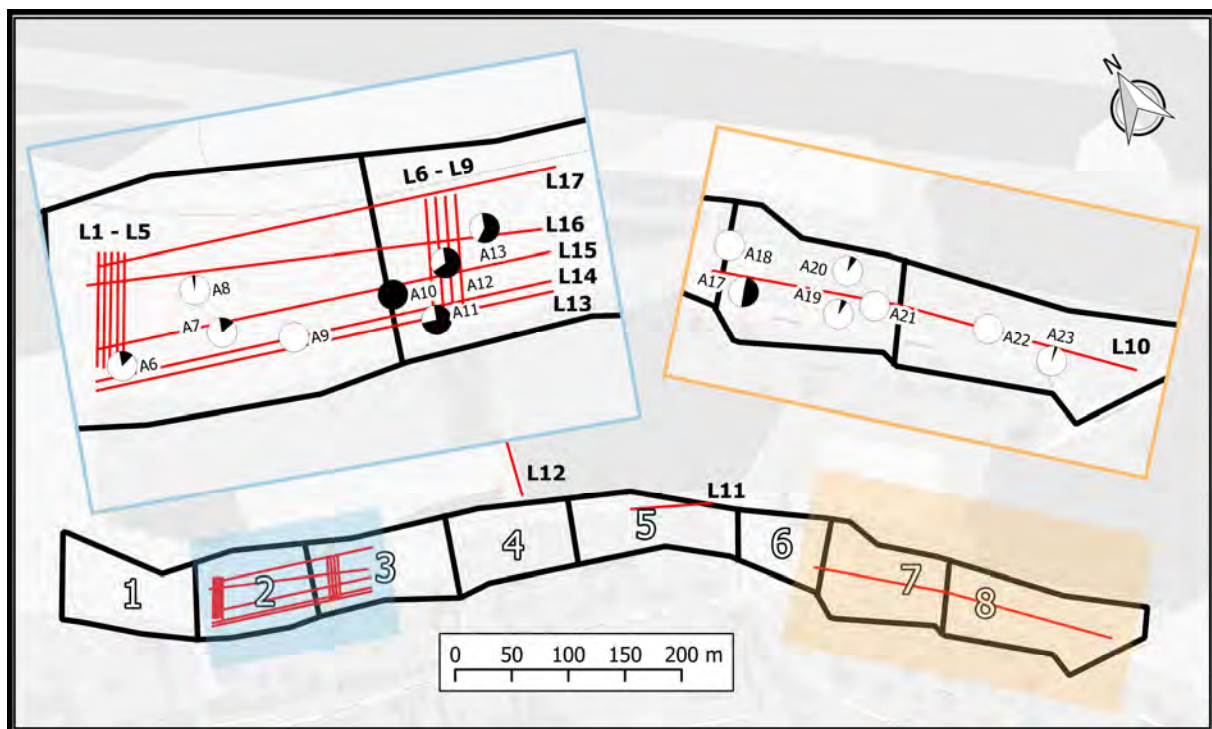
199 In case of the metal-free sediments, the polarization of the Stern layer is what causes the
200 secondary electrical field in IP measurements. This polarization effect is dependent on the
201 electrochemical properties of the interface, such as surface charge and surface area (Leroy et
202 al., 2008; Revil et al., 2014; 2017). In case of metallic minerals, as also illustrated in Figure 1,
203 the application of an external field (i.e., current injection) also enhances the polarization of the
204 electronic semi-conductor, thus, resulting in a stronger polarization effect, the so-called
205 electrode polarization mechanism. A revision on the electrode polarization mechanism is
206 presented in detail in Bückner et al. (2018 and 2019). Additionally, the models proposed by
207 Revil et al. (2015b) and Misra et al. (2016) consider the reduction of the electronic conduction
208 following the full polarization of the metals and electronic conductors, taking into account
209 that a perfect capacitor is characterized by a net zero electrical conductivity.

210 **2.3 Study area: the Heferlbach landfill**

211 Geophysical measurements were collected at the “Heferlbach” landfill, situated close to
212 Vienna (Austria), where 219,000 m³ of waste were disposed between 1965 and 1973. The
213 landfill is about 950 m long with a width varying between 50 and 150 m, and an average
214 thickness of 3.5 m; the groundwater table is found at a depth of approx. 10 m below the
215 bottom of the landfill. The disposed waste consists mainly of municipal solid waste (MSW,
216 660 kg/t moist mass), excavated soil (180kg/t moist mass) and construction and demolition
217 waste (CDW, 160 kg/t moist mass). The landfill has no membrane and leachate is not
218 collected; yet, it is fully equipped with an aeration system in order to accelerate the
219 biodegradation of organic matter aiming at mitigating subsurface migration of landfill gas into

220 neighboring buildings. The air is injected close to the bottom of the landfill and the off-gas
 221 generated is extracted and treated via bio-filter. For technical and operational reasons, the
 222 landfill was divided into eight sections (lengths varying between 80 to 140 m), which can be
 223 aerated at different rates. The latter is crucial insofar as the share of biodegradable waste (i.e.,
 224 MSW) varies considerably between the different sections (see Table 2 in the supplementary
 225 information), but also within each section, as illustrated in figure 2. Analyses of waste
 226 samples revealed pH values fluctuating around 7, water content varying between 14 and 30%,
 227 and an fluid electrical conductivity in the range between 0.3 and 2.6 mS/cm (see
 228 supplementary information). For further details about the landfill and the aeration system, we
 229 refer to and the studies of Brandstätter et al. (2016) and Fellner et al. (2015).

230



231

232 Figure 2: Geometry of the Heferbach landfill, with different areas delineating the
 233 investigation zones regarding different rates of bio-geochemical activity (directly linked to
 234 different contents of MSW). The red lines indicate the position and orientation of the IP data

235 collected along the different bio-geochemical zones of the landfill. The pie charts illustrate the
236 amount of total organic carbon (TOC) in leachate measured at different sampling points (i.e.,
237 excavations).

238

239 **2.4 IP survey – data collection and inversion**

240 IP measurements were collected using the Syscal Pro Switch 72 equipment (from IRIS
241 Instruments), using a 50 % duty cycle square wave with a pulse length of 500 milliseconds
242 (ms). Measurements were conducted along 17 profiles distributed in relevant areas of the
243 landfill (as depicted in Figure 2), and areas near excavations points, where samples were
244 collected for their chemical analysis (see supplementary information). The number of
245 electrodes, position, orientation, and the length of the different IP profiles is presented in Table
246 1. As shown in Figure 2, profiles L1 to L5 are located within landfill section 2, which is
247 characterized by low contents of MSW and thus biodegradable waste, as indicated also by low
248 contents of total organic carbon (TOC) in the leachate of the solid samples taken at the
249 excavation points A5 to A8 (see Table 3 in the Supplementary Information). Within this study,
250 we used the TOC contents measured in leachate samples as an indicator of microbial activity.
251 Profiles L6 to L9 are located in landfill section 3, corresponding to high contents of
252 biodegradable waste, as indicated by the TOC leachate contents at excavation points A10 to
253 A13 (see Table 3 in the Supplementary Information). Profile L10 was designed to go through
254 landfill sections 7 and 8, corresponding to a lateral change from organic to construction waste.
255 As illustrated in Figure 2, L10 extends from moderate high to low contents of biodegradable
256 matter, as indicated by the TOC leachate contents at excavation points A17 to A21 in section 7
257 (see Table 3 in the Supplementary Information), as well as the lowest TOC leachate content,
258 corresponding to CDW in excavation point A22 and A23. Profiles L11 and L12 were collected
259 at the border and a few meters away of the landfill to characterize the IP response of natural

260 lithology. Additionally, five roughly parallel lines (L13 to L17) were collected to map the
 261 variations between landfill sections 2 and 3, corresponding to the lowest and highest TOC
 262 contents within MSW; their distribution dictated by the existing vegetation in the landfill
 263 hindering the layout of parallel profiles.

Profile	Length (m)	# electrodes	Separation electrodes (m)	Orientation	Landfill segment	Landfill composition
1 - 5	35.0	36	1.0	N - S	2	MSW
5 - 9	35.5	72	0.5	N - S	3	MSW
10	270.0	271	1.0	E - W	7 and 8	MSW and CDW
11	71.0	72	1.0	E - W	5	MSW
12	71.0	72	1.0	N - S	--	--
13 - 17	143.0	144	1.0	E - W	2 and 3	MSW

264 Table 1: General description of the induced polarization (IP) profiles

265 The separation between electrodes was adjusted to 0.5 and 1 m according to the dimensions of
 266 the landfill, considering that increasing the electrode separation increases the depth of
 267 investigation, but decreases the lateral and vertical resolution. For the data collection, we used
 268 a dipole-dipole configuration, combining dipole lengths of 1, 2 and 3 times the separation
 269 between electrodes (i.e., DD skip 0, 1, and 2 as for example described by Flores Orozco et al.,
 270 2018a). To avoid the contamination of the data due to polarization of the electrodes themselves,
 271 the measuring sequence was designed to perform voltage measurements in electrodes always
 272 in front of the current dipole, avoiding voltage measurements with electrodes previously used
 273 for current injection. Using these settings, data collection for each profile took ca. 10 and 20
 274 minutes, for acquisitions with 36 and 72 respectively.

275 All datasets were inverted with CRTomo (by Kemna, 2000), a complex resistivity inversion
 276 algorithm, using the sensitivity-controlled focusing regularization scheme described in
 277 (Blaschek et al., 2008), which allows to solve for models with enhanced contrast compared to
 278 commonly used smoothness-constrained regularization. Moreover, CRTomo permits the
 279 inversion of the data to a confidence level determined by an error model to enhance the

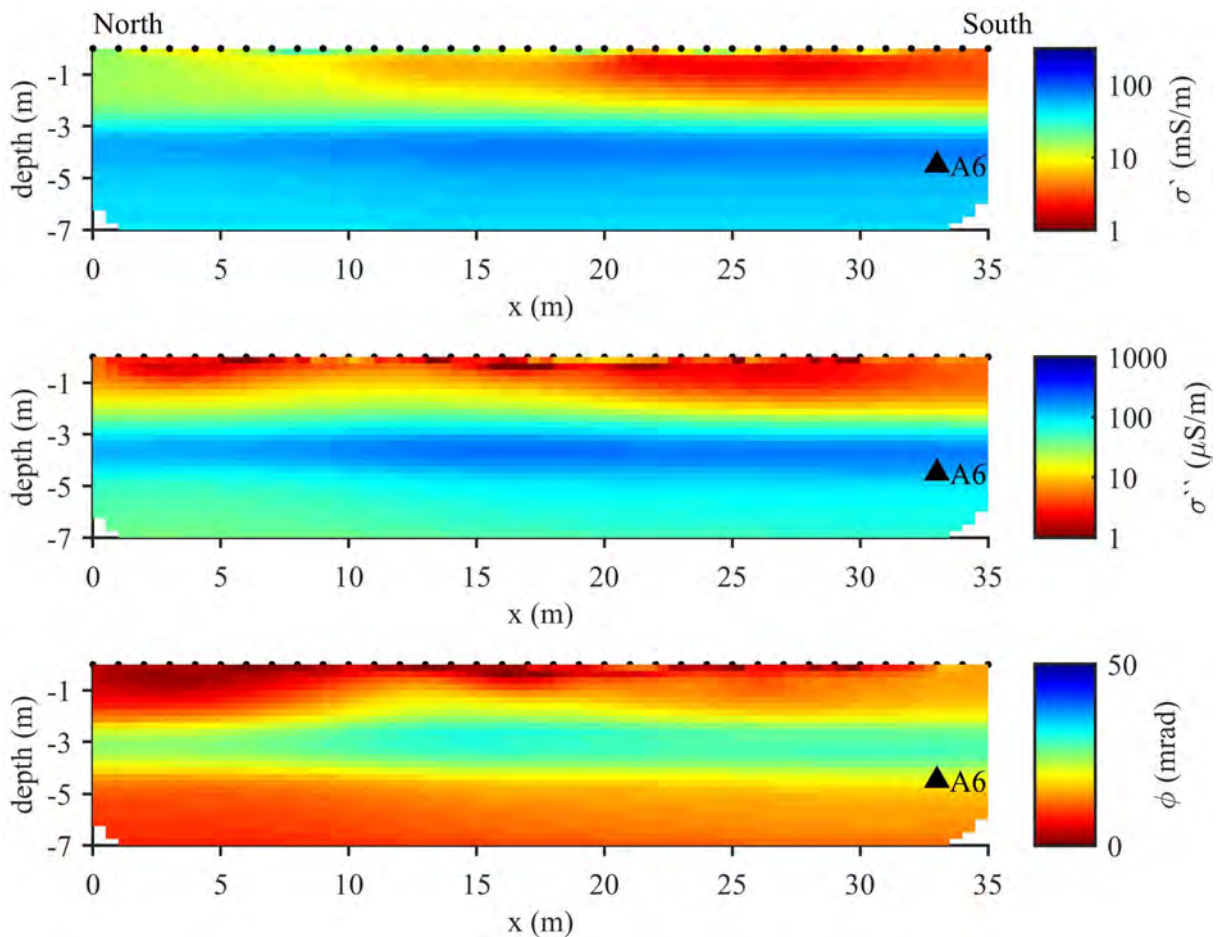
280 resolution of the electrical images and minimizing the risk of artifacts (e.g., Flores Orozco et
 281 al., 2012a). Prior to the inversion, outliers and data-error parameters were characterized through
 282 the analysis of the spatial consistency of the apparent chargeability measurements within each
 283 data set (i.e., for each independent profile), following a similar approach as Flores Orozco et al.
 284 (2018b).

285

286

3. Results and Discussion

287 3.1 Low active zones – using IP images to characterize landfill geometry



288

289 Figure 3: IP imaging results for data collected at L3 expressed in terms of the real (σ') and
 290 imaginary (σ'') component of the complex conductivity (first and second row respectively), as
 291 well as their ratio expressed in terms of the phase of the complex conductivity (ϕ). The black

292 dots at the top of each figure represent the position of the electrodes, while the triangles
293 indicate the bottom of the landfill as observed during excavations for the collection of
294 samples for ex-situ analyses, with the label indicating the number of the sample.

295

296 In Figure 3, we present the IP imaging results for data collected along L3 in an area of low
297 contents of MSW and thus biodegradable waste (see supplementary material). The imaging
298 results are expressed in terms of the real (i.e., electrical conductivity, σ') and imaginary (i.e.,
299 the polarization effect, σ'') components of the complex conductivity, revealing, in general,
300 three main layers. The shallowest layer, characterized by the lowest conductivity ($\sigma' < 5$
301 mS/m) and polarization ($\sigma'' < 5 \mu\text{S/m}$) values, corresponds to the unsaturated sand and silty
302 soils (~ 0.5 m thick) and a top waste unit (thickness between ca. 0.5 and 1 m) of excavated
303 soils and CDW (values of $\sigma' \sim 10$ mS/m and $\sigma'' \sim 5 \mu\text{S/m}$). Lateral variations within this layer
304 are interpreted as changes in the thickness of the CDW and silt content. The second layer
305 shows the highest electrical conductivity ($\sigma' > 100$ mS/m) and polarization ($\sigma'' > 100 \mu\text{S/m}$)
306 values corresponding to the MSW extending between approximately 1.5 and 4.5 m depth.
307 This layer reveals a varying thickness of the waste unit, which becomes slightly thinner to the
308 south of the landfill. Below this unit, at the expected position of the natural soils (gravel and
309 sands, with varying clay content), the electrical images reveal still high conductivity values (\sim
310 75 mS/m), yet only a moderate polarization response ($\sim 50 \mu\text{S/m}$). Inverted models for data
311 collected along L1, L2, L4 and L5 revealed results consistent with those presented in Figure 3
312 (data not shown for brevity).

313 Considering that some parameters such as salinity, temperature, porosity and saturation
314 control both components of the complex conductivity (σ'' , σ'), it is also common to present IP
315 results in terms of the phase of the complex conductivity (ϕ). Figure 3 reveals the highest ϕ
316 values corresponding to the MSW (between ca. 2 and 4.5 m depth), whereas much lower

317 values are observed in the top (soils and CDW) and bottom (sand and gravel from the host
318 formation) layers. The polarization effect in the MSW presented in Figure 3 is much higher
319 than the one observed in clay-rich sediments (ϕ between 10 and 20 mrad, or σ'' values of a
320 few hundreds of $\mu\text{S}/\text{m}$, as presented in Flores Orozco et al., 2018a). Such high IP response is
321 common in the presence of metals, due to electrode polarization mechanisms (e.g., Bückner et
322 al., 2018). However, no metallic waste (except of a few coins and tools found in the waste
323 sample taken) was reported in the excavated samples (A5 to A8) near the L1 - L5 profiles.

324 MSW is related to the high volumes of organic matter (e.g., Castaldi et al., 2005), which is
325 characterized by high surface area and surface charge (Schwartz and Furman, 2014).

326 Therefore, we explain the increase in the polarization response (ϕ as well as σ'') in the MSW
327 unit as a consequence of the polarization of the Stern layer from organic matter, similar to the
328 response observed in peat (Ponziani et al., 2012). The polarization effect is further enhanced
329 by the increase in fluid conductivity due to carbonic and organic acids (e.g., Revil and Skold,
330 2011; Weller et al., 2015; Hördt et al., 2016), as well as by a potential decrease in water
331 saturation (Jougnot et al., 2010) imposed by the aeration system. Evidence of microbial
332 activity is given by the contents of TOC in the leachate of the solid samples A5 to A8 (near
333 the position of the profile), with the polarization of biofilms representing another possible
334 contribution to the polarization response. However, field investigations have revealed that
335 field IP measurements may not be sensitive enough to the weak response of biofilms and
336 microbial cells (e.g., Flores Orozco et al., 2011; 2013).

337 In general, the layer characterized by the highest conductivity values (σ') can be used to
338 define the geometry of the landfill. However, the actual thickness of this unit is poorly
339 resolved at depth. This can be explained by the lack of contrasts in the electrical properties of
340 the landfill and the geological unit below it. Considering that the Heferbach landfill is not
341 isolated, the increase in the fluid conductivity due to leakage of leachates explains the high

342 conductivity values observed below the landfill (depth > 4.5 m), where much lower values are
343 theoretically expected due to the presence of gravel and coarse sand. Opposite to this,
344 polarization images (ϕ as well as σ'') provide a much sharper contrasts at a depth of ~ 4.5 m,
345 which corresponds to the bottom of the landfill, as reported from excavations at the site. Thus,
346 IP images provide a more accurate delineation of landfill geometry than investigations
347 performed only with ERT, sensitive only to σ' (e.g., Leroux et al., 2007; Dahlin et al., 2010;
348 Ustra et al., 2010; Gazoty et al., 2012).

349 **3.2 High IP response in biogeochemical active zones (hot-spots)**

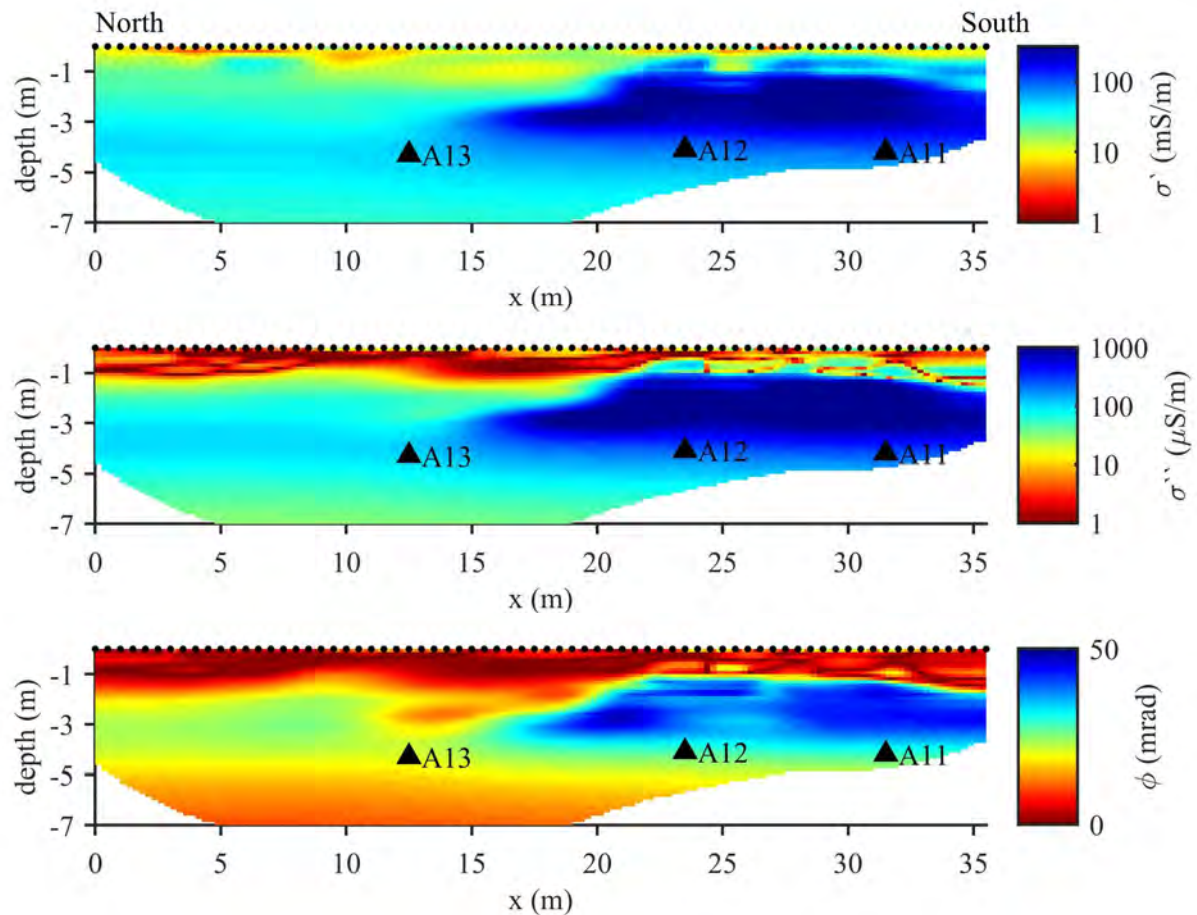
350 Figure 4 presents the imaging results for data collected along profile L6, in the landfill section
351 3, where high rates of microbial activity are expected due to the high TOC leachate contents
352 at excavation points A10 to A13 (see supplementary material). Inversion results for data
353 collected along L7 to L9 revealed a similar distribution of the complex conductivity (data not
354 shown for brevity). The imaging results show three main units consistent to those resolved for
355 profile L3 presented before. Based on data collected with a shorter separation between
356 electrodes (0.5 instead of 1 m), the cover layer is better resolved, with a thickness of ~ 50 cm,
357 corresponding to low conductivity and IP values ($\sigma' < 10$ mS/m and $\sigma'' < 10$ μ S/m
358 respectively). Accordingly, the natural sand and gravel sediments below the landfill also
359 revealed consistent results to previous lines L1 to L5, characterized by a similar IP response
360 ($\sigma'' < 100$ μ S/m and $\phi < 10$ mrad). However, the MSW in L6 to L9 reveals a much larger
361 polarization effect (both $\sigma'' > 500$ μ S/m and $\phi > 40$ mrad) than those observed in L1 to L5
362 ($\sigma'' > 100$ μ S/m and $\phi > 25$ mrad).

363 Based on excavations, the geometry of the MSW landfill near L6 is defined between ca. 0.5
364 and 5 m. Hence, the image of the phase appears to provide an accurate model of the
365 subsurface, with the MSW corresponding to the second layer with high values ($\phi > 15$ mrad).
366 Similar to the discussion above, the phase image reveals a higher contrast between the organic

367 waste and the natural sediments, than the image of the imaginary component (σ'').

368 Furthermore, the electrical conductivity (σ') again reveals poor contrasts in areas below the
369 main polarizable unit, hindering a proper delineation of landfill geometry. In accordance to
370 discussions above, the increase in both σ' and σ'' is explained by the increase in both organic
371 matter and fluid conductivity (σ_f) accompanying high rates of microbial activity, as evidenced
372 by the large production of CO₂ extracted from this landfill section.

373 Moreover, higher concentrations of biodegradable carbon (see supplementary materials and
374 TOC values of samples taken from the points A10 to A13, illustrated in Figure 2) agree with
375 high polarizable anomaly to the south of the profile. Hence, the IP images appear to be
376 sensitive to not only the landfill geometry and waste composition, as well as to bio-
377 geochemical activity. As suggested above, the increase in organic matter in MSW triggers
378 both the polarization effect and the stimulation of microbial activity (associated with the
379 production of CO₂ and leachate). The higher production of leachate and CO₂ can be suggested
380 by the 28.8 % increase in the fluid conductivity reported in samples A10 to A13 in
381 comparison to those in samples A5 to A8 (around L1 to L5), which could be indicative of
382 high microbial activity.



383

384 Figure 4: IP imaging results for data collected at L6 expressed in terms of the real (σ') and
 385 imaginary (σ'') component of the complex conductivity (first and second row respectively), as
 386 well as their ratio expressed in terms of the phase of the complex conductivity (ϕ). The black
 387 dots at the top of each figure represent the position of the electrodes, while the triangles
 388 indicate the bottom of the landfill as observed during excavations for the collection of
 389 samples for ex-situ analyses, with the label indicating the number of the sample.

390

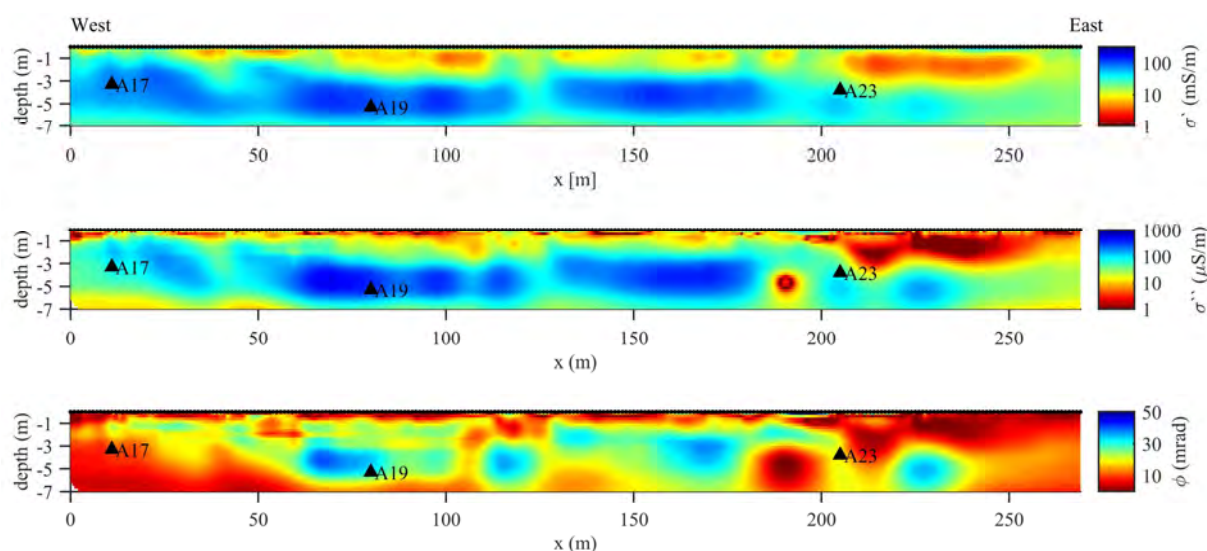
391

392 3.3 Using IP images to delineate changes in waste composition

393 To further investigate the applicability of the IP method for discriminating between

394 biogeochemically active and inactive areas, we present in Figure 5 the IP imaging results for

395 data collected along L10, which extends from MSW to CDW (see Table 3 in the
 396 Supplementary Information). In areas containing mainly MSW, high rates of microbial
 397 activity are expected considering the high TOC leachate contents, whereas CDW landfills
 398 represent biogeochemically inactive zones, as evidenced by the lowest TOC and negligible
 399 CO₂ production (Brandstätter et al., submitted). The electrical images in Figure 5 are
 400 consistent to those presented in Figure 3 and Figure 4, represented by three main layers. The
 401 waste unit is located between 0.5 and 5 m depth, with important lateral variations in ϕ images,
 402 whereas plots of the real and imaginary components (σ' and σ'') reveal practically the same
 403 features.



404
 405 Figure 5: IP imaging results for data collected at L10 expressed in terms of the real (σ') and
 406 imaginary (σ'') component of the complex conductivity (first and second row respectively), as
 407 well as their ratio expressed in terms of the phase of the complex conductivity (ϕ). The black
 408 dots at the top of each figure represent the position of the electrodes, while the triangles
 409 indicate the bottom of the landfill as observed during excavations for the collection of
 410 samples for ex-situ analyses, with the label indicating the number of the sample.

411

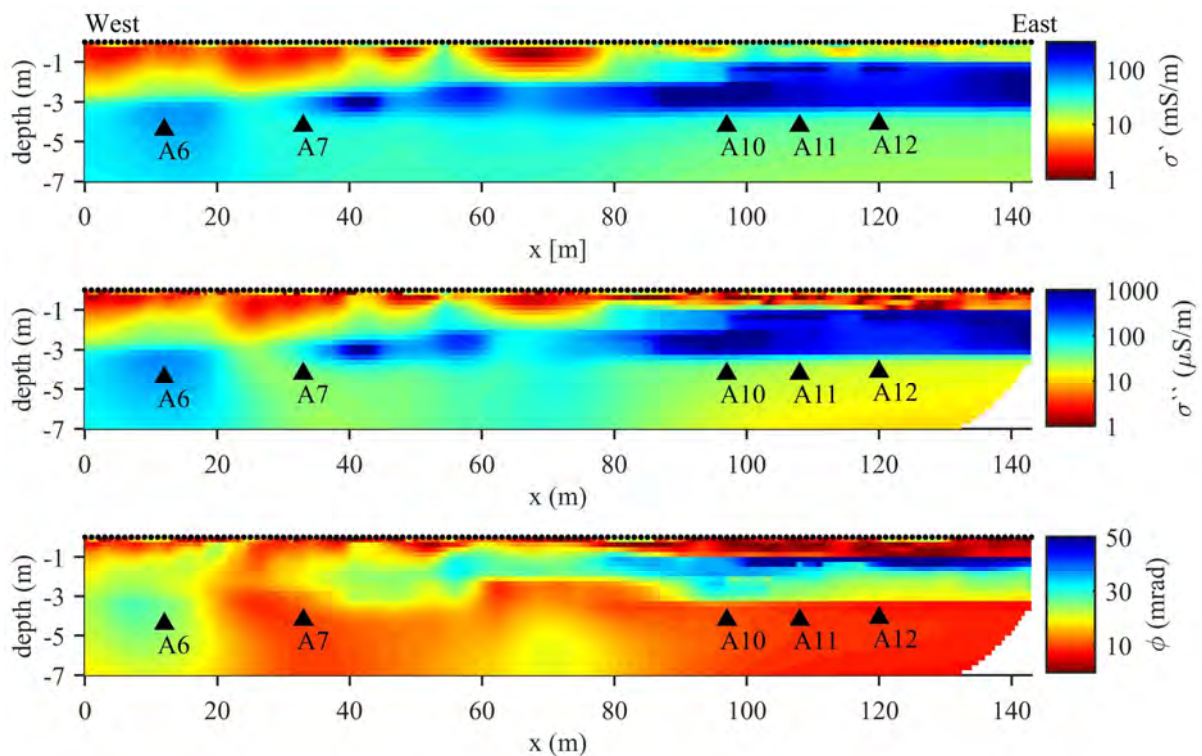
412 Consistent with previous results and information from the site, the top layer is resolved with a
413 thickness varying between 1 and 1.5 m, which consists of the cover material and excavated
414 soils. Underneath, highly conductive and polarizable material characterizes the landfill, with
415 the gravel and sandy sediments on the bottom associated with a low polarization response.
416 Moreover, Figure 5 reveals that the contact between MSW and CDW is located at ca. 210 m
417 along profile direction, characterized by a lateral change in the electrical properties from high
418 to moderate σ' , σ'' and ϕ values (for instance, $\phi < 15$ mrad in case of CDW and at least 2
419 times higher values for MSW).

420 The construction waste is characterized by a low surface area and, in case of non-metallic
421 surfaces, it also is characterized by low surface charge; thus, it is related to negligible IP
422 response (σ'' and ϕ), as revealed in the eastern part of profile L10. The presence of dry CDW
423 is responsible for low electrical conductivity values (σ') considering the associated low
424 saturation and fluid conductivity. However, deeper areas, on the east part of profile L10,
425 reveal moderate conductivity values (ca. 50 mS/m), which may suggest the presence of pore
426 water enhancing electrolytic conduction (σ_f in Equation 1) to a certain extent. The polarizable
427 anomaly found at ca. 225 m (along profile direction) may be related either to exposed metal or
428 the presence of wet fine grains (clay and silt) filling pores and enhancing surface conduction
429 mechanisms through the polarization of the EDL. However, no information is available to
430 confirm this interpretation.

431 In Figure 6 we present the imaging results for profile L15, extending from landfill section 2 to
432 3, both characterized by MSW, but different rates of microbial activity, as indicated by the
433 variable TOC contents in leachate samples. These imaging results are consistent with those
434 obtained for data collected along L13 to L17. Figure 6 reveals large variations in the electrical
435 properties, both laterally and vertically, stressing the complexity in landfill internal structure
436 and composition. In particular, the images reveal a lateral contact approximately at 80 m

437 along the profile direction. Model parameters to the east side of the profile (between 100 and
 438 140 m) evidence much higher conductivity values (σ'), in agreement with the high TOC
 439 concentrations reported in samples A10 to A13 over the samples A6 to A9 located on the west
 440 side of the profile. The increase in the salinity might also explain the increase in the
 441 polarization response observed in σ'' images. As suggested before, the phase images may be
 442 the best option to delineate the position of microbiologically active zones (or hot-spots),
 443 considering that they represent the ratio of two properties affected by pore-space geometry
 444 and fluid conductivity. Hence, in case of profile L13, the zone of microbiological activity is
 445 located between 80 and 120 m along profile direction and between 1 and 3.5 m depth. Such
 446 findings are in agreement with high production rate of CO₂ reported above (e.g., Brandstätter
 447 et al., submitted).

448



449

450 Figure 6: IP imaging results for data collected at L15 expressed in terms of the real (σ') and
 451 imaginary (σ'') component of the complex conductivity (first and second row respectively), as

452 well as their ratio expressed in terms of the phase of the complex conductivity (ϕ). The black
453 dots at the top of each figure represent the position of the electrodes, while the triangles
454 indicate the bottom of the landfill as observed during excavations for the collection of
455 samples for ex-situ analyses, with the label indicating the number of the sample.

456

457 Figure 5 and 6 reveal the capability of the IP method to discriminate between different waste
458 compositions in landfills. Based on our results, we may propose following categories:

459 (1) Low conductivity and phase values ($\sigma' < 15$ mS/m, $\sigma'' < 15$ μ S and $\phi < 15$ mrad):

460 corresponding to negligible microbial activity with no gas production and, thus, the lower
461 polarization response. Such response should be expected for CDW landfills or excavated
462 soils without organic matter.

463 (2) Moderate conductivity and phase values ($\sigma' < 80$ mS/m, $\sigma'' < 100$ μ S and $10 > \phi > 20$

464 mrad): corresponding to dry MSW or waste with low content of organic matter, resulting
465 in low rates of microbial activity and thus low gas and leachate production.

466 (3) High conductivity but moderate phase values ($\sigma' \sim 100$ mS/m, $\sigma'' \sim 500$ μ S and $20 > \phi <$

467 30 mrad): corresponding to MSW with some content of organic matter and potential for
468 the production of biogas. Increasing concentrations of leachate and fine grains result in
469 the increase of fluid and surface conductivity contributing to both σ' , σ'' and thus yielding
470 low ϕ values.

471 (4) Anomalous high phase values ($\sigma' > 200$ mS/m, $\sigma'' > 1000$ μ S and $\phi > 40$ mrad):

472 corresponding to bio-geochemically active zones in MSW with high organic matter,
473 which is responsible for high rates of microbial activity, as evidenced by high TOC
474 leachate contents. The high contents of organic matter result in high polarization (σ''),
475 which surpasses the high salinity and conductivity (σ'), thus, resulting in the highest

476 phase values in the landfill. Such zones need to be carefully monitored due to their
477 potential for the generation of methane, when air injection is terminated.

478

479

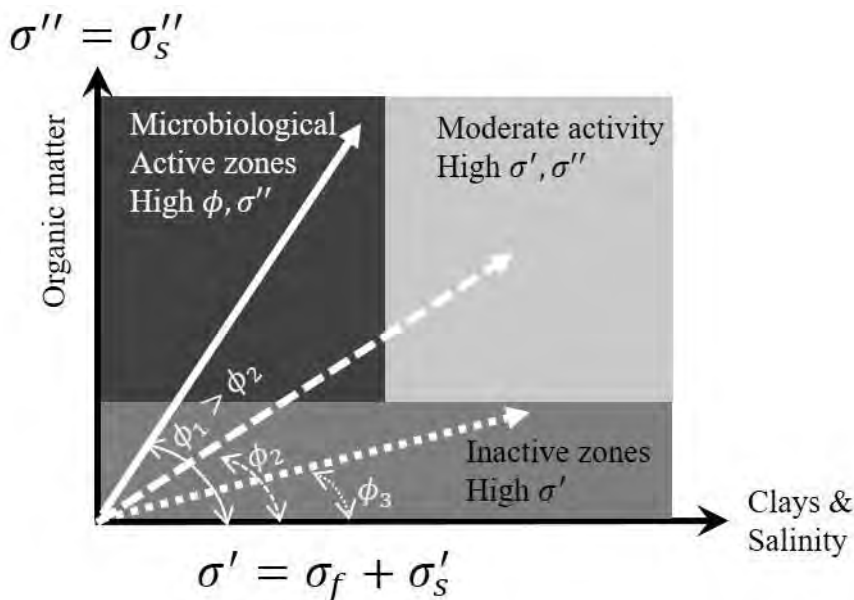
4. Conclusions

480 Our study clearly reveals the possibility to improve landfill investigations by the application
481 of induced polarization (IP) imaging methods. We demonstrated that IP imaging results
482 permit to solve for spatial variations with higher resolution than investigations solely based on
483 the analysis of excavated samples. Moreover, including images of the polarization effect,
484 either in terms of the imaginary component (σ'') or the phase (ϕ) of the complex conductivity,
485 permits an improved interpretation of the electrical conductivity, for instance to accurately
486 delineate the geometry of the landfill. The polarization effect is an important parameter in
487 landfill investigations, as it is sensitive to variations in the waste composition, especially to
488 the content of organic matter, whereas electrical conductivity appears to be dominated by the
489 increase in salinity related to leachate formation. Hence, the interpretation of landfill
490 geometry solely based on electrical conductivity images (i.e., resistivity methods) might be
491 biased due to the leachates extending below the actual contact of the landfill.

492 Polarization images (σ''), revealed a sharper contrasts between the landfill and the host
493 geology than the conductivity images (σ'); with even a better resolution observed in IP
494 imaging results expressed in terms of the phase (ϕ). The landfill geometry is properly
495 delineated by high ϕ values ($\phi > 10$ mrad), evidencing a higher polarization effect for MSW
496 than the one associated to subsurface materials. Moreover, we observed a positive correlation
497 between leachable TOC concentrations and ϕ , with the former used as an indicator of
498 microbiological activity. Accordingly, low ϕ values are observed in microbiologically inactive
499 areas; while the highest values are observed in microbiological hot-spots, associated to high
500 leachate and CO₂ production. Our results reveal that an increase in salinity (i.e., fluid

501 conductivity) plays only a secondary role in the polarization effect. Taking into account the
 502 negligible amount of metallic waste observed in samples, we suggest that the high
 503 polarization effect observed in our results is controlled by the presence of organic matter,
 504 characterized by high surface area and surface charge. Thus, IP imaging proves to be a non-
 505 invasive method to evaluate the biogeochemical status in landfills with high spatial resolution.

506 Our results show high polarization anomalies (σ'' and ϕ) in the MSW, whereas much lower
 507 values were resolved for CDW. We explain the increase in the polarization effect due to the
 508 presence of organic matter, characterized by high surface area and surface charge, two of the
 509 main parameters controlling the polarization of non-metallic materials. Thus, the IP method
 510 appears to be well-suited for the characterization of bio-geochemically active and inactive
 511 areas of the landfill. Based on our imaging results, we propose the conceptual model
 512 presented in Figure 7, which can be used for the interpretation of IP signatures in further
 513 landfill investigations.



514

515

516 Figure 7: Conceptual model proposed for the interpretation of IP imaging results for the
 517 Heferlbach landfill. IP results expressed in terms of the real, imaginary and phase of the

518 complex conductivity (σ' , σ'' , ϕ) can then be used to define active/inactive microbiological
 519 areas of the landfill. Highest ϕ values are related to high content of organic matter and
 520 potentially higher rates of microbial activity. Whereas the increase in σ' corresponds to an
 521 increase in salinity due to leachate production, or high contents of fine-grained materials
 522 associated to surface conduction mechanisms. Although not explicitly written, CDW is then
 523 related to low σ' , σ'' , ϕ values, as expected due to the low salinity, saturation and organic
 524 matter.

525
 526 However, a quantification of microbial rates based only on field data might still not be
 527 possible without further development of adequate models linking the electrical and
 528 geochemical parameters. Hence, further investigations at laboratory scale are required to
 529 permit the development of adequate geochemical models linking the IP parameters with gas
 530 production.

531 5. References

- 532 Atekwana, E. A., and Slater, L. D., 2009. Biogeophysics: A new frontier in Earth science
 533 research. *Reviews of Geophys*, 47(4). doi:10.1029/2009RG000285.
 534
 535 Barlaz, M.A., Ham, R.K., and Schaefer, D.M., 1990. Methane production from municipal
 536 refuse: A review of enhancement techniques and microbial dynamics. *Critical Reviews in*
 537 *Environmental Control*, 19(6), 557-584.
 538
 539 Binley, A., Hubbard, S.S., Huisman, J.A., Revil, A., Robinson, D.A., Singha, K. and Slater,
 540 L.D., 2015. The emergence of hydrogeophysics for improved understanding of subsurface
 541 processes over multiple scales. *Water resources research*, 51(6), 3837-3866.
 542 doi:10.1002/2015WR017016.
 543
 544 Binley, A., and Kemna, A., 2005. DC resistivity and induced polarization methods. In
 545 *Hydrogeophysics*, 129-156. Springer, Dordrecht. doi:10.1007/1-4020-3102-5_5
 546
 547 Blaschek, R., Hördt, A., and Kemna, A., 2008. A new sensitivity-controlled focusing
 548 regularization scheme for the inversion of induced polarization data based on the minimum
 549 gradient support. *Geophysics*, 73(2), F45-F54. doi:10.1190/1.2824820
 550

- 551 Brandstätter, C., Fellner, J., and Prantl, J., 2016. In-situ-Belüftung von Deponien in Feld und
552 Labor - Projekt "Heferlbach". Österreichische Wasser- und Abfallwirtschaft, 68:428.
553 doi:10.1007/s00506-016-0331-6
554
- 555 Brandstätter, C., Laner, D., and Fellner, J., 2015. Nitrogen pools and flows during lab-scale
556 degradation of old landfilled waste under different oxygen and water regimes.
557 Biodegradation, 26(5), 399-414.
558
- 559 Brandstätter, C., Prantl, R., and Fellner, J., submitted. Performance Assessment of Landfill in-
560 situ Aeration - a Case Study. Waste Management.
561
- 562 Bücken, M., Flores Orozco, A., Kemna, A., 2018. Electrochemical polarization around
563 metallic particles—Part 1: The role of diffuse-layer and volume-diffusion relaxation.
564 Geophysics, 83(4), E203-E217. doi:10.1190/geo2017-0401.1
565
- 566 Bücken, M., Undorf, S., Flores Orozco, A., and Kemna, A., 2019. Electrochemical
567 polarization around metallic particles — Part 2: The role of diffuse surface charge.
568 Geophysics, 84(2), E57-E73. doi:10.1190/geo2018-0150.1
569
- 570 Castaldi, P., Alberti, G., Merella, R. and Melis, P., 2005. Study of the organic matter
571 evolution during municipal solid waste composting aimed at identifying suitable parameters
572 for the evaluation of compost maturity. Waste Management, 25(2), 209-213.
573 doi:10.1016/j.wasman.2004.12.011
574
- 575 Chiemchaisri, C., Chiemchaisri, W., Kumar, S., and Hettiaratchi, J.P.A., 2007.
576 Solid waste characteristics and their relationship to gas production in tropical landfill.
577 Environmental Monitoring and Assessment, 135 (1-3), 41-48.
578
- 579 Christensen, T. H. and Kjeldsen, P., 1989. Basic Biochemical Processes in Landfills. In
580 Sanitary Landfilling: Process, Technology and Environmental Impact. Academic Press.
581
- 582 Dahlin, T., Rosqvist, H. and Leroux, V., 2010. Resistivity-IP mapping for landfill
583 applications. First Break, 28(8).
584
- 585 De Carlo, L., Perri, M.T., Caputo, M.C., Deiana, R., Vurro, M. and Cassiani, G., 2013.
586 Characterization of a dismissed landfill via electrical resistivity tomography and mise-à-la-
587 masse method. Journal of Applied Geophysics, 98, 1-10. doi:10.1016/j.jappgeo.2013.07.010
588
- 589 Dumont, G., Pilawski, T., Hermans, T., Nguyen, F. and Garré, S., 2018. The effect of initial
590 water distribution and spatial resolution on the interpretation of ERT monitoring of water
591 infiltration in a landfill cover. Hydrol. Earth Syst. Sci. Discuss. doi:10.5194/hess-2018-163
592
- 593 Fellner, J., Döberl, G., Allgairer, G. and Brunner, P.H., 2009. Comparing field investigations
594 with laboratory models to predict landfill leachate emissions. Waste Management, 29(6),
595 1844-1851. doi:10.1016/j.wasman.2008.12.022
596
- 597 Fellner, J., Brandstätter, C., and Laner, D., 2015. Landfill Gas Migration Modelling – A
598 Prerequisite for Determining Environmentally Compatible Gas Generation Rates. In: CD-
599 Proceedings Sardinia 2015, 15th International Waste Management and Landfill Symposium,
600 5-9 Oct. 2015, S. Margherita di Pula (Cagliari), Sardinia, Ed.: Cossu, R., Pinjing, H.,

- 601 Kjeldsen, P., Matsufuji, Y., Reinhart, D., Stegmann, R., CISA Publisher, Sardina, paper 119,
602 p 1-11, ISSN 2282-0027
603
- 604 Flores Orozco, A., Williams, K. H., Long, P. E., Hubbard, S. S., and Kemna, A., 2011. Using
605 complex resistivity imaging to infer biogeochemical processes associated with bioremediation
606 of an uranium-contaminated aquifer. *Journal of Geophysical Research: Biogeosciences*,
607 116(G3). doi:10.1029/2010JG001591
608
- 609 Flores Orozco, A., Kemna, A., Oberdörster, C., Zschornack, L., Leven, C., Dietrich, P., and
610 Weiss, H., 2012. Delineation of subsurface hydrocarbon contamination at a former
611 hydrogenation plant using spectral induced polarization imaging, *J. of Cont. Hydrology* 136-
612 137, 131-144. doi:10.1016/j.jconhyd.2012.06.001
613
- 614 Flores Orozco, A., Williams, K. H., and Kemna, A., 2013. Time-lapse spectral induced
615 polarization imaging of stimulated uranium bioremediation. *Near Surface Geophysics*, 11(5),
616 531-544. doi:10.3997/1873-0604.2013020
617
- 618 Flores Orozco, A., Bucker, M., Steiner, M., and Malet, J. P., 2018a. Complex-conductivity
619 imaging for the understanding of landslide architecture. *Engineering geology*, 243, 241-252.
620 doi:10.1016/j.enggeo.2018.07.009
621
- 622 Flores Orozco, A., Gallistl, J., Bucker, M., and Williams, K. H., 2018b. Decay curve analysis
623 for data error quantification in time-domain induced polarization. *Geophysics* 83 (2), E75 –
624 E86. doi:10.1190/geo2016-0714.1
625
- 626 Frid, V., Doudkinski, D., Liskevich, G., Shafran, E., Averbakh, A., Korostishevsky, N. and
627 Prihodko, L., 2010. Geophysical-geochemical investigation of fire-prone landfills.
628 *Environmental Earth Sciences*, 60(4), 787-798. doi:10.1007/s12665-009-0216-0
629
- 630 Gazoty, A., Fiandaca, G., Pedersen, J., Auken, E., Christiansen, A.V. and Pedersen, J.K.,
631 2012. Application of time domain induced polarization to the mapping of lithotypes in a
632 landfill site. *Hydrology and Earth System Sciences*, 16(6), 1793-1804. doi:10.5194/hess-16-
633 1793-2012
634
- 635 Gurijala, K. R., and Suflita, J. M., 1993. Environmental factors influencing methanogenesis
636 from refuse in landfill samples. *Environmental Science and Technology*, 27(6), 1176-1181.
637 doi:10.1021/es00043a018
638
- 639 Huber-Humer, M., Gebert, J., and Hilger, H. 2008. Biotic systems to mitigate landfill methane
640 emissions. *Waste Management and research*, 26 (1), 33-46.
641
- 642 Hördt, A., Bairlein, K., Bielefeld, A., Bucker, M., Kuhn, E., Nordsiek, S. and Stebner, H.,
643 2016. The dependence of induced polarization on fluid salinity and pH, studied with an
644 extended model of membrane polarization. *Journal of Applied Geophysics*, 135, 408-417.
645 doi:10.1016/j.jappgeo.2016.02.007
646
- 647 Jougnot, D., Ghorbani, A., Revil, A., Leroy, P. and Cosenza, P., 2010. Spectral induced
648 polarization of partially saturated clay-rocks: A mechanistic approach. *Geophysical Journal*
649 *International*, 180(1), 210-224. doi:10.1111/j.1365-246X.2009.04426.x
650
- 651 Kemna, A., 2000. *Tomographic Inversion of Complex Resistivity: Theory and Application*.

- 652 Der Andere Verlag Osnabrück, Germany.
653
- 654 Konstantaki, L.A., Draganov, D., Heimovaara, T., and Ghose, R., 2013. Imaging scatterers in
655 landfills using seismic interferometry: *Geophysics*, 78 (6), EN107-EN116.
656
- 657 Konstantaki, L.A., Ghose, R., Draganov, D., and Heimovaara, T., 2016. Wet and gassy zones
658 in a municipal landfill from P- and S-wave velocity fields: *Geophysics*, 81 (6), EN75-EN86.
659
- 660 Laner, D., Fellner, J. and Brunner, P.H., 2011. Future landfill emissions and the effect of final
661 cover installation—A case study. *Waste management*, 31(7), 1522-1531.
662 doi:10.1016/j.wasman.2011.02.022
663
- 664 Laner, D., Fellner, J., and Brunner, P.H., 2012. Site-specific criteria for the completion of
665 landfill aftercare. *Waste Manage. Res.* 30, 88–99. doi:10.1177/0734242X12453610
666
- 667 Leroux, V., Dahlin, T. and Svensson, M., 2007. Dense resistivity and induced polarization
668 profiling for a landfill restoration project at Härlöv, Southern Sweden. *Waste Management*
669 *and Research*, 25(1), 49-60. doi:10.1177/0734242X07073668
670
- 671 Leroy, P., Revil, A., Kemna, A., Cosenza, P., and Ghorbani, A. (2008). Spectral induced
672 polarization of water-saturated packs of glass beads. *J. Colloid Interface Sci*, 321(1), 103-117.
673
- 674 Misra, S., Torres-Verdín, C., Revil, A., Rasmus, J., and Homan, D., 2016. Interfacial
675 polarization of disseminated conductive minerals in absence of redox-active species—Part 2:
676 Effective electrical conductivity and dielectric permittivity. *Geophysics*, 81(2), E159-E176.
677 doi: <https://doi.org/10.1190/geo2015-0400.1>
678
- 679 Neyamadpour, A., 2019. 3D monitoring of volumetric water content using electrical
680 resistivity tomography in municipal solid waste landfill. *Environmental Earth Sciences*,
681 78(14), 426. doi:10.1007/s12665-019-8436-4
682
- 683 Nguyen, F., Ghose, R., Isunza Manrique, I., Robert, T., and Dumont, G. (2018). Managing
684 past landfills for future site development: A review of the contribution of geophysical
685 methods. In *Proceedings of the 4th International Symposium on Enhanced Landfill Mining*
686 (pp. 27-36).
687
- 688 Ntarlagiannis, D., Williams, K.H., Slater, L. and Hubbard, S., 2005. Low-frequency electrical
689 response to microbial induced sulfide precipitation. *Journal of Geophysical Research:*
690 *Biogeosciences*, 110(G2). doi:10.1029/2005JG000024
691
- 692 Osterman, G., Sugand, M., Keating, K., Binley, A., and Slater, L. (2019). Effect of clay
693 content and distribution on hydraulic and geophysical properties of synthetic sand-clay
694 mixtures. *Geophysics*, 84(4), E239-E253. doi:10.1190/geo2018-0387.1
695
- 696 Ponziani, M., Slob, E.C., Vanhala, H. and Ngan-Tillard, D.J.M., 2012. Influence of physical
697 and chemical properties on the low-frequency complex conductivity of peat. *Near Surface*
698 *Geophysics*, 10(6), 491-501. doi:10.3997/1873-0604.2011037
699
- 700 Revil, A. and Skold, M., 2011. Salinity dependence of spectral induced polarization in sands
701 and sandstones. *Geophysical Journal International*, 187(2), 813-824. doi:10.1111/j.1365-
702 246X.2011.05181.x

- 703
 704 Revil, A., Atekwana, E., Zhang, C., Jardani, A. and Smith, S., 2012. A new model for the
 705 spectral induced polarization signature of bacterial growth in porous media. *Water Resources*
 706 *Research*, 48(9). doi:10.1029/2012WR011965
 707
- 708 Revil, A., Kessouri, P, and Torres-Verdún, C., 2014. Electrical conductivity, induced
 709 polarization, and permeability of the Fontainebleau sandstone, *Geophysics*, 79(5), D301–
 710 D318, doi:10.1190/GEO2014-0036.1
 711
- 712 Revil, A., Binley, A., Mejus, L., and Kessouri, P., 2015a, Predicting permeability from the
 713 characteristic relaxation time and intrinsic formation factor of complex conductivity spectra:
 714 *Water Resources Research*, 51, 6672–6700. doi:10.1002/2015WR017074
 715
- 716 Revil, A., Florsch, N., and Mao, D., 2015b. Induced polarization response of porous media
 717 with metallic particles—Part 1: A theory for disseminated semiconductors. *Geophysics*, 80(5),
 718 D525-D538. doi:10.1190/geo2014-0577.1
 719
- 720 Revil, A., Coperey, A., Shao, Z., Florsch, N., Fabricius, I.L., Deng, Y., Delsman, J.R., Pauw,
 721 P.S., Karaoulis, M., de Louw, P.G.B. and van Baaren, E.S., 2017. Complex conductivity of
 722 soils. *Water Resources Research*, 53(8), 7121-7147. doi:10.1002/2017WR020655
 723
- 724 Rinne, J., Pihlatie, M., Lohila, A., Thum, T., Aurela, M., Tuovinen, J.P., Laurila, T. and
 725 Vesala, T., 2005. Nitrous oxide emissions from a municipal landfill. *Environmental science*
 726 *and technology*, 39(20), 7790-7793. doi:10.1021/es048416q
 727
- 728 Ritzkowski, M., Heyer, K.-U., and Stegmann, R., 2006. Fundamental processes and
 729 implications during in situ aeration of old landfills. *Waste Management*, 26 (4), 356-372.
 730
- 731 Ritzkowski, M., and Stegmann, R., 2013. Landfill aeration within the scope of post-closure
 732 care and its completion. *Waste Management*, 33 (10), 2074-2082.
 733
- 734 Schwarz, G. (1962). A theory of the low-frequency dielectric dispersion of colloidal particles
 735 in electrolyte solution1, 2. *The Journal of Physical Chemistry*, 66(12), 2636-2642.
 736
- 737 Schwartz, N. and Furman, A., 2014. On the spectral induced polarization signature of soil
 738 organic matter. *Geophysical Journal International*, 200(1), 589-595. doi:10.1093/gji/ggu410
 739
- 740 Seigel, H., M. Nabighian, D.S. Parasnis, and Vozoff, K., 2007. The early history of the
 741 induced polarization method: *The Leading Edge*, 26(3), 312-321. doi:10.1190/1.2715054
 742
- 743 Soupios, P. and Ntarlagiannis, D., 2017. Characterization and monitoring of solid waste
 744 disposal sites using geophysical methods: current applications and novel trends. In *Modelling*
 745 *Trends in Solid and Hazardous Waste Management (75-103)*. Springer, Singapore.
 746 doi:10.1007/978-981-10-2410-8_5
 747
- 748 Sumner, J.S., 1976. *Principles of induced polarization for geophysical prospecting*. Elsevier,
 749 Amsterdam.
 750
- 751 Tsourlos, P., Vargemezis, G.N., Fikos, I. and Tsokas, G.N., 2014. DC geoelectrical methods
 752 applied to landfill investigation: case studies from Greece. *first break*, 32(8), pp.81-89.
 753

- 754 Ustra, A.T., Elis, V.R., Mondelli, G., Zuquette, L.V. and Giacheti, H.L., 2012. Case study: a
755 3D resistivity and induced polarization imaging from downstream a waste disposal site in
756 Brazil. *Environmental Earth Sciences*, 66(3), 763-772. doi:/10.1007/s12665-011-1284-5
757
- 758 Wainwright, H. M., Flores Orozco, A., Bücken, M., Dafflon, B., Chen, J., Hubbard, S. S., and
759 Williams, K. H., 2016. Hierarchical Bayesian method for mapping biogeochemical hot spots
760 using induced polarization imaging. *Water Resources Research*, 52(1), 533-551.
761 doi:10.1002/2015WR017763
762
- 763 Ward, S. H., 1988. The resistivity and induced polarization methods. In *Symposium on the*
764 *Application of Geophysics to Engineering and Environmental Problems 1988* (pp. 109-250).
765 Society of Exploration Geophysicists. doi:10.4133/1.2921804
766
- 767 Waxman, M. H., and Smits, L. J. M., 1968. Electrical conductivities in oil-bearing shaly
768 sands. *Society of Petroleum Engineers Journal*, 8(02), 107-122. doi:10.2118/1863-A
769
- 770 Weller, A., Zhang, Z. and Slater, L., 2015. High-salinity polarization of sandstones.
771 *Geophysics*, 80(3), D309-D318. doi:10.1190/geo2014-0483.1
772
- 773 Williams, K. H., Kemna, A., Wilkins, M. J., Druhan, J., Arntzen, E., N'Guessan, A. L., Long,
774 P. E., Hubbard, S. S., and Banfield, J. F., 2009. Geophysical monitoring of coupled microbial
775 and geochemical processes during stimulated subsurface bioremediation. *Environmental*
776 *Science and Technology*, 43(17), 6717-6723. doi:10.1021/es900855j
777
- 778 Zhang, C., Guo, Y., Wang, X., and Chen, S., 2019. Temporal and spatial variation of
779 greenhouse gas emissions from a limited-controlled landfill site, *Environment international*,
780 127, 387-394.
781
782
783
784

785

An analytical membrane-polarization model to predict the complex conductivity signature of immiscible liquid hydrocarbon contaminants

Matthias Buecker^{1,2,*}, Adrián Flores Orozco², Andreas Hördt³ and Andreas Kemna¹

¹ Department of Geophysics, Steinmann Institute, University of Bonn, 53115 Bonn, Germany

² Research Group Geophysics, Department of Geodesy and Geoinformation, TU-Wien, 1040 Vienna, Austria

³ Institute for Geophysics and Extraterrestrial Physics, TU Braunschweig, 38106 Braunschweig, Germany

Received February 2017, revision accepted October 2017

ABSTRACT

An analytical membrane-polarization model is developed to predict the frequency-dependent complex conductivity of hydrocarbon-contaminated sediments. In the absence of hydrocarbon contaminants, the effect of membrane polarization can be approximated using a recently developed analytical model, which describes the pore space as a sequence of two cylindrical pores of different lengths and radii. Different cation and anion concentrations in the electrical double layer at the pore wall lead to an ion-selective behaviour causing the membrane-polarization effect. This model can readily be adjusted to account for a wetting liquid hydrocarbon covering the pore wall. To model the effect of non-wetting hydrocarbon, we extend the analytical model by introducing a second cylindrical body into the cylindrical pores that represents a discrete droplet of the contaminant phase. In order to account for the high electrical resistivity of liquid hydrocarbons, the corresponding volumes are assumed to be electrically insulating. Because most liquid hydrocarbon surfaces are negatively charged when in contact with an electrolyte, they are covered by a second electrical double layer, which can easily be incorporated into the analytical model. We use our extended model to study the effect of varying saturations of wetting and non-wetting hydrocarbon on the complex electrical conductivity of the pore system. Our results predict that conductivity magnitude and conductivity phase generally decrease with hydrocarbon saturation. However, if the surface potential at the surface of non-wetting hydrocarbon droplets is larger than the one at the pore wall, we can observe an increase in the conductivity magnitude with the hydrocarbon saturation and a slight increase in the conductivity phase at intermediate hydrocarbon concentrations. This finding is particularly interesting as it offers a possible explanation for the relation between complex conductivity and hydrocarbon saturation observed in different field and laboratory experiments.

INTRODUCTION

Due to their low solubility in water, liquid hydrocarbon (HC) contaminants, also referred to as non-aqueous phase liquids (NAPLs), released into the subsurface environment often persist as residual or free phase (e.g., Soga, Page and Illangasekare 2004). Commonly, the detection of these separate HC phases is an important objective of site characterisation because they constitute a main source for continued contamination of groundwater (e.g., Atekwana and Atekwana 2010). The characterisation of these source zones usually relies on direct soil and/or groundwater sampling, which results in a limited spatial resolution of the site investigation due to the relatively high cost of drilling-based methods (e.g., Flores Orozco *et al.* 2012). Furthermore, screened

wells generally used to monitor the progress of remediation measures are known to be unable to detect trapped (and thus immobile), residual HC. Even though, mobile free-phase thicknesses measured in monitoring wells (i.e., the thickness of the immiscible liquid HC layer floating on top of the groundwater) typically exceed the real free-phase thicknesses in the formation, an effect that can be explained to be the effect of capillary forces (Newell *et al.* 1995 and the references therein).

If combined with conventional site characterisation and monitoring techniques, geophysical exploration methods potentially help overcome some of the aforementioned limitations (Atekwana and Atekwana 2010) as they provide spatially quasi-continuous and highly resolved information on subsurface properties. In particular, direct current (DC) and induced polarization (IP) imaging techniques have received much attention because of

* buecker.matthias@yahoo.de

the distinct electrical properties of liquid HC contaminants. Due to the high electrical resistivity of most liquid HCs, fresh spills usually stand out as resistive anomalies (e.g., Börner, Grubne and Schön 1993; Chambers *et al.* 2004; Cassiani *et al.* 2009; Johansson, Fiandaca and Dahlin 2015). However, over time, the presence of HC often enhances microbial activity and organic acids are released into the groundwater, which promote mineral weathering and dissolution of ions (e.g., Sauck 2000; Cassidy *et al.* 2001). As a consequence, aged HC spills are often associated with high electrical conductivity values (e.g., Atekwana, Sauck and Werkema 2000; Flores Orozco *et al.* 2012; Cassiani *et al.* 2014; Caterina, Flores Orozco and Nguyen 2017). Although an indication of contaminated subsurface volumes based on DC resistivity anomalies alone might be sufficient in some cases, several studies report circumstances under which no significant resistivity anomaly could be detected (e.g., Börner *et al.* 1993; Ustra *et al.* 2012; Kemna, Binley and Slater 2004).

In order to explore the potential of the IP method, also known as complex resistivity or complex conductivity method, for the detection of HC contaminants, laboratory and field experiments have been undertaken with promising but seemingly contradictory results. While an increase in the measured IP phases or chargeability values with HC saturation (e.g., Olhoeft 1985, 1992; Vanhala, Soininen and Kukkonen 1992; Kemna, Räkera and Dresen 1999; Kemna *et al.* 2004; Abdel Aal, Slater and Atekwana 2006; Sogade *et al.* 2006; Cassiani *et al.* 2009; Schmutz *et al.* 2010; Revil, Schmutz and Batzle 2011; Abdel Aal and Atekwana 2013; Deceuster and Kaufmann 2012; Flores Orozco *et al.* 2015) was reported in many studies, some results display the reverse effect (e.g., Vanhala *et al.* 1992; Weller and Börner 1996; Weller *et al.* 1997; Vanhala 1997; Chambers *et al.* 2004; Martinho, Almeida and Matias 2006; Cassiani *et al.* 2009; Revil *et al.* 2011) or even an increase in the polarization magnitude until a critical saturation is reached followed by a decrease towards higher HC concentrations (e.g., Titov *et al.* 2004; Martinho *et al.* 2006; Flores Orozco *et al.* 2012; Johansson *et al.* 2015). As only a limited number of studies under certain conditions report weak or insignificant variations of the polarization response resulting from changes in HC concentration (Olhoeft 1985; Ustra *et al.* 2012), the potential of the IP method for the characterisation of HC-contaminated sites seems evident but urges a more detailed knowledge of the underlying polarization effect mechanisms.

In order to connect experimental observations to the pore-scale configuration of immiscible liquid HC, several conceptual models have been developed by various authors (e.g., Titov *et al.* 2004; Martinho *et al.* 2006; Schmutz *et al.* 2010; Revil *et al.* 2011; Flores Orozco *et al.* 2012; Abdel Aal and Atekwana 2013; Johansson *et al.* 2015). Most of these distinguish between two possible scenarios: (1) the solid phase is covered by a water film and the HC forms discrete or interconnected droplets, a condition commonly referred to as “water-wet”, whereas (2) under “hydrocarbon-wet” conditions, the two liquids interchange their roles and an HC film separates the aqueous phase from the solid

phase. All authors then attribute the resulting polarization responses to mainly three mechanisms: (a) polarization of the electrical double layer (EDL) at the solid–water interface, (b) polarization of the EDL at the water–liquid HC interface, and/or (c) membrane polarization due to geometrical constrictions in the electrolyte-filled pore space.

In order to verify the conceptual models and quantify individual contributions of the polarization mechanisms to the overall response, mechanistic models are needed. The polarization of the EDL at the solid–water interface has been intensively studied (O’Konski 1960; Schwarz 1962; Schurr 1964), and a robust mechanistic model that links the IP effect in granular media to the polarization of the Stern layer is available (Leroy *et al.* 2008; Leroy and Revil 2009). Recently, this model has been extended to include the effect of non-wetting oil as an electrically insulating but non-polarizable phase (Schmutz *et al.* 2010). The extended model predicts a monotonous increase in the conductivity phase with oil saturation and has been tested successfully against experimental data. It also contains the only empirical model that had been developed earlier (Vinegar and Waxman 1984) as a limiting case. However, the model of Schmutz *et al.* (2010) does not answer all open questions because it cannot explain measured IP responses that decrease with HC saturation or show a maximum behaviour at intermediate concentrations.

Although there are good reasons to assume that the EDL at the HC–water interface also contributes to the overall polarization (e.g., Abdel Aal *et al.* 2013; Johansson *et al.* 2015), the model of Schmutz *et al.* (2010) does not consider the polarization response around liquid HC droplets or HC-covered mineral grains.

Membrane polarization, the third possible source mechanism, explains the measured IP response with the presence of ion-selective zones along the current pathway, which leads to the build-up of (salt) concentration gradients under the effect of an external electric field (Marshall and Madden 1959). Generally, geometrical pore constrictions (pore throats and narrow passages) or clay minerals are assumed to cause the ion-selective behaviour because of the unequal cation and anion concentrations in the EDL (e.g., Buchheim and Irmer 1979; Vinegar and Waxman 1984). Titov *et al.* (2004) undertake the only published attempt to adapt a mechanistic membrane-polarization model, i.e., the model of Titov *et al.* (2002), to explain the IP response of HC-contaminated sediments. In their laboratory experiments, they observed a chargeability increase up to a critical HC saturation followed by a decrease at higher saturations. Although their discussion suggests that this maximum behaviour of chargeability is in agreement with the developed model, no rigorous quantitative treatment is provided.

Because of the evident lack of a more detailed understanding of membrane-polarization processes in HC-contaminated sediments and rocks, the main objective of this study is to place an analytical model to the disposal of the community. To this end, we first adapt the existing conceptual models and extract those parameters relevant to membrane polarization. Then, we adapt a recently pre-

sented membrane polarization model, which allows considering the effect of the EDL at the pore wall and varying pore radii (Bücker and Hördt 2013b) to simulate the effect of both wetting and non-wetting liquid HCs in the pore space on the membrane-polarization mechanism. The discussion focuses on the possible implications for the interpretation of measured IP responses.

THEORY

Conceptual model

HC contaminants in granular subsurface materials partition into four phases, namely, vapour, aqueous (dissolved in water), separate (residual or free phase), and sorbed to solid particles (e.g., Newell *et al.* 1995). The physiochemical properties of all involved materials (i.e., HC, water, and solid) and the contamination history determine the degree to which the contaminant partitions into each of the four phases. Separate liquid HC trapped in the pore space often acts as a source for continuing contamination of groundwater (e.g., Atekwana and Atekwana 2010), which makes the delineation of the source zone one of the main objectives of site characterisation and management. This study therefore focuses on the effect of immiscible liquid HC contaminants on the expected IP response. For the sake of simplicity, we will furthermore limit our treatment to the saturated zone, i.e., the pore space is completely occupied by pore water and liquid

(free-phase) HC at different ratios and no gaseous phase is considered. Following the approach of earlier studies, we will treat the cases of liquid HC as non-wetting and wetting phases separately (Martinho *et al.* 2006; Schmutz *et al.* 2010; Revil *et al.* 2011; Abdel Aal and Atekwana 2013; Johansson *et al.* 2015).

In most natural granular materials, water is the wetting fluid (e.g., Kanicky *et al.* 2001) and the liquid HC is trapped in the open pore space forming discrete droplets or ganglia (Figure 1a). The geometrical configuration of the non-wetting liquid HC depends on pore geometry and capillary pressure (e.g., Sahloul, Ioannidis and Chatzis 2002). In this study, we assume that the solid surface is covered by a continuous water film, which separates the HC droplet from the solid phase. Low pore-throat diameter ratios (often referred to as aspect ratio in the literature) and/or high HC saturations favour the formation of bridges between HC droplets in adjacent pore spaces (Chatzis, Morrow and Lim 1983), as depicted in Figure 1b. Incoming water leads to the rupture of the bridge if the HC saturation decreases below a critical value, referred to as “snap-off” (e.g., Sahloul *et al.* 2002). Besides low HC saturations, also high pore-throat diameter ratios promote the formation of discrete HC droplets (see Figure 1c). The corresponding capillary models (Figures 1b and 1c) to be considered in this study represent these two limiting cases.

Surface-active components in the pore water can change the interfacial tensions and, consequently, the wettability of NAPLs (e.g., Zhao and Ioannidis 2007). In particular, organic acids and biosurfactants released as metabolic by-products during biodegradation (e.g., Cassidy *et al.* 2001) presumably promote the change to the less usual HC-wet situation. In such a case, liquid HC and water reverse roles compared with the water-wet situation (Figure 2a). Again, predominantly controlled by pore-throat diameter ratio and HC saturation, water either forms interconnected droplets (Figure 2b) or is trapped as discrete droplets in the larger pore spaces (Figure 2c). In both limiting cases, a continuous HC film is assumed to coat the solid surface.

Besides the geometrical configuration of water and contaminant phases in the pore space, the electrical and electrochemical properties of the two phases and the liquid–liquid interface need to be considered. The large resistivity contrast between the aqueous phase and most liquid HCs justifies the assumption of electrically insulating HC droplets and films (e.g., Schmutz *et al.* 2010).

As proposed by Abdel Aal and Atekwana (2013) and Johansson *et al.* (2015), besides the EDL at the solid–water interface, we include a second EDL at the interface between liquid HC and pore water into our model. We consider this second EDL essential because the magnitude of the ζ -potential at the HC–water interface can be of the same order of magnitude or even higher (e.g., Buckley, Takamura and Morrow 1989; Busscher, Van de Belt-Gritter and Van der Mei 1995) than that at the surface of common sediment minerals (e.g., Leroy *et al.* 2008). The corresponding surface charge can be explained based on the presence of interfacially active polar

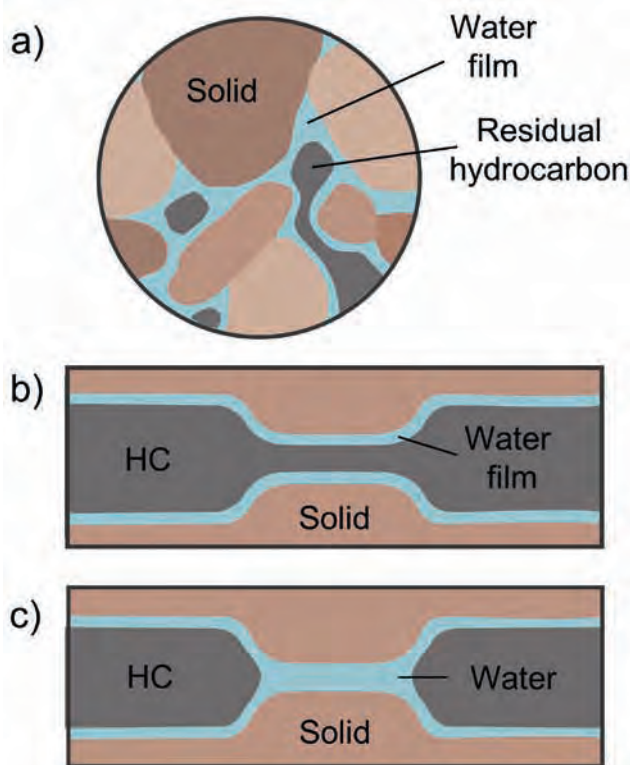


Figure 1 (a) Conceptual model of the geometrical distribution of immiscible HC droplets under water-wet conditions. Corresponding simplified capillary models for the cases of (b) interconnected and (c) separate HC droplets.

components in the liquid HC; at normal pH, the dissociation of acidic interfacial groups is responsible for the build-up of a negative surface charge, and at very low pH, the protonation of basic interfacial groups results in a positive surface charge (e.g., Farooq *et al.* 2012). Specific adsorption of hydroxide ions (OH⁻) can act as an additional source of interfacial charges even in the absence of polar components (Marinova *et al.* 1996). Usually, HC mixtures with a higher fraction of short-chained HCs will show lower absolute ζ -potentials than mixtures of longer-chained HCs (e.g., Stachurski and Michałek 1996). Beside this strong dependence on the composition of the liquid HC, water pH and electrolyte concentration influence the ζ -potential (e.g., Farooq *et al.* 2012).

As the ζ -potential at the HC–water interface strongly depends on the presence of interfacially active components, the wetting conditions in contaminated media become dependent on the signs and relative magnitudes of the ζ -potentials at both interfaces (i.e., HC–water and solid–water). In general, an increasing number of polar components and, thus, an increasing ζ -potential at the HC–water interface will favour the transition to HC-wet conditions (e.g., Revil *et al.* 2011). Because a detailed modelling of the transition between the two regimes is beyond the scope of this study, we will not *a priori* limit the parameter ranges to be studied.

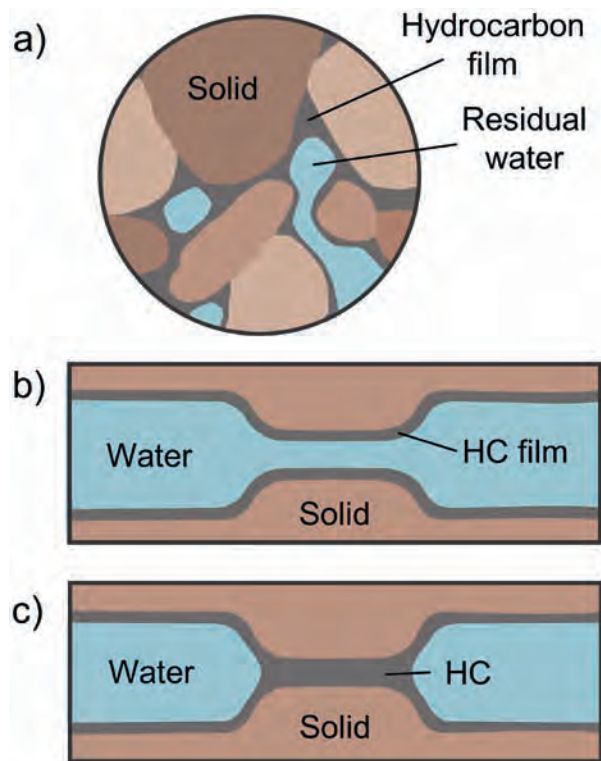


Figure 2 (a) Conceptual model of the geometrical distribution of immiscible HC droplets under HC-wet conditions. Translation into the simplified capillary model for the cases of (b) interconnected and (c) separate water droplets.

Analytical model

Recently, Bückler and Hördt (2013b) proposed a model that considers a sequence of wide and narrow cylindrical pores with pore radii R_1 and R_2 and pore lengths L_1 and L_2 . The pores are saturated with an electrolyte solution with a bulk ion concentration of c_0 (in mol/m³), and the pore wall or matrix is assumed to be non-conducting. A generally negative surface charge at the pore wall attracts an excess of cations, which accumulate in the Stern layer and the diffuse layer of the EDL, and causes a deficit of anions in the diffuse layer. The ζ -potential is used to approximate the electric potential at the interface between the Stern layer and the diffuse layer. The Gouy–Chapman theory permits quantifying the radial variation of electric potential $U(r)$ and ion concentrations $c_{p,n}(r)$ in the diffuse layer (subscripts p and n denote cation and anion properties, respectively). For a cylindrical pore of radius R_i , the electric potential can be approximated by solving the linearised Poisson–Boltzmann equation in cylindrical coordinates ($r = 0$ on the axis of the cylinder) with the boundary condition $U(R_i) = \zeta_m$ (e.g., Hunter 1981):

$$U_i(r) = \zeta_m \frac{J_0(j\kappa r)}{J_0(j\kappa R_i)}. \quad (1)$$

Here, j is the imaginary unit with $j^2 = -1$, J_0 is the Bessel function of the first kind and order zero, and $\kappa = \lambda_D^{-1}$ is the inverse of the Debye length λ_D , which is a measure of the thickness of the diffuse layer. Subscripts $i = 1, 2$ denote the properties of the wide and narrow pores, respectively. For symmetric monovalent electrolytes, the Debye length can be expressed as

$$\lambda_D = \sqrt{\frac{\epsilon_0 \epsilon_r k_B T}{2c_0 e F}}. \quad (2)$$

Here, ϵ_0 is the vacuum permittivity ($8.854 \cdot 10^{-12}$ C/(Vm)), ϵ_r is the relative permittivity of the pore fluid (≈ 80 for water), k_B is Boltzmann's constant ($1.380\,6482 \cdot 10^{-23}$ J/K) (Gaiser *et al.* 2017), T is the absolute temperature, e is the elementary charge ($1.6022 \cdot 10^{-19}$ C), and F is Faraday's constant ($96,485.3$ C/mol). The radial variation of the ion concentrations is connected to the electric potential via (e.g., Butt, Graf and Kappl 2003)

$$c_{(p,n)i}(r) = c_0 \exp\left(\mp \frac{eU_i(r)}{k_B T}\right). \quad (3)$$

Note that, at large distances from the pore wall (i.e., $r \gg \lambda_D$), the potential approaches the reference potential of 0 mV and both ion concentrations become equal to the bulk ion concentration c_0 .

Bückler and Hördt (2013b) argue that the electric current through the system of wide and narrow pores, in a first approximation, will be determined by the mean ion concentrations. They average the ion concentrations over the pore cross sections as follows:

$$\bar{b}_{(p,n)i} = \frac{2\pi}{c_0 A_1} \int_0^{R_i} r c_{(p,n)i}(r) dr. \quad (4)$$

Note that the integrated concentrations \bar{b} are normalised by the bulk ion concentration c_0 and the area of the wide pore $A_1 = \pi R_1^2$.

The latter accounts for the reduction of the total current through the narrow pore due to the smaller cross section (see Bückner and Hördt 2013b). The dimensionless mean concentrations are then used to define average transference numbers for both pores as follows:

$$t_{(p,n)i} = \frac{\mu_{p,n} \bar{b}_{(p,n)i}}{\mu_p \bar{b}_{pi} + \mu_n \bar{b}_{ni}}, \quad (5)$$

where $\mu_{p,n}$ are the ion mobility of cations and anions, respectively. By means of this approximation, the 3D cylindrical pore system can be collapsed to a sequence of 1D pores, the frequency-dependent impedance of which was studied in detail by Marshall and Madden (1959). As proposed by Bückner and Hördt (2013a), we express the Marshall–Madden impedance \times area $Z(\omega)$ in terms of its low-frequency limit $Z_0 = \lim_{\omega \rightarrow 0} Z(\omega)$, a dimensionless polarizability η_0 , and two time constants τ_i :

$$Z(\omega) = Z_0 \left[1 - \eta_0 \left(1 - \frac{\frac{L_1 + L_2}{\tau_1 + \tau_2}}{\frac{L_1}{\tau_1} \sqrt{j\omega\tau_1} \coth \sqrt{j\omega\tau_1} + \frac{L_2}{\tau_2} \sqrt{j\omega\tau_2} \coth \sqrt{j\omega\tau_2}} \right) \right], \quad (6)$$

$$Z_0 = \frac{k_B T}{ec_0 F} \left[\frac{L_1}{D_{p1} + D_{n1}} + \frac{L_2}{D_{p2} + D_{n2}} + \frac{8(t_{n2}t_{p1} - t_{n1}t_{p2})^2}{L_1/\tau_1 + L_2/\tau_2} \right], \quad (7)$$

$$\eta_0 = \frac{k_B T}{ec_0 F} \frac{8(t_{n2}t_{p1} - t_{n1}t_{p2})^2}{L_1/\tau_1 + L_2/\tau_2} \frac{1}{Z_0}, \quad (8)$$

$$\tau_i = \frac{L_i^2}{8D_{pi}t_{ni}}, \quad \text{where} \quad (9)$$

$$D_{(p,n)i} = \frac{\mu_{p,n} \bar{b}_{(p,n)i} k_B T}{e} \quad (10)$$

are corrected ion diffusion coefficients. Note that this correction for the diffusion coefficients and the modification of the transference numbers are the only changes in the Marshall–Madden impedance \times area introduced by Bückner and Hördt (2013b).

To facilitate the direct comparison with measured data, Bairlein *et al.* (2016) propose a conversion of the impedance \times area to effective conductivity:

$$\sigma_{\text{eff}}(\omega) = \frac{A_1}{Z(\omega)} \frac{L^2 \Phi}{A_1 L_1 + A_2 L_2}. \quad (11)$$

Here, Φ is the porosity of the material, $L = L_1 + L_2$ is the sum of the two pore lengths, and $A_i = \pi R_i^2$ are the cross-sectional areas of the two pores.

Adaptation of the analytical model

The analytical model can readily be adapted to account for the effect of non-wetting HC droplets (water-wet model) as a second

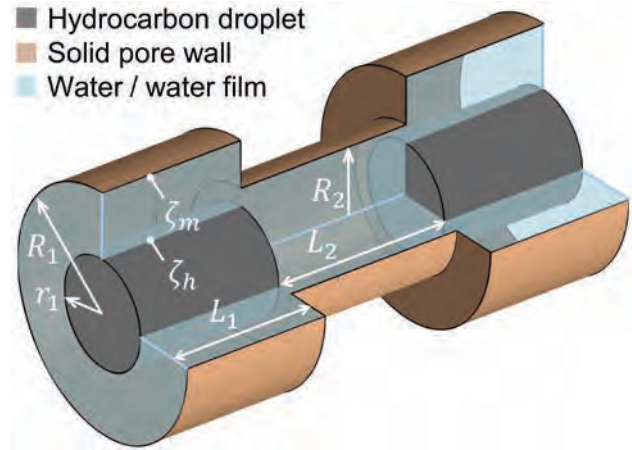


Figure 3 Three-dimensional sketch of the capillary model, including HC droplets in the wide pores. Note that both surfaces enclosing the water volume, i.e. the pore wall and the surface of the HC droplet, can carry a surface charge indicated by the ζ -potentials ζ_m and ζ_h , respectively.

phase within the pore space. As in the model of Bückner and Hördt (2013b), we describe the pore space as an alternating sequence of wide and narrow cylindrical pores. The non-aqueous phase is modelled by placing a solid non-conducting cylinder at the centre of the cylindrical pore (see Figure 3). As previously discussed, the resulting HC–water interface can also be charged. Consequently, besides the fixed potential ζ_m at the pore wall ($r = R_i$), we assume a second fixed potential ζ_h at the HC surface ($r = r_i$).

The radial variation of the electric potential in equation (1) was obtained from the linearised Poisson–Boltzmann equation in cylindrical coordinates:

$$\frac{1}{r} \frac{\partial}{\partial r} \left[r \frac{\partial U_i(r)}{\partial r} \right] = \kappa^2 U_i(r). \quad (12)$$

This is a zeroth-order modified Bessel equation with the general solution (e.g., Abramowitz and Stegun 1964)

$$U_i(r) = A_i J_0(j\kappa r) + B_i Y_0(-j\kappa r), \quad (13)$$

where Y_0 is the Bessel function of the second kind. In order to estimate the radial electric potential profiles within a tubular water film between the two cylinders (as needed for the water-wet model), we impose the boundary conditions $U_i(r_i) = \zeta_h$ and $U_i(R_i) = \zeta_m$, which yields the following two coefficients:

$$A_i = \frac{\zeta_h Y_0(-j\kappa R_i) - \zeta_m Y_0(-j\kappa r_i)}{Y_0(-j\kappa R_i) J_0(j\kappa r_i) - Y_0(-j\kappa r_i) J_0(j\kappa R_i)}, \quad (14)$$

and

$$B_i = \frac{\zeta_m J_0(j\kappa r_i) - \zeta_h J_0(j\kappa R_i)}{Y_0(-j\kappa R_i) J_0(j\kappa r_i) - Y_0(-j\kappa r_i) J_0(j\kappa R_i)}. \quad (15)$$

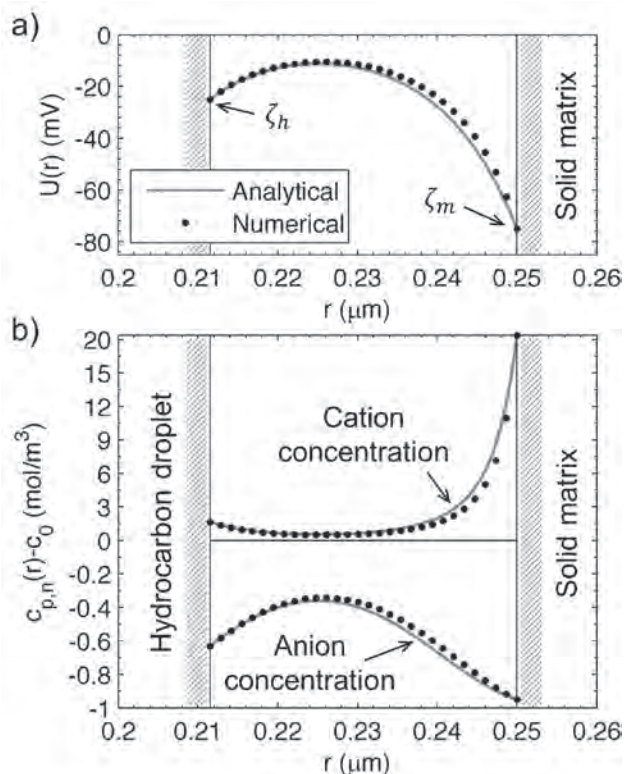


Figure 4 Radial variation of (a) the electric potential and (b) the excess ion concentrations in a tubular water film confined by two cylinders with $r \approx 0.21 \mu\text{m}$ and $R = 0.25 \mu\text{m}$ and with surface potentials $\zeta_h = -25 \text{ mV}$ and $\zeta_m = -75 \text{ mV}$, respectively. The thickness of the water film is equal to four Debye lengths (here, $\lambda_D \approx 0.01 \mu\text{m}$). Solid lines represent the analytical solutions of the linearised Poisson–Boltzmann equation, and black dots represent the full numerical solution. Note the different scaling of cation and anion concentrations (factor 15). The remaining parameter values are as follows: $c_0 = 1 \text{ mol/m}^3$, $\epsilon_r = 80$, $T = 293 \text{ K}$, and $\mu_p = \mu_n = 5 \cdot 10^{-8} \text{ m}^2/(\text{Vs})$.

Figure 4a illustrates the variation of the electric potential within a thin water film of approximately four Debye lengths ($\lambda_D \approx 0.01 \mu\text{m}$ for the chosen parameter values). The corresponding ion concentration profiles (Figure 4b) can be obtained by inserting the electric potential into the Boltzmann distribution (see equation (3)). Strictly speaking, the linearised Poisson–Boltzmann equation (12) is only valid for small surface potentials $e\zeta/k_B T \ll 1$ (or $|\zeta| \ll 25 \text{ mV}$ at room temperature) (e.g., Butt *et al.* 2003).

As typical ζ -potentials of silica minerals (e.g., Leroy *et al.* 2008) and liquid HCs (e.g., Buckley *et al.* 1989; Busscher *et al.* 1995) are in the range of -25 to -100 mV , we carry out numerical modelling to test how severe the violation of the condition of small potentials is. For this purpose, we solve the full Poisson–Boltzmann equation in cylindrical coordinates

$$\frac{1}{r} \frac{\partial}{\partial r} \left[r \frac{\partial U_i(r)}{\partial r} \right] = \kappa^2 \frac{k_B T}{e} \sinh \frac{e}{k_B T} U_i(r), \quad (16)$$

using the boundary conditions $U(r) = \zeta_h = -25 \text{ mV}$ and $U(R) = \zeta_m = -75 \text{ mV}$.

Figure 4 shows that analytical and numerical results agree fairly well for typical ζ -potentials and a sufficiently thick water film between HC droplet and solid matrix. As long as the thickness of the water film is larger than four Debye lengths (Figure 4), the small observable deviations can be considered negligible compared to other limitations of our model. However, within thinner water films, the two diffuse layers covering the HC droplet and the solid surface overlap significantly and the predictions of the analytical model become increasingly inaccurate. In this study, we will therefore clearly indicate modelling results related to water film thicknesses below four Debye lengths.

In the next step, we calculate the mean ion concentrations normalised by the bulk concentration c_0 and the cross-sectional area of the wide pore A_1 as

$$\bar{b}_{(p,n)i} = \frac{2\pi}{c_0 A_1} \int_{r_i}^{R_i} r c_{(p,n)i}(r) dr. \quad (17)$$

Figure 5 shows the variation of these dimensionless mean ion concentrations with the droplet radius for different potentials at the droplet surface. For $\zeta_h = 0 \text{ mV}$, the dimensionless mean cation concentration \bar{b}_p decays monotonously with the droplet radius. This is an immediate consequence of the displacement of the electrolyte by the insulating droplet. For $\zeta_h < 0 \text{ mV}$, \bar{b}_p initially increases with increasing droplet radius. Here, the excess cation concentration of the EDL at the growing droplet surface overcompensates the displacement of the electrolyte by the insulating droplet. At water film thicknesses of approximately four Debye lengths (here, at $r > 0.21 \mu\text{m}$), this increase in \bar{b}_p becomes even steeper before \bar{b}_p decays to zero for $r \rightarrow R$. As aforementioned, the results obtained for such small water film thicknesses must be treated with caution due to the limited validity of the analytical solution in this case of significantly overlapping diffuse layers. The dimensionless mean anion concentrations \bar{b}_n decay monotonously with the droplet radius. The deficit anion concentration in the EDL at the droplet surface makes the initial \bar{b}_n decay stronger the larger the magnitude of ζ_h is.

Like in the original model of Bückler and Hördt (2013b), we use the dimensionless mean concentrations to calculate average transference numbers $t_{(p,n)i}$ via equation (5) and correct the ion diffusion coefficients $D_{(p,n)i}$ using equation (10). In this manner, we cast the effective transport properties of the capillary model into the 1D Marshall–Madden impedance given by equations (6) to (9). Note that, unlike the original model, we do not consider a correction for the contribution of the Stern layer (i.e., the partition coefficient is assumed to be zero). The reason is the lack of information on the partitioning of cations into the Stern and diffuse layers at the HC–water interface.

Our approach allows us to study the variation of the frequency-dependent impedance of the pore sequence as a function of the radii of the HC droplets. We will assume that the water films in both pores are of the same thickness, such that the radii of the

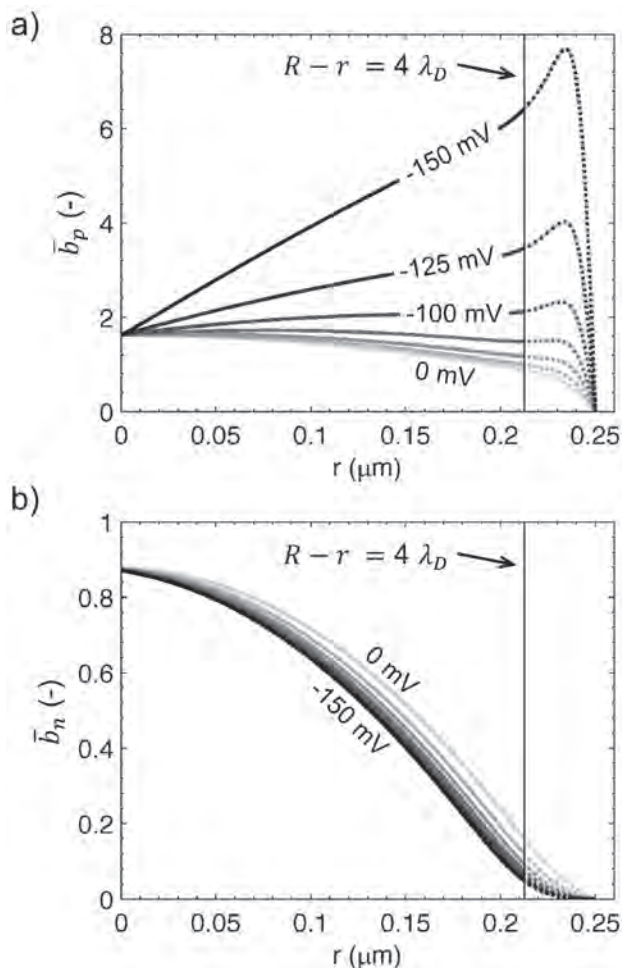


Figure 5 Variation of (a) the dimensionless mean cation concentration and (b) the dimensionless mean anion concentration with the droplet radius r given by equation (17). The radius of the pore $R = 0.25 \mu\text{m}$ and the potential at the pore wall $\zeta_m = -75 \text{ mV}$ are kept constant. The dimensionless mean concentration versus droplet radius curves are displayed for different potentials ζ_h between 0 mV and -125 mV (step width between curves is 25 mV). The vertical lines indicate the critical droplet radius, at which the water film thickness reaches the critical value of four Debye lengths. The remaining parameter values are the same as those in Figure 4.

two HC droplets are coupled via $R_1 - r_1 = R_2 - r_2$. For simplicity, in our model, the HC bridge across the narrow pore ruptures (snaps off) as soon as the film thickness is larger than the radius of the narrow pore (i.e., when $R_2 \leq R_1 - r_1$). This simplification ignores that, as a result of surface tensions, droplets are expected to snap off at much higher HC saturations, which has to be taken into account in the interpretation of the results.

In order to facilitate the comparison with measured data, we convert the obtained droplet radii to equivalent residual water saturations. To this end, we express the total pore volume V_p and the total volume of the two droplets V_h as

$$V_p = \pi R_1^2 L_1 + \pi R_2^2 L_2 \quad \text{and} \quad V_h = \pi r_1^2 L_1 + \pi r_2^2 L_2. \quad (18)$$

Then, the total HC saturation and the residual water saturation are given by

$$S_h = V_h / V_p \quad \text{and} \quad S_w = 1 - S_h, \quad (19)$$

respectively.

To model the case of the liquid HC as a wetting phase, we can simply use the original model of Bückner and Hördt (2013b), i.e., equations (1) to (11). By substituting ζ_m by ζ_h in equation (1) and R_i by r_i in equations (1) and (4), we account for the fact that, here, the pore wall is completely covered by the HC film and the water droplet (of radius r_i) is in contact with the HC surface only. Accordingly, the total volume of the HC film becomes

$$V_h = \pi (R_1^2 - r_1^2) L_1 + \pi (R_2^2 - r_2^2) L_2 \quad (20)$$

in the HC-wet model. According to the precautions taken in the case of subcritical water film thicknesses (smaller than four Debye lengths), we will clearly indicate all modelling results obtained for droplet radii smaller than two Debye lengths, where the diffuse layers covering the opposite boundaries of the water droplet significantly overlap. All other expressions remain unchanged.

RESULTS

Unless otherwise stated, the following standard model parameter values are used to obtain the complex conductivity responses presented in this section. The bulk ion concentration in the pore-filling electrolyte is set to $c_0 = 1 \text{ mol/m}^3$. Cation and anion mobility values are $\mu_p = \mu_n = 5 \cdot 10^{-8} \text{ m}^2/(\text{Vs})$, which is approximately equal to the mobility of the sodium cation (e.g., Atkins and De Paula 2013). In the water-wet case, the ζ -potential at the pore wall is assumed to be $\zeta_m = -75 \text{ mV}$ (with respect to reference potential of 0 mV at large distances from all interfaces), which is a typical value for silica mineral surfaces (e.g., Leroy *et al.* 2008). We use pore lengths of $L_1 = 50 \mu\text{m}$ and $L_2 = 5 \mu\text{m}$ and a porosity of $\Phi = 30\%$, which are representative values for fine sand or fine-grained sandstone (e.g., Morris and Johnson 1967). In order to provide a significant polarization response of the capillary model, we use pore radii $R_1 = 2.5 \mu\text{m}$ and $R_2 = 0.25 \mu\text{m}$. The resulting (aspect) ratios between pore lengths and pore diameters, i.e., $L_i / (2R_i)$, are equal to 10 for both pores. This value is large compared with typical aspect ratios of 2 to 2.5 in sedimentary rocks (e.g., Chatzis *et al.* 1983; Schmitt *et al.* 2016) but corresponds to the highest realistic aspect ratio proposed by Hördt *et al.* (2017).

Water-wet model

Figure 6 shows the spectral response of the water-wet model for varying residual water saturations and an absolute electric potential at the pore wall that is higher than the one at the HC surface (i.e., $\zeta_h / \zeta_m < 1$). In the left panel (Figure 6a), we observe an increase in the conductivity magnitude with water saturation.

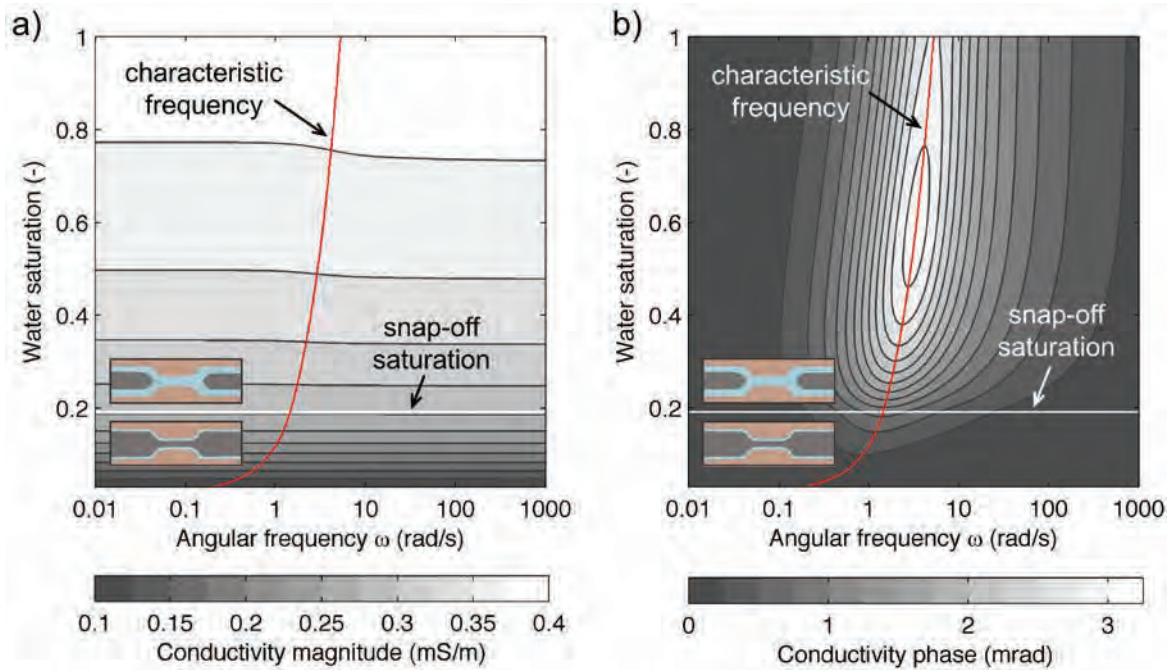


Figure 6 Frequency and saturation dependence of the effective conductivity of the water-wet model with surface potential $\zeta_h = -25$ mV. (a) Magnitude and (b) phase spectra as a function of residual water saturations. Contour lines are every 0.025 mS/m in (a) and every 0.25 mrad in (b). The white horizontal lines mark the snap-off saturation ($S_w \approx 0.19$); the two insets above and below the white line illustrate the corresponding simplified capillary models. The red lines show the variation of the characteristic angular frequency ω_c (see the main text for further details). Both plots are truncated at a saturation of $S_w \approx 0.03$, where the water film thickness falls below four Debye lengths.

The conductivity increase is most pronounced at low water saturations ($S_w < 0.19$), where the HC droplet is continuous across both pores. Minor frequency variations of the conductivity magnitude only become visible at high water saturations.

Frequency variations of the conductivity phase are much more evident (Figure 6b). Maximum phase values (ca. 3.1 mrad) occur at high water saturations, monotonously decrease with the water saturation, and practically vanish as saturation reaches the critical snap-off value. This phase decrease with decreasing water saturation can be understood by analysing equation (8), which directly relates variations of the polarization magnitude (here, in terms of the polarizability) to the squared difference between the transference numbers of the two pores $(t_{n2}t_{p1} - t_{n1}t_{p2})^2$. Making use of the equality $t_{ni} = 1 - t_{pi}$, we can simplify this term to $(t_{p1} - t_{p2})^2$. At high water saturations, the EDL at the pore wall makes the narrow pore more ion-selective than the wide pore ($t_{p2} > t_{p1}$), which results in relatively high maximum phases. As water saturation decreases and the radius of the HC droplet in the wide pore increases, the wide pore also becomes ion-selective (due to the EDL at the HC surface) and the difference between the transference numbers decreases, leading to a reduction of the observed phases. At water saturations < 0.19 , the HC droplet penetrates the narrow pore and the water films in both pores are of the same thickness. As a result, the transference numbers in both pores are almost the same and no significant phases can be observed.

The decrease in the phase is accompanied by a decrease in the characteristic angular frequency ω_c , which we define as the angular frequency, at which the phase peak is observed. For each water saturation, the phase spectrum comprises the phase values computed at 500 discrete angular frequencies (logarithmically equidistant between 0.01 rad/s and 1000 rad/s); ω_c is then approximated by the discrete angular frequency, at which the calculated phase shift is maximum. At high water saturations ($S_w = 1$), the phase peak is centred at 5.3 rad/s; at the snap-off saturation ($S_w = 0.19$), it is encountered at 1.4 rad/s and reduces to 0.2 rad/s at the lowest saturation ($S_w = 0.03$).

This behaviour can be understood as follows. The characteristic angular frequency ω_c or its inverse, i.e., the characteristic time constant $\tau_c = 1 / \omega_c$, is controlled by either of the two time constants τ_i , as discussed in detail by Bückner and Hördt (2013a). According to equations (9) and (10), both time constants τ_i depend on the dimensionless mean concentrations and the modified transference numbers as expressed by the proportionality $\tau_i \propto 1 / (\bar{b}_{pi}t_{ni})$ or equivalently $\tau_i \propto 1 / (\bar{b}_{ni}t_{pi})$. For negative surface potentials, the dimensionless mean concentration \bar{b}_{ni} shows a steep decrease from ≤ 0.9 at small droplet radii to 0 at large droplet radii (see Figure 5), whereas the transference number t_{pi} only slightly increases from ~ 0.7 to 1 (as can also be inferred from Figure 5). Consequently, with increasing droplet radii r_i , i.e., with decreasing water saturation, both time constants τ_i are expected to increase, which explains the decrease in the characteristic angular frequency.

Although, in practice, high absolute values of ζ_h will most probably result in a transition to HC-wet conditions, in Figure 7, we show that the variation of the effective conductivity significantly changes when the absolute electric potential at the HC surface becomes larger than the one at the pore wall (i.e., $\zeta_h/\zeta_m > 1$). Instead of the increase observed for $\zeta_h/\zeta_m < 1$, here, the conductivity magnitude varies only slightly with increasing water saturation. This observation might seem counterintuitive, but it can be explained by the high cation excess concentration in the EDL at the HC surface, which overcompensates the displacement of the aqueous electrolyte by the insulating HC droplet.

In comparison with the case $\zeta_h/\zeta_m < 1$, maximum phases decrease much faster with decreasing water saturation. This is a direct consequence of the large excess cation concentration in the EDL at the HC–water interface, which renders the wide pore ion selective at much higher water saturations (compared with the case $\zeta_h/\zeta_m < 1$). Interestingly, around the snap-off saturation (i.e., before the HC droplet penetrates the narrow pore) the wide pore becomes more ion-selective than the narrow pore. The reason is that the ion concentrations in the small pore are not yet affected by the large absolute ζ -potential at the HC surface. As a result, a second phase maximum is obtained. However, once the snap-off (HC) saturation is exceeded, phase values decrease rapidly with decreasing water saturation as the difference of the transference numbers of both zones decreases too. At the same time, the vari-

ation of the characteristic angular frequency becomes more pronounced; from 5.3 rad/s ($S_w = 1$), it reduces to 0.1 rad/s ($S_w = 0.03$).

Obviously, the ratio ζ_h/ζ_m has a strong influence on the effective conductivity response of the capillary model. In order to study this dependence in more detail, we extract the magnitude and phase versus saturation curves for different ratios ζ_h/ζ_m at an angular frequency of $\omega = 1$ rad/s, a typical value used for single-frequency IP measurements. Figure 8 shows that (i) the transition between the two limiting situations observed above is continuous while increasing the ratio ζ_h/ζ_m ; (ii) the critical value of this ratio seems to be $\zeta_h/\zeta_m = 1$; and (iii) for larger ratios, the second phase maximum begins to occur around the snap-off saturation. This behaviour of the phase response can also be reproduced for other electric surface potentials at the pore wall (not shown here for brevity).

Hydrocarbon-wet model

In the HC-wet model, liquid HC and water interchange roles. In particular, there is no EDL at the water–pore wall interface (characterised by ζ_m) because the pore wall is completely covered by an HC film. Consequently, the conductivity of the pore sequence will be completely determined by the radii of the residual water droplets and the potential ζ_h at the HC surface.

Figure 9 shows the spectral response of this HC-wet model. The conductivity magnitude increases almost linearly with the

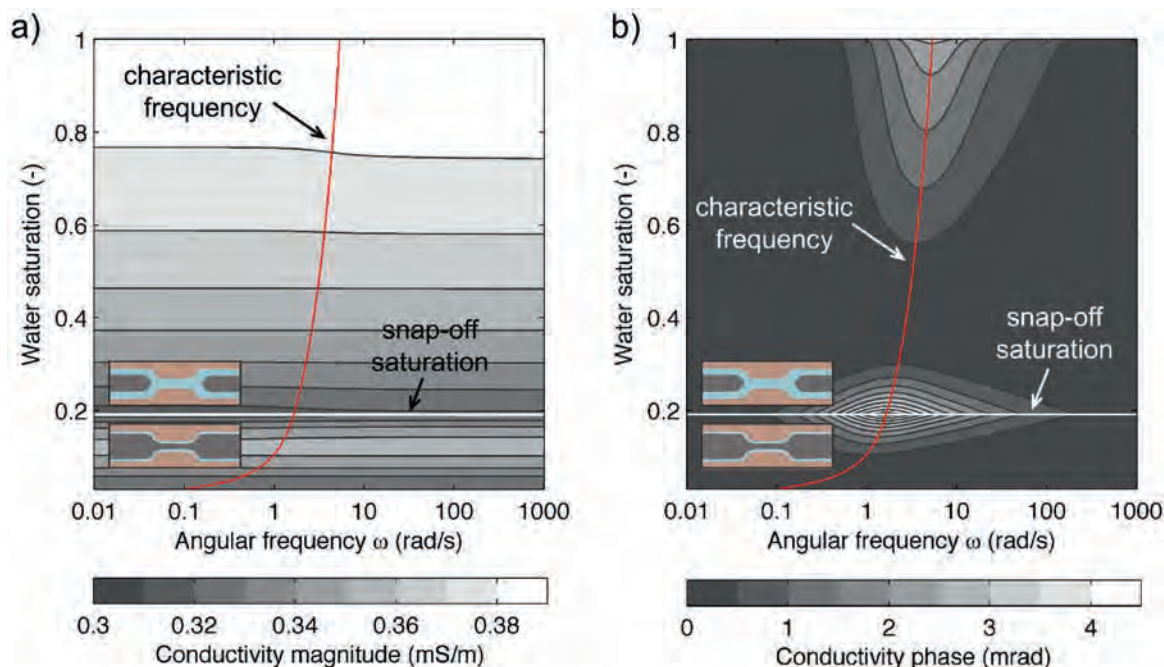


Figure 7 Frequency and saturation dependence of the effective conductivity of the water-wet model with surface potential $\zeta_h = -125$ mV. (a) Magnitude and (b) phase spectra as a function of residual water saturations. Contour lines are every 0.01 mS/m in (a) and every 0.5 mrad in (b). The white horizontal lines mark the snap-off saturation ($S_w \approx 0.19$); the two insets above and below the white line illustrate the corresponding simplified capillary models. The red lines show the variation of the characteristic angular frequency ω_c with the water saturation. Both plots are truncated at a saturation of $S_w \approx 0.03$, where the water film thickness falls below four Debye lengths.

water saturation, which simply reflects the fact that the effective (water-filled) cross section increases with the water saturation. Note that as soon as the water saturation falls below the snap-off saturation ($S_w \approx 0.81$), the entire cross section of the narrow pore throat is occupied by the insulating liquid HC, which completely blocks electric current.

In contrast to the behaviour of the water-wet model, the maximum phases observed in the HC-wet model first increase slightly with increasing HC saturation (decreasing water saturation) and then decrease rapidly towards the critical saturation. Based on the simple analysis of the term $(t_{p1} - t_{p2})^2$ made above, one would expect a monotonous increase in the phase response

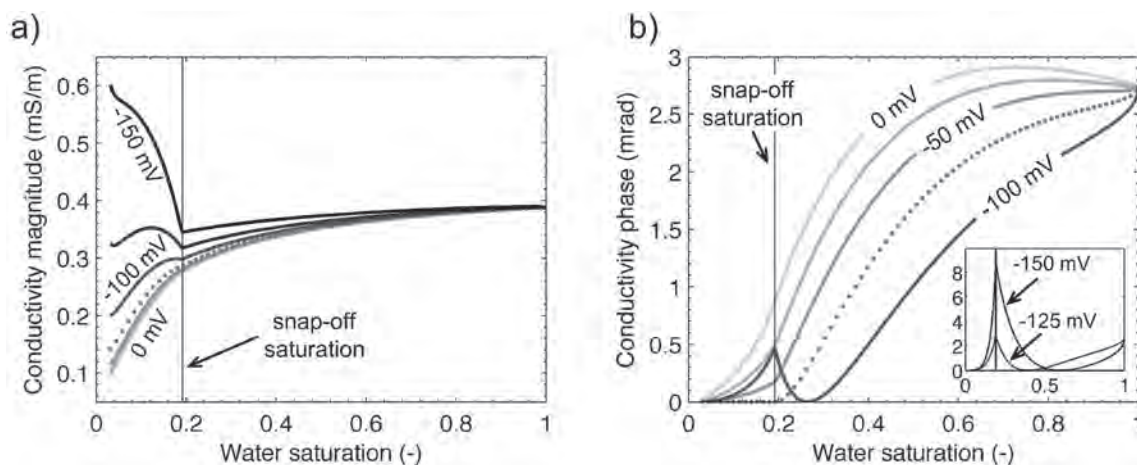


Figure 8 Variation of conductivity: (a) magnitude and (b) phase of the water-wet model with the water saturation at $\omega = 1$ rad/s. While the surface potential at the pore wall is fixed at $\zeta_m = -75$ mV, the one at the HC–water interface ζ_h is varied from 0 to -150 mV in steps of 25 mV. The dotted lines indicate the curve for the critical surface potential of $\zeta_h = -75$ mV. The solid vertical lines mark the snap-off saturation ($S_w \approx 0.19$). All curves are truncated at the saturation of $S_w \approx 0.03$, where the water film thickness falls below four Debye lengths.

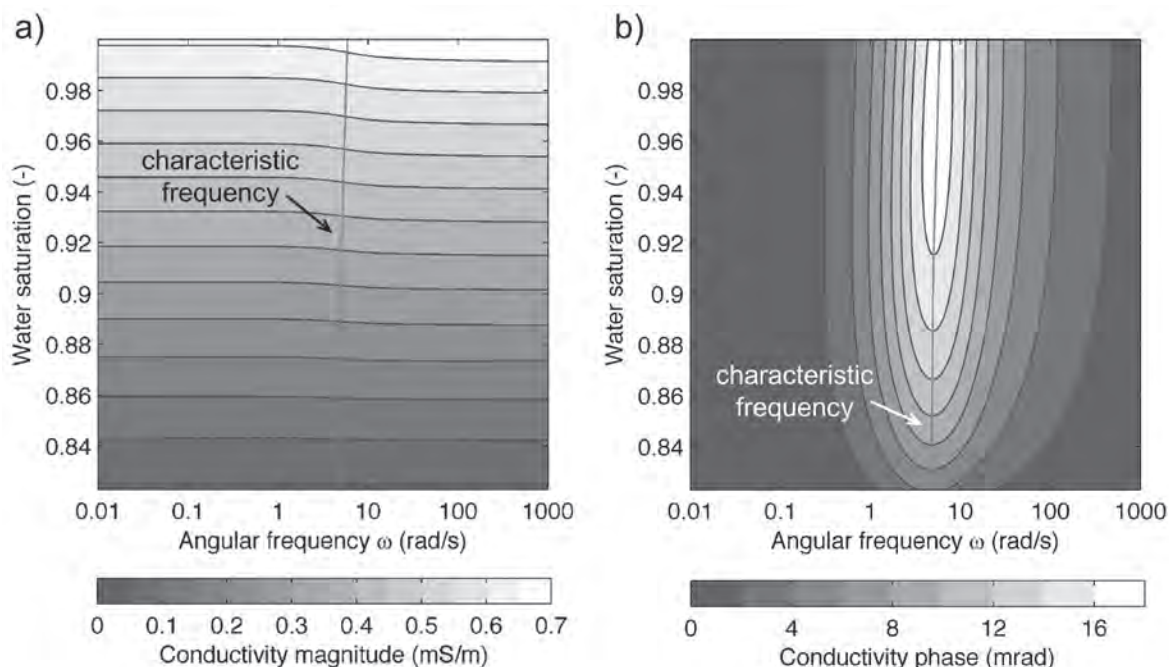


Figure 9 Frequency and saturation dependence of the effective conductivity of the HC-wet model with surface potential $\zeta_h = -125$ mV. (a) Magnitude and (b) phase spectra as a function of residual water saturation. Contour lines are every 0.05 mS/S in (a) and every 2 mrad in (b). The red lines mark the variation of the characteristic angular frequency ω_c with the water saturation. Both plots are truncated at the critical saturation of $S_w \approx 0.82$, where the radius of the water droplet in the narrow pore falls below two Debye lengths; at a slightly lower water saturation value ($S_w \approx 0.81$), the residual water becomes discontinuous in the narrow pore.

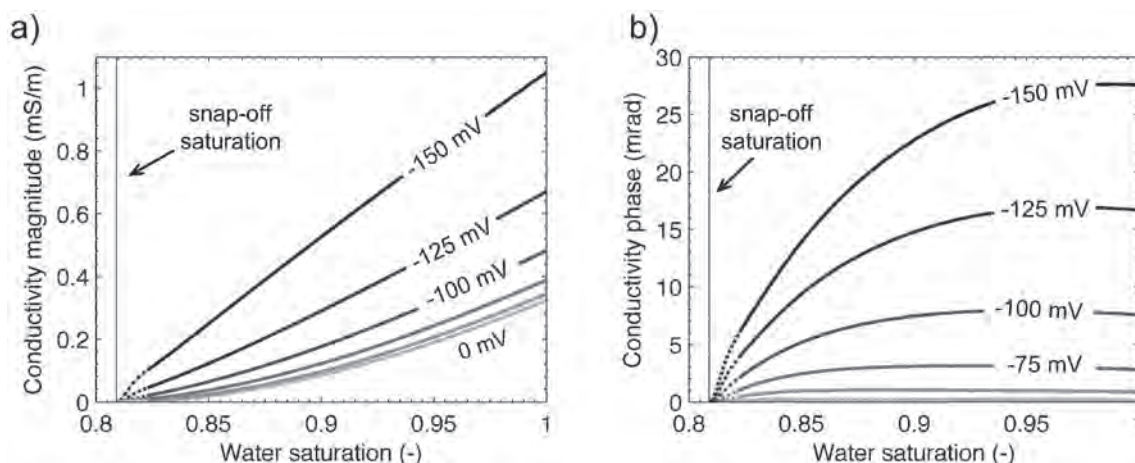


Figure 10 Variation of conductivity: (a) magnitude and (b) phase of the HC-wet model with the water saturation at $\omega = 1$ rad/s. The surface potential at the HC–water interface ζ_h is varied from 0 to -150 mV in steps of 25 mV. The vertical lines mark the snap-off saturation. Note that, as soon as the water droplet is expelled from the narrow pore, no electric current can pass and the pore system becomes insulating. Dotted lines indicate parts of the curve, which correspond to water-droplet radii below two Debye lengths.

with HC saturation as a result of the increasingly ion-selective behaviour of the narrow pore. However, as discussed before by Bückner and Hördt (2013b) and recently substantiated by Hördt *et al.* (2017), the ratio of pore radii that provides maximum phases also depends on the length ratio of the pores (more specifically, phases are maximum if $R_1^2 / R_2^2 = L_1 / L_2$). Decreasing the radius of the narrow pore beyond this optimum ratio does not further increase the phase response. In the present example, this optimum ratio is reached approximately midway between full water saturation and the critical saturation at $S_w \approx 0.81$ (Figure 9b).

The characteristic angular frequency varies little over the narrow range of relevant saturations (from 5.9 rad/s at $S_w = 1$ to 4.7 rad/s at $S_w = 0.28$). At the same time, the corrected ion diffusivity in the narrow pore must vary strongly as a result of the reduction of the effective cross section; see equations (4) and (10) (including the substitution $R_i \rightarrow r_i$). From the negligible effect of the corrected ion diffusivity in the narrow pore on the characteristic angular frequency, we can conclude that the relaxation process is largely controlled by the time constant of the wide pore. This behaviour corresponds to the long narrow pore or wide pore regime discussed in detail in Bückner and Hördt (2013a) and Hördt *et al.* (2017), in which the concentration gradients that cause the membrane-polarization effect are largely generated and relaxed via the wide pore.

To study possible effects due to the variation of ζ_h , we display magnitude and phase versus water saturation curves at $\omega = 1$ rad/s for seven different values of ζ_h . Because of the increasingly large excess cation concentration in the EDL, the conductivity magnitude increases monotonically with the absolute value of the surface potential. The almost linear increase in the conductivity magnitude with water saturation can be observed for all values of ζ_h .

As a result of the increasing difference between the transference numbers of the two pores as the absolute surface potential

increases, the phase response increases too. At the same time, the water saturation, at which the phase maximum is observed, increases from approximately $S_w = 0.87$ at $\zeta_h = -25$ mV to $S_w = 0.99$ at $\zeta_h = -150$ mV. We attribute the two last observations to the aforementioned optimum ratio of pore radii. Furthermore, Hördt *et al.* (2017) show that the optimum ratio also depends on the ζ -potential, an effect expected to become important at large absolute ζ -potentials.

DISCUSSION

Comparison with experimental data: conductivity magnitude

The general trend of a decreasing conductivity magnitude with increasing HC saturation predicted by both the water-wet and the HC-wet model is in agreement with most laboratory experiments on HC-contaminated sediments that have not undergone biodegradation (Olhoeft 1985, 1992; Vanhanla *et al.* 1992; Börner *et al.* 1993; Daily *et al.* 1995; Chambers *et al.* 2004; Titov *et al.* 2004; Ustra *et al.* 2012; Martinho *et al.* 2006; Cassiani *et al.* 2009; Schmutz *et al.* 2010; Abdel Aal and Atekwana 2013). Only for high absolute ζ -potentials at the HC surface (i.e., for mixtures containing a larger fraction of long-chain components) in the case of a non-wetting HC, we observe a reversal of this pattern. We explained the resulting increase in conductivity with HC saturation with the high cation concentration in the EDL that outbalances the displacement of conducting electrolyte by the insulating HC droplet.

Revil *et al.* (2011) anticipated a similar relationship in their discussion of the conductivity increase observed on sand samples that were contaminated with a wetting oil characterised by a larger fraction of polar components (i.e., resins and asphaltenes) and, consequently, with a higher absolute ζ -potential. Additional experimental evidence for the conductivity magnitude increase with the saturation of wetting oil can be found in Li, Tercier and

Knight (2001). The predictions of our model, which only indicate this increase if HC is the non-wetting phase, do not seem to fit the experimental findings. A possible explanation is the cylindrical geometry of our model, which, in the case of a wetting HC, results in a decrease in the surface area of the HC–water interface with increasing HC saturation. As the contribution of the EDL to the total electric current scales with the surface area, our HC-wet model predicts a conductivity decrease with HC saturation. However, in 3D media consisting of mineral grains, the surface area of the grain-coating HC will definitely increase with increasing HC saturation, at least for low to intermediate HC saturations.

Comparison with experimental data: conductivity phase

To our best knowledge, the proposed models (i.e., the water-wet and the HC-wet model) represent the first mechanistic approach offering a possible explanation for the decrease in IP phase shifts with increasing HC saturation and, under certain conditions, for the occurrence of a phase maximum at intermediate saturations. While the model of Schmutz *et al.* (2010) predicts a monotonous increase in IP phase shifts with HC contamination, various authors (e.g., Martinho *et al.* 2006; Flores Orozco *et al.* 2012; Johansson *et al.* 2015) mention the possibility of a different behaviour often linked to the yet unconsidered effect of membrane polarization but always in terms of conceptual models. In our models, we can explain the variations of the phase response based on the modification of the relation between the respective transport properties of the large pore spaces (wide pore) and the pore throats (narrow pore).

In the absence of HC contamination, membrane polarization is a result of the interplay of ion-selective pore throats and non-selective open pore spaces. In the case of a non-wetting HC, discontinuous droplets (and their EDL) also render the wide pores ion-selective, which decreases the membrane polarization effect with increasing HC saturation. A high absolute value of ζ_h enhances this effect to such an extent that the wide pore (together with the trapped droplet) becomes more ion-selective than the pore throat. As a result, we observe a local phase maximum at intermediate HC saturations before the droplet penetrates the pore throat and becomes continuous over various neighbouring pores. Part of this mechanism has been anticipated by Johansson *et al.* (2015) in their model A.

In the case of the liquid HC as a wetting phase, we observe a slight increase in the phase with HC saturation before it rapidly decreases to zero as the saturation approaches the critical snap-off value. As the discussion of Johansson *et al.* (2015) (their model D) illustrates, the initial increase in the membrane-polarization phase seems intuitive as the pore throats are expected to become increasingly ion-selective with increasing HC saturation. Yet, after the initial increase, our quantitative modelling predicts an overall decrease in the phase consistent with the experimental results reported by Revil *et al.* (2011) for measurements on sand samples contaminated with wetting oil.

Furthermore, we observe good agreement of the predictions of our HC-wet model with the experimentally determined phase versus benzene concentration curve reported by Flores Orozco *et al.* (2012). In their results, the sudden decrease in IP phases appears at benzene concentrations just above the solubility of benzene in water. Although these concentrations are just enough to indicate the presence of free-phase benzene, actual concentrations of the separate HC in the formation are often considerably higher than those determined from ground-water samples (e.g., Abdul, Kia and Gibson 1989). The comparison with our model predictions suggests that (i) the conditions at the site studied by Flores Orozco *et al.* (2012) are predominantly HC-wet and (ii) the separate benzene phase occupies those narrow pore throats with a significant membrane polarization response.

The only spectral IP parameter considered in our modelling study is the characteristic frequency. Its decrease with increasing HC saturation, which is predicted by the water-wet and HC-wet models, is in agreement with most experimental studies that allow assessing this parameter (e.g., Olhoeft 1992; Kemna *et al.* 1999; Cassiani *et al.* 2009; Schmutz *et al.* 2010; Revil *et al.* 2011; Flores Orozco *et al.* 2012). Most authors attribute the corresponding increase in the relaxation time to an increase in the characteristic length scale of the system, such as mean grain diameters, pore lengths, or pore throat diameters. This is straightforward as the diffusion time $\tau \propto L^2 / D$ (e.g., Bückler and Hördt 2013a) is proportional to the square of the characteristic length scale L . In our model, both pore lengths are kept constant. Instead, the variation of the effective pore cross sections and the mean concentrations determine transport rates within the electrolyte, which affects the relaxation time via the diffusivity D . As discussed in more detail above, with increasing HC saturation, the increasing constriction of the volume of the aqueous electrolyte reduces the corrected (or effective) diffusivity and, thereby, delays the relaxation process.

Implications for the detectability of free-phase hydrocarbon

The detectability of free-phase HC contamination is primarily determined by the contrast between the IP signatures (i.e., conductivity magnitude and phase) of the contaminated and the clean host medium. Although, in practice, macroscopic IP signatures will comprise responses of various polarization mechanisms at different amounts (e.g., membrane polarization and Stern layer polarization), we can deduce some qualitative relationships between the physical and electrochemical properties of the HC and the host medium on the one hand and the magnitude of the membrane-polarization response due to the contaminant phase on the other hand. In our model, the magnitude of the ζ -potential at the HC surface, the wettability conditions, and the geometrical parameters of the two cylindrical pores significantly influence the HC-induced variation of the response.

Under water-wet conditions (*cf.* Figure 8), the relation between conductivity magnitude and HC saturation is ambiguo-

ous: depending on the particular value of the ζ -potential at the HC surface, the modelled conductivity magnitude can increase, keep almost constant, or decrease with the HC concentration. The phase response of the water-wet model, in contrast, shows an unambiguous variation between the clean host medium (full water saturation), where the phase response is large, and a highly contaminated medium (water saturation close to zero), where the phase response reduces to zero. The only exception from this tendency has been discussed before and consists in the phase maximum observed around the snap-off-saturation in the case of high magnitudes of the ζ -potential at the HC surface. In summary, these model predictions imply strong detectability of source zones (i.e., zones with high HC and low water saturations close to zero) by variations of the conductivity phase.

At the same time, our results suggest that the ζ -potential at the (non-wetting) HC surface does not affect the efficiency of the IP method for the characterisation of HC-impacted sites. Instead, variations of this surface property only influence the particular shape of the phase response versus water saturation curves of the water-wet model. The maximum contrast between clean and highly contaminated media, and thus the source-zone detectability, is completely independent of the ζ -potential at the HC surface. Instead, this contrast is controlled by the magnitude of the membrane-polarization response of the clean medium: in general, narrow pores with relatively small cross sections favour the generation of high maximum phase shifts. Consequently, the membrane-polarization response of the clean medium (and, thus, the maximum contrast between clean and highly contaminated media) can be expected to increase with decreasing pore size. For a more detailed discussion of the geometrical constraints of the polarization response of the clean membrane-polarization model, we refer to Hördt *et al.* (2017).

In our HC-wet model, both parts of the complex conductivity show similar variations with the HC saturation and the ζ -potential at the HC surface: while an increasing HC saturation results in a clear decrease in conductivity magnitude and conductivity phase, the contrast between slightly and highly contaminated sediments increases with the magnitude of the ζ -potential at the HC surface. Consequently, our model predicts a higher sensibility of both parts of the IP response, i.e., conductivity magnitude and phase, to variations of HC saturation. However, also in the HC-wet model, the complex conductivity contrasts between a completely clean medium and a highly contaminated medium, and thus the detectability of source zones, are limited by the maximum response of the clean medium.

Scope of the proposed model

The scope of the proposed model can be extended to partially saturated sediments and rocks. As observed experimentally, quite similar effects on the IP response are obtained when the pore-filling electrolyte is displaced either by a (non-wetting) liquid HC or air (e.g., Titov *et al.* 2004; Cassiani *et al.* 2009). As far as modelling aspects are concerned, this observation is completely plausible

because (1) non-wetting liquid HC droplets and air bubbles/ganglia are expected to take similar geometrical configurations within the pore space (e.g., Titov *et al.* 2004; Johansson *et al.* 2015), (2) both liquid HC (high resistivities) and air (insulator) have much higher resistivities than pore water, and (3) the air–water interface is usually negatively charged (e.g., Yang *et al.* 2001; Jia, Ren and Hu 2013) as it is the case with the HC–water interface.

However, the predictive power of the proposed model is limited by a series of severe simplifications. First of all, in order to treat the underlying physical problem analytically, the complex 3D pore system of real subsurface materials is cast into a simple (2D) capillary model and the complex conductivity values presented in this study reflect the response of a bundle of such parallel 1D capillaries. While this restriction might already be significant in the HC-free case, it becomes considerably more important in the presence of the liquid HC. Depending on the dynamic contamination history, the latter can take highly complex 3D geometrical configurations on both the pore scale (e.g., Gvirtzman and Roberts 1991) and the pore-network scale (e.g., Chatzis *et al.* 1983; Zhao and Ioannidis 2003, 2007). In this sense, the responses of the proposed model need to be understood either as the basic responses of elementary cells, which are part of a larger cell network, or as the responses of bundles of pores of similar size and with similar geometrical configurations of the liquid HC.

Important aspects that have not been incorporated in our model are biodegradation and stimulated microbial activity. Notwithstanding, the metabolic degradation and/or transformation of HC compounds by indigenous soil microorganisms and products released by redox reactions potentially affect all relevant model parameters. The release of CO₂ and organic acids changes the pH in the pore water in contact with liquid (or dissolved) HC (e.g., Sauck 2000). Such acids, ions directly released by reduction processes, and dissolved minerals of the aquifer sediments that become instable under the changed pH conditions usually lead to an increase in water conductivity (e.g., Sauck 2000). Both pH and ion concentration in the pore water are the most important parameters controlling the ζ -potential at the mineral–water interface (e.g., Leroy *et al.* 2008) and the HC–water interface (e.g., Buckley *et al.* 1989; Busscher *et al.* 1995). The effect of variable ion concentration and pH on our membrane polarization model was studied in some detail by Hördt *et al.* (2016). In summary, the polarization magnitude increases monotonically with pH, whereas it increases with ion concentrations only at low to moderate salinities and decreases at high salinities. These model predictions are in good qualitative agreement with the experimental findings of Weller, Slater and Nordsiek (2013) and Weller, Zhang and Slater (2015). Biodegradation also changes the composition of the residual HC as it generally increases the fraction of polar and long-chained components, which leads to an increase in the absolute surface potential and might possibly alter wettability. Geometrical parameters can be affected too. On the one hand, changes of the ζ -potential and the release of surface-active compounds as by-

products of the degradation reactions (e.g., Kanicky *et al.* 2001) can alter interfacial tensions and wettability conditions, which can result in the geometrical reconfiguration of the two liquid phases in the pore space. On the other hand, mineral dissolution and the formation of new stable minerals (e.g., Schumacher 1996) can alter the solid phase and affect porosity, pore radii and lengths, and the interconnectivity of the pore system. In some cases, the precipitated solids might be electronically conducting (e.g., Cozzarelli *et al.* 1999), which would give rise to electrode polarization (e.g., Wong 1979) as an additional source mechanism.

Dissolution of HC into the pore water and sorption of dissolved compounds to the solid surface are also not considered. There are good reasons to believe that dissolved HC compounds do change neither the conductivity magnitude of the pore water (e.g., Lee *et al.* 2003) nor the polarization response of the composite system (e.g., Cassiani *et al.* 2009). Furthermore, these experimental observations might indicate that the effect of sorption on the polarization response is negligible too: because of their low solubility in water, dissolved HC compounds can be expected to readily sorb onto the surface of the solid phase. Although they might occupy charged surface sites and alter the ζ -potential (e.g., Forté and Bentley 2013), in the experiments conducted by Cassiani *et al.* (2009), no significant differences could be observed between samples saturated with clean water and samples saturated with water containing dissolved HCs.

CONCLUSIONS

We have developed a first mechanistic model that allows predicting how a liquid HC in the pore space affects membrane polarization in contaminated sediments or sedimentary rocks. In our model, the pore space is described as a sequence of two types of cylindrical pores with different pore radii and lengths. The separate HC-contaminant phase is considered either as an additional cylinder in the pore space or as a film covering the pore walls.

Our modelling results indicate that the EDL at the HC–water interface significantly influences the membrane-polarization response of the model system. For low absolute ζ -potentials and a non-wetting HC, the modelled conductivity magnitudes and phases decrease with HC saturation. If high ζ -potentials are assumed, increasing phases are observed for increasing HC saturation until the non-wetting HC becomes continuous across the narrow pore throats.

Regardless of the ζ -potential at the HC–water interface, our model for wetting HC predicts a monotonous decrease in the conductivity magnitude with increasing HC saturation. At the same time, the conductivity phase shows an initial increase with contaminant saturation, which is followed by a steep decrease towards the critical water saturation, at which the aqueous phase becomes discontinuous within the narrow pore throat.

As can be seen from the above results, our model provides a framework for the interpretation of phase responses that depart from the increasing phase versus HC saturation behaviour pre-

dicted by an earlier pore-scale model that attributes the IP response to the polarization of the Stern layer of the EDL at the solid–water interface (Schmutz *et al.* 2010).

Although some of the derived IP responses show good agreement with laboratory and field data, due to the strongly simplified geometry, the proposed model is definitely not meant as a sole basis for the interpretation of specific experimental data. Further developments of the proposed approach should consider more realistic pore geometries and geometric liquid HC configurations. Besides the use of numerical methods to approach more realistic pore geometries, an interesting possibility is to connect several impedances in a network, as suggested by Stebner and Hördt (2017).

ACKNOWLEDGEMENTS

This study was supported by the research project GEOCON, Advancing GEOlogical, geophysical and CONtaminant monitoring technologies for contaminated site investigation (contract 1305-00004B). The funding for GEOCON is provided by The Danish Council for Strategic Research under the Programme Commission on Sustainable Energy and Environment. Matthias Bucker gratefully acknowledges the POTHAL project (Development of geophysical exploration methods for the characterisation of mine-tailings towards exploitation) funded by the Federal Ministry of Science, Research and Economy of Austria and the German Academic Exchange Service DAAD (No. D/12/44360) for scholarships received for his participation in this study. All authors would like to recognise the detailed comments provided by two anonymous reviewers, which helped improve the original manuscript.

REFERENCES

- Abdel Aal, G.Z. G.Z.A., Slater L.D. and Atekwana E.A. 2006. Induced-polarization measurements on unconsolidated sediments from a site of active hydrocarbon biodegradation. *Geophysics* **71**(2), H13–H24.
- Abdel Aal, G.Z. G.Z.A. and Atekwana E.A. 2013. Spectral induced polarization (SIP) response of biodegraded oil in porous media. *Geophysical Journal International* **196**(2).
- Abdul A.S., Kia S.F. and Gibson T.L. 1989. Limitations of monitoring wells for the detection and quantification of petroleum products in soils and aquifers. *Groundwater Monitoring & Remediation* **9**(2), 90–99.
- Abramowitz M. and Stegun I.A. 1964. *Handbook of Mathematical Functions: With Formulas, Graphs, and Mathematical Tables*, Vol. 55. Courier Corporation.
- Atekwana E.A., Sauck W.A. and Werkema D.D. 2000. Investigations of geoelectrical signatures at a hydrocarbon contaminated site. *Journal of Applied Geophysics* **44**(2), 167–180.
- Atekwana E.A. and Atekwana E.A. 2010. Geophysical signatures of microbial activity at hydrocarbon contaminated sites: a review. *Surveys in Geophysics* **31**(2), 247–283.
- Atkins P. and De Paula J. 2013. *Elements of Physical Chemistry*. New York, NY: Oxford University Press.
- Bairlein K., Bucker M., Hördt A. and Hinze B. 2016. Temperature dependence of spectral induced polarization data: experimental results and membrane polarization theory. *Geophysical Journal International* **205**(1), 440–453.

- Börner F., Gruhne M. and Schön J. 1993. Contamination indications derived from electrical properties in the low frequency range. *Geophysical Prospecting* **41**(1), 83–98.
- Buchheim W. and Irmer G. 1979. Zur Theorie der induzierten galvanischen Polarisation in Festkörpern mit elektrolytischer Porenfüllung. *Gerlands Beiträge zur Geophysik* **88**, 53–72.
- Buckley J.S., Takamura K. and Morrow N.R. 1989. Influence of electrical surface charges on the wetting properties of crude oils. *SPE Reservoir Engineering* **4**(03), 332–340.
- Busscher H.J., Van de Belt-Gritter B. and Van der Mei H.C. 1995. Implications of microbial adhesion to hydrocarbons for evaluating cell surface hydrophobicity 1. Zeta potentials of hydrocarbon droplets. *Colloids and Surfaces B: Biointerfaces* **5**(3), 111–116.
- Butt H.-J., Graf K. and Kappl M. 2003. *Physics and Chemistry of Interfaces*. Weinheim, Germany: Wiley-VCH.
- Bücker M. and Hördt A. 2013a. Long and short narrow pore models for membrane polarization. *Geophysics* **78**(6), E299–E314.
- Bücker M. and Hördt A. 2013b. Analytical modelling of membrane polarization with explicit parametrization of pore radii and the electrical double layer. *Geophysical Journal International* **194**(2), 804–813.
- Cassiani G., Kemna A., Villa A. and Zimmermann E. 2009. Spectral induced polarization for the characterization of free-phase hydrocarbon contamination of sediments with low clay content. *Near Surface Geophysics* **7**(5–6), 547–562.
- Cassiani G., Binley A., Kemna A., Wehrer M., Orozco A.F., Deiana R. et al. 2014. Noninvasive characterization of the Trecate (Italy) crude-oil contaminated site: links between contamination and geophysical signals. *Environmental Science and Pollution Research* **21**(15), 8914–8931.
- Cassidy D.P., Werkema Jr D.D., Sauck W., Atekwana E., Rossbach S. and Duris J. 2001. The effects of LNAPL biodegradation products on electrical conductivity measurements. *Journal of Environmental & Engineering Geophysics* **6**(1), 47–52.
- Caterina D., Flores Orozco A. and Nguyen F. 2017. Long-term ERT monitoring of biogeochemical changes of an aged hydrocarbon contamination. *Journal of Contaminant Hydrology* **201**, 19–29.
- Chambers J.E., Loke M.H., Ogilvy R.D. and Meldrum P.I. 2004. Noninvasive monitoring of DNAPL migration through a saturated porous medium using electrical impedance tomography. *Journal of Contaminant Hydrology* **68**(1), 1–22.
- Chatzis I., Morrow N.R. and Lim H.T. 1983. Magnitude and detailed structure of residual oil saturation. *Society of Petroleum Engineers Journal* **23**(2), 311–326.
- Cozzarelli I.M., Herman J.S., Baedeker M.J. and Fischer J.M. 1999. Geochemical heterogeneity of a gasoline-contaminated aquifer. *Journal of Contaminant Hydrology* **40**(3), 261–284.
- Daily W., Ramirez A., LaBrecque D. and Barber W. 1995. Electrical resistance tomography experiments at the Oregon Graduate Institute. *Journal of Applied Geophysics* **33**(4), 227–237.
- Deceuster J. and Kaufmann O. 2012. Improving the delineation of hydrocarbon-impacted soils and water through induced polarization (IP) tomographies: a field study at an industrial waste land. *Journal of Contaminant Hydrology* **136**, 25–42.
- Farooq U., Simon S., Tweheyo M.T., Sjöblom J. and Øye G. 2012. Electrophoretic measurements of crude oil fractions dispersed in aqueous solutions of different ionic compositions—Evaluation of the interfacial charging mechanisms. *Journal of Dispersion Science and Technology* **34**(10), 1376–1381.
- Flores Orozco A., Kemna A., Oberdörster C., Zschornack L., Leven C., Dietrich P. et al. 2012. Delineation of subsurface hydrocarbon contamination at a former hydrogenation plant using spectral induced polarization imaging. *Journal of Contaminant Hydrology* **136**, 131–144.
- Flores Orozco A., Velimirovic M., Tosco T., Kemna A., Sapion H., Klaas N. et al. 2015. Monitoring the injection of microscale zerovalent iron particles for groundwater remediation by means of complex electrical conductivity imaging. *Environmental Science & Technology* **49**(9), 5593–5600.
- Forté S. and Bentley L.R. 2013. Effect of hydrocarbon contamination on streaming potential. *Near Surface Geophysics* **11**(1), 75–83.
- Gaiser C., Fellmuth B., Haft N., Kuhn A., Thiele-Krivoi B., Zandt T. et al. 2017. Final determination of the Boltzmann constant by dielectric-constant gas thermometry. *Metrologia* **54**(3), 280.
- Gvrtzman H. and Roberts P.V. 1991. Pore scale spatial analysis of two immiscible fluids in porous media. *Water Resources Research* **27**(6), 1165–1176.
- Hördt A., Bairlein K., Bielefeld A., Bücker M., Kuhn E., Nordsiek S. et al. 2016. The dependence of induced polarization on fluid salinity and pH, studied with an extended model of membrane polarization. *Journal of Applied Geophysics* **135**, 408–417.
- Hördt A., Bairlein K., Bücker M. and Stebner H. 2017. Geometrical constraints for membrane polarization. *Near Surface Geophysics* (this issue, submitted).
- Hunter R.J. 1981. *Zeta Potential in Colloid Science: Principles and Applications*. London, UK: Academic Press.
- Jia W., Ren S. and Hu B. 2013. Effect of water chemistry on zeta potential of air bubbles. *International Journal of Electrochemical Science* **8**, 5828–5837.
- Johansson S., Fiandaca G. and Dahlin T. 2015. Influence of non-aqueous phase liquid configuration on induced polarization parameters: conceptual models applied to a time-domain field case study. *Journal of Applied Geophysics* **123**, 295–309.
- Kanicky J.R., Lopez-Montilla J.C., Pandey S. and Shah D. 2001. Surface chemistry in the petroleum industry. In: *Handbook of Applied Surface and Colloid Chemistry*, Vol. 1, pp. 251–267.
- Kemna A., Räckers E. and Dresen L. 1999. Field applications of complex resistivity tomography. 69th SEG Annual International Meeting, 331–334.
- Kemna A., Binley A. and Slater L. 2004. Crosshole IP imaging for engineering and environmental applications. *Geophysics* **69**(1), 97–107.
- Lee J.H., Oh M.H., Park J., Lee S.H. and Ahn K.H. 2003. Dielectric dispersion characteristics of sand contaminated by heavy metal, landfill leachate and BTEX (02-104B). *Journal of Hazardous Materials* **105**(1), 83–102.
- Leroy P., Revil A., Kemna A., Cosenza A. and Ghorbani A. 2008. Complex conductivity of water-saturated packs of glass beads. *Journal of Colloid and Interface Science* **321**, 103–117.
- Leroy P. and Revil A. 2009. A mechanistic model for the spectral induced polarization of clay materials. *Journal of Geophysical Research: Solid Earth* **114**(B10).
- Li C., Tercier P. and Knight R. 2001. Effect of sorbed oil on the dielectric properties of sand and clay. *Water Resources Research* **37**(6), 1783–1793.
- Marinova K.G., Alargova R.G., Denkov N.D., Velev O.D., Petsev D.N., Ivanov I.B. et al. 1996. Charging of oil-water interfaces due to spontaneous adsorption of hydroxyl ions. *Langmuir* **12**(8), 2045–2051.
- Marshall D.J. and Madden T.R. 1959. Induced polarization, a study of its causes. *Geophysics* **24**(4), 790–816.
- Martinho E., Almeida F. and Matias M.S. 2006. An experimental study of organic pollutant effects on time domain induced polarization measurements. *Journal of Applied Geophysics* **60**(1), 27–40.
- Morris D.A. and Johnson A.I. 1967. Summary of hydrologic and physical properties of rock and soil materials, as analyzed by the hydrologic laboratory of the US Geological Survey, 1948-60 (No. 1839-D). US Government Publishing Office.
- Newell C.J., Acree S.D., Ross R.R. and Huling S.G. 1995. Light nonaqueous phase liquids. Robert S. Kerr Environmental Research Laboratory,

- Superfund Technology Support Center for Ground Water, Office of Research and Development, Office of Solid Waste and Emergency Response, United States Environmental Protection Agency.
- O'Konski C.T. 1960. Electric properties of macromolecules. V. Theory of ionic polarization in polyelectrolytes. *The Journal of Physical Chemistry* **64**(5), 605–619.
- Olhoeft G.R. 1985. Low-frequency electrical properties. *Geophysics* **50**(12), 2492–2503.
- Olhoeft G.R. 1992. Geophysical detection of hydrocarbon and organic chemical contamination. *5th EEGS Symposium on the Application of Geophysics to Engineering and Environmental Problems*.
- Revil A., Schmutz M. and Batzle M.L. 2011. Influence of oil wettability upon spectral induced polarization of oil-bearing sands. *Geophysics* **76**(5), A31–A36.
- Sahloul N.A., Ioannidis M.A. and Chatzis I. 2002. Dissolution of residual non-aqueous phase liquids in porous media: pore-scale mechanisms and mass transfer rates. *Advances in Water Resources* **25**(1), 33–49.
- Sauck W.A. 2000. A model for the resistivity structure of LNAPL plumes and their environs in sandy sediments. *Journal of Applied Geophysics* **44**(2), 151–165.
- Schmutz M., Revil A., Vaudelet P., Batzle M., Viñao P.F. and Werkema D.D. 2010. Influence of oil saturation upon spectral induced polarization of oil-bearing sands. *Geophysical Journal International* **183**(1), 211–224.
- Schumacher D. 1996. Hydrocarbon-induced alteration of soils and sediments. In: *Hydrocarbon Migration and its Near-Surface Expression, AAPG Memoir 66* (eds D. Schumacher and M.A. Abrams), pp. 71–89.
- Schurr J.M. 1964. On the theory of the dielectric dispersion of spherical colloidal particles in electrolyte solution. *The Journal of Physical Chemistry* **68**(9), 2407–2413.
- Schwarz G. 1962. A theory of the low-frequency dielectric dispersion of colloidal particles in electrolyte solution. *The Journal of Physical Chemistry* **66**(12), 2636–2642.
- Soga K., Page J.W.E. and Illangasekare T.H. 2004. A review of NAPL source zone remediation efficiency and the mass flux approach. *Journal of Hazardous Materials* **110**(1), 13–27.
- Sogade J.A., Scira-Scappuzzo F., Vichabian Y., Shi W., Rodi W., Lesmes D.P. et al. 2006. Induced-polarization detection and mapping of contaminant plumes. *Geophysics* **71**(3), B75–B84.
- Stachurski J. and Michałek M. 1996. The effect of the ζ potential on the stability of a non-polar oil-in-water emulsion. *Journal of Colloid and Interface Science* **184**(2), 433–436.
- Stebner H. and Hördt A. 2017. Simulation of membrane polarization of porous media with 2D and 3D impedance networks. *Near Surface Geophysics* (this issue, submitted).
- Titov K., Komarov V., Tarasov V. and Levitski A. 2002. Theoretical and experimental study of time domain-induced polarization in water-saturated sands. *Journal of Applied Geophysics* **50**(4), 417–433.
- Titov K., Kemna A., Tarasov A. and Vereecken H. 2004. Induced polarization of unsaturated sands determined through time domain measurements. *Vadose Zone Journal* **3**(4), 1160–1168.
- Ustra A., Slater L., Ntarlagiannis D. and Elis V. 2012. Spectral induced polarization (SIP) signatures of clayey soils containing toluene. *Near Surface Geophysics* **10**(6), 503–515.
- Vanhala H., Soininen H. and Kukkonen I. 1992. Detecting organic chemical contaminants by spectral-induced polarization method in glacial till environment. *Geophysics* **57**(8), 1014–1017.
- Vanhala H. 1997. Mapping oil-contaminated sand and till with the spectral induced polarization (SIP) method. *Geophysical Prospecting* **45**(2), 303–326.
- Vinegar H.J. and Waxman M.H. 1984. Induced polarization of shaly sands. *Geophysics* **49**(8), 1267–1287.
- Weller A. and Börner F. 1996. Measurements of spectral induced polarization for environmental purposes. *Environmental Geology* **27**, 329–334.
- Weller A., Gruhne M., Börner F.D. and Seichter M. 1997. Monitoring hydraulic experiments by complex conductivity tomography. *Symposium on the Application of Geophysics to Engineering and Environmental Problems 1997*, pp. 745–754. Society of Exploration Geophysicists.
- Weller A., Slater L. and Nordsiek S. 2013. On the relationship between induced polarization and surface conductivity: Implications for petrophysical interpretation of electrical measurements. *Geophysics* **78**(5), D315–D325.
- Weller A., Zhang Z. and Slater L. 2015. High-salinity polarization of sandstones. *Geophysics* **80**(3), D309–D318.
- Wong J. 1979. An electrochemical model of the induced-polarization phenomenon in disseminated sulfide ores. *Geophysics* **44**(7), 1245–1265.
- Yang C., Dabros T., Li D., Czarnecki J. and Masliyah J.H. 2001. Measurement of the zeta potential of gas bubbles in aqueous solutions by microelectrophoresis method. *Journal of Colloid and Interface Science* **243**(1), 128–135.
- Zhao W. and Ioannidis M.A. 2003. Pore network simulation of the dissolution of a single-component wetting nonaqueous phase liquid. *Water Resources Research* **39**(10).
- Zhao W. and Ioannidis M.A. 2007. Effect of NAPL film stability on the dissolution of residual wetting NAPL in porous media: a pore-scale modeling study. *Advances in Water Resources* **30**(2), 171–181.

Electrochemical polarization around metallic particles — Part 1: The role of diffuse-layer and volume-diffusion relaxation

Matthias Buecker¹, Adrián Flores Orozco², and Andreas Kemna³

ABSTRACT

We have developed an extension of the theory and mathematical description of the commonly used Wong model of electrode polarization. The full solution of the Poisson-Nernst-Planck system is provided, including three additional unknown coefficients, which describe the microscale polarization response at the surface of a perfectly conducting particle. The model involves two simultaneously acting polarization mechanisms. The first is related to the dynamic charging of diffuse layers induced over the poles of the particles, which relaxes on a time scale proportional to the particle radius and Debye length of the electrolyte solution. The second is a volume-diffusion mechanism, which is activated by reaction currents through the solid-liquid interface, i.e., faradaic currents due

to charge-transfer reactions. The relaxation time of the resulting concentration polarization around the particle increases quadratically with the particle radius and the fraction of electroactive cations in the electrolyte. Although diffuse-layer polarization dominates the effective response for small particles and in the absence of reactive cations, volume-diffusion polarization only affects the macroscopic behavior if the particle size exceeds a critical value. From the closed-form analytic expressions for both relaxation times that we used, we derive a critical particle radius that depends on Debye length and reactive cation concentration. Based on the improved understanding of the underlying polarization processes, we also review some recent conceptual models of metallic polarization and correct several physical misconceptions inherent to these reinterpretations of the classic theory.

INTRODUCTION

Due to the strong polarization response of metallic minerals, the induced-polarization (IP) method has been used for decades in the exploration of ore deposits (e.g., [Seigel et al., 2007](#)). From the beginning, the observed frequency dispersion of the measured electrical conductivities was attributed to the polarization of the solid-liquid interface between highly conductive mineral grains and the surrounding electrolyte (e.g., [Wait, 1958](#)), often referred to as electrode polarization. [Pelton et al. \(1978\)](#) later adapt the empirical Cole-Cole relaxation model ([Cole and Cole, 1941](#)) to describe the frequency-dependence of IP measurements, which to date is a common practice. To improve the understanding of

the microscopic causes of the polarization effect taking place around metallic particles, [Angoran and Madden \(1977\)](#) and [Klein and Shuey \(1978\)](#) study the effect of reaction currents, which arise from charge-transfer reactions of electroactive cation species at the solid-liquid interface. Because reaction currents short circuit the charge accumulations at both sides of the interface, the polarization of the particle surfaces becomes imperfect, which in turn largely affects the polarization response. The two aforementioned studies laid the foundation for the models by [Wong \(1979\)](#) and [Wong and Strangway \(1981\)](#), which directly relate the observed IP response to the geometric and electrochemical properties of highly conductive particles suspended in an electrolyte solution.

Manuscript received by the Editor 24 June 2017; revised manuscript received 13 February 2018; published ahead of production 28 March 2018; published online 31 May 2018.

¹Rheinische Friedrich-Wilhelms-Universität, Steinmann Institute, Department of Geophysics, Meckenheimer Allee 176, 53115 Bonn, Germany and TU Wien, Department of Geodesy and Geoinformation, Research Group Geophysics, Gußhausstraße 27-29/E120, 1040 Vienna, Austria. E-mail: buecker.matthias@yahoo.de.

²TU Wien, Department of Geodesy and Geoinformation, Research Group Geophysics, Gußhausstraße 27-29/E120, Vienna 1040, Austria. E-mail: adrian.flores-orozco@geo.tuwien.ac.at.

³Rheinische Friedrich-Wilhelms-Universität, Steinmann Institute, Department of Geophysics, Meckenheimer Allee 176, Bonn 53115, Germany. E-mail: kemna@geo.uni-bonn.de.

© 2018 Society of Exploration Geophysicists. All rights reserved.

During the past two decades, technical advances regarding measuring devices and imaging algorithms led to a renewed interest in the IP method (e.g., Kemna et al., 2012). Ongoing research provides detailed knowledge on complex-conductivity responses of composite geomaterials leading to a continued widening of the range of near-surface applications of the method (Kemna et al., 2012). As a result, today, the polarization response of metallic particles is also taken advantage of for environmental investigations, such as the detection and characterization of metal-bearing contaminant plumes (e.g., Placencia-Gómez et al., 2015; Günther and Martin, 2016), the accumulation of iron sulfides accompanying bioremediation (Flores Orozco et al., 2011, 2013), or naturally reduced zones related to biogeochemical hot spots (e.g., Wainwright et al., 2015), the monitoring of permeable reactive barriers (e.g., Slater and Binley, 2006), or metallic nanoparticle injections (e.g., Flores Orozco et al., 2015; Aal et al., 2017), among others.

Because the classic models cannot explain the broad variety of measured IP responses (e.g., Flores Orozco et al., 2011, 2013), the rapid experimental advances also stimulate a search for improved models and a deeper understanding of the polarization of conducting particles. Merriam (2007) emphasizes the importance of charge storage in the Stern layer — the inner fixed layer of the electrical double-layer coating the solid-liquid interface, which had so far not been taken into account explicitly. However, the limitation of his treatment to one spatial dimension might overlook the more complex responses of 2D or 3D media. Flekkøy (2013) develops a semiempirical diffusion-polarization model (also in one spatial dimension), which relates the well-known Cole-Cole relaxation model to microscopic parameters. Placencia-Gómez and Slater (2014) use the model by Wong (1979) to reproduce most characteristics of IP responses measured on artificial sulfide-sand mixtures, but they also point out important limitations of this highly parameterized model regarding the fitting of real IP spectra. In an attempt to reduce the complexity of Wong's model, Gurin et al. (2015) and Placencia-Gómez and Slater (2015) reinterpret the polarization of metallic particles in terms of the polarization of non-conducting dielectric particles (e.g., O'Konski, 1960; Schwarz, 1962; Schurr, 1964). Possible shortcomings of these recent studies will be addressed in the "Discussion" section. Because many important ore minerals are semiconductors (e.g., Pearce et al., 2006), Revil et al. (2015) and Misra et al. (2016) dispute Wong's assumption of perfectly conducting particles as inappropriate for most ore minerals and develop models for the polarization of semi-conducting particles. These models additionally include the contribution of the nonmetallic background material (e.g., of clay minerals) to the overall polarization response.

Considering the lack of a unified theory of the electrode polarization mechanisms as described above, this study further analyzes Wong's electrochemical model. Particular emphasis is placed on the control that particle size and chemical composition of the electrolyte (i.e., electrolyte concentration and fraction of electroactive ions) exert over the polarization response. In contrast to the compact treatment provided by Wong (1979), we include the derivation of the full solution of the underlying Poisson-Nernst-Planck (PNP) system of differential equations. We also derive explicit expressions for the time constants of the two main relaxation processes inherent to the model, the diffuse-layer and volume-diffusion relaxation. Our improvements of the mathematical description permit us to illustrate the spatial variation of ion concentrations and electric

potential around the particle and set the basis for a better understanding of the electrode polarization mechanism. Following our systematic analysis, it is then possible to reveal and discuss some notable misinterpretations of Wong's model that arose in the more recent literature.

THEORY

Wong (1979) bases his model of the polarization response of metal-bearing geomaterials on the treatment of perfectly conducting particles suspended in an electrolyte. The electrolyte is characterized by the concentrations of three ionic species: anions n_1 , inactive cations n_2 , and active cations n_3 . Inactive cations are those cations that are not able to penetrate the solid-liquid interface, whereas active cations engage in reduction-oxidation reactions at the metal surface, which allow electric charges to be transferred between the two phases. Typical examples for inactive cations are Na^+ or K^+ , and active cations will generally be dissolved metal ions.

Under the influence of an external electric field \mathbf{E}_{ext} , the concentrations of the three ionic species and the electric potential U are perturbed from their equilibrium values. For a periodic excitation with $E_{\text{ext}} = E_0 e^{i\omega t}$, where ω denotes the angular frequency and t is the time, the ion concentrations can be expressed in terms of uniform equilibrium concentrations in the bulk electrolyte n_j^∞ and frequency-dependent perturbation concentrations δn_j as follows:

$$n_j(\mathbf{r}, t) = n_j^\infty + \delta n_j(\mathbf{r}, \omega) e^{i\omega t}. \quad (1)$$

Unlike Wong, who defines the ion concentrations in ions/ m^3 , here, we use molar concentrations in mol/ m^3 . If no excitation is imposed, the electric potential U is zero everywhere. Consequently, under the influence of a harmonic external field, the total electric potential is equal to the corresponding perturbation potential

$$U(\mathbf{r}, t) = \delta U(\mathbf{r}, \omega) e^{i\omega t}. \quad (2)$$

In the perturbed system, concentration gradients drive diffusion currents and electric fields cause electromigration currents. For sufficiently small amplitudes E_0 of the external field, the corresponding linearized ion flux densities read

$$\mathbf{J}_j(\mathbf{r}, t) = -D_j \nabla \delta n_j(\mathbf{r}, \omega) e^{i\omega t} - \mu_j z_j n_j^\infty \nabla \delta U(\mathbf{r}, \omega) e^{i\omega t}, \quad (3)$$

where D_j , μ_j , and z_j denote the diffusion coefficient, the mobility, and the valence of the j th ionic species, respectively. With the conservation laws $\partial_t \delta n_j = -\nabla \cdot \mathbf{J}_j$ and the Einstein relation $D_j = \mu_j kT/e$ (e.g., Atkins and De Paula, 2010), equation 3 becomes

$$\frac{i\omega}{D_j} \delta n_j(\mathbf{r}, \omega) = \nabla^2 \delta n_j(\mathbf{r}, \omega) + \frac{e}{kT} z_j n_j^\infty \nabla^2 \delta U(\mathbf{r}, \omega), \quad (4)$$

where $k = 8.617 \times 10^{-5}$ eV/K denotes Boltzmann's constant, T is the absolute temperature, and $e = 1.602 \times 10^{-19}$ C is the elementary charge. Although the bulk electrolyte is electrically neutral, i.e., $n_1^\infty = n_2^\infty + n_3^\infty$, nonzero charge densities arising from unbalanced total cation and anion perturbation concentrations generate electric fields as quantified by Poisson's equation

$$\nabla^2 \delta U(\mathbf{r}, \omega) = -\frac{F}{\epsilon_0 \epsilon_r} \sum_{j=1}^3 z_j \delta n_j(\mathbf{r}, \omega). \quad (5)$$

Here, $F = 96,485$ As/mol is the Faraday's constant, $\epsilon_0 = 8.85 \times 10^{-12}$ F/m is the vacuum permittivity, and ϵ_r is the relative permittivity of the solution. Equations 4 and 5 constitute the PNP system of partial differential equations, which is used to describe ion transport through the electrolyte solution around the conducting particle.

Full analytic solution

To model the complex frequency-dependent response of a suspension of metallic particles, the PNP system is first solved for a single spherical particle of radius a centered at the origin of a polar-coordinate system r, θ, φ . Choosing $\theta = 0$ in the direction of the external field, the latter can be described by the electric potential $\delta U_{\text{ext}} = -E_0 r \cos \theta$ and the solution becomes independent of the azimuthal angle φ . To simplify the algebraic expressions, ion mobilities and diffusion coefficients are assumed to be the same for all three ionic species, i.e., $\mu_j = \mu$ and $D_j = D$ for all j , and the treatment is limited to a symmetric monovalent electrolyte, i.e., $z_1 = -1$ and $z_2 = z_3 = 1$. A general solution of the PNP system can then be given in terms of the three perturbation concentrations (Wong, 1979):

$$\delta n_1(\mathbf{r}, \omega) = -A(\omega)k_1(\lambda_1 r) \cos \theta + B(\omega)k_1(\lambda_2 r) \cos \theta, \quad (6)$$

$$\delta n_2(\mathbf{r}, \omega) = \frac{n_2^\infty}{n_1^\infty} A(\omega)k_1(\lambda_1 r) \cos \theta + [B(\omega) - M(\omega)]k_1(\lambda_2 r) \cos \theta, \quad (7)$$

$$\delta n_3(\mathbf{r}, \omega) = \frac{n_3^\infty}{n_1^\infty} A(\omega)k_1(\lambda_1 r) \cos \theta + M(\omega)k_1(\lambda_2 r) \cos \theta, \quad (8)$$

and the perturbation potential

$$\delta U(\mathbf{r}, \omega) = \left[-\frac{2F}{\lambda_1^2 \epsilon_0 \epsilon_r} A(\omega)k_1(\lambda_1 r) - E_0 r + E(\omega) \frac{a^3}{r^2} \right] \cos \theta. \quad (9)$$

The radial variation of the perturbation concentrations is controlled by the modified spherical Bessel function of the second kind

$$k_1(\lambda r) = \frac{\pi}{2} e^{-\lambda r} \left(\frac{1}{\lambda r} + \frac{1}{\lambda^2 r^2} \right), \quad (10)$$

and the two reciprocal length scales

$$\lambda_1^2 = \frac{i\omega}{D} + \kappa^2 \quad \text{and} \quad \lambda_2^2 = \frac{i\omega}{D}, \quad (11)$$

where $\kappa = [2n_1^\infty eF / (\epsilon_0 \epsilon_r kT)]^{1/2}$ is equal to the inverse of the Debye length λ_D .

The four unknown coefficients $A(\omega)$, $B(\omega)$, $E(\omega)$, and $M(\omega)$ are determined from boundary conditions on the three ion flux densities and the perturbation potential at the metal surface. For brevity, here, we only present the final expressions for the coefficients. Intermediate steps of this derivation are given in Appendix A. The coefficient $E(\omega)$ is the only provided and discussed in the treatment by Wong (1979):

$$E(\omega) = E_0 \left\{ 1 + \frac{3 \left(1 + \frac{\beta a}{D} f_3 \right) + \frac{3n_3^\infty}{n_1^\infty - 2n_1^\infty} \left(\frac{\alpha - 1}{\mu} \right)}{\frac{n_3^\infty}{n_1^\infty - 2n_1^\infty} \left[f_1 + \frac{\alpha}{\mu} (f_2 - 2) + \frac{\beta a \lambda_1^2}{D \kappa^2} + 2 \right] - (2 + f_1) \left(1 + \frac{\beta a}{D} f_3 \right)} \right\}, \quad (12)$$

where

$$f_1 := f_2 \frac{i\omega}{D \kappa^2}, \quad f_2 := \frac{\lambda_1^2 a^2 + 2\lambda_1 a + 2}{\lambda_1 a + 1}, \quad \text{and} \\ f_3 := \frac{\lambda_2 a + 1}{\lambda_2^2 a^2 + 2\lambda_2 a + 2}. \quad (13)$$

With the coefficient $E(\omega)$ at hand, the remaining unknown coefficients, which control the short-range perturbations around the polarized particle, can be expressed as

$$A(\omega) = \frac{E_0 a - E(\omega) a}{-2F / (\lambda_1^2 \epsilon_0 \epsilon_r) k_1(\lambda_1 a)}, \quad (14)$$

$$B(\omega) = \frac{E_0 - E(\omega)}{k_1'(\lambda_2 a)} \left\{ \frac{\lambda_1^2 \epsilon_0 \epsilon_r}{2F} f_2 - \frac{\mu}{D} n_1^\infty \left[f_2 + \frac{E_0 + 2E(\omega)}{E_0 - E(\omega)} \right] \right\}, \\ \text{and} \quad (15)$$

$$M(\omega) = -\frac{n_3^\infty}{n_1^\infty} \frac{E_0 - E(\omega)}{k_1'(\lambda_2 a) \left(1 + \frac{\beta a}{D} f_3 \right)} \left\{ \frac{\lambda_1^2 \epsilon_0 \epsilon_r}{2F} \left(f_2 + \frac{\beta a}{D} \right) - \frac{n_1^\infty}{D} (\mu - \alpha) \left[f_2 + \frac{E_0 + 2E(\omega)}{E_0 - E(\omega)} \right] \right\}, \quad (16)$$

where $k_1'(\lambda a)$ denotes the partial derivative of the modified spherical Bessel function of the second kind evaluated at the metal surface. Differentiation of equation 10 yields

$$k_1'(\lambda a) = \partial_r k_1(\lambda r)|_{r=a} = -\lambda k_1(\lambda a) - \frac{\pi}{2} \frac{e^{-\lambda a}}{a} \left(\frac{1}{\lambda a} + \frac{2}{\lambda^2 a^2} \right). \quad (17)$$

The four coefficients, equations 12–16, substituted into the general solution, equations 6–9, constitute the full solution of the problem, which shall now be further analyzed.

The first terms on the right sides of equations 6–8 describe the space charge $F[\delta n_2(\mathbf{r}, \omega) + \delta n_3(\mathbf{r}, \omega) - \delta n_1(\mathbf{r}, \omega)]$, which accumulates in a field-induced Gouy-Chapman diffuse layer. For sufficiently small frequencies, $\lambda_1 \approx \kappa$ and the term $k_1(\lambda_1 r)$ controlling the spatial extension of the space charge decays roughly with $e^{-\kappa r}$. The characteristic length of this decay is the Debye length

$\lambda_D = 1/\kappa$, which may thus be used to approximate the thickness of the diffuse layer. The second terms of equations 6–8, in contrast, describe electroneutral concentration perturbations, the spatial extension of which is controlled by the ratio $k_1(\lambda_2 r)/k_1'(\lambda_2 a)$. At low frequencies, i.e., for $\omega \rightarrow 0$, this ratio approaches $-a^3/(2r^2)$ and thus describes a $1/r^2$ decay, which allows the concentration perturbation to extend much deeper into the electrolyte. As an estimator for the thickness of the layer affected by the concentration perturbation, we will use the distance of $a\sqrt{e} - a$ from the surface, at which the concentration perturbations reduce to $1/e$ of their (virtual) values at the particle surface.

The total perturbation potential consists of three contributions. The first term on the right side of equation 9 corresponds to the field-induced space charge that accumulates in the diffuse layer. Just like the space charge, the related potential perturbation decays exponentially with the distance from the surface. The second term describes the contribution of the uniform external electric field. The last term corresponds to the effective or long-range induced dipole moment of the polarized particle, including the surrounding perturbation layer. The dipole potential decays quadratically with the distance from the center of the particle.

For the quantification of the macroscopic polarization response of the suspended particle, it is sufficient to know the reflection coefficient $f(\omega) = E(\omega)/E_0$, which describes the long-range potential perturbation (the third term in equation 9) produced by the

polarized particle together with the space charges that accumulate in its immediate vicinity. The effective conductivity σ_{eff} describes the effect of the suspended spherical particles on the macroscopic electrical properties of the inhomogeneous medium in terms of the conductivity of an equivalent homogeneous medium. To approximate the effective conductivity σ_{eff} of a two-phase system consisting of several metallic particles randomly dispersed in the electrolytic host medium, the dipole coefficient enters into the mixing rule (Wong, 1979)

$$\frac{\sigma_{\text{eff}}(\omega)}{\sigma_0} = \frac{1 + 2\nu f(\omega)}{1 - \nu f(\omega)}, \quad (18)$$

where $\sigma_0 = 2\mu n_1^\infty F$ denotes the electrical conductivity of the bulk electrolyte and ν is the volumetric fraction of metallic particles.

POLARIZATION MECHANISM

The treatment provided by Wong (1979) does not provide a comprehensive discussion of the contributions of the different micro-scale processes described by his theory; neither does he detail the relation between these physical processes and the model parameters, such as particle size and electrolyte composition. This lack has resulted in fundamental misconceptions of the model. Based on the full solution of the PNP system, we can provide visual insight into the polarization phenomena and more thorough explanations of the underlying physical processes. Therefore, this section aims at realigning the understanding of the Wong model in general and the parameters controlling amplitude and shape of the frequency-dependence electric conductivity in particular.

Under the influence of an external electric field, mobile charges on the perfectly conducting particle — the electrons in the case of a metallic conductor — instantaneously redistribute along its surface. Within the particle, the electric field of the resulting charge distribution exactly cancels out the external field. This property of the perfect conductor is taken into account by a zero-potential boundary condition on the particle surface (see equation A-1). As shown in Appendix B, the surface charge density required to cancel out the mere external field is given by

$$\Sigma_\infty(\theta) = 3\epsilon_0\epsilon_r E_0 \cos \theta. \quad (19)$$

On the electrolyte side, the induced surface charge Σ_∞ attracts ions of the opposite sign (counterions) and repels those of the same sign (co-ions). This situation corresponds to an excitation with high frequencies or to early times after switching on a constant external field.

In addition to this very fast polarization process, migration currents through the bulk solution further charge the electrolyte around the poles of the particle (see Figure 1). The charging continues until the effect of the electromigration currents is balanced by opposed diffusion currents around the particle. In this manner, at sufficiently low excitation frequencies, a new quasi-equilibrium situation is established, in which Gouy-Chapman diffuse layers build up at the particle surface. Because the continued accumulation of charges in the diffuse layers induces opposite image charges on the conducting sphere, this process also blows up the surface charge on the particle. In Appendix B, we show that the total charge in the fully developed diffuse layer can be approximated by

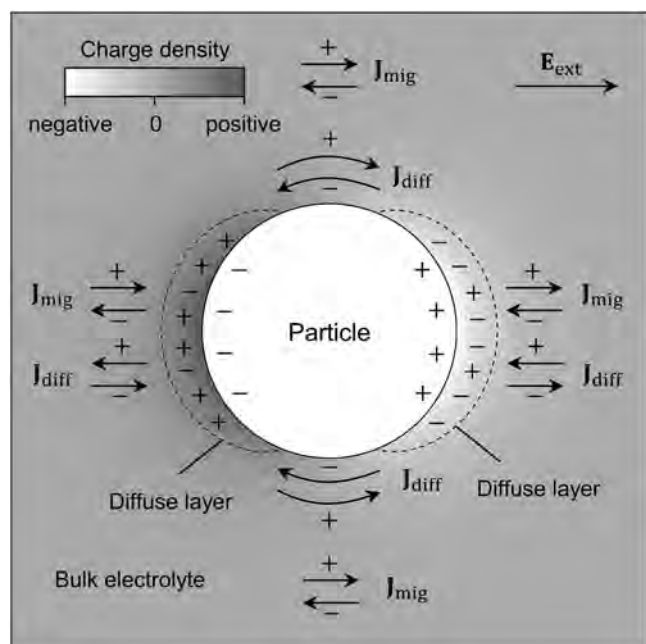


Figure 1. Schematic representation of the double-layer charging mechanism. Over the right side of the sphere, the migration current J_{mig} in the bulk electrolyte depletes cations (+) from the diffuse layer and fills it with anions (-). The resulting space charge in the diffuse layer induces positive image charges on the particle, which hold the space charge next to the surface. Over the left side, the process is the same but with opposite polarity, such that concentration gradients arise between the two hemispheres. As soon as the charging migration currents are balanced by (tangential and normal) diffusion currents J_{diff} driven by the concentration gradients, a quasi-equilibrium state is reached with a fully charged diffuse layer.

$$\Sigma_0(\theta) = \Sigma_\infty(\theta) \frac{\kappa a}{2}. \quad (20)$$

As for typical particle sizes and electrolyte concentrations, the double layer is much thinner than the particle radius and, thus, $\kappa a \gg 1$, the charge stored in the diffuse layer and mirrored on the particle surface exceeds by far the one necessary to cancel out the electric field within the sphere.

Figure 2 illustrates the field-induced perturbations around the conducting particle in terms of their real (upper half of each panel) and imaginary parts (lower half). Where indicated, small magnitudes of the imaginary components are magnified by the factors defined in the lower halves of the panels. The first line of Figure 2 shows the four perturbation quantities at the low-frequency limit, the second line at an intermediate frequency, and the third line at the high-frequency limit. For a justification of the selected frequencies, please refer to the spectral responses included at the end of this section. At the low-frequency limit, we recognize fully developed diffuse layers covering the two sides of a submicron particle ($a = 0.1 \mu\text{m}$). We select a very small particle for the visualization because it permits to distinguish the diffuse layer of thickness λ_D , as indicated by the inner dashed line. According to the orientation of the external electric field (pointing right), the induced surface charge is negative on the left side and positive on the right. Correspondingly, the polarities of the induced diffuse layers are opposite left and right of the particle.

Still in the first line of Figure 2 and outside the diffuse layer, we identify a second zone of nonzero perturbation concentrations indicated by the outer dashed line. This anomaly, which is most pronounced for the active cations, but balanced by corresponding perturbations of the concentrations of the two inactive ionic species, corresponds to the electroneutral parts of the perturbation concentrations described by the second terms of equations 6–8. The build-up of the concentration cloud is linked to reaction currents across the solid-liquid interface, and thus it disappears in the absence of active cations (not shown here for brevity). The formation of the concentration cloud can be understood in terms of the volume- or bulk-diffusion process explained in Figure 3. In summary, perturbations of the active cation concentrations produced by the reaction currents cannot be balanced by electromigration currents through the bulk electrolyte. Instead, a concentration gradient arises, which by means of diffusion, transports active cations from the anodic (cations are released into the solution) to the cathodic side of the particle (cations adsorb to the particle). Effectively, in Figure 2, we can convince ourselves that the accumulation of a n_3 surplus to the right and a deficit to the left of the particle corresponds to a concentration gradient, which drives a left-pointing diffusion current, whereas the electromigration current points right (in the direction of the external field).

The volume-diffusion process introduced in Figure 3 and the previous paragraph is similar to the semifinite diffusion problem over a planar electrode, which leads to the more familiar Warburg impedance (e.g., Bazant et al., 2004). Warburg-type impedances are generally encountered in electrochemical systems, in which the transport of ions to the electrode (if ions are consumed) or from the electrode away (if ions are produced) is primarily by diffusion and not by electromigration.

So far, we have only considered the polarization mechanism around a very small particle ($a = 0.1 \mu\text{m}$), the relaxation responses of which occur far beyond the maximum frequencies of typical field- and even laboratory-scale IP measurements. Yet, the radial concentration profiles (i.e., for $\theta = 0$) presented in Figure 4 show that diffuse layer and volume-diffusion layer also build up and have similar characteristics around much larger particles (here, $a = 10 \text{ nm}$) associated with relaxations at typical IP frequencies. For comparison, Figure 5 shows the radial concentration profiles around the small particle in the same fashion. Besides obvious scaling effects, the most significant difference between the radial profiles of differently sized particles concerns the perturbation concentrations of the active cations δn_3 within the diffuse layer. Whereas to the right of the small particle (Figures 2 and 5), the perturbation concentrations are negative, i.e., active cations are depleted compared with the bulk electrolyte, they become positive in the case of a much larger particle (Figure 4b) representing an increase over the active cation bulk concentration.

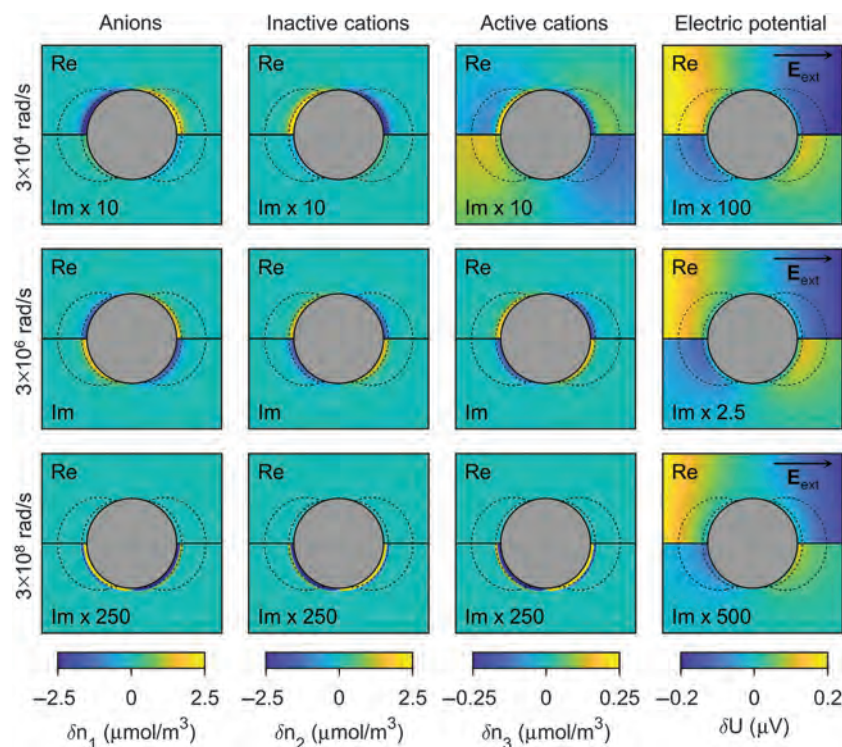


Figure 2. Perturbation concentrations and potentials around a perfectly conducting sphere of radius $a = 0.1 \mu\text{m}$ for three different angular frequencies. The upper part of each panel shows the real part, and the lower part shows the imaginary part. Note that some imaginary parts were scaled to make small variations visible. The inner dashed line indicates the diffuse double layer, and the outer dashed line indicates the volume-diffusion layer. The parameter values are $\epsilon_r = 80$, $\mu = 5 \times 10^{-8} \text{ m}^2/(\text{Vs})$, $n_1^\infty = 1 \text{ mol/m}^3$, $n_3^\infty = 0.12n_1^\infty$, $\alpha = 1 \cdot 10^{-10} \text{ m}^2/(\text{Vs})$, $\beta = 1 \times 10^{-2} \text{ m/s}$, $T = 293 \text{ K}$, and $E_0 = 1 \text{ V/m}$.

We explain this observation by the different overlaps of diffuse (thickness λ_D) and volume-diffusion layer (thickness $\approx 0.65a$). Around the submicron particle, the diffuse layer occupies a large fraction of $\lambda_D/(0.65a) = 0.15$ of the volume-diffusion layer, which seems to be large enough to inhibit a full development of the volume-diffusion layer. Around the large particle, this fraction is much smaller (10^{-6}) and the volume-diffusion layer fully develops. Further below, the strong control the ratio λ_D/a or its inverse ka exerts on the volume-diffusion polarization will be reconfirmed.

When the frequency of the external excitation is increased until it approaches the respective characteristic frequency (i.e., 3×10^6 and 0.1 rad/s around the small and the large particle, respectively), large imaginary parts of the perturbation concentrations appear within the electrical double layer indicating that a relaxation is taking place. At the same time, the perturbation concentrations in the volume-diffusion layer practically disappear around the small (second line in Figures 2 and 5) and reduce significantly around the large particle (see $\omega = 0.1$ rad/s in Figure 4). A reduced diffuse layer persists in both cases.

If the frequency is further increased, the temporal variation of the excitation is too fast to permit the ions to rearrange and form the diffuse layer. As a consequence, in the respective high-frequency limits, real and imaginary part of the perturbation concentrations approach zero.

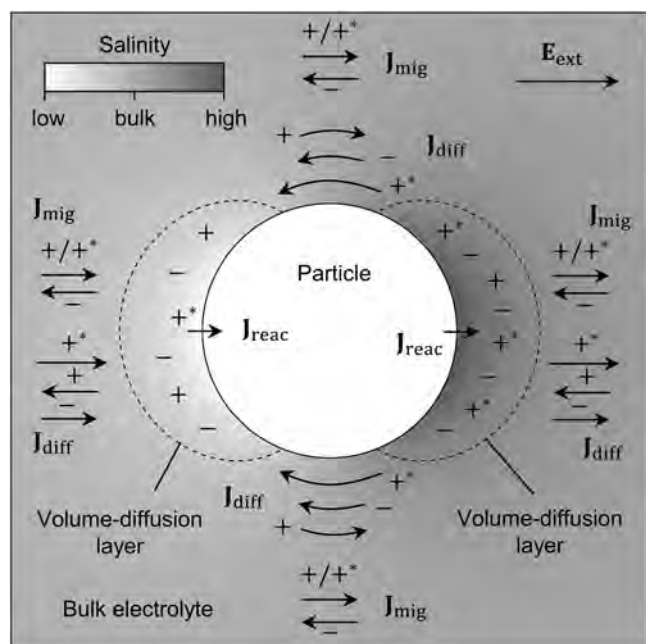


Figure 3. Schematic representation of the volume-diffusion mechanism. For the sake of clarity, the diffuse layer is omitted, although in reality it would be superimposed. The reaction current \mathbf{J}_{reac} depletes active cations ($+^*$) from the left and fills the right volume-diffusion layer with active cations. The migration currents \mathbf{J}_{mig} through the bulk electrolyte transport active ($+^*$) and inactive cations ($+$) with the fixed proportion n_3^∞/n_2^∞ and can therefore not balance the resulting concentration surpluses and deficits. Instead, these perturbation concentrations increase until the resulting concentration gradients between the two opposite sides of the particle are sufficiently large to drive diffusion currents \mathbf{J}_{diff} , which compensate the excess of active ion current caused by \mathbf{J}_{reac} .

As we can see from the perturbation potential (Figure 6), the development of a quasi-equilibrium diffuse layer at low frequencies largely screens (counterbalances) the field-induced surface charge Σ on the conducting particle. As a result, outside the diffuse layer, the potential distribution approaches the one of an insulating particle, the reflection coefficient of which can be obtained as $f = -1/2$ from potential theory. The remaining difference to the potential of an insulating sphere is due to the large nonzero exchange currents (a consequence of the large active cation concentration $n_3^\infty = 0.12 \text{ mol/m}^3$), but it disappears, if $n_3^\infty \rightarrow 0$ (not shown here for brevity). As mentioned above, with increasing frequency, the diffuse layer cannot fully develop and the screening of the surface charge becomes increasingly imperfect. At the high-frequency limit, the potential distribution therefore approaches that of a perfect conductor (the reflection coefficient f of a sphere

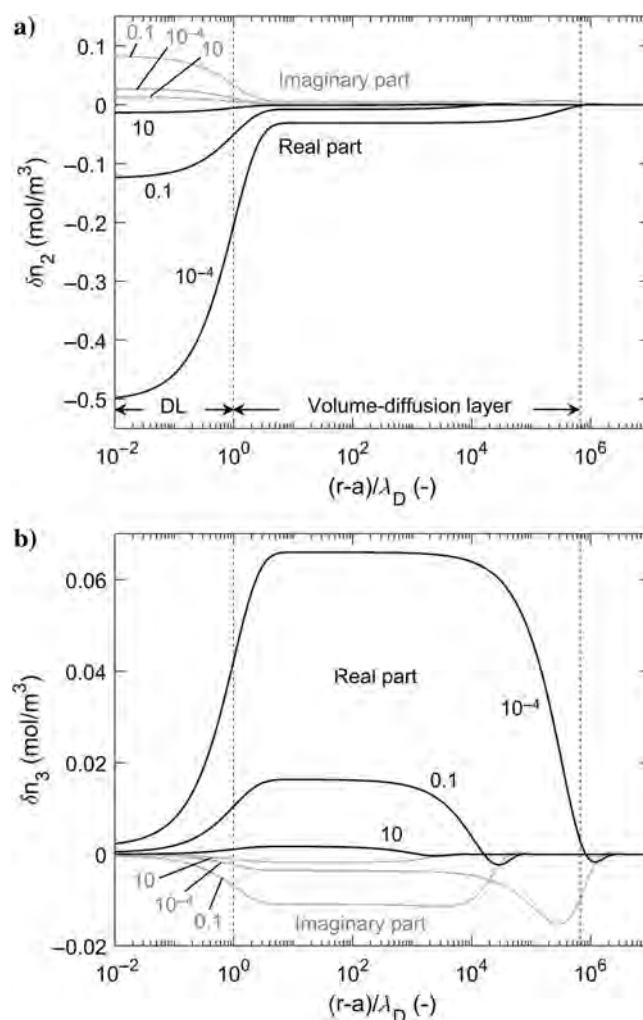


Figure 4. Radial variation (r is the distance from the center of the spherical particle) of the cation perturbation concentrations δn_2 (inactive) and δn_3 (active) along the symmetry axis ($\theta = 0$) in the vicinity of a metallic sphere of radius $a = 10 \text{ nm}$ at three different angular frequencies ($\omega = 10^{-4}, 0.1, 10 \text{ rad/s}$). The left dashed line indicates the extensions of the diffuse layer (DL, distance to surface λ_D), and the right dashed line indicates those of the volume-diffusion layer (distance $a\sqrt{\epsilon} - a$). Besides the much larger particle radius, all other parameters are as in Figure 2.

with conductivity σ_s embedded in a medium with homogeneous conductivity σ_m is $(\sigma_s - \sigma_m)/(\sigma_s + 2\sigma_m)$; e.g., Maxwell, 1891) with $f = 1$ (see, again, Figure 6).

The microscopic frequency dependencies around a single spherical particle directly relate to the macroscopic response of a suspension of a larger number of equal particles. Figure 7 shows the spectral response of a suspension with a volumetric particle content of $\nu = 0.12$ in terms of the real σ' and imaginary part σ'' of the effective electric conductivity defined in equation 18. The spectra of the two particle sizes discussed in detail in this section (i.e., $a = 0.1 \mu\text{m}$ and 10mm) appear as limiting cases, and they are accompanied by additional spectra that correspond to intermediate particle sizes. To start differentiating between the macroscopic effects of diffuse-layer polarization and volume-diffusion relaxation, Figure 7

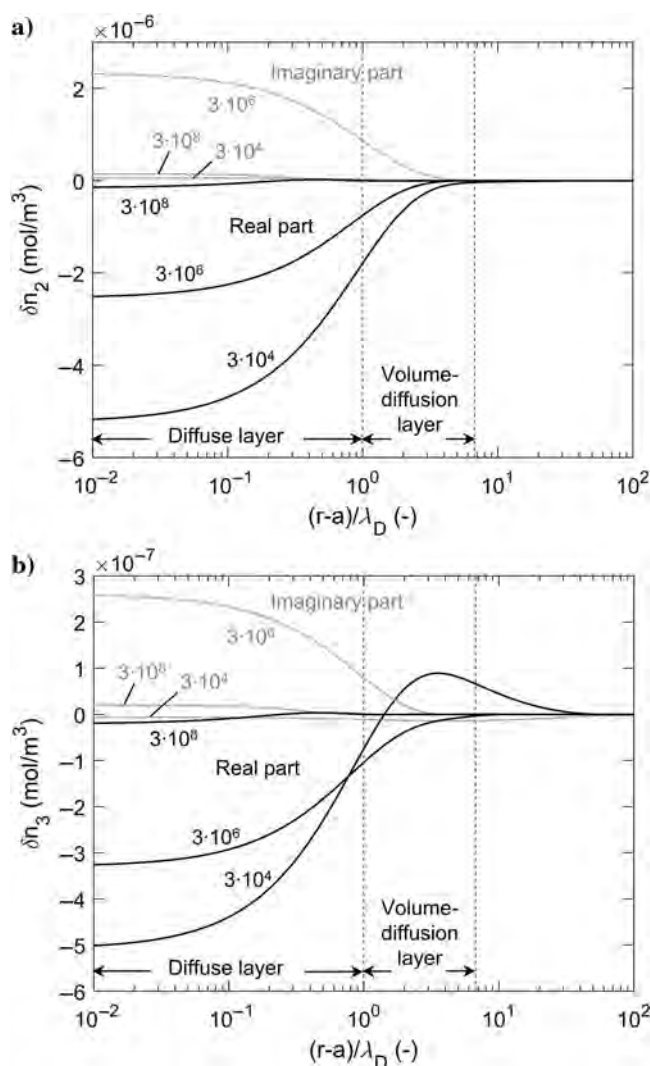


Figure 5. Radial variation (r is the distance from the center of the spherical particle) of the cation perturbation concentrations δn_2 (inactive) and δn_3 (active) along the symmetry axis ($\theta = 0$) in the vicinity of a metallic sphere of radius $a = 0.1 \mu\text{m}$ at three different angular frequencies ($\omega = 3 \times 10^4, 3 \times 10^6, 3 \times 10^8 \text{ rad/s}$). The left dashed line indicates the extensions of the diffuse layer (DL, distance to surface λ_D), and the right dashed line indicates those of the volume-diffusion layer (distance $a\sqrt{\epsilon} - a$). All parameters are as in Figure 2.

includes spectra for $n_3^\infty = 0$ (without a reaction current, the dashed curves) and $n_3^\infty = 0.12n_1^\infty$ (with a large reaction current, the solid curves).

Regardless of particle size and the concentration of active cations, the low- and high-frequency limits of all σ' spectra are (almost) the same. At low frequencies, they all approach a direct-current conductivity σ_{DC} well below σ_0 . In this limit, the diffuse layer builds up, which fully screens the electric field of the induced surface charges and gives the particle (not the suspension) a vanishing effective conductivity. As a result, the particles — although perfect conductors — decrease the effective conductivity of the suspension below the conductivity of the electrolyte. Only the contribution of the reaction current through the particle slightly increases σ_{DC} and thus

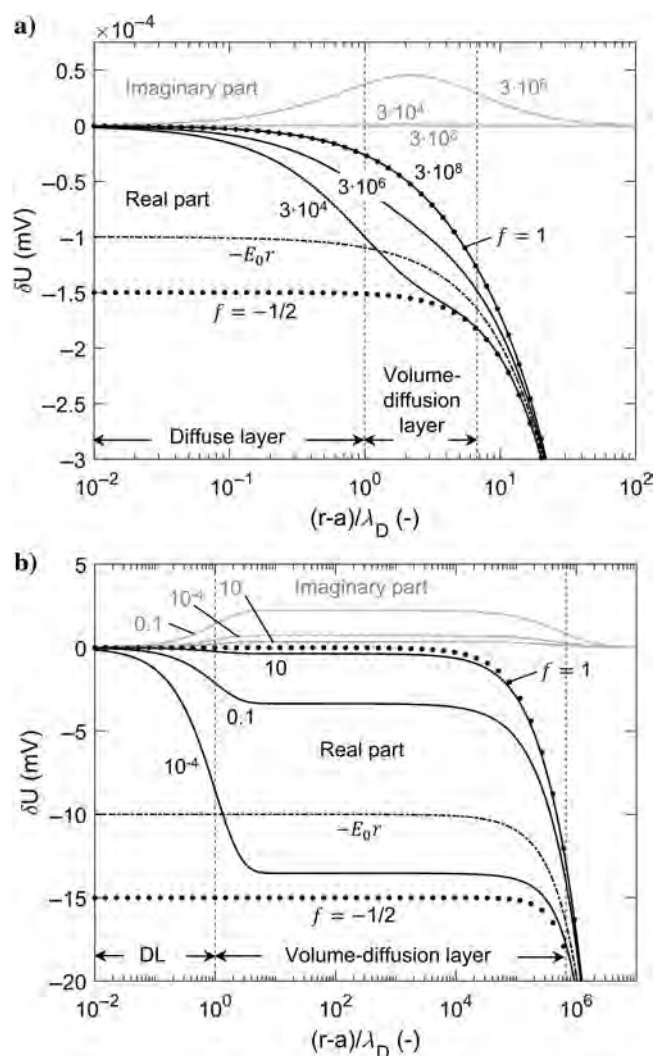


Figure 6. Radial variation (r is the distance from the center of the spherical particle) of the electric perturbation potential δU along the symmetry axis ($\theta = 0$) in the vicinity of metallic spheres of (a) radius $a = 0.1 \mu\text{m}$ at the angular frequencies $\omega = 3 \times 10^4, 3 \times 10^6, \text{ and } 3 \times 10^8 \text{ rad/s}$ and (b) radius $a = 10 \text{mm}$ at $\omega = 10^{-4}, 0.1, \text{ and } 10 \text{ rad/s}$. The left dashed lines indicate the extensions of the diffuse layer (DL, distance to surface λ_D), the right those of the volume-diffusion layer (distance $a\sqrt{\epsilon} - a$). Besides the much larger particle radius in (b), all other parameters are as in Figure 2.

explains the small deviations between the values of σ_{DC} of the models with and without reaction currents.

At the high-frequency limit, the diffuse layer does not develop, induced charges are not screened, and the particle behaves like a perfect conductor. Consequently, the suspended particles significantly increase the conductivity of the mixture. Obviously, even the contribution of the reaction currents cannot further increase the (already infinite) effective conductivity of the sphere and no differences are observed between the high-frequency limits with and without reaction currents.

The particle size and active cation concentrations, however, largely affect the transition between these limits. If no active cations are present, i.e., in the absence of the volume-diffusion process, the relaxation of the diffuse layer controls the increase of σ' and causes a narrow peak of σ'' . The flanks of the σ'' peak increase and decrease with steep slopes $\propto \omega$ and $\propto 1/\omega$, respectively. This

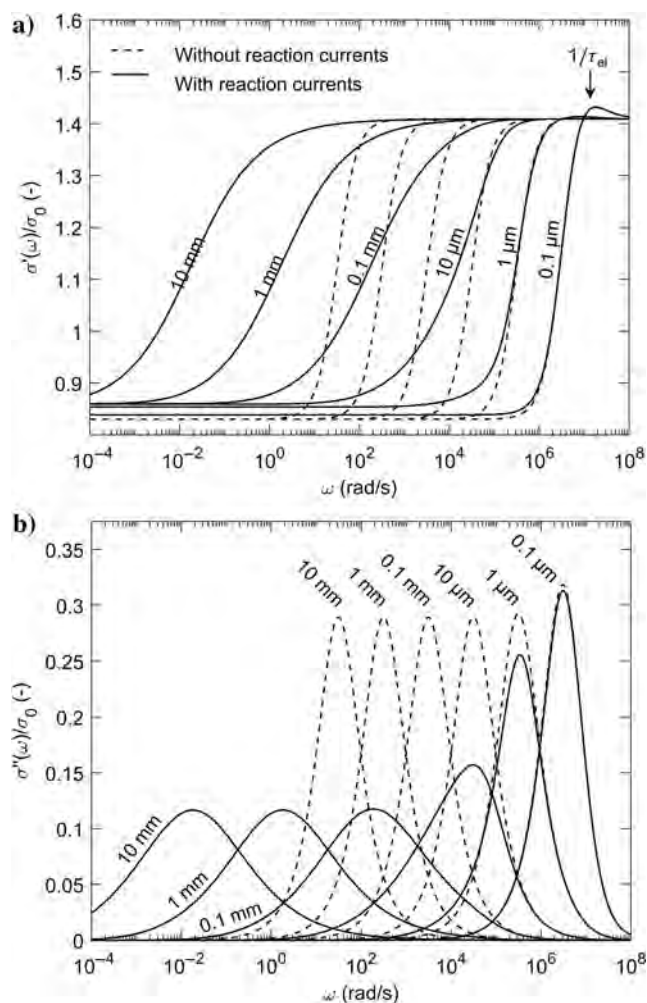


Figure 7. Effective normalized conductivity spectra for particles with different radii a between $0.1 \mu\text{m}$ and 10 mm . Responses in absence (dashed lines) and presence (solid lines) of active cations responsible for the occurrence reactions currents are included. The complex-valued conductivities are expressed in terms of (a) real σ' and (b) imaginary effective conductivity σ'' . The arrow in (a) marks the characteristic frequency $\omega_{el} = 1/\tau_{el}$ discussed further below. Volumetric fraction of conducting spheres $\nu = 0.12$; all other model parameters are as in Figure 2.

frequency dependence corresponds to the behavior of a resistor-capacitor (RC) circuit, which is a plausible parallelism for a charge-relaxation process, as is the case with the diffuse-layer polarization. An increase of the particle size shifts the characteristic angular frequency ω_c , i.e., the frequency at which the σ' transition and σ'' peak are observed, to lower angular frequencies, whereas it practically does not affect the maximum of σ'' (except for very small particles).

The presence of active cations changes the spectral response significantly. As we observe in Figure 7, the contribution of the associated volume-diffusion process driven by the nonzero reaction currents broadens the σ' transition region and the σ'' peak, reduces the maximum of σ'' , and notably shifts ω_c toward lower frequencies. These changes are almost imperceptible for small particles, whereas they become most pronounced for large particles. Because in this context, metallic minerals in the submillimeter range are considered large particles, it cannot be stressed enough that besides geometry, fluid chemistry also exerts great control over the characteristic frequency. The slopes of the broadened peaks (e.g., for $a = 10 \text{ mm}$) increase and decrease with $\propto \sqrt{\omega}$ and $\propto 1/\sqrt{\omega}$, respectively. As previously mentioned by Wong (1979) and in accordance with our present understanding of the volume-diffusion process, the occurrence of the quantity $1/\sqrt{i\omega}$ is typical for purely diffusion-controlled relaxations and can therefore also be encountered in the Warburg impedance (e.g., Merriam, 2007). In comparison with the case without reaction currents, the decrease of ω_c with the particle size is much more pronounced.

The comparison of the two cases also has an important practical implication. Although the presence of active cations largely affects the spectral response of the suspension, it is clearly not a necessary condition for a polarization process to occur. This conclusion is in agreement with the findings of other recent studies into the polarization response of conducting particles with inert surfaces (J. Quian and P.N. Sen, personal communication, 2016). However, the absence of active cations can — especially in the case of relatively large particles — shift the overall polarization response to much higher frequencies, where it can typically not be observed with IP field or laboratory instruments.

RELAXATION TIME SCALES

Due to the above observed dependence on the particle size, the characteristic frequency — or its inverse, the relaxation time — can often be used to infer this important geometric parameter from spectral IP data. However, as we also recognized in Figure 7, relaxation times for one particle size vary considerably depending on the concentration of active cations. The analysis of this subject provided by Wong (1979) is brief; he only states that for smaller particles the relaxation time varies with $\propto a\lambda_D/D$ and for larger particles with $\propto a^2/D$ and does not explicitly refer to the chemical composition of the pore water. Because of its importance as a proxy for the particle size and because it potentially determines if a relaxation can be detected at all using band-limited measuring devices (see the discussion at the end of the previous section), in this section, we will investigate the relaxation times of the polarization model in more detail.

Figure 8 shows the variation of the relaxation times, determined from modeled spectra as $\tau_c = 1/\omega_c$, with the particle radius for three different concentrations of active cations (the solid lines). For nonzero active cation concentrations, the curves reconfirm

the transition from a linear increase of τ_c with a for small particles to a quadratic increase for large particles as reported by Wong (1979). In the case of vanishing active cation concentrations, the linear increase of τ_c continues even for large particles. As without active cations, no reaction currents are active, only the diffuse-layer polarization develops, and the linear increase must be related to the charge-relaxation process of the diffuse layer. Consequently, the presence of volume-diffusion processes in the opposite case must be responsible for the quadratic increase. Although reaction currents are also active at the surface of small particles, the overall polarization response seems to be dominated by the relaxation of the diffuse layer. As Figure 8 further indicates, the critical particle radius, at which the transition between the two regimes is observed, strongly varies with the fraction of active cations in the electrolyte solution.

Relaxation of the electrolyte solution

The fastest polarization process inherent to this model is related to the relaxation of the electrolyte solution. The corresponding relaxation time (e.g., Shilov et al., 2001)

$$\tau_{\text{el}} = \frac{\epsilon_0 \epsilon_r}{\sigma_0} = \frac{\lambda_D^2}{D} \quad (21)$$

is a measure of the time that it takes the ions of the solution to screen the initial surface charge Σ_∞ before the charging of the diffuse layer takes effect. The term τ_{el} is also referred to as Debye time or the time scale of charge relaxation (e.g., Bazant et al., 2004). Its inverse ω_{el} marks the angular frequency, at which point the characteristic magnitudes of conduction and displacement current density become equal. Therefore, in the treatment of the dielectric dispersion of suspensions, ω_{el} is used to define the limit between the low- and high-frequency ranges (e.g., Shilov et al., 2001). In the equations of the Wong model, ω_{el} marks the angular frequency, at which point the real and imaginary parts of λ_1 (equation 11) are equal.

In the spectra in Figure 7, the relaxation of the electrolyte solution can be related to the small overshoot of more than the high-frequency asymptote of the σ' spectra for small particle sizes. This overshoot and its relaxation at ω_{el} are present in the spectra of larger particles, too, but they can only be distinguished at highly magnified levels (not shown here for brevity). Also, we note that in the context of induced-polarization studies with frequency ranges that hardly reach 1 kHz, the relaxation of the electrolyte is of little relevance because for typical aqueous solutions in geomaterials, it corresponds to characteristic frequencies ≥ 1 MHz.

Diffuse-layer relaxation

The first relevant time scale can be related to the relaxation of the space charge stored in the field-induced diffuse layer covering the poles of the particle. Because this polarization persists even if reaction currents are absent, an approximate expression for the corresponding time scale can be obtained by evaluating equation 12 in the limit $n_3^\infty \rightarrow 0$. As we show in more detail in Appendix C, this yields the expression

$$\tau_{\text{dl}} = \frac{a \lambda_D}{2D} \quad (22)$$

for the relaxation time of the diffuse-layer polarization. Generally, time scales $\propto \lambda_D L/D$, where L denotes the characteristic system length, are often found in the description of problems involving dynamic charging of electric double layers. Because these processes involve simultaneously acting diffusion and electromigration currents, the bulk conductivity σ_0 (via λ_D) and the geometric scale a of the problem control this “mixed” time scale (Bazant et al., 2004). The same time scale, as expressed in equation 22, was also found by J. Quian and P.N. Sen (personal communication, 2016) for the diffuse-layer relaxation of inert conducting particles.

In the context of the Wong model, excess and deficiency ion concentrations within the diffuse layers covering the two poles of the particle are controlled by a complex balance of tangential and normal electromigration and diffusion currents around the particle. Consequently, the time it takes the ions to move to their new quasi-equilibrium positions τ_{dl} depends on both processes. The contribution of the electromigration process causes dependence on λ_D , whereas the diffuse transport introduces dependence on the particle radius a . The induced double layers (the diffuse layers and their image charges on the particle surface) on the two poles of the particle can be interpreted as capacitors connected in parallel through the bulk electrolyte, which acts like an ohmic resistance. The relaxation time of such an RC circuit increases linearly with the resistance and the capacitance (e.g., Pelton et al., 1978). In the context of the Wong model, the dependence on the resistance corresponds to the variation of τ_{dl} with the resistivity of the bulk electrolyte $\rho_0 = 1/\sigma_0$. The capacitance is the charge stored in the capacitor per applied voltage, which according to equation 20 in our model scales with ak and multiplied by $1/\sigma_0$ results in a relaxation time $\propto a/\sqrt{\sigma_0}$ as predicted by τ_{dl} .

Figure 8 shows that τ_{dl} describes the variation of the modeled relaxation time τ_c with a quite well, as long as no active cations exist in the electrolyte, i.e., $n_3^\infty = 0$, and the diffuse-layer polarization dominates. Therefore, even for $n_3^\infty > 0$, the modeled

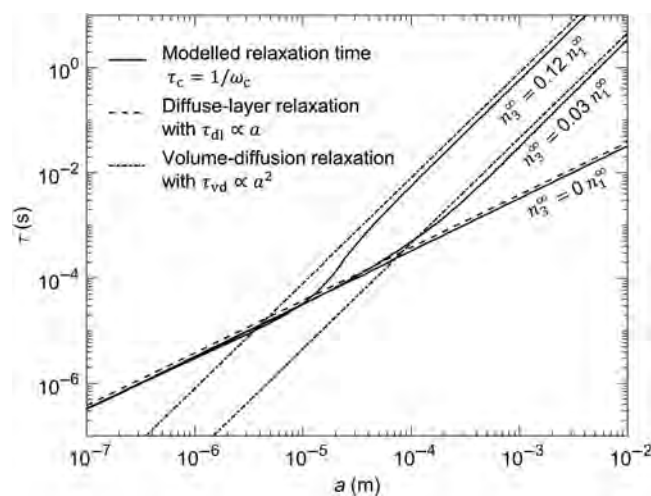


Figure 8. Variation of relaxation times τ with the particle radius a for three different concentrations of active anions $n_3^\infty/n_1^\infty = 0, 0.03$, and 0.12 . Modeled relaxation times τ_c correspond to the inverse of the characteristic angular frequency ω_c , at which point the peak of the imaginary is observed. The dashed lines correspond to the relaxation time of the diffuse layer τ_{dl} (equation 22), and the dashed-dotted lines correspond to the relaxation time of the volume diffusion τ_{vd} (equation 23). All other parameter values are as in Figure 2.

curves coincide with τ_{dl} as long as the particle radius is sufficiently small.

Volume-diffusion relaxation and critical particle size

The second relevant time scale is related to the relaxation of electroneutral perturbations of the electrolyte concentration caused by the volume-diffusion process driven by nonzero reaction currents through the particle surface. In Appendix C, we derive the characteristic time scale

$$\tau_{vd} = \frac{a^2}{4D(1 - 2n_1^\infty/n_3^\infty)^2} \quad (23)$$

for this process, which only becomes evident if the particles are large enough. Time scales $\propto L^2/D$, where L is the characteristic system length, are typical for concentration-polarization processes also referred to as volume-diffusion or bulk-diffusion processes (Shilov et al., 2001; Bazant et al., 2004). In contrast to the relaxation of the diffuse layer, these relaxation processes are controlled by diffusion only, which is reflected by the fact that τ_{vd} does not vary with $1/\sqrt{\sigma_0}$, as was the case with τ_{dl} . This is plausible because diffusion currents only depend on concentration gradients and not on bulk ion concentrations (see, e.g., equation 3).

Although the bulk conductivity does not affect τ_{vd} , equation 23 predicts a clear dependence on the fraction of active cations via n_1^∞/n_3^∞ . From Figure 8, it is obvious that for a fixed bulk conductivity $\sigma_0 \propto n_1^\infty$, an increase of the fraction of active cations shifts the critical radius a_c ; i.e., the radius at which the transition between the two relaxation time regimes happens, toward smaller particle sizes. By equating τ_{dl} and τ_{vd} , we can approximate

$$a_c = 2\lambda_D(1 - 2n_1^\infty/n_3^\infty)^2 = 8\lambda_D \left(\frac{n_1^\infty}{n_3^\infty} \right)^2. \quad (24)$$

Besides the ratio n_1^∞/n_3^∞ , the critical particle radius also depends on the Debye length λ_D . Around small particles with $a\kappa < 8(n_1^\infty/n_3^\infty)^2$, the relaxation of the field-induced diffuse layer dominates the response, whereas around larger particles with $a\kappa > 8(n_1^\infty/n_3^\infty)^2$, the volume-diffusion mechanism related to the field-induced concentration gradients controls the effective conductivity.

Equation 24 also reconfirms the strong control that the ratio $a\kappa$, i.e., the overlap of the diffuse and the volume-diffusion layers, exerts over the development of the volume-diffusion layer and thus its relaxation. For small particles, the relatively thick diffuse layer inhibits the full development of a volume-diffusion layer. As a consequence, the relaxation of the diffuse layer with $\tau_{dl} \propto a\lambda_D$ dominates the response. Around much larger particles, the volume-diffusion layer can fully develop and its relaxation becomes dominant as can be seen from the variation of the relaxation time with the particle radius $\tau_{vd} \propto a^2$. It should be noted that, in complete absence of the diffuse double layer, i.e., where $\omega_{vd} \gg \omega_{dl}$, the exchange current approaches zero (not shown here for brevity), which inhibits the buildup of a concentration gradient even if $\omega < \omega_{vd}$. In other words, for the volume-diffusion process to be activated, the presence of a diffuse layer seems to be a necessary condition.

The relaxation time of the volume-diffusion process as well as the critical particle radius defined in equations 23 and 24, respectively, underscore the important role of active cations in the electrolyte solution in the determination of the polarization response of the model.

Although implicit in the treatment by Wong, their effect on the overall relaxation time has not been discussed in detail nor quantified as done here.

DISCUSSION

An important achievement of the present study is the improved general understanding of the processes inherent to Wong's polarization model. The detailed mathematical analysis and the — to the best of our knowledge — first visualization of the physical processes provide an appropriate basis to correct some misleading reinterpretations of the model, which can be found in the more recent literature.

Based on the theory developed by Wong (1979) and Wong and Strangway (1981), Gurin et al. (2015) and Placencia-Gómez and Slater (2015) propose conceptual models aiming at a description of the polarization response of metallic particles by means of a complex frequency-dependent surface conductivity. Their approach is motivated by the difficulties to fit real IP spectra based on Wong's model (Placencia-Gómez and Slater, 2014). To derive a simpler model, which meets the requirements of interpreting real IP data, they resort to theories describing the polarization response of suspensions of nonconducting particles (e.g., O'Konski, 1960; Schwarz, 1962; Schurr, 1964; Leroy et al., 2008). These theories consider dielectric particles with nonzero surface charge densities (e.g., due to cation exchange reactions) surrounded by an electrical double layer. Complex surface conductivities are then defined to describe the polarization of the fixed Stern layer and the diffuse layer caused by an external electric field. Critical analysis reveals two important discrepancies between the rigorous treatment by Wong and these new conceptual models:

- 1) In the absence of active cations, Gurin et al. (2015) and Placencia-Gómez and Slater (2015) attribute the polarization response of metallic particles to a complex surface conductivity related to the excess of ions in an electrical double layer at the particle surface. Surface conductivity generally considers the contribution of the equilibrium diffuse and Stern layer covering nonconducting particles (e.g., Schurr, 1964; Leroy et al., 2008), and it does not consider the charging of the field-induced diffuse layer responsible for the large electrode-polarization response. Furthermore, the Wong model does not even consider fixed surface charges or equilibrium double layers at the surface of the metallic particle. Rather, from Poisson's equation 5, it is clear that without external excitation, the electrolyte solution is electroneutral — even at the very particle surface. The only double layers described by the Wong model are field induced. In conclusion, the conceptual models developed by Gurin et al. (2015) and Placencia-Gómez and Slater (2015) are not suited to reproduce the electrode polarization process described by the Wong model. Rather, they suppose a different polarization mechanism around metallic particles, which has not yet been studied in a mathematically rigorous way. Although the existence of such a mechanism cannot be discarded beforehand, the proposed conceptual models should be used with caution.
- 2) A further difficulty arises from the conceptual model by Gurin et al. (2015), which contains the argumentation that in the absence of active cations, i.e., if no reaction current through the interface is considered, "the metallic particle behaves as an insulator." This conclusion is a fundamental misconception

because the determination of whether a particle behaves like a perfect conductor or an insulator does not depend on the amount of charges that can be transferred across its surface. Rather, the criterion must be the distribution of the electric field within the particle. Although the electric field is always zero within a perfect conductor (this is warranted by an instantaneous redistribution of charges along the surface), the electric field readily penetrates the nonconducting particle. Mathematically, the first case requires a zero or constant potential boundary condition at the particle surface as realized in the Wong model (see equation A-1). The second case, in contrast, implies a significant variation of the electric potential along the particle surface. This difference between the two cases is not a mathematical subtlety, but it gives rise to fundamentally different polarization processes (and magnitudes). Therefore, the polarization response of a highly conducting particle can by no means be interpreted as a special case of the polarization of the corresponding nonconducting sphere.

Of course, the assumption of an infinite conductivity of the particle represents an important limitation of the Wong model. In their contributions, [Revil et al. \(2015\)](#) and [Misra et al. \(2016\)](#) indicate a physically sensitive way to include finite particle conductivity into a mechanistic polarization model for semiconducting particles. Although pioneering, the models of these authors do not yet include the effect of reaction currents through the solid-liquid interface. As stressed repeatedly in the present paper, the effect of reaction currents through the particle in conjunction with the resulting volume-diffusion mechanism has a huge impact on the relaxation response. Therefore, future improvements of the polarization models for semiconducting particles should definitely include the effect of electroactive ions.

Although they explicitly address the important role of active cations, the interpretation provided by [Flores Orozco et al. \(2011\)](#) for the polarization response of metallic precipitates deviates in an important point from the predictions made by the Wong model. During a field-scale biostimulation experiment, these researchers observed a decrease of the polarization response (in terms of the imaginary conductivity) during phases with low concentrations of active cations (here, Fe(II)) in the pore water. Furthermore, below a critical concentration of Fe(II), no significant polarization response was observed at all. [Flores Orozco et al. \(2011\)](#) attribute this behavior to the strong control that active ions exert over the polarization magnitude, and they conclude that in the absence of active ions, electrode polarization becomes negligible (at least in the investigated frequency band). As far as the predictions of the Wong model are concerned, this perception is erroneous because the presence of active cations is not a necessary condition for the occurrence of diffuse-layer polarization, which produces high polarization magnitudes (in terms of the maximum imaginary conductivity). From Figure 7, it is evident that the maximum imaginary conductivity rather increases with the decreasing concentration of active cations, which in the present study could be linked to the decreasing influence of the volume-diffusion mechanism. At the same time, the characteristic frequency moves toward higher frequencies. Interestingly, [Flores Orozco et al. \(2011\)](#) observe that the decrease of Fe(II) concentrations was accompanied by a decrease of the phase response at low frequencies (0.25 Hz), whereas the phase increased at higher frequencies (4 Hz). Rather than an overall reduction of the polariza-

tion magnitude, this experimental finding indicates a shift of the polarization maximum to higher frequencies, when the dissolved Fe(II) is depleted from the solution, which is in good agreement with the predictions of the Wong model.

Although the preceding discussion may suggest that the Wong model can still be considered as one of the most complete polarization models for metal-bearing geomaterials, it also shows that there is room for further improvements:

- 1) The eventual effect of surface charges at the metal surface and the associated electrical double layer on the polarization response of conducting particles is not included. For instance, on bare metal surfaces of synthetic iron and gold nanoparticles ζ -potentials can be up to -40 mV at neutral pH ([Sonavane et al., 2008](#); [Comba and Sethi, 2009](#)). Particularly in the context of applications of the IP method for the monitoring of fate and transport of metallic nanoparticles injections (e.g., [Flores Orozco et al., 2015](#)), an improved discrimination between the effects due to electrolyte composition (in particular the role of electroactive ions), particle geometry, and the electrochemical state of the surface (e.g., ζ -potential and reactivity) seems necessary.
- 2) Following the argumentation of [Misra et al. \(2016\)](#), many metallic targets — whether natural ore minerals or metal-oxide nanoparticles — are semiconductors rather than metallic conductors. The polarization of such a semiconducting particle including the effect of reaction currents through the solid-liquid interface could be studied incorporating the corresponding boundary condition of the Wong model into the approach of [Misra et al. \(2016\)](#).
- 3) For the 1D system investigated in his treatment, [Merriam \(2007\)](#) stresses the relative importance of the frequency-dependent impedance of the Stern or Helmholtz layer in the electrode polarization process. The Wong model does not consider effects related to the charging of the Stern layer at the metal surface.
- 4) The effective medium approach used by [Wong \(1979\)](#) to determine the response of an ensemble of more than one particle (see equation 18) does not consider any interaction between neighboring particles. In particular, the relatively long-range perturbations related to the volume-diffusion process described by his polarization model are likely to overlap if the average distance between particles becomes equal to or smaller than the particle diameter. Furthermore, the volume-diffusion mechanism may eventually couple to long-range polarization layers around the nonconducting grains of the background material, such as the concentration polarization due to a static double layer (e.g., [Shilov et al., 2001](#)). Interactions between densely packed metallic particles and with the nonmetallic background material should be investigated in more detail.
- 5) Although suited to develop a gross idea of the expected polarization response, the simple geometric models used in the analytic approaches (spheres and ellipsoids in [Wong, 1979](#); [Wong and Strangway, 1981](#)) are necessarily a poor representation of the generally irregular shapes of natural mineral grains. From studies on nonconducting particles, we already know that surface roughness can produce an additional relaxation at higher frequencies (e.g., [Leroy et al., 2008](#)). Indeed, IP measurements on slug grains carried out by [Nordsiek and Weller \(2008\)](#) provide indications that surface roughness may contribute in a similar manner to the polarization of metallic particles.

- 6) It has been shown that the application of Wong's model to real data can be tedious (Placencia-Gómez and Slater, 2014) or result in a poor fitting of experimental IP spectra (Gurin et al., 2015; Placencia-Gómez and Slater, 2015). One of the main drawbacks is the relatively large number of parameters, of which particularly the electrochemical parameters are poorly constrained. Although further improvements of the model addressing the first five issues of this list likely result in an even larger number of model parameters, future research should not lose sight of the need for simpler conceptualizations and mathematical descriptions of the polarization of metallic particles — especially for the interpretation of real laboratory or field data.

This list is certainly not complete, but it shows that to date many possibly important effects can still not be accounted for on the basis of existing mathematical theories. At the same time, the constant delivery of new, interesting experimental IP data therefore urges the development of improved theoretical models for their interpretation.

CONCLUSION

We complete the solution of the PNP system of partial differential equations around a perfectly conducting particle under consideration of charge-exchange reactions at the particle surface. This model was initially developed by J. Wong to describe the induced-polarization response of disseminated sulfide ores. We extend his treatment and derive the full analytic solution consisting of three unknown coefficients, which control short-range perturbations of ion concentrations and electric potential close to the particle surface. Although not needed for the determination of the effective polarization response of the suspended particle, the knowledge of such short-range perturbations allows a much more comprehensive analysis of the underlying polarization mechanisms.

We discuss the two relaxation processes inherent to the model and, as a further extension of the classical theory, provide analytic approximations for the characteristic time scales of both. Based on the full solution provided in the present study, we are able to visualize the microscopic manifestations of the two relaxation processes in terms of perturbations of the ion concentrations in the electrolyte solution. Promoted by a deepened understanding of the underlying mechanisms, we associate the two relaxation times with the relaxation of (1) field-induced diffuse layers and (2) field-induced concentration gradients. The first process corresponds to the buildup of diffuse double layers that screen field-induced surface charges at the particle surface. Its relaxation time is proportional to the Debye length of the electrolyte solution and the particle radius. The second process only occurs if charge-exchange reactions are considered, which are directly related to the buildup of concentration gradients in the electroneutral electrolyte beyond the diffuse layer. Its relaxation time is proportional to the particle radius squared, which is typical for volume or bulk-diffusion phenomena.

Provided that active cations are present, both polarization mechanisms occur simultaneously. However, around sufficiently small particles, the diffuse-layer relaxation dominates the overall polarization response, whereas volume-diffusion relaxation becomes dominant around larger particles. The transition between the two regimes is observed at a critical particle radius, which is approximately proportional to the thickness of the diffuse layer (λ_D) and the inverse of the normalized concentration of active anions squared $[(n_1^\infty/n_3^\infty)^2]$.

Because under typical conditions, this critical radius is related to characteristic frequencies >1 kHz, to our best knowledge, no experiment for the transition has been published. Our findings can open the possibility to design laboratory measurements — by increasing the Debye length and adjusting the active ion concentration — that may be suited to detect the predicted transition and further test the theoretical model.

ACKNOWLEDGMENTS

We gratefully acknowledge three anonymous reviewers and L. Slater for their insightful comments that helped to improve the manuscript. Financial support for this study was provided by the Austrian Federal Ministry of Science, Research and Economy (project: Development of geophysical exploration methods for the characterization of mine-tailings towards exploitation), the German Academic Exchange Service (DAAD), and the research project GEOCON, Advancing GEOlogical, geophysical and CONTaminant monitoring technologies for contaminated site investigation (contract 1305-00004B). We thank E. Placencia-Gómez and L. Slater for valuable discussions that motivated this study.

APPENDIX A

DERIVATION OF THE THREE REMAINING UNKNOWN COEFFICIENTS

The potential on the surface of the perfectly conducting particle must have a constant value, and from the symmetry of the external excitation, it follows that this constant value must be zero. Because this condition must hold for any θ , we write (from equation 9)

$$-2F/(\lambda_1^2 \epsilon_0 \epsilon_r) A(\omega) k_1(\lambda_1 a) - E_0 a + E(\omega) a = 0. \quad (\text{A-1})$$

The two inactive ionic species do not react at the particle surface, such that the corresponding fluxes through the surface must also be zero. From equation 3, we get

$$\begin{aligned} & -D \partial_r [-A(\omega) k_1(\lambda_1 r) + B(\omega) k_1(\lambda_2 r)] \\ & + \mu n_1^\infty \partial_r \left[-2F/(\lambda_1^2 \epsilon_0 \epsilon_r) A(\omega) k_1(\lambda_1 r) - E_0 r + E(\omega) \frac{a^3}{r^2} \right] = 0 \end{aligned} \quad (\text{A-2})$$

evaluated at $r = a$ for the anion flux density and

$$\begin{aligned} & -D \partial_r \{ n_2^\infty / n_1^\infty A(\omega) k_1(\lambda_1 r) + [B(\omega) - M(\omega)] k_1(\lambda_2 r) \} \\ & - \mu n_2^\infty \partial_r \left[-2F/(\lambda_1^2 \epsilon_0 \epsilon_r) A(\omega) k_1(\lambda_1 r) - E_0 r + E(\omega) \frac{a^3}{r^2} \right] = 0 \end{aligned} \quad (\text{A-3})$$

evaluated at $r = a$ for the flux density of the passive cations. Only the normal flux of the active cations through the metal surface does not vanish. It depends on the perturbation concentration of the active cations δn_3 and the radial electric field $-\partial_r U$ at the particle surface. This boundary condition writes

$$\begin{aligned}
& -D\partial_r[n_3^\infty/n_1^\infty A(\omega)\kappa_1(\lambda_1 r) + M(\omega)\kappa_1(\lambda_2 r)] \\
& -\mu n_3^\infty \partial_r \left[-2F/(\lambda_1^2 \epsilon_0 \epsilon_r) A(\omega)\kappa_1(\lambda_1 r) - E_0 r + E(\omega) \frac{a^3}{r^2} \right] \\
& = -\beta [n_3^\infty/n_1^\infty A(\omega)\kappa_1(\lambda_1 r) + M(\omega)\kappa_1(\lambda_2 r)] \\
& -\alpha n_3^\infty \partial_r \left[-2F/(\lambda_1^2 \epsilon_0 \epsilon_r) A(\omega)\kappa_1(\lambda_1 r) - E_0 r + E(\omega) \frac{a^3}{r^2} \right]
\end{aligned} \tag{A-4}$$

evaluated at $r = a$. The right side of equation A-4 is the exchange current across the metal electrolyte interface as defined by Wong (1979) in terms of the electrochemical reaction-current parameters α (in Cs/kg) and β (in m/s). In our treatment, the reaction current is given in mol/(m²s), which has to be multiplied by Faraday's constant $F = eN_A$ to obtain the corresponding electric current density in A/m² actually defined by Wong (1979) (his equation 28).

Note that boundary conditions far away from the particle surface, here zero perturbation concentrations and a perturbation potential equal to the external electric field, are implicit in the selection of the modified spherical Bessel function of the second kind $k_1(\lambda r)$.

Because the coefficient $E(\omega)$ given in equation 12 can be looked up in Wong (1979), we do not include its lengthy derivation. To solve equations A-1–A-4 for the three remaining unknown coefficients, we first carry out the partial derivatives ∂_r , introduce the abbreviation $k'_1(\lambda a) := \partial_r k_1(\lambda r)|_{r=a}$, and do some minor manipulations, which yields

$$A(\omega) = \frac{E_0 a - E(\omega) a}{-2F/(\lambda_1^2 \epsilon_0 \epsilon_r) k_1(\lambda_1 a)}, \tag{A-5}$$

$$\begin{aligned}
& DA(\omega)k'_1(\lambda_1 a) - DB(\omega)k'_1(\lambda_2 a) \\
& + \mu n_1^\infty [-2F/(\lambda_1^2 \epsilon_0 \epsilon_r) A(\omega)k'_1(\lambda_1 a) - E_0 - 2E(\omega)] = 0,
\end{aligned} \tag{A-6}$$

$$\begin{aligned}
& Dn_2^\infty/n_1^\infty A(\omega)k'_1(\lambda_1 a) + D[B(\omega) - M(\omega)]k'_1(\lambda_2 a) \\
& + \mu n_2^\infty [-2F/(\lambda_1^2 \epsilon_0 \epsilon_r) A(\omega)k'_1(\lambda_1 a) - E_0 - 2E(\omega)] = 0,
\end{aligned}$$

and

$$\tag{A-7}$$

$$\begin{aligned}
& -Dn_3^\infty/n_1^\infty A(\omega)k'_1(\lambda_1 a) - DM(\omega)k'_1(\lambda_2 a) \\
& -\mu n_3^\infty [-2F/(\lambda_1^2 \epsilon_0 \epsilon_r) A(\omega)k'_1(\lambda_1 a) - E_0 - 2E(\omega)] \\
& = -\beta [n_3^\infty/n_1^\infty A(\omega)k_1(\lambda_1 a) + M(\omega)k_1(\lambda_2 a)] \\
& -\alpha n_3^\infty [-2F/(\lambda_1^2 \epsilon_0 \epsilon_r) A(\omega)k'_1(\lambda_1 a) - E_0 - 2E(\omega)].
\end{aligned} \tag{A-8}$$

Equation A-5 already expresses the coefficient $A(\omega)$ in terms of the known coefficient $E(\omega)$, and no further manipulation is needed.

Using the solution for $A(\omega)$ from equation A-5 and the definition of f_2 in equation 13, the coefficient $B(\omega)$ is readily obtained from equation A-6 as

$$B(\omega) = \frac{E_0 - E(\omega)}{k'_1(\lambda_2 a)} \left\{ \frac{\lambda_1^2 \epsilon_0 \epsilon_r}{2F} f_2 - \frac{\mu}{D} n_1^\infty \left[f_2 + \frac{E_0 + 2E(\omega)}{E_0 - E(\omega)} \right] \right\}. \tag{A-9}$$

For the last unknown coefficient $M(\omega)$, we rearrange equation A-8 using the definitions of f_2 and f_3 in equation 13 and substituting $A(\omega)$ from equation A-5, which yields

$$\begin{aligned}
M(\omega) = & \frac{-n_3^\infty/n_1^\infty [E_0 - E(\omega)]}{k'_1(\lambda_2 a)(1 + \frac{\beta a}{D} f_3)} \left\{ \frac{\lambda_1^2 \epsilon_0 \epsilon_r}{2F} \left(f_2 + \frac{\beta a}{D} \right) \right. \\
& \left. - \frac{n_1^\infty}{D} (\mu - \alpha) \left[f_2 + \frac{E_0 + 2E(\omega)}{E_0 - E(\omega)} \right] \right\}.
\end{aligned} \tag{A-10}$$

APPENDIX B

DERIVATION OF INDUCED SURFACE CHARGE DENSITY

The charge density Σ on the surface of the perfectly conducting sphere can be related to the normal component of the electric field at its surface as

$$\Sigma(\theta, \omega) = -\epsilon_0 \epsilon_r \partial_r \delta U(\mathbf{r}, \omega)|_{r=a}. \tag{B-1}$$

Inserting equations 9 and 14 and carrying out the partial derivative with respect to r yields

$$\Sigma(\theta, \omega) = \epsilon_0 \epsilon_r E_0 \left\{ [1 - f(\omega)] \frac{\lambda_1^2 a^2 + 2\lambda_1 a + 2}{\lambda_1 a + 1} + 1 + 2f(\omega) \right\} \cos \theta. \tag{B-2}$$

At the high-frequency limit, i.e., for $\omega \rightarrow \infty$, the reflection coefficient $f(\omega)$ approaches one and the surface charge density reduces to $\Sigma_\infty(\theta) = 3\epsilon_0 \epsilon_r E_0 \cos \theta$. In this limit, the excitation is too fast to permit the diffuse layer to build up and Σ_∞ is the minimal charge required to cancel out the electrical field within the sphere. The same result can be obtained from standard electrostatic potential theory for a perfectly conducting sphere surrounded by a medium of finite conductivity.

At the low-frequency limit, i.e., for $\omega \rightarrow 0$, the reflection coefficient approaches $-1/2$ and λ_1 becomes κ . For sufficiently large particles, $\kappa a \gg 1$ and the surface can be approximated by $\Sigma_0(\theta) = 3/2\epsilon_0 \epsilon_r E_0 \kappa a \cos \theta$. In this limit, the external excitation is sufficiently slow so as to permit the diffuse layer to fully develop. The charge stored on the electrolyte side induces image charges on the particle surface, which increases Σ by the large factor of $\kappa a/2$.

APPENDIX C

DERIVATION OF RELAXATION TIMES

Diffuse-layer relaxation

To derive an expression for the relaxation time of the diffuse-layer polarization, we consider the limiting case of vanishing concentrations of active cations in the electrolyte solution. Evaluating equation 12 for $n_3^\infty \rightarrow 0$ yields the frequency-dependent reflection coefficient

$$f(\omega) = E(\omega)/E_0 = 1 - \frac{3/2}{1 + f_1/2}, \quad (\text{C-1})$$

where $f_1 = f_2 i \omega \lambda_D^2 / D$. If we further limit our analysis to frequencies $\omega \ll \omega_{el} = 1$ MHz, which is appropriate for the particle sizes that we are mainly interested in, we can approximate λ_1 by $\kappa = 1/\lambda_D$. For sufficiently thin diffuse double layers compared with the particle radius, i.e., $a/\lambda_D \gg 1$, the coefficient f_2 defined in equation 13 approaches a/λ_D . In this limit, the frequency-dependent reflection coefficient becomes

$$f(\omega) = 1 - \frac{3/2}{1 + i \omega \frac{a \lambda_D}{2D}}. \quad (\text{C-2})$$

From equation C-2, we can extract the approximate relaxation time of the double-layer polarization $\tau_{dl} = a \lambda_D / (2D)$.

Volume-diffusion relaxation

To identify the relaxation time of the volume-diffusion polarization, we evaluate the appropriate limit of the reflection coefficient f . As argued before for the relaxation of the diffuse layer, the characteristic frequency of the volume-diffusion relaxation will also be $\omega \ll \omega_{el}$, from which follows that $\lambda_1 = \lambda_D^{-1}$. For sufficiently thin diffuse double layers compared with the particle radius, we still have $a/\lambda_D \gg 1$. Furthermore, we will assume that for angular frequencies ω around the characteristic frequency of the volume-diffusion relaxation ω_{vd} , the inequality $\lambda_2 a \gg 1$ holds. We leave it to the reader to verify this assumption by evaluating $\lambda_2 a$ at the angular frequency $\omega_{vd} = \tau_{vd}^{-1}$, where τ_{vd} refers to the final result of this derivation. Under the above assumptions, the three coefficients f_i can be approximated by

$$f_1 = i \omega \frac{a \lambda_D}{D}, \quad f_2 = \frac{a}{\lambda_D} \gg 1, \quad \text{and} \quad f_3 = \frac{1}{a \lambda_2}. \quad (\text{C-3})$$

From Figure 8, it is obvious that $\tau_{vd} > \tau_{dl}$ for all particle sizes with dominant volume-diffusion relaxation. Consequently, for sufficiently large particles, the characteristic frequency of this relaxation must be searched for at frequencies $\omega \ll \omega_{dl}$. Substituting this inequality into the above expression for f_1 yields $f_1 \ll 2i$. Using the same inequality, we obtain $\beta a / (D \lambda_2) \gg 1$ for typical parameter values (i.e., $\beta = 10^{-2}$ m/s). In summary, under the above approximations and assumptions, the frequency-dependent reflection coefficient from equation 12 becomes

$$f(\omega) = E(\omega)/E_0 = 1 + \frac{3 \frac{\beta}{D \lambda_2} + \frac{3 n_3^\infty}{n_3^\infty - 2 n_1^\infty} \left(\frac{a}{\mu} - 1 \right)}{\frac{n_3^\infty}{n_3^\infty - 2 n_1^\infty} \left[\frac{a a}{\mu \lambda_D} + \frac{\beta a}{D} + 2 \right] - 2 \frac{\beta}{D \lambda_2}}. \quad (\text{C-4})$$

This expression can be further simplified, if we take into account that $a/\mu \ll 1$ and $\alpha D / (\mu \lambda_D \beta)$ for typical parameter values [i.e., $\alpha = 10^{-10} \text{ m}^2 / (\text{Vs})$] as well as $\beta a / D \gg 1$ for all relevant particle sizes. Together with our last assumption of sufficiently small concentrations of active cations $n_3^\infty \ll n_1^\infty$ and after some manipulations, we obtain

$$f(\omega) = 1 - \frac{3/2}{1 - \sqrt{\frac{i \omega}{4D} \frac{a}{1 - 2 n_1^\infty / n_3^\infty}}}. \quad (\text{C-5})$$

From equation C-5, we can extract the approximate relaxation time of the volume-diffusion polarization $\tau_{vd} = a^2 / [4D(1 - 2 n_1^\infty / n_3^\infty)^2]$.

REFERENCES

- Aal, G. A., E. A. Atekwana, and D. D. Werkema, 2017, Complex conductivity response to silver nanoparticles in partially saturated sand columns: Journal of Applied Geophysics, **137**, 73–81, doi: [10.1016/j.jappgeo.2016.12.013](https://doi.org/10.1016/j.jappgeo.2016.12.013).
- Angoran, Y., and T. R. Madden, 1977, Induced polarization: A preliminary study of its chemical basis: Geophysics, **42**, 788–803, doi: [10.1190/1.1440747](https://doi.org/10.1190/1.1440747).
- Atkins, P., and J. De Paula, 2010, Elements of physical chemistry: Oxford University Press.
- Bazant, M. Z., K. Thornton, and A. Ajdari, 2004, Diffuse-charge dynamics in electrochemical systems: Physical Review E, **70**, 021506, doi: [10.1103/PhysRevE.70.021506](https://doi.org/10.1103/PhysRevE.70.021506).
- Cole, K. S., and R. H. Cole, 1941, Dispersion and absorption in dielectrics. I: Alternating current characteristics: The Journal of Chemical Physics, **9**, 341–351, doi: [10.1063/1.1750906](https://doi.org/10.1063/1.1750906).
- Comba, S., and R. Sethi, 2009, Stabilization of highly concentrated suspensions of iron nanoparticles using shear-thinning gels of xanthan gum: Water Research, **43**, 3717–3726, doi: [10.1016/j.watres.2009.05.046](https://doi.org/10.1016/j.watres.2009.05.046).
- Flekkøy, E. G., 2013, A physical basis for the Cole-Cole description of electrical conductivity of mineralized porous media: Geophysics, **78**, no. 5, D355–D368, doi: [10.1190/geo2012-0478.1](https://doi.org/10.1190/geo2012-0478.1).
- Flores Orozco, A., M. Velimirovic, T. Tosco, A. Kemna, H. Sapion, N. Klaas, R. Sethi, and L. Bastiaens, 2015, Monitoring the injection of microscale zerovalent iron particles for groundwater remediation by means of complex electrical conductivity imaging: Environmental Science & Technology, **49**, 5593–5600, doi: [10.1021/acs.est.5b00208](https://doi.org/10.1021/acs.est.5b00208).
- Flores Orozco, A., K. H. Williams, and A. Kemna, 2013, Time-lapse spectral induced polarization imaging of stimulated uranium bioremediation: Near Surface Geophysics, **11**, 531–544, doi: [10.3997/1873-0604.2013020](https://doi.org/10.3997/1873-0604.2013020).
- Flores Orozco, A., K. H. Williams, P. E. Long, S. S. Hubbard, and A. Kemna, 2011, Using complex resistivity imaging to infer biogeochemical processes associated with bioremediation of an uranium-contaminated aquifer: Journal of Geophysical Research: Biogeosciences, **116**, G03001, doi: [10.1029/2010JG001591](https://doi.org/10.1029/2010JG001591).
- Günther, T., and T. Martin, 2016, Spectral two-dimensional inversion of frequency-domain induced polarization data from a mining slag heap: Journal of Applied Geophysics, **135**, 436–448, doi: [10.1016/j.jappgeo.2016.01.008](https://doi.org/10.1016/j.jappgeo.2016.01.008).
- Gurin, G., K. Titov, Y. Ilyin, and A. Tarasov, 2015, Induced polarization of disseminated electronically conductive minerals: A semi-empirical model: Geophysical Journal International, **200**, 1555–1565, doi: [10.1093/gji/ggu490](https://doi.org/10.1093/gji/ggu490).
- Kemna, A., A. Binley, G. Cassiani, E. Niederleithinger, A. Revil, L. Slater, K. H. Williams, A. F. Orozco, F.-H. Haegel, A. Hoerd, S. Kruschwitz, V. Leroux, K. Titov, and E. Zimmermann, 2012, An overview of the spectral induced polarization method for near-surface applications: Near Surface Geophysics, **10**, 453–468.
- Klein, J., and R. Shuey, 1978, Nonlinear impedance of mineral-electrolyte interfaces. Part I: Pyrite: Geophysics, **43**, 1222–1234, doi: [10.1190/1.1440889](https://doi.org/10.1190/1.1440889).
- Leroy, P., A. Revil, A. Kemna, P. Cosenza, and A. Ghorbani, 2008, Complex conductivity of water-saturated packs of glass beads: Journal of Colloid and Interface Science, **321**, 103–117, doi: [10.1016/j.jcis.2007.12.031](https://doi.org/10.1016/j.jcis.2007.12.031).

- Maxwell, J. C., 1891, *A treatise on electricity and magnetism*: Clarendon Press.
- Merriam, J., 2007, Induced polarization and surface electrochemistry: *Geophysics*, **72**, no. 4, F157–F166, doi: [10.1190/1.2732554](https://doi.org/10.1190/1.2732554).
- Misra, S., C. Torres-Verdín, A. Revil, J. Rasmus, and D. Homan, 2016, Interfacial polarization of disseminated conductive minerals in absence of redox-active species. Part 1: Mechanistic model and validation: *Geophysics*, **81**, no. 2, E139–E157, doi: [10.1190/geo2015-0346.1](https://doi.org/10.1190/geo2015-0346.1).
- Nordsiek, S., and A. Weller, 2008, A new approach to fitting induced-polarization spectra: *Geophysics*, **73**, no. 6, F235–F245, doi: [10.1190/1.2987412](https://doi.org/10.1190/1.2987412).
- O’Konski, C. T., 1960, Electric properties of macromolecules. V: Theory of ionic polarization in polyelectrolytes: *The Journal of Physical Chemistry*, **64**, 605–619, doi: [10.1021/j100834a023](https://doi.org/10.1021/j100834a023).
- Pearce, C. I., R. A. Patrick, and D. J. Vaughan, 2006, Electrical and magnetic properties of sulfides: *Reviews in Mineralogy and Geochemistry*, **61**, 127–180, doi: [10.2138/rmg.2006.61.3](https://doi.org/10.2138/rmg.2006.61.3).
- Pelton, W., S. Ward, P. Hallof, W. Sill, and P. H. Nelson, 1978, Mineral discrimination and removal of inductive coupling with multifrequency IP: *Geophysics*, **43**, 588–609, doi: [10.1190/1.1440839](https://doi.org/10.1190/1.1440839).
- Placencia-Gómez, E., A. Parviainen, L. Slater, and J. Leveinen, 2015, Spectral induced polarization (SIP) response of mine tailings: *Journal of Contaminant Hydrology*, **173**, 8–24, doi: [10.1016/j.jconhyd.2014.12.002](https://doi.org/10.1016/j.jconhyd.2014.12.002).
- Placencia-Gómez, E., and L. D. Slater, 2014, Electrochemical spectral induced polarization modeling of artificial sulfide-sand mixtures: *Geophysics*, **79**, no. 6, EN91–EN106, doi: [10.1190/geo2014-0034.1](https://doi.org/10.1190/geo2014-0034.1).
- Placencia-Gómez, E., and L. D. Slater, 2015, On the pore water chemistry effect on spectral induced polarization measurements in the presence of pyrite: *Journal of Applied Geophysics*, **135**, 474–485, doi: [10.1016/j.jappgeo.2015.11.001](https://doi.org/10.1016/j.jappgeo.2015.11.001).
- Revil, A., N. Florsch, and D. Mao, 2015, Induced polarization response of porous media with metallic particles. Part 1: A theory for disseminated semiconductors: *Geophysics*, **80**, no. 5, D525–D538, doi: [10.1190/geo2014-0577.1](https://doi.org/10.1190/geo2014-0577.1).
- Schurr, J., 1964, On the theory of the dielectric dispersion of spherical colloidal particles in electrolyte solution: *The Journal of Physical Chemistry*, **68**, 2407–2413, doi: [10.1021/j100791a004](https://doi.org/10.1021/j100791a004).
- Schwarz, G., 1962, A theory of the low-frequency dielectric dispersion of colloidal particles in electrolyte solution: *The Journal of Physical Chemistry*, **66**, 2636–2642, doi: [10.1021/j100818a067](https://doi.org/10.1021/j100818a067).
- Seigel, H., M. Nabighian, D. S. Parasnis, and K. Vozoff, 2007, The early history of the induced polarization method: *The Leading Edge*, **26**, 312–321, doi: [10.1190/1.2715054](https://doi.org/10.1190/1.2715054).
- Shilov, V., A. Delgado, F. Gonzalez-Caballero, and C. Grosse, 2001, Thin double layer theory of the wide-frequency range dielectric dispersion of suspensions of non-conducting spherical particles including surface conductivity of the stagnant layer: *Colloids and Surfaces A: Physicochemical and Engineering Aspects*, **192**, 253–265, doi: [10.1016/S0927-7757\(01\)00729-4](https://doi.org/10.1016/S0927-7757(01)00729-4).
- Slater, L., and A. Binley, 2006, Synthetic and field-based electrical imaging of a zerovalent iron barrier: Implications for monitoring long-term barrier performance: *Geophysics*, **71**, no. 5, B129–B137, doi: [10.1190/1.2235931](https://doi.org/10.1190/1.2235931).
- Sonavane, G., K. Tomoda, and K. Makino, 2008, Biodistribution of colloidal gold nanoparticles after intravenous administration: Effect of particle size: *Colloids and Surfaces B: Biointerfaces*, **66**, 274–280, doi: [10.1016/j.colsurfb.2008.07.004](https://doi.org/10.1016/j.colsurfb.2008.07.004).
- Wainwright, H. M., A. Flores Orozco, M. Bücker, B. Dafflon, J. Chen, S. S. Hubbard, and K. H. Williams, 2015, Hierarchical Bayesian method for mapping biogeochemical hot spots using induced polarization imaging: *Water Resources Research*, **52**, 533–551, doi: [10.1002/2015WR017763](https://doi.org/10.1002/2015WR017763).
- Wait, J. R., 1958, A phenomenological theory of induced electrical polarization: *Canadian Journal of Physics*, **36**, 1634–1644, doi: [10.1139/p58-164](https://doi.org/10.1139/p58-164).
- Wong, J., 1979, An electrochemical model of the induced-polarization phenomenon in disseminated sulfide ores: *Geophysics*, **44**, 1245–1265, doi: [10.1190/1.1441005](https://doi.org/10.1190/1.1441005).
- Wong, J., and D. Strangway, 1981, Induced polarization in disseminated sulfide ores containing elongated mineralization: *Geophysics*, **46**, 1258–1268, doi: [10.1190/1.1441264](https://doi.org/10.1190/1.1441264).

Electrochemical polarization around metallic particles — Part 2: The role of diffuse surface charge

Matthias Buecker¹, Sabine Undorf², Adrián Flores Orozco³, and Andreas Kemna⁴

ABSTRACT

Numerical simulations are carried out to study the induced-polarization response of a charged metallic sphere, which immersed in electrolyte solution is covered by a static diffuse layer. The metallic sphere itself is assumed to be perfectly conductive; electromigration and diffusion processes in bulk electrolyte and diffuse layer are modeled by the Poisson-Nernst-Planck system of partial differential equations. To include the effect of a fixed diffuse charge, we consider a constant electric ζ -potential at the surface of the particle, which leads to the buildup of a static diffuse layer. Furthermore, a minor fraction of electroactive cations engages in oxidation-reduction reactions at the particle surface, which allows charges to be transferred across the solid-liquid interface. Upon excitation by a low-frequency electric field, we observe the coupling of three polarization processes in the composite material consisting of metallic particle and surrounding

electrolyte. The first is related to the dynamic charging of field-induced diffuse layers immediately outside the two hemispheres of the sphere. The other two are volume-diffusion processes: (1) one driven by the reaction currents through the particle surface and (2) the other driven by the unequal electromigration transport of anions and cations through the static diffuse layer. Diffuse-layer relaxation and volume diffusion due to reaction currents can also be observed around uncharged metallic particles and clearly dominate the macroscopic polarization response. The ζ -surface potential at the particle surface, and thus the static diffuse layer, only moderately change the relaxation of the field-induced diffuse layer: With the increasing magnitude of the ζ -potential, we observe an increase of the low-frequency electrical conductivity of the particle in suspension, a reduction of its polarization magnitude, and a shift of its characteristic frequency toward lower frequencies. The volume-diffusion process due to the reaction currents remains practically unaffected by the static diffuse layer.

INTRODUCTION

In a previous study (Buecker et al., 2018), we have presented the full analytical solution for the classic electrode-polarization model of the induced-polarization (IP) response of uncharged metallic particles proposed by Wong (1979). In the present paper, we extend this polarization model and develop a numerical scheme to study the response of charged metallic particles. The precharged surfaces of such particles immersed in an electrolyte solution are covered by static diffuse clouds of counter charges known as the diffuse part of

the electric double layer (EDL), which must not be confused with the field-induced diffuse layers caused by an external excitation. Neither the classic model by Wong (1979) nor the more recent numerical modeling study carried out by Abdulsamad et al. (2017), nor the semiconductor-polarization models developed by Revil et al. (2015b) and Misra et al. (2016a) consider the effect of such a static diffuse charge. Although it was claimed to be the actual cause of the polarization response of highly conductive particles in the conceptual models proposed by Gurin et al. (2015)

Manuscript received by the Editor 23 February 2018; revised manuscript received 12 September 2018; published ahead of production 12 November 2018; published online 4 February 2019.

¹TU Braunschweig, Institute for Geophysics and Extraterrestrial Physics, Mendelssohnstraße 3, Braunschweig 38106, Germany, Rheinische Friedrich-Wilhelms-Universität, Steinmann Institute, Department of Geophysics, Meckenheimer Allee 176, Bonn 53115, Germany, and TU-Wien, Department of Geodesy and Geoinformation, Research Group Geophysics, Gußhausstraße 27-29/E120, Vienna 1040, Austria. E-mail: m.buecker@tu-bs.de (corresponding author).

²University of Edinburgh, School of GeoScience, Crew Building, The King's Buildings, Alexander Crum Brown Road, Edinburgh EH9 3FF, UK. E-mail: s.undorf@ed.ac.uk.

³TU-Wien, Department of Geodesy and Geoinformation, Research Group Geophysics, Gußhausstraße 27-29/E120, Vienna 1040, Austria. E-mail: adrian.flores-orozco@geo.tuwien.ac.at.

⁴Rheinische Friedrich-Wilhelms-Universität, Steinmann Institute, Department of Geophysics, Meckenheimer Allee 176, Bonn 53115, Germany. E-mail: kemna@geo.uni-bonn.de.

© 2019 Society of Exploration Geophysicists. All rights reserved.

and Placencia-Gómez and Slater (2015), to date, no mechanistic polarization model has been developed to describe the effect of a fixed surface charge — independently of whether it is located in the inner Stern layer or the outer diffuse layer.

Depending on the chemical composition and the concentration of the electrolyte, diffuse charges on the surfaces of pure metals and metal-bearing minerals vary over a wide range of positive and negative values. The potential drop across the diffuse layer, which can be approximated by the experimentally determinable ζ -potential at the plane of shear, is often used to parameterize the charge stored in the diffuse layer. The ζ -potential of metallic and metal-bearing surfaces ranges from values as low as -50 mV on stainless steel at 10 mM NaCl and pH 7 (Boulangé-Petermann et al., 1995) to $+20$ mV on pyrite at 1 mM KNO_3 and pH 6 (Reyes-Bozo et al., 2015). Because these values differ significantly from zero, a possible effect of the corresponding static EDL over the polarization response of metallic particles should not be discarded a priori. Reversely, recent laboratory and field studies with metallic nanoparticles (e.g., Joyce et al., 2012; Flores Orozco et al., 2015; Abdel Aal et al., 2017) indicate that it might be possible to use IP measurements to retrieve information on the in situ chemical condition and reactivity of the surfaces of metallic particles (Shi et al., 2015), which is strongly correlated with the ζ -potential.

It is the objective of the present study to develop a model that describes the polarization response due to a static diffuse layer covering the surface of the metallic particles and to study the effect of varying charge densities in this layer. Our theoretical treatment is based on a modification of the system of partial differential equations (PDEs) proposed by Wong (1979); therefore, it also permits including the effect of reaction currents through the metal-electrolyte interface. Because to our best knowledge the modified problem, which includes the polarization response of a static diffuse layer, cannot be solved analytically, we adopt a finite-element approach to obtain a numerical solution. Our results comprise the microscale perturbations of ion concentrations and electrical potential around the particle as well as the effect of the static diffuse layer on the effective electrical conductivity spectra of the composite system. Here, we focus on the impact of the diffuse charge on relevant descriptive parameters such as the direct-current (DC) conductivity, relaxation time, and maximum polarization response. In the “Discussion” section, we further analyze the practical relevance of our findings and implications for the interpretation of IP measurements.

THEORY

The electrochemical polarization model introduced by Wong (1979) and Wong and Strangway (1981) describes the IP response of metal-bearing ores based on the frequency-dependent complex conductivity of perfectly conducting particles (e.g., metallic conductors) immersed in an electrolyte solution. As discussed in detail by Bücker et al. (2018), the primary polarization phenomenon inherent to this model is related to the dynamic charging of field-induced diffuse layers at the particle surface (for a comprehensive discussion of diffuse-charge dynamics, see Bazant et al., 2004). This mechanism does not require the presence of electroactive ions to establish. Rather, electroactive ions additionally allow reaction currents to cross the solid-liquid interface and trigger a volume-diffusion mechanism, which largely changes the polarization response, particularly around larger particles.

Fundamental equations and extended model

Like Wong (1979), we consider a perfectly conducting sphere immersed in an electrolyte solution that consists of three ionic species. The supporting electrolyte consists of anions (subscript 1) and inactive cations (subscript 2), which do not engage in electrochemical reactions at the particle surface (e.g., Cl^- and Na^+). A smaller fraction of active cations (subscript 3), in contrast, does participate in reduction and oxidation reactions at the metallic surface, which allows a net electric current to cross the solid-liquid interface. Upon excitation by the uniform electric field $\mathbf{E}_{\text{ext}} = \mathbf{E}_0 e^{i\omega t}$, where ω and t denote the angular frequency and time, respectively, the electric potential U and the ion concentrations n_j (in mol/m^3) around the particle will be perturbed from their equilibrium values. In 3D coordinates, the total ion flux densities caused by the external excitation are described by the Nernst-Planck equations (Nernst, 1888, 1889; Planck, 1890):

$$\mathbf{J}_j(\mathbf{r}, t) = -D_j \nabla n_j(\mathbf{r}, t) - \mu_j z_j n_j(\mathbf{r}, t) \nabla U(\mathbf{r}, t), \quad (1)$$

where D_j , μ_j , and z_j denote the diffusion coefficient, mobility, and signed valence of the j th ionic species. The first term on the right side of equation 1 describes a diffusion current, whereas the second term corresponds to a conduction or electromigration current. For the sake of simplicity, we limit our treatment to monovalent ions of symmetric electrolytes, i.e., $z_1 = -1$ and $z_2 = z_3 = 1$. Assuming, furthermore, the conservation of each ionic species expressed by the continuity equation $\nabla \cdot \mathbf{J}_j(\mathbf{r}, t) = -\partial_t n_j(\mathbf{r}, t)$, equation 1 becomes

$$\partial_t n_j(\mathbf{r}, t) = \nabla [D_j \nabla n_j(\mathbf{r}, t) + \mu_j z_j n_j(\mathbf{r}, t) \nabla U(\mathbf{r}, t)]. \quad (2)$$

We use the compact notation $\partial_{x,f} := \partial f / \partial x$ for partial derivatives with respect to x . The three ion concentrations are coupled among each other and to the total electric potential via Poisson’s equation:

$$\nabla^2 U(\mathbf{r}, t) = -\frac{F}{\epsilon_0 \epsilon_r} \sum_{j=1}^3 z_j n_j(\mathbf{r}, t), \quad (3)$$

where $F = 96,485$ C/mol is Faraday’s constant, $\epsilon_0 = 8.85 \times 10^{-12}$ C/(Vm) is the vacuum permittivity, and ϵ_r is the constant relative permittivity of the aqueous electrolyte. The system of PDEs described in equations 2 and 3 is also known as the Poisson-Nernst-Planck (PNP) system for ion transport.

Following the treatment by Wong (1979), we decompose the concentration of the j th ionic species into a static background concentration $n_j^{(0)}(\mathbf{r})$ and a perturbation $\delta n_j(\mathbf{r})$ imposed by the oscillating external field:

$$n_j(\mathbf{r}, t) = n_j^{(0)}(\mathbf{r}) + \delta n_j(\mathbf{r}) \cdot e^{i\omega t}. \quad (4)$$

In a similar fashion, the total electric potential can be decomposed into the background potential $U^{(0)}(\mathbf{r})$ and a perturbation potential $\delta U(\mathbf{r})$ as follows:

$$U(\mathbf{r}, t) = U^{(0)}(\mathbf{r}) + \delta U(\mathbf{r}) \cdot e^{i\omega t}. \quad (5)$$

Unlike in Wong’s model, the background concentration $n_j^{(0)}(\mathbf{r})$ is not equal to the bulk concentration n_j^∞ but includes the excess and defect concentrations caused by a fixed diffuse charge density at the

particle surface. For the same reason, the background potential $U^{(0)}(\mathbf{r})$ can no longer be assumed to be zero as done in Wong's model.

Besides the differentiation between active and passive cations made here, equations 2–5 are essentially the same as those used, e.g., by Chew and Sen (1982a, 1982b) to describe ion transport through the electrolyte around a charged particle. Although these authors model the polarization response of nonconducting particles, the physics controlling the response of the electrolyte solution is identical. The fundamentally different electrical characteristics of the suspended particles (nonconducting versus perfectly conducting) are later taken into account by imposing appropriate boundary conditions at the particle surface.

According to these authors, the problem can be decomposed into the solution of a static part of the problem, which essentially yields the equilibrium ion concentrations $n_j^{(0)}(\mathbf{r})$ and electric potentials $U^{(0)}(\mathbf{r})$ in the static diffuse layer and the bulk electrolyte (Chew and Sen, 1982b), and the solution of a frequency-dependent part (Chew and Sen, 1982a), which yields the perturbation quantities $\delta n_j(\mathbf{r})$ and $\delta U(\mathbf{r})$ caused by the external excitation. Although the static part does not depend on the perturbation quantities, the frequency-dependent solution couples to the static solution. Both parts of the solution are introduced in the following two subsections.

Static solution

In a variation of the approach by Chew and Sen (1982a, 1982b), in the absence of an external field, i.e., for $\delta n_j(\mathbf{r}) = 0$ for all j and $\delta U(\mathbf{r}) = 0$, we write (from equation 2)

$$0 = \nabla[D_j \nabla n_j^{(0)}(\mathbf{r}) + \mu_j z_j n_j^{(0)}(\mathbf{r}) \nabla U^{(0)}(\mathbf{r})]. \quad (6)$$

We assume that in equilibrium, i.e., without an external excitation, all three ion current densities through the particle surface vanish. This is obvious for the inactive ionic species, which do not penetrate the particle surface by definition, and is also sensible for the active cations (for more details, see Appendix A). Under this condition, equation 6 is solved by the Boltzmann-distributed concentrations (e.g., Chew and Sen, 1982b)

$$n_j^{(0)}(\mathbf{r}) = n_j^\infty \exp\left(-\frac{z_j e}{kT} U^{(0)}(\mathbf{r})\right), \quad (7)$$

where e denotes the elementary charge (1.602×10^{-19} C), k is Boltzmann's constant (8.617×10^{-5} eV/K), and T is the absolute temperature. The spatial variation of the static background potential $U^{(0)}(\mathbf{r})$ is coupled to the space charge resulting from equation 7 via Poisson's equation (from equation 3)

$$\nabla^2 U^{(0)}(\mathbf{r}) = -\frac{F}{\epsilon_0 \epsilon_r} \sum_{j=1}^3 z_j n_j^{(0)}(\mathbf{r}). \quad (8)$$

Inserting equation 7 into 8 gives the well-known Poisson-Boltzmann equation, which together with the boundary conditions at the particle surface,

$$U^{(0)}(\mathbf{r}) \Big|_{\text{surface}} = \zeta, \quad (9)$$

and at a far distance from the particle

$$U^{(0)}(\mathbf{r}) \xrightarrow{r \rightarrow \infty} 0, \quad (10)$$

determines the static background potential. Note that we placed the origin of our coordinate system ($r = 0$) in the center of the particle.

Because the static boundary conditions, i.e., equations 9 and 10, are the same as those used to describe the diffuse layer around a nonconducting particle, an approximate solution of the static potential $U^{(0)}(\mathbf{r})$ can be looked up in Chew and Sen (1982b) and inserted into equation 7 to obtain the static concentrations $n_j^{(0)}(\mathbf{r})$. Nevertheless, because the frequency-dependent solution requires the use of numerical methods in the present study, we will solve the static problem numerically, too.

Frequency-dependent solution

The static solution can then be used to obtain the perturbation potential $\delta U(\mathbf{r})$ and the perturbation ion concentrations $\delta n_j(\mathbf{r})$. Assuming that the amplitude $E_0 = |\mathbf{E}_0|$ of the external field is small (i.e., $E_0^2 \ll E_0$), all perturbation quantities are approximately proportional to the external excitation E_0 . Extending the approach by Chew and Sen (1982a) to the case of three ionic species, the linearized frequency-dependent part of equation 2 is written as

$$\begin{aligned} i\omega \delta n_j(\mathbf{r}, \omega) &= \nabla\{D_j \nabla \delta n_j(\mathbf{r}, \omega) \\ &+ \mu_j z_j [n_j^{(0)}(\mathbf{r}) \nabla \delta U(\mathbf{r}, \omega) + \delta n_j(\mathbf{r}, \omega) \nabla U^{(0)}(\mathbf{r})]\} \\ &+ \mathcal{O}(E_0^2), \end{aligned} \quad (11)$$

where the term $\mathcal{O}(E_0^2)$ represents the neglected products of two perturbation quantities and the perturbation potential satisfies Poisson's equation:

$$\nabla^2 \delta U(\mathbf{r}, \omega) = -\frac{F}{\epsilon_0 \epsilon_r} \sum_{j=1}^3 z_j \delta n_j(\mathbf{r}, \omega). \quad (12)$$

Equations 11 and 12 constitute four coupled differential equations that describe the variation of the perturbation quantities within the electrolyte, and it only remains to specify suitable boundary conditions. At a distance far from the particle, the perturbation potential should approach values corresponding to the external electric field, i.e.,

$$\delta U(\mathbf{r}, \omega) \xrightarrow{r \rightarrow \infty} -\mathbf{E}_{\text{ext}} \cdot \mathbf{r}, \quad (13)$$

whereas the ion concentrations should approach the static solution; i.e., the perturbation concentrations should vanish as described by

$$\delta n_j(\mathbf{r}, \omega) \xrightarrow{r \rightarrow \infty} 0. \quad (14)$$

We will assume that the particle can be considered a perfect conductor, such that the perturbation potential must be constant along the particle surface (see the "Discussion" section for a more detailed analysis of this assumption). If the external excitation is symmetric around the sphere, this constant potential must be zero; i.e.,

$$\delta U(\mathbf{r}, \omega) \Big|_{\text{surface}} = 0. \quad (15)$$

Because inactive ions are neither produced nor consumed at the particle surface, the normal fluxes of both inactive ionic species through the surface, i.e., equation 1 for $j = 1, 2$, must also be zero:

$$\{-D_j \nabla \delta n_j(\mathbf{r}, \omega) - \mu_j z_j [n_j^{(0)}(\mathbf{r}, \omega) \nabla \delta U(\mathbf{r}, \omega) + \delta n_j(\mathbf{r}, \omega) \nabla U^{(0)}(\mathbf{r}, \omega)]\} \cdot \mathbf{n} \Big|_{\text{surface}} = 0, \quad (16)$$

with \mathbf{n} denoting the unit normal vector to the surface (pointing into the electrolyte). Only the normal flux of the active cations through the metal surface is nonzero due to the oxidation-reduction reactions. The rate of ion production or consumption at the surface depends on the perturbation concentration of the active ions and the electric field at the surface as expressed by

$$\{-D_3 \nabla \delta n_3(\mathbf{r}, \omega) - \mu_3 [n_3^{(0)}(\mathbf{r}, \omega) \nabla \delta U(\mathbf{r}, \omega) + \delta n_3(\mathbf{r}, \omega) \nabla U^{(0)}(\mathbf{r}, \omega)]\} \cdot \mathbf{n} \Big|_{\text{surface}} = -\alpha(\zeta) n_3^{(0)}(\mathbf{r}, \omega) \nabla \delta U(\mathbf{r}, \omega) \cdot \mathbf{n} - \beta(\zeta) \delta n_3(\mathbf{r}, \omega), \quad (17)$$

where we already made use of the equality $z_3 = 1$. As we show in more detail in Appendix A, the right side of equation 17 corresponds to the exchange current across the metal electrolyte interface defined by Wong (1979) adapted to our extended model. The two parameters α (in Cs/kg) and β (in m/s) control the dependence of the reaction current on the overpotential at the particle surface and the perturbation of the active ion concentration, respectively. Details on the exchange current can be found in Appendix A. In the same appendix, we show that — assuming a constant reaction-current density i_0 — the two reaction-current parameters vary with the ζ -potential as follows:

$$\alpha(\zeta) = \alpha(0) \exp\left(\frac{e\zeta}{kT}\right), \quad \beta(\zeta) = \beta(0) \exp\left(\frac{e\zeta}{kT}\right), \quad (18)$$

where $\alpha(0)$ and $\beta(0)$ describe the reaction current in the absence of a static surface potential as used in the study by Wong (1979). Note that

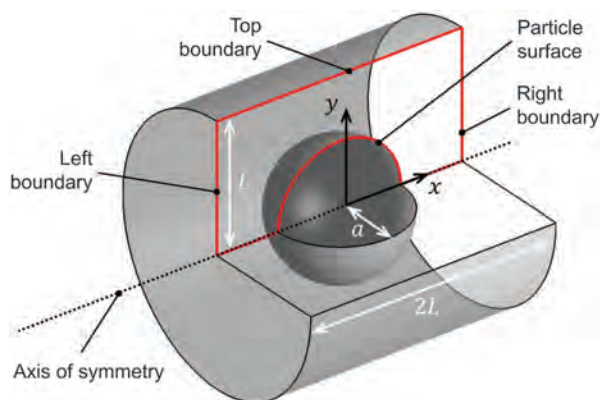


Figure 1. Three-dimensional sketch of the modeled volume. The spherical particle of radius a is enclosed by a cylinder of radius L and height $2L$ representing the surrounding electrolyte solution. The red lines mark the actual 2D model domain discretized for the particular simulation. Due to the particular set of boundary conditions on the surface of the particle, it is not necessary to model any of the perturbation quantities in its interior.

in our case, the reaction current is given in terms of an ion flux density in mol/(m²s), which has to be multiplied by Faraday's constant F to obtain the corresponding electric current density in A/m² as defined by Wong (1979) (his equation 28).

NUMERICAL IMPLEMENTATION

To our best knowledge, no closed analytical solution of the problem set up by the PDEs 11 and 12 and the boundary conditions expressed in equations 13–17 exists in the literature. This is also true for similar systems of PDEs with boundary conditions adjusted to the problem of charged nonconducting particles, for which only approximate analytical (e.g., Chew and Sen, 1982a; Shilov et al., 2001) or numerical solutions (e.g., DeLacey and White, 1981) have been reported.

Here, we use the finite-element software package COMSOL Multiphysics to successively obtain the static and the frequency-dependent solution. Although the numerical solution would also permit study of irregularly shaped particles, here we limit our treatment to spherical particles. This enables us to compare our results for the charged particle with the predictions of the analytical Wong model for an uncharged particle of equal size. Figure 1 illustrates the modeled volume with the particle of radius a centered at the origin of coordinates. The uniform external field is imposed, such that $\mathbf{E}_0 = E_0 \mathbf{e}_x$.

Due to the cylindrical symmetry of the problem, the numerical simulation only needs to be carried out on the 2D model domain of length $2L$ (in the x -direction) and height L (in the y -direction) marked in red in Figure 1. This approach, which helps to solve the numerical problem efficiently, is based on taking the x -coordinate of the Cartesian space as the z -coordinate of the cylindrical coordinate system and the y -coordinate as the radial coordinate r . As the problem is completely symmetric around the x - or z -axis, there is no variation in azimuthal direction. In addition, this approach requires a suitable coordinate transformation that accounts for the different form of the differential operators in cylindrical coordinates (for details, see Appendix B).

As we saw earlier, in the case of vanishing equilibrium reaction current densities, the static problem reduces to the solution of the Poisson-Boltzmann equation, which contains $U^{(0)}(\mathbf{r})$ as only unknown variable. The boundary conditions, equations 9 and 10, are translated into the following boundary conditions for the numerical simulation: $U^{(0)} = \zeta$ on the particle surface, $U^{(0)} = 0$ on the left, right, and top boundaries (see Figure 1), and $\partial_y U(0) = 0$ on the axis of symmetry. For technical details on the implementation in COMSOL Multiphysics, see Appendix B.

Because bulk values are imposed as boundary conditions on the left, right, and top boundaries, these should be placed sufficiently far away from the static diffuse layer and the frequency-dependent induced perturbations around the particle. As a trade-off between computational cost and accuracy, we use a standard domain size L of four times the particle radius, i.e., $L = 4a$. We checked the suitability of this length scale by comparing the modeled perturbation potential at the boundary (for $\zeta = 0$) with the corresponding values of the analytical solution (Wong, 1979; Bücker et al., 2018). Because our modeling results do not yield a longer scale perturbation caused by the effect of the static diffuse layer (see the next section), this criterion will turn out to be sufficient.

Furthermore, the discretization of the 2D modeling domain should account for the expected small-scale variation of the solution

within the diffuse layer at the particle surface. While particle sizes of at least 1 mm may be of interest, the thickness of the diffuse layer is only of the order of one Debye length

$$\lambda_D = \left(\frac{\epsilon_0 \epsilon_r kT}{2n_1^\infty eF} \right)^{1/2}, \quad (19)$$

which for typical ionic strengths of the electrolyte is as small as 10^{-8} m. To be able to resolve the diffuse layer, we therefore discretize the electrolyte next to the surface with a special boundary-layer mesh consisting of rectangular elements with a size of $\pi a/400$ along the boundary (tangential direction). In the radial direction, this boundary-layer mesh is much finer and consists of a fixed number of eight elements with sizes increasing from $\lambda_D/2$ at the surface to $\approx 1.8\lambda_D$ at the outer limit of the boundary layer. The remaining volume is filled with triangular elements, the maximum sizes of which increase from $\lambda_D/2$ at the outer limit of the boundary-layer mesh to $L/20$ at the remote boundaries. Resulting meshes consist of ≈ 9250 elements for particle sizes between 0.1 μm and 10 mm, of which the constant number of 3200 elements corresponds to the boundary-layer mesh.

After having solved the static problem, the frequency-dependent solution is obtained using the same mesh. The static background ion concentrations needed for the frequency-dependent solution, are computed by inserting $U^{(0)}(\mathbf{r})$ into equation 7. For a detailed implementation of the PDEs 11–12 in COMSOL Multiphysics, see Appendix B. The analytical boundary conditions for the frequency-dependent problem, equations 13–17, merge into the following numerical formulation: They are unchanged on the particle surface; $\delta n_j = 0$ for all j and $\delta U = \pm E_0 L$ on the left and right boundary, respectively; and $\mathbf{J}_j = 0$ for all j and $\partial_y \delta U = 0$ on the top boundary and the axis of symmetry. While the static solution only needs to be computed once for each set of model parameters (i.e., a , ζ , and n_j^∞), the frequency-dependent problem has to be solved for each value of the angular frequency ω separately.

Further below, we will display the modeling results either directly, i.e., the actual solutions for the four perturbation quantities, or in terms of the effective conductivity of the modeled volume. The latter can be obtained from a numerical integration of the total ionic fluxes through the left (or right) boundary; i.e.,

$$\sigma_{\text{mod}} = \frac{2}{E_0 L^2} \int_0^L \sum_{j=1}^3 \mathbf{J}_j(x=L, y) \mathbf{e}_x y dy, \quad (20)$$

where the term $y dy$ accounts for the area element of the circular surface of the boundary and the factor $2/L^2$ stems from the normalization to its total area.

As mentioned above, the standard domain size is $L = 4a$ to ensure that the boundaries are located far enough from the polarized particle. However, this corresponds to a rather small particle volume fraction of $\nu_{\text{mod}} \approx 0.01$. To facilitate the comparison with the spectral responses discussed in part 1 of this series (Bücker et al., 2018), the modeled effective conductivities σ_{mod} are scaled to the volumetric content of $\nu = 0.12$ using the Maxwell-Garnett mixing rule (e.g., Wong, 1979):

$$\frac{\sigma_{\text{eff}}}{\sigma_0} = \frac{1 + 2\nu f}{1 - \nu f}, \quad (21)$$

where $\sigma_0 = 2\mu n_1^\infty F$ is the bulk conductivity of the electrolyte and

$$f = \frac{1}{\nu_{\text{mod}}} \frac{\sigma_{\text{mod}} - \sigma_0}{\sigma_{\text{mod}} + 2\sigma_0} \quad (22)$$

is the modeled frequency-dependent reflection coefficient of the spherical particle.

Due to the lack of an appropriate analytical model, the numerical solution around the charged particle itself cannot be validated rigorously. However, for the limiting case of a particle without diffuse charge, i.e., $\zeta = 0$, the numerical solution can be compared with the analytical solutions provided by Wong (1979) and Bücker et al. (2018) to detect possible problems due to an inappropriate discretization or other issues arising from the numerical implementation. In the “Results” section, all numerical results are therefore presented along with the corresponding analytical solutions for an uncharged particle.

RESULTS

Unless otherwise stated, the standard model parameters listed in Table 1 are used to obtain the results presented in this section. As mentioned above, all numerical results are scaled to a standard volumetric content of 12%, which ensures a significant spectral variation of the effective conductivity. The ζ -potential on the surface of the charged particle is set to $\zeta = -50$ mV, which is a typical value for stainless steel surfaces at neutral pH (Boulangé-Petermann et al., 1995) and is high enough to render the small changes of the spectral response induced by the static diffuse layer visible. In a similar fashion, we use a relatively high bulk concentration of the active cations of $n_3^\infty = 0.12$ mol/m³ to also highlight the effect of the reaction current. The values of the reaction current parameters $\alpha(0)$ and $\beta(0)$ for the uncharged particle are taken over from Wong (1979). A uniform ion mobility of $\mu_1 = \mu_2 = \mu_3 = \mu = 5 \times 10^{-8}$ m²/(Vs), which is approximately the mobility of the sodium cation at room temperature (e.g., Atkins and De Paula, 2013), is assumed for all three ionic species.

Table 1. Standard parameter values for numerical modeling studies.

Parameter (unit)	Symbol	Value
Absolute temperature (K)	T	293
Volumetric metal content (-)	ν	0.12
Particle radius (μm)	a	0.1
ζ -potential (mV)	ζ	-50
Relative permittivity of the fluid (-)	ϵ_r	80
Ion mobility [m ² /(Vs)]	μ	5×10^{-8}
Signed ion valences (-)	z_1, z_2, z_3	-1, 1, 1
Bulk anion concentration (mol/m ³)	n_1^∞	1
Bulk concentration of active cations (mol/m ³)	n_3^∞	0.12
Reaction-current parameter [m ² /(Vs)]	$\alpha(0)$	10^{-10}
Reaction-current parameter (m/s)	$\beta(0)$	10^{-2}
Magnitude of external field (V/m)	E_0	1

Polarization mechanism

In part I (Bücker et al., 2018), we analyzed the two main relaxation processes inherent to Wong's electrochemical polarization model: The first is related to the accumulation and relaxation of electrical charges in thin diffuse layers induced next to the two hemispheres of the particle. This dynamic charging relaxes on a characteristic time scale that increases linearly with the particle radius as $\tau_{dl} = a\lambda_D/(2D)$. The second is a volume-diffusion process related to the buildup of an electrically neutral concentration gradient around the particle. This gradient is required to balance reac-

tion currents through the particle, and it is therefore only observed in the presence of active cations (i.e., $n_3^\infty > 0$) and a nonzero exchange current (i.e., $\alpha(0), \beta(0) > 0$) at the particle surface. The relaxation of the concentration gradient occurs on a time scale $\tau_{vd} \propto a^2/D$ and becomes dominant around particles with radius $8\lambda_D(n_1^\infty/n_3^\infty)^2$ or larger (see Bücker et al., 2018).

Figures 2, 3, 4, and 5 give an insight into the microscale manifestations of both mechanisms and the changes produced by adding a static diffuse layer. The first row of Figure 2 shows the (purely radial) variation of the background ion concentrations $n_j^{(0)}(\mathbf{r})$ and the background potential $U^{(0)}(\mathbf{r})$ within such a static diffuse layer

around a charged submicron particle with a radius of $0.1 \mu\text{m}$ and a ζ -potential of -50 mV . The dashed line indicates the approximate thickness $\lambda_D \approx 10 \text{ nm}$ of the diffuse layer. Although the negative charges at the particle surface deplete anions (co-ions) almost completely from the diffuse layer, they increase both cation concentrations (counterions) at the surface by a factor of ≈ 7.2 . Because the excess of counterions outnumbers the deficit of co-ions, the effective conductivity of the interfacial layer is larger than the one of the bulk electrolyte. Outside the diffuse layer, all three ion concentrations approach their respective bulk concentrations and the static potential decays to 0 mV .

The other four rows of Figure 2 show particles of the same size ($0.1 \mu\text{m}$) but with different surface characteristics under the influence of an external field. The selected angular frequency of $\omega = 3 \times 10^4 \text{ rad/s}$ of the external excitation is well below the characteristic frequencies of all relaxations of interest, such that the corresponding perturbations can fully develop. Figure 2 displays the real parts of the complex-valued perturbation quantities. The corresponding imaginary parts are not displayed because they are much (at least by a factor of 10) smaller at the selected low angular frequency.

Complex-valued concentrations and potentials might be less familiar to some readers. But in the mathematical formalism used here, which describes harmonic oscillations by complex numbers, the occurrence of nonzero imaginary parts indicates that these quantities are out of phase compared with the external electrical field, the phase of which is given by the product ωt .

Upon excitation by the external field, the perfectly conducting sphere always responds with a quasi-instantaneous redistribution of charges along its surface. The resulting induced surface charges $\Sigma_\infty \propto \epsilon_0 \epsilon_r 3E_0$ (see, e.g., Bücker et al., 2018) ensure that the external field is canceled out within the particle, which is being accounted for by the boundary condition 15. This early-time or high-frequency behavior of the particle itself is the same, regardless of reaction currents through the particle surface or the assumption of a fixed diffuse surface charge. However, due to slower

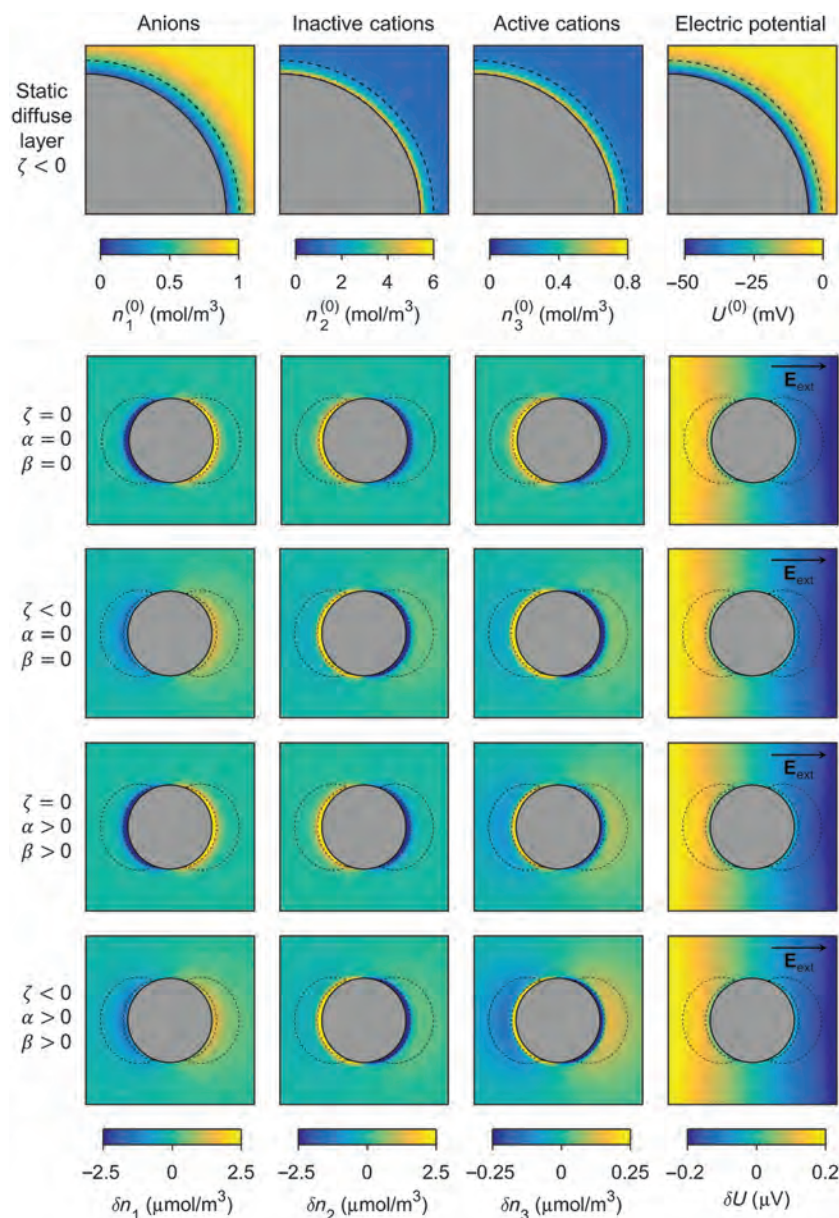


Figure 2. Static diffuse layer (the first row) and field-induced perturbations around a submicron particle with $a = 0.1 \mu\text{m}$ at the low-frequency limit $\omega = 3 \times 10^4 \text{ rad/s}$ (the other four rows). Only the real parts of the complex-valued perturbation quantities are illustrated; the respective imaginary parts are much smaller at the low-frequency limit displayed here. The inner dashed line indicates the diffuse layer, and the outer line indicates the volume-diffusion layer. All remaining parameters as listed in Table 1.

processes, the variation of the late-time or low-frequency perturbations of ion concentrations and electric potentials within the electrolyte next to the particle depends largely on the particular set of surface properties. In the following, we will discuss the different effects of ζ -potential and reaction currents in detail.

The second row of Figure 2 and the solid-gray curves in Figures 3 and 4 illustrate the low-frequency polarization of the uncharged conducting particle, i.e., $\zeta = 0$, with no reaction currents through the solid-liquid interface, here realized by setting $\alpha(0), \beta(0) = 0$. Under these conditions, only the effect of the diffuse-layer polarization can be observed, the fundamental polarization of the perfect conductor. As discussed in more detail by Bückner et al. (2018), normal electromigration currents around the poles of the particle charge the electrolyte next to the particle surface until they are balanced by opposed diffusion currents driven by the resulting concentration gradients. At sufficiently small frequencies or after sufficiently long

times, the total charge stored in the diffuse layer and mirrored on the particle is by a factor $\alpha\kappa$ (where $\kappa = 1/\lambda_D$) larger than the quasi-instantaneously induced surface charge Σ_∞ (Bückner et al., 2018). The perturbation concentrations in the diffuse layer decay approximately exponentially with the distance from the surface, i.e., $\propto \exp[-\kappa(r-a)]$ (Wong, 1979; Bückner et al., 2018). The inner dashed lines in Figures 2–4 mark the distance at which the perturbations decay to $1/e$ of their respective values at the particle surface indicating the spatial extension of the field-induced diffuse layers.

From the third row of Figure 2 and the dashed-gray curves in Figures 3 and 4, it is evident that the situation changes if a fixed surface potential of $\zeta = -50$ mV is considered: Here, we observe a significant reduction of the anion perturbation concentrations within the diffuse layer (the first panel), whereas the resulting lack of charge is compensated by an amplification of the cation perturbation concentrations in the diffuse layer (the second and third panels, better recognizable from the radial sections in Figures 3 and 4).

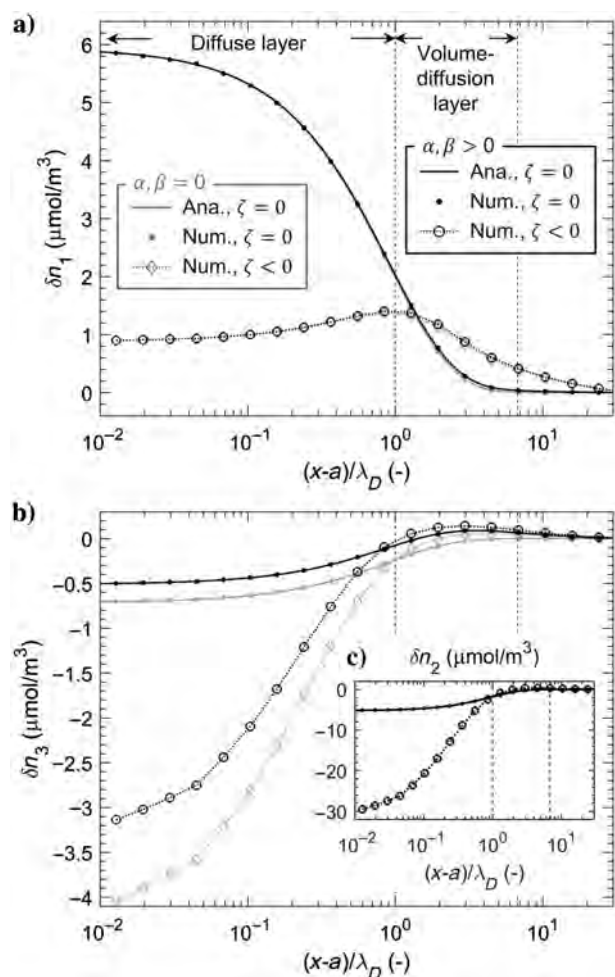


Figure 3. Radial profiles ($y = 0, x > 0$) of the real parts of the perturbation concentrations of (a) anions, (b) active, and (c) passive cations at $\omega = 3 \times 10^4$ rad/s. For $\zeta = 0$, numerical results (the filled circles) are plotted along with the respective analytical solutions (the solid lines) from Bückner et al. (2018). For $\zeta < 0$, only numerical results (the open symbols, dashed lines) exist. For both cases, results without (gray) and with (black) the reaction current are displayed. The vertical dashed lines indicate the extensions of the diffuse layer (DL, left line) and the volume-diffusion layer (right line). All of the other parameter values are as in Table 1.

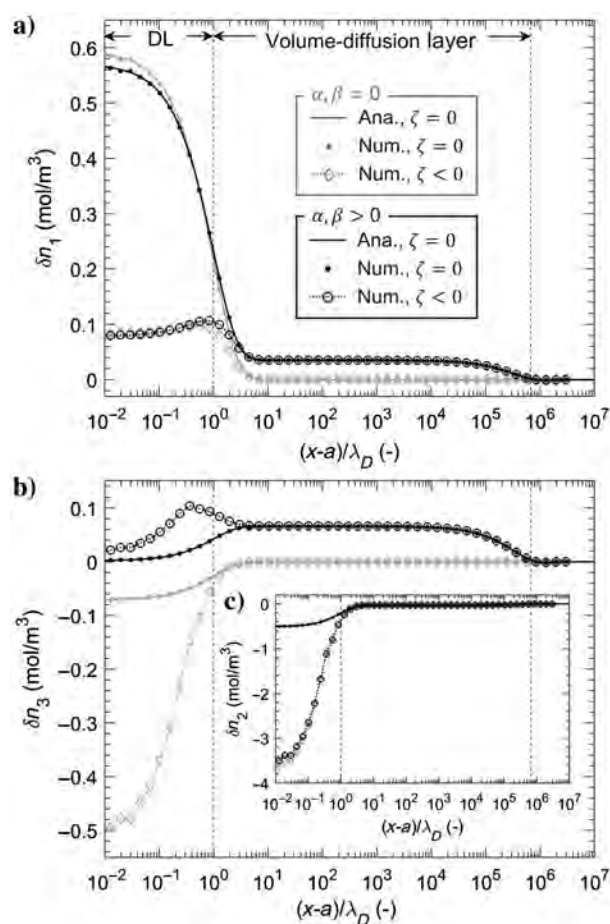


Figure 4. Radial profiles ($y = 0, x > 0$) of the real parts of the perturbation concentrations of (a) anions, (b) active, and (c) passive cations in the vicinity of a conducting sphere of radius $a = 10$ nm at $\omega = 10^{-4}$ rad/s. For $\zeta = 0$, numerical results (the filled circles) are plotted along with the respective analytical solutions (the solid lines) from Bückner et al. (2018). For $\zeta < 0$, only numerical results (the open symbols, dashed lines) exist. For both cases, results without (gray) and with (black) reaction current are displayed. The vertical dashed lines indicate the extensions of the diffuse layer (DL, left line) and volume-diffusion layer (right line). All other parameter values as in Table 1.

Beyond the diffuse layer covering the submicron particle (Figures 2 and 3), all ion concentrations increase (or, respectively, decrease) uniformly on the two opposite sides of the particle resulting in an electrically neutral salinity gradient around the particle. The development of this relatively long-range concentration gradient can be understood as a direct consequence of the unequal contributions of anions and cations to the conductivity of the static diffuse layer. Tangentially to the surface, electromigration currents transport much more cations than anions, which in Figure 2 depletes cations to the left of the particle and accumulates them to the right. At the same time, more anions arrive at (are pulled away from) the right (left) side of the particle than can be transported through the diffuse layer, which explains the net electroneutrality of the perturbation. The concentrations increase until the resulting opposite diffusion currents can balance the effect of the electromigration currents, leading to the quasiequilibrium situation shown in Figure 2. The process described in this paragraph is a volume-diffusion mechanism, which is similar to but should not be confused with the one arising from the reaction currents discussed in the next paragraph. Obviously, this mechanism is much weaker around the larger particle (Figure 4), where the presence of a static diffuse layer does not result in recognizable changes of the ion concentration in the zone marked as the volume-diffusion layer.

The fourth row of Figure 2 and the black solid curves in Figures 3 and 4 show the influence of nonzero reaction currents, i.e., $\alpha, \beta > 0$, on the perturbations around an uncharged particle, i.e., $\zeta = 0$ mV. Here, not the unequal population of the static diffuse layer with anions and cations but the exclusive release and absorption of active cations at the surface causes an imbalance of electromigration fluxes between the electrolyte far away and in the vicinity of the particle. As discussed in more detail previously (Bücker et al., 2018), the result is a coupling of the diffuse-layer polarization and the volume-diffusion process. Although the perturbations caused by the volume-diffusion process around charged particles (the previous paragraph) appear clearly and have the same sign in all three ion concentrations; the reaction currents mainly affect the concentration of the active ions (see δn_3) and electro-neutrality in the volume-diffusion region is ensured by a small reduction of δn_2 and a small increase of δn_1 . The radial profiles in Figures 3 and 4 illustrate these distinct effects clearly.

The radial profiles in Figure 4 also show a second important difference between the concentration gradients due to the two different volume-diffusion mechanisms, which cannot be distinguished around the small particle: Only the reaction currents produce the plateaus observed in the region marked as the volume-diffusion layer (the black lines and symbols), which together with the decay at larger distances represent the $1/r^2$ dependence of the corresponding perturbation concentrations. The absence of these plateaus in the perturbation concentrations related to the asymmetric transport in the static diffuse layer (the gray lines and symbols in Figure 4) indicates a much faster — probably exponential — decay with the distance from the particle surface and thus a much smaller thickness of the volume affected by the concentration gradient.

The last row of Figure 2 and the dashed black curves in Figures 3 and 4 show the coupling of all three polarization processes. From a direct comparison among the different maps and profiles, it can be seen that, in this case, (1) the perturbation concentrations within the diffuse layer around small and large particles are largely controlled by the static diffuse layer, (2) those in the volume-diffusion region

around the large particle only by the reaction current through the particle surface, and (3) those in the volume-diffusion region around the small particle by the reaction current through the particle surface and the static diffuse layer.

Although the effects and interactions between the different polarization mechanisms are clearly reflected in the perturbation concentrations around the submicron particle, the resulting electric perturbation potentials (the last column in Figure 2) hardly show any noticeable variation. The radial profiles of the perturbation potentials presented in Figure 5 also show only subtle differences. In both cases, the perturbation potential primarily shows the steep exponential decrease due to the space charge stored in the diffuse layer followed by a plateau due to the $1/r^2$ decay of the effective dipole moment of the particle. If no reaction currents are considered, i.e., for $\alpha, \beta = 0$, the charges of the diffuse layer fully screen the electric field. In this case, the potential profile outside the diffuse layer is equal to the one around a perfectly insulating sphere, the reflection coefficient of which can be obtained as $f = -1/2$ from potential theory. The reflection coefficient f of a sphere with conductivity σ_s embedded in a medium with homogeneous conductivity σ_m is $(\sigma_s - \sigma_m)/(\sigma_s + 2\sigma_m)$ (e.g., Maxwell, 1891). Reaction currents through the interface (i.e., $\alpha, \beta > 0$) leak charges from the diffuse layer into the particle (and vice versa), which reduces the effective dipole moment of the particle and thus the perturbation potential along the plateau in Figure 5. The almost-identical variations of the potential around charged (the open symbols) and uncharged (the filled symbols) particles suggest that the static diffuse layer has hardly any effect on the macroscopic response of the particle.

As mentioned in the previous section, Figures 3–5 show a good agreement of numerical (the solid lines) and analytical (the filled circles) results for the case of the uncharged particle, i.e., $\zeta = 0$ mV. The full analytical solution for all four perturbation quantities can be looked up in Bücker et al. (2018). Slight deviations between numerical and analytical solutions only become visible very close to the particle surface. As an explanation, we recall that the smallest radial element size of our finite-element mesh is $\lambda_D/2$, which is a factor of 50 larger than the smallest radial distance displayed in the radial profiles in Figures 3–5. Thus, the observed misfit does not indicate a systematic error but could be reduced by increasing the resolution of the mesh.

Spectral response

Figure 6 displays the effective conductivity spectra obtained for the submicron particle, i.e., $a = 0.1$ μm , in terms of the respective real ($\sigma'(\omega)$) and imaginary ($\sigma''(\omega)$) parts. The diffuse-layer relaxation, which dominates around such small particles, leads to a steep transition between the low- and high-frequency limits of σ' and a narrow peak in the σ'' spectra. The small overshoots of σ' at the angular frequency $1/\tau_{\text{el}} = \sigma_0/(\epsilon_0\epsilon_r) \approx 10^{-7}$ rad/s can be attributed to the relaxation of the electrolyte solution (Bücker et al., 2018), and they obey the Kramers-Kronig relations with the corresponding imaginary spectra (not shown here for brevity). The effect of a nonzero ζ -potential on the spectra in Figure 6 can be summarized under the following three main changes: The presence of a static diffuse layer (1) increases the DC limit of σ' (subsequently denominated by σ_{DC}), (2) reduces the maximum of σ'' (subsequently σ''_{max}), and (3) shifts the characteristic angular frequency,

at which σ''_{\max} is encountered, toward lower frequencies (subsequently ω_c).

Figure 7 shows that the effect of a nonzero ζ -potential on the spectral response of the large particle with $a = 10 \text{ nm}$ is different. For vanishing reaction currents, i.e., $\alpha(0), \beta(0) = 0$, we still observe the steep transition of σ' and the narrow peak of σ'' related to the diffuse-layer polarization. However, here σ_{DC} and σ''_{\max} remain unaffected by the static diffuse layer and only the shift of ω_c to lower frequencies can be observed. If nonzero reaction currents through the surface of the large particle are taken into account, i.e., for $\alpha(0), \beta(0) > 0$, the volume-diffusion process becomes dominant resulting in a broadening of the transition region, a broadening and reduction of the σ'' -peak, and a substantial reduction of the characteristic angular frequency ω_c . In this regime, no effect of the static diffuse layer on the spectral response can be detected.

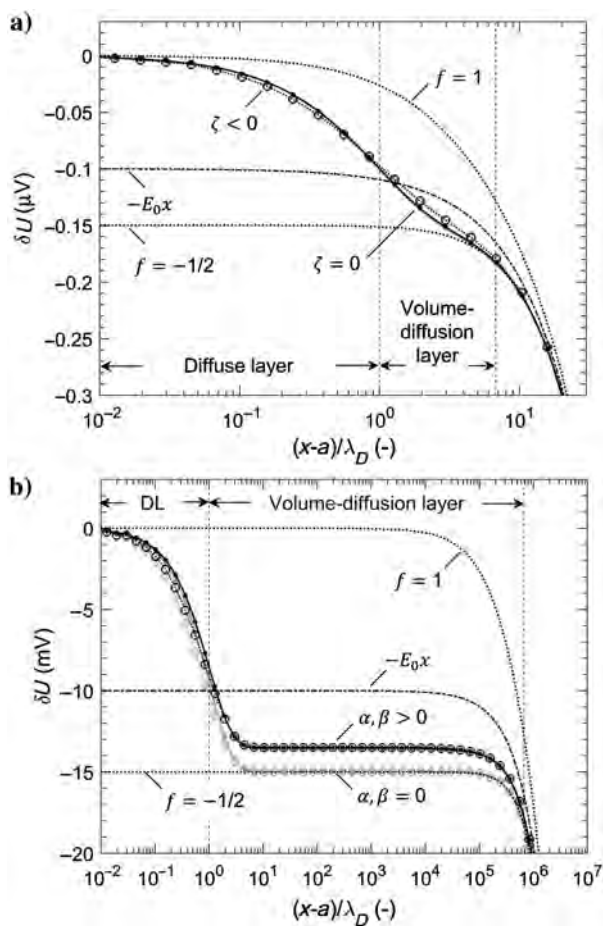


Figure 5. Radial profiles ($y = 0, x > 0$) of the real part of the perturbation potential in the vicinity of conducting spheres (a) of radius $a = 0.1 \text{ } \mu\text{m}$ at $\omega = 3 \times 10^4 \text{ rad/s}$ and (b) of radius $a = 10 \text{ nm}$ at $\omega = 10^{-4} \text{ rad/s}$. For $\zeta = 0$, numerical results (the filled circles) are plotted along with the respective analytical solutions (the solid lines) from [Bücker et al. \(2018\)](#). For $\zeta < 0$, only numerical results (the open symbols, dashed lines) exist. For both cases, results without (gray) and with (black) the reaction current are displayed. The potential $-E_0x$ associated with the uniform external field \mathbf{E}_{ext} as well as the potentials around a nonconducting ($f = -1/2$) and a perfectly conducting ($f = 1$) sphere are also included. The vertical dashed lines indicate the extensions of the diffuse layer (DL, the left line) and the volume-diffusion layer (the right line). All of the other parameter values are as in [Table 1](#).

In the following, we will study the dependency of the three spectral parameters σ_{DC} , σ''_{\max} , and ω_c on the ζ -potential in more detail and provide some possible explanations for the observed changes.

Figure 8a shows the variation of σ_{DC} with the ζ -potential for two different particle radii ($a = 0.1$ and $31.6 \text{ } \mu\text{m}$). As we know, an increasing magnitude of the (negative) ζ -potential results in an increase of cation and a decrease of anion concentrations in the static diffuse layer. Because the increase of the cation concentrations with ζ is much larger than the decrease of the anion concentration, the surface conductivity increases with the magnitude of the ζ -potential, which results in the increase of σ_{DC} observed in [Figure 8](#). Because the total volume fraction occupied by the static diffuse layer of fixed thickness λ_D decreases with increasing particle size, the increase of σ_{DC} with ζ is most pronounced around the smaller particle ($0.1 \text{ } \mu\text{m}$) and becomes almost negligible around the larger ($31.6 \text{ } \mu\text{m}$) particle.

Above, we saw that — provided that no reaction currents are allowed to cross the surface — a fully developed induced diffuse

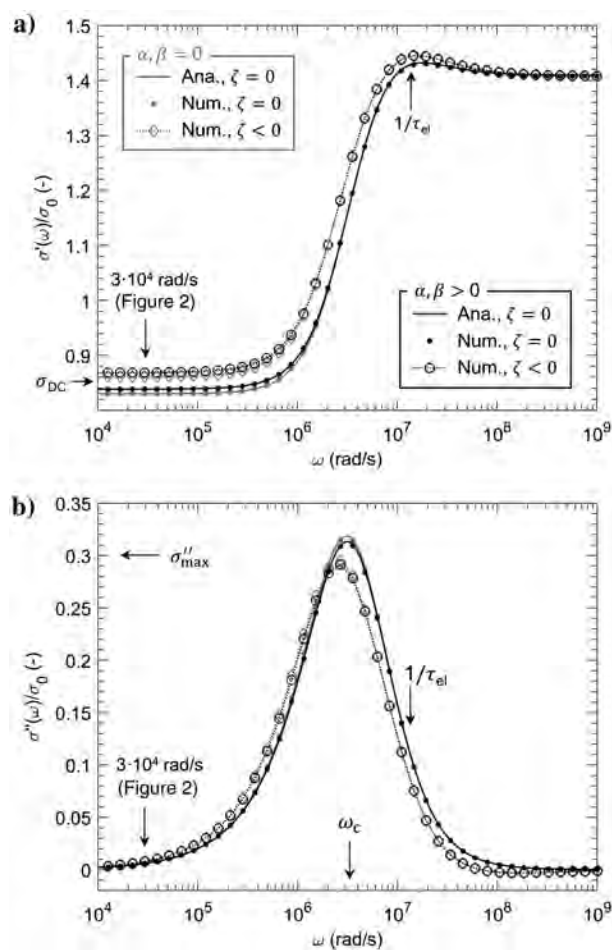


Figure 6. Variation of (a) real (σ') and (b) imaginary (σ'') part of the effective normalized conductivity with angular frequency. For the uncharged particle ($\zeta = 0$), numerical spectra (the filled circles) can be compared with the analytical solution (the solid lines) from [Wong \(1979\)](#). For the charged particle ($\zeta < 0$), only numerical spectra (the open symbols, dashed lines) exist. For uncharged and charged particles, spectra without (gray) and with (black) the reaction currents are displayed. All of the other parameter values are as in [Table 1](#).

layer lets the perfectly conducting particle effectively (i.e., outside the diffuse layer) behave like a nonconducting particle (see Figure 5). At the same time, the static diffuse layer partly compensates the effect of the induced diffuse layer and slightly increases the effective conductivity. To understand the contribution of the static diffuse layer, we can try to describe the variation of σ_{DC} with ζ by the corresponding expressions known from the classic theory for nonconducting particles.

According to O’Konski (1960), the effect of the surface conductivity K can be taken into account by adding the conductivity $2K/a$ to the conductivity of the particle. If the particle is nonconducting, which in our case is true in the low-frequency limit and outside the induced diffuse layer, the effective conductivity of the particle is given by

$$\sigma_p = \frac{2K}{a}. \quad (23)$$

Because our model does not include a Stern layer, K only considers the conductivity increment due to the static diffuse layer. For a thin static diffuse layer, i.e., $a\kappa \gg 1$, the surface conductivity K can be approximated using Bikerman’s formula (e.g., Shilov et al., 2001). Because we do not consider electro-osmotic coupling, we evaluate this formula in the high-viscosity limit, where

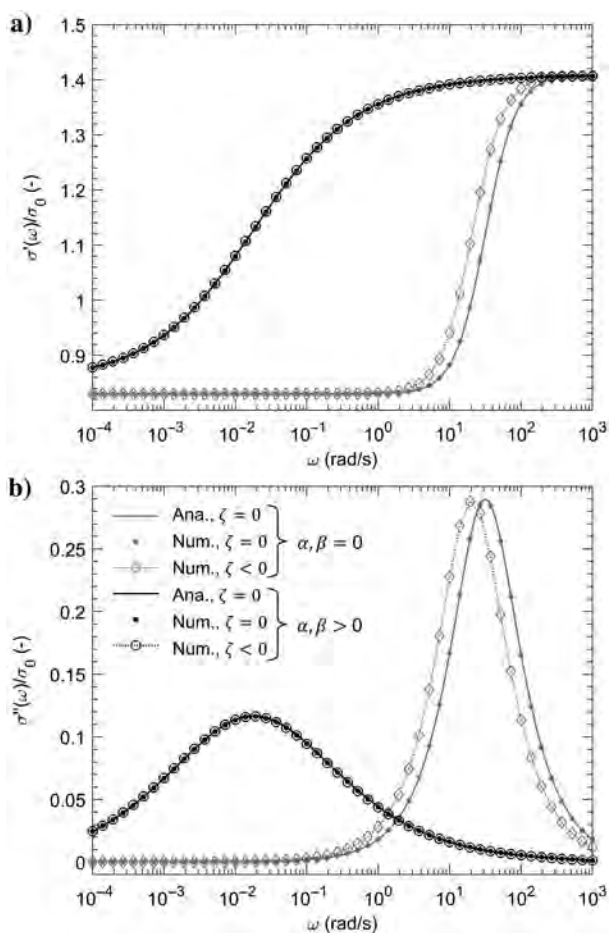


Figure 7. As Figure 6 but for a larger particle with $a = 10$ mm.

$$K \approx 2\sigma_0\lambda_D \left[\cosh\left(\frac{e\zeta}{2kT}\right) - 1 \right]. \quad (24)$$

The effective DC conductivity of a particle with conductivity σ_p immersed in a medium of conductivity σ_0 can be obtained from inserting the effective reflection or dipole coefficient (e.g., from Shilov et al., 2001)

$$f_{DC} = \frac{\sigma_p - \sigma_0}{\sigma_p + 2\sigma_0}, \quad (25)$$

into the Maxwell-Garnett mixing rule (equation 21). The predicted variation of σ_{DC} with ζ is illustrated in Figure 8a (the solid lines) along with the corresponding numerical results (the black open symbols).

Particularly for the smaller particle, this analytical approximation overestimates the conductivity increment produced by the static diffuse layer. There are various reasons for the observed deviation: Equations 23–25 are only valid in the thin double layer limit, i.e., $a \gg \lambda_D$. Furthermore, the Bikerman model of surface conductivity does not consider the volume-diffusion polarization of the static diffuse layer observed in our simulation results, which is expected to reduce the effective conductivity increment, nor the coupling with the induced diffuse layer. Despite these shortcomings, the qualitative agreement with the modeled response is relatively good and provides an additional plausibility check of our numerical implementation.

Note that the comparison with the response of a nonconducting particle is only sensible in the low-frequency limit, where the perfectly conducting particle behaves like an insulator. At higher frequencies, the different natures of the particles lead to fundamen-

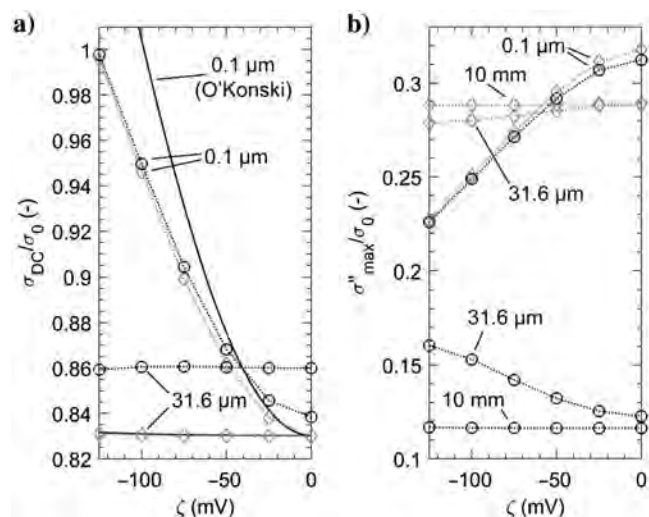


Figure 8. Variation of the low-frequency limit of the (a) effective conductivity σ_{DC} and the (b) maximum imaginary conductivity σ''_{max} with the ζ -potential for radii $a = 0.1 \mu\text{m}$, $31.6 \mu\text{m}$ (a and b), and 10 mm (b only). Conductivity variations are displayed for simulations with (the black circles) and without (the gray diamonds) reaction currents. The black solid lines illustrate the analytical approximation of σ_{DC} based on the surface conductivity according to O’Konski (1960). Besides a and ζ , all of the parameter values are as in Table 1.

tally different frequency dependencies of the effective conductivity (see the “Discussion” section for more detail).

Figure 8b shows the variation of σ''_{\max} (i.e., the value of σ'' at the characteristic frequency of each individual spectral response), which is often taken as a measure of the magnitude of the polarization. If no reaction currents are considered (the gray diamonds), σ''_{\max} decreases with the magnitude of ζ . This decrease is most pronounced for the smallest particle, i.e., $a = 0.1 \mu\text{m}$, and is hardly noticeable for the largest, i.e., $a = 10 \text{ mm}$. For the smallest particle, the variation of σ''_{\max} with ζ does almost not change when reaction currents are added to the model (the black circles). All responses discussed so far are dominated by the relaxation of the diffuse layer, such that we can conclude that the magnitude of this polarization process generally decreases with the increasing diffuse charge density at the particle surface. The opposite is the case when the volume-diffusion process becomes dominant: σ''_{\max} increases with the magnitude of ζ . We observe this around the intermediate particle, i.e., $a = 31.6 \mu\text{m}$, if reaction currents are considered. In addition, in the case of nonzero reaction currents, the effect of ζ becomes almost imperceptible around the largest particle, i.e., $a = 10 \text{ mm}$.

Relaxation time

Due to its strong dependence on geometric parameters, the relaxation time τ , here defined as the inverse of the characteristic angular frequency ω_c , is often used as a proxy for the size of the conducting particles. Hence, a good understanding of the effect of the ζ -potential on this important spectral parameter would be desirable. Figure 9 illustrates the variation of τ with the particle radius a for different surface characteristics. The response of uncharged particles shows the typical division into two regimes (e.g., Bückner et al., 2018): The $\tau \propto \lambda_D a$ increase can be attributed to the diffuse-layer relaxation, whereas the much steeper $\tau \propto a^2$ variation is related to

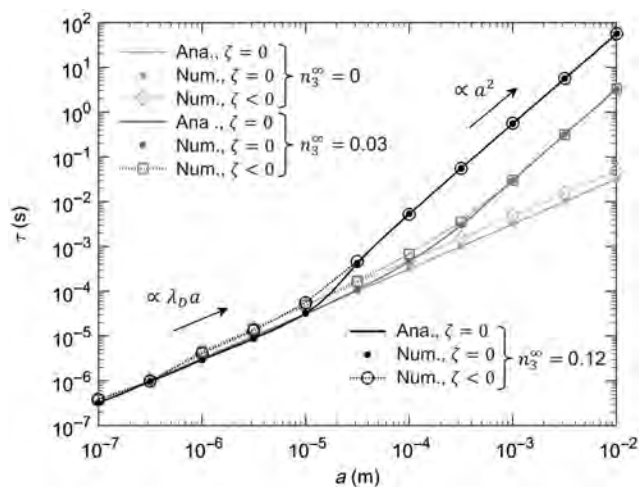


Figure 9. Variation of relaxation times τ with particle radius a for three different concentrations of active anions $n_3^\infty = 0, 0.03,$ and 0.12 mol/m^3 (light gray, dark gray, and black, respectively). For the uncharged particle ($\zeta = 0$), numerical results (the filled circles) can be compared with the analytical solution (the solid lines) from Wong (1979). For the charged particle ($\zeta < 0$), only numerical results (the open symbols, dashed lines) can be displayed. Besides a , ζ , and n_3^∞ , all of the other parameters are as in Table 1.

the volume-diffusion mechanism, which dominates around larger particles if reaction currents through the particle surface are taken into account. This division into two regimes is also valid for charged particles, i.e., $\zeta = -50 \text{ mV}$. The only effect of the static diffuse layer around the particles is a slight increase of the relaxation times of the diffuse layer ($\propto \lambda_D a$) for radii $a > 1 \mu\text{m}$. The relaxation times of the volume-diffusion polarization ($\propto a^2$), in contrast, remain practically unaffected.

Figure 10, which illustrates the variation of the relaxation times with the ζ -potential for three differently sized particles, confirms this general observation. We also see that the variation of the relaxation time of the diffuse layer, i.e., $\alpha(0), \beta(0) = 0$, with ζ is relatively flat at approximately 0 mV , becomes steepest at approximately $\pm 25 \pm 75 \text{ mV}$, and then again flattens out toward higher magnitudes of ζ . This behavior is symmetric with respect to $\zeta = 0 \text{ mV}$; thus, it is not affected by the sign of the diffuse surface charge. In contrast, the practically constant relaxation time of the volume-diffusion mechanism (the black lines and symbols in Figure 10) presents a slightly asymmetric behavior, which becomes most noticeable at large magnitudes of the ζ -potential.

At first glance, the increase of the relaxation time of the diffuse layer with ζ seems counter intuitive: The static diffuse layer increases the conductivity in the vicinity of the particle as described by the surface conductivity K . At the same time, the relaxation time is proportional to the Debye length and thus to the square root of the inverse of the conductivity of the electrolyte around the particle, i.e., $\tau \propto 1/\sqrt{\sigma_0}$ (e.g., from Bückner et al., 2018), which would imply a decrease of τ with ζ . However, the concentration polarization produced by the unequal anion and cation fluxes through the static diffuse layer seem to delay charging and relaxation of the induced diffuse layers related to the observed increase of τ with ζ .

The relative insensitivity of the relaxation time of the volume-diffusion process (the one produced by the reaction currents) to changes in ζ is in accordance to the fact that the corresponding volume-diffusion layer is practically unaffected by the presence of the static diffuse layer (see, e.g., Figure 4). Obviously, this proc-

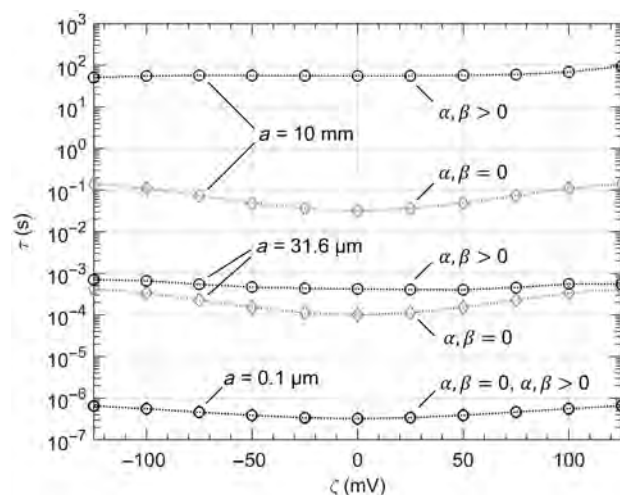


Figure 10. Variation of relaxation times τ with the ζ -potential for three different particle radii $a = 10^{-7}, 3.16 \times 10^{-5},$ and 10^{-2} m with (the black) and without (the gray) reaction currents. All of the other parameter values are equal to those given in Table 1.

ess does not respond to changes in the (surface) conductivity, which is plausible for a purely diffusion-controlled mechanism.

DISCUSSION

Perfectly conducting versus nonconducting particles

Treatments of the low-frequency polarization response of charged (nonconducting) dielectric particles can be roughly classified into two groups; models of the first group stress the polarization response of the Stern or Helmholtz layer of counterions tightly bound to the particle surface (e.g., Schwarz, 1962; Schurr, 1964; Leroy et al., 2008). Under the influence of an external electric field, these charges rearrange along the surface but cannot leave (or enter) the Stern layer. The maximum polarization is assumed to be controlled by an equilibrium between tangential electromigration and diffusion currents resulting in the typical relaxation time scale of the Stern layer $\tau = a^2/(2D)$. The influence of the outer diffuse layer is only considered in terms of the real-valued conductivity increment $2K/a$ proposed by O'Konski (1960), which does not actively contribute to the polarization. Models of the second group, in contrast, only study the polarization response of the diffuse layer. Although most treatments neglect the polarization response of the Stern layer (e.g., DeLacey and White, 1981; Chew and Sen, 1982a), there are also approaches attempting to incorporate its effect (e.g., Shilov et al., 2001). The polarization of the static diffuse layer arises due to the unequal cation and anion transport by electromigration currents along the surface and usually also relaxes on a time scale $\tau \propto a^2/D$. In the absence of a fixed diffuse surface charge and thus for a vanishing ζ -potential, the models of both groups do not predict any polarization response, except for the Maxwell-Wagner polarization at high frequencies (i.e., $\approx 1/\tau_{ei}$).

In comparison to these polarization mechanisms around nonconducting particles, the case of perfectly conducting particles is fundamentally different. Here, the main mechanism responsible for the large low-frequency dispersion of the effective conductivity of the suspension is the dynamic charging of the field-induced (and not the static) diffuse layer, which is a direct consequence of the high conductivity contrast between particle and electrolyte. In contrast to both mechanisms observed for nonconducting particles, the pure polarization of the field-induced diffuse layer relaxes on a time scale $\tau = \lambda_D a/(2D)$. Only if reaction currents, which have not been addressed in the theories for nonconducting particles, are taken into account, the coupling with the resulting volume-diffusion mechanism yields a relaxation time $\tau \propto a^2$.

The present numerical study indicates that the effect of the ζ -potential and static diffuse layer should be considered of secondary importance for the effective conductivity of suspensions of perfectly conducting particles — at least for typical parameter values. Interestingly, the corresponding surface conductivity decreases the polarization magnitude, i.e., σ''_{\max} , and thus, its effect is exactly opposite to the one it has in the case of nonconducting particles.

In the case of nonconducting particles, the Stern layer usually plays an even more important role for the observed polarization phenomena (e.g., Schwarz, 1962; Schurr, 1964; Leroy et al., 2008) than the diffuse layer. However, our model does not include any polarization effect due to the Stern layer. We justify this simplification based on the assumed infinite conductivity of the particle, which results in a vanishing tangential electric field along the particle surface (and at small distances from the surface). This is due to

an immediate redistribution of charges, which cancels out any electric field within the particle volume and along its surface. Thus, tangential electromigration currents within a thin Stern layer, which cause a large polarization around nonconducting particles, should either be zero or very small.

In summary, the role of surface conductivity around perfectly conducting particles is completely different to the one it plays for the polarization of nonconducting particles. Therefore, the polarization of the static diffuse layer around perfectly conducting particles should by no means be confused with the main polarization mechanisms due to the dynamic charging of the diffuse layer and the volume-diffusion process driven by reaction currents.

Potential for nanoparticle characterization

To date, only a few studies have investigated the particular IP response of metallic nanoparticles (Joyce et al., 2012; Shi et al., 2015; Abdel Aal et al., 2017), but the obtained results encourage further research to advance this exciting new application. The strong response of metallic particles and the well-known fact that the polarization magnitude scales with the volumetric metal content (e.g., Wong, 1979; Misra et al., 2017) make it a suitable method to monitor nanoparticle injection experiments (Flores Orozco et al., 2015). Besides the mere localization and quantification, some researchers have even suggested that IP measurements could aid in the characterization of the in situ chemical condition and reactivity of the particle surfaces (e.g., Shi et al., 2015). The strong correlation between the ζ -potential (i.e., the fixed diffuse surface charge) on the surface reactivity (e.g., Sund et al., 2011) and on the IP response of nonconducting particles (e.g., Leroy et al., 2008) justified this hope.

Generally speaking, our modeling results also indicate that the sheer size of nanoparticles favors such applications of the IP method: From Figure 8, we see that the smaller the particle is, the more sensitive σ_{DC} and σ''_{\max} become with respect to variations of the ζ -potential. For the 0.1 μm particle, the maximum relative changes of both spectral parameters are approximately 15% over the studied range of ζ -potentials from 0 to -125 mV. These variations are small but detectable. With increasing particle size, the sensitivity of both parameters to changes in ζ decreases rapidly. Already, for microscale particles, here 31.6 μm , they are expected to be almost insensitive — except for σ''_{\max} in the case of nonzero reaction currents.

The situation is very different with regard to the sensitivity of the relaxation time to variations of the ζ -potential. Figures 9 and 10 show that here, in contrast to σ_{DC} and σ''_{\max} , a significant increase of the relaxation time can only be observed for microparticles or larger, i.e., $a > 1$ μm , and in the absence of reaction currents. Under these conditions, the relaxation time of the pure diffuse-layer polarization increases by a factor of five from 0 to ± 125 mV, with the highest sensitivity in the range between ± 25 and ± 75 mV. As the same two figures show, the relaxation time of the volume-diffusion process, which dominates for larger particles sizes and nonzero reaction currents, is expected to be practically insensitive to changes of the ζ -potential. However, in this regime, the relaxation time is highly sensitive to the reaction current through the particle surface, which in turn is a direct measure for the reactivity of the particle surface. This effect can be of interest to monitor particle-injection experiments, in which particle-surface properties change over time (e.g., engineered particle coatings, Flores Orozco et al., 2015), or

conditions with varying availability of active ionic species, e.g., due to biogeochemical processes (e.g., Flores Orozco et al., 2011).

Despite of the theoretical potential of the IP method to characterize surface properties such as ζ -potential and reactivity, the high characteristic frequencies of the relaxation processes around nanoparticles impose a practical limit: Typical laboratory setups only permit determining the complex conductivity response of material samples up to frequencies of 1–40 kHz, and can therefore only resolve the increasing flank of the relaxation peak (e.g., Abdel Aal et al., 2017). In this case, the determination of the characteristic frequency might become too imprecise to detect the small variations of τ with ζ . Other researchers, in contrast, were able to observe the relaxation peak of submicron silver and zero-valent iron particles at sufficiently low frequencies (Joyce et al., 2012). In field experiments with array lengths in the meter to dekameter range, electromagnetic induction usually masks the IP response at frequencies >10–100 Hz (e.g., Flores Orozco et al., 2011, 2012), which further reduces the detectability of nanoparticles in larger scale applications.

Limitations of the model

In part 1 of this series (Bücker et al., 2018), we discussed the limitations inherent to the model by Wong (1979) — including our own extensions. Obviously, the numerical model presented in this second part suffers from the same set of shortcomings inherited from the base model. To mention some of the remaining issues, (1) it ignores the fact that most metal-bearing minerals are rather semiconductors than metallic conductors, (2) it does not consider dynamic charging of the Stern layer (e.g., Merriam, 2007), (3) it neglects particle-particle interactions between adjacent grains, which is inherent to the mixing rule used for the up-scaling, (4) it does not treat the effects of nonspherical geometries or surface roughness, and (5) having even more model parameters, its application to real data is expected to be even more tedious (e.g., Placencia-Gómez and Slater, 2014).

In the light of recently developed semiconductor-polarization models (e.g., Revil et al., 2015b; Misra et al., 2016a, 2016b; Abdulsamad et al., 2017), it is worth reconsidering the assumption of an infinite conductivity of the metallic particle. In his analysis, Wong (1979) argues that if “the conductivity [...] of the mineral is a hundred or a thousand times the conductivity [...] of the surrounding medium” (i.e., the electrolyte), the particle could be considered a perfect conductor. However, this argumentation only assesses the (DC) conductivity of the involved materials, which is not sufficient in the context of a frequency-dependent model.

The situation described by the zero-potential boundary condition 15 requires the charges on the particle to relax much faster than the variation of the external excitation. In metallic conductors, the charge relaxation time can be roughly approximated by two times the collision time of the free electrons (e.g., Ashby, 1975). At room temperature, typical collision times in elemental metals are in the order of 10^{-15} – 10^{-14} s, such that the characteristic frequency of charge relaxation is well beyond the relevant frequency range and the assumption of a perfect conductor remains justified. The analysis by Revil et al. (2015a, 2015b) suggests that the situation changes fundamentally if semiconducting minerals, such as pyrite or magnetite, are considered. Here, the diffusion-controlled relaxation of the charge carriers inside the semiconducting particle not only leads to a much slower response of the solid particle but it seems to be the

main polarization mechanism in the typical IP frequency range. With this in mind, the application of the present polarization model (as well as any model that rests on the assumption of a perfectly conductive solid phase) should clearly be limited to the case of metallic conductors.

In addition to the known limitations (1–5), the assumption of a constant ζ -potential used in this study might also be unrealistic. In particular, the large field-induced variations of the ion concentrations close to the particle surface raise doubts whether the constant- ζ -potential boundary condition, i.e., equation 15, can be adequate. This limitation is also inherited from the Wong model, which — from our new perspective — describes the special case of $\zeta = 0$, i.e., at the point of zero charge of the metal surface. Determining the ζ -potential self-consistently from a speciation model for the particle-electrolyte interface might result in a more realistic boundary condition, which can account for the complex mutual dependency between the diffuse layer and the surface (including the Stern layer).

CONCLUSION

We have developed a numerical approach to study the effect of a static diffuse layer on the electrochemical polarization of a perfectly conducting particle. In comparison to the response of a particle without such a static diffuse layer, the observed changes are relatively small, which implies that the effect of surface conductivity is of secondary importance for the polarization of perfectly conducting or metallic particles. In particular around relatively large particles (compared with the Debye length), the diffuse surface charge on the particle is practically not expected to influence the macroscopic response at all.

For nano- and small microscale particles, however, the three important spectral parameters — the low-frequency limit of the effective conductivity σ_{DC} , the polarization magnitude σ''_{max} , and the relaxation time τ — do reveal measurable responses to variations of the ζ -potential (or the constant diffuse surface charge). Therefore, our findings are of particular interest for the interpretation of IP experiments designed to find a link between the complex conductivity response and the chemical surface conditions of metallic nano- and microscale particles.

The present study advances the basic understanding of the polarization mechanism around perfectly conducting particles, quantifies the previously completely disregarded effect of the diffuse surface charge on the polarization response, and opens the possibility for an application of the IP method for the improved characterization of the chemical state of metallic nano- and microscale particles.

ACKNOWLEDGMENTS

We gratefully acknowledge A. Revil and two anonymous reviewers for their insightful comments that helped to substantially improve the manuscript. This study was supported by the research project GEOCON, Advancing geological, geophysical and contaminant monitoring technologies for contaminated site investigation (contract 1305-00004B). The funding for GEOCON is provided by The Danish Council for Strategic Research under the Programme Commission on Sustainable Energy and Environment. M. Bücker gratefully acknowledges the Austrian Federal Ministry of Science, Research and Economy (project: Development of geophysical exploration methods for the characterization of mine-tailings towards

exploitation) and the German Academic Exchange Service (DAAD) for scholarships received for his participation in this study. Additional funding was provided by the Austrian Academy of Science (ÖAW) through the project ATMOperm: Atmosphere — permafrost relationship in the Austrian Alps — atmospheric extreme events and their relevance for the mean state of the active layer.

DATA AND MATERIALS AVAILABILITY

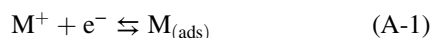
Data associated with this research are available and can be obtained by contacting the corresponding author.

APPENDIX A

ADAPTATION OF THE EXCHANGE CURRENT

Our description of the exchange current strictly adheres to the one proposed by Wong (1979). However, although Wong can assume the bulk concentration of the active cations n_3^0 at the particle surface, according to equation 7, the equilibrium concentration at a charged surface is given by $n_3^{(0)}(\zeta) = n_3^\infty \exp[-e\zeta/(kT)]$, which requires some adaptations of the known expressions.

The fundamental metal deposition-dissolution reaction:



remains unchanged. Here, M^+ denotes the metal cation in solution, e^- is an electron, and $M_{(\text{ads})}$ is a metal atom adsorbed to the particle surface. The net exchange-current density due to the above reaction is written as equation 23 in Wong, (1979)

$$i = k_- [M_{(\text{ads})}] e \exp[e\eta/(2kT)] - k_+ [M^+] e \exp[-e\eta/(2kT)], \quad (\text{A-2})$$

where we have already assumed a symmetry factor of 1/2. The parameters k_+ and k_- are the rate constants, $[M_{(\text{ads})}]$ and $[M^+]$ are the concentrations of active cations and adsorbed atoms (in ions/m³), and η is the current-producing overpotential.

Under undisturbed conditions, i.e., without any external excitation, the overpotential η is zero by definition and the modified concentration of active cations at the particle surface is given by $n_3^{(0)}(\zeta)$, which includes the cation excess in the static diffuse layer caused by the nonvanishing surface potential ζ . Wong's expression for the equilibrium exchange current, his equation 24, therefore, becomes

$$i_0 = k_- [M_{(\text{ads})}] e = k_+ n_3^{(0)}(\zeta) N_A e, \quad (\text{A-3})$$

where N_A is Avogadro's constant (6.0221×10^{23} mol⁻¹).

As Wong (1979) discusses in more detail, for small overpotentials $\eta \ll e/(2kT)$, the nonequilibrium exchange current due to a nonzero overpotential can be linearized resulting in

$$i \approx i_0 e\eta/(kT) \text{ or } i \approx i_0 e/(kT) \mathbf{E} \cdot \mathbf{n}l, \quad (\text{A-4})$$

where $\mathbf{E} \cdot \mathbf{n}$ is the component of the electrical field normal to the particle surface (\mathbf{n} is the unit normal vector pointing into the electrolyte) and l is the characteristic distance of closest approach by the active cations to the surface.

Even in the absence of a current-producing overpotential, a perturbation $\delta n_3(\zeta)$ of the active cation concentration from the equilibrium value $n_3^{(0)}(\zeta)$ can generate the net exchange current

$$\begin{aligned} i &= k_- [M_{(\text{ads})}] e - k_+ [n_3^{(0)}(\zeta) + \delta n_3(\zeta)] N_A e \\ &= i_0 - i_0 - k_+ \delta n_3(\zeta) N_A e \\ &= -k_+ \delta n_3(\zeta) N_A e. \end{aligned} \quad (\text{A-5})$$

Note that the net current density due to a positive $\delta n_3(\zeta)$ is negative (toward the center of the particle).

The total exchange current density is then obtained as the sum of the one caused by a nonzero overpotential and a perturbation of the active cation concentration from the equilibrium and writes

$$i \approx \alpha(\zeta) n_3^{(0)}(\zeta) N_A e \mathbf{E} \cdot \mathbf{n} - \beta(\zeta) \delta n_3(\zeta) N_A e, \quad (\text{A-6})$$

where $\alpha(\zeta) = i_0 l / [n_3^{(0)}(\zeta) N_A kT]$ and $\beta = k_+ = i_0 / [n_3^{(0)}(\zeta) N_A e]$ are the functions of the ζ -potential. Wong (1979) estimates his values of $\alpha(0) = i_0 l / (n_3^\infty N_A kT)$ and $\beta(0) = i_0 / (e n_3^\infty N_A)$ from experimentally determined values of the equilibrium reaction current density i_0 . If we use the same experimental values as starting point and assume that the particles used also had a nonvanishing static surface potential, we find $\alpha(\zeta) = \alpha(0) \exp[e\zeta/(kT)]$ and $\beta(\zeta) = \beta(0) \exp[e\zeta/(kT)]$ (by comparison with the expressions by Wong). Note that equation A-6 defines an electrical current density in A/m², i.e., the corresponding current densities in mol/(m²s) as needed for the corresponding boundary condition, equation 17, can be obtained by dividing i by $F = N_A e$.

APPENDIX B

IMPLEMENTATION INTO THE COMSOL COEFFICIENT FORM PDE

The COMSOL PDE interface in coefficient form allows the specification of PDEs and systems of PDEs of the general type

$$e_a \frac{\partial^2 u}{\partial t^2} + d_a \frac{\partial u}{\partial t} + \nabla \cdot (-c \nabla u - \alpha u + \gamma) + \beta \cdot \nabla u + a u = f \quad (\text{B-1})$$

with general boundary conditions

$$-\mathbf{n} \cdot (-c \nabla u - \alpha u + \gamma) = g - q u \quad (\text{B-2})$$

and

$$u = s, \quad (\text{B-3})$$

where u denotes the dependent variable and \mathbf{n} is the inward-pointing unit normal vector (i.e., into the electrolyte) on the respective boundary. Note that actually COMSOL defines the normal vector reversely (outward-pointing); consequently, it appears with reversed sign in equation B-2. The coefficients e_a , d_a , c , α , γ , β , a , f , q , g , and s are used to describe the specific problem to be modeled. Equation B-2 is a generalized Neumann boundary condition, and equation B-3 is a Dirichlet boundary condition.

Static solution

With these definitions, the numerical implementation of the static problem from equations 7 and 8 with boundary conditions 9 and 10 is straightforward. If we define the dependent variable $u_1 = U^{(0)}(\mathbf{r})$, the PDE coefficients must be

$$c = 1 \quad (\text{B-4}) \quad \text{and}$$

and

$$f = \frac{F}{\epsilon_0 \epsilon_r} \sum_{j=1}^3 z_j n_j^\infty \exp\left(-\frac{z_j e}{kT} u\right). \quad (\text{B-5})$$

Note that throughout this step-by-step instruction we will use the convention that all coefficients that are not mentioned specifically are assumed to be zero. Assuming monovalent ions $|z_j| = 1$ and making use of the electroneutrality condition in the bulk electrolyte $n_1^\infty = n_2^\infty + n_3^\infty$, the coefficient f can be simplified to

$$f = -\frac{2n_1^\infty F}{\epsilon_0 \epsilon_r} \sinh\left(\frac{e}{kT} u\right). \quad (\text{B-6})$$

On the top boundary (at $y = L$), on the left ($x = -L$), and on the right ($x = L$) boundary, we define

$$s = 0, \quad (\text{B-7})$$

while for the metal surface (at $x^2 + y^2 = a^2$ for the spherical particle), we set

$$s = \zeta \quad (\text{B-8})$$

to implement the Dirichlet boundary conditions 10 and 9, respectively. Defining the axis $y = 0$ as the symmetry axis (selecting rotational symmetry in the model setup), no specific boundary conditions must be defined on this boundary.

Frequency-dependent solution

For the solution of the frequency-dependent case, we need to implement the system of the four coupled PDEs described in equations 11 and 12. In the system case, the dependent variable u in equation B-1 becomes a column vector of length four. We define

$$\mathbf{u}_2 = \begin{bmatrix} u_{21} \\ u_{22} \\ u_{23} \\ u_{24} \end{bmatrix} = \begin{bmatrix} \delta n_1(\mathbf{r}, \omega) \\ \delta n_2(\mathbf{r}, \omega) \\ \delta n_3(\mathbf{r}, \omega) \\ \delta U(\mathbf{r}, \omega) \end{bmatrix}. \quad (\text{B-9})$$

Assuming isotropy of all of its elements, the coefficient c becomes a 4-by-4 coefficient matrix. In our case, \underline{c} is written as

$$\underline{c} = \begin{bmatrix} D & 0 & 0 & -\mu_1 n_1^\infty \exp\left(\frac{e}{kT} u_1\right) \\ 0 & D & 0 & \mu_2 n_2^\infty \exp\left(-\frac{e}{kT} u_1\right) \\ 0 & 0 & D & \mu_3 n_3^\infty \exp\left(-\frac{e}{kT} u_1\right) \\ 0 & 0 & 0 & 1 \end{bmatrix}, \quad (\text{B-10})$$

where u_1 denotes the scalar static solution (for the electrical potential only). The coefficient matrices

$$\underline{\alpha} = \begin{bmatrix} -\mu_1 \nabla u_1 & 0 & 0 & 0 \\ 0 & \mu_2 \nabla u_1 & 0 & 0 \\ 0 & 0 & \mu_3 \nabla u_1 & 0 \\ 0 & 0 & 0 & 0 \end{bmatrix} \quad (\text{B-11})$$

$$\underline{a} = \begin{bmatrix} i\omega & 0 & 0 & 0 \\ 0 & i\omega & 0 & 0 \\ 0 & 0 & i\omega & 0 \\ \frac{F}{\epsilon_0 \epsilon_r} & -\frac{F}{\epsilon_0 \epsilon_r} & -\frac{F}{\epsilon_0 \epsilon_r} & 0 \end{bmatrix} \quad (\text{B-12})$$

complete the description of our system of PDEs in coefficient form. Note that each element $\alpha_{i,j} = [\alpha_{i,j,1}, \alpha_{i,j,2}]^T$ is a two-element column vector in which the third indices correspond to the spatial coordinates x and y .

As mentioned in the main text, because of the cylindrical symmetry, the solution of the system of PDEs can be carried out on a 2D modeling domain with coordinates x and y (see Figure 1). Thus, the position vector and the gradient operator become

$$\mathbf{r} = \begin{bmatrix} x \\ y \end{bmatrix} \quad \text{and} \quad \nabla = \begin{bmatrix} \partial_x \\ \partial_y \end{bmatrix}, \quad (\text{B-13})$$

respectively. Although we are actually interested in solving the system of PDEs in cylindrical coordinates, we will first proceed with the formulation of the system in the two Cartesian coordinates x and y and further below we will provide a simple conversion to cylindrical coordinates.

The problem description for the numerical modeling is completed by the following boundary conditions. Far from the particle surface (i.e., for $r \rightarrow \infty$), we requested the perturbation potential to approximate the exciting potential $-\mathbf{E} \cdot \mathbf{r}$ and the perturbation ion concentrations to vanish. Therefore, on the *left and right boundaries*, we define the Dirichlet boundary conditions by setting

$$\mathbf{s} = \begin{bmatrix} 0 \\ 0 \\ 0 \\ E_0 L \end{bmatrix} \quad \text{and} \quad \mathbf{s} = \begin{bmatrix} 0 \\ 0 \\ 0 \\ -E_0 L \end{bmatrix}, \quad (\text{B-14})$$

respectively.

On the *top boundary*, we implement a zero-flux boundary condition for all four dependent variables. This results in vanishing normal fluxes for all three ionic species and a vanishing normal electrical field. Again, due to the rotational symmetry, no boundary conditions must be defined on the symmetry axis (i.e., along $y = 0$).

On the *particle surface*, we implement mixed boundary conditions consisting of one Dirichlet condition for the electric potential, equation 15, and generalized Neumann conditions for the three ion fluxes, equations 16 and 17. To define the boundary conditions on the ion fluxes, we set

$$\underline{q} = \begin{bmatrix} 0 & 0 & 0 & 0 \\ 0 & 0 & 0 & 0 \\ 0 & 0 & \beta(\zeta) & 0 \\ 0 & 0 & 0 & 0 \end{bmatrix} \quad (\text{B-15})$$

and

$$\mathbf{g} = \begin{bmatrix} 0 \\ 0 \\ \alpha(\zeta)n_3^\infty \exp\left(-\frac{e}{kT}u_1\right)\mathbf{n} \cdot \nabla u_{24} \\ 0 \end{bmatrix}, \quad (\text{B-16})$$

where $\mathbf{n} \cdot \nabla u_{24} = n_x \partial_x u_{24} + n_y \partial_y u_{24}$. A Dirichlet boundary condition component is specified for the fourth component by setting

$$s = 0, \quad (\text{B-17})$$

which overwrites the above no-flux boundary condition (only for the perturbation potential). The Dirichlet boundary condition for the first three components is deactivated, and the generalized Neumann boundary conditions described by \underline{q} and \mathbf{g} remain valid for the first three components.

Conversion to cylindrical coordinates

As mentioned above, the software expects the equations to be defined in a Cartesian system with two space dimensions. That means that if we assume isotropic media (i.e., \underline{c} is a 4-by-4 matrix), the i th equation of our system is given by

$$\sum_j [-(\partial_x c_{i,j} \partial_x + \partial_y c_{i,j} \partial_y) u_j - (\partial_x \alpha_{i,j,1} + \partial_y \alpha_{i,j,2}) u_j + a_{i,j} u_j] = 0, \quad (\text{B-18})$$

where we have already dropped all vanishing coefficients (i.e., e_a , d_a , and γ). However, we actually seek to solve a system in cylindrical coordinates, the i th component of which should write

$$\sum_j \left[-\left(\frac{1}{r} \partial_r r c_{i,j} \partial_r + \partial_z c_{i,j} \partial_z \right) u_j - \left(\frac{1}{r} \partial_r r \alpha_{i,j,1} + \partial_z \alpha_{i,j,2} \right) u_j + a_{i,j} u_j \right] = 0 \quad (\text{B-19})$$

instead. If we multiply the entire system by r , we get

$$\sum_j [-(\partial_r r c_{i,j,1,1} \partial_r + \partial_z r c_{i,j,2,2} \partial_z) u_j - (\partial_r r \alpha_{i,j,1} + \partial_z r \alpha_{i,j,2}) u_j + r a_{i,j} u_j] = 0, \quad (\text{B-20})$$

which can be converted to the form supported by software. Defining r as y and z as x yields the modified system:

$$\nabla \cdot (-y \underline{c} \nabla \mathbf{u} - y \underline{a} \mathbf{u}) + y \underline{a} \mathbf{u} = 0. \quad (\text{B-21})$$

Thus, it is sufficient to multiply the three coefficient matrices \underline{c} , \underline{a} , and \underline{a} by y to transform the problem to cylindrical coordinates. Note that the boundary coefficients \underline{q} and \mathbf{g} have to be multiplied by y , too, whereas \mathbf{r} remains unchanged.

REFERENCES

Abdel Aal, G. Z., E. A. Atekwana, and D. D. Werkema, 2017, Complex conductivity response to silver nanoparticles in partially saturated sand columns: *Journal of Applied Geophysics*, **137**, 73–81, doi: [10.1016/j.jappgeo.2016.12.013](https://doi.org/10.1016/j.jappgeo.2016.12.013).
 Abdulsamad, F., N. Florsch, and C. Camerlynck, 2017, Spectral induced polarization in a sandy medium containing semiconductor materials:

Experimental results and numerical modelling of the polarization mechanism: *Near Surface Geophysics*, **15**, 669–683.
 Ashby, N., 1975, Relaxation of charge imbalances in conductors: *American Journal of Physics*, **43**, 553–555, doi: [10.1119/1.9787](https://doi.org/10.1119/1.9787).
 Atkins, P., and J. De Paula, 2013, *Elements of physical chemistry*: Oxford University Press.
 Bazant, M. Z., K. Thornton, and A. Ajdari, 2004, Diffuse-charge dynamics in electrochemical systems: *Physical Review E*, **70**, 021506, doi: [10.1103/PhysRevE.70.021506](https://doi.org/10.1103/PhysRevE.70.021506).
 Boulangé-Petermann, L., A. Doren, B. Baroux, and M.-N. Bellon-Fontaine, 1995, Zeta potential measurements on passive metals: *Journal of Colloid and Interface Science*, **171**, 179–186, doi: [10.1006/jcis.1995.1165](https://doi.org/10.1006/jcis.1995.1165).
 Bücker, M., A. Flores Orozco, and A. Kemna, 2018, Electrochemical polarization around metallic particles — Part 1: The role of diffuse-layer and volume-diffusion relaxation: *Geophysics*, **83**, no. 4, E203–E217, doi: [10.1190/geo2017-0401.1](https://doi.org/10.1190/geo2017-0401.1).
 Chew, W., and P. Sen, 1982a, Dielectric enhancement due to electrochemical double layer: Thin double layer approximation: *The Journal of Chemical Physics*, **77**, 4683–4693, doi: [10.1063/1.444369](https://doi.org/10.1063/1.444369).
 Chew, W., and P. Sen, 1982b, Potential of a sphere in an ionic solution in thin double layer approximations: *The Journal of Chemical Physics*, **77**, 2042–2044, doi: [10.1063/1.444060](https://doi.org/10.1063/1.444060).
 DeLacey, E. H., and L. R. White, 1981, Dielectric response and conductivity of dilute suspensions of colloidal particles: *Journal of the Chemical Society, Faraday Transactions 2: Molecular and Chemical Physics*, **77**, 2007–2039, doi: [10.1039/f29817702007](https://doi.org/10.1039/f29817702007).
 Flores Orozco, A., A. Kemna, C. Oberdörster, L. Zschornack, C. Leven, P. Dietrich, and H. Weiss, 2012, Delineation of subsurface hydrocarbon contamination at a former hydrogenation plant using spectral induced polarization imaging: *Journal of Contaminant Hydrology*, **136**, 131–144, doi: [10.1016/j.jconhyd.2012.06.001](https://doi.org/10.1016/j.jconhyd.2012.06.001).
 Flores Orozco, A., M. Velimirovic, T. Tosco, A. Kemna, H. Sapion, N. Klaas, R. Sethi, and L. Bastiaens, 2015, Monitoring the injection of microscale zerovalent iron particles for groundwater remediation by means of complex electrical conductivity imaging: *Environmental Science and Technology*, **49**, 5593–5600, doi: [10.1021/acs.est.5b00208](https://doi.org/10.1021/acs.est.5b00208).
 Flores Orozco, A., K. H. Williams, P. E. Long, S. S. Hubbard, and A. Kemna, 2011, Using complex resistivity imaging to infer biogeochemical processes associated with bioremediation of an uranium-contaminated aquifer: *Journal of Geophysical Research: Biogeosciences*, **116**, G03001, doi: [10.1029/2010JG001591](https://doi.org/10.1029/2010JG001591).
 Gurin, G., K. Titov, Y. Ilyin, and A. Tarasov, 2015, Induced polarization of disseminated electronically conductive minerals: A semi-empirical model: *Geophysical Journal International*, **200**, 1555–1565, doi: [10.1093/gji/ggu490](https://doi.org/10.1093/gji/ggu490).
 Joyce, R. A., D. R. Glaser, D. D. Werkema, and E. A. Atekwana, 2012, Spectral induced polarization response to nanoparticles in a saturated sand matrix: *Journal of Applied Geophysics*, **77**, 63–71, doi: [10.1016/j.jappgeo.2011.11.009](https://doi.org/10.1016/j.jappgeo.2011.11.009).
 Leroy, P., A. Revil, A. Kemna, P. Cosenza, and A. Ghorbani, 2008, Complex conductivity of water-saturated packs of glass beads: *Journal of Colloid and Interface Science*, **321**, 103–117, doi: [10.1016/j.jcis.2007.12.031](https://doi.org/10.1016/j.jcis.2007.12.031).
 Maxwell, J. C., 1891, *A treatise on electricity and magnetism*: Clarendon Press.
 Merriam, J., 2007, Induced polarization and surface electrochemistry: *Geophysics*, **72**, no. 4, F157–F166, doi: [10.1190/1.2732554](https://doi.org/10.1190/1.2732554).
 Misra, S., C. Torres-Verdín, D. Homan, and J. Rasmus, 2017, Dispersive and directional electrical conductivity and dielectric permittivity of conductive-mineral-bearing samples derived from multifrequency tensor electromagnetic induction measurements: *Geophysics*, **82**, no. 4, D211–D223, doi: [10.1190/geo2016-0336.1](https://doi.org/10.1190/geo2016-0336.1).
 Misra, S., C. Torres-Verdín, A. Revil, J. Rasmus, and D. Homan, 2016a, Interfacial polarization of disseminated conductive minerals in absence of redox-active species — Part 1: Mechanistic model and validation: *Geophysics*, **81**, no. 2, E139–E157, doi: [10.1190/geo2015-0346.1](https://doi.org/10.1190/geo2015-0346.1).
 Misra, S., C. Torres-Verdín, A. Revil, J. Rasmus, and D. Homan, 2016b, Interfacial polarization of disseminated conductive minerals in absence of redox-active species — Part 2: Effective electrical conductivity and dielectric permittivity: *Geophysics*, **81**, no. 2, E159–E176, doi: [10.1190/geo2015-0400.1](https://doi.org/10.1190/geo2015-0400.1).
 Nernst, W., 1888, Zur Kinetik der in Lösung befindlichen Körper: *Zeitschrift für physikalische Chemie*, **2**, 613–637.
 Nernst, W., 1889, Die elektromotorische Wirksamkeit der Ionen: *Zeitschrift für physikalische Chemie*, **4**, 129–181.
 O’Konski, C. T., 1960, Electric properties of macromolecules. V. Theory of ionic polarization in polyelectrolytes: *The Journal of Physical Chemistry*, **64**, 605–619, doi: [10.1021/j100834a023](https://doi.org/10.1021/j100834a023).
 Placencia-Gómez, E., and L. D. Slater, 2014, Electrochemical spectral induced polarization modeling of artificial sulfide-sand mixtures: *Geophysics*, **79**, no. 6, EN91–EN106, doi: [10.1190/geo2014-0034.1](https://doi.org/10.1190/geo2014-0034.1).
 Placencia-Gómez, E., and L. D. Slater, 2015, On the pore water chemistry effect on spectral induced polarization measurements in the presence of

- pyrite: *Journal of Applied Geophysics*, **135**, 474–485, doi: [10.1016/j.jappgeo.2015.11.001](https://doi.org/10.1016/j.jappgeo.2015.11.001).
- Planck, M., 1890, Ueber die Erregung von Electricität und Wärme in Electrolyten: *Annalen der Physik*, **275**, 161–186, doi: [10.1002/andp.18902750202](https://doi.org/10.1002/andp.18902750202).
- Revil, A., G. Z. Abdel Aal, E. A. Atekwana, D. Mao, and N. Florsch, 2015a, Induced polarization response of porous media with metallic particles — Part 2: Comparison with a broad database of experimental data: *Geophysics*, **80**, no. 5, D539–D552, doi: [10.1190/geo2014-0578.1](https://doi.org/10.1190/geo2014-0578.1).
- Revil, A., N. Florsch, and D. Mao, 2015b, Induced polarization response of porous media with metallic particles — Part 1: A theory for disseminated semiconductors: *Geophysics*, **80**, no. 5, D525–D538, doi: [10.1190/geo2014-0577.1](https://doi.org/10.1190/geo2014-0577.1).
- Reyes-Bozo, L., M. Escudey, E. Vyhmeister, P. Higuera, A. Godoy-Faúndez, J. L. Salazar, H. Valdés-González, G. Wolf-Sepúlveda, and R. Herrera-Urbina, 2015, Adsorption of biosolids and their main components on chalcopyrite, molybdenite and pyrite: Zeta potential and FTIR spectroscopy studies: *Minerals Engineering*, **78**, 128–135, doi: [10.1016/j.mineng.2015.04.021](https://doi.org/10.1016/j.mineng.2015.04.021).
- Schurr, J., 1964, On the theory of the dielectric dispersion of spherical colloidal particles in electrolyte solution: *The Journal of Physical Chemistry*, **68**, 2407–2413, doi: [10.1021/j100791a004](https://doi.org/10.1021/j100791a004).
- Schwarz, G., 1962, A theory of the low-frequency dielectric dispersion of colloidal particles in electrolyte solution: *The Journal of Physical Chemistry*, **66**, 2636–2642, doi: [10.1021/j100818a067](https://doi.org/10.1021/j100818a067).
- Shi, Z., D. Fan, R. L. Johnson, P. G. Tratnyek, J. T. Nurmi, Y. Wu, and K. H. Williams, 2015, Methods for characterizing the fate and effects of nano zerovalent iron during groundwater remediation: *Journal of Contaminant Hydrology*, **181**, 17–35, doi: [10.1016/j.jconhyd.2015.03.004](https://doi.org/10.1016/j.jconhyd.2015.03.004).
- Shilov, V., A. Delgado, F. Gonzalez-Caballero, and C. Grosse, 2001, Thin double layer theory of the wide-frequency range dielectric dispersion of suspensions of non-conducting spherical particles including surface conductivity of the stagnant layer: *Colloids and Surfaces A: Physicochemical and Engineering Aspects*, **192**, 253–265, doi: [10.1016/S0927-7757\(01\)00729-4](https://doi.org/10.1016/S0927-7757(01)00729-4).
- Sund, J., H. Alenius, M. Vippola, K. Savolainen, and A. Puustinen, 2011, Proteomic characterization of engineered nanomaterial-protein interactions in relation to surface reactivity: *ACS Nano*, **5**, 4300–4309, doi: [10.1021/nn101492k](https://doi.org/10.1021/nn101492k).
- Wong, J., 1979, An electrochemical model of the induced-polarization phenomenon in disseminated sulfide ores: *Geophysics*, **44**, 1245–1265, doi: [10.1190/1.1441005](https://doi.org/10.1190/1.1441005).
- Wong, J., and D. Strangway, 1981, Induced polarization in disseminated sulfide ores containing elongated mineralization: *Geophysics*, **46**, 1258–1268, doi: [10.1190/1.1441264](https://doi.org/10.1190/1.1441264).

JGR Solid Earth

RESEARCH ARTICLE

10.1029/2019JB017679

On the Role of Stern- and Diffuse-Layer Polarization Mechanisms in Porous Media

Matthias Bucker^{1,2,3} , Adrián Flores Orozco² , Sabine Undorf^{3,4} , and Andreas Kemna³ 

¹Institute for Geophysics and extraterrestrial Physics, TU Braunschweig, Braunschweig, Germany, ²Department of Geodesy and Geoinformation, Research Group Geophysics, TU Wien, Vienna, Austria, ³Institute of Geosciences, Geophysics Section, Rheinische Friedrich-Wilhelms-Universität Bonn, Bonn, Germany, ⁴School of GeoSciences, University of Edinburgh, Edinburgh, UK

Key Points:

- We investigate Maxwell-Wagner, Stern-layer and diffuse-layer, and membrane polarization in porous media in a generalized mathematical framework
- Numerical and analytical solutions are mutually verified, and existing analytical models of the four mechanisms are improved
- Low-frequency Stern-layer polarization is stronger than diffuse-layer polarization if the electrical double layer is discontinuous, only

Correspondence to:

M. Bucker,
m.buecker@tu-bs.de

Citation:

Bücker, M., Flores Orozco, A., Undorf, S., & Kemna, A. (2019). On the role of Stern- and diffuse-layer polarization mechanisms in porous media. *Journal of Geophysical Research: Solid Earth*, 124. <https://doi.org/10.1029/2019JB017679>

Received 12 MAR 2019

Accepted 24 MAY 2019

Accepted article online 31 MAY 2019

Abstract Water-saturated porous media exhibit a low-frequency (<1 MHz) dispersion of the electrical conductivity caused by the polarization of the electrical double layer (EDL) coating the charged solid-liquid interface. We develop a mathematical framework describing the polarization caused by field-induced perturbations of the ion densities in the Stern and the diffuse layer of the EDL for two different geometrical configurations of solid and liquid phase. For spherical grains immersed in an electrolyte we derive an improved analytical description by combining suitable models for diffuse- and Stern-layer polarization. The selected models differ from those usually used in geophysical literature and improve the agreement with the corresponding finite-element solution significantly. We then employ the validated finite-element model to examine the EDL in a pore-constriction geometry, which is often used to study membrane polarization. Here, a suitable analytical model can only be set up for a pure diffuse-layer polarization. The results for the coupled Stern- and diffuse-layer polarization in both geometries indicate that (1) the polarization of the Stern layer is much stronger than the polarization of the diffuse layer as long as the EDL is not connected at the system scale; (2) this dominance of the Stern-layer polarization can be observed in both geometries, but (3) the contribution of the diffuse layer increases with increasing compaction as represented by the pore-constriction geometry; and (4) the contributions of both parts of the EDL reach similar levels, when the EDLs on different surfaces are interconnected at the system scale.

1. Introduction

Complex-conductivity measurements assess the frequency-dependent electrical conduction and polarization properties of soil and subsurface materials. Because macroscopic measurements are correlated to pore and/or grain geometry, electrochemical characteristics of the solid-liquid interface, and of the pore-filling electrolyte, the method has a huge potential for novel hydrogeophysical (e.g., Börner et al., 1996; Hördt et al., 2009) and biogeophysical (e.g., Atekwana & Slater, 2009; Flores Orozco et al., 2011; Wainwright et al., 2015) applications. Although empirical relations based on these correlations are increasingly used in near-surface studies, there is no widely accepted model linking macroscopic polarization effects to microscopic properties (e.g., Kemna et al., 2012). In absence of conductive minerals, four mechanisms contribute to the low-frequency (<1 MHz) dispersion of complex conductivity, all of which are sensitive to the polarization of different parts of the electrical double layer (EDL) at the solid-liquid interface (e.g., Lesmes & Morgan, 2001): (1) Maxwell-Wagner polarization, (2) polarization of the Stern layer, (3) polarization of the diffuse layer, and (4) membrane polarization.

Maxwell (1892) and Wagner (1914) studied interfacial polarization in heterogeneous media consisting of two or more phases of different electrical conductivity and/or dielectric constant: unequal conduction and displacement current densities in the different phases are balanced by an accumulation of charge along the geometrical boundaries. O'Konski (1960) extended the Maxwell-Wagner theory to include the polarization of charges bound to the surface of charged particles. Later, Garcia et al. (1985) treated the case of uncharged dielectric particles in electrolyte solution. In contrast to earlier theories, which assume homogeneous conductivities in both phases resulting in true surface charge distributions, their treatment accounts for local field-induced concentration variations in the electrolyte and thus volume charge of finite extension. The characteristic time scales of the different types of Maxwell-Wagner polarization are short, such that this relaxation usually occurs at the high-frequency limit (kHz) of the complex-conductivity response (e.g., Leroy et al., 2008; Lesmes & Morgan, 2001).

A first theory describing the polarization of the Stern layer was presented by Schwarz (1962) and improved by Schurr (1964). Schwarz' theory accounts for the diffusion-controlled polarization of the Stern layer of bound counterions. Schurr combined this model with the one by O'Konski to include the effect of surface conductivity due to the diffuse layer. Because the contribution of the diffuse layer is frequency independent in this model, the dispersion of the complex conductivity is attributed to Stern-layer polarization, and the diffuse layer only results in a uniform increase of the real part of the conductivity. Later, Schurr's model provided the basis for the treatment by Leroy et al. (2008), which includes a detailed electrochemical model to quantify the partition of charges into Stern and diffuse layer (see, e.g., Revil & Glover, 1997, 1998) and also accounts for a grain-size distribution. This model successfully predicted the response of glass beads (Leroy et al., 2008) and was extended to sand-oil-water mixtures later (Schmutz et al., 2010).

The polarization of the diffuse layer has been studied by Dukhin and Shilov (1974), who developed a theory for the ion fluxes through thin diffuse layers, which induce concentration variations in the diffuse layer and the adjacent electrolyte. This concentration-polarization mechanism has also been treated analytically by Fixman (1980), Chew and Sen (1982a), and Hinch et al. (1984) among others. A numerical solution removing many of the limitations of the analytical approaches—for example, the assumption of a thin diffuse layer compared to the particle radius, a sufficiently small surface potential, and a monovalent symmetric electrolyte—was presented by DeLacey and White (1981). Later, Shilov et al. (2001) included the effect of Maxwell-Wagner polarization into the classical Dukhin-Shilov theory yielding a good agreement with the numerical model by DeLacey and White (1981).

Different attempts have been made to determine the relative importance of Stern- and diffuse-layer polarization and to develop combined models. Lyklema et al. (1983) generalized the Schwarz-Schurr model by including the coupling of charges in the Stern layer to those in the diffuse layer, which mainly results in a decrease of the relaxation time scale. Leroy et al. (2017) applied this approach to model the polarization response of calcite precipitations on glass beads. de Lima and Sharma (1992) analyzed the models by Schwarz, Schurr, and Fixman separately in order to assess their relative contribution to the overall polarization response. By superposing the individual responses, Lesmes and Morgan (2001) developed a combined model considering all three polarization mechanisms, that is, Stern-/diffuse-layer and Maxwell-Wagner polarization. The authors also included a volume-averaging approach to study water-particle mixtures characterized by a grain-size distribution. Based on the work of Kijlstra et al. (1992), Shilov et al. (2001) modified the Dukhin-Shilov theory to account for the contribution of the Stern layer to surface conductivity.

Most theories describing the first three polarization mechanisms rest on the analytical solution of the underlying system of partial differential equations (PDEs) around one isolated spherical particle. The induced dipole moment of the polarized particle obtained from such treatment can then be used to derive the effective conductivity (or the effective dielectric constant) of ensembles of more than one particle. The effective medium theory provides mixing laws for dilute suspensions (e.g., Maxwell, 1892; Wagner, 1914) or mixtures with higher particle concentrations (e.g., Bruggeman, 1935; Hanai, 1960).

Membrane polarization is generally studied on pore networks with different levels of complexity. Marshall and Madden (1959) developed the first model for a sequence of two types of one-dimensional pores or zones. The membrane effect is introduced by assuming different mobilities for cations and anions in the "active" zone. While these authors do not further specify the origin of mobility variations, later developments related ion selectivity to the unequal contributions of cations and anions to the surface conductivity at the pore wall (Buchheim & Irmer, 1979; Fridrikhsberg & Sidorova, 1961; Titov et al., 2002, 2004). Blaschek and Hördt (2009) carried out numerical simulations on one- and two-dimensional pore networks, where the ion-selective behavior of narrow pores is still parameterized in terms of ion mobilities, which are constant over the pore cross section. Volkmann and Klitzsch (2010) improved this approach and limited the ion selectivity—expressed in terms of unequal effective ion mobilities—to a thin layer covering the pore walls.

Bücker and Hördt (2013a) proposed an analytical model, which allows to explicitly include pore radii and surface conductivity due to Stern and diffuse layer into the one-dimensional impedance model by Marshall and Madden. This model has later been extended to model the effect of temperature, fluid salinity, pH, and immiscible hydrocarbon contaminants on the polarization response (Bairlein et al., 2016; Bücker et al., 2017; Hördt et al., 2016). Based on the same model, Stebner et al. (2017) used impedance networks to model the membrane polarization of porous media. Because the model by Bücker and Hördt typically requires large

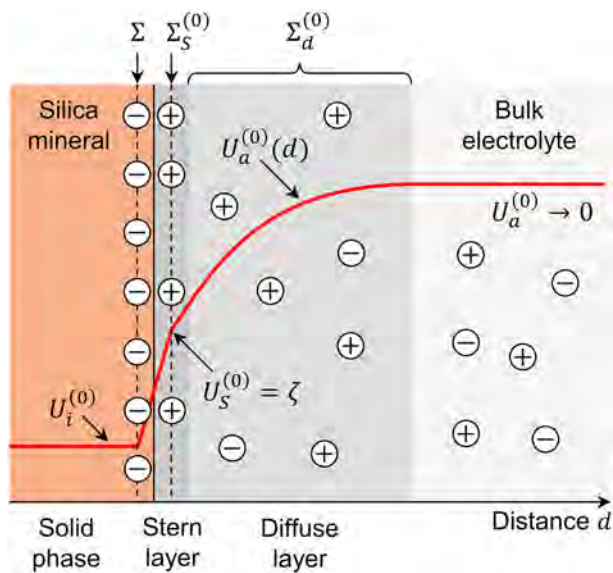


Figure 1. Simplified model of the equilibrium electrical double layer (EDL) at the charged silica surface. Due to the deprotonation of silanol surface sites, the mineral surface acquires the surface charge Σ . In the electrolyte, this usually negative charge is screened by an equal number of the positive charges distributed over the Stern layer ($\Sigma_S^{(0)}$) and the diffuse layer ($\Sigma_D^{(0)}$). The red line sketches the spatial variation of the electrical potential $U^{(0)}$ across the different parts of the electrical double layer.

aspect ratios, length of a pore divided by its diameter, to produce measurable polarization magnitudes, Hördt et al. (2017) further investigated into the geometrical constraints of this membrane-polarization model.

Besides geometrical constraints, the simplified consideration of the Stern layer is a major limitation of the existing theoretical treatment of membrane polarization. While combined treatments of Stern-layer, diffuse-layer, and Maxwell-Wagner polarization mechanisms exist for grain-based models, the coupling between these three mechanisms is often largely simplified in pore-constriction models. Irrespective from the model geometry, the complexity of the equations for the fully coupled system describing all three mechanisms puts a challenge on analytical solutions, which therefore all suffer from strong simplifications or only treat limiting cases.

The present paper addresses the repeatedly stated need for “a mechanistic approach and [...] general framework in which all these mechanisms are explained and quantified in their relative importance” (Kemna et al., 2012). In the theory section, we compile the mathematical descriptions of all relevant physical processes and provide a mathematical framework, which allows modeling the fully coupled interplay of Stern- and diffuse-layer polarization on arbitrary geometries. Subsequently, we derive an improved analytical approximation for the polarization of a single grain, which matches the results obtained from numerically solving the equations of the generalized mathematical framework. The validated numerical model is then applied to the pore-constriction geometry. Based on the comparison of numerical and analytical results, we improve the membrane-polarization model by Bückler and Hördt (2013a) and for the first time study the fully coupled Stern- and diffuse-layer polarization in a pore-constriction geometry.

2. Theory

2.1. EDL Model

Most solid surfaces in contact with aqueous solutions are charged. We will consider silica surfaces in contact with a monovalent electrolyte, such as NaCl, where the deprotonation of silanol surface sites produces a negative surface-charge density Σ over a wide pH range (e.g., Leroy et al., 2008; Somasundaran, 2006). In the electrolyte next to the silica surface, the electric field of Σ attracts counterions (cations, if $\Sigma < 0$) and repels coions (here anions) giving rise to the development of two layers: The inner layer—also known as Stern or Helmholtz layer—consists of counterions adsorbed to the silica surface. The outer layer—also known as diffuse or Gouy-Chapman layer—is mainly populated by counterions and a minor fraction of coions both obeying Poisson-Boltzmann statistics.

We adopt the simplified model displayed in Figure 1. The Stern layer is treated as an infinitely thin layer of counterions (e.g., Leroy et al., 2008; Schwarz, 1962; Schurr, 1964) and is characterized by the uniform surface charge density $|\Sigma_S^{(0)}| < |\Sigma|$ (the superscript (0) indicates quantities in the equilibrium state, that is, without external excitation), which partly shields the electric field of Σ . Furthermore, we assume that charges in the Stern layer can only move along the surface, which reflects a strong binding of counter-ions to the surface.

The movement of the ions in the diffuse layer is not restricted to the surface; that is, these ions can move in all directions. As a result of an equilibrium between simultaneously acting electrostatic forces and thermal fluctuations, counterion excess and coion deficit concentrations smoothly decay with the distance d from the surface. At a far distance from the surface, both ion concentrations approach their values in the bulk electrolyte. Together with $\Sigma_S^{(0)}$, the total positive charge density $\rho(d)$ in the diffuse layer screens the negative surface charge Σ . By integrating $\rho(d)$ across the diffuse layer, we obtain the equivalent surface charge density $\Sigma_D^{(0)}$ of the diffuse layer. In equilibrium, the EDL consisting of charged surface sites, Stern layer, and diffuse layer is electroneutral, that is, $\Sigma_S^{(0)} + \Sigma_D^{(0)} = -\Sigma$.

The electric potential at the inner limit of the diffuse layer is usually identified with the ζ -potential at the plane of shear (e.g., Leroy et al., 2008; Bückner & Hördt, 2013a). Due to the space charge ρ , the electric potential $U_a^{(0)}$ in the electrolyte decays from ζ at the solid-liquid interface to zero in the bulk electrolyte. Note that in the simplified model sketched in Figure 1, the (equilibrium) potential in the Stern layer $U_S^{(0)}$ is equal to ζ .

2.2. Basic Equations

2.2.1. Bulk Electrolyte and Diffuse Layer

The bulk electrolyte is characterized by the ion valences z_{\pm} , mobilities μ_{\pm} , and bulk concentrations C_{\pm}^{∞} , as well as the relative permittivity ϵ_a . For the sake of simplicity, we assume that the mobilities of cations (subindex +) and anions (subindex -) are equal, that is, $\mu_+ = \mu_- = \mu$, and limit our treatment to monovalent electrolytes, that is, $z_{\pm} = \pm 1$. In the case of a dilute solution, the electrical conductivity of the bulk electrolyte is then given by $\sigma_a = 2e\mu C_{\pm}^{\infty}$.

Spatial and temporal variations of the ion concentrations $C_{\pm}(\mathbf{r}, t)$ and the electrical potential $U_a(\mathbf{r}, t)$ in the solution, that is, in the diffuse layer and the bulk electrolyte, are controlled by the steady state Nernst-Planck, mass continuity, and Poisson equations (e.g., Garcia et al., 1985):

$$\mathbf{J}_{\pm}(\mathbf{r}, t) = -D\nabla C_{\pm}(\mathbf{r}, t) - z_{\pm}\mu C_{\pm}(\mathbf{r}, t)\nabla U_a(\mathbf{r}, t), \quad (1)$$

$$\nabla \mathbf{J}_{\pm}(\mathbf{r}, t) = -\partial_t C_{\pm}(\mathbf{r}, t), \quad (2)$$

$$\nabla^2 U_a(\mathbf{r}, t) = -\frac{e}{\epsilon_0 \epsilon_a} [C_+(\mathbf{r}, t) - C_-(\mathbf{r}, t)]. \quad (3)$$

Here, D denotes the diffusion coefficient, $e = 1.602 \times 10^{-19}$ C is the elementary charge, and $\epsilon_0 = 8.85 \times 10^{-12}$ F/m is the vacuum permittivity. In absence of specific interaction between the different ion species, the Einstein relation $D = \mu k_B T / e$ can be used to connect diffusion coefficient and mobility of the ions. Here, $k_B = 1.381 \times 10^{-23}$ J/K is Boltzmann's constant, and T is the absolute temperature. The current densities \mathbf{J}_{\pm} defined by the steady state Nernst-Planck equation (1) consider diffusion $-D\nabla C_{\pm}$ and electromigration $-z_{\pm}\mu C_{\pm}\nabla U_a$ ion fluxes.

If the system is excited by a time-harmonic electric field $E_0 e^{i\omega t}$, where ω and t denote angular frequency and time, respectively, the ion concentrations $C_{\pm}(\mathbf{r}, t)$ can be expressed by the sums of the static equilibrium concentrations $C_{\pm}^{(0)}$ and perturbation concentrations δC_{\pm} (e.g., Garcia et al., 1985):

$$C_{\pm}(\mathbf{r}, t) = C_{\pm}^{(0)}(\mathbf{r}) + \delta C_{\pm}(\mathbf{r}, \omega) \cdot e^{i\omega t}. \quad (4)$$

The electrical potential $U_a(\mathbf{r}, t)$ can also be decomposed into the static equilibrium potential $U_a^{(0)}$ and the perturbation $|\delta U_a| \ll U_a^{(0)}$:

$$U_a(\mathbf{r}, t) = U_a^{(0)}(\mathbf{r}) + \delta U_a(\mathbf{r}, \omega) \cdot e^{i\omega t}. \quad (5)$$

By inserting equations (4) and (5) into equations (1) through (3) and Fourier-transforming the resulting system, the problem can be decomposed into a static part and a frequency-dependent part (e.g., Chew & Sen, 1982b, 1982a). While the frequency-dependent part couples to the static solution, the static part can be solved independently.

To obtain the static part of the system, we set $\delta C_{\pm}, \delta U_a, \partial_t = 0$. After a few additional manipulations, this yields the Boltzmann-distributed equilibrium ion concentrations (Chew & Sen, 1982b)

$$C_{\pm}^{(0)}(\mathbf{r}) = C_{\pm}^{\infty} \exp \left[-\frac{z_{\pm} e}{k_B T} U_a^{(0)}(\mathbf{r}) \right] \quad (6)$$

and the Poisson-Boltzmann equation (e.g., Chew & Sen, 1982b)

$$\nabla^2 U_a^{(0)}(\mathbf{r}) = -\kappa^2 \frac{k_B T}{e} \sinh \left[\frac{e}{k_B T} U_a^{(0)}(\mathbf{r}) \right], \quad (7)$$

where $\kappa = [2e^2 C_{\pm}^{\infty} / (\epsilon_0 \epsilon_r k_B T)]^{1/2}$ is the inverse Debye screening length. Together with the boundary conditions discussed below, equations (6) and (7) describe the equilibrium ion concentrations C_{\pm}^{∞} and the static electrical potential $U_a^{(0)}$ in the diffuse layer and the bulk electrolyte.

In order to obtain the solution of the frequency-dependent system under the influence of a weak external field $E_0 \exp(i\omega t)$, the steady state Nernst-Planck equation (1) is inserted into the continuity equation (2), Fourier-transformed and linearized, which gives (e.g., Chew & Sen, 1982a)

$$i\omega \delta C_{\pm}(\mathbf{r}, \omega) = \nabla \cdot \left\{ D \nabla \delta C_{\pm}(\mathbf{r}, \omega) + \mu z_{\pm} \left[C_{\pm}^{(0)}(\mathbf{r}) \nabla \delta U_a(\mathbf{r}, \omega) + \delta C_{\pm}(\mathbf{r}, \omega) \nabla U_a^{(0)}(\mathbf{r}) \right] \right\} + \mathcal{O}(E_0^2). \quad (8)$$

The frequency-dependent perturbation concentrations of the two ion species and the potentials are coupled to each other by the Fourier-transformed Poisson equation (e.g., Chew & Sen, 1982a)

$$\nabla^2 \delta U_a(\mathbf{r}, \omega) = -\frac{e}{\epsilon_0 \epsilon_r} \left[\delta C_+(\mathbf{r}, \omega) - \delta C_-(\mathbf{r}, \omega) \right]. \quad (9)$$

Equations (8) and (9) constitute three coupled PDEs that describe the spatial variations of the perturbation quantities. As the boundary conditions at the solid surface link the solution in the electrolyte to the corresponding solutions in the Stern layer and the interior of the solid, we will discuss the boundary conditions further below.

2.2.2. Stern Layer

The Stern layer is modeled as a thin layer situated at the solid-liquid interface. In absence of an external excitation, the surface-charge density $\Sigma_S^{(0)}$ in this layer is uniform. Under the influence of the electrical field $E_0 \exp(i\omega t)$, the counterions move along the surface, but no charge exchange with the electrolyte nor the solid is considered. We describe the surface-charge density in the Stern layer in terms of the constant equilibrium value $\Sigma_S^{(0)}$ and the perturbation $|\delta \Sigma_S| \ll \Sigma_S^{(0)}$, such that

$$\Sigma_S(\mathbf{r}_S, t) = \Sigma_S^{(0)} + \delta \Sigma_S(\mathbf{r}_S, \omega) \exp(i\omega t), \quad (10)$$

where \mathbf{r}_S denotes the position vector in local coordinates along the solid-liquid interface. Adopting the treatment of the bound surface-charge densities on spherical particles proposed by Schwarz (1962) and Schurr (1964), the perturbation of the surface-charge density in the Stern layer is controlled by

$$i\omega \delta \Sigma_S(\mathbf{r}_S, \omega) = \nabla_S \cdot \left[D_S \nabla_S \delta \Sigma_S(\mathbf{r}_S, \omega) + \mu_S \Sigma_S^{(0)} \nabla_S \delta U_S(\mathbf{r}_S, \omega) \right] + \mathcal{O}(E_0^2), \quad (11)$$

where ∇_S is the surface Laplacian operating on functions defined on the geometrical boundary (also known as Laplace-Beltrami operator), μ_S is the mobility, D_S is the diffusion coefficient, and δU_S is the perturbation potential in the Stern layer. Note that equation (11) is the surface equivalent of equation (8) describing diffusion and electromigration surface-flux densities within the Stern layer. Only the third term on the right-hand side of equation (8) has no equivalent because the constant potential results in a vanishing tangential electrical field $-\nabla_S U_S^{(0)}$.

For spherical particles of radius a centered at the origin of the spherical coordinate system (r, θ, ϕ) and an excitation parallel to the polar axis $\theta = 0$, equation (11) takes the form (e.g., Schurr, 1964; Schwarz, 1962)

$$i\omega \delta \Sigma_S(\theta, \omega) = \frac{1}{a^2 \sin \theta} \frac{\partial}{\partial \theta} \left[D_S \sin \theta \frac{\partial}{\partial \theta} \delta \Sigma_S(\theta, \omega) + \mu_S \Sigma_S^{(0)} \sin \theta \frac{\partial}{\partial \theta} \delta U_S(\theta, \omega) \right]. \quad (12)$$

There is no particular surface equivalent of Poisson's equation (9). Instead, the continuity of the electrical potential at the solid surface (in conjunction with the vanishing thickness of the Stern layer) directly couples δU_S and the surface-charge density $\delta \Sigma_S$ to the adjacent perturbation potentials in electrolyte and solid.

2.2.3. Solid Dielectric

The solid dielectric has a relative permittivity ϵ_i and zero electrical conductivity. The spatial variation of the potential within the solid is governed by the Laplace equation $\nabla^2 U_i(\mathbf{r}, t) = 0$. In equilibrium, the static electrical potential $U_i^{(0)}$ must be equal to the (constant) ζ -potential on the surface, and $U_i^{(0)}$ must be constant throughout the solid. The Fourier-transformed frequency-dependent Laplace equation writes

$$\nabla^2 \delta U_i(\mathbf{r}, \omega) = 0, \quad (13)$$

which in conjunction with the spatially varying surface potential $\delta U_S(\mathbf{r}_S, \omega)$ determines the perturbation potential $\delta U_i(\mathbf{r}, \omega)$ within the solid.

2.3. Boundary Conditions

At far distances d from the surface, the static background potential in the electrolyte should approach zero, that is,

$$U_a^{(0)} \xrightarrow{d \rightarrow \infty} 0. \quad (14)$$

At the surface, we take advantage of our knowledge of the constant potential $U_i^{(0)}$ inside of the solid (see above) and use the continuity of the displacement current to define the Neumann boundary condition

$$-\epsilon_0 \epsilon_a \nabla U_a^{(0)} \Big|_{\text{surface}} \cdot \mathbf{n} = \Sigma + \Sigma_S^{(0)}, \quad (15)$$

where \mathbf{n} denotes the unit normal vector to the solid surface (pointing out of the solid into the electrolyte) and $\Sigma + \Sigma_S^{(0)} = -\Sigma_d^{(0)}$ is the net surface-charge density. The boundary conditions on the equilibrium ion concentrations $C_{\pm}^{(0)}$ are implicit to equation (6).

The perturbation potential at far distances d from the surface must be equal to values corresponding to the external electrical field, that is,

$$\delta U_a(\mathbf{r}, \omega) \xrightarrow{d \rightarrow \infty} -\mathbf{E}_{\text{ext}}(\mathbf{r}) \cdot \mathbf{r}, \quad (16)$$

while the ion concentrations should approach their bulk values, that is,

$$\delta C_{\pm}(\mathbf{r}, \omega) \xrightarrow{d \rightarrow \infty} 0. \quad (17)$$

At the surface of the solid, the solutions for the three model domains—electrolyte, Stern layer, and solid—are pieced together. The continuity of the electrical potential demands the three perturbation potentials to be equal at any point \mathbf{r}_S on the surface, that is,

$$\delta U_i(\mathbf{r}_S, \omega) = \delta U_S(\mathbf{r}_S, \omega) = \delta U_a(\mathbf{r}_S, \omega). \quad (18)$$

We assume that on the time scales of interest, ions of the solution do not engage in surface reactions; thus, they are neither produced nor consumed, and the normal fluxes through the surface are zero, that is,

$$\left\{ -D \nabla \delta C_{\pm}(\mathbf{r}, \omega) - \mu z_{\pm} \left[C_{\pm}^{(0)}(\mathbf{r}, \omega) \nabla \delta U_a(\mathbf{r}, \omega) + \delta C_{\pm}(\mathbf{r}, \omega) \nabla U_a^{(0)}(\mathbf{r}, \omega) \right] \right\} \Big|_{\mathbf{r}=\mathbf{r}_S} \cdot \mathbf{n} = 0. \quad (19)$$

The continuity of the displacement current implies that (e.g., Schwarz, 1962)

$$\left[-\epsilon_0 \epsilon_a \nabla \delta U_a(\mathbf{r}, \omega) + \epsilon_0 \epsilon_i \nabla \delta U_i(\mathbf{r}, \omega) \right] \Big|_{\mathbf{r}=\mathbf{r}_S} \cdot \mathbf{n} = \delta \Sigma_S(\mathbf{r}_S), \quad (20)$$

which completes the set of boundary conditions.

3. Polarization of Spherical Grains

The model setup in the previous section describes the charge polarization of the Stern layer and the concentration polarization produced by unequal contributions of anions and cations to electrical conduction through the diffuse layer. In this section, we will study the relative importance of both polarization mechanisms for the case of dilute suspensions of dielectric spheres. Because even for spherical particles no analytical solution of the fully coupled problem is known, we first obtain a suitable analytical approximation of the coupled polarization process, which combines (i) the Stern-layer polarization model by Schwarz (1962), including the correction of the corresponding relaxation time proposed by Lyklema et al. (1983), and (ii) the diffuse-layer polarization model developed by Dukhin and Shilov (1974). In order to assess the quality of our analytical model and open the possibility to model the polarization response of more complex geometrical configurations, we also present a numerical finite-element solution.

3.1. Analytical Model

At distances far from a spherical particle of radius a centered at the origin of the spherical coordinate system $\mathbf{r} = (r, \theta, \phi)$, all approximate analytical solutions take the form (e.g., Dukhin & Shilov, 1974; Maxwell, 1892; Schurr, 1964; Wagner, 1914)

$$\delta U_a(\mathbf{r}, \omega) = E_0 \left[-r + \frac{f(\omega)a^3}{r^2} \right] \cos \theta, \quad (21)$$

if the external excitation is parallel to the polar axis, that is, $\theta = 0$. The first term of this expression accounts for the potential due to the external field, and the second term describes the effective long-range dipole moment of the polarized particle. The reflection coefficient $f(\omega)$ contains the complete information on the macroscopic polarization response of the particle. For a pure Maxwell-Wagner polarization, it writes

$$f(\omega) = \frac{\sigma_i^*(\omega) - \sigma_a^*(\omega)}{2\sigma_a^*(\omega) + \sigma_i^*(\omega)}, \quad (22)$$

where $\sigma_a^*(\omega) = \sigma_a + i\omega\epsilon_0\epsilon_a$ and $\sigma_i^*(\omega) = i\omega\epsilon_0\epsilon_i$ are the complex conductivity of the bulk electrolyte and the nonconducting particle, respectively.

With $f(\omega)$ for one spherical particle at hand, the effective complex conductivity $\sigma^*(\omega)$ of a dilute suspension of a number of equal particles can be obtained using a generalized form of the theory by Wagner (1914)

$$\frac{\sigma^*(\omega)}{\sigma_a^*} = \frac{1 + 2\nu f(\omega)}{1 - \nu f(\omega)}, \quad (23)$$

where ν denotes the volume fraction of suspended particles. Together with the complex conductivities σ_a^* and σ_i^* , equations (22) and (23) describe the Maxwell-Wagner polarization of suspensions of dielectric particles in a medium with homogeneous complex conductivity $\sigma_a^*(\omega)$.

O'Konski (1960) included the effect of a uniform surface charge density Σ_x into this model. He found that the effect of charge carriers that move freely along the particle surface can be taken into account by adding the effective conductivity increment $\sigma_x = 2\mu_x\Sigma_x/a$ to the complex conductivity σ_i^* of the particle. According to this idea, the effective conductivity of the diffuse layer can be expressed as

$$\sigma_d = |\sigma_{d+} + \sigma_{d-}| = \frac{2\mu|\Sigma_{d+}^{(0)} - \Sigma_{d-}^{(0)}|}{a}, \quad (24)$$

where the contributions of the two types of ions to the effective conductivity of the diffuse layer are defined as

$$\sigma_{d\pm} = \frac{\pm 2\mu\Sigma_{d\pm}^{(0)}}{a}. \quad (25)$$

For sufficiently thin diffuse layers, that is, $\kappa a \ll 1$, the equivalent surface charge densities in the diffuse layer can be related to the surface charge using a variation of Bikerman's equation for the surface conductivity near a (highly) charged plane surface (e.g., Shilov et al., 2001)

$$\Sigma_{d\pm}^{(0)} = \pm \frac{2eC_{\pm}^{\infty}}{\kappa} \left[\exp\left(\mp \frac{e\zeta}{2k_B T}\right) - 1 \right]. \quad (26)$$

Note that while the total charge stored in the diffuse layer is represented by the sum of both contributions, that is, $\Sigma_d^{(0)} = \Sigma_{d+}^{(0)} + \Sigma_{d-}^{(0)}$, the total surface conductivity of the diffuse layer σ_d is proportional to their difference. For a given surface charge density $\Sigma_D^{(0)}$, the ζ -potential can be obtained from

$$\zeta(\Sigma_d^{(0)}) = -\frac{2k_B T}{e} \sinh^{-1} \left(\Sigma_d^{(0)} \frac{\kappa}{4eC_{\pm}^{\infty}} \right). \quad (27)$$

This relation can readily be obtained from equation (26). Resolved for $\Sigma_d^{(0)}(\zeta)$, it is also known as Grahame equation (Grahame, 1947).

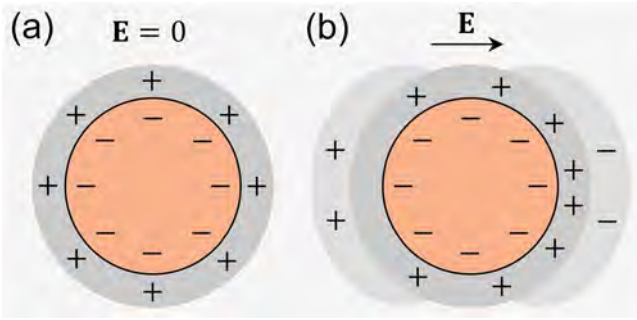


Figure 2. Sketch of the polarization of the Stern layer: (a) negatively charged particle and Stern layer in equilibrium; (b) under the influence of the external field \mathbf{E} , cations in the Stern layer move along the surface, deplete on the left side and accumulate on the right side of the particle. The resulting net surface charge $\delta\Sigma_S$ causes field-induced diffuse layers of opposite charge to build up in the electrolyte next to the charged surfaces (e.g., Lyklema et al., 1983).

The surface-charge density of the Stern layer can be expressed in terms of the effective conductivity

$$\sigma_S = \frac{2\mu_S |\Sigma_S^{(0)}|}{a}. \quad (28)$$

In the present study, the partition of counterions into diffuse layer and Stern layer will be expressed in terms of the ratio $p = -\Sigma_S^{(0)}/\Sigma$. Note that this definition is slightly different from the partition coefficient $f_Q = \Sigma_S^{(0)}/(\Sigma_{d+}^{(0)} + \Sigma_S^{(0)})$ introduced by Leroy and Revil (2004).

3.1.1. Stern-Layer Polarization

If the entire counter charge is located in the Stern layer (i.e., $p = 1$), and no diffuse layer is present (i.e., $\Sigma_d^{(0)}, \zeta = 0$), the low-frequency response of the particle is caused by the polarization of the Stern layer only (see Figure 2). In the thin double layer limit, that is, $\kappa a \ll 1$, the solution of the polarization problem can be approximated as done by Schwarz (1962). In terms of the reflection coefficient f defined in equation (21), the final result obtained by Schwarz (1962) can be expressed as (from his equation 13)

$$f_S(\omega) = \frac{\sigma_S^*(\omega) - \sigma_a^*(\omega)}{2\sigma_a^*(\omega) + \sigma_S^*(\omega)}, \quad (29)$$

where σ_S^* is the effective complex conductivity of the spherical particle, which writes (from Schwarz, 1962, equations 14 and 16)

$$\sigma_S^*(\omega) = \sigma_S \frac{i\omega\tau_S}{1 + i\omega\tau_S} + i\omega\epsilon_0\epsilon_i. \quad (30)$$

Note that the particle is assumed to be nonconducting, that is, $\sigma_i = 0$. The relaxation time of the Stern-layer polarization τ_S can be expressed as (Lyklema et al., 1983, equation 36)

$$\tau_S = \frac{a^2}{2D_S M}, \quad (31)$$

where the coefficient M defined as (Lyklema et al., 1983, equation 34)

$$M = 1 + \frac{\kappa \Sigma_S^{(0)}}{2eC_{\pm}^{\infty} \cosh[e\zeta/(2k_B T)]} \quad (32)$$

accounts for the coupling of the charges in the Stern layer to the electrolyte, which had not been considered in the original model by Schwarz (1962).

Because $\zeta = 0$ if $p = 1$, there is no equilibrium diffuse layer, and the polarization response is only due to the polarization of the Stern layer, first term in equation (30), and the Maxwell-Wagner polarization caused by the conductivity and permittivity contrasts between particle and electrolyte.

3.1.2. Diffuse-Layer Polarization

In the opposite case, in which no Stern layer exists (i.e., $p = 0$) and the entire counter charge is located in the diffuse layer, only the diffuse layer polarizes (see Figure 3). This scenario has been treated by Dukhin and Shilov (1974) for the limit of thin diffuse layers. If electro-osmotic effects are neglected; that is, in the limit of an infinitely large fluid viscosity, the result of the classical Dukhin-Shilov theory can be expressed in terms of the reflection coefficient (e.g., Grosse & Shilov, 1996; Shilov et al., 2001)

$$f_d(\omega) = \frac{2Du(\zeta) - 1}{2Du(\zeta) + 2} - \frac{3S}{2} \frac{(\sigma_{d+} - \sigma_{d-})^2}{\sigma_a^2 [2Du(\zeta) + 2]^2} \left[1 - \frac{i\omega\tau_a}{1 + \sqrt{i\omega 2\tau_a/S + i\omega\tau_a}} \right], \quad (33)$$

where $Du(\zeta) = \sigma_d/(2\sigma_a)$ is the Dukhin number. The coefficient S , which appears in the expression for f_d , writes

$$S = \frac{[Du(\zeta) + 1] \sigma_a^2}{(\sigma_{d+} + \sigma_a)(\sigma_{d-} + \sigma_a)} \quad (34)$$

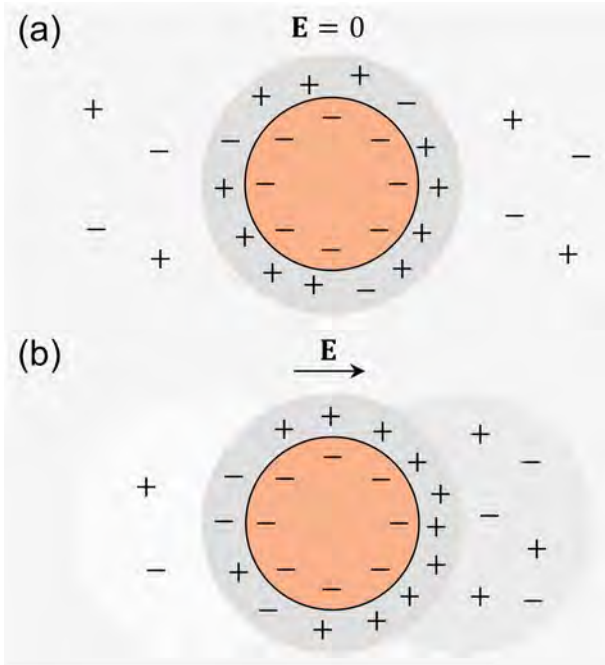


Figure 3. Sketch of the polarization of the diffuse layer: (a) negatively charged particle, diffuse layer, and bulk electrolyte in equilibrium; (b) under the influence of the external field \mathbf{E} , the high effective conductivity of the diffuse layer leads to an accumulation of positive charge on the right side and negative charge on the left side of the particle. In addition, unequal migration flux densities of cations and anions through the diffuse layer are counterbalanced by an electroneutral salinity gradient that builds up next to the particle.

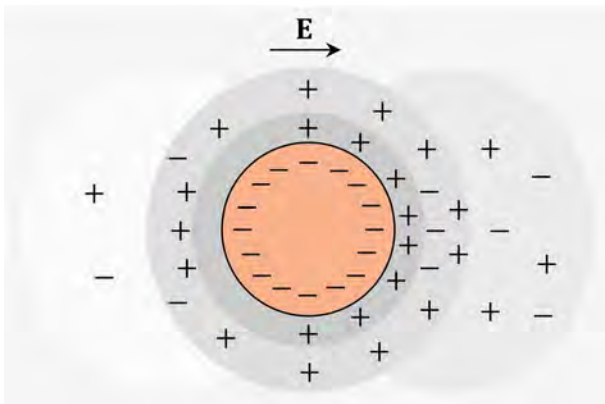


Figure 4. Sketch of the coupled polarization of Stern and diffuse layer: Due to the presence of a diffuse layer, the net surface density in the polarized Stern layer $\delta\Sigma_S$ is larger than in the case without diffuse layer (Lyklema et al., 1983). In the inner part of the diffuse layer, $\delta\Sigma_S$ attracts opposite charges (here positive on the right and negative on the left side of the particle). In the outer part, the charge in the diffuse layer changes its sign, which compensates for the high effective conductivity of this layer (as in Figure 3). The salinity gradient in the electrolyte next to the particle is a result of the unequal migration flux densities of cations and anions through the diffuse layer.

and the time constant is defined as $\tau_a = a^2S/(2D)$. The effective conductivity of the suspension can be obtained by substituting f by f_d in equation (23). Note that this formulation only accounts for the polarization of the diffuse layer; an extension including Maxwell-Wagner polarization can be found in Shilov et al. (2001).

3.1.3. Coupled Polarization

For any value $0 < p < 1$, the counter charges are distributed over Stern and diffuse layer, which leads to a simultaneous polarization of both parts of the EDL (see Figure 4). As argued by Lesmes and Morgan (2001), the coupled polarization can be approximated by a superposition of the individual responses, that is, by adding the effective complex dielectric constants of the particle (or the corresponding effective complex-conductivity increments). In order to obtain an effective conductivity increment describing the diffuse-layer polarization, we rearrange equation (22) as follows:

$$\sigma_d^*(\omega) = \sigma_a^*(\omega) \frac{1 + 2f_d(\omega)}{1 - f_d(\omega)}. \quad (35)$$

The effective conductivity σ_s^* , which accounts for Stern-layer and Maxwell-Wagner polarization, is given by equations (30) through (32), and, thus, the total effective conductivity of the particle including all three mechanisms writes

$$\sigma_c^*(\omega) = \sigma_d^*(\omega) + \sigma_s^*(\omega) = \sigma_d^*(\omega) + \sigma_s \frac{i\omega\tau_S}{1 + i\omega\tau_S} + i\omega\epsilon_0\epsilon_i. \quad (36)$$

Note that this expression is almost the same as the one obtained by Schurr (1964) except for the decrease of τ_S by the factor M and the substitution of σ_d by $\sigma_d^*(\omega)$, that is, including the frequency-dependent contribution of the diffuse layer defined by equations (33) through (35).

The new coupled model described here is also similar to the one proposed by Lesmes and Morgan (2001), from which it differs with regard to (i) the relaxation time of the Stern layer τ_S , where we use the correction by Lyklema et al. (1983); (ii) the low-frequency contribution σ_s of the Stern layer (their equations 5 and 6), which we do not consider because it contradicts the assumption of a strongly bound Stern-layer; and (iii) the selection of the model describing the diffuse-layer polarization, where we use the Dukhin-Shilov theory instead of the model by Fixman (1980). Fixman's assumption that the coion contribution to the surface conductivity can be ignored for sufficiently high ζ -potentials does not hold for the range of ζ -potentials studied here. We found that this simplification significantly affects the real part of the complex conductivity (not shown here for brevity).

3.2. Numerical Model

Figure 5 shows the geometrical setup used for the numerical modeling. The dielectric particle of radius a is centered at the origin of coordinates, and the external electric field is imposed in x direction, that is, $\mathbf{E}_{\text{ext}} = E_0\mathbf{e}_x$, where \mathbf{e}_x denotes the unit vector in x direction. Due to the cylindrical symmetry of the problem, the numerical simulation can be carried out on the two-dimensional model domain in Cartesian coordinates $\mathbf{r} = (x, y)$ marked in red in Figure 5.

We use the finite-element software COMSOL Multiphysics to successfully obtain the static and the frequency-dependent solution. We first

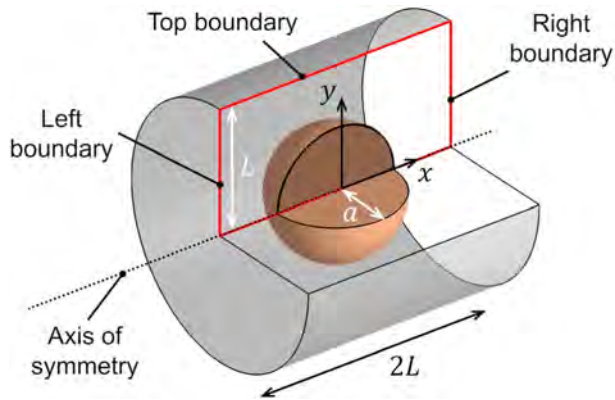


Figure 5. Three-dimensional sketch of the geometrical setup used for the numerical simulation of the polarization around spherical particles. The particle of radius a is enclosed by a cylinder of radius L and height $2L$, which represents the electrolyte. The red rectangle marks the actual two-dimensional model domain.

solve the Poisson-Boltzmann equation (7), which contains $U^{(0)}(\mathbf{r})$ as only unknown variable. For the numerical implementation, boundary conditions (14) and (15) are translated as follows: $U^{(0)} = 0$ on the left, right, and top boundary; $[\epsilon_0 \epsilon_i \nabla U_i^{(0)} - \epsilon_0 \epsilon_a \nabla U_a^{(0)}] \mathbf{n} = -\Sigma_d^{(0)}$ on the particle surface; and $\partial U^{(0)}/\partial y = 0$ on the axis of symmetry. The static background ion concentrations are computed by inserting $U_a^{(0)}$ into equation (6).

Subsequently, we solve the frequency-dependent part described by equations (8), (9), (11), and (13) and the boundary conditions (16) through (20). For the numerical solution, the latter are adjusted as follows: $\delta n_{\pm} = 0$ and $\delta U_a = \pm E_0 L$ on the left and right boundary, respectively; $\mathbf{J}_{\pm} = 0$ and $\partial \delta U / \partial y = 0$ on top boundary and on the axis of symmetry; unchanged on the particle surface. While the static solution only needs to be computed once for each set of model parameters (i.e., a , Σ , and p), the frequency-dependent problem has to be solved for each value of the angular frequency ω separately.

Because bulk values are implicitly assumed on the left, right, and top boundary, these boundaries must be placed sufficiently far away from the particle surface, where the polarization is expected to cause nonzero per-

turbations. As a trade-off between precision and computational cost, we define a standard domain size of $L = 10a$. For more technical details on the implementation, see the appendix.

The effective conductivity of the model can be obtained from the numerical integration of the total ion flux densities through the left (or likewise the right) boundary, that is,

$$\sigma_{\text{mod}}^* = \frac{2}{E_0 L^2} \int_0^L [\mathbf{J}_+(y) + \mathbf{J}_-(y)] \mathbf{e}_x y dy, \quad (37)$$

where the term $y dy$ accounts for the area element of the boundary and the factor $2/L^2$ stems from the normalization with the total area.

The standard domain size is $L = 10a$ and corresponds to a rather small volume fraction of dielectric particles. Therefore, we scale the modeled effective conductivities $\sigma_{\text{mod}}^*(\omega)$ to a more realistic volumetric content of $\nu = 0.4$ using the mixing rule defined in equation (23) with

$$f(\omega) = \frac{1}{\nu_{\text{mod}}} \frac{\sigma_{\text{mod}}^*(\omega) - \sigma_a^*(\omega)}{\sigma_{\text{mod}}^*(\omega) + 2\sigma_a^*(\omega)}. \quad (38)$$

3.3. Comparison of Analytical and Numerical Solution

Unless otherwise stated, the following parameter values are used to obtain both numerical and analytical results: The relative permittivities are $\epsilon_a = 80$ for the aqueous electrolyte and $\epsilon_i = 4.5$ for the solid, which is a typical value for quartz sand (e.g., Robinson & Friedman, 2003). The uniform ion mobility is $\mu = 5 \cdot 10^{-8} \text{ m}^2/(\text{Vs})$, which is approximately equal to the mobility of the sodium cation (e.g., Atkins & De Paula, 2013) and will be used for both ion species in the electrolyte. The mobility of the counterions in the Stern layer is only 10% of the ion mobility in the bulk electrolyte, that is, $\mu_S = \mu/10$. This value corresponds to the reduction of the cation mobility in the Stern layer inferred for K^+ on latex surfaces by Zukoski and Saville (1986) and for Na^+ on clay surfaces by Revil and Glover (1998) and Revil et al. (1998). For near-neutral pH of the solution and ion concentrations in the bulk electrolyte of $C_{\pm}^{\infty} = 1 \text{ mol/m}^3$, it is adequate to assume a surface charge density of $\Sigma = -0.01 \text{ C/m}^2$ (e.g., Kosmulski, 2006). The absolute temperature of $T = 293 \text{ K}$ (room temperature) and the above-mentioned volumetric content of $\nu = 0.4$ complete the set of standard model parameters.

Figure 6 displays the conductivity spectra of a suspension of spherical particles of radius $a = 5 \mu\text{m}$ for six values of p between 0 and 1. The effective conductivity of the mixture σ^* is expressed in terms of the corresponding real (σ') and imaginary (σ'') parts. In Figure 6a, we observe a continuous decrease of σ' with increasing p . This means that the surface conductivity due to counterions in the diffuse layer is much larger than the one of the Stern layer. This is due, on the one hand, to the significantly reduced mobility of the counterions in the Stern layer, which affects all frequencies equally. On the other hand, at low frequencies,

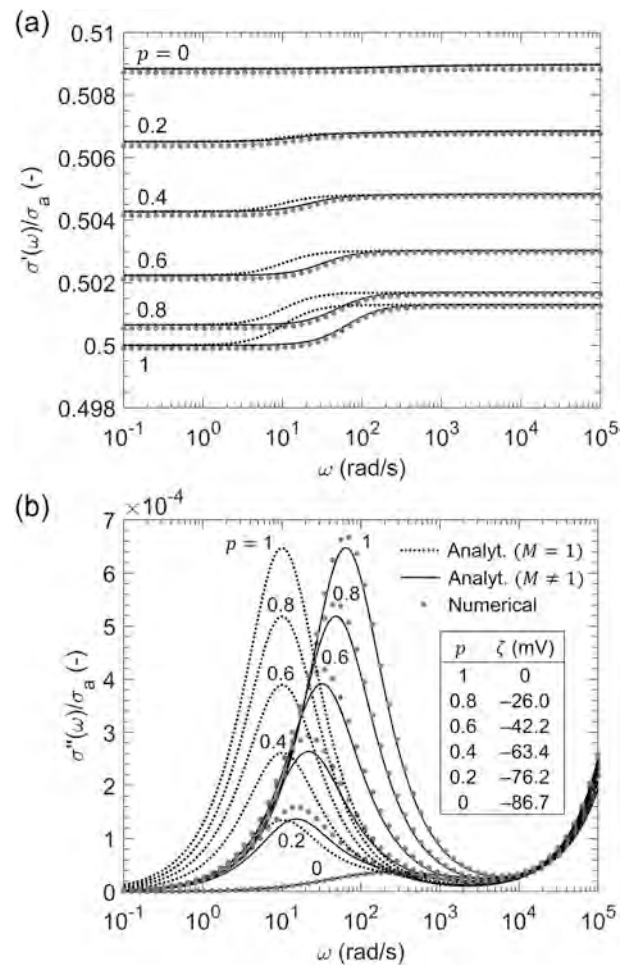


Figure 6. Complex-conductivity spectra of a suspension of dielectric particles of radius $a = 5 \mu\text{m}$ at different ratios $p = -\Sigma_s^{(0)}/\Sigma$, that is, the surface charge in the Stern layer increases with p . Complex-valued conductivities in terms of real (a) and imaginary (b) parts normalized to the bulk conductivity σ_a . Numerical results (gray circles) are displayed along with the corresponding analytical models according to equation (36) using the simple relaxation time after Schwarz, (1962; $M = 1$ in equation (31), dotted line) and using the corrected relaxation time after Lyklema et al. (1983; $M \neq 1$, solid line). The values of ζ shown in (b) are computed from equation (27).

the Stern layer is completely polarized and does not contribute to the DC conductivity because we assume that it cannot exchange ions with the bulk electrolyte. However, the Stern layer does contribute to the high-frequency limit of σ' , that is, at frequencies larger than the characteristic frequency of the Stern-layer polarization. The higher p and thus the surface conductivity σ_s , the larger becomes the difference between high- and low-frequency limits of σ' , which is largest in the case of a pure Stern-layer polarization ($p = 1$). In contrast, in the case of a sole diffuse-layer polarization ($p = 0$), we hardly recognize any variation of σ' with the angular frequency.

The peak imaginary conductivity σ'' (Figure 6b) increases almost linearly with p , that is, the charge density in the Stern layer. For the same surface-charge densities, the Stern-layer polarization ($p = 1$) results in a maximum of σ'' , which is approximately an order of magnitude larger than the peak produced by the corresponding diffuse-layer polarization ($p = 0$). From Figure 7, which shows a close-up of the small imaginary conductivities generated in the case of a depopulated Stern layer, it is evident that even a small fraction of 20% of positive charge located in the Stern layer produces a stronger response than the other 80% located in the diffuse layer. It is worth mentioning that the polarization magnitude (here in terms of the maximum of σ'') largely varies with the mobility of the counterions in the Stern layer. In a separate analysis, we observed a difference between the magnitudes of the two polarization processes of 2 orders of magnitude when a larger mobility of $\mu_S = \mu/2$ was assumed (not shown). This observation is in agreement with the

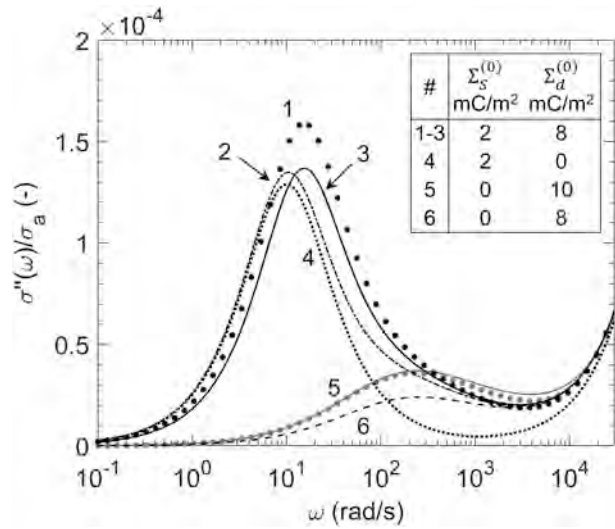


Figure 7. Numerical (filled circles) and analytical (lines) imaginary conductivity spectra for small surface charge densities $\Sigma_s^{(0)}$ in the Stern layer. Analytical curves are calculated from equation (36), using the values of $\Sigma_s^{(0)}$ and $\Sigma_d^{(0)}$ given in this Figure. Curve 1, numerical solution for the coupled Stern and diffuse-layer polarization; curves 2 and 3, analytical solution for the coupled Stern and diffuse-layer polarization using $M = 1$ and $M \neq 1$ in equation (31), respectively; curve 4, analytical solution for a pure Stern-layer polarization using $M = 1$; curves 5 and 6, numerical and analytical solutions for a pure diffuse-layer polarization and two different surface charge densities $\Sigma_d^{(0)}$ in the diffuse layer.

results obtained earlier by Lesmes and Morgan (2001) and confirms their conclusion that the Stern-layer polarization produces a much stronger frequency dispersion than the diffuse-layer polarization.

For sufficiently small values of p , Figure 7 also shows that the contribution of the diffuse-layer polarization results in a slight increase of the polarization magnitude and the characteristic angular frequency (curves 1 and 3) as compared to the pure Stern-layer polarization (curve 4). The latter is related to the higher characteristic frequency of the diffuse-layer relaxation as a consequence of the shorter relaxation time, here $\tau_a \approx \tau_s/2$ because $S \approx 1$.

The comparison of the corresponding curves in Figures 6 and 7 also serves as a mutual validation of our finite-difference implementation and the new analytical approximation for the coupled polarization response. For angular frequencies between 0.1 and 10^4 mrad/s, the relative deviation between analytical and numerical results is $<0.3\%$ in the real part and $<20\%$ in the imaginary part of the effective conductivity. Here, the analytical approximation clearly underestimates the polarization magnitude. A good agreement, however, is observed between the characteristic frequency, that is, the angular frequency at which the σ'' peaks are observed. Apart from the underestimated polarization magnitude, the good agreement between numerical and analytical curves confirms the approach to model the coupled polarization process by a simple superposition of the individual responses of Stern and diffuse layer.

4. Membrane Polarization

Besides the polarization of Stern and diffuse layer around grains, the polarization of ion-selective pore constrictions can also cause a low-frequency dispersion of the complex conductivity. In the present section, we study this membrane-polarization mechanism based on an alternating series of wide and narrow cylinders. The cylinder walls are negatively charged and covered by an EDL consisting of a Stern and a diffuse layer, both contributing to the macroscopic polarization of the system. In order to assess their relative contributions, effective conductivity spectra are computed for varying charge densities in the two layers. Because no analytical model is available for the coupled response in this geometry, we resort to the numerical finite-element implementation validated in the previous section. We also show that after a slight modification presented here, the analytical membrane-polarization model proposed by Bückner and Hördt (2013a) reproduces the numerical results for the sole diffuse-layer polarization fairly well.

4.1. Analytical Model for Diffuse-Layer Polarization

Bückner and Hördt (2013a) considered the sequence of wide and narrow pores sketched in Figure 8. The pores are characterized by their radii R_i and lengths L_i ; the indices 1 and 2 denote properties of the wide and the narrow pore, respectively. A nonzero ζ -potential at the cylinder walls causes diffuse layers to build up. According to Bückner and Hördt (2013a), upon excitation by an external electrical field, the electrical current parallel to the symmetry axis will be controlled by the mean ion concentrations

$$b_{\pm,i} = \frac{2\pi}{C_{\pm}^{\infty} A_1} \int_0^{R_i} r C_{\pm,i}^{(0)}(r) dr. \quad (39)$$

These mean ion concentrations are averaged over the pore cross-section and normalized with the bulk ion concentration C_{\pm}^{∞} . An additional normalization with the area of the wide pore $A_1 = \pi R_1^2$ accounts for the reduction of the total current through the narrow pore due to the reduced cross-section (see Bückner & Hördt, 2013a).

For sufficiently small ζ -potentials, that is, $\zeta \ll k_B T/e$, the radial variation of the electrical potential in the pore can be approximated by solving the linearized Poisson-Boltzmann equation in cylindrical coordinates,

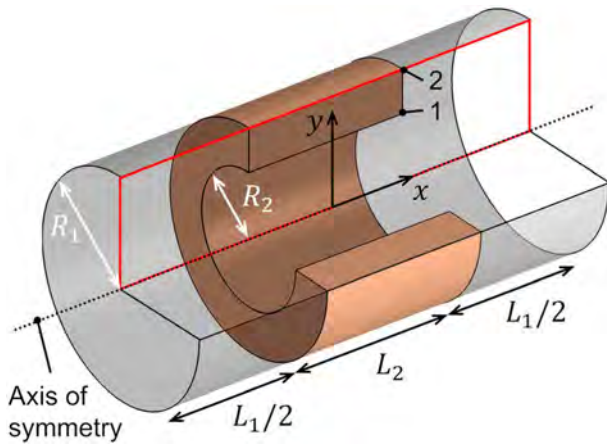


Figure 8. Three-dimensional sketch of the geometrical setup used for the numerical simulation of membrane polarization in a pore constriction. The two wide cylinders of length $L_1/2$ and radius R_1 and the narrow cylinder of length L_2 and radius R_2 are saturated with electrolyte solution. The volume around the narrow cylinder belongs to the nonconducting matrix with dielectric constant ϵ_i . The red rectangle marks the actual two-dimensional model domain.

which gives (Hunter, 1981; Bückner & Hördt, 2013a)

$$U_a^{(0)}(r) = \zeta \frac{J_0(i\kappa r)}{J_0(i\kappa R)}, \quad (40)$$

where J_0 is the Bessel function of the first kind and order zero. The radial variation of the ion concentrations $C_{\pm i}^{(0)}(r)$ are obtained by inserting $U_a^{(0)}(r)$ into equation (6).

For the typically much higher ζ -potential values of up to -100 mV on silica surfaces (here, $\Sigma = -0.01$ C/m²), the solution of the linearized Poisson-Boltzmann equation becomes imprecise. If we instead limit our treatment to sufficiently wide pore radii, that is, $\kappa R_i \gg 1$, we can make use of Bikerman's equation 26, which is more adequate for highly charged surfaces. The dimensionless mean ion concentrations can then be approximated by

$$b_{\pm i} \approx \frac{A_i}{A_1} \left(\frac{\pm 2\Sigma_{d\pm}^{(0)}}{eC_{\pm}^{\infty}R_i} + 1 \right). \quad (41)$$

Either of these definitions of $b_{\pm i}$, that is, equation 39 proposed by Bückner and Hördt (2013a) or equation (41) proposed here, can be used to express the effective transference numbers

$$t_{\pm 1} = \frac{b_{\pm i}}{b_{+i} + b_{-i}}. \quad (42)$$

By means of this approximation, the three-dimensional cylindrical pore system is collapsed to a sequence of one-dimensional pores, the frequency-dependent impedance of which was derived by Marshall and Madden (1959). Following Bückner and Hördt (2013b) and Bückner et al. (2017), the Marshall-Madden impedance can be written as

$$Z(\omega) = \frac{2}{\sigma_a} \left[\frac{L_1}{b_{+1} + b_{-1}} + \frac{L_2}{b_{+2} + b_{-2}} + \frac{8D(t_{+1} - t_{+2})^2}{\frac{L_1}{\tau_1} \sqrt{i\omega\tau_1} \coth \sqrt{i\omega\tau_1} + \frac{L_2}{\tau_2} \sqrt{i\omega\tau_2} \coth \sqrt{i\omega\tau_2}} \right], \quad (43)$$

where the frequency dependence is controlled by the two time constants

$$\tau_i = \frac{L_i^2}{2D} S_i \quad \text{with} \quad S_i = \frac{1}{4b_{+i}t_{-i}}. \quad (44)$$

In order to stress the structural similarities between these two relaxation times and the relaxation time of the diffuse layer around spherical grains, we can rewrite the dimensionless mean ion concentrations $b_{\pm i}$ defined in equation (41) in terms of a Dukhin number for cylindrical geometries, which we define as

$$Du(\zeta, R_i) = \frac{\sigma_d(R_i)}{2\sigma_a} = \frac{|\sigma_{d+}(R_i) + \sigma_{d-}(R_i)|}{2\sigma_a}. \quad (45)$$

In analogy to equation (25), the surface conductivities write $\sigma_{d\pm}(R_i) = \pm 2\mu\Sigma_{d\pm}^{(0)}/R_i$. The coefficients S_i take the form

$$S_i = \frac{A_1}{2A_i} \frac{[2Du(\zeta, R_i) + 1]\sigma_a^2}{[2\sigma_{d+}(R_i) + 1][2\sigma_{d-}(R_i) + 1]}. \quad (46)$$

Besides the factor $A_1/(2A_i)$ and the factors 2, with which the Dukhin numbers and the individual conductivities $\sigma_{d\pm}$ are multiplied, this definition of S_i is equivalent to the definition of S in equation (34), which controls the relaxation time of the diffuse layer around spherical particles.

4.2. Numerical Model for the Coupled Polarization

The numerical modeling is carried out using COMSOL Multiphysics. Again, the cylindrical symmetry of the problem permits limiting the computation to a two-dimensional model domain (red rectangle in Figure 8).

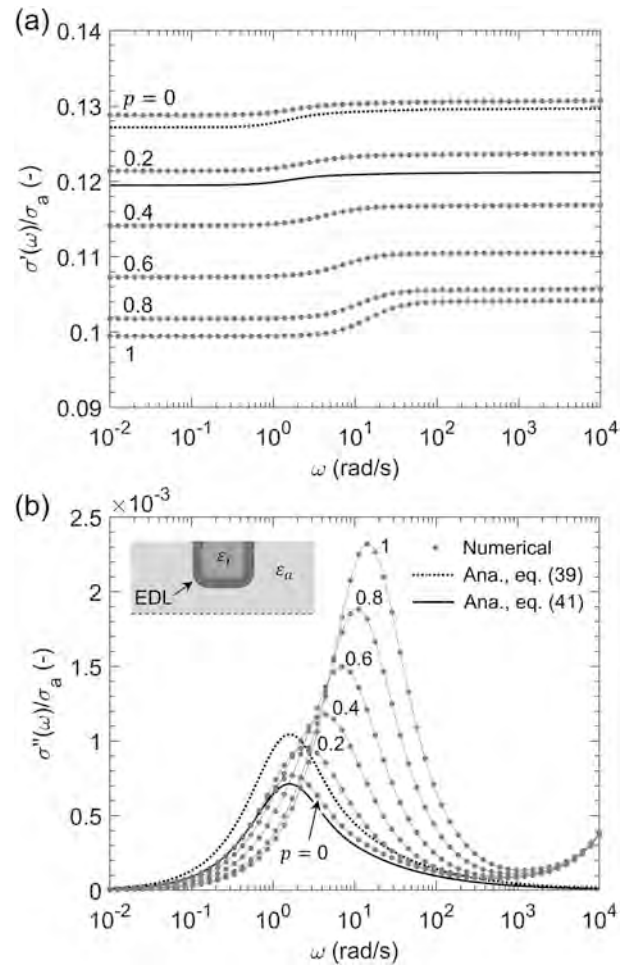


Figure 9. Complex-conductivity spectra of the membrane-polarization model for different ratios $p = -\Sigma_S^{(0)}/\Sigma$. Complex-valued conductivity in terms of real (a) and imaginary parts (b) normalized to the bulk conductivity σ_a . Numerical results (gray circles, lines are to guide the eye only) for all values of p are displayed along with the analytical models for $p = 0$ after Bückner and Hördt (2013a) using the average ion concentrations from equation (39) (dotted line) and from equation (41) (solid line). The sketch in (b) shows that the electrical double layer (EDL) is discontinuous in the wide pore. Pore lengths and radii are $L_1 = 90 \mu\text{m}$, $L_2 = 10 \mu\text{m}$, $R_1 = 2 \mu\text{m}$, and $R_2 = 0.2 \mu\text{m}$; all other parameter values are the same as in Figure 6.

The systems of PDEs describing the static and the frequency-dependent parts of the polarization problem remain unchanged, and only boundary conditions and finite-element mesh need to be adapted to the different geometry.

The boundary conditions for the static solution, that is, equations (14) and (15), merge into $U^{(0)} = 0$ on the left and right boundary; $[\epsilon_0 \epsilon_i \nabla U_i^{(0)} - \epsilon_0 \epsilon_a \nabla U_a^{(0)}] \mathbf{n} = -\Sigma_d^{(0)}$ on the solid-liquid interface; and $\partial U^{(0)}/\partial y = 0$ on the axis of symmetry and the entire top boundary. This setup represents a discontinuous EDL, which only covers the surfaces of the volume shown in brown in Figure 8. Additionally, we compute the response of a setup, where the EDL is continuous in the wide pore and the boundary condition on the corresponding parts of the top boundary writes $[-\epsilon_0 \epsilon_a \nabla U_a^{(0)}] \mathbf{n} = -\Sigma_d^{(0)}$.

For the frequency-dependent part of the problem, the boundary conditions described in equations (16) through (20) are adjusted as follows: $\delta n_{\pm} = 0$ and $\delta U_a = \pm E_0 L$ on the left and right boundary, respectively; $\mathbf{J}_{\pm} = 0$ and $\partial \delta U / \partial y = 0$ on the axis of symmetry and the top boundary; equations (18) through (20) remain unchanged on the solid-liquid interface. In the setup with the continuous EDL, the boundary conditions on those parts of the top boundary, which delimit the wide pore, are given by the unchanged zero-flux condition (19) and the continuity of the displacement current, which here writes $-\epsilon_0 \epsilon_a \nabla \delta U_a(\mathbf{r}_S) \cdot \mathbf{n} = \delta \Sigma_S(\mathbf{r}_S)$.

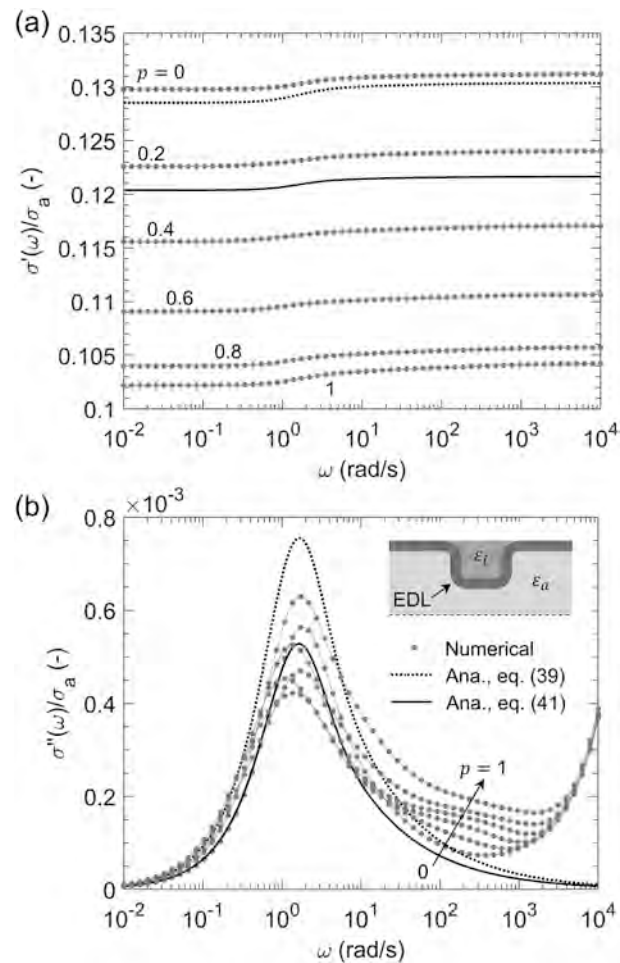


Figure 10. Complex-conductivity spectra of the membrane-polarization model with a continuous electrical double layer (EDL) in terms of the normalized real (a) and imaginary conductivity (b). Numerical results (gray circles lines are to guide the eye only) for different values of p are displayed along with the analytical models for $p = 0$ after Bückner and Hördt (2013a) using the average ion concentrations from equation (39) (dotted line) and from equation (41) (solid line). The sketch in (b) shows the continuous EDL in the wide pore; all other parameter values are the same as in Figure 9.

In order to avoid artifacts related to sharp corners covered by an EDL, the vertex 1 in Figure 8 is rounded off for the model with a discontinuous EDL, whereas the vertices 1 and 2 are rounded off for the model with a continuous EDL. In both cases, the radius of curvature is $(R_1 - R_2)/2$. For further technical details on the implementation, see the appendix.

The effective conductivity of the model can be obtained from numerically integrating the total ion flux densities through the left (or right) boundary. The resulting expression is equal to equation (37), if L substituted by R_1 . In the model with the continuous EDL, the surface current through the Stern layer has to be considered, too. The corresponding conductivity increment $-2/(E_0 R_1)[D_S \partial \delta \Sigma_S / \partial x + \mu_S \Sigma_S \partial \delta U_S / \partial x]$ has to be added to σ_{mod}^* . The analytical expression for the effective conductivity writes $\sigma_{\text{eff}}(\omega) = (L_1 + L_2)/Z(\omega)$, where $Z(\omega)$ is defined in equation (43).

4.3. Comparison of Analytical and Numerical Solution

The effective-conductivity spectra obtained from the model with the discontinuous EDL are shown in Figure 9. In the analytical models (for the case $p = 0$), the absence of the EDL in the wide pore has to be taken into account by setting $b_{\pm,1} = 1$ instead of using equation (39) or (41). The length of the narrow pore $L_2 = 10 \mu\text{m}$ was selected to match the diameter of the spherical particle treated above; the length of the wide pore $L_1 = 90 \mu\text{m}$ as well as the two pore radii $R_1 = 2 \mu\text{m}$ and $R_2 = 0.2 \mu\text{m}$ were adjusted to achieve a significant polarization response. As discussed in more detail in Hördt et al. (2017), the polarization magnitude of

the model by Bückner and Hördt (2013a) largely depends on the relation between the two ratios R_1/R_2 and L_1/L_2 .

In Figure 9a, we observe a similar variation of the magnitude of σ' with the ratio p as for the polarization around a spherical particle. In both cases, the surface conductivity increases σ' if the countercharges are mainly located in the diffuse layer. At low frequencies, the Stern layer polarizes and does not contribute to σ' ; at high frequencies, its contribution is limited by the low ion mobility in the Stern layer (remember that $\mu_S = \mu/10$). Moreover, the variation of the imaginary part σ'' with p (Figure 9b) is similar to the one observed for the spherical particle. Again, the σ'' peak increases with the amount of countercharges located in the Stern layer, that is, with increasing p , and shifts toward higher angular frequencies.

Figure 9 also shows that computing the mean ion concentrations from equation (41) instead of equation (39) improves the agreement with the numerical solution: for $p = 0$, the relative deviations between the analytical and the numerical σ'' curves are $<20\%$ for the modified and $<50\%$ for the original model at angular frequencies <100 rad/s. Because the analytical model does not consider Maxwell-Wagner polarization, which becomes dominant at high frequencies, the misfit increases at angular frequencies >100 rad/s. The original membrane polarization model, however, matches the real part (σ') better. Here, the relative deviation between the analytical models and the numerical solution are $\approx 7\%$ for the modified and $<1\%$ for the original model.

The fair overall agreement of analytical and numerical curves for $p = 0$ confirms the validity of the model developed by Bückner and Hördt (2013a) for a sole diffuse-layer polarization. The same authors also proposed a simple modification of the mean counterion concentration to take into account the contribution of the Stern layer. However, their model rather predicts a continuous decrease of the polarization magnitude with increasing p and practically a constant characteristic frequency (not shown here for brevity), indicating that the Stern-layer polarization is more complex than assumed by Bückner and Hördt (2013a).

The polarization response changes significantly if the EDL is assumed to be continuous in the wide pore (Figure 10). Here, magnitude and characteristic frequency of the main σ'' peak located around 2 rad/s decrease only slightly from $p = 0$ to $p = 0.4$ and increase not much steeper for larger values of p . In comparison to the significant variation of the main peak observed in Figure 9 for the discontinuous EDL, here, the σ'' peak remains almost unchanged. Furthermore, at frequencies between 100 and 1,000 rad/s, a smaller secondary polarization peak appears for $p > 0$ and increases monotonically with p . The real part σ' shows the usual decrease of surface conductivity with increasing p . The relative deviations between the numerical results for $p = 0$ and the two analytical models are similar to those reported above for a discontinuous EDL.

5. Discussion

The new analytical model presented here describes Maxwell-Wagner, Stern-layer, and diffuse-layer polarization around spherical grains and permits analyzing the frequency response due to a superposition of all three mechanisms. Numerical and analytical results for typical model parameters consistently confirm the results of earlier studies: The contribution of the diffuse-layer polarization to the macroscopic response is significantly smaller than the one of the Stern-layer polarization (e.g., de Lima & Sharma, 1992; Lesmes & Morgan, 2001). In most practical cases, the polarization of the diffuse layer can therefore safely be neglected.

The comparison of numerical and analytical results also confirmed the strong coupling of the surface charge in the Stern layer with charges in the electrolyte as predicted by Lyklema et al. (1983). The model proposed by Lyklema and coworkers can easily be obtained from the model by Schwarz (1962) by adjusting the relaxation time of the Stern layer: For a charge density in the Stern layer of $\Sigma_S^{(0)} \approx 0.01$ C/m² and a bulk ion concentration of 1 mol/m³, equation (32) predicts a reduction of the relaxation time by a factor $M \approx 6.4$. This effect can also be interpreted in terms of an effective diffusion coefficient $D_S^{\text{eff}} = D_S M$, which in our case (i.e., $D_S = D/10$) is only a factor ≈ 2 smaller than the diffusion coefficient of the ions in the bulk electrolyte.

This observation is of particular interest, as it offers an explanation for the large diffusion coefficients D_S needed to adjust the model by Leroy et al. (2008) to measured complex-conductivity spectra. The model by Leroy and coworkers does not include the correction of the relaxation time proposed by Lyklema et al. (1983). Thus, it often requires the assumption of similar diffusion coefficients in Stern layer and bulk electrolyte (e.g., Leroy & Revil, 2009; Leroy et al., 2008; Revil & Florsch, 2010; Schmutz et al., 2010). Independent determinations of the diffusion coefficient in the Stern layer from experimental surface-conductivity and

particle-mobility data, however, normally result in a reduction of the counterion mobility by a factor 10 or larger (e.g., Zukoski & Saville, 1986; Revil & Glover, 1998). A recent extension of the model by Leroy et al. (2008) already considers the corrected relaxation time and successfully adjusts the polarization response of calcite precipitations on glass beads (Leroy et al., 2017). Together with our findings that support the theory by Lyklema et al. (1983), this indicates that the difference between the predictions of the two experiments could be reduced significantly, if the Stern-layer relaxation time used in the model by Leroy et al. (2008) (and subsequent studies) was replaced by the one defined in equations (31) and (32).

Although the correction of the relaxation time might be able to justify the (to date) unexplained assumption inherent to the model by Leroy et al. (2008), it also questions the often-used simple relation between relaxation time and grain size by introducing an additional dependence on chemical properties of pore fluid and solid surface: The coefficient M strongly depends on the electrolyte concentration and the surface-charge density in the Stern layer. Consequently, besides the grain diameter and the diffusion coefficient in the Stern layer, variations of experimentally determined relaxation times might partly be due to variations of these chemical parameters.

We have also applied our finite-element model to study membrane polarization, which had not been investigated in the same detail as the polarization around spherical grains before. In the limiting case of a sole diffuse-layer polarization, we found that an improved analytical formulation based on the work by Marshall and Madden (1959) and Bückner and Hördt (2013a) yields a good agreement with the numerical results. However, the analytical model does not reproduce the numerical results for the coupled polarization of diffuse and Stern layer. Consequently, the incorporation of the Stern-layer polarization in the model by Bückner and Hördt (2013a) is insufficient in its current form, and our numerical results can contribute substantially to our understanding of the role of the Stern layer in the context of membrane polarization.

Even in the pore-constriction geometry, the polarization of the Stern layer can control the frequency response, especially if the EDL is discontinuous. Certain similarities of the coupled responses of both geometries stand out—namely, the generally larger response of the Stern-layer polarization and the simultaneous increase of characteristic frequency and polarization magnitude with the surface charge in the Stern layer. However, we also observed that the particular geometrical configuration of the EDL in the pore-constriction model can largely reduce the difference between the respective magnitudes of diffuse-layer and Stern-layer polarization: If the EDL becomes continuous, the contributions of both mechanisms can become practically the same.

Although we have taken an important step toward this long-term goal, it is beyond the scope of the present study to provide an analytical model that integrates membrane polarization and the polarization around spherical grains. Nevertheless, we can put our results into a broader context and draw some preliminary conclusions regarding the relative contributions of the various polarization mechanisms.

Grain-based polarization models are best suited for the modeling of dilute suspensions of dielectric particles because they only account for grain-electrolyte interactions and largely ignore grain-grain interactions. For practical purposes, these models can even be applied to high particle concentrations, and the responses of unconsolidated granular media (e.g., Leroy et al., 2008) have been matched successfully with this type of models. For typical parameter combinations, the polarization of isolated grains is only controlled by the Stern layer, and contributions of a simultaneously occurring diffuse-layer polarization can be neglected.

With increasing degree of compaction and cementation, grain-grain interactions are expected to become more important (e.g., Lesmes & Morgan, 2001). These interactions include (i) the interaction of polarization dipoles of adjacent grains as well as (ii) percolating diffuse and Stern layers. Based on the good agreement between experimental data and the responses of grain-based polarization models, the interaction of polarization dipoles can safely be neglected. To date, the effect of percolating diffuse and Stern layers on the polarization response has only been touched in passing: For instance, Leroy et al. (2008) argue that a diffuse layer above the percolation threshold cannot polarize and only consider an increase of the low-frequency conductivity. In the same sense, they postulate that the Stern layers of adjacent particles are discontinuous because the model based on the Stern-layer polarization accurately describes experimental observations. While the result of this argumentation—the small contribution of the diffuse-layer polarization and the dominating role of the Stern layer—agrees with our findings, the physical picture should be reconsidered: Around isolated particles, the polarization of the diffuse layer is negligible, too, such that it is not necessary

to assume that the diffuse layers are percolating. In addition, we have shown that even in the case of continuous (or percolating) diffuse and Stern layers in the pore-constriction model, both layers can polarize. Consequently, the discontinuity of neither of the two layers is needed to generate a polarization response.

The similarity of the polarization response of grain-based and pore-constriction geometry indicates a gradual transition between the two models with increasing degree of compaction and cementation. As long as the EDLs are assumed to be discontinuous, the Stern layer dominates the polarization response of both models, which makes the distinction between effects related to individual grains and effects related to pore constrictions a mere question of the point of view. Our results suggest that responses caused by pore constrictions, that is, typical membrane-polarization responses, can—at least to a certain degree—be adjusted using grain-based models and vice versa. This is particularly plausible, if we consider that in granular media made of near-spherical particles, pore diameters and pore lengths are of the same order of magnitude as the typical grain sizes and thus all relaxation times are controlled by similar characteristic lengths.

6. Conclusions

We have investigated the low-frequency electrical conductivity of porous media by means of analytical and numerical models for single-grain and pore-constriction geometries. Our results allowed us to assess the relative contributions of polarization mechanisms originating from the diffuse part and the Stern layer of the EDL covering charged mineral surfaces. Because our models also include Maxwell-Wagner polarization, they are useful for a broad frequency range.

To match our numerical results, we assembled a new analytical model for the grain-based geometry by combining the Dukhin-Shilov model (Dukhin & Shilov, 1974), which accounts for the diffuse-layer polarization, with Schurr's Stern-layer polarization model (Schurr, 1964) including a correction of the Stern-layer relaxation time proposed by Lyklema et al. (1983). The corrected relaxation time, which accounts for the interaction of the charges in the Stern layer with the electrolyte solution, significantly improves the agreement of analytical and numerical results. Without the correction, untypically high diffusion coefficients of the counterions in the Stern layer have to be assumed to fit the spectral response. For typical model parameters, the relative contribution of the diffuse-layer polarization was seen to be insignificant in comparison to the large response of the Stern layer.

Our numerical results for the pore-constriction geometry agree with the analytical membrane-polarization model by Bückner and Hördt (2013a) if we relate the mean ion concentrations of the cylindrical pores to Bikerman's expression for the surface conductivity of highly charged surfaces (Bikerman, 1933) and as long as no Stern layer is considered. We also propose detailed model to describe Stern-layer polarization in a typical membrane-polarization geometry. As in the grain-based model, the diffuse layer makes a much smaller contribution to the total response than the Stern layer—at least as long as the charged surfaces are below the percolation threshold; that is, the individual EDLs are not interconnected at the system scale.

In conclusion, the responses of grain-based and pore-constriction geometries are more similar than usually assumed, particularly if the polarization of both parts of the EDL are taken into account. Below the percolation threshold, the Stern-layer dominates the macroscopic response, but as soon as the EDL becomes percolating, this dominance breaks down and both mechanisms contribute to a similar extend. More detailed studies on specific pore geometries are required to conclusively assess the relative importance of the different polarization mechanisms, but our study is a significant step toward this long-term goal and sets the basis for extensive numerical studies.

Appendix A: Numerical Implementation

The COMSOL PDE interface in coefficient form allows the definition of PDEs and systems of PDEs of the general type

$$e_a \frac{\partial^2 u}{\partial t^2} + d_a \frac{\partial u}{\partial t} + \nabla \cdot (-c \nabla u - a u + \gamma) + \beta \cdot \nabla u + a u = f \quad (\text{A1})$$

with the general boundary conditions

$$-\mathbf{n} \cdot (-c \nabla u - a u + \gamma) = g - q u \quad \text{and} \quad (\text{A2})$$

$$u = s, \tag{A3}$$

where u denotes the dependent variable and \mathbf{n} the inward-pointing unit normal vector.

Due to their cylindrical symmetry, the problems can be solved on two-dimensional domains (see Figures 5 and 8) with coordinates $\mathbf{r} = (x, y)^T$ and gradient operator $\nabla = (\partial/\partial x, \partial/\partial y)^T$. As explained in more detail in Bückner et al. (2018), multiplying all coefficients in equations (A1) and (A2) by y yields a transformation to cylindrical coordinates.

A1. Static Solution

The static problem set up by equations (6) and (7) is implemented by setting $u_1 = U^{(0)}(\mathbf{r})$, $c_1 = y\epsilon_0\epsilon_a$, $f_1 = -y2C_{\pm}^{\infty}e \sinh(u_1e/(kT))$ in the electrolyte as well as $c_1 = y\epsilon_0\epsilon_a$ and $f_1 = 0$ in the solid phase. Note that in this appendix, coefficients are assumed to be zero if not specified differently.

The fixed surface-charge boundary condition (15) is realized by setting $g = -y\Sigma_d^{(0)}$ on all charged boundaries. The definition of the zero reference potential, equation (14), depends on the specific model: In the grain geometry, we set $s = 0$ on the left, right, and top boundary; in the membrane geometry, we define the point-wise constraint $u_1 = 0$ at two positions ($x = \pm(L_1 + L_2)/2, y = 0$) located on the left and right boundary, respectively. In this case, standard no-flow boundary conditions are set on the remaining parts of left and right boundary, as well as on the uncharged parts of the top boundary. Because $y = 0$ is the symmetry axis (selecting rotational symmetry in the model setup), no specific boundary conditions are defined on this boundary.

A2. Frequency-Dependent Solution

For the frequency-dependent problem set up by the coupled PDEs (8) and (9), which describe the physics in the electrolyte, the Laplace equation (13), which controls the electrical field in the solid phase, and equation (11), which controls the surface charge in the Stern layer, need to be solved simultaneously. We use the same dependent variable u_2 in the electrolyte and in the solid phase and define suitable PDE coefficients on each of the two subdomains. The variable u_2 writes

$$\mathbf{u}_2 = \begin{bmatrix} u_{21} \\ u_{22} \\ u_{23} \end{bmatrix} = \begin{bmatrix} \delta C_{-}(\mathbf{r}, \omega) \\ \delta C_{+}(\mathbf{r}, \omega) \\ \delta U(\mathbf{r}, \omega) \end{bmatrix}. \tag{A4}$$

Assuming isotropic properties, the coefficient c_2 is a 3-by-3 coefficient matrix. In the electrolyte it writes

$$c_2 = \begin{bmatrix} yD & 0 & -y\mu C_{-}^{\infty} \exp(\frac{e}{kT}u_1) \\ 0 & yD & y\mu C_{+}^{\infty} \exp(-\frac{e}{kT}u_1) \\ 0 & 0 & y\epsilon_0\epsilon_a \end{bmatrix}, \tag{A5}$$

and in the solid phase

$$c_2 = \begin{bmatrix} 0 & 0 & 0 \\ 0 & 0 & 0 \\ 0 & 0 & y\epsilon_0\epsilon_i \end{bmatrix}. \tag{A6}$$

The variable u_1 is the static part of the electrical potential. The coefficient matrix $\underline{\alpha}$ writes

$$\underline{\alpha}_2 = \begin{bmatrix} -y\mu\nabla u_1 & 0 & 0 \\ 0 & y\mu\nabla u_1 & 0 \\ 0 & 0 & 0 \end{bmatrix} \tag{A7}$$

in the electrolyte and is equal to the null matrix in the solid phase. Note that on our two-dimensional modeling domain, each element of the matrix $\underline{\alpha}_2$ is a two-element vector. The matrix \underline{a}_2 is

$$\underline{a}_2 = \begin{bmatrix} yi\omega & 0 & 0 \\ 0 & yi\omega & 0 \\ yF & -yF & 0 \end{bmatrix} \tag{A8}$$

in the electrolyte. In the solid phase, \underline{a}_2 is the same except for the last line, which has to be filled with zeros instead.

Equation (11) describing the perturbation surface-charge density $\delta\Sigma_S$ is solved on the solid-liquid interface only. By means of a so-called lower-dimensional physics interface, the curvature of this interface is taken into account. Because the electrical potential in the Stern layer has to be equal to the potentials δU_i and δU_a on the corresponding boundaries, the only dependent variable on the interface is $u_3 = \delta\Sigma_S(\mathbf{r}_S, \omega)$. The coefficients are $c_3 = yD_S$, $a_3 = yi\omega$, and $\gamma_3 = -y\mu_S\Sigma_S^{(0)}\nabla u_{23}$, where u_{23} denotes the perturbation potentials on the adjacent two-dimensional subdomains.

The boundary condition (16) describing the external excitation and the condition on the perturbation concentrations (17) are realized by setting $\mathbf{s}_2 = (0, 0, \pm E_0 L)^T$. In the membrane-polarization model with the continuous EDL, this boundary is not located at a far distance from the charged surface. However, because of the symmetry of the problem with respect to $x = 0$, we expect the perturbation ion concentrations to vanish in this geometry, too (see, e.g., concentration profiles in Blaschek & Hördt, 2009). For the same reason, the perturbation surface-charge density $\delta\Sigma_S$ is also expected to vanish on the left and right boundary, and we set $s_3 = 0$ (only for a continuous EDL).

On the solid-liquid interface, we implement the zero-flux boundary conditions (19) and the condition on the displacement current (20) by defining $\mathbf{g} = (0, 0, yu_3)^T$.

On the top boundary, we implement zero-flux boundary condition on all three components of u_2 resulting in vanishing normal ion fluxes and a vanishing normal electrical field. In the membrane-polarization model with the continuous EDL, parts of the top boundary represent charged surfaces and are furnished with the corresponding boundary conditions described above. In the membrane-polarization model with the discontinuous EDL, the one-dimensional domain representing the Stern layer ends at the top boundary. In this case, we also define no-flux boundary conditions for u_3 .

A3. Model Discretization

Special care has to be taken with the model discretization: While particle and pore sizes are in the micrometer to millimeter range, the thickness of the diffuse layer is orders of magnitude smaller. We use a special quadrangle boundary-layer mesh at the solid-liquid interface, which in radial direction consists of eight elements with sizes increasing from $\lambda_D/2$ at the surface to $\approx 1.8\lambda_D$ at the outer edge. In tangential direction (i.e., along the boundaries), the elements have a size of $\pi a/400$ in the grain-based model and $R_2/5$ in the pore-constriction geometry. The remaining volume is filled with triangular elements, the maximum size of which increases from $\pi a/400$ (or $R_2/5$) at the edge of the boundary-layer meshes to $L/20$ (or $R_1/5$) at the remote boundaries. For a spherical particle of radius $a = 5\ \mu\text{m}$, this results in a total of $\approx 20,900$ elements, of which 6,400 elements correspond to the boundary-layer mesh. For pore lengths $L_1 = 90\ \mu\text{m}$ and $L_2 = 10\ \mu\text{m}$ and pore radii $R_1 = 2\ \mu\text{m}$ and $R_2 = 0.2\ \mu\text{m}$, the meshes consist of $\approx 14,700$ elements ($\approx 11,000$ for the continuous EDL), of which $\approx 5,200$ ($\approx 7,600$) elements make the boundary-layer mesh.

References

- Atekwana, E. A., & Slater, L. D. (2009). Biogeophysics: A new frontier in earth science research. *Reviews of Geophysics*, 47, RG4004. <https://doi.org/10.1029/2009RG000285>
- Atkins, P., & De Paula, J. (2013). *Elements of Physical Chemistry*. USA: Oxford University Press.
- Bairlein, K., Bückner, M., Hördt, A., & Hinze, B. (2016). Temperature dependence of spectral induced polarization data: experimental results and membrane polarization theory. *Geophysical Journal International*, 205, 440–453.
- Bikerman, J. (1933). Ionentheorie der Elektromose, der Strömungsströme und der Oberflächenleitfähigkeit. *Zeitschrift für Physikalische Chemie A*, 163, 378–394.
- Blaschek, R., & Hördt, A. (2009). Numerical modelling of the IP effect at the pore scale. *Near Surface Geophysics*, 7(5-6), 579–588.
- Börner, F., Schopper, J., & Weller, A. (1996). Evaluation of transport and storage properties in the soil and groundwater zone from induced polarization measurements. *Geophysical Prospecting*, 44(4), 583–601.
- Bruggeman, D. A. G. (1935). Berechnung verschiedener physikalischer Konstanten von heterogenen Substanzen. I. Dielektrizitätskonstanten und Leitfähigkeiten der Mischkörper aus isotropen Substanzen. *Annalen der Physik*, 416(7), 636–664.
- Buchheim, W., & Irmner, G. (1979). Zur Theorie der induzierten galvanischen Polarisation in Festkörpern mit elektrolytischer Porenfüllung. *Gerlands Beiträge zur Geophysik*, 88, 53–72.
- Bückner, M., Flores Orozco, A., Hördt, A., & Kemna, A. (2017). An analytical membrane-polarization model to predict the complex conductivity signature of immiscible liquid hydrocarbon contaminants. *Near Surface Geophysics*, 15(6), 547–562.
- Bückner, M., & Hördt, A. (2013a). Analytical modelling of membrane polarization with explicit parametrization of pore radii and the electrical double layer. *Geophysical Journal International*, 194, 804–813.
- Bückner, M., & Hördt, A. (2013b). Long and short narrow pore models for membrane polarization. *Geophysics*, 78(6), E299–E314.

Acknowledgments

M. Bückner acknowledges the Austrian Federal Ministry of Science, Research and Economy (project Development of Geophysical Exploration Methods for the Characterization of Mine-Tailings Towards Exploitation) and the German Academic Exchange Service (DAAD) for scholarships received for his work on this study. All authors gratefully acknowledge P. Leroy and one anonymous reviewer for their insightful comments that helped to improve the manuscript. Scripts, numerical models, and data used for this manuscript are available at Zenodo (<https://doi.org/10.5281/zenodo.3067277>).

- Bücker, M., Undorf, S., Flores Orozco, A., & Kemna, Andreas. (2018). Electro-chemical polarization around metallic particles-Part 2: The role of diffuse surface charge. *Geophysics*, *84*(2), 1–64.
- Chew, W., & Sen, P. (1982a). Potential of a sphere in an ionic solution in thin double layer approximations. *The Journal of Chemical Physics*, *77*(4), 2042–2044.
- Chew, W., & Sen, P. (1982b). Dielectric enhancement due to electrochemical double layer: Thin double layer approximation. *The Journal of Chemical Physics*, *77*(9), 4683–4693.
- de Lima, O. A., & Sharma, M. M. (1992). A generalized Maxwell-Wagner theory for membrane polarization in shaly sands. *Geophysics*, *57*(3), 431–440.
- DeLacey, E. H., & White, L. R. (1981). Dielectric response and conductivity of dilute suspensions of colloidal particles. *Journal of the Chemical Society, Faraday Transactions 2: Molecular and Chemical Physics*, *77*(11), 2007–2039.
- Dukhin, S., & Shilov, V. (1974). *Dielectric phenomena and the double layer in disperse systems and polyelectrolytes*. New York: Wiley.
- Fixman, M. (1980). Charged macromolecules in external fields. I. The sphere. *The Journal of Chemical Physics*, *72*(9), 5177–5186.
- Flores Orozco, A., Williams, K. H., Long, P. E., Hubbard, S. S., & Kemna, A. (2011). Using complex resistivity imaging to infer biogeochemical processes associated with bioremediation of an uranium-contaminated aquifer. *Journal of Geophysical Research*, *116*, G03001. <https://doi.org/10.1029/2010JG001591>
- Fridrikhsberg, D. A., & Sidorova, M. P. (1961). A study of relationship between the induced polarization phenomenon and the electro-kinetic properties of capillary systems (in Russian). *Vestnik Leningradskogo Universiteta, Seria Chimia*, *4*, 222–226.
- Garcia, A., Grosse, C., & Brito, P. (1985). On the effect of volume charge distribution on the Maxwell-Wagner relaxation. *Journal of Physics D: Applied Physics*, *18*(4), 739.
- Grahame, D. C. (1947). The electrical double layer and the theory of electrocapillarity. *Chemical Reviews*, *41*(3), 441–501.
- Grosse, C., & Shilov, V. N. (1996). Theory of the low-frequency electrorotation of polystyrene particles in electrolyte solution. *The Journal of Physical Chemistry*, *100*(5), 1771–1778.
- Hördt, A., Bairlein, K., Bielefeld, A., Bücker, M., Kuhn, E., Nordsiek, S., & Stebner, H. (2016). The dependence of induced polarization on fluid salinity and pH, studied with an extended model of membrane polarization. *Journal of Applied Geophysics*, *135*, 408–417.
- Hanaï, T. (1960). Theory of the dielectric dispersion due to the interfacial polarization and its application to emulsions. *Kolloid-Zeitschrift*, *171*(1), 23–31.
- Hinch, E. J., Sherwood, J. D., Chew, W. C., & Sen, P. N. (1984). Dielectric response of a dilute suspension of spheres with thin double layers in an asymmetric electrolyte. *Journal of the Chemical Society, Faraday Transactions 2: Molecular and Chemical Physics*, *80*(5), 535–551.
- Hördt, A., Druiventak, A., Blaschek, R., Binot, F., Kemna, A., Kreye, P., & Zisser, N. (2009). Case histories of hydraulic conductivity estimation with induced polarization at the field scale. *Near Surface Geophysics*, *7*(5–6), 529–545.
- Hördt, A., Bairlein, K., Bücker, M., & Stebner, H. (2017). Geometrical constraints for membrane polarization. *Near Surface Geophysics*, *15*, 579–592.
- Hunter, R. (1981). *Zeta potential in colloid science: Principles and applications*. London: Academic Press.
- Kemna, A., Binley, A., Cassiani, G., Niederleithinger, E., Revil, A., Slater, L., et al. (2012). An overview of the spectral induced polarization method for near-surface applications. *Near Surface Geophysics*, *10*(6), 453–468.
- Kijlstra, J., van Leeuwen, H. P., & Lyklema, J. (1992). Effects of surface conduction on the electrokinetic properties of colloids. *Journal of the Chemical Society, Faraday Transactions*, *88*(23), 3441–3449.
- Kosmulski, M. (2006). Electric charge density of silica, alumina, and related surfaces. In P. Somasundaran (Ed.), *Encyclopedia of surface and colloid science* (Vol. 3, pp. 1857–1867). New York, London: CRC press.
- Leroy, P., Li, S., Jougnot, D., Revil, A., & Wu, Y. (2017). Modelling the evolution of complex conductivity during calcite precipitation on glass beads. *Geophysical Journal International*, *209*(1), 123–140.
- Leroy, P., & Revil, A. (2004). A triple-layer model of the surface electrochemical properties of clay minerals. *Journal of Colloid and Interface Science*, *270*(2), 371–380.
- Leroy, P., & Revil, A. (2009). A mechanistic model for the spectral induced polarization of clay materials. *Journal of Geophysical Research*, *114*, B10202. <https://doi.org/10.1029/2008JB006114>
- Leroy, P., Revil, A., Kemna, A., Cosenza, P., & Ghorbani, A. (2008). Complex conductivity of water-saturated packs of glass beads. *Journal of Colloid and Interface Science*, *321*(1), 103–117.
- Lesmes, D. P., & Morgan, F. D. (2001). Dielectric spectroscopy of sedimentary rocks. *Journal of Geophysical Research*, *106*(B7), 13,329–13,346.
- Lyklema, J., Dukhin, S., & Shilov, V. (1983). The relaxation of the double layer around colloidal particles and the low-frequency dielectric dispersion: Part I. Theoretical considerations. *Journal of Electroanalytical Chemistry and Interfacial Electrochemistry*, *143*(1–2), 1–21.
- Marshall, D. J., & Madden, T. R. (1959). Induced polarization, a study of its causes. *Geophysics*, *24*(4), 790–816.
- Maxwell, J. C. (1892). *A treatise on electricity and magnetism* (3rd ed.). Oxford, England: Clarendon.
- O’Konski, C. T. (1960). Electric properties of macromolecules. V. Theory of ionic polarization in polyelectrolytes. *The Journal of Physical Chemistry*, *64*(5), 605–619.
- Revil, A., Cathles, L., Losh, S., & Nunn, J. (1998). Electrical conductivity in shaly sands with geophysical applications. *Journal of Geophysical Research*, *103*(B10), 23,925–23,936.
- Revil, A., & Florsch, N. (2010). Determination of permeability from spectral induced polarization in granular media. *Geophysical Journal International*, *181*(3), 1480–1498.
- Revil, A., & Glover, P. W. J. (1997). Theory of ionic-surface electrical conduction in porous media. *Physical Review B*, *55*(3), 1757.
- Revil, A., & Glover, P. W. J. (1998). Nature of surface electrical conductivity in natural sands, sandstones, and clays. *Geophysical Research Letters*, *25*(5), 691–694.
- Robinson, D. A., & Friedman, S. P. (2003). A method for measuring the solid particle permittivity or electrical conductivity of rocks, sediments, and granular materials. *Journal of Geophysical Research*, *108*(B2), 2076. <https://doi.org/10.1029/2001JB000691>
- Schmutz, M., Revil, A., Vaudelet, P., Batzle, M., Viñao, P. F., & Werkema, D. (2010). Influence of oil saturation upon spectral induced polarization of oil-bearing sands. *Geophysical Journal International*, *183*(1), 211–224.
- Schurr, J. (1964). On the theory of the dielectric dispersion of spherical colloidal particles in electrolyte solution. *The Journal of Physical Chemistry*, *68*(9), 2407–2413.
- Schwarz, G. (1962). A theory of the low-frequency dielectric dispersion of colloidal particles in electrolyte solution. *The Journal of Physical Chemistry*, *66*(12), 2636–2642.
- Shilov, V. N., Delgado, A. V., Gonzalez-Caballero, F., & Grosse, C. (2001). Thin double layer theory of the wide-frequency range dielectric dispersion of suspensions of non-conducting spherical particles including surface conductivity of the stagnant layer. *Colloids and Surfaces A: Physicochemical and Engineering Aspects*, *192*(1), 253–265.

- Somasundaran, P. (2006). *Encyclopedia of surface and colloid science* (Vol. 2). New York, London: CRC press.
- Stebner, H., Halisch, M., & Hördt, A. (2017). Simulation of membrane polarization of porous media with impedance networks. *Near Surface Geophysics*, *15*, 563–578.
- Titov, K., Kemna, A., Tarasov, A., & Vereecken, H. (2004). Induced polarization of unsaturated sands determined through time domain measurements. *Vadose Zone Journal*, *3*(4), 1160–1168.
- Titov, K., Komarov, V., Tarasov, V., & Levitski, A. (2002). Theoretical and experimental study of time domain-induced polarization in water-saturated sands. *Journal of Applied Geophysics*, *50*(4), 417–433.
- Volkman, J., & Klitzsch, N. (2010). Frequency-dependent electric properties of microscale rock models for frequencies from one millihertz to ten kilohertz. *Vadose Zone Journal*, *9*(4), 858–870.
- Wagner, Karl W. (1914). Erklärung der Dielektrischen Nachwirkungsvorgänge auf Grund Maxwellscher Vorstellungen. *Electrical Engineering (Archiv für Elektrotechnik)*, *2*(9), 371–387.
- Wainwright, H. M., Flores Orozco, A., Bucker, M., Dafflon, B., Chen, J., Hubbard, S. S., & Williams, K. H. (2015). Hierarchical Bayesian method for mapping biogeochemical hot spots using induced polarization imaging. *Water Resources Research*, *52*, 533–551. <https://doi.org/10.1002/2015WR017763>
- Zukoski, C. F., & Saville, D. A. (1986). The interpretation of electrokinetic measurements using a dynamic model of the stern layer: II. Comparisons between theory and experiment. *Journal of colloid and interface science*, *114*(1), 45–53.

Assistant Prof. Dr. rer. nat. Adrián Flores Orozco

adrian.flores-orozco@geo.tuwien.ac.at

Business Address

Wiednerhauptst. 8-10
1040-Vienna, Austria
tel. +4315880112834

Private address

Strohgasse 43, Nr. 10
1030-Vienna, Austria
tel. +4367763487555

Personal information

Date of birth: 17.01.1980
Nationality: Mexican

PROFILE

I am a geophysicist interested in understanding the feedback between bio-geochemical processes and geophysical signatures. I have more than ten years of experience in the application of geophysical methods in hydrogeological and environmental investigations. My area of expertise are the electrical and electromagnetic methods, with special emphasis in the Spectral induced Polarization. Currently I am working on the mapping of biogeochemical activity in shallow aquifers and contaminated sites.



CURRENT POSITION

Assistant Professor at the Department of Geodesy and Geoinformation, TU-Wien; Vienna, Austria, 03.2016 – present

Head of the Geophysics Research Division at the Department of Geodesy and Geoinformation, TU-Wien; Vienna, Austria, 01.2016 – present

WORKING EXPERIENCE

University Assistant (Post-Doc) in the Geophysics Research Division, Department of Geodesy and Geoinformation, TU-Wien; Vienna, Austria, 05.2013 –12.2015

Postdoctoral Researcher in the Applied Geophysics Department, University of Bonn; Bonn, Germany, 09.2012 – 04.2013

Doctoral Researcher in Applied Geophysics Department, University of Bonn; Bonn, Germany, 01.2008 – 08.2012

EDUCATION

Ph.D. Geophysics

University of Bonn; Bonn, Germany — 2008-2012

Final Grade: magna cum laude ("very good")

Ph.D. Thesis: "Characterization of contaminated sites and monitoring of processes accompanying bioremediation using spectral induced polarization imaging"

Referent: Prof. Dr. Andreas Kemna

Co-referent: Prof. Dr. Andrew Binley

M.Sc., Applied Environmental Geosciences

University of Tübingen; Tübingen, Germany — 2004-2006

Final Grade: 1.7 (maximum: 1)

M.Sc. Thesis: "Comparison of DC-Surface, Direct-Push and Borehole Geoelectrical surveys – Monitoring measurements during the MOSAM test in Leipzig"

Dipl. Ing. (Geophysics)

Universidad Nacional Autonoma de Mexico; Mexico City, México — 1997-2004

Final Grade: 9.32 (maximum: 10)

B.Sc. Thesis: "Comparison of Vertical Electrical Surveys (VES) and Transient ElectroMagnetic (TEM) Surveys for the characterization of the aquifer in San Miguel de Allende, Queretaro, Mexico"

SERVICE TO THE PROFESSION

Member of the technical committee of the 5th International Workshop on Induced Polarization, 2018

Guest-Editor for the Near Surface Geophysics Special Issue on Induced Polarization, 2017

Member of the scientific committee of the 4th International Workshop on Geoelectrical Monitoring - GELMON, 2017

Member of the scientific committee of the 4th International Workshop on Induced polarization, 2016

Member of the executive board from the Austrian Geophysical Society (AGS), 2016 – present

Member of the organization committee of the 1th International Workshop on Induced Polarization, 2009

External examiner for PhD defenses

- David Caterina: "Towards a better understanding of time-lapse electrical resistivity properties associated to organic contaminants and bioremediation processes in the subsurface", 2014 - University of Liege, Belgium

Scientific reviewer for

- Journals: Geophysics, Near Surface Geophysics, Journal of Applied Geophysics, Water Resources Research, Natural Hazards, Geophysics Journal International, etc.
- Research projects: Israel Science Foundation (ISF); Research Foundation – Flanders (FWO)

AREAS OF SCIENTIFIC INTEREST

- Biogeophysics: Understanding the bio-geochemical controls on the response measured by means of electrical and electromagnetic methods. The development of adequate models linking geophysical and biogeochemical data.
- Limnogeophysics: Application of waterborne geophysical methods to improve the understanding of surface-groundwater interactions in rivers, lakes, coastal aquifers.
- Contaminant hydrology: Application of electrical and electromagnetic methods for the characterization of contaminant sites and the monitoring of natural and stimulated transformation of contaminants transformations.
- Engineering geology: Combined application of electrical, electromagnetic and seismic methods (active and passive) for the characterization of mountain slopes for both geotechnical and hydrogeological investigations, with special focus on assessing the vulnerability to landslide and rock falls.

THIRD-PARTY FUNDED RESEARCH PROJECTS**SIP-ICE – Improved ice quantification at alpine permafrost sites based on electrical and electromagnetic measurements of spectral induced polarization**

Funded by the Swiss National Science Foundation (SNF) – German Research Foundation (DFG) – DACH collaborative proposal

Duration: 01.08.2019 – 31.7.2021

Project Partner, Joint supervisor PhD Student

SEIS-SIP - Research collaboration between the TU-Wien Research group Geophysics and the Pöyry Infra GmbH

Based on joint activities in the private sector, funded by Pöyry Infra GmbH

Duration: 01.01.2017 – 31.12.2020

Principal investigator

GEOCON - GEOphysical methods for the characterization of CONTaminated sites

Funded by the Italy-Israel Scientific and Technological Cooperation Programme

Duration: 01.02.2019 – 31.07.2019

Project Partner

HYDROSLIDE: HYDRO-geophysical observations for an advanced understanding of clayey landsLIDES

Funded by Austrian Science Fund (FWF) – Agence Nationale de la Recherche (ANR), 2016
 French-Austrian Joint Projects Call
 Duration: 01.04.2016 – 31.12.2019
 Co-Principal Investigator

Explo-Graf -Development of new geophysical methods for the prospection of graphite-rich formations

Funded by BMWF (Austrian) Federal Ministry of Science, Research and Economy, Raw Materials Initiative Call
 Duration: 01.12.2017 – 31.12.2019
 Co-Principal Investigator

TU-Seisnet - National Collaboration for the transfer in real-time of seismologic data between the TU-Wien and the ZAMG

Funded by the Zentralanstalt für Meteorologie und Geodynamik — ZAMG
 Duration: 01.06.2017 – 30.12.2019
 Principal Investigator

GeoCHARTH - Geophysikalische Charakterisierung von tonigen Hangrutschungen,

Funded by the Amt der Niederösterreichischen Landesregierung (Office of the Provincial Government of Lower Austria)
 Duration: 07.09.2017 – 01.06.2018
 Principal Investigator

GEO-tief: Geophysical - Hydrogeological characterization of deep flowpaths

Funded by TU-Vienna, Innovative Projects – Infrastructure Call 2017
 Principal Investigator

POTHAL: Development of geophysical exploration methods for the characterization of mine-tailings towards exploitation

Funded by BMWF (Austrian) Federal Ministry of Science, Research and Economy, Raw materials initiative
 Duration: 01.10.2016 – 30.09.2018
 Co-Principal Investigator

GeoHIT: Geophysical-Hydrological Investigation technique

Funded by TU-Vienna, Innovative Projects – Infrastructure Call 2015
 Principal Investigator

ATMOperm: Atmosphere – permafrost relationship in the Austrian Alps – atmospheric extreme events and their relevance for the mean state of the active layer

Funded by the Austrian Academy of Sciences (ÖAW), Research Program Earth System Sciences (ESS)

Duration: 1.12.2015 - 30.11.2018

Co-Principal Investigator

Delineation of biogeochemical “Hot-spots” in fluvial environments

Funded by Lawrence Berkeley National Laboratory - Subcontract of US DOE

Duration: 01.06.2013 – 30.01.2014

Principal Investigator

AWARDS

2018 Ludger Mintro Awaras from the European Association of Geoscientists and Engineers (EAGE) for the paper “An analytical membrane-polarization model to predict the complex conductivity signature of immiscible liquid hydrocarbon contaminants”, published in Near Surface Geophysics, 15 (6), 2017

Best paper Award 2015 from the Faculty of Mathematic and Geoinformation, TU-Wien: “Monitoring the injection of microscale zero-valent iron particles for groundwater remediation by means of complex electrical conductivity imaging”

Special mention for Outstanding Student Paper Award (OSPA) Fall 2011 AGU Meeting: "Delineation of Subsurface Hydrocarbon Contamination at a Former Hydrogenation Plant Using Spectral Induced Polarization Imaging", co-authored by Andreas Kemna, Christoph Oberdoerster, Ludwig Zschornack, Carsten Leven, Peter Dietrich, and Holger Weiss, 2011

CONACyT-DAAD Master’s program scholarship, 2004 – 2006

CONACyT-DAAD Doctoral program scholarship, 2006 – 2010

PEER-REVIEWED PUBLICATIONS

1. **Flores Orozco A.**, Micic V., Bücken, M., Gallistl, J., Hofmann, T., and Nguyen F. 2019. Complex-conductivity monitoring to delineate aquifer pore clogging during nanoparticles injection. *Geophysical Journal International* 218, 1838 - 1852
2. **Flores Orozco A.**, Kemna, A., Binley, A., and Cassiani, G. 2019. Analysis of time-lapse data error in complex conductivity imaging to alleviate anthropogenic noise for site characterization. Submitted to *Geophysics* 84(2), B181 – B193
3. Bücken M., **Flores Orozco, A.**, Undorf, S., and Kemna, A. 2019. On the Role of Stern- and Diffuse-layer polarization mechanisms in porous media. *Journal of Geophysical Research: Solid Earth* 124, 1-22
4. Bücken M., Undorf, S., **Flores Orozco, A.**, and Kemna, A. 2019. Electrochemical polarization around metallic particles — Part 2: The role of diffuse surface charge. *Geophysics* 84(2), E57 – E73
5. Mollaret, C., Hilbich, C., Pellet, C., **Flores Orozco, A.**, Delaloye R., and Hauck, C. 2019. Mountain permafrost degradation documented through a network of permanent electrical resistivity tomography sites. *The Cryosphere Discussion*
6. **Flores Orozco, A.**, Bücken, M., Steiner, M., and Malet, J-P. 2018. Complex-conductivity imaging for the understanding of landslide architecture. *Journal of Environmental Geology* 243, 241-252
7. **Flores Orozco, A.**, Gallistl, J., Bücken, M., and Williams, K. H. 2018. Decay curve analysis for data error quantification in time-domain induced polarization imaging. *Geophysics* 83 (2), E75 – E86
8. Bücken M., **Flores Orozco, A.**, and Kemna, A. 2018. Electro-chemical polarization around metallic particles – Part 1: The role of diffuse-layer and volume-diffusion relaxation *Geophysics* 83(4), E203 – E217
9. Funk, B., **Flores Orozco, A.**, Maierhofer, T., and Plan, L. 2018. Anwendung geophysikalischer Methoden zur Detektion zweier Höhlen nahe Lunz am See (NÖ). *Die Höhle* 69(1-4), 109 - 117
10. Gallistl, J., Weigand, M., Stumvoll, M., Ottowitz, D., Glade, T., and **Flores Orozco, A.** 2018. Delineation of subsurface variability in clay-rich landslides through spectral induced polarization imaging and electromagnetic methods. *Journal of Environmental Geology* 245, 292 – 308
11. Ntarlagiannis, D., Ustra, A., Kessouri, P., Flores Orozco, A. 2018. The untapped potential of the Induced Polarization method: characterizing and monitoring hydrocarbon contamination in soils. *Fast TIMES* 23 (4), 63 - 73
12. Bücken, M., **Flores Orozco, A.**, Hördt, A., and Kemna, A. 2017. An analytical membrane-polarization model to predict the complex conductivity signature of immiscible liquid hydrocarbon contaminants. *Near Surface Geophysics* 15, 547 - 562
13. Bücken, M., Lozano García, S., Ortega Guerrero, B., Caballero, M., Pérez, L., Caballero, L.,... **Flores Orozco, A.**, Brown, E., ..., and Garay-Jiménez, F. 2017. Geoelectrical and Electromagnetic methods applied to paleolimnological studies: Two examples from es-

- sicated lakes in the basin of Mexico. *Boletín de la Sociedad Geológica Mexicana* 69 (2), 279 - 298
14. Caterina, D., **Flores Orozco, A.**, and Nguyen, F. 2017. Long-term ERT monitoring of biogeochemical changes of an aged hydrocarbon contamination. *Journal of Contaminant Hydrology* 201, 19 – 29
 15. Lesperre, N., Nguyen, F., Kemna, A., Robert, T., Hermans, T., Daouri, M., and **Flores Orozco, A.** 2017. A new approach for time-lapse data weighting in electrical resistivity tomography. *Geophysics* 82 (6), E325 – E333
 16. Wainwright, H. M., **Flores Orozco, A.**, Bücker, M., Dafflon, B., Chen, J., Hubbard, S.S., and Williams, K.H. 2017, Hierarchical Bayesian method for mapping biogeochemical hot spots using induced polarization imaging. *Water Resources Research* 52 (1), 533 - 551
 17. Weigand, M., **Flores Orozco, A.**, and Kemna, A. 2017. Reconstruction quality of SIP parameters in multi-frequency complex resistivity imaging. *Near Surface geophysics* 15, 187 – 199.
 18. Blöschl, G., Blaschke, A., Broer, M., Bucher, C., Carr, G., Chen, X., Eder, A., Exner-Kittridge, M., Farnleiner, A., **Flores Orozco, A.**, Haas, P., Hogan, P., Oismüller, M., ..., and Zessner, M. 2016. The hydrological Open Air Laboratory (HOAL) in petzenkirchen: a hypothesis-driven observatory. *Hydrol. Earth Syst. Sci.* 20, 227 – 255.
 19. **Flores Orozco, A.**, Velimirovic, M., Tosco, T., Kemna, A., Sapion, H., Klaas, N., Sethi, R., and Leen, B. 2015. Monitoring the injection of microscale zero-valent iron particles for groundwater remediation by means of complex electrical conductivity imaging. *Environmental Science and Technology* 49, 5593 – 5600
 20. Cassiani, G., Binley, A., Kemna, A., Weher, M., **Flores Orozco, A.**, Deiana, R., Boaga, J., Rossi, M., Dietrich, P., Werban, U., Godio, A., and Deida, G.P., 2014, Non-invasive characterization of the Trecate (Italy) crude-oil contaminated site: links between contamination and geophysical signals. *Environmental Science and Pollution Research* 21, 8914-8931.
 21. **Flores Orozco, A.**, Williams, H.K., and Kemna, A., 2013. Time-lapse spectral induced polarization imaging of stimulated uranium bioremediation. *Near Surface Geophysics* 11, 531-544.
 22. **Flores Orozco, A.**, Kemna, A., Oberdörster, C., Zschornack, L., Leven, C., Dietrich, P., Weiss, H., 2012, Delineation of subsurface hydrocarbon contamination at a former hydrogenation plant using spectral induced polarization imaging, *Journal of Contaminated Hydrology* 136-137, 131-144.
 23. **Flores Orozco, A.**, Kemna, A., and Zimmermann, E., 2012, Data error quantification in spectral induced polarization imaging, *Geophysics* 77(3), E227-E237.
 24. Chen, J., Hubbard, S.S., Williams, H.K., **Flores Orozco, A.**, and Kemna, A. 2012. Estimating the spatio-temporal distribution of geochemical parameters associated with biostimulation using spectral induced polarization data and hierarchical bayesian models. *Water Resources Research* 48, W05555.

25. Kemna, A., Binley, A., Cassiani, G., Niederleithinger, E., Revil, A., Slater, L., Williams, H.K., **Flores Orozco, A.**, Haegel, F.-H., Hördt, A., Kruschwitz, S., Leroux, V., Titov, K., and Zimmermann, E., 2012, An overview of the spectral induced polarization method for near-surface applications. *Near Surface Geophysics* 10(6), 453-468
26. **Flores Orozco, A.**, Williams H.K., Long, P.E., Hubbard, S.S., and Kemna, A., 2011, Using complex resistivity imaging to infer biogeochemical processes associated with bioremediation of an uranium-contaminated aquifer, *Journal of Geophysical Research* 116, G03001.
27. Krautblatter, M., Verleysdonk, S., **Flores Orozco, A.**, and Kemna, A., 2010. Temperature-calibrated imaging of seasonal changes in permafrost rock walls by quantitative electrical resistivity tomography (Zugspitze, German/Austrian Alps): *Journal of Geophysical Research* 115, F02003.

UNDER REVISION

Flores Orozco, A., Gallistl, J., Steiner, M., Brandstätter, C., and Fellner J. Imaging biogeochemical active zones in landfills with induced polarization. Submitted to *Waste Management Journal*

Flores Orozco, A., and Gallistl, J., Investigation of cable effects in spectral induced polarization imaging using multicore and coaxial cables. Submitted to *Geophysics*

Nordsiek, S., Peiffer, S., Gilfedder, B., **Flores Orozco, A.**, Frei, S. Monitoring the formation of iron sulfides with the method of spectral induced polarization in a column experiment. Submitted to *ACS Earth and Space Chemistry*

BOOK CHAPTERS

Flores Orozco, A., Bücker, M., Rucker, C., Kemna, A., and Börner, F. Applications of the Induced Polarization imaging for site characterization and the evaluation of remediation techniques methods. In: Grinat, M., Hock, S., and Lehmann, K., eds. *Die Roten Blätter der DGG – The red pages of the German Geophysical Society. Sonderband I/2019. Deutsche Geophysikalische Gessellschaft e.V.*, 2019: 23-37

Tina Martin, Weigand, M. and **Flores Orozco, A.** Induzierte Polarization in der Biogeophysik. In: Grinat, M., Hock, S., and Lehmann, K., eds. *Die Roten Blätter der DGG – The red pages of the German Geophysical Society. Sonderband I/2019. Deutsche Geophysikalische Gessellschaft e.V.*, 2019: 59-71

Kemna, A., Huisman, J. A., Zimmermann, R., Zhao, Y., Treichel, A., **Flores Orozco, A.**, and Fechner, T. Broadband Electrical Impedance Tomography for Subsurface Characterization Using Improved Corrections of Electromagnetic Coupling and Spectral Regularization. In: Weber, M., and Münch, U., eds. *Tomography of the Earth's Crust: From Geophysical Sounding to Real-Time Monitoring. Springer Int. Publishing*, 2014: 1-20.

Cassiani, G., Binley, A., Kemna, A., **Flores Orozco, A.**, JafarGandomi, A., Bastani, M., Maineult, A., Rizzo, E., Titov, K., A geophysical multi-method approach to contaminated site characterization. In Kästner, M., Braeckevelt, M., Döberl, G., Cassiani, G., Petrangeli-Papini, M., Leven-Pfister, C., van Ree, D., eds. Model-driven soil probing, site assessment and evaluation- Guidance on Technologies. Rome: Sapienza Università Editrice, 2012: 94-131

CONFERENCE PAPERS (EXTENDED ABSTRACTS)

Flores Orozco A., Steiner, M., Gallistl, J., and Ivanova, A. 2018. Geophysikalische Bildgebung zur Charakterisierung von Deponien und der internen Abfallzusammensetzung. Nov 2018 Recy & DepoTech 2018: VORTRÄGE-Konferenzband zur 14. Recy & DepoTech Band. Vol. 14, p. 509 - 514

Flores Orozco, A., Maiherhofer, T., Aigner, L., and Hilbich, C. 2018. Measurements of the Induced Polarization effect in alpine permafrost using transient electromagnetic and complex resistivity methods, In: Philip Deline, Xavier Bodin, Ludovic Ravel. 5th European Conference on Permafrost, Book of Abstract. Edited by Philip Deline, Xavier Bodin and Ludovic Ravel. France. Edytem, 2018.

Steiner, M., Maierhofer, T., Chwatal, W., Heinrich, G., Pfeiler, G., and **Flores Orozco, A.**, 2018. 3D refraction seismic tomography investigations in alpine permafrost at Hoher Sonnblick (Austria), In: Philip Deline, Xavier Bodin, Ludovic Ravel. 5th European Conference on Permafrost, Book of Abstract. Edited by Philip Deline, Xavier Bodin and Ludovic Ravel. France. Edytem, 2018

Flores Orozco, A. and Bucker, M. 2017. Electrical monitoring of nano- and micro-scale particle injections for in-situ groundwater remediation: GELMON 2017: 4th International Workshop on Geoelectrical Monitoring: Book of Abstracts: November 22nd - November 24th, 2017, Vienna, Austria. "Berichte der Geologischen Bundesanstalt", 124, p13, Vienna

Kemna, A., Weigand, M., **Flores Orozco, A.**, Wagner, F., Hilbich, C., and Hauck, C. 2017. Use of geoelectrical monitoring methods for characterizing thermal state, ice content and water flow in permafrost environments - In Hoyer, S. (Ed.) (2017): GELMON 2017: 4th International Workshop on Geoelectrical Monitoring: Book of Abstracts: November 22nd - November 24th, 2017, Vienna, Austria. "Berichte der Geologischen Bundesanstalt", 124, p19, Vienna

Flores Orozco, A., Gallistl, J., Bucker, M., Williams, K.H. 2016. Decay-curve analysis for the quantification of data error in time-domain induced polarization imaging: 4th Int. Workshop on Induced Polarization, Aarhus (Denmark), June 6-8, 4p.

Gallistl, J., **Flores Orozco, A.**, Bucker, M. 2016. Characterization of abandoned mine-tailings by means of time- and frequency-domain induced polarization imaging: 4th Int. Workshop on Induced Polarization, Aarhus (Denmark), June 6-8, 4p

Bücker M., Flores Orozco, A., Pita, C., and Kemna, A. 2014. The effect of anthropogenic noise on induced polarization measurements for environmental applications: a case study: 2nd Latin American Geosciences Student Conference (LAGSC) from the EAGE, Mexico City (Mexico), 4-7 August 2014, 4p

Flores Orozco, A., Williams, K.H., and Kemna, A., 2010. Monitoring redox processes with spectral induced polarization in a stimulated bioremediation experiment: 1st Int. Conf. Frontiers in Shallow Subsurface Technology, Delft (Holland), January 20-22, 4p

INVITED TALKS

Electrical monitoring of nano- and micro-scale particle injections for in-situ groundwater remediation:

Keynote lecture in GELMON 2017: 4th International Workshop on Geoelectrical Monitoring, 22-24 September 2017, Vienna, Austria

Electrical imaging of subsurface nano- and micro-scale particle injections for in situ groundwater remediation:

BayCEER Kolloquium, Lectures in Ecology and Environmental Research WS 2017/18 at the University of Bayreuth, 26 October 2017, Bayreuth, Germany

Complex conductivity imaging for the characterization of contaminant plumes in industrial areas prior to injection of nano- and micro-scale-particles:

Keynote lecture in the 23rd European Meeting of Environmental and Engineering Geophysics from the EAGE, Workshop 2: Geophysics for mapping and monitoring of contaminated ground and buried waste, 2 September 2017, Malmö, Sweden

Acquisition and processing of SIP field data:

Invited lecture in the Short Course in frame of 4th International Workshop on Induced Polarization, 5 June, 2016, Aarhus, Denmark

Electrical resistivity and Induced Polarization applied in the assessment of contaminated sites and the monitoring of remediation processes

Lecturer in the Second Latin American EAGE meeting, Geosciences Student Conference, Short Workshop, 2-3 August 2014, Mexico City, Mexico.

Using complex resistivity imaging to infer biogeochemical processes associated with bioremediation of a uranium-contaminated aquifer

Lecture in the Colloquiums of Geosciences and Geography: University of Fribourg
15 October 2013, Fribourg, Switzerland

TEACHING EXPERIENCE

Exploration with non-seismic methods (now: Exploration with electrical and electromagnetic methods) – Theoretical lecture including exercises

MA Geodesy and Geomatics Engineering at the TU-Vienna, Summer term 2014 to 2017

MA Geodesy and Geomatics Engineering at the TU-Vienna, Winter term 2018 to 2019

Geophysical data processing – Exercise lecture

MA Geodesy and Geomatics Engineering at the TU-Vienna, Winter term 2018 to 2019

Geophysical Field Lecture

BA Geodesy and Geomatics Engineering at the TU-Vienna, Summer term 2014 to 2018

Applied Geophysics – Theoretical lecture

BA Geodesy and Geomatics Engineering at the TU-Vienna, Winter term 2013 to 2019

Applied Geophysics – Exercise lecture

BA Geodesy and Geomatics Engineering at the TU-Vienna, Winter term 2013 to 2019

Fundamentals of Geophysics – Theoretical lecture

BA Geodesy and Geomatics Engineering at the TU-Vienna, Winter term 2017 to 2019

Fundamentals of Geophysics – Exercise lecture

BA Geodesy and Geomatics Engineering at the TU-Vienna, Winter term 2017 to 2019

Seminar of Geosciences (Geophysics)

MA Geodesy and Geomatics Engineering at the TU-Vienna, Summer term 2014 to 2019

Multidisciplinary Project

BA Geodesy and Geomatics Engineering at the TU-Vienna, Summer term 2014 to 2018

Applied Hydrogeophysics – Field lecture

MA Geosciences at the University of Bonn, Germany, Summer term 2009 to 2012

Applied Geophysics – Exercise lecture

BA Geosciences at the University of Bonn, Germany, Winter term 2009 to 2010

INVITED LECTURER

Landslide Dynamics – Project module

MA in Geography at the University of Vienna (Austria), Winter term 2018 and Summer term 2019

Applied Geophysics – Theoretical lecture including exercises (1 week Block)

MA in Earth Sciences at the University of Vienna (Austria), 9 – 13 February, 2015

Electrical Resistivity and Induced Polarization imaging for the characterization of contaminated sites and monitoring of remediation processes – Theoretical lecture including exercises (1 week Block)

Colegio de Geofísicos (The National College of Geophysics), Mexico City (Mexico), 23 – 27 February, 2015

Geophysical electrical imaging methods for site characterization – Theoretical lecture including exercises (1 week Block)

Postgraduate Program, Institute of Geophysics, National Autonomous University of Mexico (UNAM), Mexico City (Mexico), 20 – 24 January, 2014

SUPERVISION OF STUDENTS

Ongoing Ph.D. students

- Jakob Gallistl (TU-Wien): Development of the Spectral induced Polarization imaging method for the hydrogeological modeling of clay rich landslides
- Matthias Steiner (TU-Wien): Coupled passive and active seismic and electromagnetic methods to characterize hydrogeological processes in fractured media
- Theresa Maierhofer (joint PhD TU-Wien and U. Fribourg): Improved ice quantification at alpine permafrost sites based on electrical and electromagnetic measurements of spectral induced polarization
- Timea Katona (TU-Wien): Understanding the electrochemical response in microbiological hot spots and mine-tailings

Ongoing M.Sc. Students (TU-Wien)

- Armin Kren: Joint investigation of landslides through borehole data, seismic and electrical methods
- Doris Schlögelhofer: The application of the transient electromagnetic method for near-surface investigations
- David Wundsam: The use of geophysical imaging to delineate tunnels built by worms and other animals in soils
- Lukas Aigner: Engineering applications of the Transient Electromagnetic Method
- Martin Mayr: Permafrost investigations through coupled electrical and seismic methods

Concluded M.Sc. Students (TU-Wien)

- Barbara Funk: "Electrical imaging for cave detection: numerical and field studies", concluded in March 2019
- Theresa Maierhofer: "Electrical modelling for an improved understanding of GPR signatures in alpine permafrost", concluded in March 2018
- Jakob Gallistl: "Data-error quantification in time-domain induced polarization imaging based on the analysis of the decay curve", concluded in April 2017
- Benjamin Lehner: "Characterization of hydrogeological parameters at the floodplain scale by the means of electrical imaging", concluded in April 2015

Concluded B.Sc. Students (TU-Wien)

- Raphael Vasak: Auswertung von ERT-Daten im Hangrutschungsgebiet mit Abschätzung der Messfehler
- Nathalie Roser: Electrical properties in Vineyards
- Raphael Palisek: Data analysis in DC-resistivity measurements collected in a landslide and the Diendorfer fault

- Antonia Golab: Delineation of soil structures and the plough horizon through electrical imaging: laboratory investigations, concluded in January 2018
- Martin Mayr and Herbert Wicker: Detection of cavities and metallic ores through geophysical methods in the Alpine region, concluded in November 2017
- Armin Kren and Yannic Öhlknecht: Characterization of subsurface properties in the vicinity of a landfill in Tumeltsham, Low Austria, concluded in November 2017
- Anastasia Ivanova: Geoelectrical characterization of a landfill ongoing aeration, concluded in September 2017
- Julia Geiger: "Hydrogeological Characterization at the HOAL Site by Means of Induced Polarization Imaging, Low Induction-Number Electromagnetic Induction and Ground Penetrating Radar.", concluded in October 2016
- Manuel Schmitzer: Geophysical characterization of the Donau island, concluded in October 2016
- Thummerer Jakob: Hydrogeophysical characterization of the Donau Island, concluded in October 2016
- Lisa Riedel: Extensive geophysical characterization at the Hydrological Open Air Laboratory, concluded in September 2016
- David Wundsam: "Comparison of data quality between time- and frequency-domain Induced Polarization measurements", concluded in September 2016
- Astrid Denk: Evaluation of electrical conductivity measurements through low induction electromagnetic methods at the HOAL site, concluded March 2016
- Gabriel Stollhof: "Characterization of data quality in shallow induced polarization (IP) measurements", concluded in November 2015
- Sebastian Flöry: "Digitalization of electrical models and optimization of electrode configuration in electrical imaging", concluded in November 2014

CONFERENCE ABSTRACTS

2019

1. **Flores Orozco, A.**, Gallistl, J., Aigner, L., Bücken, M., and Kostial, D. 2019. Induced Polarization imaging for the investigation of clay-rich landslides. 7. Jahrestagung der DGG, Braunschweig 4 - 8. March, 2019
2. Aigner, L., Gallistl, J., Bücken, M., Steine, M., Chwatal, W., Kostial, D., and **Flores-Orozco, A.** 2019. Characterization of a clayey landslide by integral application of multiple geophysical and geotechnical methods. 7. Jahrestagung der DGG, Braunschweig 4 - 8. March, 2019
3. Bücken, M., **Flores Orozco, A.**, Gallistl, J., Buckel, J., Pita de la Paz, C., and Pérez, L. 2019. Zu Wasser und zu Lande: Elektrische und elektromagnetische Erkundung von Sedimentablagerungen im Seengebiet Nahá und Metzabok in Chiapas (Mexiko). 7. Jahrestagung der DGG, Braunschweig 4 - 8. March, 2019

4. Katona, T., Aigner, L., Bücken, M., Römer, A., Nordsiek, S., and **Flores Orozco, A.** 2019. Spectral induced polarization imaging of a graphite deposit. 7. Jahrestagung der DGG, Braunschweig 4 - 8. March, 2019
5. Maierhofer, T., Hilbich, C., Hauck, C., and **Flores-Orozco, A.** 2019. Towards operational application of Spectral Induced Polarization for alpine permafrost environments – improvement of data quality. 7. Jahrestagung der DGG, Braunschweig 4 - 8. March, 2019
6. Martin, T., **Flores Orozco, A.**, Günther, T., and Dahlin, T. 2019. Evaluation of spectral induced polarization field measurements in time- and frequency-domain. 7. Jahrestagung der DGG, Braunschweig 4 - 8. March, 2019
7. Steiner, M., Wagner, F., Schöner, W., Maierhofer, T., and **Flores Orozco, A.** 2019. Assessment of data fusion strategies with regard to an enhanced characterization of alpine permafrost. 7. Jahrestagung der DGG, Braunschweig 4 - 8. March, 2019
8. Maierhofer, T., Aigner, L., Hilbich, C., Hauck, C., and **Flores Orozco, A.**, 2019. Spectral Induced Polarization for permafrost environments in the Swiss and Austrian Alps – Improvement of data quality and first applications and results. Geophysical Research Abstracts Vol. 21, EGU2019-16749, 2019. EGU General Assembly 2019
9. Radvanyi, P., Hoehn, P., **Flores Orozco, A.**, and Hofmann, T. Impact of streambed hydraulic conductivity estimates from induced polarization on the predictive uncertainty of a groundwater flow model, Geophysical Research Abstracts Vol. 21, EGU2019-9452, 2019.
10. Katona T., Gallistl, J., Nordsiek, S., Bücken, M., Frei, S., Durejka, S., Gilfedder, B., and **Flores Orozco, A.** 2019. Characterization of biogeochemical hot spots using induced polarization, Geophysical Research Abstracts Vol. 21, EGU2019-9433, 2019, EGU General Assembly 2019
11. Bücken, M., **Flores Orozco, A.**, Undorf, S., and Kemna, A., Pore-Scale Induced-Polarization Modelling: A Synopsis of Basic Mechanisms, Geophysical Research Abstracts Vol. 21, EGU2019-3937, 2019, EGU General Assembly 2019

2018

12. **Flores Orozco A.**, Steiner, M., Gallistl, J., and Ivanova, A. 2018. Geophysikalische Bildgebung zur Charakterisierung von Deponien und der internen Abfallzusammensetzung. Nov 2018 Recy & DepoTech 2018: VORTRÄGE-Konferenzband zur 14. Recy & DepoTech Band. Vol. 14, p. 509 - 514
13. **Flores Orozco, A.**, Maierhofer, T., Aigner, L., and Hilbich, C. 2018. Measurements of the Induced Polarization effect in alpine permafrost using transient electromagnetic and complex resistivity methods, In: Philip Deline, Xavier Bodin, Ludovic Ravel. 5th European Conference on Permafrost, Book of Abstract. Edited by Philip Deline, Xavier Bodin and Ludovic Ravel. France. Edytem, 2018.
14. Steiner, M., Maierhofer, T., Chwatal, W., Heinrich, G., Pfeiler, G., and **Flores Orozco, A.** 2018. 3D refraction seismic tomography investigations in alpine permafrost at Hoher Sonnblick (Austria), In: Philip Deline, Xavier Bodin, Ludovic Ravel. 5th Euro-

- pean Conference on Permafrost, Book of Abstract. Edited by Philip Deline, Xavier Bodin and Ludovic Ravel. France. Edytem, 2018
15. Chwatal, W, Kostial, D., **Flores Orozco, A.**, Preuth, T. 2018. Begleitende geophysikalische Messungen zu verschiedenen geologischen Fragestellungen im Tunnel Feuerbach, Stuttgart 21: 78. Jahrestagung der DGG, Leoben 12. - 15. February, 2018
 16. Freudenthaler, A., Chwatal, W., **Flores Orozco, A.**, and Schmid, C. 2018. Altreifendeponie Ohlsdorf - Fallbeispiel einer ungewöhnlichen Deponieerkundung: 78. Jahrestagung der DGG, Leoben 12. - 15. February, 2018
 17. Freudenthaler, A., Chwatal, W., and **Flores Orozco, A.** 2018. Umfahrung Bergheim - Geophysikalische Verfahren einer Tunneltrasse: 78. Jahrestagung der DGG, Leoben 12. - 15. February, 2018
 18. Funk, B., **Flores Orozco, A.**, and Plan L. 2018. Detection of caves by geophysical methods to prevent natural hazards – Two case studies from Lower Austria: EGU General Assembly 2018, Geophysical Research Abstracts, Vol. 20, EGU2018-17194, 2018
 19. Gallistl, J., Steiner, M., Maierhofer, T., Aigner, L., Birgit, B., Malet, J-P., and **Flores Orozco, A.** 2018. On the use of multi-method geophysical investigations for the delineation of hydrogeological connectivity in landslides: EGU General Assembly 2018, Geophysical Research Abstracts, Vol. 20, EGU2018-17422-1, 2018
 20. Gómez-Nicolás, M., Ojeda, E., Salles, P., and **Flores Orozco, A.** 2018. Structural characterization of a coastal aquifer using time-lapse electrical resistivity tomography: EGU General Assembly 2018, Geophysical Research Abstracts, Vol. 20, EGU2018-11853, 2018
 21. Hintersberger, E. Decker, K., Ranftl, E., Aigner, L., **Flores Orozco, A.** 2018. Insights of Quaternary movement at the southern Diendorf Fault (Austria): EGU General Assembly 2018, Geophysical Research Abstracts, Vol. 20, EGU2018-17866, 2018
 22. Karl, C., Stumvoll, M., Gallistl, J., **Flores Orozco, A.**, and Glade, T. 2018. Delineation of internal landslide structures using complex conductivity imaging and geotechnical investigations – case study Hofermühle, Lower Austria: EGU General Assembly 2018, Geophysical Research Abstracts, Vol. 20, EGU2018-13516, 2018
 23. Steiner M., Maierhofer, T., and **Flores Orozco, A.** 2018. Constraining Refraction Seismic Tomography (RST) by means of Ground-Penetrating Radar (GPR) models for an improved spatial characterization of alpine permafrost: EGU General Assembly 2018, Geophysical Research Abstracts, Vol. 20, EGU2018-17277, 2018
 24. Steiner, M., Straka, W., and **Flores Orozco, A.** 2018. Event detection in ambient seismic noise by means of robust outlier detection: EGU General Assembly 2018, Geophysical Research Abstracts, Vol. 20, EGU2018-17365-1, 2018
 25. Schlögel I, **Flores Orozco, A.**, Trebsche, P., and Gallistl, J. 2018. Geophysikalische Erkundung des spätbronzezeitlichen Bergbaus Priggwitz-Gasteil in Niederösterreich: 78. Jahrestagung der DGG, Leoben 12. - 15. February, 2018

2017

26. Bückner M., Undorf, S., **Flores Orozco, A.**, and Kemna, A. 2017. Numerical modelling of electrochemical polarization around charged metallic particles: EGU General Assembly 2017, Vol. 19, EGU2017-7589-1, 2017
27. **Flores Orozco, A.**, Gallistl, J., Schmid, D., Micic Batka, V., Bückner M., and Hofmann, T. 2017. Electrical imaging of subsurface nanoparticle propagation for in-situ groundwater remediation: EGU General Assembly 2017, Vol. 19, EGU2017-7854, 2017
28. Gallistl, J., **Flores Orozco, A.**, Ottowitz, D., Gautier, S., and Malet, J-P. Induced polarization (IP) imaging for the improved characterization of clay-rich landslides: EGU General Assembly 2017, Vol. 19, EGU2017-6441, 2017
29. Hoehn, P., **Flores Orozco, A.**, and Hofmann, T. 2017. Waterborne spectral induced polarization imaging to investigate stream-aquifer exchange: EGU General Assembly 2017, Vol. 19, EGU2017-8617, 2017
30. Malet, J-P., Supper, R., **Flores Orozco, A.**, Gautier, S., and Boagard, T. High-frequency HYDRO-geophysical observations for an advanced understanding of clayey landSLIDES: the HYDROSLIDE research project: EGU General Assembly 2017, Vol. 19, EGU2017-15434, 2017
31. Steiner, M., Maierhofer, T., Pfeiler, S., Chwatal, W., Behm, M., Reisenhofer, S., Schöner, S., Straka, W., and **Flores Orozco, A.** 2017. Active and passive seismic investigations in Alpine Permafrost at Hoher Sonnblick (Austria). EGU General Assembly 2017, Vol. 19, EGU2017-8578, 2017
32. Wilde, M., Rodríguez Elizarrarás, S., Morales Barrera, W. V., Schindt, D., Bückner, M., **Flores Orozco, A.**, García García, E., Pita de la Paz, C., and Tehorst, B. 2017. Multidisciplinary approach for the characterization of landslides in volcanic areas – a case study from the Palma Sola-Chiconquiaco Mountain Range, Mexico: EGU General Assembly 2017, Vol. 19, EGU2017-16475-1, 2017

2016

33. **Flores Orozco, A.**, Kemna, A., Cassiani, G., and Binley, A. 2016. Improved site contamination through time-lapse complex resistivity imaging: EGU General Assembly 2016, Vol. 18, EGU2016-18287, 2016
34. **Flores Orozco, A.**, Gallistl, J., Schlögel, I., Chwatal, W., Oismüller, M., and Blöschl, G. 2016. Geophysical characterization of Hydrogeological processes at the catchment scale: EGU General Assembly 2016, Vol. 18, EGU2016-16834, 2016
35. Bückner, M., Undorf, S., Kemna, A., and **Flores Orozco, A.** 2016. Analytical and numerical modelling of electrochemical polarization around charged metallic particles immersed in electrolyte solution. Annual meeting of the Mexican Geophysical Union (UGM), Puerto Vallarta, Mexico

2015

36. **Flores Orozco, A.**, Kreutzer, I., Bücken, M., Nguyen, F., Hofmann, T., and Döberl, G. 2015. Integration of Induced Polarization Imaging, Ground Penetrating Radar and geochemical analysis to characterize hydrocarbon spills, EGU General Assembly 2015, Vol. 17, EGU2015-12763, 2015
37. Bücken, M., **Flores Orozco, A.**, Pita, C., and Kemna, A., 2015. Case Study on the Effect of Anthropogenic Noise on Induced Polarization Images of an Oil-Spill Site in an Urban Environment: 75. Jahrestagung der DGG, Hannover 23. - 26. März.
38. Bücken, M., Kemna, A., **Flores Orozco, A.**, 2015. Der Effekt von Kohlenwasserstoffverunreinigungen auf Messungen der Induzierten Polarisation: Modellierungsansätze auf der Porenskala: 75. Jahrestagung der DGG, Hannover 23. - 26. März.
39. Gallistl, J., **Flores Orozco, A.**, Bücken, M., and Williams, K.H. 2015. Characterization of data error in time-domain induced polarization tomography based on the analysis of decay curves, EGU General Assembly 2015, Vol. 17, EGU2015-3806, 2015
40. Wainwright, H., **Flores-Orozco, A.**, Bücken, M., Dafflon, B., Chen, J., Hubbard, S., Williams, K., 2015. Noninvasive Characterization of Biogeochemical Hotspots Using Induced Polarization Imaging. Goldschmidt Conference, Czech Republic..

2014

41. **Flores Orozco, A.**, Bücken, M., Williams, K., 2014. Characterization of Natural Attenuation in a uranium-contaminated site by means of Induced Polarization Imaging, Oral presentation, EGU General Assembly 2014, Vienna, Austria.
42. **Flores Orozco, A.**, Bücken, M., Williams, K., 2014. Induced polarization imaging at the floodplain scale for the delineation of naturally reduced zones, Oral presentation, 3rd International Workshop on Induced Polarization, Ile d'Oléron, France.
43. Haruko M. W., **Flores Orozco, A.**, Bücken, M., Dafflon, B., Williams, H.K., and Hubbard, S.S., 2014. Reactive Transport Modeling parameterization using geophysical Datasets. Complex SoilSystem Conference. Berkeley, California, USA.
44. Williams, K.H., Bücken, M., **Flores Orozco, A.**, Hobson, C., and Robbins, M., 2014. Novel approaches for delineating and studying "hotspots" and "hot moments" in fluvial environments): Eos Trans. AGU, 95, Fall Meet. Suppl., Abstract B33B-0163.
45. Williams, K.H., **Flores Orozco, A.**, Bücken, M., Hobson, C., Wainwright, H., Dafflon, B., Conrad, M., Tokunaga, T., Bargar, J., and Hubbard, S., 2014. Floodplains as Biogeochemical Reactors: Using Multi-scale Approaches to Quantify Hot Spots and Hot Moments at DOE's Rifle, Colorado Field Site. Posterbeitrag auf dem TES/SBR Joint Investigators Meeting in Potomac, Maryland, USA.

2013

46. **Flores Orozco, A.**, Williams, K., Kemna, A., 2013. 5D SIP monitoring of stimulated uranium bioremediation. 2nd International Workshop on Geoelectrical Monitoring. Vienna, Austria
47. **Flores Orozco, A.**, Hilbich, C., Kemna, A., Hauck, C., 2013. Data error quantification for improved time-lapse ERT monitoring of Alpine permafrost. 2nd International Workshop on Geoelectrical Monitoring. Vienna, Austria
48. Villanueva Estrada, R.E., Rocha Miller, R., Arango Galván, C., López Álvarez, A., Bücken, M., Castro González, A., Arvizu Fernández, J.L., **Flores Orozco, A.**, 2013. Estudio del Sitio de Disposición Final Prados de la Montaña para Evaluar el Potencial para el Posible Aprovechamiento de la Energía Residual. Resumen en extenso, 3er Congreso Nacional de Investigación en Cambio Climático, Mexico City, Mexico.
49. Bücken, M., Arango Galván, C., **Flores Orozco, A.**, Villanueva Estrada, R.E., Rocha Miller, R., Pita de la Paz, C., Kemna, A., 2013. Landfill Delineation Using Time and Frequency-Domain Induced Polarization: A Case Study. Oral presentation, Reunión Anual 2013 of the Unión Geofísica Mexicana, Puerto Vallarta, Jalisco, Mexico.

SKILLS**Languages:**

- Spanish (mother tongue), English (fluent speaking, writing and understanding), German (fluent speaking and understanding), Italian (fluent understanding)

Programming:

- Matlab, Octave, Python, C++, Fortran